UNIVERSITY OF CALIFORNIA, SAN DIEGO

Studies of Isocyano Analogues to Manganese Carbonyls and the Development of Low-Valent Coordination Polymers using Multitopic *m*-Terphenyl Isocyanides

A dissertation submitted in partial satisfaction of the
requirements for the degree of Doctor of Philosophy

in

Chemistry

by

Douglas Walter Agnew

Committee in charge:

Joshua S. Figueroa, Chair
Katherine A. Barbeau
Seth M. Cohen
Jospeh M. O'Connor
William C. Trogler
Haim Weizman

2017

The dissertation of Douglas Walter Agnew is approved, and it is acceptable in quality and form for publication on microfilm and electronically:

_____

_____

_____

_____

_____

_____

Chair

University of California, San Diego

2017

DEDICATION

For my parents, Kathy and Duncan

EPIGRAPH

"The truth will set you free.
But not until it is finished with you."
-David Foster Wallace, *Infinite Jest*

TABLE OF CONTENTS

SIGNATURE PAGE iii

DEDICATION iv

EPIGRAPH v

TABLE OF CONTENTS iv

LIST OF ABBREVIATIONS x

LIST OF FIGURES xv

LIST OF SCHEMES xxv

LIST OF TABLES xxvii

ACKNOWLEDGEMENTS xxix

VITA xxxiv

ABSTRACT OF THE DISSERTATION xxxv

Chapter 1 Coordination Chemistry of Low-Valent Transition Metal Ions 1

1.1 Low Coordinate Metal Carbonyls – An Unexamined Nodal Archetype 1

1.2 *m*-Terphenyl Isocyano Analogues to Transition Metal Carbonyls 3

1.3 Utilizing Low-Valent Coordination Complexes as Directing Nodes in Polymeric Materials 6

1.4 Outlook 11

1.5 References 12

Chapter 2 Insights into the Chemistry of Zero-Valent Manganese: Isolation of a Pentacoordinate Manganese(0) Monoradical 17

2.1 Introduction 17

2.2 Preparation and Characterization of $Mn(CO)_3(CNAr^{Dipp2})_2$ 19

2.3 Reactivity of $Mn(CO)_3(CNAr^{Dipp2})_2$ 23

2.4 Nucleophilic and Radical Initiated Routes to Manganese-Main Group Complexes 39

2.5 Synthetic Procedures and Characterization Data 52

2.6 EPR Procedures and Measurements 70

2.7 Results from Computational Studies 72

2.8 Crystallographic Structure Determinations 89

2.9 Acknowledgements 97

2.10 References 98

Chapter 3 Electrochemical Properties and CO_2-Reduction Ability of *m*-Terphenyl Isocyanide-Supported Manganese Tricarbonyl Complexes 105

3.1 Introduction 105

3.2 Electrochemical Properties of $XMn(CO)_3(CNAr^{Dipp2})_2$ Complexes 108

3.3 Electrochemical and Stochiometric Reactivity of $XMn(CO)_3(CNAr^{Dipp2})_2$ Complexes with CO_2 117

3.4 Concluding Remarks 124

3.5 Synthetic Procedures and Characterization Data 125

3.6 Representative Solution IR Spectra 131

3.7 Experimental Design of Electrochemical Experiments 133

3.8 Crystallographic Structure Determinations 135

3.9 Acknowledgements 137

3.10 References 137

Chapter 4 Controlled *cis*-Labilization of CO from Manganese(I) Mixed Carbonyl/Isocyanides: An Entry Point to Coordinatively Unsaturated Metallo-Lewis Acids 142

4.1 Introduction 142

4.2 Synthesis of Manganese(I) κ^2-Carboxylates via Dissociative Loss of CO 145

4.3 Carboxylate Removal to Generate Open Coordination Sites 152

4.4 Concluding Remarks 167

4.5 Synthetic Procedures and Characterization Data 168

4.6 Selected ^{1}H NMR Spectra 186

4.7 Crystallographic Structure Determinations 191

4.8 Acknowledgements 197

4.9 References 198

Chapter 5 Robust, Transformable and Crystalline Single-Node Organometallic Networks Constructed from Ditopic *m*-Terphenyl Isocyanides 203

5.1 Introduction 203

5.2 Preparations and Properties of Cu(I)-Isocyanides Coordination Polymers 204

5.3 Nanoscale Morphological Characteristics of Cu-^{ISO}CN-3 214

5.4 Concluding Remarks 220

5.5 Synthetic Procedures and Characterization Data 221

5.6 Crystallographic Structure Determinations 238

5.7 Contact Angle Measurements, TGA/DSC and Gas Sorption Analyses 244

5.8 Computational Studies 248

5.9 Acknowledgements 261

5.10 References 262

Chapter 6 Further Development of Multi-Topic *m*-Terphenyl Isocyanide Ligands for Supramolecular Chemistry 266

6.1 Introduction 266

6.2 Multinuclear Complexes Bridged by [CNAr^{Mes2}]$_2$ 267

6.3 Development of Additional Ditopic and Tritopic *m*-Terphenyl Isocyanide Ligands 282

6.4 Concluding Remarks 286

6.5 Synthetic Procedures and Characterization Data 286

6.6 Crystallographic Structure Determinations 297

6.7 Acknowledgements 299

6.8 References 300

Chapter 7 Development of Multidimensional Coordination Polymers of Ni(0) 303

7.1 Introduction 303

7.3 A Redox-Active Coordination Polymer Derived from Tricoordinate Ni(0) Nodes 303

7.3 Preparation of a 3-Dimensional Porous Framework with Zerovalent Ni Nodes 314

7.4 Synthetic Procedures and Experimental Details 320

7.5 Characterization Data 327

7.6 Crystallographic Structure Determinations 335

7.7 Acknowledgements 344

7.8 References 345

LIST OF ABBREVIATIONS

Å = Angstrom (10^{-10} m)

a = unit cell axis a

Anal. = combustion analysis (elemental)

Ar = aryl

ATR = attenuated total reflectance

α = unit cell angle α, orientation of magnetic nuclei aligned with an extern magnetic field

b = unit cell axis b

β = unit cell angle β, position two atoms removed, orientation of magnetic nuclei aligned against an external magnetic field

br = broad

C_{ipso} = arene ring carbon attached to substituent

C_{iso} = terminal isocyanide carbon

CNR = isocyanide

CO = carbon monoxide, carbonyl

COD = 1,5–cyclooctadiene (C_8H_{12})

Cp = cyclopentadienyl (C_5H_5)

Cy = cyclohexyl (*cyclo*–C_6H_{11})

c = unit cell axis c

calcd. = calculated

cm^{-1} = wavenumber

°C = degrees Celsium

d = doublet, days, deuterated

DSC = Differential Scanning Coulemetry

DFT = Density Functional Theory

Dipp = 2,6,–diisopropylphenyl (2,6–$^{i}Pr_2C_6H_3$)

δ = chemical shift

η^n = hapticity of a ligand with n contiguous atoms bound to a metal center

E = energy, main–group atom

EI = electron impact

equiv = equivalents

EPR = Electron Paramagnetic Resonance

Et_2O = diethyl ether

eV = electron volts

FTIR = Fourier Transform Infrared Spectroscopy

GC–MS = Gas Chromatography – Mass Spectrometry

GoF = Goodness of Fit

g = grams

γ = unit cell angle γ

HOMO = Highest Occupied Molecular Orbital

HRMS = High Resolution Mass Spectrometry

Hz = Hertz (s^{-1})

h = hours

IR = Infared

^{i}Pr = isopropyl ($CH(CH_3)_2$)

J = NMR coupling constant, magnetic coupling constant

κ^n = hapticity of a ligand win n non–contiguous atoms bound to a metal center

K = degrees Kelvin

kcal = kilocalories

L = ligand (neutral), liters

LDA = lithium diisopropylamide

LUMO = Lowest Unoccupied Molecular Orbital

M = transition–metal, mega– (10^6), molar (mol/L)

Me = methyl (CH_3)

$(Me_3Si)_2O$ = bis–trimethylsilyl ether

MeCN = acetonitrile

Mes = mesityl, 2,4,6–trimethylphenyl (2,4,6–$Me_3C_6H_2$)

MO = Molecular Orbital

m = *meta* position

m = multiplet, mili– (10^{-3})

min = minutes

mol = moles

μ = bridging ligands, absorption coefficient (X–Ray crystallography), magnetic moment

NMR = Nuclear Magnetic Resonance

ν = infrared stretching frequency

OTf = triflate, trifluoromethylsulfonate ($[OSO_2CF_3]$)

o = *ortho* position

Ph = phenyl (C_6H_5)

p = *para* position

ppm = parts per million

π = pi

q = quartet

R = organic group, alkyl group

R = residual value (X–ray crystallography)

RT = room temperature

S = single electronic state

S = electronic spin

SOF = Site Occupancy Factor

SOMO = Singly Occupied Molecular Orbital

SQUID = Superconducting Quantum Interference Device

s = singlet, seconds

σ = sigma

T = temperature, triplet electronic state

TGA = ThermoGravimetric Analysis

THF = tetrahydrofuran

t = triplet

Tol = toluene, tolyl (C_7H_8)

^{t}Bu = tertiary–butyl ($C(CH_3)_3$)

Tripp = triisopropylphenyl (2,4,6–^{i}Pr$_3$C$_6$H$_2$)

V = unit cell volume

VT = variable temperature

X = halide or pseudo halide

Xyl = xylyl

Z = number of molecules in unit cell

LIST OF FIGURES

Figure 1.1. Calculated geometries for several coordinatively and/or electronically unsaturated transition metal carbonyls..... 2

Figure 1.2. Molecular orbital scheme depicting the isolobal relationship between isocyanides and carbonyls..... 4

Figure 1.3. Three examples of isolated isocyano analogues to metal carbonyls; from right to left $Na_2[Fe(CNAr^{Mes2})_4]$, $Co(CNAr^{Mes2})_4$, and $Ni(CNAr^{Mes2})_3$.. 5

Figure 1.4. Examples of *m*-terphenyl isocyanides employed by the Figueroa group 6

Figure 2.1. EPR spectrum of $Mn(CO)_3(CNAr^{Dipp2})_2$ (**1**) at 295 K in Et_2O (0.05 mM), with simulated spectrum in black 21

Figure 2.2. Molecular structure of $Mn(CO)_3(CNAr^{Dipp2})_2$ (**1**), with selected isopropyl groups rings and H atoms omitted for clarity 22

Figure 2.3. Spin density plot of $Mn(CO)_3(CNXyl)_2$ showing predominant spin build-up on the Mn metal center 22

Figure 2.4. Molecular structure of $(Bu_3Sn)Mn(CO)_3(CNAr^{Dipp2})_2$ (**3**)..... 24

Figure 2.5. Molecular structure of $(Cl_2HC)Mn(CO)_3(CNAr^{Dipp2})_2$ (**4**), with the proton on the $CHCl_2$ unit located in the electron density map 24

Figure 2.6. Molecular structure of $ClMn(CO)_3(CNAr^{Dipp2})_2$ (**5**)..... 25

Figure 2.7. Molecular structure of $(m_2\text{-}k^1\text{:}k^1\text{-}OC_6Me_4O)[Mn(CO)_3(CNAr^{Dipp2})_2]_2$ (**6**) 26

Figure 2.8. Molecular structure of *cis,mer:trans,mer*-$[Mn(CO)_3(CNAr^{Dipp2})_2]_2(\mu\text{-}\eta^1\text{:}\eta^1\text{-}P_4)$ (**7**) 27

Figure 2.9. Molecular structure of CS_2-manganese dimer..... 28

Figure 2.10. Molecular structure of $Mn(NO)(CO)_2(CNAr^{Dipp2})_2$ 30

Figure 2.11. Molecular structure of $(\eta^2\text{-}N,O\text{-}PhNO)Mn(CO)_2(CNAr^{Dipp2})_2$ (**8**), with select *iso*-propyl groups omitted for clarity 32

Figure 2.12. EPR spectrum of $(h^2\text{-}N,O\text{-}PhNO)Mn(CO)_2(CNAr^{Dipp2})_2$ (**8**) at 295 K in toluene (0.05 mM) 33

Figure 2.13. Spin density plot of $(\eta^2\text{-}N,O\text{-}PhNO)Mn(CO)_2(CNXyl)_2$ showing spin localization onto the phenylnitroxide radical..... 33

Figure 2.14. Molecular structure of (η^2-*N,O*-*m*-TolNO)Mn(CO)$_2$(CNAr^{Dipp2})$_2$ (**9**) 34

Figure 2.15. EPR spectrum of (h^2-*N,O*-*m*-TolNO)Mn(CO)$_2$(CNAr^{Dipp2})$_2$ (**9**) at 295 K in toluene (0.05 mM) 34

Figure 2.16. Spin density plot of (η^2-*N,O*-*m*-TolNO)Mn(CO)$_2$(CNXyl)$_2$ showing spin localization onto the tolylnitroxide radical..... 35

Figure 2.17. Molecular structure of (η^2-*N,O*-*p*-PhNO)Mn(CO)$_2$(CNAr^{Dipp2})$_2$ (**10**) 35

Figure 2.18. EPR spectrum of (h^2-*N,O*-*p*-TolNO)Mn(CO)$_2$(CNAr^{Dipp2})$_2$ (**10**) at 295 K in toluene (0.05 mM) 36

Figure 2.19. Spin density plot of (η^2-*N,O*-*p*-TolNO)Mn(CO)$_2$(CNXyl)$_2$ showing spin localization onto the tolylnitroxide radical..... 36

Figure 2.20. Relative Bonding Energies (DH^{SCF}) for the conversion of (κ^1-*N*-PhNO)Mn(CO)$_3$(CNXyl)$_2$ to (η^2-*N,O*-PhNO)Mn(CO)$_2$(CNXyl)$_2$ and CO.. 37

Figure 2.21. Relative Bonding Energies (DH^{SCF}) for the conversion of (κ^1-*N*-PhNO)Mn(CO)$_5$ to (η^2-*N,O*-PhNO)Mn(CO)$_4$ and CO 38

Figure 2.22. Solid state structures of Mn(BiCl$_2$)(CO)$_3$(CNAr^{Dipp2})$_2$ (*top*) and Mn(SbF$_2$)(CO)$_3$(CNAr^{Dipp2})$_2$, with selected Dipp rings and H atoms omitted for clarity..... 43

Figure 2.23. Molecular structure of Mn(FHF)(CO)$_3$(CNAr^{Dipp2})$_2$, with H atoms omitted for clarity 47

Figure 2.24. ^{1}H NMR (300.1 MHz, C$_6$D$_6$, 20 ˚C) of mixture resulting from decomposition of MnF(CO)$_3$(CNAr^{Dipp2})$_2$..... 48

Figure 2.25. Inset view of ^{1}H NMR (300.1 MHz, C$_6$D$_6$, 20 ˚C) of upfield doublet resonance in mixture resulting from decomposition of MnF(CO)$_3$(CNAr^{Dipp2})$_2$..... 49

Figure 2.26. (*Top*) Formation of the Mn-aluminyl complex Mn(AlCl$_2$·THF)(CO)$_3$(CNAr^{Dipp2})$_2$ (*Bottom*) Solid state structure of Mn(AlCl$_2$·THF)(CO)$_3$(CNAr^{Dipp2})$_2$ 50

Figure 2.27. Molecular structure of (OTf)Mn(CO)$_3$(CNAr^{Dipp2})$_2$..... 92

Figure 3.1. Molecular structure of IMn(CO)$_3$(CNAr^{Dipp2})$_2$ (**3**) 109

Figure 3.2. Cyclic voltammograms (CVs) of **1** (red), **2** (green), **3** (blue), and **4** (black) in THF with 0.1 M TBAPF$_6$ under dinitrogen..... 109

Figure 3.3. Cyclic voltammograms (CVs) of **2** in THF 111

Figure 3.4. Cyclic voltammograms (CVs) of **4** in THF with 0.1 M $TBAPF_6$ under dinitrogen with the varying equivalents of MeCN added 112

Figure 3.5. IR-SEC of **4** in THF with 0.1 M $TBAPF_6$ under dinitrogen..... 113

Figure 3.6. IR-SEC of **2** in THF with 0.1 M TBAPF6 under dinitrogen..... 114

Figure 3.7. Cyclic voltammograms (CVs) of **2** in THF with 0.1 M $TBAPF_6$ under dinitrogen (black) and under CO_2 (red) 118

Figure 3.8. Cyclic voltammograms (CVs) of **4** in THF with 0.1 M TBAPF6 under dinitrogen (black) and under CO2 (red)..... 118

Figure 3.9. Solid state structures of $Mn_2(CO)_8(CNAr^{Dipp2})_2$ (**8**, A) and $Mn_2(CO)_7(CNAr^{Dipp2})_3$ (**7**, B) at 100K..... 119

Figure 3.10. Inset view of $^{13}C\{^1H\}$ NMR spectrum in C_6D_6 of product mixture isolated from the addition of $^{13}CO_2$ to $Na[Mn(CO)_3(CNAr^{Dipp2})_2]$ 121

Figure 3.11. $^{13}C\{^1H\}$ NMR spectrum of $Na_2{}^{13}CO_3$ in D_2O (*i.e.* $Na[DCO_3]$), isolated from the addition of $^{13}CO_2$ to $Na[Mn(CO)_3(CNAr^{Dipp2})_2]$..... 121

Figure 3.12. Infrared spectrum of $BrMn(CO)_3(CNAr^{Dipp2})_2$ (**2**) in C_6D_6..... 131

Figure 3.13. Infrared spectrum of $HMn(CO)_3(CNAr^{Dipp2})_2$ in THF 132

Figure 3.14. Infrared spectrum of $[Mn(CO)_3(CNAr^{Dipp2})_2]OTf$ (**4**) in THF 132

Figure 3.15. Infrared spectrum of $[Mn(CO)_3(CNAr^{Dipp2})_2]^0$ (**5**) in C_6D_6..... 132

Figure 3.16. Infrared spectrum of $Na[Mn(CO)_3(CNAr^{Dipp2})_2]$ (**6**) in THF 133

Figure 3.17. IR-SEC data for $BrMn(CO)_3(CNAr^{Dipp2})_2$ (**2**) 134

Figure 3.18. IR-SEC data for $[Mn(CO)_3(CNAr^{Dipp2})_2]OTf$ (**4**) without solvent subtraction..... 135

Figure 3.19. Raw IR-SEC data for $BrMn(CO)_3(CNAr^{Dipp2})_2$ (**2**) in $^{13}CO_2$-sparged THF without solvent subtraction or baseline normalization..... 135

Figure 4.1. Solid-state structures of A) $Mn(\kappa^2\text{-}(O_2C(t\text{Bu})))(CO)_2(CNAr^{Dipp2})_2$ (**1**), B) $Mn(\kappa^2\text{-}(O_2CCH_3))(CO)_2(CNAr^{Dipp2})_2$ (**2**), C) $Mn(\kappa^2\text{-}(O_2CC_6H_5))(CO)_2(CNAr^{Dipp2})_2$ (**3**) and D) $Mn(\kappa^2\text{-}(O_2CH))(NC_5H_5)(CO)_2(CNAr^{Dipp2})_2$ (**4-pyr**) 147

Figure 4.2. Solid state structure of *trans,mer*-$(\kappa^1\text{-}(O_2CC_6H_5))Mn(CO)_3(CNAr^{Dipp2})_2$ (**5**), with H atoms omitted for clarity 149

Figure 4.3. *Top*: Synthesis of *trans,mer-(*κ^1-O_2CCF_3)$Mn(CO)_3(CNAr^{Dipp2})_2$ (**6**). *Bottom*: Solid state structure of **6**, with disordered atoms and H atoms omitted for clarity 151

Figure 4.4. Structure of [$K(Et_2O)$][(η^4-4-Ar^{Dipp}-6,10-diisopropylazabenz[*b*]azulene)$Mn(CO)_2$-($CNAr^{Dipp2}$)] (**7**)..... 154

Figure 4.5. Solid state structure of Mn((κ^2-*H,H'*-BH_4))$(CO)_2(CNAr^{Dipp2})_2$ (**8**), with selected H atoms omitted for clarity 157

Figure 4.6. *Top*: Synthesis of Mn(κ^2-$F_3CSO_3BH_3$)$(CO)_2(CNAr^{Dipp2})_2$ (**8-OTf**). *Bottom*: Solid state structure of **8-OTf** 158

Figure 4.7. A) Solid state structure of Mn(OTf)(THF)$(CO)_2(CNAr^{Dipp2})_2$ (**9-THF**). B) Solid state structure of [$Mn(OEt_2)_2(CO)_2(CNAr^{Dipp2})_2$]$BAr^F{}_4$ (**10**) 161

Figure 4.8. Solid state structure of $Mn(CO)_2(CNAr^{Dipp2})$(h^2-(*C,H*-CH_3)$(CH_3)_2CCO_2B(C_6F_5)_3$) (**11**) with a Dipp ring and H atoms omitted for clarity 163

Figure 4.9. Molecular structure of $(C_6F_5)_3B{\leftarrow}CNAr^{Dipp2}$, with H atoms omitted for clarity 164

Figure 4.10. Two perspectives of the molecular structure of $Mn(CO)_2$(η^2-*C,N*-(H_3CCNAr^{Dipp2}))($CNAr^{Dipp2}$) (**12**) 176

Figure 4.11. ^{1}H NMR spectrum (500.1 MHz, 20 ˚C, C_6D_6) of Mn(κ^2-*O,O*-(O_2CCH_3))$(CO)_2(CNAr^{Dipp2})_2$..... 186

Figure 4.12. ^{1}H NMR spectrum (400.1 MHz, 20 ˚C, C_6D_6) of Mn(κ^2-*O,O*-($O_2C(C_6H_5)$)$(CO)_2(CNAr^{Dipp2})_2$ (**3**) 186

Figure 4.13. ^{1}H NMR spectrum (500.1 MHz, 20 ˚C, C_6D_6) of Mn(κ^1-*O*-(O_2CH))$(CO)_2$(Pyr)$(CNAr^{Dipp2})_2$) **(4-pyr)** 187

Figure 4.14. ^{1}H NMR spectrum (500.1 MHz, 20 ˚C, C_6D_6) of Mn(κ^1-*O*-((C_6H_5)CO_2))$(CO)_3(CNAr^{Dipp2})_2$ **(5)**. 187

Figure 4.15. ^{1}H NMR spectrum (500.1 MHz, 20 ˚C, C_6D_6) of Mn(κ^1-*O*-(O_2CCF_3))$(CO)_3(CNAr^{Dipp2})_2$ **(6)**. 188

Figure 4.16. ^{1}H NMR spectrum (500.1 MHz, 20 ˚C, C_6D_6) of Mn(κ^2-*H,H*-($F_3CSO_3BH_3$))$(CO)_2(CNAr^{Dipp2})_2$ **(8-OTf)**. 188

Figure 4.17. ^{1}H NMR spectrum (400.1 MHz, 20 ˚C, C_6D_6) of Mn(OTf)$(CO)_2(CNAr^{Dipp2})_2$ **(9)** in reaction mixture resulting from S1.14, Method A 189

Figure 4.18 ^{1}H NMR spectrum (400.1 MHz, 20 ˚C, C_6D_6) of $Mn(OTf)(CO)_2(CNAr^{Dipp2})_2$ **(9)** in reaction mixture resulting from S1.14, Method B 189

Figure 4.19. ^{1}H NMR spectrum (500.1 MHz, 20 ˚C, C_6D_6) of $[Mn(CO)_2(CNAr^{Dipp2})_2(OEt_2)_2]BAr^{F}{}_4$ **(10)**. The symbol (*) denotes free *n*-pentane 190

Figure 4.20. ^{1}H NMR spectrum (500.1 MHz, 20 ˚C, C_6D_6) of $Mn(CO)_2(CNAr^{Dipp2})(h^2\text{-}(C,H\text{-}CH_3)(CH_3)_2CCO_2B(C_6F_5)_3)$ **(11)** 190

Figure 5.1. **A**: Synthesis of Cu-^{ISO}CN-1. **B**: The interpenetrated diamondoid lattice of Cu-^{ISO}CN-1 along the *ac* plane, **C**: Cu(I) tetrakis-isocyanide node. **D**: Space-filling diagram of node..... 207

Figure 5.2. Stacked ATR-IR spectra for the thermolysis of Cu-^{ISO}CN-1 in the solid state at 125 ºC over the course of 2 days. 208

Figure 5.3. Solid-state CP-MAS ^{13}C NMR spectrum of Cu-^{IS0}CN-1 211

Figure 5.4. *Left*: View down the *c* axis of Cu-^{ISO}CN-2. *Middle*: View of Cu-^{ISO}CN-3 down the *ac* plane. *Right*: $[Cu(THF)([CNAr^{Mes2}]_2)_3]^+$ node 211

Figure 5.5. ATR-IR (left) and PXRD (right) of Cu-^{ISO}CN-3 after 2 day exposure to a) 1 N NaOH, b) 1 N HCl, c) 1 N HNO_3, d) iPrOH, e) MeOH, f) H_2O. g) Cu-^{ISO}CN-3 213

Figure 5.6. Generalized illustration of the geometric parameters used to define the pyramilization of $[Cu(L_a)(L_b)_3]^+$ species 215

Figure 5.7. Molecular structure of $[Cu(PMe_3)(CNAr^{Mes2})_3]OTf$ (OTf = O_3SCF_3), with THF solvent molecules omitted for clarity 216

Figure 5.8. Optimized structures of $[Cu(CNXyl)_3]^+$ (**A**), $[Cu(OH_2)(CNXyl)_3]^+$ (**B**), $[Cu(PMe_3)(CNXyl)_3]^+$ (**C**), and $[Cu(THF)(CNXyl)_3]^+$ (**D**) 216

Figure 5.9. TEM image of Cu-^{ISO}CN-3 sheets prepared by sonication in H_2O 217

Figure 5.10. TEM image of Cu-^{ISO}CN-3 sheets prepared by sonication in H_2O ... 218

Figure 5.11. TEM image of Cu-^{ISO}CN-3 sheets prepared by sonication in H_2O ... 218

Figure 5.12. TEM image of Cu-^{ISO}CN-3 sheets prepared by sonication in H_2O ... 219

Figure 5.13. TEM images of Cu-^{ISO}CN-3 after sonication in a 20 mM solution of $NaBAr^{F}$ in MeOH 220

Figure 5.14. ^{1}H NMR spectrum ($CDCl_3$, 400.1 MHz, 20 ˚C) of $H_2N(p\text{-}BrAr^{Mes2})$ 227

Figure 5.15. ^{1}H NMR spectrum ($CDCl_3$, 400.1 MHz, 20 ˚C) of H_2N(*p*-(BPin)Ar^{Mes2}) 227

Figure 5.16. ^{1}H NMR spectrum ($CDCl_3$, 400.1 MHz, 20 ˚C) of $[H_2NAr^{Mes2}]_2$ 228

Figure 5.17. ^{1}H NMR spectrum ($CDCl_3$, 400.1 MHz, 20 ˚C) of $[HC(O)HNAr^{Mes2}]_2$ 228

Figure 5.18. ^{1}H NMR spectrum ($CDCl_3$, 400.1 MHz, 20 ˚C) of $[CNAr^{Mes2}]_2$..... 229

Figure 5.19. Solution IR spectrum ($CDCl_3$, 20 ˚C) of $[HC(O)HNAr^{Mes2}]_2$ 229

Figure 5.20. Solution IR spectrum ($CDCl_3$, 20 ˚C) of $[CNAr^{Mes2}]_2$..... 230

Figure 5.21. Solid-state ATR-IR spectra of **(a)** Cu-^{ISO}CN-3, **(b)** Cu-^{ISO}CN-2, and **(c)** Cu-^{ISO}CN-1 233

Figure 5.22. Experimental and predicted PXRD patterns for Cu-^{ISO}CN-3. **(a)** As-isolated crystalline phase; **(b)** predicted pattern of Cu-^{ISO}CN-3 233

Figure 5.23. Powder X-ray diffraction patterns for **(a)** Cu-^{ISO}CN-2 (experimental), **(b)** Cu-^{ISO}CN-2 (predicted), **(c)** Cu-^{ISO}CN-1 (experimental), **(d)** Cu-^{ISO}CN-1 (predicted). 234

Figure 5.24. ATR-IR of Cu-^{ISO}CN-1 heated at 50 ºC for 5 days. Inset view shows the isocyanide region 234

Figure 5.25. ATR-IR of Cu-^{ISO}CN-1 heated at 125 ˚C over a 48 h period. No further changes in the ATR-IR spectra are observed after 36 h 235

Figure 5.26. Powder X-ray diffraction pattern of Cu-^{ISO}CN-1 heated at 125 ºC for 2 days in the solid state (**top**) and representative pattern of Cu-^{ISO}CN-1 as prepared (**bottom**)..... 235

Figure 5.27. Solid-state ATR-IR spectra of Cu-^{ISO}CN-3 after suspension. **(a)** 1 N NaOH, **(b)** 1 N HCl, **(c)** 1 N HNO_3, **(d)**, iPrOH, **(e)** MeOH, (**f**) H_2O, (**g**) Cu-^{ISO}CN-3 236

Figure 5.28. Powder X-ray diffraction of Cu-^{ISO}CN-3 after suspension in **(a)** MeOH, **(b)** iPrOH, **(c)** 1 N NaOH, **(d)** 1 N HNO_3, **(e)** 1 N HCl, **(f)** H_2O. 237

Figure 5.29. Solid-state ATR-IR spectra of the isocyanide region of Cu-^{ISO}CN-3 after activation at 200 ºC and gas sorption analysis. 237

Figure 5.30. Powder X-ray diffraction of Cu-^{ISO}CN-3 after activation at 200 ºC and gas sorption analysis. 238

Figure 5.31. Asymmetric unit of Cu-^{ISO}CN-1, with THF solvent molecules of co-crystallization omitted for clarity and disordered $[PF_6]^-$ shown 239

Figure 5.32. Channels formed along *a* axis in Cu-^{ISO}CN-1. The channels along the *c* axis are crystallographically identical 240

Figure 5.33. Asymmetric unit of Cu-^{ISO}CN-2 240

Figure 5.34. Channels along the *b* axis in Cu-^{ISO}CN-2 241

Figure 5.35. Asymmetric unit of Cu-^{ISO}CN-3, with positionally disordered $[PF_6]^-$ counteranions included 241

Figure 5.36. View along the *a* axis of Cu-^{ISO}CN-3. *Left*: Inset view of pore, showing Cu-THF unit pointed towards channel. *Right*: Zig-zag pattern formed by channels 242

Figure 5.37. Molecular structure of $[CNAr^{Mes2}]_2$, with diethyl ether solvent molecules of co-crystallization omitted for clarity 242

Figure 5.38. CO_2 sorption isotherms of activated Cu-^{ISO}CN-3; red = adsorption, black = desorption 245

Figure 5.39. CO_2 sorption isotherms of activated Cu-^{ISO}CN-3 after exposure to 1 N HNO_3; red = adsorption, black = desorption 246

Figure 5.40. CO_2 sorption isotherms of activated Cu-^{ISO}CN-3 after exposure to 1 M NaOH; red = adsorption, black = desorption 246

Figure 5.41. Thermogravimetric analyses of Cu-^{ISO}CN-3 (red), Cu-^{ISO}CN-2 (blue), and Cu-^{ISO}CN-1 (black) 247

Figure 5.42. A representative image of the contact angle meter upon addition of a drop of H_2O to Cu-^{ISO}CN-3 (left). Close-up view of a bead of water on top of Cu-^{ISO}CN-3 (right) 248

Figure 6.1. Molecular structure of $[(CO)_4FeCNAr^{Mes2}]_2$, with H atoms omitted for clarity 269

Figure 6.2. Molecular structure of $[PdCl(\eta^3\text{-allyl})CNAr^{Mes2}]_2$, with FBz solvent molecule and H atoms omitted for clarity 270

Figure 6.3. Molecular structure of $[(CO)_5CrCNAr^{Mes2}]_2$, with H atoms omitted for clarity 272

Figure 6.4. Unit cell of Co-^{ISO}CN-1, with *m*-terphenyl groups displayed in wireframe and free THF solvent molecule and H atoms omitted for clarity273

Figure 6.5. (*Left*) Covalent connectivity in Co-^{ISO}CN-1, revealing the formation of a 1-D Co(II) coordination polymer. (*Right*) Packing of 1-D chains 275

Figure 6.6. Molecular structure of $[(CO)_5MoCNAr^{Mes2}]_2$, with H atoms omitted for clarity 277

Figure 6.7. Downfield region of the $^{13}C\{^1H\}$ NMR spectrum of $[(CO)_4Mo(CNAr^{Mes2})_2$ 279

Figure 6.8. UV-Vis spectra (C_6H_6, 20 ˚C) of $[(CO)_5MoCNAr^{Dipp2}]_2$ (blue) and $[(CO)_4Mo(CNAr^{Dipp2})_2]_2$ (red)..... 280

Figure 6.9. UV-Vis spectra (C_6H_6, 20 ˚C) of $[(CO)_4Mo(CNAr^{Dipp2})_2]_2$ (red) and its decomposition product (black) 282

Figure 6.10. Molecular structure of *p*-QTPh-$[CNAr^{Mes2}]_2$ 284

Figure 7.1. A linear strand of Ni-^{ISO}CN-1, showing the ladder-like topology..... 306

Figure 7.2. (*left*) the unusual C_s-symmetry about Ni enforced by the rigid framework of Ni-^{ISO}CN-1; (*right*) plot of the isocyanide region in the ATR-IR spectrum of Ni-^{ISO}CN-1 307

Figure 7.3. Synchrotron XANES data for Ni-^{ISO}CN-1, $[Ni(CNAr^{Mes2})_4]OTf$, and $Ni(CNAr^{Mes2})_3$ 308

Figure 7.4. (*Left*) Solid-state structure of Ni(TlOTf)-^{ISO}CN-1; (*Right*) Stacked plot of ATR-IR spectra of Ni-^{ISO}CN-1 exposed to 1 mM (**a**), 10 mM (**b**), and 100mM (**c**) MeCN solutions of TlOTf..... 309

Figure 7.5. XANES spectra for Ni(TlOTf)-^{ISO}CN-1 and Ni-^{ISO}CN-1, verify retention of Ni(0) oxidation state after addition of TlOTf..... 310

Figure 7.6. Redox activity of Ni-^{ISO}CN-1 312

Figure 7.7. Synchrotron XANES data for Ni-^{ISO}CN-2, $[Ni(CNAr^{Mes2})_4]OTf$, and $Ni(CNAr^{Mes2})_4$ 315

Figure 7.8. (*top*) View down 100 axis of Ni-^{ISO}CN-2·$([CNAr^{Mes2}]_2)_{0.5}$, with free $[CNAr^{Mes2}]_2$ omitted; (*bottom left*) Pore generated by two unique Ni(0) nodes, with the partially occupied free $[CNAr^{Mes2}]_2$ shown in blue; (*bottom right*) ATR-IR spectrum of Ni-^{ISO}CN-2..... 317

Figure 7.9. ATR-IR spectra of Ni-^{ISO}CN-2·$([CNAr^{Mes2}]_2)_{0.5}$ (black), as prepared Ni-^{ISO}CN-2 (red), and Ni-^{ISO}CN-2 after heating in THF (blue) 319

Figure 7.10. PXRD pattern of as-synthesized Ni-^{ISO}CN-1 at 100K (middle, black) and the predicted pattern from SXRD (bottom, red). The top pattern,

collected at 295K, in blue results for Ni-^{ISO}CN-1 upon desolvation under vacuum 327

Figure 7.11. Full PXRD patterns of Ni-^{ISO}CN-1 undergoing redox-cycling. Starting Ni-^{ISO}CN-1 (bottom, blue); after full oxidation to Ni(I) using FcOTf (middle); after reduction to Ni(0) using Cp_2Co (top) 327

Figure 7.12. PXRD pattern for Ni(TlOTf)-^{ISO}CN-1; (*top)* 100K, (*bottom*) 295K 328

Figure 7.13. PXRD pattern for Ni-^{ISO}CN-1 after reduction from Ni(I)-^{ISO}CN-1; (*top)* 100K, (*bottom*) 295K 328

Figure 7.14. Comparison of PXRD patterns (298K) of Ni-^{ISO}CN-1 (blue) and re-reduced Ni-^{ISO}CN-1 after exposure of Ni(I)-^{ISO}CN-1 to Fc^* for one day ... 329

Figure 7.15. Solid-state ATR-IR spectrum of Ni-^{ISO}CN-1 329

Figure 7.16. Solid-state ATR-IR spectra of Ni-^{ISO}CN-1 after exposure to MeCN solutions of TlOTf; (top) 100mM, (middle) 10 mM, (bottom) 1 mM 330

Figure 7.17. View of isocyanide region for ATR-IR spectra of Ni-^{ISO}CN-1 after placement in degassed H_2O under a N_2 atmosphere; (bottom*)* two days, (top) four days 330

Figure 7.18. ATR-IR of Ni(I)-^{ISO}CN-1 331

Figure 7.19. ATR-IR of mixed-valence Ni-^{ISO}CN-1 331

Figure 7.20. ATR-IR of Ni-^{ISO}CN-1 after reduction with Fc^* in MeCN; inset shows isocyanide region 331

Figure 7.21. X-band EPR spectra of $[Ni(CNAr^{Mes2})_3]OTf$ (top, red) and Ni(I)-^{ISO}CN-1 (bottom, black) collected at 150K 332

Figure 7.22. PXRD pattern of Ni-^{ISO}CN-1 after reduction from Ni(I)-^{ISO}CN-1; (*top*) 100K, (*bottom*) 295K 332

Figure 7.23. Comparison of PXRD patterns (298K) of Ni-^{ISO}CN-1 (blue) and re-reduced Ni-^{ISO}CN-1 after exposure of Ni(I)-^{ISO}CN-1 to Fc^* for one day ... 333

Figure 7.24. Representative DSC trace for Ni-^{ISO}CN-1. The large exotherm has an onset temperature of 261 ˚C 333

Figure 7.25. Solid-state ATR-IR spectrum of Ni-^{ISO}CN-2 334

Figure 7.26. PXRD pattern of as-synthesized, desolvated Ni-^{ISO}CN-1 (top, black) and the predicted pattern of Ni-^{ISO}CN-1·$[CNAr^{Mes2}]_2$ from SC-XRD (bottom, red) 334

Figure 7.27. Representative DSC trace for Ni-^{ISO}CN-2. The large exotherm has an onset temperature of 302 ˚C 335

Figure 7.28. Asymmetric unit of Ni-^{ISO}CN-1, with MeCN solvent molecules omitted for clarity 338

Figure 7.29. Asymmetric unit of Ni(TlOTf)-^{ISO}CN-1, with one MeCN solvent molecule and disordered Tl^{+} omitted for clarity 338

Figure 7.30. (Left) View of single polymer of Ni(TlOTf)-^{ISO}CN-1; (Right) View down the *ab* plane. The *meta*-terphenyl substituents are displayed in wireframe for clarity. Additionally, the triflate counteranion has also been omitted for clarity 339

Figure 7.31. Asymmetric unit of Ni(0/I)-^{ISO}CN-2. The disordered Ni site was modeled and refined anisotropically, with a SOF = 0.26 for Ni(I) (shown in magenta) 339

Figure 7.32. Asymmetric unit of Ni-^{ISO}CN-2·[CNAr^{Mes2}]$_2$, with THF solvent molecule and disordered mesityl rings omitted for clarity 340

Figure 7.33. Adamantoid cage formed by 10 Ni(0) nodes in Ni-^{ISO}CN-2. The mesityl groups on [CNAr^{Mes2}]$_2$ have been omitted for clarity 340

Figure 7.34. View down the 100 axis, with free [CNAr^{Mes2}]$_2$ omitted. The independent nets are colored in blue and pink, respectively, highlighting the two-fold interpenetration in Ni-^{ISO}CN-2 341

Figure 7.35. Optical microscope photograph of a single crystal of Ni-^{ISO}CN-1. The 100 axis lies approximately orthogonal to the face of the parallelogram. The Ni-^{ISO}CN-2 polymers are aligned along the 010 axis 341

Figure 7.36. Optical microscope photograph of single crystals of Ni-^{ISO}CN-1 suspended in Trilene oil 342

LIST OF SCHEMES

Scheme 1.1. Formation of low-coordinate Cu(I) complexes via the addition of sterically encumbering isocyanides a Cu(I) precursor 7

Scheme 1.2. The reactivity of three isoelectronic manganate complexes with MeI. 9

Scheme 2.1. Preparation of $Mn(CO)_3(CNAr^{Dipp2})_2$ *via* three different routes..... 19

Scheme 2.2. Reaction pinwheel for complex **1** 23

Scheme 2.3. Addition of CS_2 results in the formation of a four-member manganocyclic dimer, which is believed to result from α-migratory insertion following initial formation of CS_2-bridged dimer .....

Scheme 2.4. Addition of $NO_{(g)}$ to **1** causes the dissociation of CO *en route* to the formation of $Mn(NO)(CO)_2(CNAr^{Dipp2})_2$ 29

Scheme 2.5. Reactivity of $Mn(CO)_3(CNAr^{Dipp2})_2$ with $BiCl_3$, $SnCl_2$ and SbF_3 41

Scheme 2.6. Addition of XeF_2 in C_6H_5F results in the formation of $MnF(CO)_3(CNAr^{Dipp2})_2$. Decomposition *via* an adventitious proton source results in the bifluoride complex..... 46

Scheme 3.1. A schematic view of the complexes involved in this study..... 108

Scheme 3.2. Proposed mechanism for CO_2 reductive disproportionation by $Na[Mn(CO)_3(CNAr^{Dipp2})_2]$ 123

Scheme 4.1. *Left:* Scheme depicting the route typically used towards the generation of monovacant Mn(I) complexes..... 143

Scheme 4.2. Generalized synthesis of Mn(I) κ^2-carboxylates **1**-**4** 146

Scheme 4.3. Synthesis of *trans,mer*-(κ^1-$(O_2CC_6H_5)$)$Mn(CO)_3(CNAr^{Dipp2})_2$ (**5**) from $Mn(CO)_3(CNAr^{Dipp2})_2$ and benzoyl peroxide..... 149

Scheme 4.4. Proposed mechanistic sequence leading to the formation of **7**, with pre-insertion complex on the bottom right..... 153

Scheme 4.5. Reaction pinwheel of **1** showing the deprotection strategies employed. 155

Scheme 4.6. Synthesis of $Mn(CO)_2(\eta^2$-*C,N*-$(H_3CCNAr^{Dipp2}))(CNAr^{Dipp2})$ (**12**) and *t*$BuC(O)OAlMe_3$ 165

Scheme 4.7. The addition of CO to $Mn(CO)_2(\eta^2$-*C,N*-$(H_3CCNAr^{Dipp2}))(CNAr^{Dipp2})$ (**12**) causes the deinsertion of the alkyl group 167

Scheme 5.1. Synthesis of the ditopic isocyanide $[CNAr^{Mes2}]_2$ 205

Scheme 6.1. Preparation of $[(CO)_4FeCNAr^{Mes2}]_2$ and $[PdCl(\eta^3$-allyl$)CNAr^{Mes2}]_2$ 268

Scheme 6.2. Synthesis of $[(CO)_5CrCNAr^{Mes2}]_2$ 271

Scheme 6.3. Preparation of the 1-D coordination polymer Co-^{ISO}CN-1 273

Scheme 6.4. Preparation of the dinuclear complex $[(CO)_5MoCNAr^{Dipp2}]_2$ from $Mo(CO)_6$ 276

Scheme 6.5. Formation of the tetranuclear complex $[(CO)_4Mo(CNAr^{Mes2})_2]_4$ 278

Scheme 6.6. Preparation of *p*-QTPh-$[CNAr^{Mes2}]_2$ from H_2N(*p*-(BPin)Ar^{Mes2}) and 4,4'-dibromobiphenyl..... 283

Scheme 6.7. Preparation of 1,3,5-$(CNAr^{Mes2})_3$-triphenylbenzene from H_2N(*p*-(BPin)Ar^{Mes2}) and 1,3,5-tris(4-bromophenyl)benzene 285

Scheme 7.1. Synthesis of Ni-^{ISO}CN-1 305

LIST OF TABLES

Table 2.1. Thermodynamic Calculations for CO Dissociation and Formation of η^2-Nitroxide Species from $XMn(CO)_3(CNXyl)_2$ Complexes..... 73

Table 2.2. Thermodynamic Calculations for CO Dissociation and Formation of η^2-Nitroxide Species from $XMn(CO)_5$ Complexes (X = Phenylnitroxide)..... 73

Table 2.3. Crystallographic Data Collection and Refinement Information 93

Table 2.4. Crystallographic Data Collection and Refinement Information 94

Table 2.5. Crystallographic Data Collection and Refinement Information 95

Table 2.6. Crystallographic Data Collection and Refinement Information 96

Table 2.7. Crystallographic Data Collection and Refinement Information 97

Table 3.1 Crystallographic Data Collection and Refinement Information 136

Table 4.1. Selected NMR and IR spectroscopic data for **1-4** with comparison to the σ_p value for the respective *R* group of the carboxylate..... 151

Table 4.2 Crystallographic Data Collection and Refinement Information 193

Table 4.3 Crystallographic Data Collection and Refinement Information 194

Table 4.4 Crystallographic Data Collection and Refinement Information 195

Table 4.5 Crystallographic Data Collection and Refinement Information 196

Table 4.6 Crystallographic Data Collection and Refinement Information 197

Table 5.1. Comparison of the calculated *vs*. experimental values for **P** for the set of complex under study..... 215

Table 5.2. Crystallographic Data Collection and Refinement Information. 243

Table 5.3. Crystallographic Data Collection and Refinement Information 243

Table 5.4. Calculated Relative Energies as a Function of Linker Torsion Angle for $[CNAr^{Mes2}]_2$..... 249

Table 6.1. Crystallographic Data Collection and Refinement Information 298

Table 6.2. Crystallographic Data Collection and Refinement Information 299

Table 7.1. Tl occupancy data determined from crystallographic analysis..... 337

Table 7.2 Crystallographic Data Collection and Refinement Information 343

Table 7.3 Crystallographic Data Collection and Refinement Information **.....** 344

ACKNOWLEDGEMENTS

There is no question that I would not have finished this enormous project without the love and support of my family and friends throughout this process. Thank you for encouraging me, for being patient with me, and especially rolling your eyes at me.

Professor Joshua S. Figueroa, it has been a privilege to be your student. You have shown me how to be a good scientist, which as I have learned over the last 5 years is no easy feat. Thank you for introducing me to the world of badass organometallic chemistry, and giving me the toolset to go out and crush molecules and get shit done™. Most importantly, thank you for imparting the deeply critical mindset necessary to sniff out BS – this is perhaps the most valuable lesson you have taught me.

To the other faculty in the chemistry department, thank you for your advice, wisdom, and support. In particular, I would like to thank Professor Seth Cohen, whose support over the last 2 years was so important to the success of my research. Additionally, Profs William Trogler, Michael Sailor, Arnold Rheingold, Clifford Kubiak, Jeffrey Reinhardt, Carlos Guerrero, Michael Tauber, Nathan Gianneschi, and Joseph O'Connor – thank you for thoughtful discussions and insights into my research. Your help made my research get to the next level.

The Figueroa Research Group – you guys are nuts (the apple doesn't fall far from the tree). Treff, you have been a huge influence on my growth scientifically, and you're an awesome friend. Alex, the same goes for you too; I'd say the two years we lived together was one long group meeting (but the good kind). I look forward to

puttering around the Gulf with you in the near future. Charles aka Chuck, you're a goddamn beast in the lab, and I'm stoked to be your friend and colleague in the coming years. Brandon, I look forward to seeing your research grace the cover of *Science* in the future. To you all, I look forward to watching us continue to dominate the chemical space around us and never missing a chance to fuck shit up. To the next generation, you have all the power and resources to do amazing things, and it's great to see you doing it! Kyle, stay strong and continue to be the great leader in lab you are. Myles, just get the structure! Joanne, keep crushing it. Mike and Alejandra, you guys are doing great, and remember to keep the old crew in check!

There are so many people at UCSD that have been critical to my growth as a scientist. First and foremost, Curtis Moore and Milan Gembicky, without your help in the crystal palace I would be DOA. Seriously, the place is a second home for me on campus, and I will sorely miss you guys. Anthony Mrse, the NMR labs wouldn't be the same without you, and thank you for help and (importantly) genuine interest in getting the best possible results for me. Thank you to Joseph Patterson and Mollie Touve for all things nano, you certainly have opened my eyes to bigger things (get it?). A big shout out to Michael Denny, Jr., you were so helpful for understanding the material world. The same goes for Matt Sampson, you electrochemical wizard; thank you for putting up with my weird project for so long. There are so many other people to thank, with whom I've had inspiring conversations and have shared the bumps and bruises of graduate school: Corey Weinstein, Andrew Ostericher, Lewis Churchill, Sergio Ayala, Cy Credille, Melissa Helm, Sarah Barnhill, Gabriel Canzi, Kyle Grice, Stephen Cope,

Mohand Melaimi, Matt Millard, Matt Del Bel … Thanks to you all, and to anyone I have neglected to mention here.

The SD section – thanks for bringing me out of the lab and outa the grad school frame of mind. Ryan and Ian, the afternoons on the deck drinking MLs will always be a special memory, and I look forward to many more. Clifford Kapono and Robbie, thank you for dragging me out of bed at 5am to go surf some amazing waves. To all those in the North County; Charles, Rich and Megahn, Spencer, Matt – thank you. Jonathan and Max, you're basically my other family, and I wouldn't be where I am now if I had not spent years (both young and old) roaming the sand castle.

Not many grad students live 5 minutes away from their family home, but I can tell you it is great. The close proximity of my family, their love and support (as well as a delicious meal) was such a luxury during these years. Mom, Dad, and Isabel – thank you for being there and providing such stability in an otherwise fairly chaotic time.

Ulrika, meeting you was the best thing that's happened in my life, and I am so grateful for your unconditional love and support throughout these years. There is so much I could say here it would dwarf the rest of this dissertation, but I'll just say this: I'm eagerly looking forward to spending the rest of my life with you.

Chapter 2 is adapted in part from "Kinetic Destabilization of Metal-Metal Single Bonds: Isolation of a Pentacoordinate Manganese(0) Monoradical" by Douglas W. Agnew, Curtis E. Moore, Arnold L. Rheingold, and Joshua S. Figueroa, *Angewandte Chemie, International Edition* **2015** *54*, 12673-12677, Copyright 2015 Wiley-VCH Verlag GmbH & Co., and "Comparison of Nucelophilic- and Radical-Based Routes to the Formation of Manganese-Group Element Single Bonds" by

Douglas W. Agnew, Curtis E. Moore, Arnold L. Rheingold, and Joshua S. Figueroa, which has been submitted for publication. Permission to include published material in this dissertation has been obtained from all coauthors. The dissertation author is the first author of both papers.

Chapter 3 is adapted from "Electrochemical Properties and CO_2-Reduction Ability of *m*-Terphenyl Isocyanide Supported Manganese Tricarbonyl Complexes" by Douglas W. Agnew, Matthew D. Sampson, Curtis E. Moore, Arnold L. Rheingold, Clifford P. Kubiak, and Joshua S. Figueroa, *Inorganic Chemistry* **2016** *55* (23), 12400-12408. Copyright 2016, American Chemical Society. Permission to include published material in this dissertation has been obtained from all coauthors. The dissertation author is the first author of this paper.

Chapter 4 is adapted from "Controlled cis Labilization of CO from Manganese(I) Mixed Carbonyl/Isocyanide Complexes: An Entry Point to Coordinatively Unsaturated Metallo-Lewis Acids" by Douglas W. Agnew, Curtis E. Moore, Arnold L. Rheingold, and Joshua S. Figueroa, *Organometallics* 2017 *36* (2), 363-371. Copyright 2017, American Chemical Society. Permission to include published material in this dissertation has been obtained from all coauthors. The dissertation author is the first author of this paper.

Chapter 5 is in part adapted from "Robust, Transformable, and Crystalline Single-Node Organometallic Networks Constructed from Ditopic *m*-Terphenyl Isocyanides" by Douglas W. Agnew, Milan Gembicky, Curtis E. Moore, Arnold L. Rheingold, and Joshua S. Figueroa, *Journal of the American Chemical Society* **2016** *138* (46), 15138-15141. Copyright 2016, American Chemical Society. Permission

to include published material in this dissertation has been obtained from all coauthors. The dissertation author is the first author of this paper. Chapter 5 contains unpublished material produced in collaboration with Professor Nathan Gianneschi, Dr. Joseph Patterson, and Mollie Touve, who are thanked for the acquisition of TEM images of Cu-^{ISO}CN-3. Professor Stanley Opella and Dr. Anna de Angelis are thanked for the acquisition of the CP-MAS ^{13}C NMR spectrum of Cu-^{ISO}CN-3. Professor Seth Cohen and Michael S. Denny, Jr., are thanked for helpful discussions and assistance with physical measurements.

Professor Michael Sailor, Nicole Chan, and Dr. Tushar Kumeria are thanked for their assistance with the UV-Vis measurements performed in Chapter 6, particularly with the design of the air-free system utilized in the described study.

Chapter 7 is adapted from two manuscripts currently being prepared for publication by D. W. Agnew, I. D. Dimucci, C. E. Moore, S. N. MacMillan, A. L. Rheingold, K. M. Lancaster, and J. S. Figueroa. Permission to include published material in this dissertation has been obtained from all coauthors. The dissertation author is the first author of this paper.

VITA

2017 Doctor of Philosophy, University of California, San Diego

2014 Master of Science, University of California, San Diego

2010 Bachelor of Arts, Reed College

PUBLICATIONS

Agnew, D. W.; Moore, C. E.; Rheingold, A. L.; Figueroa, J. S. "Comparison of Nucleophilic- and Radical-Based Routes to the Formation of Manganese-Main Group Element Single Bonds." *Dalton Transactions*. Accepted

Mokhtarzadeh, C. C.; Carpenter, A. E.; Spence, D. P. Melaimi, M.; **Agnew, D W.**; Weidemann, N.; Moore, C. E.; Rheingold, A. L.; Figueroa, J. S. "Geometric and Electronic Structure Analysis of the Three-Membered Electron-Transfer Series $[(\mu\text{-}CNR)_2[CpCo]_2]^n$ (n = 0, 1–, 2–) and its Relevance to the Classical Bridging-Carbonyl System." *Organometallics*. Accepted

Agnew, D. W.; Moore, C. E.; Rheingold, A. L.; Figueroa, J. S. "Controlled *cis*-labilization of CO from Manganese Mixed Carbonyl/Isocyanides: An Entry-Point to Coordinatively Unsaturated Metallo-Lewis Acids." *Organometallics*. **2017**, *36*, 363-371.

Agnew, D. W.; Gembicky, M.; Moore, C. M. Rheingold, A. L.; Figueroa, J. S. "Robust, Transformable and Crystalline Single-Node Organometallic Networks Constructed from Ditopic m-Terphenyl Isocyanides." *Journal of the American Chemical Society*. **2016**, *138*, 15138–15141.

Agnew, D. W.; Sampson, M. D.; Moore, C. E.; Kubiak, C. P.; Figueroa, J. S. "Electrochemical Properties and CO_2-Reduction Ability of m-Terphenyl Isocyanide Supported Manganese Tricarbonyl Complexes." *Inorganic Chemistry*. **2016**, *55*, 12400–12408.

Agnew, D. W.; Moore, C. E.; Rheingold, A. L.; Figueroa, J. S. "Kinetic Destabilization of Metal-Metal Single Bonds: Isolation of a Pentacoordinate Manganese (0) Monoradical." *Angewandte Chemie, Int. Ed*. **2015**, *54*, 12673-12677.

Ditri, T. B.; Barnett, B. R.; Carpenter, A. E.; **Agnew, D. W.**; Mokhtarzardeh, C. C.; Figureoa, J. S. "*m*–Terphenyl Isocyanides Featuring 2,6-dimesityl and 2,6-bis-(2,6-di-isopropyl)phenyl Substitution Patterns." *Inorganic Syntheses*. In Press.

ABSTRACT OF THE DISSERTATION

Studies of Isocyano Analogues to Manganese Carbonyls and the Development of Low-Valent Coordination Polymers using Multitopic *m*-Terphenyl Isocyanides

by

Douglas Walter Agnew

Doctor of Philosophy in Chemistry

University of California, San Diego, 2017

Professor Joshua S. Figueroa, Chair

The work presented in this dissertation is best apportioned into two distinct parts; the first part (Chapters 2-4) describes several investigations of low-valent manganese carbonyl/isocyanide complexes, while the second part (Chapters 5-7) details the generation of coordination polymers and other supramolecular complexes

using the ditopic isocyanide $[CNAr^{Mes2}]_2$. With this division in mind, the attentive reader will hopefully observe that the interrogative method utilized in studies of discrete, molecular complexes can be translated efficiently and effectively to materials development.

In the first part, the mixed carbonyl/isocyanide complex $Mn(CO)_3(CNAr^{Dipp2})_2$ was isolated in gram scale with the aid of the sterically encumbering isocyanide $CNAr^{Dipp2}$. This green solid, which is electronically and structurally similar to the homoleptic carbonyl $Mn(CO)_5$, displays the radical-based chemistry expected for an open-shelled, low-spin d^7 organometallic species. However, the kinetic stabilization engendered by the *m*-terphenyl groups has allowed for a careful study of reaction products, with the notable isolation of several manganese η^2-*N,O*-nitroxide radicals. The identification of these species raises doubts concerning earlier work regarding nitrosoarene spin-trapping of photolytically generated $Mn(CO)_5$, and underscores the importance of the *cis*-labilizing effect in low-valent Mn chemistry. This latter fact has been elaborated upon with the generation of multiple Mn κ^2-carboxylates (eg. $(\kappa^2$-*O,O*'-$RCO_2)Mn(CO)_2(CNAr^{Dipp2})_2$) via the *cis*-labilization of CO from the $[Mn(CO)_3(CNAr^{Dipp2})_2]$ framework using a variety of metal carboxylate reagents. These Mn carboxylate species can serve as viable sources of the $[Mn(CO)_2(CNAr^{Dipp2})_2]^+$ fragment under reductive conditions or with the use of Lewis acidic reagents. Finally, the stability of $Mn(CO)_3(CNAr^{Dipp2})_2$ permitted a thorough electrochemical study of the Mn(-1/0/1) redox couple, with particular attention paid to the reduction of CO_2 by the manganate $[Mn(CO)_3(CNAr^{Dipp2})_2]^-$. The results of this

study are informative towards the design of improved Mn-based molecular catalysts for the catalytic reduction of CO_2.

In the second part of this dissertation, the development of isocyanide coordination polymers derived from the sterically encumbering diisocyanide $[CNAr^{Mes2}]_2$ is described. In particular, it was found that control over nodal geometry and ligand coordination number is accomplished for Cu(I) isocyanide coordination polymers in direct analogy to previously surveyed chemistry for molecular Cu(I) *m*-terphenyl isocyanide complexes. The ability to favor low isocyanide coordination was further utilized in the preparation of Ni-^{ISO}CN-1, the first authenticated metal-organic material utilizing zerovalent metal sites as nodes. Similar to the aforementioned Cu(I) polymers, Ni-^{ISO}CN-1 features low isocyanide coordination, which results in a formal 16 e^- count at each Ni(0) site. An assessment of the physical properties of these and other polymers is presented, providing a first glimpse into the chemistry of crystalline transition metal-isocyanide coordination polymers.

Chapter 1

Coordination Chemistry of Low-Valent Transition Metal Ions

1.1 Low Coordinate Metal Carbonyls – An Unexamined Nodal Archetype

Metal carbonyl chemistry has enjoyed a rich history beginning with the discovery of $Ni(CO)_4$ by L. Mond in 1890.[1] Since that time, carbonyl complexes of all mid-to-late transition metals have been isolated and been subjected to numerous synthetic and spectroscopic studies. A particular focus within these studies has been the development of structural and molecular orbital descriptions for coordinatively and/or electronically unsaturated metal carbonyl species, such as $Mn(CO)_5$, $Fe(CO)_4$, $Co(CO)_4$, and $Ni(CO)_3$ (Figure 1.1).[2-3] This is due to the recognition of these species as active intermediates in a variety of catalytic transformations, such as olefin isomerization, hydroformylation, and carbonylation.[4-9] However, a comprehensive evaluation of the structural and electronic parameters of this species class has been hampered by the kinetic instability inherent to many of these complexes. As a result, much of the information regarding unsaturated metal carbonyls has been derived from spectroscopic studies in cryogenic matrix-isolation and gas-phase experiments, preventing a detailed understanding of their behavior in solution.[10-20] These studies have nevertheless been crucial in the development of a proper theoretical description of the electronic structure of these species.

A case in point is the bonding and geometries of coordinatively unsaturated Mo carbonyls. Valence Shell Electron Pair Repulsion (VSEPR) and other valence

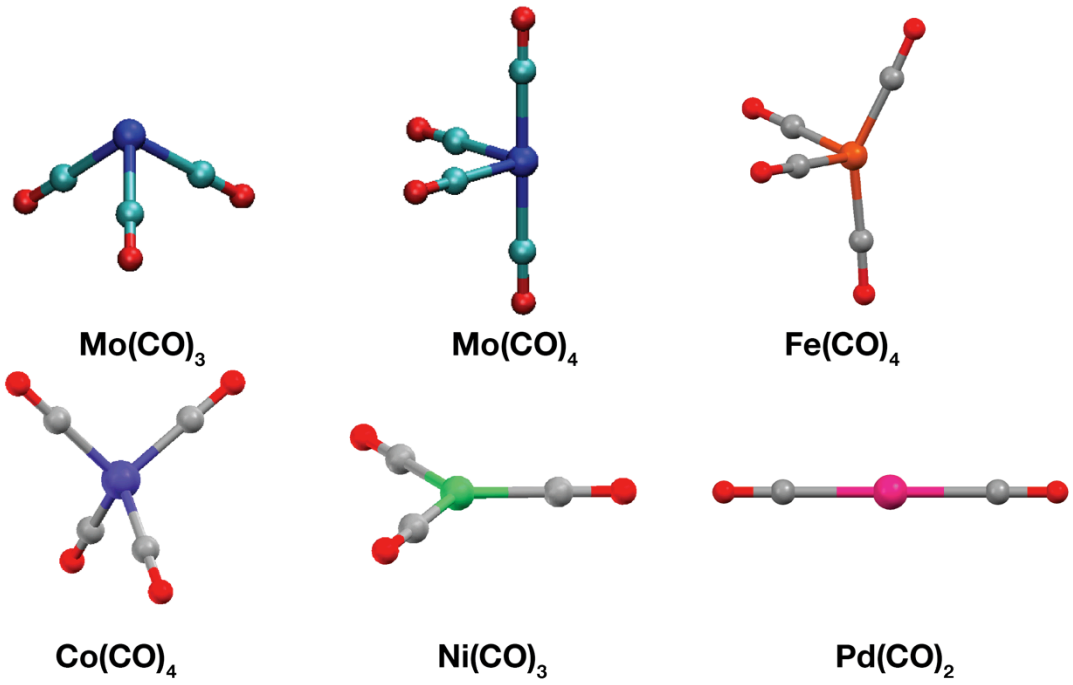

Figure 1.1. Calculated geometries for several coordinatively and/or electronically unsaturated transition metal carbonyls.

bond theories predict that the transient species $Mo(CO)_4$, $Mo(CO)_3$, and $Mo(CO)_2$ would exhibit square planar (D_{4h}), trigonal planar (D_{3h}), and linear ($C_{\infty v}$) geometries, respectively. However, it was proposed by Hoffman and Burdett that these species will instead possess *cis*-divacant octahedral (C_{2v}), trigonal pyramidal (C_{3v}), and bent (C_{2v}) geometries, respectively, to account for maximum π-backdonation from the Mo(0) metal center to the carbonyl π^*-manifold.[2, 21] This was found to be true with multiple other metal-carbonyl species, such as $Ni(CO)_3$, which contrary to VSEPR prediction adopts a trigonal planar (D_{3h}) geometry.[22] Indeed, detailed IR studies of photogenerated unsaturated metal carbonyls in the 1970s and 1980s provided experimental verification of these proposed geometric and electronic descriptions, and established a molecular orbital-based approach to understanding organometallic complexes.

It should be noted that while the aforementioned matrix-isolation studies confirmed the predictions of Hoffman and Burdett, a significant sensitivity to matrix identity was observed to affect the precise geometries of many of the unsaturated metal carbonyls under study. For example, $Fe(CO)_4$ was found to interact with both Xe and CH_4 matrices, resulting in the formation of a pseudo trigonal-bipyramidal geometry with a corresponding singlet electronic ground state, as opposed to the predicted triplet state.[23] Additionally, EPR evidence indicates that $Mn(CO)_5$, generated from γ-irradiation of $HMn(CO)_5$, forms a weak chemical bond to the Kr matrix that surrounds it.[24] Indeed, these and other data emphasize the extremely high reactivity of this species class, as well as the pitfalls of matrix-isolation and gas-phase studies.

The unusual geometries of unsaturated metal carbonyls, as well as their established reactivity patterns, would make them interesting species from which to generate polymeric networks. Accordingly, analogous complexes that effectively model the geometries and electronic ground states of metal carbonyls but permit the use of bridging ligands is necessary for this to be achieved. We have therefore targeted isocyano analogues of unsaturated metal carbonyls for the development of unique coordination polymers, using studies of molecular, mononuclear analogues as prototypical models.

1.2 *m*-Terphenyl Isocyano Analogues to Transition Metal Carbonyls

By virtue of their orthogonal and degenerate π*-orbitals, isocyanides function as effective electronic mimics of carbonyls in their capacity to engage in π-backdonation with electron rich metals (Figure 1.2).[25] A notable advantage of isocyanides lies in the variability of the ancillary –R group, which can be modified with aryl, alkyl, and even

amino[26] substituents. This has granted chemists the ability to tune both the electronic structure on the isocyanide functional group as well as adapt the steric environment to the requirements of the system at hand. Some noteworthy examples of transition metal-isocyanide complexes include N. J. Cooper's isocyanide metallates, K(18-c-6)[$Mn(CNXyl)_5$][27] and $Na[Co(CNXyl)_4]$[28], as well as J. Ellis's ferrate $Na_2[Fe(CNXyl)_4]$[29] (Xyl = 2,6-$(CH_3)_2$-(C_6H_4)), which effectively mimic the structural environment of their carbonyl analogues. These results firmly established the efficacy of isocyanide-for-CO substitution in generating molecular, isolable analogues of low-valent transition metal carbonyls. Importantly, however, like their thermally stable carbonyl counterparts, the transition metal-isocyanide complexes prepared in this fashion feature coordinative saturation at the metal center, precluding the observation of isocyano-analogues to unsaturated metal carbonyls. Accordingly, further adjustment of the ancillary –R group was deemed necessary to effect significantly higher kinetic stability to coordinatively unsaturated metal species to permit a thorough interrogation of their properties.

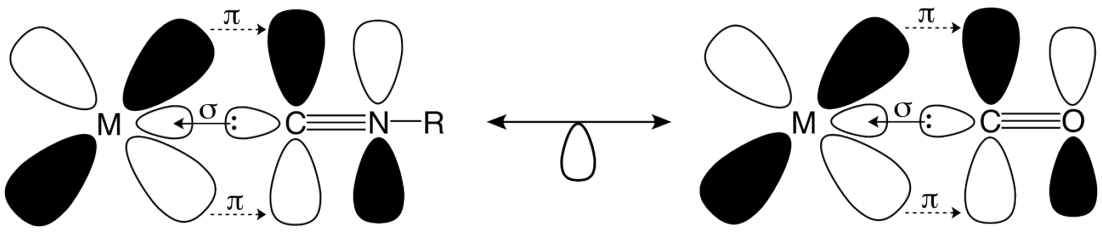

Figure 1.2. Molecular orbital scheme depicting the isolobal relationship between isocyanides and carbonyls.

Over the course of the last decade, a series of transition metal-isocyanide species have been prepared by the Figueroa group in which the isocyanide ligand incorporates a sterically encumbering *m*-terphenyl substituent as the R group (Figure 1.3).[30-47] The *m*-terphenyl group has found widespread application in organometallic chemistry as both a σ-type aryl ligand[48] as well as a supporting substituent to amido[49], phenoxy[50] and carboxylate[51] ligand types. Indeed, an important advantage of *m*-terphenyl groups is the opportunity to modulate the steric profile with alkyl and halide substituents, leading to a diverse set of applications with electronically similar ligand parameters (Figure 1.4). This has been established with *m*-terphenyl isocyanides through the quite extensive chemistry explored for mid-to-late transition metals within the Figueroa group, which has include a detailed assessment of the electronic influences of varied *m*-terphenyl groups on the isocyanide ligand character.[44]

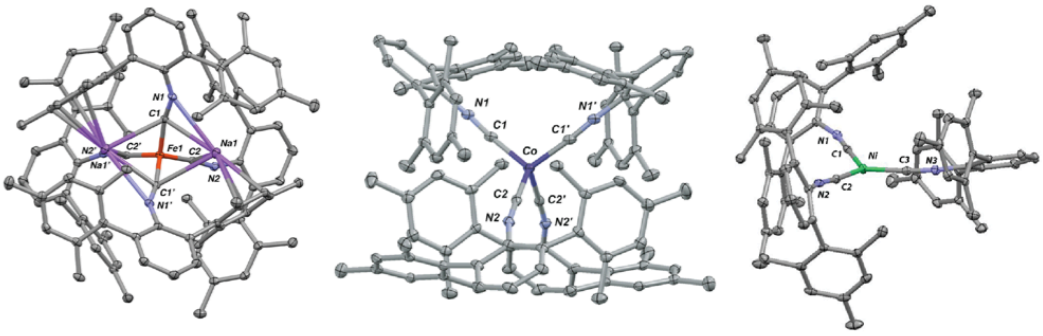

Figure 1.3. Three examples of isolated isocyano analogues to metal carbonyls; from right to left $Na_2[Fe(CNAr^{Mes2})_4]$, $Co(CNAr^{Mes2})_4$, and $Ni(CNAr^{Mes2})_3$.

The ability to generate metal species with low coordination number was established in the first report from Figueroa and coworkers, which described the preparation of a number of Cu(I)-isocyanide species using $CNAr^{Mes2}$

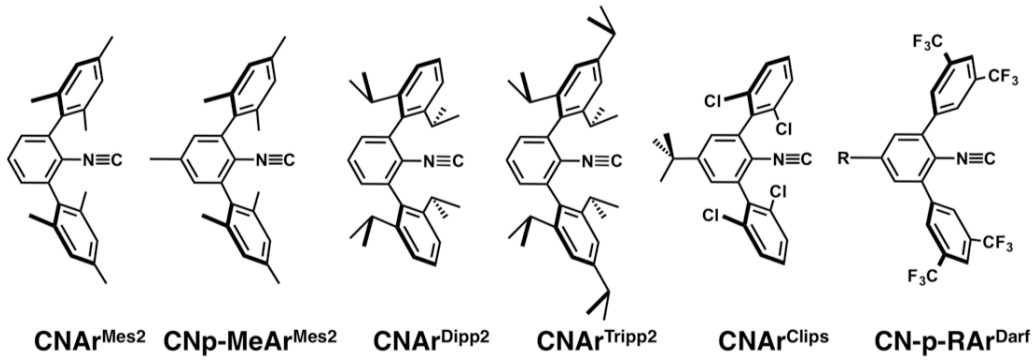

Figure 1.4. Examples of *m*-terphenyl isocyanides employed by the Figueroa group.

(Ar^{Mes2} = 2,6-(2,4,6-$Me_3C_6H_2)_2C_6H_3$).[30] Contrary to previous reports of cationic Cu(I) isocyanides[52], in which four-coordinate, tetrahedral complexes were generated, the received species when using the bulky *m*-terphenyl isocyanide $CNAr^{Mes2}$ were three-coordinate and trigonal pyramidal (Scheme 1.1), with a solvent ligand bound apically to achieve electronic saturation. Importantly, this solvento-adduct was found to be kinetically labile, allowing for access to a highly Lewis acidic Cu^+ metal center that was shown to bind benzene in an η^1-fashion. In a later report, it was found that upon moving to the more sterically-imposing $CNAr^{Dipp2}$ ligand (Ar^{Dipp2} = 2,6-(2,6-$iPrC_6H_3)_2C_6H_3$), lower isocyanide coordination numbers could be achieved such that two coordination sites were now occupied by kinetically-labile THF or the trifluoromethanesulfonate counteranion.[32] These results demonstrated the efficacy of the *m*-terphenyl ancillary substituent in aryl isocyanides for generating low-coordinate metal species.

Importantly, this concept has found success in preparing a number of isocyano analogues to low-valent, coordinatively unsaturated transition metal carbonyls. A notable example is the syntheses of $Ni(CNAr^{Mes2})_3$ and $Ni(CNAr^{Dipp2})_3$, which mirror

the geometric environment and electronic character of $Ni(CO)_3$.[31, 37] This unsaturated binary carbonyl has only been observed in gas-phase studies[22], rendering a detailed description

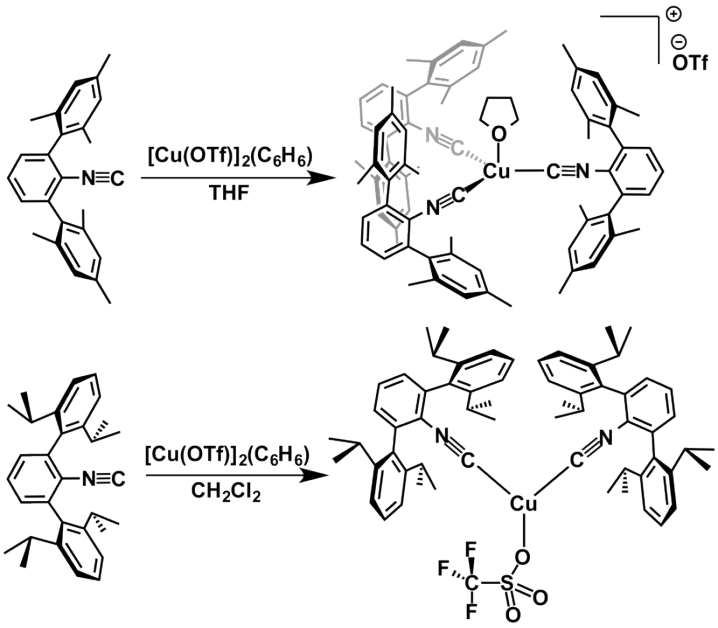

Scheme 1.1. Formation of low-coordinate Cu(I) complexes via the addition of sterically encumbering isocyanides a Cu(I) precursor.

of its geometry and general reactivity warranted. Indeed, the discovery of the above-mentioned isocyano analogues was notable in that they provided a close correlation to the electronic structure of $Ni(CO)_3$, with a non-bonding filled d_{z^2} orbital. Previous attempts to model NiL_3 analogues using phosphines resulted in a significantly altered orbital ordering in the Ni(0) center.[37, 53-54]

As a last note – one that is key to understanding the motivation behind chapters 2-4 – the isocyanide-for-carbonyl analogy has limits, many of which are exposed upon moving to mid-row transition metals. An early example of this is found in N. J. Cooper's manganese isonitrilate K(18-c-6)[$Mn(CNXyl)_5$], which despite being an adequate geometric model of the analogous carbonyl manganate $[Mn(CO)_5]^-$

demonstrated divergent reactivity under similar reaction conditions (Scheme 1.2). It has been known for some time that addition of MeI to $Na[Mn(CO)_5]$ readily generates $Mn(CH_3)(CO)_5$ in appreciable yield[55-56]; however, repetition of these synthetic conditions with the homoleptic isonitrilate instead generates a Mn(I) κ^2-1,2-diazabutadien-2yl complex via double isocyanide insertion and ligand redistribution.[57] This process is believed to occur as a result of the much higher electron density on Mn by virtue of the higher σ-donor/π-acceptor ratio for isocyanides with respect to carbonyls.[58-61]

Based upon these results, Figueroa and coworkers initially sought a mixed isocyanide/carbonyl ligand field in their studies of *m*-terphenyl isocyanide-supported Mn complexes, as the higher π-acidity of the carbonyls would help mitigate electron density buildup at the metal center. An appropriate compromise was found with the complex $Na[Mn(CO)_3(CNAr^{Dipp2})_2$, which mirrored much of the previously surveyed reaction chemistry of $[Mn(CO)_5]^-$ (Scheme 1.2).[34] Importantly, however, the sterically crowded environment fostered by the *m*-terphenyl ancillary group rendered unusual metal species isolable, and has enabled new reactivities to emerge. Accordingly, this ligand framework was utilized to further delineate reactivity trends for low-valent Mn in π-acidic ligand fields.

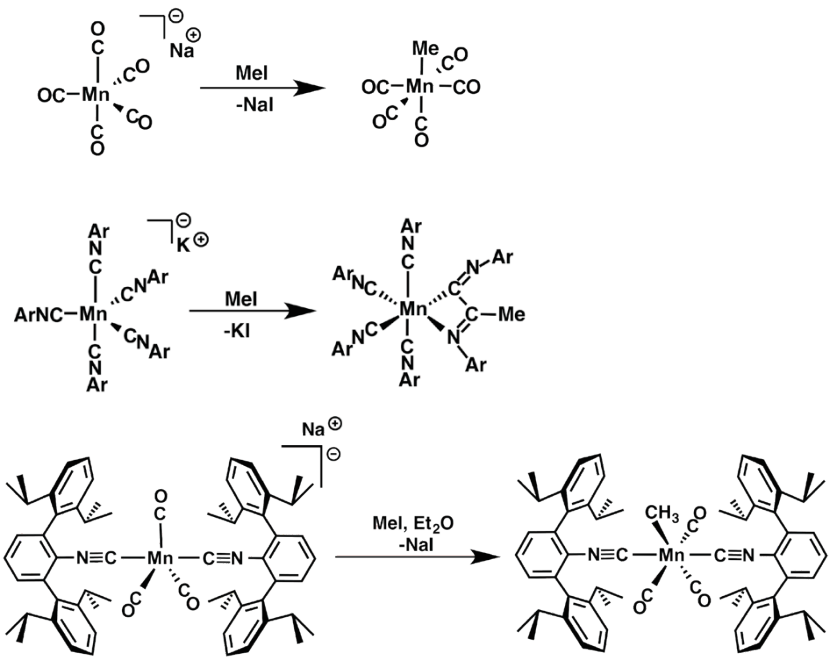

Scheme 1.2. The reactivity of three isoelectronic manganate complexes with MeI.

1.3 Utilizing Low-Valent Coordination Complexes as Directing Nodes in Polymeric Materials

The advent of modern coordination chemistry, as defined by Alfred Werner, was a watershed moment in the progress of inorganic chemistry.[62] Knowledge of preferred coordination, valence, and geometry about metal ions ushered in dramatic advances in the synthesis, structure and reactivity of novel molecular complexes. However, it was not until over half a century later was it realized that these coordination properties could be utilized in the generation of multidimensional polymeric networks, termed *coordination polymers*, wherein metal-ligand geometry established the underlying topology and connectivity of the superstructure.[63] The variety of available geometries, metal-ligand combinations, and ion valences has resulted in the rapid growth of coordination polymer research, and has enabled

targeted designs for applications such as gas storage[64-65], gas separations[66], sensing[67], catalysis[68], and more recently electronics[69] and energy storage.[70-71] As a result, coordination polymer research continues to be an area of intense interest in the chemical and engineering community.

A key feature found in almost all coordination polymers reported to date has been the reliance on high-valent metal ions for nodal formation.[72] This is a result of the well-known geometries encountered for these ions, as well as their general stability towards aqueous and aerobic conditions. Accordingly, a complementary set of anionic ligand types have been employed for framework formation, such as carboxylates, tetrazolates, and imidazolates, with pyridines and nitriles being the notable exception as neutral ligands.[73] While significant effort to modulate the properties of these ligands has been undertaken in the last 20 years[74-75], the consistent use of high-valent metal ions effectively restricts the potential of coordination polymers to address certain challenges in heterogeneous catalysis and gas separations. By refocusing on the development of alternative nodal metal ions, such as those in low-valent oxidation states, the principle of geometric framework design can be preserved while allowing for unprecedented functionality.

The geometries that describe the coordination environment for metal complexes in low valent oxidation states (eg. -2, -1, 0) are generally the same as those for higher valent metal species.[76] For example, the zerovalent group 6 carbonyls (Cr, Mo, W) form octahedrons with six carbonyl ligands, an identical geometry to that observed for the ferricyanide ion (Fe^{III}), which forms the metal-ligand node for the ubiquitous Prussian Blue dye.[77] Alternatively, $Ni(CO)_4$ and $[Co(CO)_4]^-$, both of which

contain d^{10} metal ions, assume tetrahedral geometries like those of the Cu(I)-tetracyano nodes underlying R. Robson's groundbreaking metal-organic material described in 1989.[78] Indeed, many more geometric comparisons can be drawn between currently employed nodal sites and molecular examples of low-valent organometallic species, underscoring the feasibility of using low-valent metal ions as the directing nodes in coordination polymers.

Interestingly, early attempts to incorporate this rationale predate the large bulk of coordination polymer research. In 1980, Efraty, Feinstein and coworkers described the preparation of a material in which diisocyanoarene ligands were used to link [Rh(I)Cl] metal centers to form infinite 2-dimensional sheets.[79] The choice of isocyanide ligands resulted from the similar ligand properties to carbonyls, a common ligand for reduced metal ions; both are linear with comparable σ-donor/π-acceptor qualities, and can stabilize a range of electron-rich metals, as discussed in section 1.2.[58, 80-81] Moreover, linear diisocyanoarene ligands are structurally inflexible, enabling the formation of rigid, multidimensional metal-organic solids.[82] As a result, multiple reports were made that described materials developed from the addition of diisocyanoarenes to other Rh(I) starting materials[83-85], as well as low-valent Cr(0), Mo(0), W(0), Mn(I), Pd(0) and Cu(I) precursors.[86-89] However, while spectroscopic evidence was found to support the formation of polymeric solids containing low-valent metals, a complete structural description of these materials remained unaccomplished. Perhaps as a result of this, research into this subset of coordination polymers largely disappeared throughout the 1990s and 21st century, and accordingly there is a paucity of data regarding coordination polymer materials of this type.

1.4Outlook

Enabling stability for low-valent metal species, often in low-coordination, is a central theme throughout this thesis. This is applied in the study not just of their intrinsic reactivity but also in evaluating coordinative preference in solution and solid states. Chapters 2-4 will discuss this in the context of molecular Mn carbonyl/isocyanide chemistry. The extrapolation of this theme will be conducted in Chapters 5-7, wherein the conceptual groundwork discussed in sections 1.2 and 1.3 will be applied to generating infinite framework materials.

1.5 References

1. Mond, L.; Langer, C.; Quincke, F., *Journal of the Chemical Society, Transactions* **1890,** *57*, 749.
2. Elian, M.; Hoffmann, R., *Inorg. Chem.* **1975,** *14*, 1058.
3. Burdett, J. K., *Inorg. Chem.* **1975,** *14*, 375.
4. Bailey, D. C.; Langer, S. H., *Chem. Rev.* **1981,** *81*, 109.
5. Moggi, L.; Juris, A.; Sandrini, D.; Manfrin, M. F., *Reviews of Chemical Intermediates* **1981,** *4*, 171.
6. Schroeder, M. A.; Wrighton, M. S., *J. Am. Chem. Soc.* **1976,** *98*, 551.
7. A. Schroeder, M.; S. Wrighton, M., *J. Organomet. Chem.* **1977,** *128*, 345.
8. Andrews, M. A.; Cheng, C. W. F., *J. Am. Chem. Soc.* **1982,** *104*, 4268.
9. Franke, R.; Selent, D.; Börner, A., *Chem. Rev.* **2012,** *112*, 5675.
10. Wrighton, M. S.; Ginley, D. S., *J. Am. Chem. Soc.* **1975,** *97*, 2065.
11. Perutz, R. N.; Turner, J. J., *J. Am. Chem. Soc.* **1975,** *97*, 4791.
12. Perutz, R. N.; Turner, J. J., *Inorg. Chem.* **1975,** *14*, 262.
13. Fletcher, T. R.; Rosenfeld, R. N., *J. Am. Chem. Soc.* **1985,** *107*, 2203.

14. Fletcher, T. R.; Rosenfeld, R. N., *J. Am. Chem. Soc.* **1986,** *108*, 1686.

15. Ishikawa, Y.; Hackett, P. A.; Rayner, D. M., *The Journal of Physical Chemistry* **1988,** *92*, 3863.

16. Ganske, J. A.; Rosenfeld, R. N., *The Journal of Physical Chemistry* **1989,** *93*, 1959.

17. Andrews, L.; Zhou, M.; Gutsev, G. L., *Journal of Physical Chemistry A* **2003,** *107*, 990.

18. Symons, M. C. R.; Sweany, R. L., *Organometallics* **1982,** *1*, 834.

19. Church, S. P.; Poliakoff, M.; Timney, J. A.; Turner, J. J., *J. Am. Chem. Soc.* **1981,** *103*, 7515.

20. Breeze, P. A.; Burdett, J. K.; Turner, J. J., *Inorg. Chem.* **2002,** *20*, 3369.

21. Burdett, J. K.; Graham, M. A.; Perutz, R. N.; Poliakoff, M.; Rest, A. J.; Turner, J. J.; Turner, R. F., *J. Am. Chem. Soc.* **1975,** *97*, 4805.

22. Rest, A. J.; Turner, J. J., *Journal of the Chemical Society D: Chemical Communications* **1969**, 1026.

23. Poliakoff, M.; Turner, J. J., *Angewandte Chemie International Edition* **2001,** *40*, 2809.

24. Fairhurst, S. A.; Morton, J. R.; Perutz, R. N.; Preston, K. F., **1984,** *3*, 1389.

25. It is important to note that isocyanides are generally recognized to exhibit higher σ-donor/π-acceptor ratios than carbonyls, which in some cases leads to substantive differences in the electronic structure of the resulting metal complexcompared to the corresponding metal carbonyl.

26. Fehlhammer, W. P.; Schoder, F.; Weinberger, B.; Stolzenberg, H.; Beck, W., *Z. Anorg. Allg. Chem.* **2009,** *635*, 1367.

27. L Utz, T.; A Leach, P.; J Geib, S.; John Cooper, N., *Chem. Commun.* **1997**, 847.

28. Warnock, G. F.; Cooper, N. J., *Organometallics* **1989,** *8*, 1826.

29. Brennessel, W. W.; Ellis, J. E., *Angewandte Chemie International Edition* **2007,** *46*, 598.

30. Fox, B. J.; Sun, Q. Y.; DiPasquale, A. G.; Fox, A. R.; Rheingold, A. L.; Figueroa, J. S., *Inorg. Chem.* **2008,** *47*, 9010.

31. Fox, B. J.; Millard, M. D.; DiPasquale, A. G.; Rheingold, A. L.; Figueroa, J. S., *Angewandte Chemie International Edition* **2009,** *48*, 3473.

32. Ditri, T. B.; Fox, B. J.; Moore, C. E.; Rheingold, A. L.; Figueroa, J. S., *Inorg. Chem.* **2009,** *48*, 8362.

33. Labios, L. A.; Millard, M. D.; Rheingold, A. L.; Figueroa, J. S., *J. Am. Chem. Soc.* **2009,** *131*, 11318.

34. Stewart, M. A.; Moore, C. E.; Ditri, T. B.; Labios, L. A.; Rheingold, A. L.; Figueroa, J. S., *Chem. Commun.* **2010,** *47*, 406.

35. Margulieux, G. W.; Weidemann, N.; Lacy, D. C.; Moore, C. E.; Rheingold, A. L.; Figueroa, J. S., *J. Am. Chem. Soc.* **2010,** *132*, 5033.

36. Ditri, T. B.; Moore, C. E.; Rheingold, A. L.; Figueroa, J. S., *Inorg. Chem.* **2011,** *50*, 10448.

37. Emerich, B. M.; Moore, C. E.; Fox, B. J.; Rheingold, A. L.; Figueroa, J. S., *Organometallics* **2011,** *30*, 2598.

38. Carpenter, A. E.; Margulieux, G. W.; Millard, M. D.; Moore, C. E.; Weidemann, N.; Rheingold, A. L.; Figueroa, J. S., *Angewandte Chemie International Edition* **2012,** *51*, 9412.

39. Ditri, T. B.; Carpenter, A. E.; Ripatti, D. S.; Moore, C. E.; Rheingold, A. L.; Figueroa, J. S., *Inorg. Chem.* **2013,** *52*, 13216.

40. Barnett, B. R.; Moore, C. E.; Rheingold, A. L.; Figueroa, J. S., *J. Am. Chem. Soc.* **2014,** *136*, 10262.

41. Carpenter, A. E.; McNeece, A. J.; Barnett, B. R.; Estrada, A. L.; Mokhtarzadeh, C. C.; Moore, C. E.; Rheingold, A. L.; Perrin, C. L.; Figueroa, J. S., *J. Am. Chem. Soc.* **2014,** *136*, 15481.

42. Mokhtarzadeh, C. C.; Margulieux, G. W.; Carpenter, A. E.; Weidemann, N.; Moore, C. E.; Rheingold, A. L.; Figueroa, J. S., *Inorg. Chem.* **2015,** *54*, 5579.

43. Agnew, D. W.; Moore, C. E.; Rheingold, A. L.; Figueroa, J. S., *Angewandte Chemie International Edition* **2015,** *54*, 12673.

44. Carpenter, A. E.; Mokhtarzadeh, C. C.; Ripatti, D. S.; Havrylyuk, I.; Kamezawa, R.; Moore, C. E.; Rheingold, A. L.; Figueroa, J. S., *Inorg. Chem.* **2015,** *54*, 2936.

45. Carpenter, A. E.; Rheingold, A. L.; Figueroa, J. S., *Organometallics* **2016,** *35*, 2309.

46. Mokhtarzadeh, C. C.; Rheingold, A. L.; Figueroa, J. S., *Dalton Trans.* **2016**, 14561.

47. Agnew, D. W.; Sampson, M. D.; Moore, C. E.; Rheingold, A. L.; Kubiak, C. P.; Figueroa, J. S., *Inorg. Chem.* **2016,** *55*, 12400.

48. Clyburne, J. A. C.; McMullen, N., *Coord. Chem. Rev.* **2000,** *210*, 73.

49. Gavenonis, J.; Tilley, T. D., *Organometallics* **2002,** *21*, 5549.

50. Dickie, D. A.; MacIntosh, I. S.; Ino, D. D.; He, Q.; Labeodan, O. A.; Jennings, M. C.; Schatte, G.; Walsby, C. J.; Clyburne, J. A. C., *Can. J. Chem.* **2008,** *86*, 20.

51. Yoon, S.; Lippard, S. J., *J. Am. Chem. Soc.* **2005,** *127*, 8386.

52. Bowmaker, G. A.; Hanna, J. V.; Hahn, F. E.; Lipton, A. S.; Oldham, C. E.; Skelton, B. W.; Smith, M. E.; White, A. H., *Dalton Trans.* **2008**, 1710.

53. Gosser, L. W.; Tolman, C. A., *Inorg. Chem.* **1970,** *9*, 2350.

54. Aresta, M.; Nobile, C. F.; Sacco, A., *Inorg. Chim. Acta* **1975,** *12*, 167.

55. Andersen, J.-A. M.; Moss, J. R., *Organometallics* **1994,** *13*, 5013.

56. Noack, K.; Calderazzo, F., *J. Organomet. Chem.* **1967,** *10*, 101.

57. Utz, T. L.; Leach, P. A.; Geib, S. J.; Cooper, N. J., *Organometallics* **1997,** *16*, 4109.

58. Sarapu, A. C.; Fenske, R. F., *Inorg. Chem.* **1975,** *14*, 247.

59. Treichel, P. M., *Adv. Organomet. Chem.* **1973,** *11*, 2.

60. Mueh, H. J.; Treichel, P. M., **1977,** *22*, 265.

61. Barybin, M. V.; Meyers, J. J.; Neal, B. M., Renaissance of Isocyanoarenes as Ligands in Low-Valent Organometallics. In *Isocyanide Chemistry*, Wiley-VCH Verlag GmbH & Co. KGaA: 2012; pp 493.

62. Bowman-James, K., *Acc. Chem. Res.* **2005,** *38*, 671.

63. Bailar, J. C., *Prep. Inorg. React.* **1964,** *1*.

64. Yaghi, O. M.; Li, H.; Eddaoudi, M.; O'Keeffe, M., *Nature* **1999,** *402*, 276.

65. Murray, L. J.; Dinca, M.; Long, J. R., *Chem. Soc. Rev.* **2009,** *38*, 1294.

66. Li, J.-R.; Sculley, J.; Zhou, H.-C., *Chem. Rev.* **2012,** *112*, 869.

67. Kreno, L. E.; Leong, K.; Farha, O. K.; Allendorf, M.; Van Duyne, R. P.; Hupp, J. T., *Chem. Rev.* **2012,** *112*, 1105.

68. Lee, J.; Farha, O. K.; Roberts, J.; Scheidt, K. A.; Nguyen, S. T.; Hupp, J. T., *Chem. Soc. Rev.* **2009,** *38*, 1450.

69. Stavila, V.; Talin, A. A.; Allendorf, M. D., *Chem. Soc. Rev.* **2014,** *43*, 5994.

70. Aubrey, M. L.; Long, J. R., *J. Am. Chem. Soc.* **2015,** *137*, 13594.

71. Sheberla, D.; Bachman, J. C.; Elias, J. S.; Sun, C.-J.; Shao-Horn, Y.; Dinca, M., *Nat. Mater.* **2017,** *16*, 220.

72. Cook, T. R.; Zheng, Y.-R.; Stang, P. J., *Chem. Rev.* **2013,** *113*, 734.

73. Kitagawa, S.; Kitaura, R.; Noro, S.-i., *Angewandte Chemie International Edition* **2004,** *43*, 2334.

74. Wang, Z.; Cohen, S. M., *Chem. Soc. Rev.* **2009,** *38*, 1315.

75. Cohen, S. M., *Chem. Rev.* **2012,** *112*, 970.

76. Cotton, F. A.; Wilkinson, G., *Advanced Inorganic Chemistry*. 5th ed.; John Wiley and Sons: 1988.

77. Greenwood, N. N.; Earnshaw, A., *Chemistry of the Elements*. 2nd ed.; Elsevier: 2015.

78. Hoskins, B. F.; Robson, R., *J. Am. Chem. Soc.* **1989,** *111*, 5962.

79. Efraty, A.; Feinstein, I.; Frolow, F.; Wackerle, L., *J. Am. Chem. Soc.* **1980,** *102*, 6341.

80. Bonati, F.; Malatesta, L., *Isocyanide Complexes of Metals*. Wiley: 1969.

81. Yamamoto, Y., **1980,** *32*, 193.

82. Efraty, A.; Feinstein, I.; Wackerle, L.; Goldman, A., *The Journal of Organic Chemistry* **1980,** *45*, 4059.

83. Efraty, A.; Feinstein, I.; Wackerle, L.; Frolow, F., *Angewandte Chemie International Edition* **1980,** *19*, 633.

84. Feinstein-Jaffe, I.; Efraty, A., *Macromolecules* **1986,** *19*, 2076.

85. Efraty, A.; Feinstein, I.; Frolow, F.; Goldman, A., *J. Chem. Soc., Chem. Commun.* **1980**, 864.

86. Efraty, A.; Feinstein, I.; Wackerle, L., *J. Organomet. Chem.* **1981,** *220*, 333.

87. Feinstein-Jaffe, I.; Biran, I.; Mahalu, D.; Cohen, S.; Lawrence, S. A., *Inorg. Chim. Acta* **1988,** *154*, 129.

88. Feinstein-Jaffe, I.; Efraty, A., *J. Mol. Catal.* **1986,** *35*, 285.

89. Feinstein-Jaffe, I.; Maisuls, S. E., *J. Organomet. Chem.* **1988,** *350*, 57.

Chapter 2

Insights into the Chemistry of Zero-Valent Manganese: Isolation of a Pentacoordinate Manganese(0) Monoradical

2.1 Introduction

For decades, transiently generated $17e^-$ monoradicals have occupied a central role in the development of atom-transfer and radical-mediated processes in organometallic chemistry.[1-3] A prototypical example of this class is the zerovalent manganese pentacarbonyl radical, $Mn(CO)_5$, which has been extensively investigated for its role in radical-type olefin hydrogenation,[4,5] as well as in the photolytic cleavage of the Mn-Mn bond of $Mn_2(CO)_{10}$.[6] Despite these studies, $Mn(CO)_5$ is well recognized as a highly unstable, organometallic transient, which rapidly dimerizes to $Mn_2(CO)_{10}$ via Mn-Mn bond formation. Accordingly, this instability has necessitated that $Mn(CO)_5$ be characterized and studied under cryogenic conditions,[7-10] or at higher temperatures by using either ultrafast spectroscopic[11] or nitrosoarene spin-trapping techniques.[12-14] Importantly, efforts to prepare stabilized variants of $Mn(CO)_5$ by substitution of one or more CO ligands with more encumbering ligands such as phosphines (PR_3) have been shown to extend the lifetime of MnL_5-type radicals to the order of hours in solution.[15-18] However, such derivatized $Mn(CO)_{5-n}L_n$ complexes have remained susceptible to facile dimerization/redistribution processes when concentrated and isolable examples remain unknown. In addition, investigations into the $1e^-$ activation chemistry of $Mn(CO)_{5-n}L_n$ species with small molecule substrates are limited.[16,17]

Given the challenges faced in exploring the properties of $Mn(CO)_5$ and related zerovalent MnL_5 complexes, it is notable that they continue to be of significant interest as transient species. For example, MnL_5 monoradicals of the type $Mn(CO)_3(bipy)$ (bipy = 2,2'-bipyridine) are now recognized as the key intermediates on the pathway to catalyst deactivation (via Mn-Mn bond formation) in electrocatalytic CO_2 reduction.[19-21] Accordingly, successful strategies leading to the kinetic stabilization and isolation of such MnL_5 monoradicals, while explicitly preventing the formation of the common Mn-Mn single bond motif, are of importance in these processes. Furthermore, access to long-lived MnL_5 monoradicals offer a potential avenue for the development of selective, well-defined metal-mediated $1e^-$ transformations. Herein we describe the isolation, structure and spectroscopic features of the neutral monoradical $Mn(CO)_3(CNAr^{Dipp2})_2$ (Ar^{Dipp2} = 2,6-(2,6-(*i*-Pr)$_2$C$_6$H$_3$)$_2$C$_6$H$_3$) featuring two *m*-terphenyl isocyanide ligands.[22,23] The encumbering nature of this isocyanide ligand effectively prevents the formation of Mn-Mn single bonds, thus rendering this $17e^-$ radical both isolable in the solid state and persistent in solution. In addition, due to the isolobal analogy between carbon monoxide (CO) and organoisocyanides (C≡NR),[22,24] $Mn(CO)_3(CNAr^{Dipp2})_2$ serves as a precise electronic structure mimic of archetypical $Mn(CO)_5$. Most importantly, a survey of the chemistry accessible to $Mn(CO)_3(CNAr^{Dipp2})_2$ has afforded new insights into classic spin-trapping experiments of $Mn(CO)_5$ due to the ability to conveniently investigate a kinetically stabilized MnL_5 monoradical under ambient conditions.

2.2 Preparation and Characterization Of $Mn(CO)_3(CNAr^{Dipp2})_2$.

Monoradical $Mn(CO)_3(CNAr^{Dipp2})_2$ (**1**) can be generated by three independent synthetic routes (Scheme 2.1). Oxidation of the sodium salt[25] $Na[Mn(CO)_3(CNAr^{Dipp2})_2]$ with 1.0 equiv of thallium triflate (TlOTf; OTf = $[O_3SCF_3]^-$) leads to **1** with loss of Tl metal and NaOTf, while comproportionation of $Na[Mn(CO)_3(CNAr^{Dipp2})_2$ and the triflate complex, $Mn(OTf)(CO)_3(CNAr^{Dipp2})_2$, delivers **1** with only NaOTf as a byproduct. In addition, **1** can be obtained under photolytic conditions by irradiation of $Mn_2(CO)_{10}$ in the presence of 4.0 equiv of $CNAr^{Dipp2}$. In all preparations, complex **1** is obtained as a dark-green crystalline solid that possesses limited solubility in alkanes solvents, but is well solubilized in both ethereal and aromatic solvents. Of these three methods, comproportionation of $Na[Mn(CO)_3(CNAr^{Dipp2})_2$ and $Mn(OTf)(CO)_3(CNAr^{Dipp2})_2$ delivers **1** most cleanly and in highest isolated yield (92%). Upon isolation, **1** retains its integrity for days in solution at elevated temperatures (C_6D_6, 80 ˚C) and shows no sign of dimerization and/or ligand redistribution when concentrated to a solid.

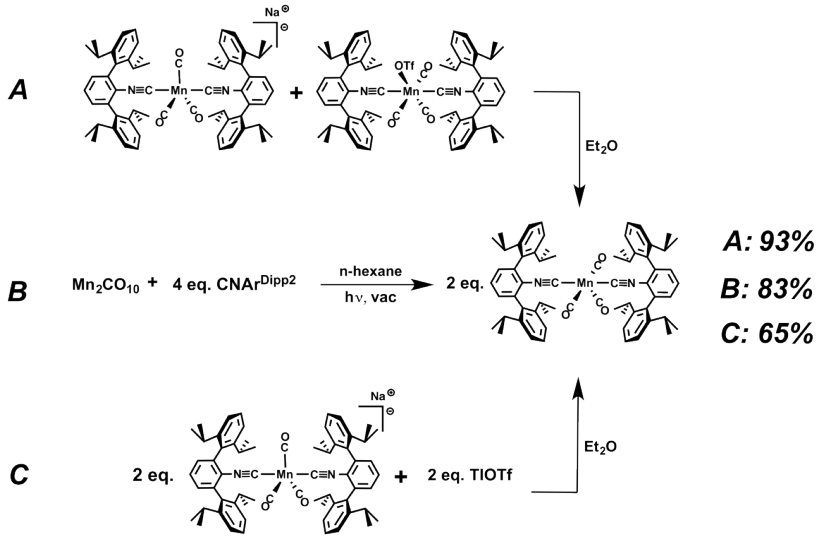

Scheme 2.1. Preparation of $Mn(CO)_3(CNAr^{Dipp2})_2$ *via* three different routes.

In both solution and the solid state, complex **1** possesses several spectroscopic and structural features consistent with a d^7 monoradical formulation. The ^{1}H NMR spectrum of **1** in C_6D_6 features broad, shifted resonances characteristic of a paramagnetic species, while Evans method magnetic moment determination (C_6D_6, 20 ˚C) revealed a m_{eff} value of 1.89(±0.04) μ_B indicative of an S = ½ ground state. The room temperature EPR spectrum of **1** (Figure 2.1) supports this assignment and shows a well-resolved six line pattern consistent with a single unpaired electron within a ^{55}Mn I = 5/2 spin environment. Importantly, the isotropic g and Mn hyperfine coupling values of g_{iso} = 2.075 and $A_{iso}(^{55}Mn)$ = 11.4 G are similar to those determined for persistent, but non-isolable, $Mn(CO)_3(PR_3)_2$ complexes[15,18] and accordingly reflect the presence of a low-spin, zerovalent Mn center. In addition, the IR spectrum (C_6D_6) of **1** features a ν_{CN} band centered at 2048 cm^{-1}. This band is located at an intermediate energy relative to the formally Mn(I) and Mn(–1) complexes $Mn(OTf)(CO)_3(CNAr^{Dipp2})_2$ (2131 cm^{-1}) and $Na[Mn(CO)_3(CNAr^{Dipp2})_2]$ (1910 cm^{-1}),[25] respectively, and is likewise indicative of a zerovalent Mn center.

Single crystals of $Mn(CO)_3(CNAr^{Dipp2})_2$ **1** were reproducibly obtained by crystallization from a layered Et_2O/*n*-pentane mixture at –35 ˚C.In the solid-state, **1** adopts a square-pyramidal coordination geometry (Addison–Reedijk τ_5 geometry index[26] = 0.03) with *trans*-spanning $CNAr^{Dipp2}$ ligands within the equatorial plane (Figure 2.2). This geometry is consistent with a $e(xz,yz)^4b_2(xy)^2a_1(z^2)^1b_1(x^2\text{-}y^2)^0$ d-orbital splitting pattern in idealized C_{4v} symmetry, as has been proposed for the ground state geometry and electronic configuration for the d^7 monoradical $Mn(CO)_5$.[27] In addition, the molecular structure of **1** possesses an average C-Mn-C angle between the

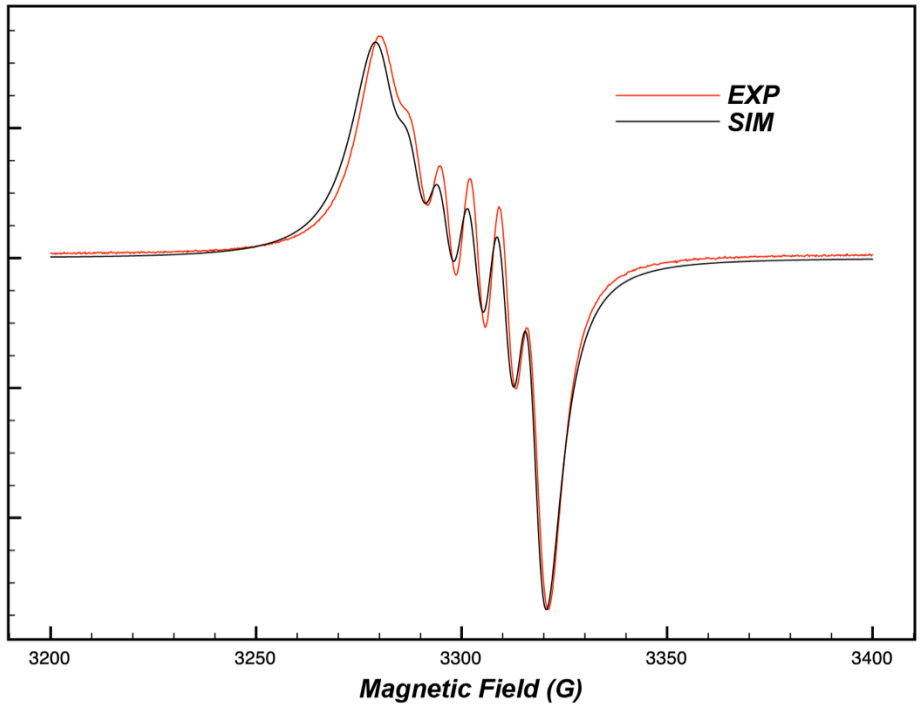

Figure S2.1. EPR spectrum of $Mn(CO)_3(CNAr^{Dipp2})_2$ (**1**) at 295 K in Et_2O (0.05 mM), with simulated spectrum in black. Simulation of the spectrum yielded the isotropic values g_{iso} = 2.0755; $A_{iso}(Mn)$ = 11.4 G; μ_{eff} = 1.797 μ_B. The parameters used for the fit are *g* = [2.0737, 2.0695, 2.0833]; A(Mn) = [9.34, 12.39, 12.44] (in G); line broadening (Gaussian) = 0.0052; rotational correlation time: 1 x $10^{-7.7891}$ s. The slight anisotropy in the simulated spectrum arises from rotational tumbling below the diffusion limit. For other examples of small molecule EPR spectra within the fast, but not isotropic, motion regime, see: a) K. A. Earle, D. E. Budil, J. H. Freed *J. Phys. Chem.* **1993**, *97*, 13289-13297. b) S. Stoll, A. Schweiger *Biol. Magn. Reson.* **2007**, *27*, 299-321.

axial carbonyl and the basal plane ligands of 96.4(+/- 2.7)˚. This structural property is in excellent agreement with the axial/basal plane angle of 98˚ predicted by Hoffmann for the C_{4v}-symmetric d^7 monoradical $Mn(CO)_5$, and arises in order to maximize p-backbonding interactions between the partially occupied Mn dz^2 orbital and the basal plane ligands.[27] Indeed, a DFT-derived spin-density plot for the model complex $Mn(CO)_3(CNXyl)_2$ (Xyl = 2,6-$Me_2C_6H_3$) is fully consistent with this prediction and shows that spin density is located predominantly on the Mn center, but also distributed over the out-of-plane π* orbitals of the basal CO and isocyanide ligands (Figure 2.3). In addition, it is important to note that $Mn(CO)_5$ isolated in a CO matrix at 20 K has also been determined to possess an axial/basal plane angle of 96(+/- 3˚) by IR

spectroscopy.[10] Accordingly, the spectroscopic and structural features of **1** render it a precise electronic structure analogue to the highly unstable $Mn(CO)_5$ monoradical.

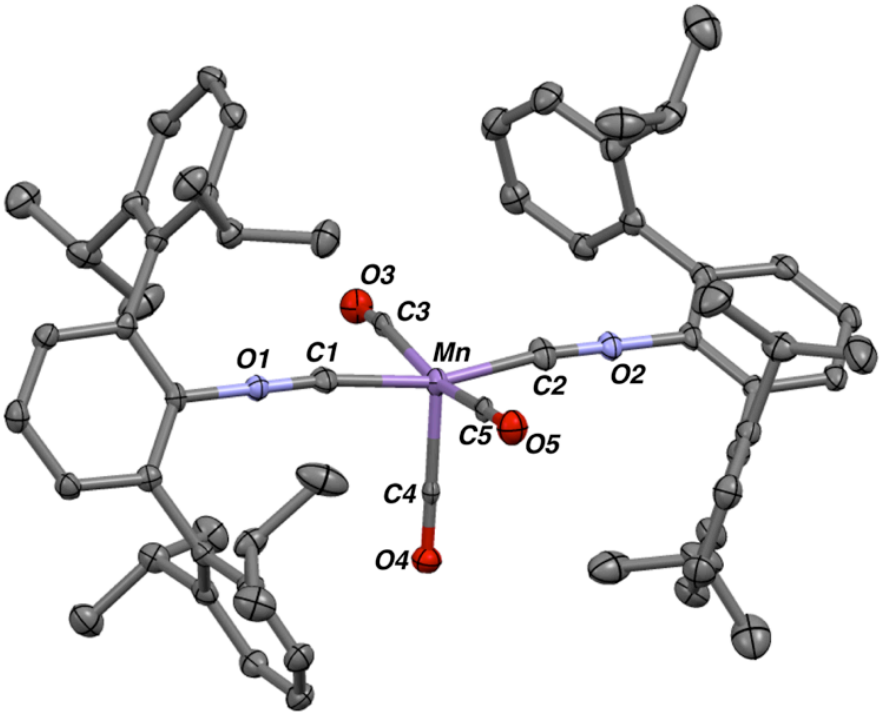

Figure 2.2. Molecular structure of $Mn(CO)_3(CNAr^{Dipp2})_2$ (**1**), with selected isopropyl groups rings and H atoms omitted for clarity. Selected bond distances (Å) and angles (˚): Mn-C1 = 1.909(3); Mn-C2 = 1.912(3); Mn-C3 = 1.882(6); Mn-C4 = 1.883(5); C1-Mn-C2 = 164.78(6); C3-Mn-C5 = 166.7(5).

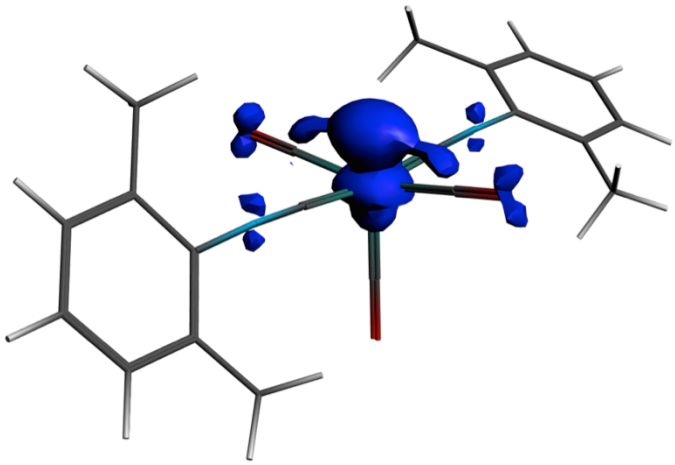

Figure 2.3. Spin density plot of $Mn(CO)_3(CNXyl)_2$ showing predominant spin build-up on the Mn metal center with delocalization onto the out-of-plane π* orbitals of the basal ligands.

2.3 Reactivity Of $Mn(CO)_3(CNAr^{Dipp2})_2$.

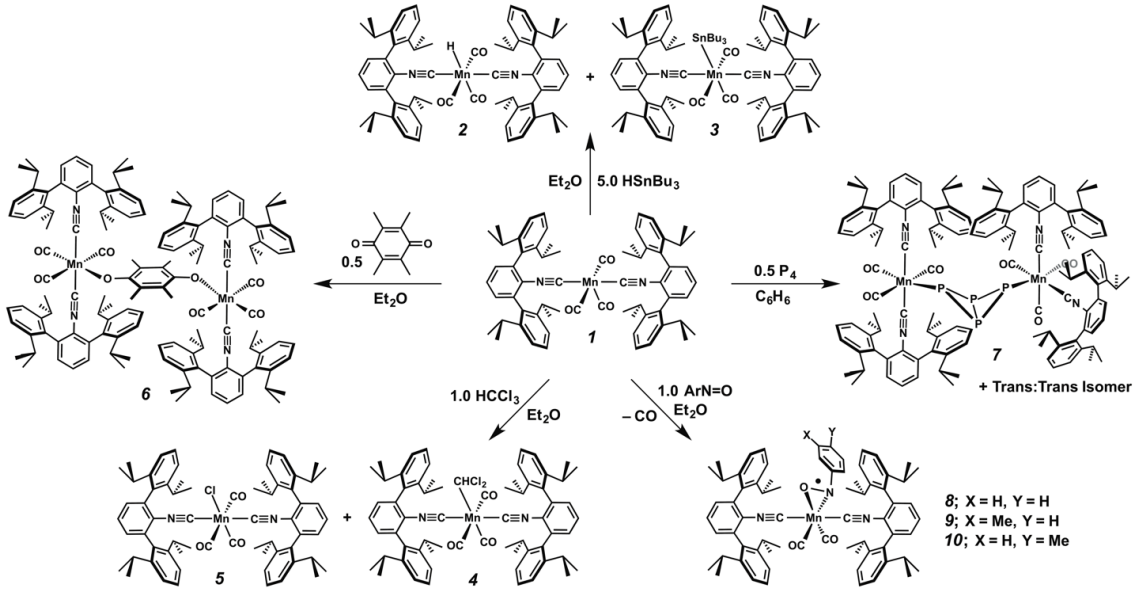

Scheme 2.2. Reaction pinwheel for complex **1**.

In addition to serving as an electronic structure model, monoradical **1** mimics the main reactivity patterns established for $Mn(CO)_5$. For example, **1** engages in hydrogen-atom abstraction reactions with substrates possessing weak H-E bonds. Treatment of **1** with an excess (> 10 equiv) of $HSnBu_3$ or stoichiometric H_2SnPh_2 in benzene solution readily affords the monohydride complex, $HMn(CO)_3(CNAr^{Dipp2})_2$ (**2**).[25] However, when **1** is exposed to lower concentrations of $HSnBu_3$ (< 5.0 equiv), an equimolar mixture of **2** and the stannyl complex $(Bu_3Sn)Mn(CO)_3(CNAr^{Dipp2})_2$ (**3**) is obtained (Figure 2). This product distribution indicates that **1** is a highly efficient radical scavenger and intercepts the tri-*n*-butyltin radical at a rate competitive with dimerization to $Bu_3Sn\text{-}SnBu_3$.[28] Similarly, **1** reacts with chloroform (1.0 equiv) in Et_2O solution to produce a 1:1 mixture of the dichloromethyl complex $(Cl_2HC)Mn(CO)_3(CNAr^{Dipp2})_2$ (**4**) and the chloride complex $ClMn(CO)_3(CNAr^{Dipp2})_2$

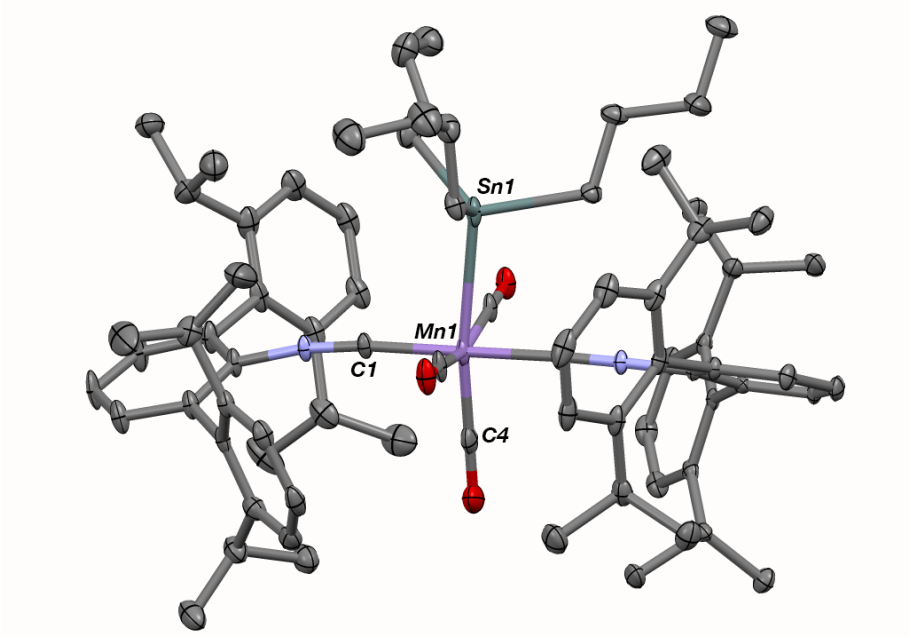

Figure 2.4. Molecular structure of $(Bu_3Sn)Mn(CO)_3(CNAr^{Dipp2})_2$ (**3**). Selected bond distances (Å) and angles (˚): Mn1-Sn1 = 2.6915(8); Mn1-C1 = 1.893(3); Mn1-C4 = 1.765(7); Sn1-Mn1-C1 = 95.13(10); Sn1-Mn1-C4 = 169.98(19).

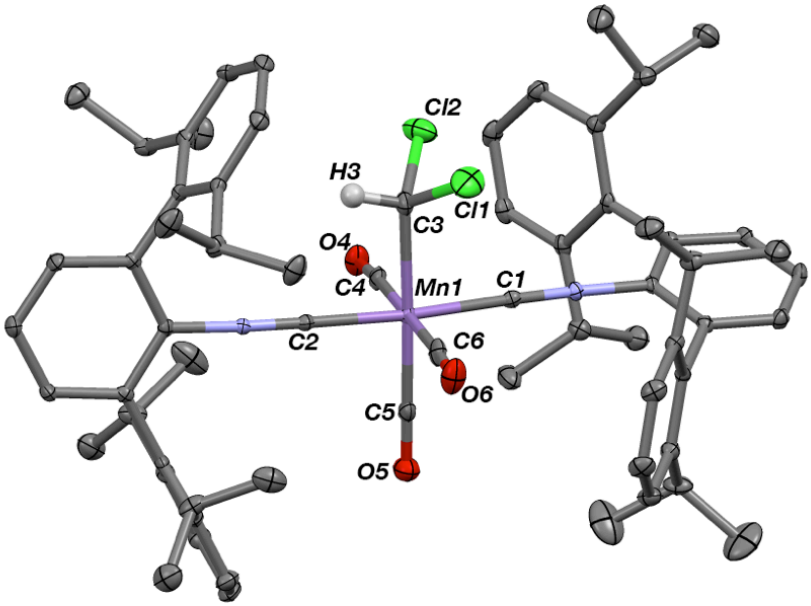

Figure 2.5. Molecular structure of $(Cl_2HC)Mn(CO)_3(CNAr^{Dipp2})_2$ (**4**), with the proton on the $CHCl_2$ unit located in the electron density map. Selected bond distances (Å) and angles (˚): Mn1-C3 = 2.113(3); C6-O6 = 1.067(4); C5-O5 = 1.110(4); C6-Mn1-C3 = 92.17(25); Mn1-C3-Cl1 = 116.29(18); Cl1-C3-Cl2 = 105.99(18).

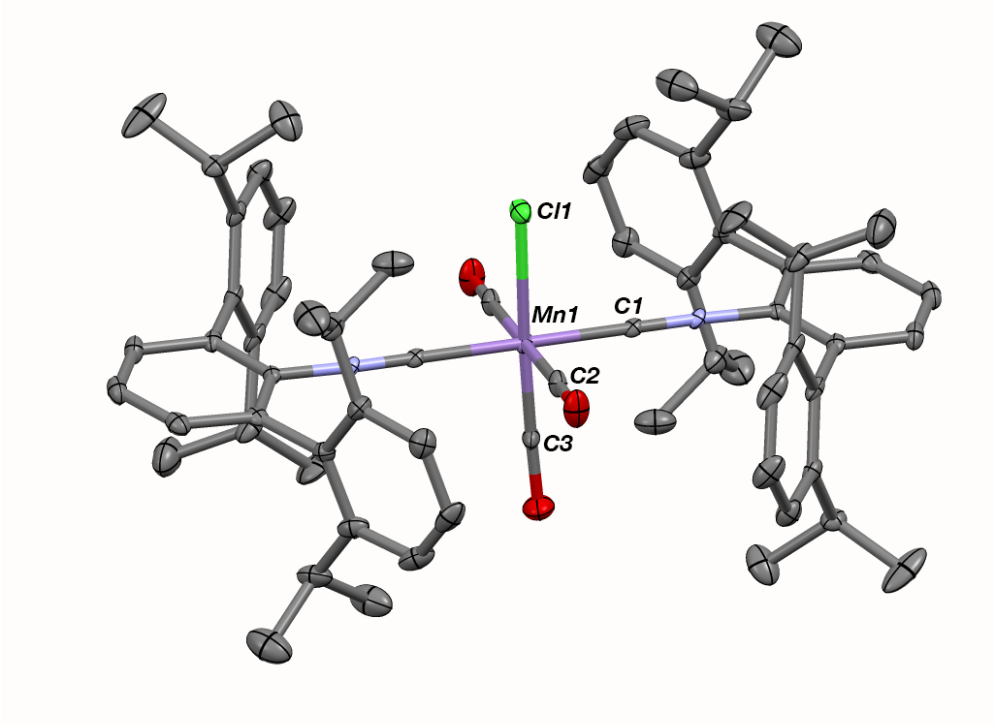

Figure 2.6. Molecular structure of $ClMn(CO)_3(CNAr^{Dipp2})_2$ (**5**). Selected bond distances (Å) and angles (°): Mn1-Cl1 = 2.416(4); Mn1-C1 = 1.922(4); Mn1-C3 = 1.732(12); Cl1-Mn1-C1 = 88.92(12); Cl1-Mn1-C3 = 177.2(4).

(**5**), again indicating a competency for both atom-abstraction and radical-scavenger reactivity patterns.

Two molecules of **1** can also cooperatively effect the $2e^-$ reduction of certain substrates. As shown in Figure 2, treatment of **1** with 0.5 equiv. of tetramethylbenzoquinone leads to reductive aromatization en route to the diamagnetic, aryloxide-bridged dimer, $(\mu_2\text{–}\kappa^1\text{:}\,\kappa^1\text{–}OC_6Me_4O)[Mn(CO)_3(CNAr^{Dipp2})_2]_2$ (**6**), as determined by ^1H NMR spectroscopy and X-ray diffraction. In addition, **1** reacts quantitatively with 0.5 equiv. of P_4 at room temperature to produce the P_4-butterfly-bridged complex $(\mu_2\text{–}\eta^1\text{:}\eta^1\text{–}P_4)[Mn(CO)_3(CNAr^{Dipp2})_2]_2$ (**7**; Figure 2.7 and 2.8).[29] Whereas the $\mu_2\text{–}\eta^1\text{:}\eta^1\text{–}P_4$ butterfly-motif is a common structural outcome from the reaction of main-group radicals and anions with P_4,[30] it is very rarely observed during

the activation of white phosphorus by transition metal complexes.[31-34] Accordingly, the stability of 17e⁻ **1** in solution, coupled with the encumbering *m*-terphenyl ancillary groups, allows for the selective radical-type,[33] transition- metal-based activation of P_4 at ambient conditions.

This observed cooperative 2 e⁻ reduction also can be extended to some heteroallene substrates. As shown in Scheme 2.3, addition of CS_2 to two equivalents of monoradical **1** results in the formation of a unusual dimeric species wherein the two Mn metal centers are bridged by the SCS-group. Additionally, α-insertion to one of

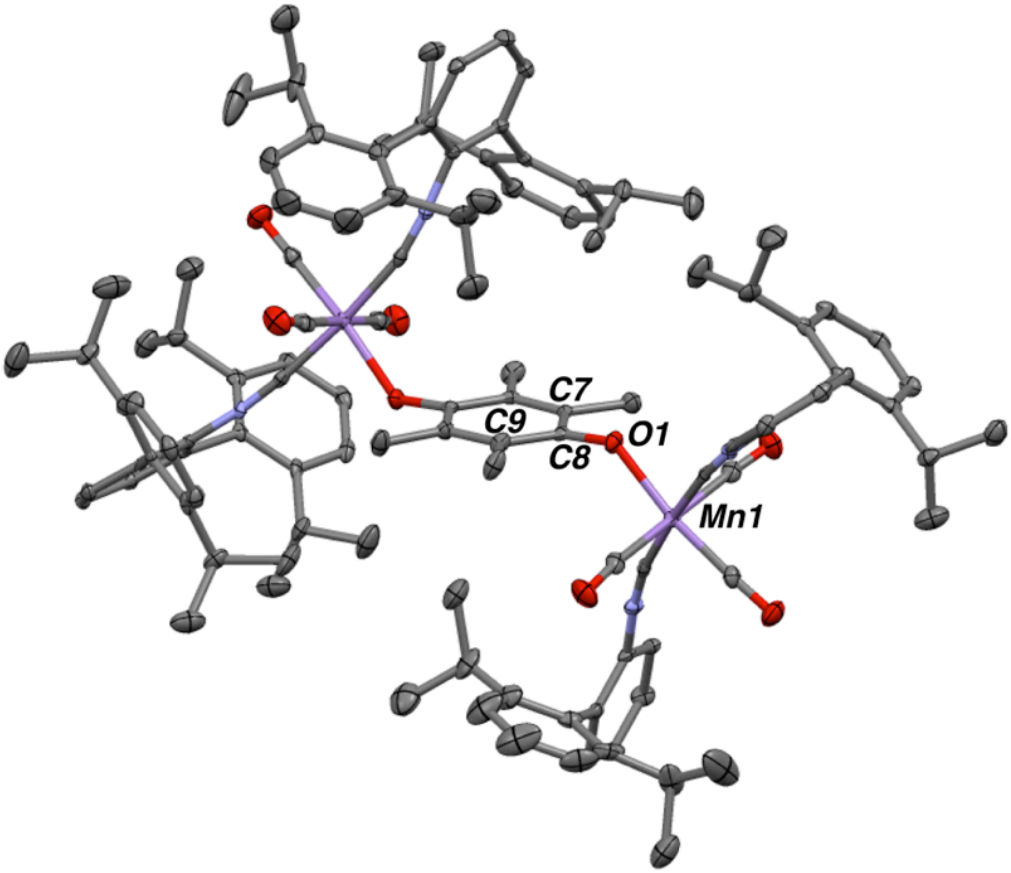

Figure 2.7. Molecular structure of $(\mu_2\text{-}\kappa^1\text{:}\kappa^1\text{-}OC_6Me_4O)[Mn(CO)_3(CNAr^{Dipp2})_2]_2$ (**6**). Selected bond distances (Å) and angles (°): Mn1-O1 = 2.0258(19); O1-C8 = 1.361(3); C8-C9 = 1.404(4); C8-C7 = 1.411(4); Mn1-O1-C8 = 130.81(18); C9-C8-C7 = 118.7(3).

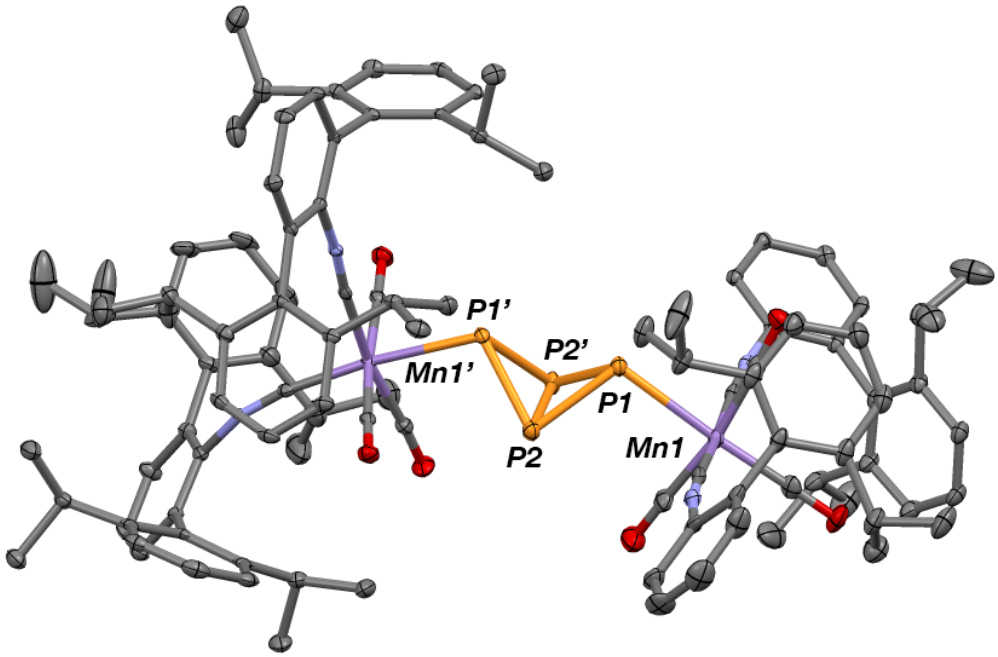

Figure 2.8. Molecular structure of *cis,mer:trans,mer*-[$Mn(CO)_3(CNAr^{Dipp2})_2]_2(\mu\text{-}\eta^1\text{:}\eta^1\text{-}P_4)$ (**7**). Selected bond distances (Å) and angles (˚): Mn1'-P1' = 2.4703(9); Mn1-P1 = 2.4627(9); P2'-P2 = 2.1699(12); P1'-P2 = 2.2123(12); Mn1'-P1'-P2 = 107.70(4); P1'-P2-P1 = 80.29(4).

the supporting isocyanide ligands is evident from the molecular structure (Figure 2.9), as determined by X-ray crystallography. This results in the formation of a formally acyclic carbene ($d_{Mn1\text{-}C1}$ = 2.049(3) Å), with a ^{13}C resonance at 261.1 ppm (C_6D_6, 20 ˚C), which is also part of the four-membered metallocycle formed about Mn. Similar to the aforementioned P_4-butterfly complex **7**, isomerization of the $CO/CNAr^{Dip2}$ ligands also occurs on one of the Mn centers, likely to accommodate the formation of a short-bridged dimer. We contend that this product results from two, one-electron activations of CS_2, resulting in an intermediately formed CS_2-dimeric species. This then migrates to the isocyanide α-carbon, resulting in the formation of the isolated product. Unfortunately, attempts to extend this chemistry to CO_2 did not result in any observed reactivity.

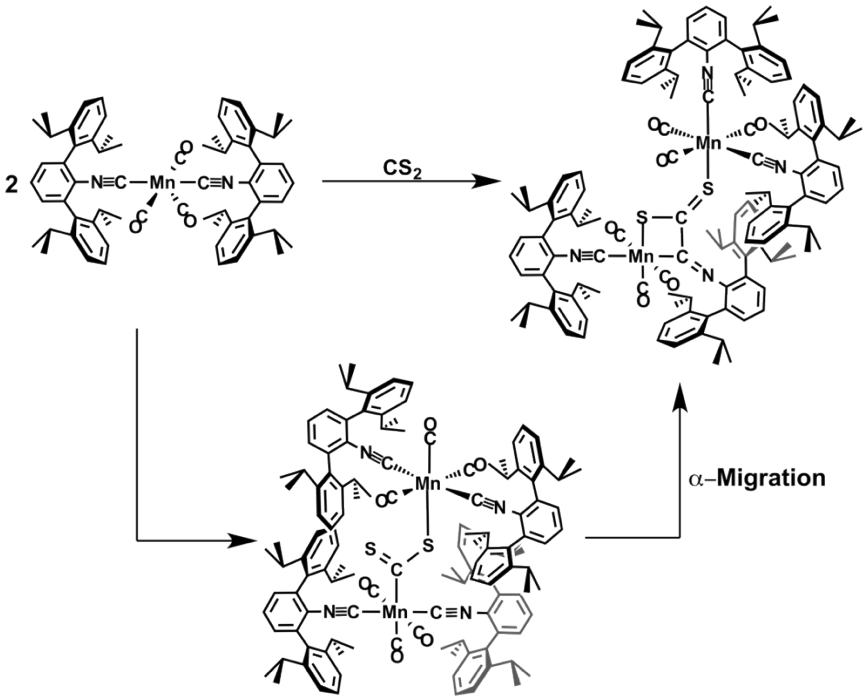

Scheme 2.3. Addition of CS_2 results in the formation of a four-member manganocyclic dimer, which is believed to result from α-migratory insertion following initial formation of CS_2-bridged dimer.

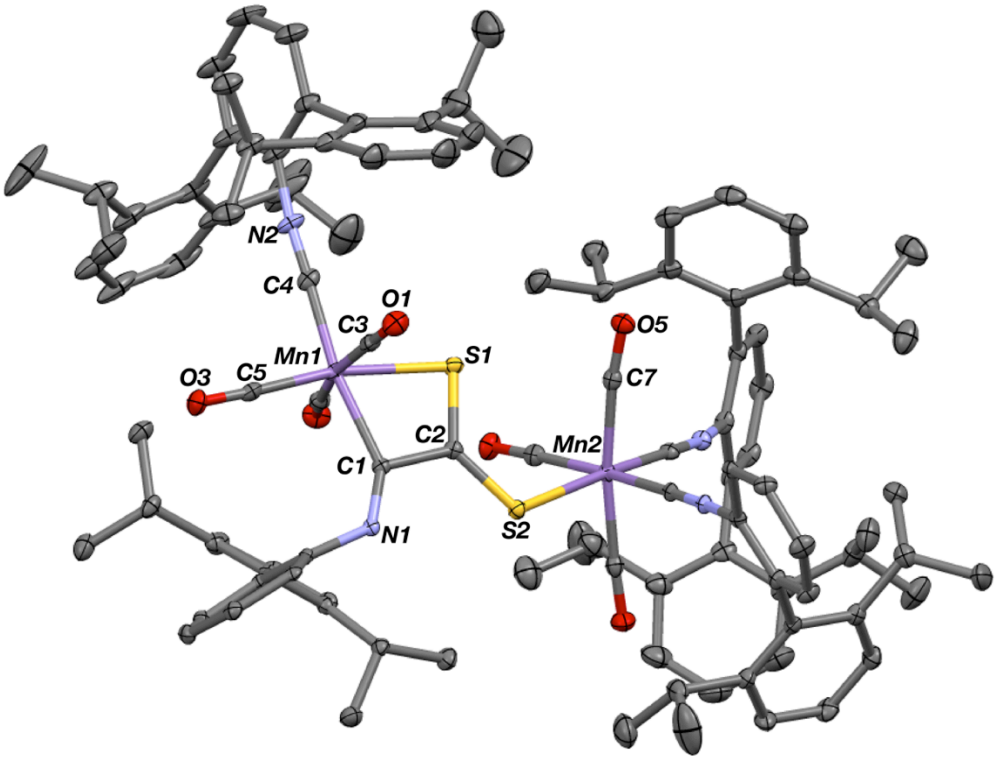

Figure 2.9. Molecular structure of CS_2-manganese dimer. Selected bond distances (Å) and angles (°): Mn1-S1 = 2.3750(9); Mn2-S2 = 2.3718(8); C2-S1 = 1.674(3); C2-S2 = 1.680(3); C2-C1 = 1.524(4); C1-N1 = 1.269(3); S1-Mn1-C1 = 71.05(8); S1-C2-S2 = 128.56(16); C1-C2-S2 = 123.54(19); C2-S2-Mn2 = 112.48(9).

Consistent with the chemistry outlined above for monoradical **1**, addition of $NO_{(g)}$ (1 atm) to a degassed benzene solution of **1** causes a distinct color change to deep red over one minute. Analysis of the mixture reveals the clean formation a new product (Scheme 2.4), which notably displays only one resonance at 226.1 ppm in the $^{13}C\{^{1}H\}$ spectrum (C_6D_6, 20 ˚C) corresponding to the carbonyl ligands. Additionally, only two bands at 1983 cm^{-1} and 1922 cm^{-1} are observed in the isocyanide region of the IR spectrum, with a third, strong band at 1702 cm^{-1}. Consistent with these observations, crystallographic analysis of single crystals grown from Et_2O reveals the formation of $Mn(NO)(CO)_2(CNAr^{Dipp2})_2$, which adopts a trigonal bipyramidal structure in the solid state (Figure 2.10). Only two CO ligands are observed, indicating CO dissociation *en route* to the formation of $Mn(NO)(CO)_2(CNAr^{Dipp2})_2$. The band at 1702 cm^{-1}, corresponding to the κ^1-*N*-NO ligand, is consistent with that observed for the analogous complex $Mn(NO)(CO)_4$.[45] This result provides an early indication in the *cis*-labilizing effect certain ligands can have in this mixed carbonyl/isocyanide system, which will be discussed in the following paragraphs and in Chapter 4.

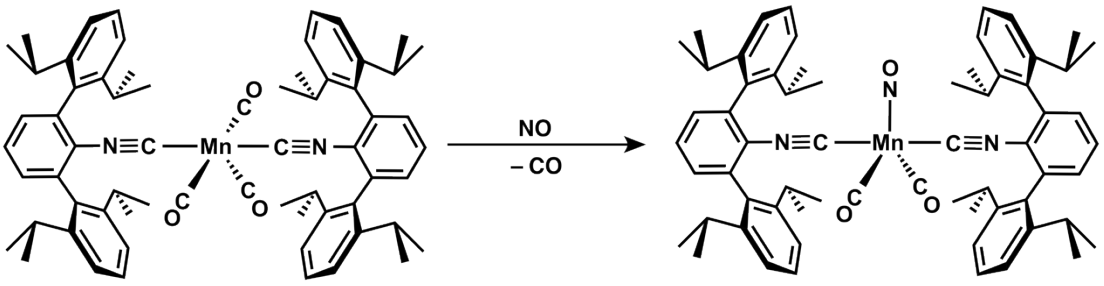

Scheme 2.4. Addition of $NO_{(g)}$ to **1** causes the dissociation of CO *en route* to the formation of $Mn(NO)(CO)_2(CNAr^{Dipp2})_2$.

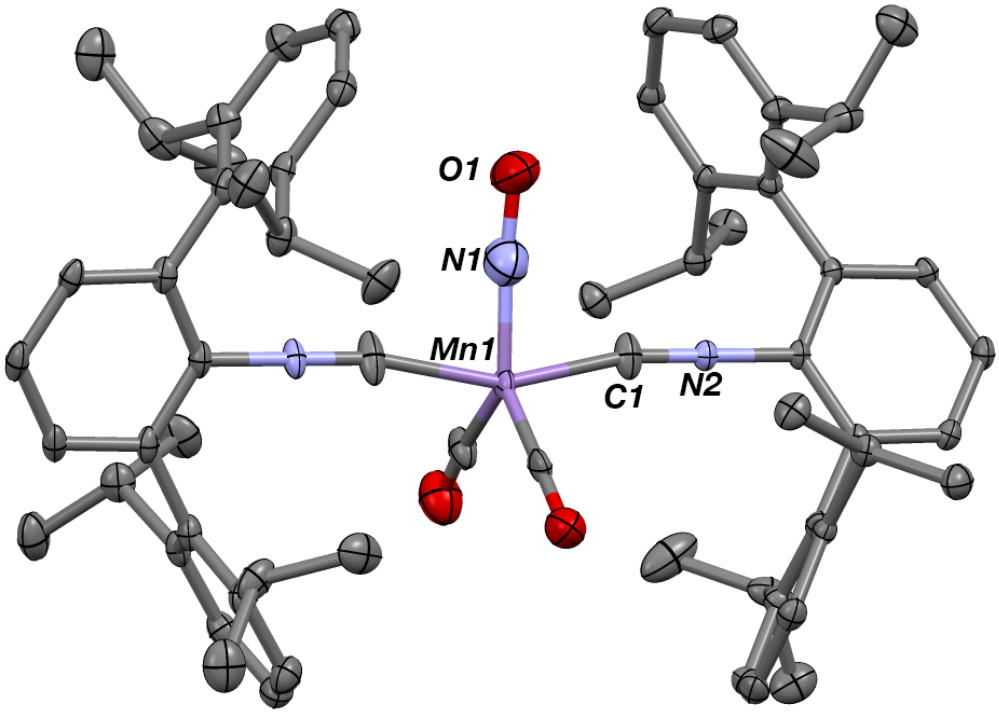

Figure 2.10. Molecular structure of $Mn(NO)(CO)_2(CNAr^{Dipp2})_2$.

The well-defined and persistent nature of **1** has also allowed for a survey of its reactivity toward nitrosoarenes (*i.e.* ArN=O). These reactions can be viewed as a model system for nitrosoarene spin-trapping studies of $Mn(CO)_5$, which provided some of the earliest EPR evidence for the formation of $Mn(CO)_5$ radicals in fluid solution.[2-14] It is generally accepted that $Mn(CO)_5$ reacts with nitrosoarenes to form simple κ^1-*N* nitroxide-radical spin adducts (*i.e.* (κ^1-*N*-ArNO)$Mn(CO)_5$), which give rise to *g* values near that of the free electron (2.002), indicative of NO p* system-centered radicals. However, like $Mn(CO)_5$ itself, these nitroxide spin adducts are not amenable to isolation and their characterization is limited to EPR spectroscopic detection at temperatures near –30 °C.[12-14] It is therefore significant that treatment of **1** with 1.0 equiv. of nitrosobenzene (PhNO) in thawing Et_2O solution produces the η^2-

N,*O* phenylnitroxide radical complex (η^2-*N*,*O*-PhNO)Mn(CO)$_2$(CNAr^{Dipp2})$_2$ (**8**) with loss of one CO ligand as determined by X-ray diffraction (Figure 2 and 3). Furthermore, this outcome is not limited to nitrosobenzene, as treatment of **1** with either *m*-nitrosotoluene (*m*-TolNO) or *p*-nitrosotoluene (*p*-TolNO) results in the complexes (η^2-*N*,*O*-*m*- TolNO)Mn(CO)$_2$(CNAr^{Dipp2})$_2$ (**9**) and (η^2-*N*,*O*-*p*-TolNO)Mn(CO)$_2$(CNAr^{Dipp2})$_2$ (**10**), respectively, with CO loss (Figure 2).

The structural and spectroscopic features of complexes **8**-**10** are strongly reflective of the presence of η^2-coordinated arylnitroxide radical ligands (*i.e.* [ArNO]$^{1-\bullet}$]) (Figures 2.10-2.18). In the solid state, complexes **8**-**10** feature N-O bond distances of 1.264(10) Å, 1.284(9) Å and 1.320(2) Å, respectively, and show a marginal lengthening in response to the inductive properties of the ArNO aryl substituent. However, these bond distances all fall at values intermediate of those typical for NO double (~1.19 Å) and single bonds (~ 1.45 Å),[35] and thus provide strong support for a formal NO bond order of 1.5. In addition, the nitroxide aryl groups in complexes **8**-**10** adopt an in-plane orientation relative to the Mn center (Figure 3). This feature contrasts distinctly with structurally characterized η^2-*N*,*O* nitrosoarene complexes (*i.e.* metalloxaziridines),[36] in which the aryl groups adopt a perpendicular orientation relative to the metal center on account of in-plane M→p*(NO) backbonding. Accordingly, the solid-state structures of complexes **8**-**10** strongly suggest that the η^2-ArNO ligands do not bind according to the standard Dewar-Chatt-Duncanson model of M→L p-backbonding. Rather, the structural properties of **8**-**10** indicate that the η^2-ArNO ligands function as L_2-type, not X_2-type, donors,[37] with an unpaired electron localized in a NO p* orbital oriented perpendicular to the plane of the Mn center. The

room-temperature EPR spectra of complexes **8**-**10** in toluene solution support this description and give rise to g_{iso} values of 2.004, 2.008, and 2.005, respectively, indicative of organic radicals (Figure 3, S2.3 and S2.4). Notably, while persistent nitroxide-radical complexes are uncommon, structurally characterized examples exhibiting κ^1-*N*,[36,38,39] κ^1-*O*[40] and bridging m-($1\kappa^1$-*N*:$2\kappa^1$-*O*)[41] coordination modes have been reported. However, complexes **8**-**10** represent unique examples of side-on bound η^2-*N,O* nitroxide radicals.

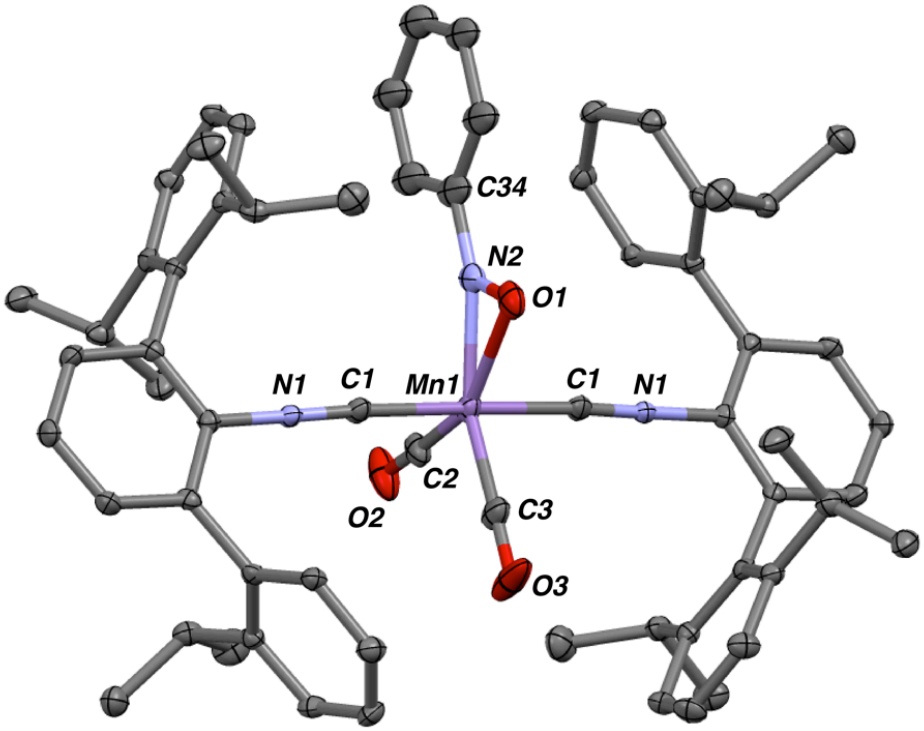

Figure 2.11. Molecular structure of (η^2-*N,O*-PhNO)Mn(CO)$_2$(CNAr^{Dipp2})$_2$ (**8**), with select *iso*-propyl groups omitted for clarity. Selected bond distances (Å) and angles (°): N2-O1 = 1.264(10); N2-Mn1 = 1.977(8); O1-Mn1 = 2.132(7); Mn1-C2 = 1.740(9); Mn1-C3 = 1.798(9); N2-Mn1-O1 = 35.6(3); O1-Mn1-N2 = 78.9(5); C34-N2-O1 = 127.4(8).

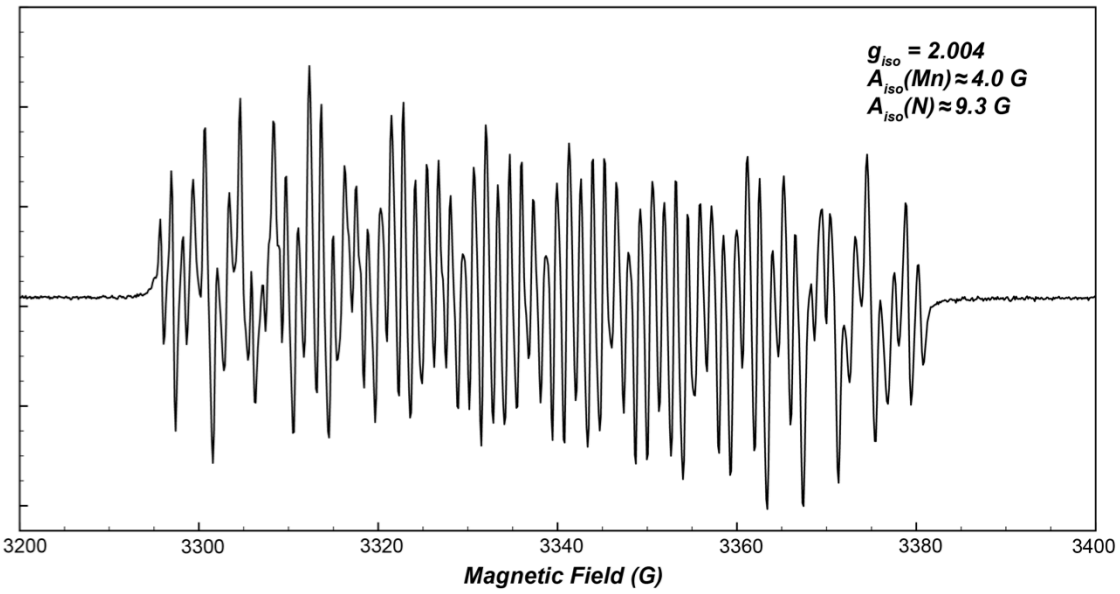

Figure 2.12. EPR spectrum of (η^2-*N,O*-PhNO)Mn(CO)$_2$(CNAr^{Dipp2})$_2$ (**8**) at 295 K in toluene (0.05 mM).

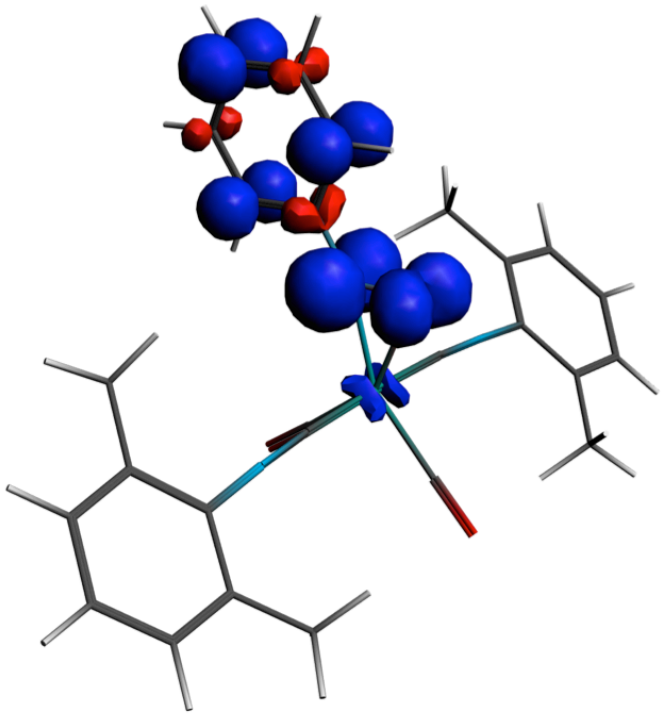

Figure 2.13. Spin density plot of (η^2-*N,O*-PhNO)Mn(CO)$_2$(CNXyl)$_2$ showing spin localization onto the phenylnitroxide radical and the origin of ^{1}H hyperfine coupling from the phenyl ring.

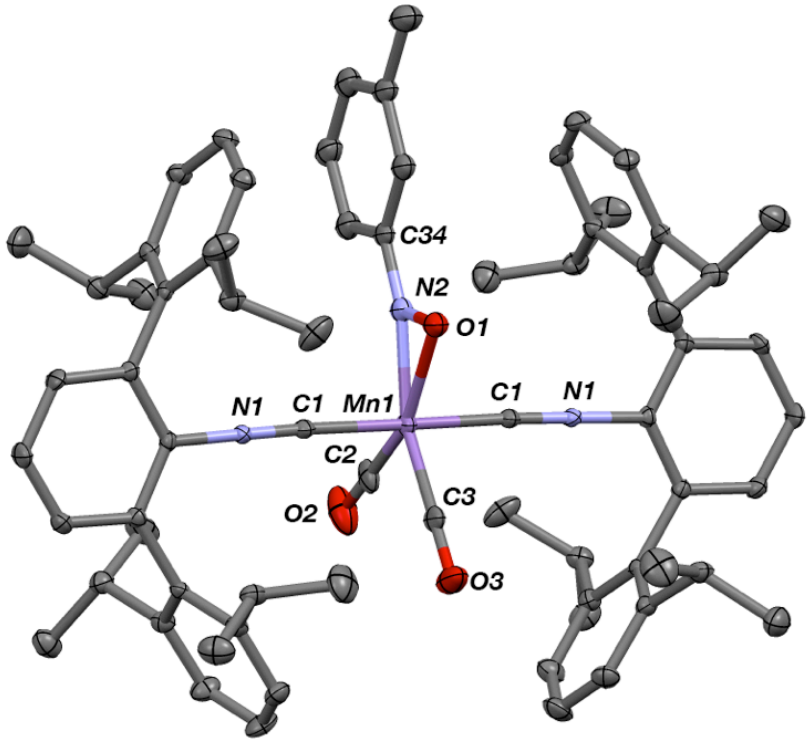

Figure 2.14. Molecular structure of (η^2-*N,O*-*m*-TolNO)Mn(CO)$_2$(CNAr^{Dipp2})$_2$ (**9**). Selected bond distances (Å) and angles (˚): N2-O1 = 1.284(9); N2-Mn1 = 1.916(7); O1-Mn1 = 2.084(5); Mn1-C2 = 1.730(8); Mn1-C3 = 1.834(8); N2-Mn1-O1 = 37.1(3); O1-N2-Mn1 = 78.5(4); C34-N2-O1 = 123.9(8).

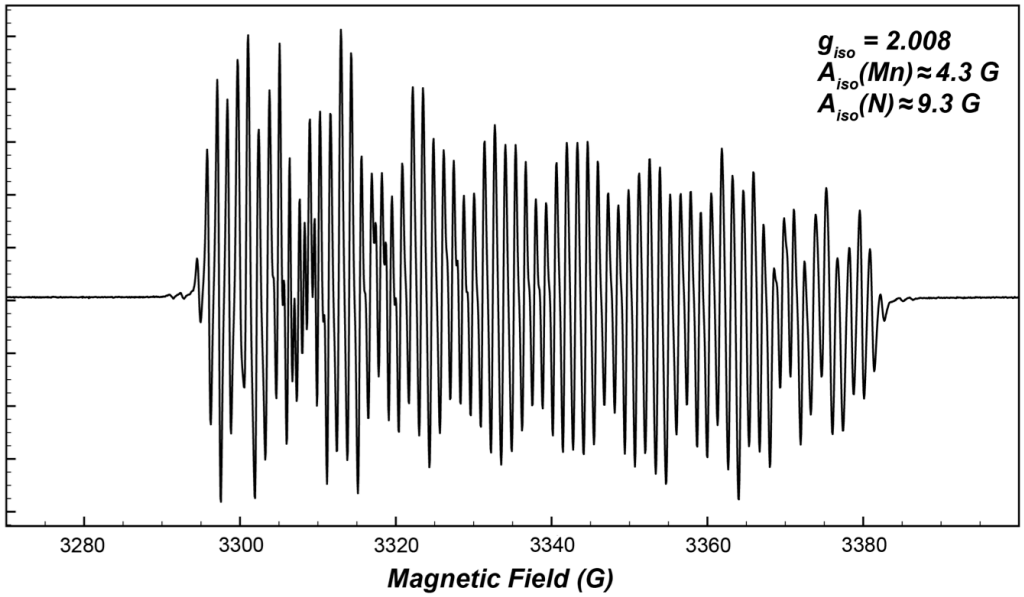

Figure 2.15. EPR spectrum of (η^2-*N,O*-*m*-TolNO)Mn(CO)$_2$(CNAr^{Dipp2})$_2$ (**9**) at 295 K in toluene (0.05 mM).

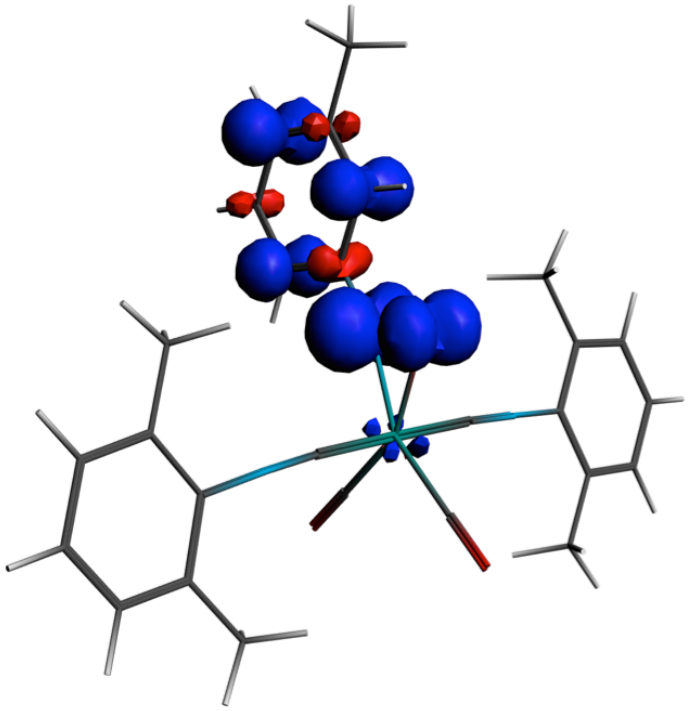

Figure 2.16. Spin density plot of (η^2-*N,O*-*m*-TolNO)Mn(CO)$_2$(CNXyl)$_2$ showing spin localization onto the tolylnitroxide radical and the origin of ^{1}H hyperfine coupling from the tolyl ring.

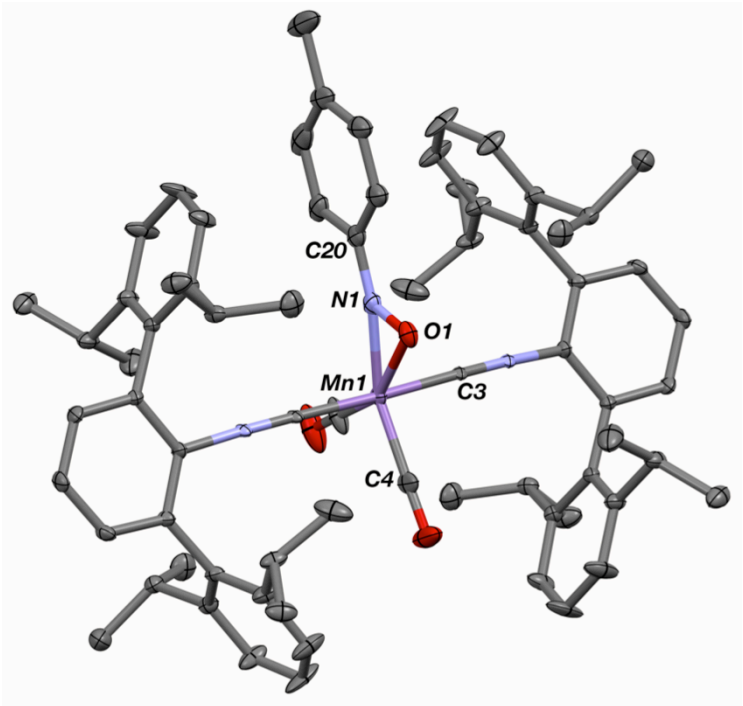

Figure 2.17. Molecular structure of (η^2-*N,O*-*p*-PhNO)Mn(CO)$_2$(CNAr^{Dipp2})$_2$ (**10**). Selected bond distances (Å) and angles (˚): N2-O1 = 1.337(6); N2-Mn1 = 1.928(5); O1-Mn1 = 2.076(5); Mn1-C3 = 1.991(3); N2-Mn1-O1 = 38.79(18); O1-N2-Mn1 = 76.6(3); C20-N2-O1 = 121.5(5).

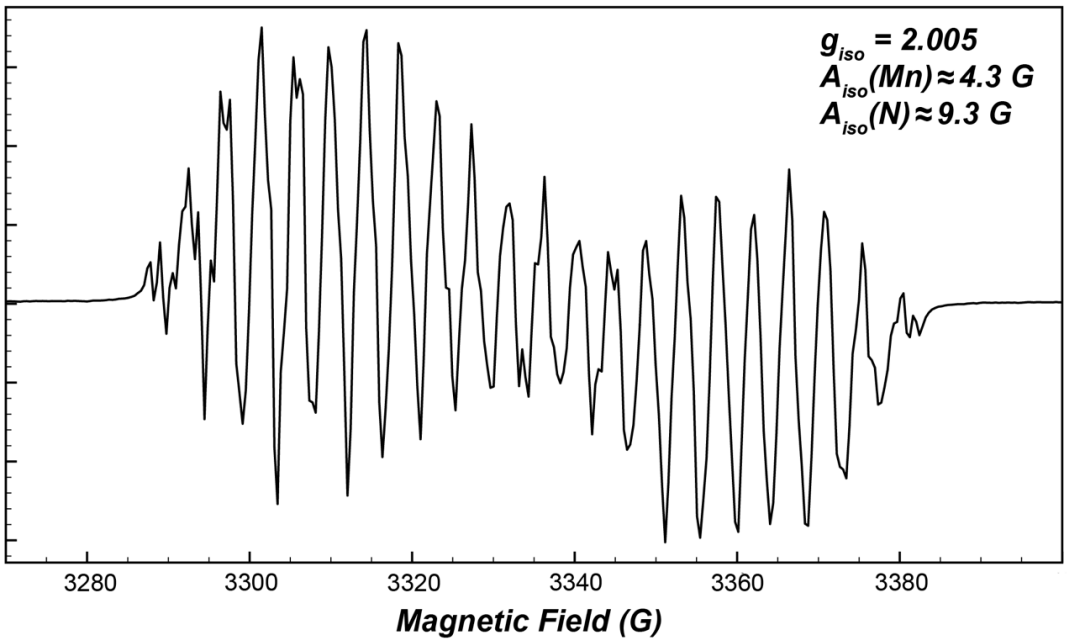

Figure 2.18. EPR spectrum of (η^2-*N,O-p*-TolNO)Mn(CO)$_2$(CNAr^{Dipp2})$_2$ (**10**) at 295 K in toluene (0.05 mM).

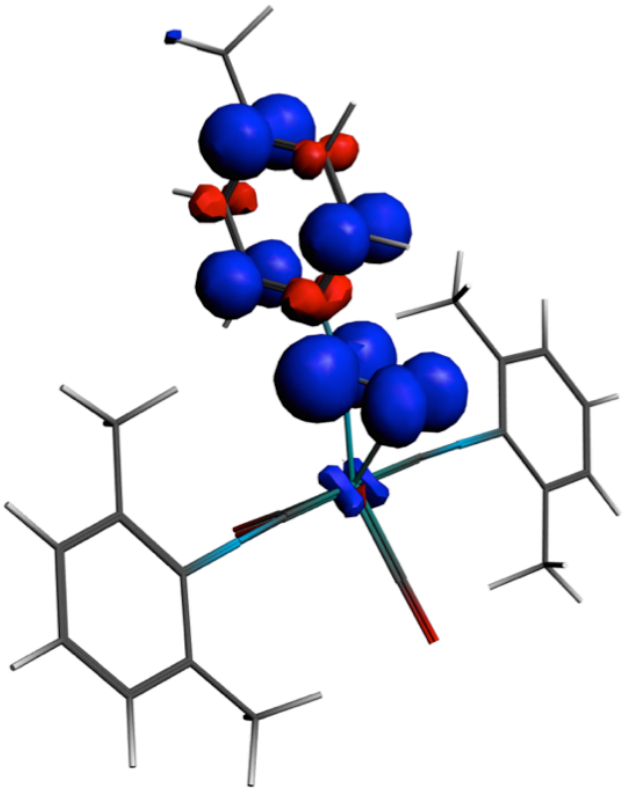

Figure 2.19. Spin density plot of (η^2-*N,O-p*-TolNO)Mn(CO)$_2$(CNXyl)$_2$ showing spin localization onto the tolylnitroxide radical and the origin of ^{1}H hyperfine coupling from the tolyl ring.

Whereas it appears that monoradical **1** and transiently generated $Mn(CO)_5$ display divergent reactivity toward nitrosoarenes, it is important to note that ^1H NMR and IR spectroscopy indicated that the formation of complexes **8**-**10** is complete upon mixing. Furthermore, intermediate species indicative of a κ^1-*N* nitroxide radical complex are not detected during these transformations at temperatures as low as –35 ˚C. To this end, DFT calculations for the conversion of the putative κ^1-*N* nitroxide radical complex, $(\kappa^1$-*N*-PhNO)$Mn(CO)_3(CNXyl)_2$, to $(\eta^2$-*N*,*O*-PhNO)$Mn(CO)_2(CNXyl)_2$ and free CO reveal that the process is enthalpically disfavored by 10.2 kcal/mol (Figure 2.19). Similarly, the calculated conversion of $(\kappa^1$-*N*-PhNO)$Mn(CO)_5$ to $(\eta^2$-*N*,*O*-PhNO)$Mn(CO)_4$ and CO is enthalpically disfavored by 5.9 kcal/mol (Figure 2.20).

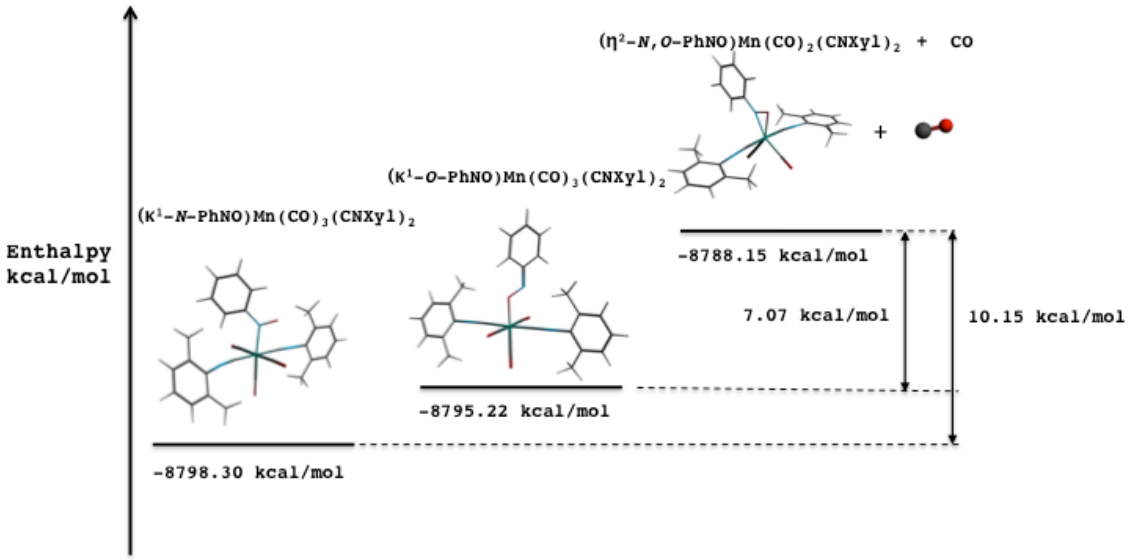

Figure 2.20. Relative Bonding Energies (ΔH^{SCF}) for the conversion of $(\kappa^1$-*N*-PhNO)$Mn(CO)_3(CNXyl)_2$ to $(\eta^2$-*N*,*O*-PhNO)$Mn(CO)_2(CNXyl)_2$ and CO.

Based on these results, the formation of complexes **8**-**10** likely arises from a strong kinetic *cis*-CO labilizing effect[42] by an unobserved κ^1-*N*-coodinated arylnitroxide radical (*i.e.* $(\kappa^1$-*N*-ArNO)$Mn(CO)_3(CNAr^{Dipp2})_2$). Indeed, κ^1-*N*

arylnitroxide ligands are expected to exhibit weak s- and strong p-donor capacity and therefore function as efficient *cis*-labilizing ligands in six-coordinate $XMnL_5$ complexes.[42-44] However, as the π-acidity properties of isocyanides are known to match those of CO with respect to *cis*-labilizing ability,[43] isocyanide for CO substitution on Mn should not dramatically affect reaction outcomes. Therefore, it is plausible that (η^2-*N*,*O*-ArNO)$Mn(CO)_4$, rather than (κ^1-*N*-PhNO)$Mn(CO)_5$, species may more accurately reflect the results of $Mn(CO)_5$ spin-trapping studies.[12-14] This notion is further supported by the fact that **8**-**10** give rise to Mn and N hyperfine coupling constants (A_{iso}(Mn) ≈ 4.0 G; A_{iso}(N) ≈ 9.0 G) that are markedly similar to those measured during nitrosoarene spin-trapping studies of $Mn(CO)_5$.[12-14]

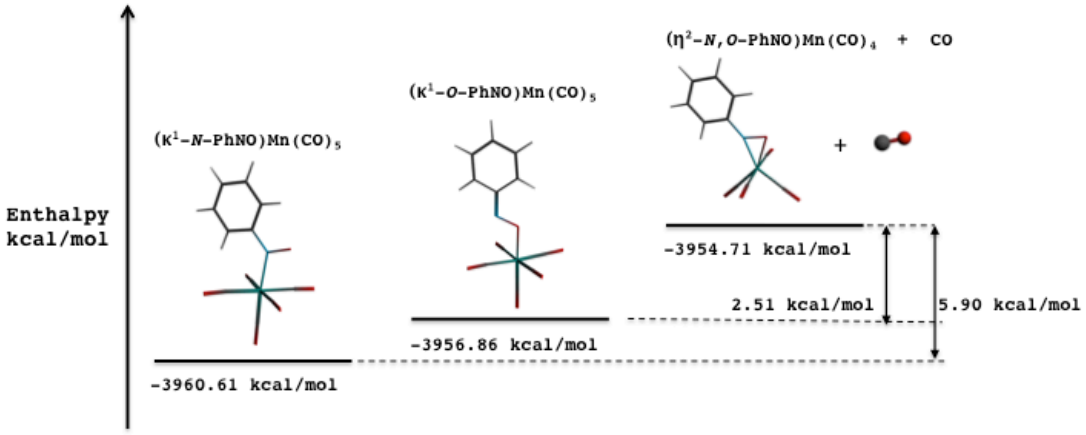

Figure 2.21. Relative Bonding Energies (ΔH^{SCF}) for the conversion of (κ^1-*N*-PhNO)$Mn(CO)_5$ to (η^2-*N*,*O*-PhNO)$Mn(CO)_4$ and CO.

This suggestion highlights an important aspect of the ability to isolate monoradical **1** and explore its behavior in a well-defined manner. As the transient nature of $Mn(CO)_5$ and other organometallic monoradicals has most often precluded systematic studies of their reactivity properties, variants that are kinetically stabilized in both solution and the solid state can be employed to further develop selective

transformations. Just as importantly, kinetic stabilization in the manner exhibited by **1** can afford a more detailed assessment of reaction outcomes in such transformations.

2.4 Nucleophilic and Radical Initiated Routes to Manganese-Main Group Complexes

Bifunctional catalysis mediated by transition metal-main group compounds is becoming an increasingly effective means towards facilitating difficult bond-lysis steps in catalytic cycles.[46] While this concept has found wide applicability with ancillary boryl ligands,[47-50] it has recently been shown that other Group 13 element fragments,[51-52] as well as fragments featuring heavier pnictogen atoms,[53-54] can fill the role as an effective Lewis acid. However, the generation of these complexes remains a particular challenge due to the difficulty in preparing stable main-group nucleophiles to functionalize various metal species.[55-56] Additionally, the development of synthetic routes using binary main group halides remains largely limited to either oxidative addition with late-row transition metals[49-50, 57-58] or nucleophilic reactions with classical carbonyl metallates.[59]

For nucleophilic derivatization reactions, complications can arise as a result of multiple additions in sterically uncongested systems,[60-61] as well as the tendency of main-group halides to function as oxidants[62] towards reduced metal species. This often results in irreversible dimerization of the transition metal complex as a consequence of metalloradical formation. However, in limited cases some dinuclear metal complexes are capable of homo-fragmentation to produce short-lived metalloradicals, which can subsequently react with a main group fragment.[63-65] This strategy has proven to be

particularly powerful in generating unique transition metal-main group species.[65] To examine this pathway in more detail, we have investigated the activation of binary main group halides with the stable manganese metalloradical $Mn(CO)_3(CNAr^{Dipp2})_2$,[66] with comparison to nucleophilic reaction pathways accomplished by the corresponding manganate $Na[Mn(CO)_3(CNAr^{Dipp2})_2]$ (Ar^{Dipp2} = 2,6-(2,6-(*i*-$Pr)_2C_6H_3)_2C_6H_3$).[67] Importantly, we have found that the use of sterically encumbering *m*-terphenyl isocyanides[68-86] facilitates the formation of unique, terminal main group substituents without dimerization occurring.

We recently reported the preparation of $Mn(CO)_3(CNAr^{Dipp2})_2$, a zerovalent, square-pyramidal complex that serves as an analogue to the unstable metalloradical $Mn(CO)_5$.[66] Consistent with its low-spin, d^7 ground state, $Mn(CO)_3(CNAr^{Dipp2})_2$ acts as a potent atom abstraction reagent and competent radical scavenger in solution. For example, addition of 1 equiv $CHCl_3$ to $Mn(CO)_3(CNAr^{Dipp2})_2$ results in the generation of $MnCl(CO)_3(CNAr^{Dipp2})_2$ and $Mn(CHCl_2)(CO)_3(CNAr^{Dipp2})_2$ in a 1:1 ratio. Interestingly, this reactivity was found to carry over to Sn(IV) species as well. For example, reaction of 1 equiv of $HSn(n\text{-}Bu)_3$ with $Mn(CO)_3(CNAr^{Dipp2})_2$ was found to produce an equimolar mixture of $MnH(CO)_3(CNAr^{Dipp2})_2$ as well as the stannyl complex $Mn(Sn(n\text{-}Bu)_3)(CO)_3(CNAr^{Dipp2})_2$. This suggested that the intrinsic reactivity of $Mn(CO)_3(CNAr^{Dipp2})_2$ could be used to facilitate the formation of unique, low-valent manganese adducts with substrates containing homolytically cleavable E-X bonds. This mode of reactivity should thus be complementary to the manganate complex $Na[Mn(CO)_3(CNAr^{Dipp2})_2]$, which has been established to react with tin(II) dichloride to form the unique chloro-substituted metallostannylene, $Mn(SnCl)(CO)_3(CNAr^{Dipp2})_2$.

Accordingly, herein we show that complexes possessing manganese/main group element bonds can be readily accessed by a radical type approach using the neutral metalloradical $Mn(CO)_3(CNAr^{Dipp2})_2$. These reactions proceed with high atom-economy and can succeed in some cases where nucleophilic-derivitization/salt elimination routes fail to easily provide the desired product. In addition, in the course of this study we have prepared the monofluoro complex $MnF(CO)_3(CNAr^{Dipp2})_2$, which serves as an analogue to the unknown simple organometallic fluoride $FMn(CO)_5$.[87]

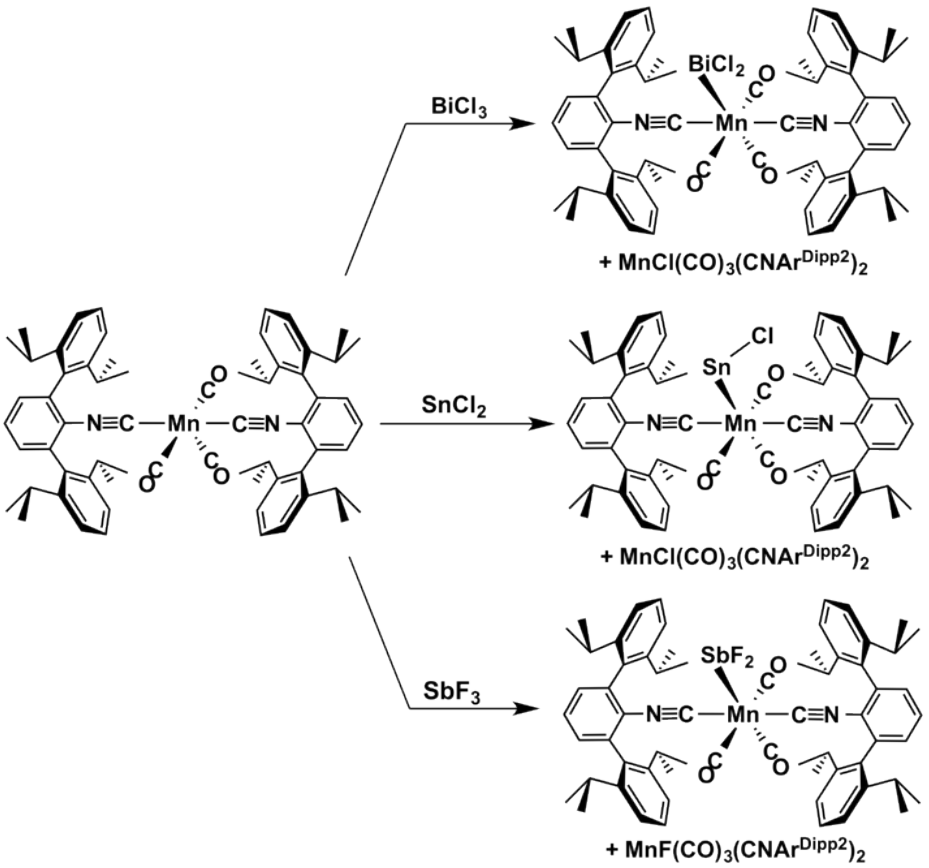

Scheme 2.5. Reactivity of $Mn(CO)_3(CNAr^{Dipp2})_2$ with $BiCl_3$, $SnCl_2$ and SbF_3.

Based upon the observed reactivity of $Mn(CO)_3(CNAr^{Dipp2})_2$ with $CHCl_3$ and $HSn(n\text{-}Bu)_3$, we anticipated that a simple 1:1 stoichiometry between $Mn(CO)_3(CNAr^{Dipp2})_2$ and a main group halide should result in a product mixture

containing the Mn-main group adduct and the corresponding halide complex $MnX(CO)_3(CNAr^{Dipp2})_2$. Indeed, addition of $SnCl_2$ to a stirring diethyl ether solution of $Mn(CO)_3(CNAr^{Dipp2})_2$ provides $MnCl(CO)_3(CNAr^{Dipp2})_2$[66] and the previously reported metallostannylene complex, $Mn(SnCl)(CO)_3(CNAr^{Dipp2})_2$,[67] in approximately a 1.3:1 ratio, as assayed by ^1H NMR spectroscopy. Isolation of $Mn(SnCl)(CO)_3(CNAr^{Dipp2})_2$ is readily accomplished via *n*-pentane extraction of the product mixture, as $MnCl(CO)_3(CNAr^{Dipp2})_2$ is insoluble in *n*-pentane, providing green microcrystals in 32% yield upon removal of volatiles. While this yield falls below that previously reported for the corresponding salt metathesis route using $Na[Mn(CO)_3(CNAr^{Dipp2})_2]$, it is notable that the metalloradical pathway allows for nearly quantitative recovery of Mn metal centers (as $Mn(SnCl)(CO)_3(CNAr^{Dipp2})_2$ and $MnCl(CO)_3(CNAr^{Dipp2})_2$by mass balance. As shown previously, the chloride complex can be easily reduced by one or two electrons to regenerate $Mn(CO)_3(CNAr^{Dipp2})_2$ or $[Mn(CO)_3(CNAr^{Dipp2})_2]^-$, respectively, which can then be reused in further reactions. Importantly, this result supports a metalloradical approach towards Sn(II) derivatization, similar to that previously observed for the related reactivity with Sn(IV) substrates.

To further explore the generality of this metalloradical approach and its comparison to salt elimination using $Na[Mn(CO)_3(CNAr^{Dipp2})_2]$, we examined the

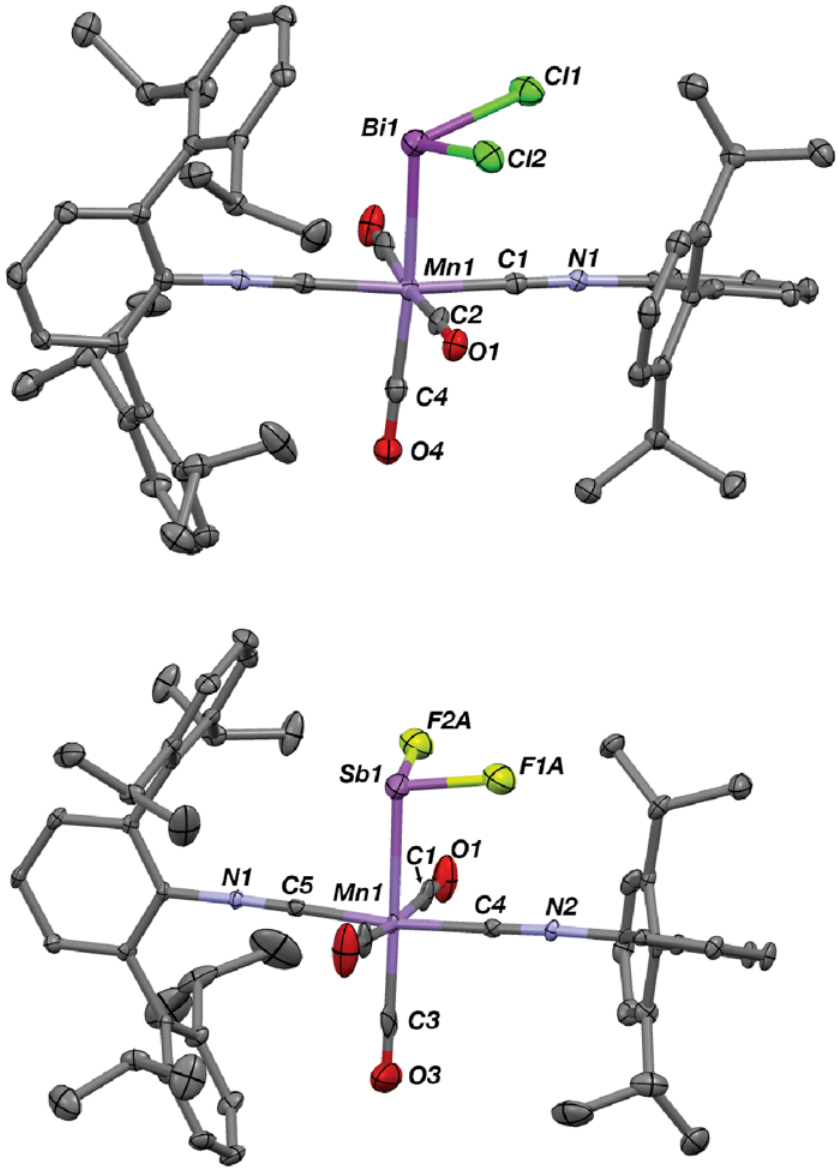

Figure 2.22. Solid state structures of $Mn(BiCl_2)(CO)_3(CNAr^{Dipp2})_2$ (*top*) and $Mn(SbF_2)(CO)_3(CNAr^{Dipp2})_2$, with selected Dipp rings and H atoms omitted for clarity. Selected bond distances (Å) and angles (º) ($Mn(BiCl_2)(CO)_3(CNAr^{Dipp2})_2$): Mn1-Bi1 = 2.6809(10); C5-N2 = 1.153(8); Bi1-Cl1 = 2.500(2); Cl1-Bi1-Cl2 = 95.06(7); Bi1-Mn1-C5 = 83.81(18). ($Mn(SbF_2)(CO)_3(CNAr^{Dipp2})_2$): Mn1-Sb1 = 2.6111(6); C5-N1 = 1.157(4); Sb-F2A = 1.900(6); F2A-Sb1-F2A = 92.2(3); Sb1-Mn1-C5 = 86.92(10).

reactivity with several readily available main group halides. It was discovered that the character of the halide played an important role in facilitating a favorable transformation. Indeed, while $SbCl_3$ and SbI_3 led solely to $MnCl(CO)_3(CNAr^{Dipp2})_2$

and $MnI(CO)_3(CNAr^{Dipp2})_2$[84], respectively, it was found that SbF_3 reacts with $Mn(CO)_3(CNAr^{Dipp2})_2$ over several days in DME solution to form $Mn(SbF_2)(CO)_3(CNAr^{Dipp2})_2$ and $MnF(CO)_3(CNAr^{Dipp2})_2$ in approximately a 1:1 ratio. Analysis of the product mixture by ^{19}F NMR spectroscopy reveals two singlets at -58.6 ppm and -166.0 ppm, and solution infrared spectroscopy supports the presence of two C_{2v}-symmetric molecular complexes with isocyanide stretches at 2118 cm^{-1} and 2086 cm^{-1}. Indeed, crystallization of the product mixture in THF produces a combination of bright yellow and orange crystals. Extraction of this mixture with *n*-pentane followed by recrystallization in pyridine was found to provide $Mn(SbF_2)(CO)_3(CNAr^{Dipp2})_2$ in 43% yield, which gives rise to the ^{19}F NMR signal at -166.0 ppm. Crystallographic analysis of $Mn(SbF_2)(CO)_3(CNAr^{Dipp2})_2$ revealed an octahedral geometry about manganese in the solid state with a Mn-Sb distance of 2.6111(6) Å. The three-coordinate Sb center adopts a distorted pyramidal geometry (average of two positionally disordered $-SbF_2$ fragments: ∠(Mn-Sb-F) = 100.3(4)°; F-Sb-F = 92.0(5)°). Notably, while three-coordinate, terminal transition metal stibyl halides (*eg*. L_nMSbX_2) are known for chloro-derivatives[58, 60, 88], $Mn(SbF_2)(CO)_3(CNAr^{Dipp2})_2$ represents a unique example of a monomeric difluorostibyl complex without intermolecular catenation between $-SbF_2$ centers.[89] Notably, it was found that $Mn(SbF_2)(CO)_3(CNAr^{Dipp2})_2$ could also be synthesized via a salt elimination route from $Na[Mn(CO)_3(CNAr^{Dipp2})_2]$ and SbF_3 in 54% yield, thus revealing a complementarity between the nucleophilic displacement and atom abstraction approaches. However, as observed for the reactivity with $SnCl_2$, the atom abstraction route allows nearly quantitative recovery of Mn centers (as

$Mn(SbF_2)(CO)_3(CNAr^{Dipp2})_2$ and $MnF(CO)_3(CNAr^{Dipp2})_2$), whereas 46% of the molar equivalents of Mn are lost to intractable products in the salt elimination route.

Notably, radical-type formation of Mn-bound heavier pnictogen dihalides is not limited to antimony. While, attempts to generate the corresponding $–BiF_2$ adduct using BiF_3 under similar conditions did not lead to a productive reaction, addition of 1 equiv of solid $BiCl_3$ to a stirring diethyl ether solution of $Mn(CO)_3(CNAr^{Dipp2})_2$ provided $MnCl(CO)_3(CNAr^{Dipp2})_2$ and $Mn(BiCl_2)(CO)_3(CNAr^{Dipp2})_2$ in a 2.5:1 ratio, as assayed by ^{1}H NMR spectroscopy. We contend this low ratio is the result of the thermal- and photo-sensitivity of $Mn(BiCl_2)(CO)_3(CNAr^{Dipp2})_2$ (*vide infra*). Recrystallization of the product mixture affords red and yellow crystals of $Mn(BiCl_2)(CO)_3(CNAr^{Dipp2})_2$ and $MnCl(CO)_3(CNAr^{Dipp2})_2$, respectively, which can be manually separated. Following separation, ^{1}H NMR spectroscopy of the red crystals indicates the isocyanide ligands are in identical chemical environments, supporting a *trans*- stereochemical orientation. Indeed, $Mn(BiCl_2)(CO)_3(CNAr^{Dipp2})_2$ adopts an octahedral coordination geometry about Mn in the solid state, with a Mn-Bi distance of 2.26809(10) Å, which is similar to other isolated transition metal halobismuth complexes.[57, 60, 90] While most transition metal halobismuth complexes form bridging interactions in the solid state,[91-93] $Mn(BiCl_2)(CO)_3(CNAr^{Dipp2})_2$ does not exhibit intermolecular contacts due to the encumbering nature of the $CNAr^{Dipp2}$ ligands. However, despite the increased kinetic stabilization afforded by $CNAr^{Dipp2}$, $Mn(BiCl_2)(CO)_3(CNAr^{Dipp2})_2$ is thermally unstable above –40 °C and shows significant sensitivity to light. Indeed, allowing to $Mn(BiCl_2)(CO)_3(CNAr^{Dipp2})_2$ to stir in the dark at room temperature for 3 h, or

exposing –40 ˚C solutions to ambient light for 20 minutes, resulted in the formation of $MnCl(CO)_3(CNAr^{Dipp2})_2$ and a black precipitate, which we presume to be solid Bi^0.

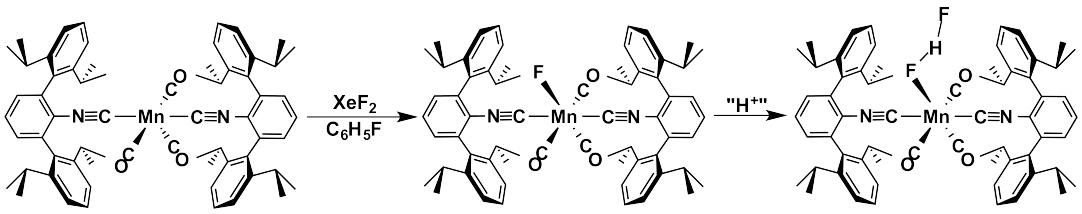

Scheme 2.6. Addition of XeF_2 in C_6H_5F results in the formation of $MnF(CO)_3(CNAr^{Dipp2})_2$. Decomposition *via* an adventitious proton source results in the formation of the bifluoride complex.

As mentioned above, $MnF(CO)_3(CNAr^{Dipp2})_2$ is among the two-component mixture resulting from reaction of $Mn(CO)_3(CNAr^{Dipp2})_2$ and SbF_3. An alternate synthesis, involving the addition of solid XeF_2 to a stirring fluorobenzene solution of $Mn(CO)_3(CNAr^{Dipp2})_2$, was found to exclusively provide $MnF(CO)_3(CNAr^{Dipp2})_2$ in 41% yield. Notably, we have not identified conditions where the use of $Na[Mn(CO)_3(CNAr^{Dipp2})_2]$ as a starting material has been found to provide $MnF(CO)_3(CNAr^{Dipp2})_2$, which highlights the utility of an open-shell starting material for the formation of this transition metal monofluoride. The infrared spectrum of $MnF(CO)_3(CNAr^{Dipp2})_2$ in C_6D_6 possesses an isocyanide band at 2118 cm^{-1} that is identical to those of the C_{2v}-symmetric halide complexes $MnCl(CO)_3(CNAr^{Dipp2})_2$, $MnBr(CO)_3(CNAr^{Dipp2})_2$, and $MnI(CO)_3(CNAr^{Dipp2})_2$.[84] This observation strongly reveals that the identity of the halide ligand does not effect the degree of π-backbonding by Mn to the isocyanide ligands. The ^{19}F NMR spectrum of $MnF(CO)_3(CNAr^{Dipp2})_2$ in C_6D_6 displays a singlet at -58.6 ppm, with no other signals observed between 200 to -500 ppm. However, the three downfield peaks in the $^{13}C\{^1H\}$ NMR spectrum of corresponding to $CNAr^{Dipp2}$, CO_{trans}, and CO_{cis} at 172.5

ppm, 210.0 ppm, and 218.0 ppm, respectively, display carbon-fluorine coupling (J_{CF} = 11 Hz (CO_{trans}), 150 Hz ($CNAr^{Dipp2}$), 172 Hz (CO_{cis})) with J_{CF} constants consistent with a *mer,trans*-stereochemical arrangement. Notably, this complex serves as an mixed isocyanide/carbonyl analogue of $MnF(CO)_5$, which to date has not been observed.[87, 94-97]

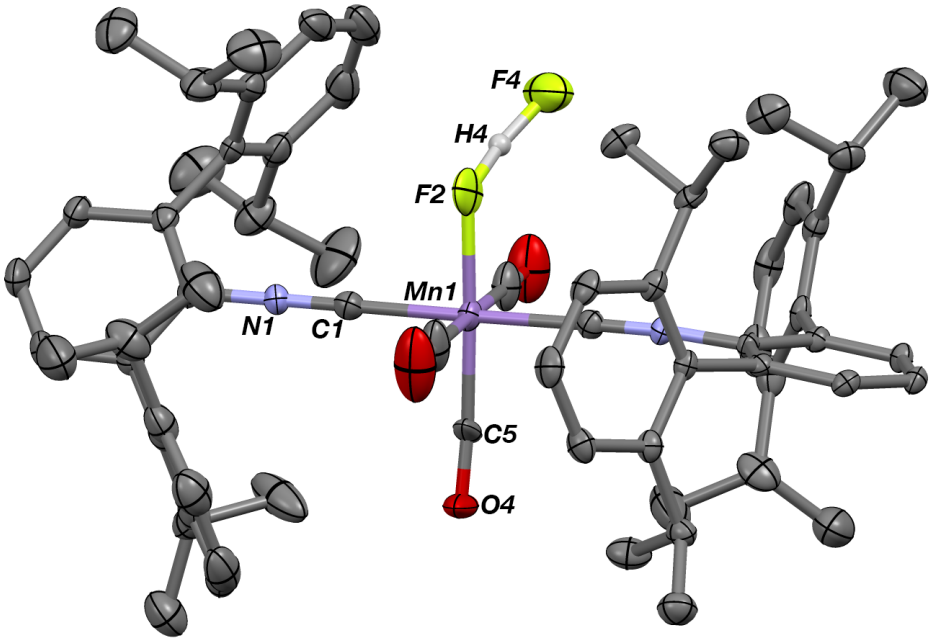

Figure 2.23. Molecular structure of $Mn(FHF)(CO)_3(CNAr^{Dipp2})_2$, with H atoms omitted for clarity. Selected bond distances (Å) and angles (º): F2-H4 = 1.10(5); F4-H4 = 1.20(5); Mn1-F2 = 1.943(11); Mn1-C5 = 1.811(12); Mn1-C1 = 1.927(2); Mn1-F2-H4 = 118(3); Mn-F1··F4 = 120.7(9); F2-Mn1-C1 = 88.7(2); F2-H4-F4 = 164(3).

In an attempt to gain further insight into the structure of $MnF(CO)_3(CNAr^{Dipp2})_2$, single crystals were grown from a concentrated diethyl ether solution at –35 ˚C and subjected to X-ray crystallographic analysis. The resultant structure solution indicated the expected *mer,trans*-stereochemical arrangement of the CO and $CNAr^{Dipp2}$ ligands, respectively, and the fluoride ligand was located in the apical position from the electron density map. However, additional electron density corresponding to another HF unit was observed in close proximity to the Mn-bound

fluoride atom, such that the structure from these crystals is more appropriately assigned as the bifluoride adduct $Mn(FHF)(CO)_3(CNAr^{Dipp2})_2$ (Figure 2), with a F···F distance of 2.276(2) Å. This is, to our knowledge, the first structurally characterized low-valent manganese biflouride complex.[98] Indeed, ^1H NMR analysis of these crystals revealed the presence of a new product (Figures 2.24 and 2.25), which displayed a doublet (J_{HF} = 411 Hz) at 10.91 ppm (C_6D_6, 20 °C). Additionally, a doublet (J_{HF} = 400 Hz) at –187.85 ppm as well as a broadened singlet at –482.20 ppm was observed in the ^{19}F NMR spectrum. These data are consistent with previously reported transition metal fluorides in which an HF molecule is strongly H-bonded to the terminal fluoride ligand.[98-99] We contend this HF molecule likely originates from the reaction of XeF_2 with adventitious water in the system.[100-101]

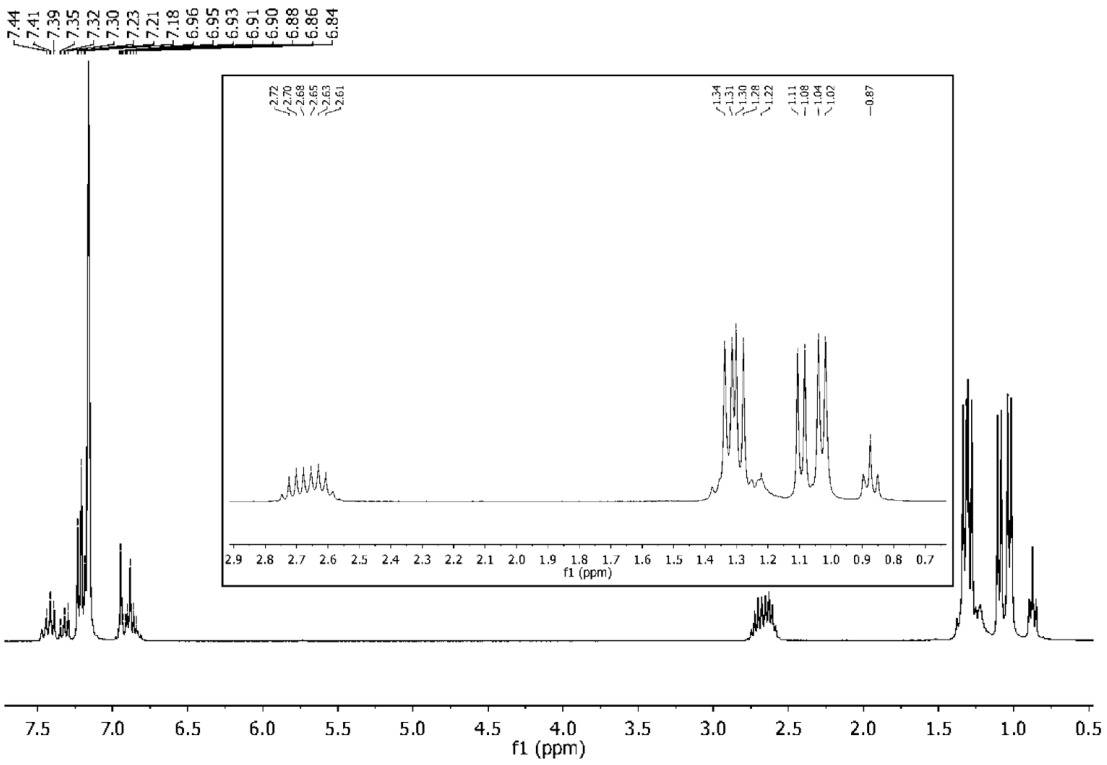

Figure 2.24. ^1H NMR (300.1 MHz, C_6D_6, 20 °C) of mixture resulting from decomposition of $MnF(CO)_3(CNAr^{Dipp2})_2$.

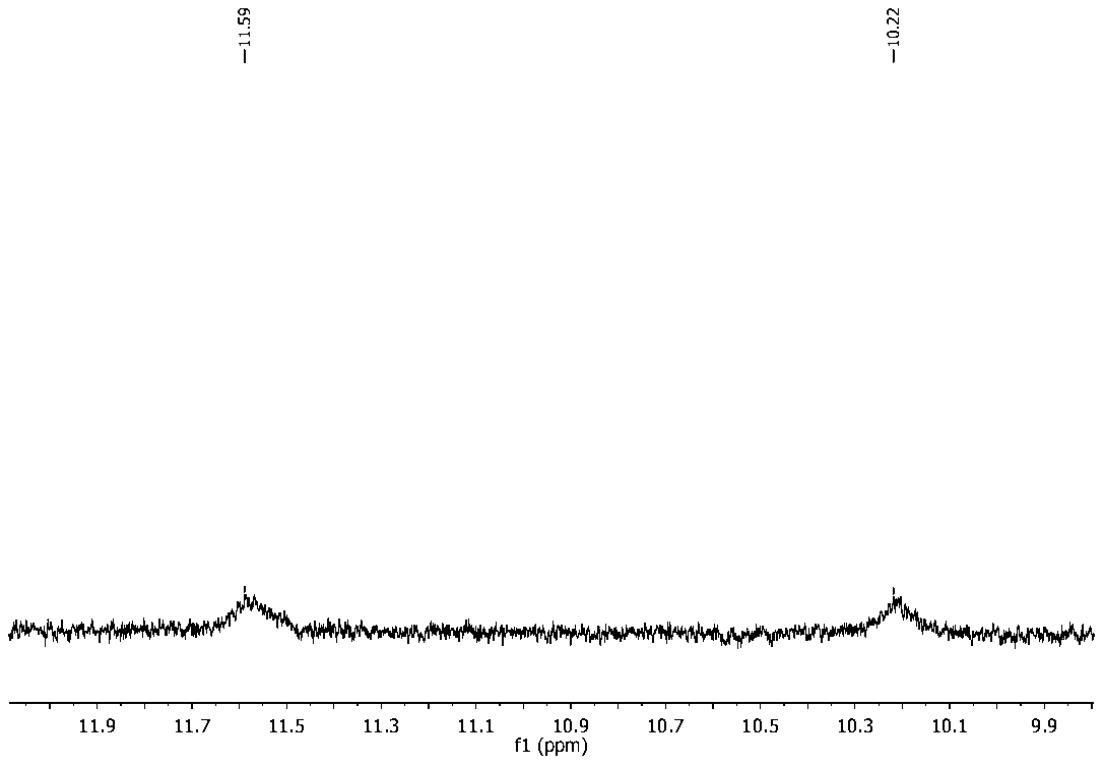

Figure 2.25. Inset view of ^{1}H NMR (300.1 MHz, C_6D_6, 20 ˚C) of upfield doublet resonance in mixture resulting from decomposition of $MnF(CO)_3(CNAr^{Dipp2})_2$.

Despite multiple attempts, we have thus far been unable to structurally characterize $MnF(CO)_3(CNAr^{Dipp2})_2$ in isolation; we nonetheless note that the formation of $MnF(CO)_3(CNAr^{Dipp2})_2$ in solution completes the halide series for mixed carbonyl/$CNAr^{Dipp2}$ manganese complexes, and provides a stable analogue to the unobserved metal carbonyl fluoride $FMn(CO)_5$.

While metalloradical $Mn(CO)_3(CNAr^{Dipp2})_2$ can be employed to generate metal bound main-group fragments, limitations were observed in several cases in attempts to more broadly extend this chemistry. For example, it was found that PCl_3, PCl_5, S_2Cl_2, and $AlCl_3$ generate $MnCl(CO)_3(CNAr^{Dipp2})_2$ as the exclusive product, and is invariant of the reaction stoichiometry. These reagents similarly produce $MnCl(CO)_3(CNAr^{Dipp2})_2$ when combined with $Na[Mn(CO)_3(CNAr^{Dipp2})_2]$, with the lone

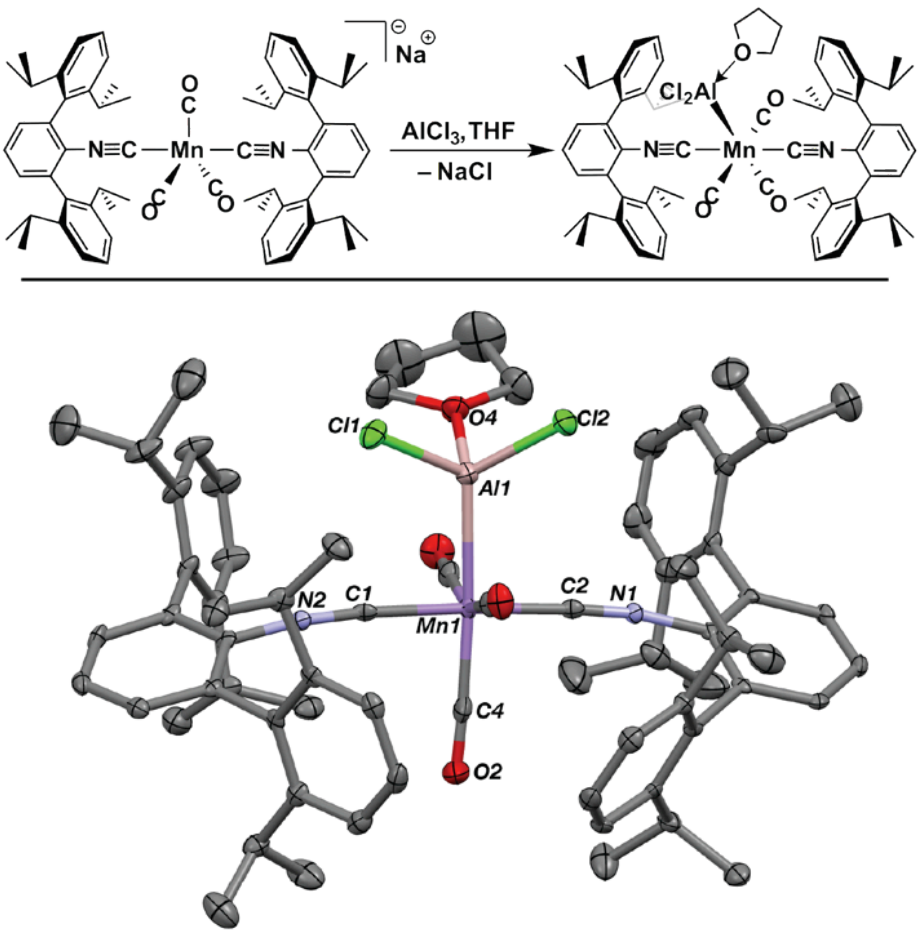

Figure 2.26. (*Top*) Formation of the Mn-aluminyl complex $Mn(AlCl_2{\cdot}THF)(CO)_3(CNAr^{Dipp2})_2$ via addition of $AlCl_3$ to $Na[Mn(CO)_3(CNAr^{Dipp2})_2]$. (*Bottom*) Solid state structure of $Mn(AlCl_2{\cdot}THF)(CO)_3(CNAr^{Dipp2})_2$, with H atoms omitted for clarity.

exception of $AlCl_3$, which generates $Mn(AlCl_2{\cdot}THF)(CO)_3(CNAr^{Dipp2})_2$ (Figure 3) in 74% yield with loss of NaCl . The molecular structure determined from X-ray crystallography reveals an octahedral complex in which the Mn-bound $AlCl_2$ group also binds a THF molecule. Importantly, both the diamagnetic NMR spectrum as well as the isocyanide IR band (ν_{CN} = 2057 cm^{-1}) are consistent with a Mn(I) oxidation state, indicating the $-AlCl_2(THF)$ group to be behaving as an X-type ligand.[102] Attempts at thermal desolvation under vacuum led to intractable mixtures and, notably, preparations involving the use of non-coordinating solvents, such as C_6H_6 or

toluene, led directly to the formation of $MnCl(CO)_3(CNAr^{Dipp2})_2$, potentially suggesting the necessity of an Al-solvento adduct in facilitating salt elimination. Interestingly, examples of transition metal-bound AlX_2 (X = halide) species are quite rare,[103-104] with only one reported metal-AlX_2 complex occurring with diamino substituents.[105] The pendant $Al(NR_2)_2$ groups in these latter complexes have been shown in some instances to behave as Lewis acidic sites and participate in cooperative reactivity with the transition metal center. Accordingly, we are currently developing an understanding of the pendant Lewis acidity in $Mn(AlCl_2{\cdot}THF)(CO)_3(CNAr^{Dipp2})_2$ towards functionalizable Lewis-basic substrates.

The above results demonstrate that, under appropriate conditions, a diverse series of manganese-main group complexes are available by both metalloradical and traditional salt elimination routes. Notably, the product distribution in the cases of $BiCl_3$ and SbF_3 are significantly dependent on the starting metal complex, indicating different reaction pathways are being accessed. While this breadth of reactivity was not observed in all cases – $AlCl_3$ being the notable example – this indicates that bimodal, complementary reactivity available to the starting metal complex should allow for facile exploration of routes towards functionalized transition metal-main group adducts. We are currently working to expand the reaction chemistry surveyed here to understand more fully its advantages and limitations.

2.5 Synthetic Procedures and Characterization Data

General Considerations. All manipulations were performed under an atmosphere of dry dinitrogen using standard Schlenk and glovebox techniques, unless otherwise stated. Solvents were dried and degassed according to standard procedures.[106] Reagent grade starting materials were purchased from commercial sources and purified according to standard procedures.[107] $SnCl_2$ was recrystallized from THF twice and thoroughly desolvated prior to use. The compounds $CNAr^{Dipp2}$,[108] $Na[Mn(CO)_3(CNAr^{Dipp2})_2]$,[109] *p*-nitrosotoluene,[110] *m*-nitrosotoluene[110] and H_2SnPh_2,[111] were prepared according to literature procedures. Benzene-d_6 (Cambridge Isotope Laboratories) was stirred over NaK alloy for two days, distilled, degassed, and stored over 4 Å molecular sieves. Photochemical substitution reactions were carried out in a standard borosilicate ampoule fitted with a gas-adapter side-arm for attachment to a vacuum line. Photolysis was performed via broad spectrum UV irradiation from an Oriel 1000 watt Universal Xenon Arc Lamp, model 8540.

Solution ^1H, $^{13}C\{^1H\}$ and $^{31}P\{^1H\}$ NMR spectra were recorded on a Bruker AVA300 spectrometer, a Varian Mercury 400 spectrometer, a Varian X-Sens 500 spectrometer, or a JEOL ECA-500 spectrometer. ^1H and $^{13}C\{^1H\}$ NMR chemical shifts are reported in ppm relative to $SiMe_4$ (^1H and $^{13}C\{^1H\}$ δ = 0.0 ppm) with reference to residual proton resonances of 7.16 ppm (^1H) and 128.06 ppm (^{13}C) for benzene-d_6.[112] $^{31}P\{^1H\}$ NMR spectra were referenced externally to 85% H_3PO_4 (δ = 0.0 ppm). Room temperature FTIR spectra were recorded on a Thermo-Nicolet iS10 FTIR spectrometer. Samples were prepared either as KBr pellets or as benzene-d_6 solutions injected into a ThermoFisher solution cell equipped with KBr windows.

Solvent peaks were digitally subtracted from all solution FTIR spectra using a previously recorded spectrum of the solvent. Combustion analyses were performed by Robertson Microlit Laboratories of Madison, New Jersey (USA).

Synthesis of $Mn(OTf)(CO)_3(CNAr^{Dipp2})_2$ (OTf = O_3SCF_3).

In a darkened glovebox, a suspension of AgOTf (0.048 g, 0.185 mmol, 1.1 eq) in 1 mL fluorobenzene was added to a fluorobenzene solution of $BrMn(CO)_3(CNAr^{Dipp2})_2$ (0.179 g, 0.168 mmol, 4 mL) and stirred at room temperature. Over the course of 1 h, a white precipitate formed in the reaction mixture. The mixture was filtered through a Celite plug and the solution was evaporated to dryness to yield $Mn(OTf)(CO)_3(CNAr^{Dipp2})_2$ as a yellow powder. Yield 0.176 g, 0.156 mmol, 95%. Single crystals suitable for X-ray diffraction were obtained from a saturated Et_2O solution stored at –35 ˚C. ^{1}H NMR (300.1 MHz, C_6D_6, 20 ˚C) δ = 7.40 (t, 2H, *J* = 8 Hz, *p*-Ar), 7.21 (d, 4H, *J* = 8 Hz, *m*-Ar), 6.93 (m, 8H, *m*-Dipp), 6.85 (dd, 4H, *J* = 8 Hz, *p*-Dipp), 2.66 (sept, 8H, *J* = 7 Hz, C*H*$(CH_3)_2$), 1.35 (d, 24H, *J* = 7 Hz, CH(C*H*$_3)_2$), 1.00 (d, 24H, *J* = 7 Hz, CH(C*H*$_3)_2$) ppm. FTIR (C_6D_6, KBr windows): ν_{CN} = 2131 cm^{-1} (vs), ν_{CO} = 2032 cm^{-1} (vs), 1954 cm^{-1} (s), also 2963, 2926, 2867, 1233, 1203, 1010, 757, 637 cm^{-1}. Anal. Calcd for $C_{66}H_{74}N_2O_6F_3SMn$: C, 69.83; H, 6.57; N, 2.47. Found: C, 68.92; H, 6.54; N, 2.36.

Synthesis of $Mn(CO)_3(CNAr^{Dipp2})_2$ (1). Method A: Comproportionation.

To a stirring Et_2O solution of $Mn(OTf)(CO)_3(CNAr^{Dipp2})_2$ (0.049 g, 0.044 mmol, 5 mL) was added $Na[Mn(CO)_3(CNAr^{Dipp2})_2]$ (0.045 g, 0.044 mmol), 5 mL) over the

course of five minutes. The solution was stirred for eight hours, during which time a white precipitate formed. The reaction mixture was filtered through Celite and filtrate was evaporated under reduced pressure. The dark green residue was washed with *n*-pentane (10 mL), extracted with Et_2O (10 mL) and filtered through Celite. Removal of the solvent *in vacuo* provided (**1**) as a green solid. Yield: 0.040 g, 0.0406 mmol, 92%. Emerald green, diffraction quality crystals were grown from a saturated Et_2O solution layered with *n*-pentane and stored at –35 ˚C overnight. ^{1}H NMR (400.1 MHz, C_6D_6, 20 ˚C) δ = 8.6 (b), 2.9 (b), 1.45 (b), 0.7 (b) ppm. FTIR (C_6D_6, KBr window, 25 ˚C): ν_{CN} = 2048 cm^{-1} (vs), 2016 cm^{-1} (w), ν_{CO} = 1944 cm^{-1} (s), 1912 cm^{-1} (m), also 2960, 2913, 1562, 1540, 1440, 1411, 1026, 755 and 639 cm^{-1}. FTIR (KBr pellet, 25 ˚C): ν_{CN} = 2051 cm^{-1} (vs), 2013 cm^{-1} (w), ν_{CO} = 1931 cm^{-1} (s), 1910 cm^{-1} (s), also 2960, 2924, 2867, 1595, 1578, 1461, 1413, 1381, 1361, 1053 and 606 cm^{-1}. Evan's Method: μ_{eff} (C_6D_6 with $(Me_3Si)_2O$ reference, 500.2 MHz, 20 ˚C, 4 runs) = 1.89(±0.04) μ_B. Anal. Calcd for $C_{65}H_{74}MnN_2O_3$: C, 79.16; H, 7.56; N, 2.84. Found: C, 78.25; H, 7.65; N, 2.86.

Synthesis of $Mn(CO)_3(CNAr^{Dipp2})_2$ (1). Method B: Photochemical Substitution.

In a 350 mL resealable ampoule equipped with a Teflon screw cap and a magnetic stirbar was added an *n*-hexane slurry of $Mn_2(CO)_{10}$ (0.216 g, 0.554 mmol, 20 mL) and $CNAr^{Dipp2}$ (0.953 g, 2.24 mmol, 4.04 equiv.). The yellow reaction mixture was subjected to three freeze/pump/thaw (F/P/T) cycles, after which it was exposed to UV irradiation for 5 minutes. The mixture was then subjected to two freeze/pump/thaw cycles to evacuate the liberated CO. The UV irradiation/(F/P/T) process was

continued, during which time the slurry became a deep orange solution with green precipitate. The process was repeated until no appreciable CO was liberated by visual inspection (~25 irradiation cycles). The ampoule was then transferred to a glovebox. The green precipitate was filtered using a medium porosity frit. The solid obtained was washed with *n*-hexane (10 mL) and cold *n*-pentane (10 mL), collected and then placed under vacuum to remove residual solvent. Yield: 0.917 g, 0.930 mmol, 83%.

Synthesis of $Mn(CO)_3(CNAr^{Dipp2})_2$ (1). Method C: Oxidation.

To a stirring Et_2O solution of $Na[Mn(CO)_3(CNAr^{Dipp2})_2]$ (0.050 g, 0.050 mmol, 6 mL) was added TlOTf (0.017 g, 0.049 mmol, 0.97 eq.) as a suspension in 1 mL Et_2O at room temperature. Over the course of 5 minutes, the deep purple solution became green-brown, with concurrent precipitation of a solid. The mixture was filtered through a fiberglass plug, and the solvent removed under reduced pressure. The resulting dark green solid was washed with *n*-pentane (5 mL) and all volatiles were removed *in vacuo*, providing **1** as a green solid. Yield: 0.032 g, 0.032 mmol, 64%.

Reaction between $Mn(CO)_3(CNAr^{Dipp2})_2$ (1) and H_2SnPh_2: Synthesis of $HMn(CO)_3(CNAr^{Dipp2})_2$ (2). A thawing Et_2O solution of $Mn(CO)_3(CNAr^{Dipp2})_2$ (**1**; 0.024 g, 0.0245 mmol, 5 ml) was combined with a frozen Et_2O solution of Ph_2SnH_2 (0.007 g, 0.0258, 1.05 eq, 2 mL), and the reaction solution was allowed to warm to room temperature while stirring. During this time, the color of the solution changed from dark green to yellow and was accompanied by precipitation of a solid. After 1 h, the solution was filtered through celite and the solvent removed under reduced

pressure to give $HMn(CO)_3(CNAr^{Dipp2})_2$ as a light yellow solid. Yield: 0.017 g, 0.0017 mmol, 70%. Characterization data for $HMn(CO)_3(CNAr^{Dipp2})_2$ has been reported previously.[4]

Reaction between $Mn(CO)_3(CNAr^{Dipp2})_2$ (1) and $HSnBu_3$: Synthesis of $HMn(CO)_3(CNAr^{Dipp2})_2$ (2) and $(Bu_3Sn)Mn(CO)_3(CNAr^{Dipp2})_2$ (3). A stirring diethyl ether solution of $Mn(CO)_3(CNAr^{Dipp2})_2$ (**1**; 0.018 g, 0.018 mmol, 5 ml) was treated with 5 equiv. of $HSnBu_3$ (0.027 g, 24 μl) and stirred at room temperature. The color of the solution changed from dark green to light yellow over the course of 8 hours, after which the solvent was removed under reduced pressure. ^{1}H NMR analysis of the crude reaction mixture showed a 1:1 mixture of $HMn(CO)_3(CNAr^{Dipp2})_2$ and $(Bu_3Sn)Mn(CO)_3(CNAr^{Dipp2})_2$ (**3**). Extraction of the crude mixture with *n*-pentane, followed by removal of solvent *in vacuo*, provided $(Bu_3Sn)Mn(CO)_3(CNAr^{Dipp2})_2$ (**3**) as a colorless solid. Yield: 0.010 g, 0.008 mmol, 44%. Recrystallization from a concentrated $Et_2O/(Me_3Si)_2O$ mixture at –35 ˚C for 2 days provided colorless single crystals of $(^nBu_3Sn)Mn(CO)_3(CNAr^{Dipp2})_2$ (**3**). Data for $(^nBu_3Sn)Mn(CO)_3(CNAr^{Dipp2})_2$: ^{1}H NMR (400.1 MHz, C_6D_6, 20 ˚C) δ 7.37 (t, 4H, J = 8 Hz, *p*-Dipp), 7.27 (d, 8H, J = 8 Hz, *m*-Dipp), 7.01 (d, 4H, J = 8 Hz, *m*-Ar), 6.87 (dd, 2H, J = 8, 7 Hz, *p*-Ar), 2.74 (sept, 8H, J = 7 Hz, C*H*$(CH_3)_2$), 1.42 (d, 24H, J = 7 Hz, CH(*CH*$_3)_2$), 1.09 (m, 18H, Sn(C*H*$_2)_3CH_3$), 1.06 (d, 24H, J = 7 Hz, CH(C*H*$_3)_2$), 0.98 (t, 9H, J = 8 Hz, $Sn(CH_2)_3CH_3$) ppm. ^{13}C{^{1}H} NMR (125.7 MHz, C_6D_6, 20 ˚C) δ = 219.4 (*cis*-*C*O), 218.6 (*trans*-*C*O), 189.4 (*C*N), 146.3, 137.9, 135.2, 130.9, 129.5, 128.3, 123.5, 31.2 ($SnCH_2(CH_2)_2CH_3$), 31.16 (C*H*$(CH_3)_2$), 28.0 ($SnCH_2(CH_2)_2CH_3$), 25.4

($CH(CH_3)_2$), 23.8 ($CH(CH_3)_2$), 14.0 ($SnCH_2(CH_2)_2CH_3$), 10.4 ($SnCH_2(CH_2)_2CH_3$) ppm (one Ar^{Dipp2} resonance obscured by the C_6D_6 residual). FTIR (C_6D_6, KBr windows, 25 ˚C): ν_{CN} = 2052 cm^{-1} (vs), ν_{CO} = 1949 cm^{-1} (vs), 1943 cm^{-1} (sh), also 2960, 2927, 2869, 2854, 1464, 1412, 757, 652, 635 cm^{-1}. HRMS (ESI-TOFMS, NCMe): Calc'd for $C_{77}H_{101}N_2O_3MnSn$ = 1276.6215. Found: *m/z* = 1293.6256 $[M+OH]^+$.

Reaction between $Mn(CO)_3(CNAr^{Dipp2})_2$ (1) and $CHCl_3$: Synthesis of $(Cl_2HC)Mn(CO)_3(CNAr^{Dipp2})_2$ (4) and $ClMn(CO)_3(CNAr^{Dipp2})_2$ (5). To an Et_2O solution of $Mn(CO)_3(CNAr^{Dipp2})_2$ (**1;** 0.014 g, 0.014 mmol, 5 mL) was added a solution of $CHCl_3$ in Et_2O (0.002 g, 0.014 mmol (1.3 μL), 1 mL), which resulted in a color change from green to light yellow. The solution was stirred for 1 minute, after which the volatiles were removed *in vacuo* to provide a 1:1 mixture of $(Cl_2HC)Mn(CO)_3(CNAr^{Dipp2})_2$ (**4**) and $ClMn(CO)_3(CNAr^{Dipp2})_2$ (**4**) as assayed by ^1H NMR. Dissolution of the mixture in Et_2O (2 mL), followed by storage at –35 ˚C for 24 h, led to selective crystallization of **4** as yellow X-ray diffraction quality crystals. Data for $(Cl_2HC)Mn(CO)_3(CNAr^{Dipp2})_2$ (**4**): ^1H NMR (400.1 MHz, C_6D_6, 20 ˚C) δ = 7.37 (t, 2H, *J* = 8 Hz, *p*-Ar), 7.23(d, 4H, *J* = 8 Hz, *m*-Ar), 6.94 (m, 8H, *m*-Dipp), 6.88 (dd, 4H, *J* = 8, 7 Hz, *p*-Dipp), 5.12 (s, 1H, $CHCl_2$), 2.69 (sept, 8H, *J* = 7 Hz, $CH(CH_3)_2$), 1.40 (d, 24H, *J* = 7 Hz, $CH(CH_3)_2$), 1.03 (d, 24H, J = 7 Hz, $CH(CH_3)_2$) ppm. FTIR (C_6D_6, KBr windows, 25 ˚C): ν_{CN} = 2096 cm^{-1} (vs), ν_{CO} = 1990 cm^{-1} (vs), 1956 cm^{-1} (w), also 2959, 2923, 2864, 1459, 1364, 1251, and 757cm^{-1}. HRMS (ESI-TOFMS, MeCN): Calc'd for $C_{66}H_{75}N_2O_3Cl_2Mn$, 1069.4614. Found *m/z* = 1069.6060 $[M]^+$.

Independent Synthesis of $ClMn(CO)_3(CNAr^{Dipp2})_2$ (5). To an Et_2O solution of $Mn(CO)_3(CNAr^{Dipp2})_2$ (**1**; 0.066 g, 0.067 mmol, 10 mL) was added PCl_5 (0.014 g, 0.067 mmol, 1.01 equiv.). The reaction mixture quickly became light yellow concomitant with the formation of a precipitate. The reaction mixture was filtered through a fiberglass plug and the solvent was removed under reduced pressure to produce a light orange solid. Recrystallization from a saturated THF solution at –40ºC produced yellow single crystals of $ClMn(CO)_3(CNAr^{Dipp2})_2$, which were dried *in* vacuo. Yield: 0.054 g, 0.053 mmol, 79%. ^{1}H NMR (500.1 MHz, C_6D_6, 20 ˚C) δ = 7.41 (t, 2H, *J* = 8 Hz, *p*-Ar), 7.19 (d, 4H, *J* = 8 Hz, *m*-Ar), 6.89 (m, 8H, *m*-Dipp), 6.82 (dd, 4H, *J* = 8, 7 Hz, *p*-Dipp), 2.63 (sept, 8H, *J* = 7 Hz, C*H*$(CH_3)_2$), 1.37 (d, 24H, *J* = 7 Hz, CH(*CH*$_3)_2$), 1.02 (d, 24H, *J* = 7 Hz, CH(C*H*$_3)_2$) ppm. ^{13}C{^{1}H} NMR (125.7 MHz, C_6D_6, 20 ˚C) δ = 217.3 (*C*O), 210.0 (*C*O), 173.2 (*C*N), 146.6, 139.7, 134.3 129.7, 129.6, 128.6, 128.3, 123.6, 31.5(C*H*$(CH_3)_2$), 24.6 (CH(C*H*$_3)_2$), 24.2 (CH(C*H*$_3)_2$) ppm. FTIR (C_6D_6, KBr windows, 25˚C): ν_{CN} = 2118 cm^{-1} (vs), ν_{CO} = 2015 cm^{-1} (vs), 2010 cm^{-1} (sh), 1940 cm^{-1} (s), also 2961, 2927, 2868, 1462, 755, 647, 630 cm^{-1}. HRMS (ESI-TOFMS, MeCN): Calc'd for $C_{65}H_{74}N_2O_3ClMn$ = 1020.4768; Found *m/z* = 985.5080 $[M–Cl]^+$.

Synthesis of $(\mu_2\text{-}\kappa^1\text{:}\kappa^1\text{-}1,4\text{-}O_2Me_4C_6)[Mn(CO)_3(CNAr^{Dipp2})_2]_2$ (6). Separately, an Et_2O solution of $Mn(CO)_3(CNAr^{Dipp2})_2$ (**1**; 0.063 g, 0.064 mmol, 10 mL) and an Et_2O solution of duroquinone (0.006 g, 0.035 mmol, 2 mL, 0.55 equiv) were prepared. The solution containing **1** was then frozen in a glovebox cold well. This frozen solution

was then placed on a stir plate and upon thawing, 1 mL of the duroquinone solution was added over 1 min, followed by stirring for an additional 2 min. The reaction mixture was then refrozen in the cold well, and the second 1 mL portion of duroquinone was added as the mixture began to thaw. The resulting mixture was stirred for 5 min, and then transferred to a –35 ºC freezer. The deep green solution became cherry red overnight and the volume was concentrated to 4 mL. Filtration of this solution through Celite, followed by removal of the solvent *in vacuo*, yielded a thermally unstable red solid. Yield: 0.027 g, 0.012 mmol, 16%. Dissolution of the solid in Et_2O, followed by storage at –40 ˚C for 2 weeks yielded red single crystals which were amenable to X-ray diffraction. ^{1}H NMR (400.1 MHz, C_6D_6, 20 ºC) δ = 7.36 (m, 4H), 7.19 (d, *J* = 8 Hz, 16H), 6.91 (d, *J* = 8 Hz, 8H), 6.90 (m, 4H), 2.63 (sept, *J* = 7 Hz, 4H), 2.2 (br s, 12H), 1.43 (d, *J* = 7 Hz, 64 H), 1.23 (d, *J* = 7 Hz, 64 H) ppm. ^{13}C{^{1}H} NMR (125.7 MHz, C_6D_6, 20 ºC) δ = 228.7 (*C*O), 224.4 (*C*O), 184.3 (*C*N), 146.2, 139.6, 135.2, 131.7, 130.1, 129.6, 125.6, 123.4, 31.5(*C*H(CH_3)), 25.7 (dur-*C*H_3), 24.6 (CH(*C*H_3)), 24.2 (CH(*C*H_3)) ppm. FTIR (C_6D_6, KBr windows, 20 ºC): $\nu_{CN/CO}$ = 2083 (s), 1976 (vs), 1958 (w), and 1906 (s) cm^{-1}; also 2962, 2928, 2867, 1460, 1410, 1263, and 1121 cm^{-1}. Due to the thermal decomposition of **6**, satisfactory combustion analysis and HRMS were not obtained.

Synthesis of (μ_2-η^1:η^1-P_4)[$Mn(CO)_3(CNAr^{Dipp2})_2]_2$ (7) (*trans,mer:cis,mer and trans,mer:trans,mer* isomers). To a stirring orange C_6H_6 solution of $Mn(CO)_3(CNAr^{Dipp2})_2$ (**1**; 0.036 g, 0.036 mmol, 5 mL) was added a solution of P_4 in C_6H_6 (0.023 g, 0.019 mmol, 0.51 eq., 2 mL) at room temperature. The solution slowly

became a light orange color over 30 minutes, after which the solvent was removed under reduced pressure. The resultant orange residue was extracted with pentane (1 x 2 mL) and filtered through a fiberglass plug. Thereafter the solvent was removed under reduced pressure to provide an orange solid. Yield: 0.032 g, 0.015 mmol, 85 %. Reddish-orange crystals of the *trans,mer:cis,mer* isomer suitable for x-ray diffraction were grown from a concentrated Et_2O solution stored at –40 ˚C. ^{1}H NMR (500.1 MHz, C_6D_6, 20 ˚C) δ = 7.15 (m, 8H, *m*-Ar), 7.09 (d, 16H, *m*-Dipp), 6.99 (m, 8H, *p*-Dipp), 6.83 (m, 4H, *p*-Ar), 2.80 (m, 16H, C*H*$(CH_3)_2$), 1.51 (d, 12H, *J* = 7 Hz, CH(C*H*$_3)_2$, *trans,mer:trans,mer* isomer), 1.50 (d, 12H, *J* = 7 Hz, CH(C*H*$_3)_2$, *trans,mer:cis,mer* isomer), 1.38 (d, 12H, *J* = 7 Hz, CH(C*H*$_3)_2$, *trans,mer:cis,mer* isomer), 1.30 (d, 12H, J = 7 Hz, CH(C*H*$_3)_2$, *trans,mer:cis,mer* isomer), 1.21 (d, 12H, *J* = 7 Hz, CH(C*H*$_3)_2$, *trans,mer:cis,mer* isomer), 1.18 (d, 24H, *J* = 7 Hz, CH(C*H*$_3)_2$, *trans,mer:cis,mer* and *trans,mer:trans,mer* isomers), 1.11 (d, 12H, *J* = 7 Hz, CH(C*H*$_3)_2$, *trans,mer:cis,mer* isomer) ppm. ^{13}C{^{1}H} NMR (125.7 MHz, C_6D_6, 20 ˚C) δ = 216.1 (*C*O), 178.5 (*C*N), 146.4, 146.3, 138.9, 138.8, 135.9, 135.1, 135.0, 131.0, 130.7, 130.6, 130.3, 130.0, 129.7, 129.4, 129.3, 129.2, 128.3, 123.9, 123.7, 123.6, 123.5, 31.4 (*C*H$(CH_3)_2$), 31.3 (*C*H$(CH_3)_2$), 31.2 (*C*H$(CH_3)_2$), 25.1 (CH(*C*H$_3)_2$), 25.0 (CH(*C*H$_3)_2$), 24.9 (CH(*C*H$_3)_2$), 24.8 (CH(*C*H$_3)_2$), 24.7 (CH(*C*H$_3)_2$), 24.3 (CH(*C*H$_3)_2$) ppm. Prolonged scanning failed to uncover the resonance for the carbonyl group on the *trans,mer:cis,mer* isomer. ^{31}P {^{1}H} NMR (202.7 MHz, C_6D_6, 20 ˚C) δ = –99.0 (dt, *J* = 264.7, 186.9 Hz, 1 P, *trans,mer:cis,mer* isomer), –116.9 (t, *J* = 186.3 Hz, 2P, *trans,mer:trans,mer* isomer), –122.2 (dt, J = 264.7, 186.9 Hz, 1 P, *trans,mer:cis,mer* isomer), –309.9 (dt, *J* = 15.5, 186 Hz, 2P, *trans,mer:cis,mer* isomer), –322.7 (t, *J* =

186.9 Hz, 2 P, *trans,mer:trans,mer* isomer). FTIR (C_6D_6, KBr windows): (*mixture of isomers)* $\nu_{CN/CO}$ = 2112 cm^{-1} (vs), 2071 cm^{-1} (vs), 2055 cm^{-1} (sh), 1967 cm^{-1} (s), 1941 cm^{-1} (m), also 2961, 2926, 2867, 1582, 1460, 1410, 1049, 844, 755, 624 cm^{-1}. Anal. Calcd for $C_{130}H_{148}Mn_2N_4O_6P_4$: C, 74.47; H, 7.12; N, 2.69. Found: C, 74.50; H, 6.99; N, 2.69.

Synthesis of (η^2-*N*,*O*-PhNO)Mn(CO)$_2$(CNAr^{Dipp2})$_2$ (8). An Et_2O solution of [$Mn(CO)_3(CNAr^{Dipp2})_2$] (**1;** 0.065 g, 0.066 mmol, 10 mL) was frozen in a cold well. Upon thawing, a cold Et_2O solution of nitrosobenzene (0.007 g, 0.0660 mmol, 2 mL) was added dropwise over 5 min with stirring. The resulting dark red solution was stirred for 15 min. and allowed to warm to room temperature. Volatiles were then removed *in vacuo*, and the resulting dark brown solid was washed with cold *n*-pentane (2 x 5 mL) to yield a red-brown solid. Yield: 0.054 g, 0.0514 mmol, 78%. Deep-red diffraction quality crystals were grown from a concentrated C_6H_{12} solution at room temperature over 2 days. ^{1}H NMR (400.1 MHz, C_6D_6, 20 ˚C) δ = 7.3, 6.5, 2.7, 1.4, 1.1 ppm. μ_{eff} (Evan's Method, C_6D_6 /$(Me_3Si)_2O$, 500.2 MHz, 20 ˚C, 4 runs) = 1.90(±0.11) μ_B. FTIR (KBr pellet, 25 ˚C): ν_{CN} = 2087 cm^{-1} (vs), ν_{CO} = 1966 cm^{-1} (s), 1907 cm^{-1} (s), also 1462, 1415, 1382, 1362, 1328 and 754 cm^{-1}. Anal. Calc'd for $C_{70}H_{79}N_3O_3Mn$: C, 78.92; H, 7.47; N, 3.94. Found: C, 77.84; H, 7.76; N, 3.70.

Synthesis of (η^2-*N*,*O*-*m*-TolNO)Mn(CO)$_2$(CNAr^{Dipp2})$_2$ (9). An Et_2O solution of $Mn(CO)_3(CNAr^{Dipp2})_2$ (**1**; 0.069 g, 0.070 mmol, 10 mL) was frozen in a cold well. Upon thawing, a cold Et_2O solution of *m*-nitrosotoluene (0.009 g, 0.073 mmol, 1.05

equiv, 2 mL) was added dropwise over 5 min. The resulting dark red solution was stirred for 15 minutes and allowed to warm to room temperature.Volatiles were then removed *in vacuo*, and the resulting dark brown solid was washed with cold *n*-pentane (2 x 5 mL) to yield a red-brown solid. Yield: 0.056 g, 0.052 mmol, 74%. X-ray diffraction quality crystals were grown from a concentrated C_6H_{12} solution at room temperature over 2 days. ^{1}H NMR (300.1 MHz, C_6D_6, 20 ˚C) δ = 7.5, 6.5, 2.7, 1.3, 1.0 ppm. μ_{eff} (Evan's Method, C_6D_6 /$(Me_3Si)_2O$, 500.2 MHz, 20 ˚C, 4 runs) = 2.25 (±0.07) μ_B. FTIR (C_6D_6, KBr windows, 25 ˚C): ν_{CN} = 2084 cm^{-1} (vs), ν_{CO} = 1964 cm^{-1} (s), 1905 cm^{-1} (s), also 2961, 2926, 2867, and 756 cm^{-1}. Anal. Calcd for $C_{71}H_{81}N_3O_3Mn$: C, 79.01; H, 7.56; N, 3.89. Found: C, 78.02; H, 7.51; N, 4.00.

Synthesis of (η^2-*N*,*O*-*p*-TolNO)Mn(CO)$_2$(CNAr^{Dipp2})$_2$ (10). An Et_2O solution of [Mn(CO)$_3$(CNAr^{Dipp2})$_2$] (**1**; 0.060 g, 0.061 mmol, 10 mL) was frozen in a cold well. Upon thawing, a cold Et_2O solution of *p*-nitrosotoluene (0.008 g, 0.0620 mmol, 1.01 equiv, 3 mL) was added dropwise over 5 min. The resulting dark red solution was stirred for 15 minutes while being allowed to warm to room temperature. Volatiles were removed *in vacuo*, and the resulting dark brown solid was washed with cold pentane (2 x 5 mL) to yield a red-brown solid. Yield: 0.049 g, 0.045 mmol, 74 %. X-ray diffraction quality crystals were grown from a concentrated C_6H_{12} solution at room temperature over 2 days. ^{1}H NMR (300.1 MHz, C_6D_6, 20 ˚C) δ = 7.4, 6.5, 2.7, 1.4, 1.1 ppm. μ_{eff} (Evan's Method, C_6D_6 /$(Me_3Si)_2O$, 500.2 MHz, 20 ˚C, 4 runs) = 1.95(±0.01) μ_B. FTIR (C_6D_6, KBr windows, 25 ˚C): ν_{CN} = 2081 cm^{-1} (vs), ν_{CO} = 1962 cm^{-1} (s),

1903 cm^{-1} (s), also 1496, 1415, 1058, 1028, and 652 cm^{-1}. Anal. Calcd for $C_{71}H_{81}N_3O_3Mn$: C, 79.01; H, 7.56; N, 3.89. Found: C, 78.03; H, 7.23; N, 3.90.

Synthesis of $((CO)_3(CNAr^{Dipp2})_2Mn(SCS)Mn(C{=}NAr^{Dipp2})(CO)_2(CNAr^{Dipp2})$. To an Et_2O solution of $[Mn(CO)_3(CNAr^{Dipp2})_2]$ (93 mg, 0.0943 mmol, 11 mL) was added an ethereal solution of CS_2 (0.094 mM, 1 mL, 1 eq) in one portion. The mixture was stirred for 6 h at room temperature, and gradually changed in color from orange to deep red. All volatiles were removed under reduced pressure, and the resulting residue was extracted with cold pentane (5 mL) and filtered. The pentane was removed *en vacuo* to provide a deep red/black solid. Yield: 66 mg, 0.0322 mmol, 34%. Storage of a concentrated Et_2O/TMS_2O solution at -35 ºC for 3 days produced red diffraction quality crystals. ^1H NMR (500.1 MHz, C_6D_6, 20 ºC) δ = 7.52 (m), 7.41 (t, J = 8 Hz), 7.34 (br s), 7.3 (d, 8 Hz), 7.08 (t, J = 7.55 Hz), 7.01 (d, J = 6 Hz), 6.94 (m), 6.84 (dt, J = 14.5, 7.3 Hz), 3.72 (br s), 3.64 (sept, J = 7 Hz), 2.84 (sept, J = 7 Hz), 2.63 (br s), 2.50 (br s), 1.64 (br s), 1.45 (br s), 1.27 (d, J = 7 ppm), 2.17 (br s), 1.15 (d, J = 7 Hz), 0.98 (br s) ppm. $^{13}C\{^1H\}$ NMR (125.7 MHz, C_6D_6, 20 ºC) δ = 261.2 (SC-*C*=N), 203.8 (S-*C*-S), 152.5, 148.4, 147.1, 146.5, 146.0, 139.4, 138.9, 138.5, 135.2, 134.9, 134.3, 31.5 (*C*H(CH_3)), 24.9 (CH(*C*H_3)) 24.7 (CH(*C*H_3)) ppm. FTIR (C_6D_6, KBr windows, 20 ºC): $\nu_{CN/CO}$ = 2140 cm^{-1} (w), 2085 cm^{-1} (s), 2049 cm^{-1} (vs), 2012 cm^{-1} (sh), 2004 cm^{-1} (s), 1964 cm^{-1} (m), 1945 cm^{-1} (s), 1919 cm^{-1} (s), also 2956, 2922, 2864, 1576, 1410, 1055, and 755 cm^{-1}. HR-MS (ESI-TOFMS): predicted for $C_{131}H_{148}Mn_2N_4O_6S_2^+$: 2047.9674; found *m/z* = 2047.9717.

Synthesis of $Mn(CO)_2(CNAr^{Dipp2})_2(NO)$. Inside a resealable glass ampoule, a benzene solution containing **1** (0.15 g, 0.152 mmol, 5 ml) was degassed by freeze-pump-thaw (3 cycles). Thereafter $NO_{(g)}$ was introduced to the atmosphere, and the solution was stirred for 5 min. During this time, the solution color changed from orange to deep red. After 5 min more stirring, the NO atmosphere was removed under vacuum. The ampoule was then brought into a glovebox, the solution filtered through a fiberglass plug, and all volatiles were removed under reduced pressure to provide a deep red solid. Yield, 0.142 g, 95%. Crystals suitable for X-ray analysis were prepared from a concentrated Et_2O solution stored at – 40 ˚C for 1 day. ^{1}H NMR (400.1 MHz, C_6D_6, 20 ºC) δ = 7.32 (t, 2H, J = 8 Hz, p-Ar), 7.16 (d, 4H, J = 8 Hz, m-Ar), 6.93 (m, 8H, m-Dipp), 6.85 (dd, 4H, J = 8.5, 6.5 Hz, p-Dipp), 2.68 (sept, 8H, J = 7 Hz, C*H*(CH3)2), 1.27 (d, 24H, J = 7 Hz, CH(*CH3*)2), 1.05 (d, 24H, J = 7 Hz, CH(C*H*3)2) ppm. $^{13}C\{^1H\}$ NMR (125.7 MHz, C_6D_6, 20 ºC) δ = 226.2 (*C*O), 184.4 (*C*N), 146.4, 138.7, 134.4, 129.7, 129.6, 128.3, 128.1, 123.5, 31.4 (C*H*$(CH_3)_2$), 24.6 (CH(C*H*$_3)_2$), 24.0 (CH(C*H*$_3)_2$) ppm. FTIR (C_6D_6, KBr windows): ν_{CN} = 2093 cm^{-1} (vs), ν_{CO} = 1983 cm^{-1} (w), ν_{CO} = 1922 cm^{-1} (s), ν_{NO} = 1702 cm^{-1}, also 2961, 2927, 2868, 1454, 1415, 755, 652, 627 cm^{-1}. Anal. Calcd for $C_{64}H_{74}MnN_3O_3$: C, 77.79%; H, 7.55%, N, 4.25%. Found: C, 75.95%; H, 7.33%; N, 4.10%.

Synthesis of $Mn(SnCl)(CO)_3(CNAr^{Dipp2})_2$ and $MnCl(CO)_3(CNAr^{Dipp2})_2$. To a stirring diethyl ether solution of $Mn(CO)_3(CNAr^{Dipp2})_2$ (0.046 g, 0.046 mmol, 5 ml) was added solid $SnCl_2$ (0.009 g, 0.046 mmol, 1 eq.). The color of the solution turned from orange to light yellow over the course of 5 minutes, and the mixture was stirred a further 15

minutes before all volatiles were removed *en vacuo*. A ^{1}H NMR of the product mixture indicated a 1:1.3 distribution between $Mn(SnCl)(CO)_3(CNAr^{Dipp2})_2$ and $MnCl(CO)_3(CNAr^{Dipp2})_2$ based upon integration of the respective ($CH(CH_3)$) protons. Extraction of the product mixture with pentane (2 X 5 ml) provides $Mn(SnCl)(CO)_3(CNAr^{Dipp2})_2$ as a green solid. Yield: 0.032 g, 32%. Characterization data has been previously published.[22]

Synthesis of $Mn(SbF_2)(CO)_3(CNAr^{Dipp2})_2$ and $MnF(CO)_3(CNAr^{Dipp2})_2$. A DME solution of $Mn(CO)_3(CNAr^{Dipp2})_2$ (0.016 g, 0.016 mmol, 4 mL) was treated with SbF_3 (0.029 g, 10 eq.) in one portion at room temperature. The mixture was stirred for 12 hours, after which the DME was removed *en vacuo*. The solid was taken up in C_6H_6 and filtered, and all volatiles were removed under reduced pressure to provide a dull yellow solid. Integration from a ^{1}H NMR spectrum reveals formation of $Mn(SbF_2)(CO)_3(CNAr^{Dipp2})_2$ and $MnF(CO)_3(CNAr^{Dipp2})_2$ in a 1:1.1 ratio, respectively, based upon integration of the respective (*p*-Ar) protons. Extraction of this mixture with *n*-pentane (5 X 10 ml), followed by cooling of the extracts to -40 ˚C caused $Mn(SbF_2)(CO)_3(CNAr^{Dipp2})_2$ to precipitate as an orange solid. Yield: 0.008 g, 43%.

Synthesis of $Mn(SbF_2)(CO)_3(CNAr^{Dipp2})_2$ using $Na[Mn(CO)_3(CNAr^{Dipp2})_2$. To a stirring THF solution of $Na[Mn(CO)_3(CNAr^{Dipp2})_2]$ (0.108 g, 0.108 mmol, 8 ml) was added SbF_3 (0.029 g, 0.162 mmol, 1.5 eq) as a solid, which turned the solution from deep purple to orange, with concurrent formation of a black precipitate. The mixture was filtered through a celite plug and the volatiles removed under reduced pressure.

The resulting orange solid was washed with pentane (4 X 5 ml) and then dissolved in benzene and filtered though a fiberglass plug. All volatiles were removed under reduced pressure, providing a light yellow solid. Yield: 0.067 g, 0.058 mmol, 54%. Diffraction quality crystals can be grown from a pyridine solution at -40 ºC. ^{1}H NMR (500.2 MHz, C_6D_6, 20 ºC) δ = 7.32 (t, 2H, J = 8 Hz, *p*-Ar), 7.18 (d, 4H, J = 8 Hz, *m*-Ar), 6.93 (m, 8H, *m*-Dipp), 6.83 (dd, 4H, J = 8.5, 6.5 Hz, *p*-Dipp), 2.68 (sept, 8H, J = 7 Hz, C*H*$(CH_3)_2$), 1.38 (d, 24H, J = 7 Hz, CH(*CH*$_3)_2$), 1.01 (d, 24H, J = 7 Hz, CH(C*H*$_3)_2$) ppm. ^{13}C NMR (125 MHz, C_6D_6, 20 ºC) = 211.6 (*C*O), 172.5 (*C*NR), 146.5, 139.2, 134.7, 130.1, 129.7, 123.6, 31.3 (*C*$(CH_3)_2$), 24.9 (C(*C*$H_3)_2$), 24.0 (C(*C*$H_3)_2$) ppm. Prolonged scanning did not uncover the second carbonyl resonance. ^{19}F NMR (470.6 Hz, C_6D_6, 20 ºC) δ = -166.0 ppm. FTIR (C_6D_6, KBr windows): ν_{CN} = 2087 cm^{-1} (vs), ν_{CO} = 1979 cm^{-1} (s), ν_{CO} = 1964 cm^{-1} (s), also 2854, 1593, 1457, 1385, 1363, 1058, 758, 645 cm^{-1}. HR-MS (ESI-TOFMS): predicted for $[M+H_3O]^+$ = $C_{65}H_{77}F_2MnN_2SbO_4$, 1163.4270; found *m/z* = 1163.4068. Repeated samples failed to provide a satisfactory elemental analysis.

Synthesis of $MnF(CO)_3(CNAr^{Dipp2})_2$. *Caution: XeF_2 is a highly reactive compound. Care must be taken to ensure limited contact with borosilicate glass containers for prolonged periods.* In a darkened glovebox, a fluorobenzene solution of $Mn(CO)_3(CNAr^{Dipp2})_2$ (0.037 g, 0.0375 mmol, 5 ml) was set stirring at room temperature in a glass scintillation vial. In a separate plastic vial, a weighed sample of XeF_2 (0.010 g, 0.056 mmol, 1.5 eq) was added in one portion to the stirring solution. The color of the solution gradually changed from orange to yellow over 5 minutes.

With continued stirring, all volatiles were removed under reduced pressure to yield a yellow solid. The solid was washed with pentane (3 X 5 ml) and extracted with diethyl ether to provide a light yellow powder. The powder was dissolved into a minimal amount of THF, filtered through a fiberglass plug, and stored at -40˚C for 2 days. The resulting crystals were washed with pentane, providing an analytically pure product. Yield: 0.015 g, 41%. ^{1}H NMR (500.1 MHz, C_6D_6, 20 ºC) δ 7.41 (t, 4H, J = 8 Hz, *p*-Dipp), 7.19 (d, 8H, J = 8 Hz, *m*-Dipp), 6.89 (d, 4H, J = 8 Hz, *m*-Ar), 6.82 (dd, 2H, J = 8, 7 Hz, *p*-Ar), 2.64 (sept, 8H, J = 7 Hz, C*H*$(CH_3)_2$), 1.38 (d, 24H, J = 7 Hz, CH(*C*$H_3)_2$), 1.02 (d, 24H, J = 7 Hz, CH(C*H*$_3)_2$) ppm. ^{13}C{^{1}H} NMR (125.7 MHz, C_6D_6, 20 ºC) δ = 218.0 (*cis-C*O, d, J = 172 Hz), 210.0 (*trans-C*O, d, J = 11 Hz), 172.5 (*C*N, d, 150 Hz), 146.4, 139.7, 134.3, 139.7, 128.6, 123.6, 31.5 (*C*H(CH_3)), 24.6 (CH(*C*$H_3)_2$), 24.3 (CH(*C*$H_3)_2$), ppm (two $CNAr^{Dipp2}$ aromatic resonances are obscured by the C_6D_6 signal). ^{19}F NMR (470.6 MHz, C_6D_6, 20 ºC, TFA standard) δ = -59.7 ppm. FTIR (C_6D_6, KBr windows): ν_{CN} = 2117 cm^{-1} (vs), ν_{CO} = 2014 cm^{-1} (vs), 2008 cm^{-1} (sh), 1942 (s), also 2961, 2926, 2868, 1568, 1480, 1437, 1133, 758, 677, 647cm^{-1}. Repeated combustion analyses routinely provided C and H values that indicated some incorporation of HF.

Synthesis of $Mn(BiCl_2)(CO)_3(CNAr^{Dipp2})_2$ and $MnCl(CO)_3(CNAr^{Dipp2})_2$. To a stirring diethyl ether solution of $Mn(CO)_3(CNAr^{Dipp2})_2$ (28 mg, 0.0284 mmol, 5 mL) was added a solution of $BiCl_3$ in diethyl ether (9 mg, 1 mL, 1 eq.). The orange solution became dark orange with concomitant precipitation of a black powder, and stirring was discontinued after 5 minutes. The solution was filtered and the solvent

was removed under reduced pressure. Integration from ^{1}H NMR spectra reveals a conversion of $Mn(CO)_3(CNAr^{Dipp2})_2$ to $Mn(BiCl_2)(CO)_3(CNAr^{Dipp2})_2$ and $MnCl(CO)_3(CNAr^{Dipp2})_2$ in a 0.4:1 ratio, respectively, based upon integration of the respective (*p*-Ar) protons. Light red single crystals of $Mn(BiCl_2)(CO)_3(CNAr^{Dipp2})_2$ are obtained from a concentrated THF solution at –40 ˚C overnight. The compound is light sensitive and slowly decomposes above –40 ˚C; decomposition provides Bi^0 (as a black solid) and $MnCl(CO)_3(CNAr^{Dipp2})_2$. Spectroscopic data for $Mn(BiCl_2)(CO)_3(CNAr^{Dipp2})_2$: ^{1}H NMR (300.1 MHz, C_6D_6, 20 ºC) δ = 7.34 (t, 2H, J = 8 Hz, *p*-Ar), 7.19 (d, 4H, J = 8 Hz, *m*-Ar), 6.92 (m, 8H, *m*-Dipp), 6.80 (dd, 4H, J = 8.5, 6.5 Hz, *p*-Dipp), 2.67 (sept, 8H, J = 7 Hz, C*H*$(CH_3)_2$), 1.35 (d, 24H, J = 7 Hz, CH(CH_3)$_2$), 0.99 (d, 24H, J = 7 Hz, CH(CH_3)$_2$) ppm. ^{13}C{^{1}H} NMR (125.7 MHz, C_6D_6, 20 ºC) δ = 209.4 (*trans*-*C*O), 203.8 (*cis*-*C*O), 164.7 (*C*N), 146.7, 139.8, 134.7, 130.4, 130.0, 123.9, 31.3 (*C*H(CH_3), 25.0 (CH(CH_3)$_2$), 24.3 (CH(CH_3)$_2$), ppm (two $CNAr^{Dipp2}$ aromatic resonances are obscured by the *proteo*-benzene impurity peak). FTIR (C_6D_6, KBr windows): ν_{CN} = 2093 cm^{-1} (vs), ν_{CO} = 1981 cm^{-1} (s), also 2964, 2926, 2869, 1458, 1030, 759, 645, 633 cm^{-1}. Attempts to collect combustion analysis of the purified material prepared as in S1.5 or S1.6 failed to provide satisfactory results. We believe this is due to the observed thermal instability which routinely provides $MnCl(CO)_3(CNAr^{Dipp2})_2$ as the sole identifiable compound.

Synthesis of $Mn(Cl_2Bi)(CO)_3(CNAr^{Dipp2})_2$ using $Na[Mn(CO)_3(CNAr^{Dipp2})_2]$. To a thawing THF solution of $Na[Mn(CO)_3(CNAr^{Dipp2})_2]$ (0.092 g, 0.091 mmol, 10 mL) was added a solution of $BiCl_3$ (0.029 g, 1.01 eq, 10 mL) over 15 minutes, slowly turning

the solution deep orange. The solution was stirred for an additional 5 minutes, after which it was filtered through a Celite plug and the solvent removed under reduced pressure to provide a red solid. Yield: 0.037 g, 32%. Light red single crystals of $Mn(BiCl_2)(CO)_3(CNAr^{Dipp2})_2$ are obtained from a concentrated THF solution at –40 °C overnight.

Synthesis of $Mn(AlCl_2{\cdot}THF)(CO)_3(CNAr^{Dipp2})_2$. A stirring THF solution of $Na[Mn(CO)_3(CNAr^{Dipp2})_2]$ (0.063 g, 0.063 mmol, 5 ml) is slowly treated with a THF solution of $AlCl_3$ (0.009 g, 0.065 mmol, 1.05 eq., 2 ml) at room temperature over 5 minutes. After approximately 30 minutes stirring, the deep purple color lightens to yellow. Thereafter, the solvent is removed *en vacuo* to provide a yellow solid. This solid is then subject to two cycles of *n*-pentane addition and removal under vacuum to desolvate remaining salts. Extraction of the yellow solid with Et_2O (3 X 2 ml), followed by evaporation of the combined extracts under vacuum, provides analytically pure $Mn(AlCl_2{\cdot}THF)(CO)_3(CNAr^{Dipp2})_2$ as a yellow solid. Yield: 0.053 g, 74 %. ^1H NMR (500.1 MHz, C_6D_6, 20 ºC) δ 7.32 (t, 4H, J = 8 Hz, *p*-Dipp), 7.23 (d, 8H, J = 8 Hz, *m*-Dipp), 7.06 (d, 4H, J = 8 Hz, *m*-Ar), 6.91 (dd, 2H, J = 8, 7 Hz, *p*-Ar), 3.44 (m, THF), 2.82 (sept, 8H, J = 7 Hz, C*H*$(CH_3)_2$), 1.48 (d, 24H, J = 7 Hz, CH(*CH*$_3)_2$), 1.27 (m, THF), 1.05 (d, 24H, J = 7 Hz, CH(C*H*$_3)_2$) ppm. $^{13}C\{^1H\}$ NMR (125.7 MHz, C_6D_6, 20 ºC) δ = 219.1 (*trans-C*O), 210.0 (*cis-C*O), 182.4 (*C*N), 146.8, 137.8, 135.7, 130.9, 129.0, 126.1, 123.4, 72.5 (THF), 31.2 (*C*H$(CH_3)_2$), 25.7 (CH(*C*H$_3)_2$), 25.0 (THF), 23.5 (CH(*C*H$_3)_2$), ppm. FTIR (C_6D_6, KBr windows): ν_{CN} = 2057 cm^{-1} (vs), ν_{CO} = 1951 cm^{-1} (s), 1918 cm^{-1} (vs), also 3065, 2961, 2925, 2865, 1578, 1458, 1411, 1385, 1363, 1331,

1056, 1004, 757, 657cm^{-1}. Anal. Calcd for $C_{69}H_{82}AlCl_2MnN_2O_4$: C, 71.66; H, 7.15; N, 2.42. Found: C, 71.93; H, 6.75; N, 1.99.

2.6 EPR Procedures and Measurements

X-Band EPR Measurements. X-Band continuous wave (CW) EPR spectra were measured on a Bruker E500 spectrometer equipped with a Bruker ER 041 X Microwave Bridge and a liquid nitrogen cooling system. Spectra were recorded in 4 mm quartz tubes, and the magnetic field was calibrated with DPPH. Samples were prepared in a dinitrogen-filled glovebox from analytical-grade crystals in concentrations ranging between 0.2-0.5 mM. Complex **1** was prepared in dry Et_2O and all other spectra were recorded in dry toluene. To ensure no decomposition products were formed during spectral acquisition, all samples were checked by ^{1}H NMR and IR spectroscopy immediately after EPR data acquisition. Spectra of $Mn(CO)_3(CNAr^{Dipp2})_2$ (**1**) and (η^2-*N,O*-PhNO)$Mn(CO)_2(CNAr^{Dipp2})_2$ (**8**) were collected at variable temperatures (295 K, 225 K, 200 K, 180 K, 151 K) to probe diffusion effects in the spectrum; it was found that at lower temperatures significant changeover to a fast-motion regime occurred. Additionally, spectra of **1** and **8** were measured at 0.005 mM, 0.05 mM, and 0.5 mM to investigate possible intermolecular effects causing additional lines. No effect was observed, but it should be noted that the spectra at 0.005 mM was particularly weak, causing spectral distortion as a result of high microwave power. Spectral quality was deemed to be the best at 0.05 mM, which are reported. Simulations for complex **1** were performed using the program

EasySpin.[113] Due to the complexity associated with ^{1}H superhyperfine coupling in the EPR spectra of complexes **8**-**10**, reasonable-quality simulations were not obtained. Spin density plots showing the origin of ^{1}H hyperfine coupling for **8**-**10** can be found in section 2.3. A_{iso}(Mn) and A_{iso}(N) values for complexes **8**-**10** are estimated from the experimental spectra.

Spectrometer Conditions

$Mn(CO)_3(CNAr^{Dipp2})_2$ (1; 0.05 mM): X-band (9.3769 GHz): centerfield/sweep-width = 3300 G/200 G; microwave power = 0.4104 mW; modulation amplitude = 1.00 G; modulation frequency = 100.0 KHz; time constant = 2.56 ms; scans = 16.

(η^2-*N,O*-PhNO)$Mn(CO)_2(CNAr^{Dipp2})_2$ (8; **0.05 mM):** X-band (9.3836 GHz): centerfield/sweep-width = 3340 G/125 G; microwave power = 6.377 mW; modulation amplitude = 0.5 G; modulation frequency = 100.0 KHz; time constant = 10.49 ms; scans = 32.

(η^2-*N,O*-*m*-TolNO)$Mn(CO)_2(CNAr^{Dipp2})_2$ (9; **0.05 mM):** X-band (9.3861 GHz): centerfield/sweep-width = 3340 G/140 G; microwave power = 0.1008 mW; modulation amplitude = 0.5 G; modulation frequency = 100.0 KHz; time constant = 20.97 ms; scans = 32.

(η^2-*N,O-p*-TolNO)Mn(CO)$_2$(CNAr^{Dipp2})$_2$ (10; 0.05 mM): X-band (9.3888 GHz): centerfield/sweep-width = 3340 G/170 G; microwave power = 0.06362 mW; modulation amplitude = 0.1 G; modulation frequency = 100.0 KHz; time constant = 20.97 ms; scans = 32.

2.7 Results from Computational Studies

Computational Details. Density Functional Theory calculations were performed using the Amsterdam Density Functional (ADF) program suite, version 2012.01.[114-116] Optimized molecular structures and spin density plots were visualized with the ADFView graphical interface of the ADF-GUI.[117] Initial geometries were derived from X-ray structure determinations and the *m*-terphenyl isocyanide ligands were abbreviated to 2,6-xylyl isocyanide (i.e. 2,6-$Me_2C_6H_3NC$) for computational expedience. We have previously shown by experimental methods that the *m*-terphenyl isocyanide CNAr^{Dipp2} and CNXyl exert a similar electronic influence on transition metal centers.[118] Relativistic effects were included in all calculations using the zeroth-order regular approximation (ZORA).[119,120] For all atoms, the triple-ζ Slater-type orbital TZ2P ADF basis set was utilized without frozen cores. The local density approximation (LDA) of Vosko, Wilk and Nusair (VWN)[121], was used in tandem with the generalized gradient approximations (CGA) described by Becke[122] and [123,124] for all electron exchange and correlation, respectively.

Table 2.1. Thermodynamic Calculations for CO Dissociation and Formation of η^2-Nitroxide Species from $XMn(CO)_3(CNXyl)_2$ Complexes (X = Phenylnitroxide).

Model Complex	**Total Bonding Energy (kcal/mol)**
(κ^1-*N*-PhNO)$Mn(CO)_3(CNXyl)_2$	–8798.30
(κ^1-*O*-PhNO)-$Mn(CO)_3(CNXyl)_2$	–8795.22
(η^2-*N*,*O*-PhNO)-$Mn(CO)_2(CNXyl)_2$	–8446.69
CO	–341.46

Note: The κ^1-*O* phenylnitroxide complex (κ^1-*O*-PhNO)$Mn(CO)_3(CNXyl)_2$ was included for completeness. The calculations reveal that the κ^1-*O* isomer is *ca*. 3.0 kcal/mol disfavored relative to the κ^1-*N* phenylnitroxide isomer.

Table 2.2. Thermodynamic Calculations for CO Dissociation and Formation of η^2-Nitroxide Species from $XMn(CO)_5$ Complexes (X = Phenylnitroxide).

Model Complex	**Total Bonding Energy (kcal/mol)**
(κ^1-*N*-PhNO)$Mn(CO)_5$	–3960.61
(κ^1-*O*-PhNO)$Mn(CO)_5$	–3956.86
(η^2-PhNO)$Mn(CO)_4$	–3613.25

Note: The κ^1-*O* phenylnitroxide complex (κ^1-*O*-PhNO)$Mn(CO)_5$ was included for completeness. The calculations reveal that the κ^1-*O* isomer is *ca*. 3.3 kcal/mol disfavored relative to the κ^1-*N* phenylnitroxide isomer.

Spin Density Plots for $Mn(CO)_3(CNXyl)_2$, (η^2-*N*,*O*-PhNO)$Mn(CO)_2(CNXyl)_2$, (η^2-*N*,*O m*-TolNO)$Mn(CO)_2(CNXyl)_2$, (η^2-*N*,*O*-*p*-TolNO)$Mn(CO)_2(CNXyl)_2$.

Sample Input File for $Mn(CO)_3(CNXyl)_2$

#########

```
$ADFBIN/adf -n8 \
 <<< "
TITLE Mn_CO3_CNXyl2 geo opt

MAXMEMORYUSAGE 23000

RELATIVISTIC ZORA

UNRESTRICTED

CHARGE 0 1
SCF

DIIS
END

XC
 LDA VWN
 GGA Becke Perdew
END

SYMMETRY NOSYM
ATOMS
Mn      -1.70624726      10.31708157       5.27289025
N       -1.57370241      13.37160776       5.09509044
N       -1.62210121       7.26080010       5.12402327
C       -1.64753550      14.74799793       5.09814094
C       -2.13532375      15.40199643       6.25341166
C       -2.56568636      14.61365102       7.46052467
C       -1.66912394       5.88594712       5.11923234
C       -2.04244260       5.21980531       3.92836803
C       -1.78205327       3.11242973       5.11469395
C       -1.62509473       8.44561489       5.16807193
C       -2.20867809      16.79729256       6.22291158
C       -2.72558548      10.32182848       3.74515231
C       -1.59000314      12.18814297       5.15607891
C       -2.37790658       6.00099982       2.68686869
C       -3.03289206      10.35141405       6.46883616
C       -1.35169743       5.18814286       6.30862684
C       -0.97022604       5.93556264       7.55769679
C       -0.72998361      14.71533979       2.73594043
C       -1.33756824      16.84759406       3.96824637
C       -0.30036494      10.29374778       6.45560540
O       -3.89580303      10.37914479       7.24938570
C       -1.81534909      17.51695954       5.09484164
O       -3.38589556      10.32275769       2.79152332
C       -2.09106470       3.82366253       3.95496750
C       -1.24177622      15.45373510       3.94328416
O        0.57935838      10.26825392       7.21100608
C       -1.41659079       3.79277516       6.27673287
H       -1.73711425      14.01415487       7.86321017
H       -3.37226590      13.90992597       7.21145326
H       -2.92437752      15.28013022       8.25296370
H       -1.82806475       2.02458515       5.11346511
H       -2.58391586      17.32247931       7.10120767
H       -1.54468202       6.65182897       2.38720871
H       -3.24671005       6.65465243       2.84940529
```

```
H      -2.60671860       5.32820853       1.85274599
H      -0.78679713       5.24251482       8.38639153
H      -1.76305396       6.63335390       7.86165110
H      -0.06246008       6.53595704       7.40358325
H      -0.41506110      15.41617353       1.95453442
H      -1.50286025      14.05604343       2.31563267
H       0.12577084      14.07579594       2.99315180
H      -1.03021535      17.41236863       3.08809609
H      -1.88206158      18.60363082       5.09356278
H      -2.37795863       3.29022923       3.04890414
H      -1.17949052       3.23496616       7.18280090


END

GEOMETRY
 Iterations 300
 GO
END

BASIS
 type TZ2P
 core none
END

END INPUT
```

Optimized Geometries of $Mn(CO)_3(CNXyl)_2$, (η^2-*N*,*O*-PhNO)$Mn(CO)_2(CNXyl)_2$, (η^2-*N*,*O*-*p*-TolNO)$Mn(CO)_2(CNXyl)_2$, (η^2-*N*,*O*-*m*-TolNO)$Mn(CO)_2(CNXyl)_2$, (κ^1-*N*-PhNO)$Mn(CO)_3(CNXyl)_2$, (κ^1-*O*-PhNO)$Mn(CO)_3(CNXyl)_2$, (κ^1-*N*-PhNO)$Mn(CO)_5$, (κ^1-*O*-PhNO)$Mn(CO)_5$, (η^2-*N*,*O*-PhNO)$Mn(CO)_4$, and CO.

```
# Mn(CO)3(CNXyl)2

Mn     -1.70624726      10.31708157       5.27289025
N      -1.57370241      13.37160776       5.09509044
N      -1.62210121       7.26080010       5.12402327
C      -1.64753550      14.74799793       5.09814094
C      -2.13532375      15.40199643       6.25341166
C      -2.56568636      14.61365102       7.46052467
C      -1.66912394       5.88594712       5.11923234
C      -2.04244260       5.21980531       3.92836803
C      -1.78205327       3.11242973       5.11469395
C      -1.62509473       8.44561489       5.16807193
C      -2.20867809      16.79729256       6.22291158
C      -2.72558548      10.32182848       3.74515231
C      -1.59000314      12.18814297       5.15607891
C      -2.37790658       6.00099982       2.68686869
C      -3.03289206      10.35141405       6.46883616
C      -1.35169743       5.18814286       6.30862684
C      -0.97022604       5.93556264       7.55769679
C      -0.72998361      14.71533979       2.73594043
C      -1.33756824      16.84759406       3.96824637
C      -0.30036494      10.29374778       6.45560540
O      -3.89580303      10.37914479       7.24938570
C      -1.81534909      17.51695954       5.09484164
O      -3.38589556      10.32275769       2.79152332
```

C	-2.09106470	3.82366253	3.95496750
C	-1.24177622	15.45373510	3.94328416
O	0.57935838	10.26825392	7.21100608
C	-1.41659079	3.79277516	6.27673287
H	-1.73711425	14.01415487	7.86321017
H	-3.37226590	13.90992597	7.21145326
H	-2.92437752	15.28013022	8.25296370
H	-1.82806475	2.02458515	5.11346511
H	-2.58391586	17.32247931	7.10120767
H	-1.54468202	6.65182897	2.38720871
H	-3.24671005	6.65465243	2.84940529
H	-2.60671860	5.32820853	1.85274599
H	-0.78679713	5.24251482	8.38639153
H	-1.76305396	6.63335390	7.86165110
H	-0.06246008	6.53595704	7.40358325
H	-0.41506110	15.41617353	1.95453442
H	-1.50286025	14.05604343	2.31563267
H	0.12577084	14.07579594	2.99315180
H	-1.03021535	17.41236863	3.08809609
H	-1.88206158	18.60363082	5.09356278
H	-2.37795863	3.29022923	3.04890414
H	-1.17949052	3.23496616	7.18280090

####

#(η^2-N,O-PhNO)Mn(CO)$_2$(CNXyl)$_2$

Mn	4.02801760	12.12097434	5.63115641
N	4.17325478	15.19372591	5.70852641
C	4.06027717	14.01760517	5.66109435
C	4.32756422	16.56073826	5.80623611
C	3.95568544	17.36766214	4.70684023
C	4.12450274	18.74907233	4.83309530
H	3.84760229	19.39113494	3.99705769
C	4.64027740	19.30940094	6.00155780
H	4.76367379	20.38848617	6.07842082
C	5.00299134	18.49044200	7.07035712
H	5.40980239	18.93055865	7.98087497
C	4.85906042	17.10204864	6.99919921
C	3.40542201	16.74810771	3.45129067
C	4.33728341	7.68227031	5.80956630
C	5.25774290	8.05191222	8.14556473
C	1.77764477	12.13580036	3.29519176
C	2.48061852	12.15374599	2.06584784
C	3.96718601	6.86754840	4.71554663
C	1.77722196	12.16884195	0.86971718
H	2.32244891	12.18401844	-0.07342583
C	0.37386288	12.16426372	0.86664516
H	-0.17167075	12.17478810	-0.07544489
O	6.58134109	12.12140657	4.17151524
O	5.15993263	12.12903461	8.36425487
O	1.93961470	12.11938551	5.63569852
N	2.49974063	12.12401749	4.45289066
C	5.58327294	12.12120195	4.77202680
C	4.73104053	12.12370240	7.28222668
C	4.15309872	5.48835820	4.84494402

H	3.87710113	4.84014600	4.01306096
C	4.68406914	4.93782286	6.01116169
H	4.82233822	3.86091339	6.08939852
C	5.04000425	5.76395581	7.07684746
H	5.45535601	5.33131167	7.98710560
C	4.87588484	7.14987789	7.00372440
C	3.39823872	7.47546376	3.46256779
C	-0.32192298	12.14505724	2.08459810
H	-1.41168852	12.14066959	2.08522912
C	0.35934330	12.13134847	3.29442275
N	4.17319127	9.04794308	5.70750478
C	4.06024422	10.22397402	5.65994719
C	5.25856926	16.20721444	8.14071832
H	4.11101518	16.02212149	3.02389845
H	3.20082040	17.51465585	2.69554091
H	2.47343655	16.20071904	3.65001471
H	5.63285747	7.46860024	8.99395615
H	4.40061994	8.64775242	8.48892747
H	6.03830787	8.76577669	7.84725726
H	3.56942925	12.15596966	2.08403882
H	4.09527942	8.20024821	3.01955782
H	2.46691467	8.02092708	3.66964067
H	3.18615319	6.70185754	2.71616035
H	-0.16567782	12.11773277	4.24708038
H	6.02817577	15.48600381	7.83211388
H	4.40533534	15.62004474	8.50792298
H	5.65619783	16.79584408	8.97496625

####

#(η^2-N,O-*p*-*Tol*NO)Mn(CO)$_2$(CNXyl)$_2$

Mn	-3.61207539	12.07550262	4.70047706
C	-3.71345069	7.62378281	4.53891618
N	-3.66185538	8.99968846	4.61768394
C	-3.34595484	5.46879643	5.53847485
H	-3.02378595	4.85979757	6.38293916
C	-3.80763671	4.85643854	4.37364525
H	-3.84461044	3.77023214	4.30869343
H	0.37046212	12.12275189	6.60006091
C	-2.79407430	7.53573833	6.90036954
C	-3.28758220	6.86096985	5.64994767
C	0.04048043	12.16375496	11.29154800
C	-3.71322919	16.52727749	4.54903531
C	-0.55723322	12.16189945	9.90705144
C	-4.22607959	5.63272366	3.29308260
H	-4.59182028	5.15168938	2.38558975
C	-1.95270397	12.13795718	9.71610406
C	-4.64747456	7.87755424	2.19368928
C	-4.19088002	7.02868303	3.34899231
C	-4.26792719	18.51383761	3.31435114
H	-4.66011904	18.99169219	2.41662688
C	-3.82259167	19.29393812	4.38131773
H	-3.86614107	20.37978963	4.31503523
H	-2.61047742	12.14705204	10.58650702
C	-3.32542271	18.68546829	5.53376193
C	-4.70894568	16.26466689	2.23056072
C	-4.22552746	17.11811103	3.37157030

H	-2.98056876	19.29646269	6.36811425
C	-3.25900781	17.29378770	5.64604713
C	-3.60785502	13.97160048	4.67950423
H	0.20854587	11.13702137	11.65359757
C	-2.72835493	16.62414614	6.88389586
N	-3.65854225	15.15170070	4.63094279
H	-3.59119063	12.09057483	8.30682318
O	-1.54272726	12.07636141	4.96857182
C	-0.26719318	12.12410462	7.48131773
C	-4.09821404	12.08168982	2.97367626
O	-6.34626660	12.07724379	5.78579328
C	-5.27176619	12.07606309	5.33555194
N	-2.24943427	12.07331036	6.07201594
C	-3.60993578	10.17952181	4.67162299
C	-1.67381111	12.09927386	7.30737653
C	0.26302228	12.15533776	8.76271728
C	-2.51175154	12.10615260	8.44769176
O	-4.39127390	12.08742148	1.84688828
H	-2.44149112	17.36720280	7.63641403
H	-2.51968376	6.79593481	7.66072374
H	-3.56123540	8.19838427	7.32456603
H	-1.91583480	8.16381382	6.69578307
H	-0.62055602	12.65834678	12.01471216
H	1.01109275	12.67593837	11.30929247
H	1.34733019	12.17822891	8.88606315
H	-3.83301066	8.51088966	1.81517502
H	-5.46012130	8.55427114	2.49234792
H	-5.00792960	7.25151059	1.36972330
H	-3.90216386	15.63326101	1.83287587
H	-5.09254159	16.88692290	1.41420983
H	-5.51087856	15.58555201	2.55192985
H	-1.85004405	16.00350144	6.65797071
H	-3.47871550	15.95537356	7.32791231

######

#(η^2-N,O-*m*-*Tol*NO)Mn(CO)$_2$(CNXyl)$_2$

Mn	-0.16128912	12.17523091	0.18843171
N	-0.15246341	9.09997593	0.08016123
C	0.28842011	17.44166829	0.95966565
C	-1.12382004	8.02405783	-2.36941061
C	0.27516553	18.82380734	0.75103808
C	-0.16773939	14.07113050	0.17653405
C	-0.58344787	5.76163837	-1.36031924
C	0.78631394	16.83918550	2.24499326
C	-0.61356668	7.15463907	-1.25221722
N	-0.17422324	15.25019396	0.08510648
C	-0.14338582	7.72693032	-0.04803819
C	-0.10897413	4.96684393	-0.31675142
C	0.33744755	6.94539040	1.02691542
C	0.34388630	5.55711373	0.86316142
C	-0.15455263	10.27917780	0.16392703
C	0.82309842	7.59641566	2.29287065
H	-1.01290729	18.96161239	-2.39778356
C	-1.16194267	16.23228935	-2.39687818
H	3.28826340	12.17367413	1.21190100
H	5.20380249	12.07215010	2.81036574
H	4.78840736	11.94454734	5.25446611

C	-0.65171875	18.53368752	-1.46288796
C	3.94590611	11.99424163	4.56391859
O	-0.48518723	12.15325451	2.25109483
H	3.11442252	11.29267711	7.06690400
O	-2.70051296	12.17482467	-1.32885086
H	1.37850923	11.56023258	6.78674720
C	-1.69545903	12.17503481	-0.74259459
H	2.46926305	12.93907047	7.00147828
N	0.77217530	12.16143142	1.88254121
H	-0.18672400	20.44825420	-0.58940598
C	2.63117572	11.98179366	5.06981027
H	0.63702411	19.47811481	1.54418146
C	-0.18379673	16.61844979	-0.08738843
C	1.56455106	12.03675639	4.17647421
C	1.79863113	12.10820446	2.78002541
C	4.18056526	12.06517661	3.18395929
H	-0.09246762	3.88338470	-0.42379965
H	0.71302746	4.93418842	1.67794851
H	0.53362939	12.02270093	4.52806115
C	-0.66285604	17.14461013	-1.30929120
C	3.12413214	12.12241064	2.28663930
C	-0.18787267	19.36885403	-0.44660434
C	0.87452899	12.18856643	-1.25330292
C	2.38350156	11.93522815	6.55941092
O	1.56602661	12.19950263	-2.19179322
H	-0.34275015	8.70673388	-2.73279643
H	-1.96258841	8.65127886	-2.03652883
H	-1.46499983	7.41334674	-3.21289020
H	-0.93844911	5.29843118	-2.28080008
H	1.65187930	16.18474236	2.07046682
H	0.01427650	16.21780302	2.71948306
H	1.08362047	17.62159394	2.95236929
H	1.12068452	6.84215388	3.02990155
H	0.04422210	8.22970774	2.73958861
H	1.68576137	8.24992122	2.10091961
H	-0.37125124	15.55043638	-2.74049632
H	-1.51448601	16.81021417	-3.25858227
H	-1.99010877	15.60309085	-2.04202958

####

#(κ^1-*N*-PhNO)Mn(CO)$_3$(CNXyl)$_2$

Mn	-0.51833757	-1.07288051	0.07044842
C	1.07121029	-1.83173303	-0.30375607
C	0.19607247	0.63039466	-0.16713725
N	-2.33883840	-0.07163581	0.37669532
C	-0.02428686	-0.94606620	1.89746334
C	-1.25426414	-2.75372625	0.23220182
C	-1.01127693	-1.07450054	-1.77460130
O	2.09522873	-2.32891761	-0.53842377
N	-1.25789998	-1.06321457	-2.92465562
N	0.39952545	-0.83877834	2.99450708
O	0.69707024	1.65200938	-0.32399973
O	-1.63800969	-3.84083529	0.27206072
O	-2.54001145	0.92185478	-0.42189439
H	-2.37419456	-2.01376129	2.26622330
C	-3.36150710	-0.34580522	1.29554511
C	-4.53582265	0.45092562	1.29629403

C	-5.56895330	0.17838673	2.18339953
C	-5.47655981	-0.88195617	3.09570549
C	-4.31609310	-1.66321696	3.10844506
C	-3.27010134	-1.40037908	2.22814568
H	-4.59519091	1.26915201	0.58349624
H	-6.46415747	0.80060566	2.16452216
H	-6.29336481	-1.09376245	3.78406755
H	-4.22419403	-2.49041366	3.81229528
H	-0.21145039	-1.89216838	-7.26714275
H	-3.85182922	0.24384827	-6.42111342
C	1.04974380	-0.68545459	4.20558252
C	0.29018363	-0.66692006	5.39568082
C	0.98155250	-0.50016509	6.59917574
C	2.36866607	-0.36146979	6.62193114
C	3.09498303	-0.38632625	5.43183079
C	2.45732458	-0.54794935	4.19894611
H	-2.26531141	-0.74156649	-8.05549911
H	0.41551242	-0.47671487	7.53026009
H	2.88666859	-0.23097181	7.57065874
H	4.17902886	-0.27656902	5.45210876
C	-1.53512762	-0.98823480	-4.27711254
C	-2.71636962	-0.33513027	-4.69310706
C	-2.95131467	-0.26035741	-6.07031181
C	-2.06007882	-0.81356648	-6.98860713
C	-0.90545755	-1.45935540	-6.54659262
C	-0.61506807	-1.56122850	-5.18373848
C	-3.68393907	0.23357356	-3.69169721
C	0.62941889	-2.24935999	-4.69062094
C	-1.20430083	-0.82518482	5.35948501
C	3.23299223	-0.57218974	2.91009726
H	-4.25386650	-0.57156122	-3.20400817
H	-4.40058688	0.90141538	-4.18282875
H	-3.17649908	0.78017484	-2.88605153
H	1.21316463	-2.64496005	-5.52932518
H	0.38617039	-3.08362401	-4.01786342
H	1.26970156	-1.55947624	-4.12312178
H	-1.67591553	-0.07887371	4.70623495
H	-1.63106494	-0.72744069	6.36377727
H	-1.48846754	-1.80962047	4.96207235
H	4.30467036	-0.44522745	3.09947322
H	2.90838878	0.23084624	2.23351360
H	3.09008688	-1.51999385	2.37234068

####

(κ^1-*O*-PhNO)Mn(CO)$_3$(CNXyl)$_2$

Mn	-0.43957910	-0.90214532	0.07664461
C	1.15523374	-1.58806028	-0.38902902
C	0.17023840	0.82332906	-0.14755311
N	-3.27096006	-0.91412273	0.34277264
C	0.06364769	-0.84447118	1.90631086
C	-1.13720063	-2.61594984	0.31828346
C	-1.04767401	-0.92433346	-1.72985618
O	2.17866910	-2.04932564	-0.69165864
N	-1.39524867	-0.94461658	-2.85402526
N	0.41978843	-0.81970707	3.02961750
O	0.56593286	1.89599166	-0.28989304

O	-1.48516616	-3.70253983	0.45373583
O	-2.22765488	-0.10645256	0.61531187
H	-5.48636951	-2.12800592	0.01089756
C	-4.48359269	-0.32328005	0.63790184
C	-4.66260141	0.99247670	1.14271494
C	-5.94445228	1.47643960	1.38156910
C	-7.07421683	0.68290526	1.13478768
C	-6.90466342	-0.61922282	0.63908499
C	-5.63309386	-1.11825728	0.39421649
H	-3.78376486	1.60510820	1.33106464
H	-6.07264120	2.48872417	1.76707308
H	-8.07300715	1.07257940	1.32754301
H	-7.77558385	-1.24575576	0.44544506
H	-0.84743615	-2.07164292	-7.22238717
H	-4.46048240	-0.02901165	-6.08080660
C	0.86733614	-0.78994120	4.33680475
C	-0.07823786	-0.91095248	5.37901039
C	0.40533748	-0.87989612	6.69069000
C	1.76691603	-0.73585459	6.95516769
C	2.67777036	-0.61784040	5.90569506
C	2.25266162	-0.64173833	4.57450406
H	-3.04567272	-1.08848115	-7.82455705
H	-0.30285692	-0.97228461	7.51395799
H	2.12066807	-0.71459996	7.98485598
H	3.74107452	-0.50494938	6.11642356
C	-1.82987822	-0.97717085	-4.16625895
C	-3.08243054	-0.40309585	-4.47842727
C	-3.49657763	-0.46082548	-5.81285077
C	-2.70143905	-1.05523019	-6.79205555
C	-1.46669528	-1.60859660	-6.45419045
C	-1.00200513	-1.58391828	-5.13640995
C	-3.92232475	0.24415258	-3.41353709
C	0.32696068	-2.17895044	-4.75540823
C	-1.54286358	-1.06889020	5.07552836
C	3.22501958	-0.51784732	3.43235599
H	-4.11590171	-0.44126490	-2.57713951
H	-4.88234928	0.57640572	-3.82276173
H	-3.41248686	1.11846708	-2.98430889
H	0.83194120	-2.59661824	-5.63355588
H	0.20819350	-2.98166670	-4.01414131
H	0.98848361	-1.42579038	-4.30489325
H	-1.92161856	-0.22931807	4.47668011
H	-2.12775049	-1.12615551	5.99984372
H	-1.73371576	-1.97988313	4.49133579
H	4.24848622	-0.39740596	3.80471859
H	2.98751486	0.34686879	2.79692487
H	3.19814844	-1.40576361	2.78496381

####

#(κ^1-*N*-PhNO)$Mn(CO)_5$

Mn	-0.21124066	-1.01032539	0.05769949
C	1.46179456	-1.41262701	-0.54486395
C	0.07862249	0.83208298	-0.18092369
N	-2.03834858	-0.39052480	0.86570304
C	0.38875556	-0.87990910	1.83436242
C	-0.54321034	-2.80536255	0.35616128

C	-0.86297850	-1.06985773	-1.67210863
O	2.51532845	-1.67971463	-0.93521244
O	-1.18366363	-1.08300001	-2.77600888
O	0.79758187	-0.82792292	2.90231532
O	0.29638182	1.94121016	-0.36115845
O	-0.65720862	-3.93318962	0.54948446
O	-1.91344805	0.59615177	1.67856583
H	-2.77766838	-2.42839785	-0.78219248
C	-3.33150574	-0.88710211	0.64648516
C	-4.41977554	-0.29587376	1.33604895
C	-5.70954492	-0.76871926	1.13710260
C	-5.96031394	-1.82888933	0.25609478
C	-4.88990541	-2.41477741	-0.42613904
C	-3.58958660	-1.95488971	-0.23561576
H	-4.20964437	0.52506522	2.01597147
H	-6.53454363	-0.30368198	1.67655138
H	-6.97531620	-2.19248895	0.10408113
H	-5.06759162	-3.23899354	-1.11545165

####

(κ^1-*O*-PhNO)Mn(CO)$_5$

Mn	1.44608689	0.61724719	0.56631477
C	3.16803446	1.10322501	0.90882453
C	0.92927852	2.36837328	0.24266101
N	-0.56827696	-1.04076411	-0.47390813
C	0.96241011	0.79317398	2.34977770
C	1.83051355	-1.20049086	0.85590545
C	1.80426673	0.39019922	-1.25956902
O	4.26285078	1.40372596	1.12365074
O	2.06308704	0.28483400	-2.37029719
O	0.67269167	0.90497823	3.45382609
O	0.60837248	3.45195982	0.04398032
O	2.13068796	-2.28465889	1.06894221
O	-0.47424705	0.12149926	0.21674664
H	-1.18958309	-3.15444684	-1.74729433
C	-1.88012796	-1.37168529	-0.74617290
C	-3.01659733	-0.60819074	-0.37234251
C	-4.28899597	-1.04958083	-0.71639636
C	-4.46773198	-2.24412664	-1.42876564
C	-3.34826873	-3.00404664	-1.79932745
C	-2.07048646	-2.57858563	-1.46545864
H	-2.87332614	0.31846461	0.17845404
H	-5.15807330	-0.45792565	-0.42892842
H	-5.46956746	-2.57903234	-1.69458688
H	-3.48001008	-3.93243805	-2.35445571

####

(η^2-N,O-PhNO)Mn(CO)$_4$

Mn	-0.12049046	12.14835184	0.06285588
O	-0.17098209	9.14581031	-0.11244286
O	1.69984151	12.14536575	-2.26293859
C	-1.68950645	12.14404931	-0.84446338
C	0.96692517	12.14679279	-1.36502207
H	3.33255357	12.15407764	1.14191107
N	0.80106518	12.15001746	1.76242881

O	-0.17677034	15.15053226	-0.12166379
C	2.60345333	12.13852127	4.96631213
C	-0.14198836	14.00775965	0.00160186
C	4.18973371	12.14501668	3.12889805
H	5.21780566	12.14547035	2.77014363
C	3.92870251	12.13836249	4.50681243
O	-2.70798795	12.14002878	-1.39195911
C	-0.13857110	10.28891840	0.00741102
C	3.14596678	12.15015263	2.21467981
C	1.54208955	12.14429820	4.07329801
O	-0.46740916	12.15139990	2.08840179
C	1.80962113	12.14956623	2.68079531
H	4.75246648	12.13344695	5.21850511
H	2.40044983	12.13368274	6.03657050
H	0.50834315	12.14356414	4.41189120

####

CO

C	-1.26006251	-2.35450079	0.00000000
O	-0.15124345	-2.10528508	0.00000000

Mulliken Spin Density Output for $Mn(CO)_3(CNXyl)_2$, (η^2-*N,O*-PhNO) $Mn(CO)_2(CNXyl)_2$, (η^2-*N,O-p*-TolNO)$Mn(CO)_2(CNXyl)_2$, (η^2-*N,O-m*-TolNO)$Mn(CO)_2(CNXyl)_2$.

$Mn(CO)_3(CNXyl)_2$

Atom	Charge	Spin density		S	P	D	F
1 Mn	-0.2689	0.6954	A:	3.1207	6.6017	3.2525	0.0073
			B:	3.0808	6.3851	2.8133	0.0075
2 N	-0.1588	0.0394	A:	1.6973	1.8690	0.0289	0.0039
			B:	1.6957	1.8309	0.0291	0.0040
3 N	-0.1565	0.0388	A:	1.6970	1.8676	0.0290	0.0039
			B:	1.6953	1.8302	0.0293	0.0041
4 C	0.1515	-0.0026	A:	1.5321	1.3379	0.0492	0.0037
			B:	1.5332	1.3404	0.0483	0.0036
5 C	-0.0072	0.0051	A:	1.5793	1.3849	0.0390	0.0030
			B:	1.5786	1.3806	0.0390	0.0030
6 C	0.5412	-0.0004	A:	1.4458	1.2625	0.0198	0.0011
			B:	1.4458	1.2629	0.0198	0.0010
7 C	0.1512	-0.0081	A:	1.5322	1.3350	0.0494	0.0037
			B:	1.5335	1.3431	0.0483	0.0036
8 C	-0.0040	0.0162	A:	1.5788	1.3895	0.0389	0.0029
			B:	1.5776	1.3743	0.0390	0.0030
9 C	0.1812	0.0188	A:	1.5416	1.3451	0.0296	0.0024
			B:	1.5403	1.3275	0.0298	0.0024
10 C	0.1156	-0.0046	A:	1.6925	1.2028	0.0409	0.0037
			B:	1.7022	1.2003	0.0383	0.0037
11 C	0.2354	-0.0013	A:	1.5326	1.3175	0.0292	0.0024
			B:	1.5327	1.3187	0.0291	0.0024
12 C	0.3448	0.0635	A:	1.6729	1.1341	0.0479	0.0045
			B:	1.6752	1.0722	0.0438	0.0046
13 C	0.1171	-0.0013	A:	1.6924	1.2036	0.0411	0.0037
			B:	1.7018	1.1982	0.0384	0.0037
14 C	0.5395	-0.0012	A:	1.4465	1.2622	0.0199	0.0011
			B:	1.4468	1.2632	0.0198	0.0010

15 C	0.4022	-0.0106	A:	1.6541	1.0851	0.0498	0.0045
			B:	1.6481	1.1040	0.0476	0.0046
16 C	-0.0071	0.0163	A:	1.5790	1.3909	0.0389	0.0029
			B:	1.5779	1.3756	0.0390	0.0030
17 C	0.5399	-0.0011	A:	1.4455	1.2630	0.0199	0.0011
			B:	1.4459	1.2639	0.0197	0.0010
18 C	0.5371	-0.0004	A:	1.4466	1.2638	0.0199	0.0011
			B:	1.4466	1.2641	0.0198	0.0011
19 C	0.2305	-0.0015	A:	1.5331	1.3193	0.0292	0.0024
			B:	1.5332	1.3207	0.0291	0.0024
20 C	0.3492	0.0612	A:	1.6723	1.1316	0.0476	0.0045
			B:	1.6746	1.0720	0.0436	0.0046
21 O	-0.3798	-0.0067	A:	1.9095	2.2453	0.0288	0.0030
			B:	1.9106	2.2508	0.0288	0.0030
22 C	0.1803	0.0038	A:	1.5411	1.3385	0.0297	0.0024
			B:	1.5408	1.3350	0.0298	0.0024
23 O	-0.3512	0.0436	A:	1.9104	2.2553	0.0287	0.0030
			B:	1.9100	2.2116	0.0291	0.0031
24 C	0.2319	-0.0069	A:	1.5328	1.3160	0.0294	0.0024
			B:	1.5336	1.3226	0.0289	0.0024
25 C	-0.0037	0.0045	A:	1.5783	1.3839	0.0390	0.0030
			B:	1.5776	1.3800	0.0390	0.0030
26 O	-0.3505	0.0431	A:	1.9105	2.2546	0.0288	0.0029
			B:	1.9101	2.2114	0.0292	0.0031
27 C	0.2313	-0.0067	A:	1.5328	1.3164	0.0293	0.0024
			B:	1.5336	1.3228	0.0289	0.0024
28 H	-0.1649	0.0003	A:	0.5378	0.0419	0.0029	0.0000
			B:	0.5375	0.0419	0.0029	0.0000
29 H	-0.1551	0.0002	A:	0.5327	0.0420	0.0029	0.0000
			B:	0.5325	0.0420	0.0029	0.0000
30 H	-0.2241	0.0000	A:	0.5680	0.0411	0.0029	0.0000
			B:	0.5680	0.0411	0.0029	0.0000
31 H	-0.1957	-0.0010	A:	0.5573	0.0374	0.0026	0.0000
			B:	0.5588	0.0370	0.0026	0.0000
32 H	-0.2037	0.0004	A:	0.5605	0.0389	0.0027	0.0000
			B:	0.5601	0.0389	0.0027	0.0000
33 H	-0.1679	0.0002	A:	0.5392	0.0420	0.0029	0.0000
			B:	0.5390	0.0420	0.0029	0.0000
34 H	-0.1576	0.0011	A:	0.5346	0.0419	0.0029	0.0000
			B:	0.5334	0.0419	0.0029	0.0000
35 H	-0.2248	0.0000	A:	0.5684	0.0411	0.0029	0.0000
			B:	0.5684	0.0411	0.0029	0.0000
36 H	-0.2246	0.0000	A:	0.5683	0.0411	0.0029	0.0000
			B:	0.5683	0.0411	0.0029	0.0000
37 H	-0.1612	0.0006	A:	0.5360	0.0419	0.0029	0.0000
			B:	0.5354	0.0420	0.0029	0.0000
38 H	-0.1606	0.0006	A:	0.5358	0.0419	0.0029	0.0000
			B:	0.5352	0.0419	0.0029	0.0000
39 H	-0.2229	0.0000	A:	0.5676	0.0410	0.0029	0.0000
			B:	0.5676	0.0410	0.0029	0.0000
40 H	-0.1594	0.0005	A:	0.5352	0.0418	0.0029	0.0000
			B:	0.5347	0.0418	0.0029	0.0000
41 H	-0.1662	0.0001	A:	0.5383	0.0419	0.0029	0.0000
			B:	0.5382	0.0419	0.0029	0.0000
42 H	-0.2033	0.0002	A:	0.5602	0.0388	0.0027	0.0000
			B:	0.5600	0.0389	0.0027	0.0000
43 H	-0.1947	-0.0002	A:	0.5574	0.0372	0.0026	0.0000
			B:	0.5577	0.0371	0.0026	0.0000
44 H	-0.2034	0.0005	A:	0.5605	0.0388	0.0027	0.0000
			B:	0.5599	0.0389	0.0027	0.0000
45 H	-0.2022	0.0004	A:	0.5598	0.0388	0.0027	0.0000

#####

(η^2-*N,O*-PhNO)Mn(CO)$_2$(CNXyl)$_2$

Atom	Charge	Spin density		S	P	D	F
1 Mn	-0.0151	0.0189	A:	3.0764	6.4175	3.0126	0.0105
			B:	3.0779	6.4243	2.9861	0.0098
2 N	-0.1580	-0.0008	A:	1.6976	1.8480	0.0289	0.0040
			B:	1.6977	1.8488	0.0289	0.0040
3 C	0.1563	0.0016	A:	1.7074	1.1724	0.0391	0.0037

			B:	1.7076	1.1708	0.0390	0.0037
4 C	0.1523	0.0007	A:	1.5327	1.3394	0.0485	0.0037
			B:	1.5326	1.3387	0.0485	0.0037
5 C	-0.0039	-0.0004	A:	1.5783	1.3815	0.0390	0.0030
			B:	1.5783	1.3818	0.0390	0.0030
6 C	0.2309	0.0001	A:	1.5329	1.3201	0.0291	0.0024
			B:	1.5329	1.3200	0.0291	0.0024
7 H	-0.2019	0.0000	A:	0.5594	0.0388	0.0027	0.0000
			B:	0.5594	0.0388	0.0027	0.0000
8 C	0.1791	-0.0003	A:	1.5410	1.3370	0.0298	0.0024
			B:	1.5410	1.3373	0.0298	0.0024
9 H	-0.1944	0.0000	A:	0.5575	0.0371	0.0026	0.0000
			B:	0.5574	0.0371	0.0026	0.0000
10 C	0.2335	0.0001	A:	1.5328	1.3190	0.0291	0.0024
			B:	1.5328	1.3189	0.0291	0.0024
11 H	-0.2034	0.0000	A:	0.5601	0.0389	0.0027	0.0000
			B:	0.5601	0.0389	0.0027	0.0000
12 C	-0.0050	-0.0003	A:	1.5782	1.3822	0.0390	0.0030
			B:	1.5782	1.3825	0.0390	0.0030
13 C	0.5486	-0.0001	A:	1.4451	1.2597	0.0198	0.0010
			B:	1.4451	1.2599	0.0198	0.0010
14 C	0.1506	0.0007	A:	1.5331	1.3398	0.0485	0.0037
			B:	1.5330	1.3392	0.0485	0.0037
15 C	0.5442	0.0000	A:	1.4459	1.2612	0.0198	0.0010
			B:	1.4459	1.2612	0.0198	0.0010
16 C	0.0482	-0.0748	A:	1.5492	1.3309	0.0543	0.0040
			B:	1.5592	1.4067	0.0439	0.0034
17 C	0.1817	0.1556	A:	1.5404	1.4168	0.0276	0.0022
			B:	1.5295	1.2705	0.0288	0.0026
18 C	-0.0047	-0.0004	A:	1.5784	1.3818	0.0390	0.0030
			B:	1.5784	1.3822	0.0390	0.0030
19 C	0.1879	-0.0663	A:	1.5353	1.3031	0.0320	0.0026
			B:	1.5428	1.3665	0.0276	0.0023
20 H	-0.1954	0.0030	A:	0.5602	0.0364	0.0026	0.0000
			B:	0.5561	0.0375	0.0026	0.0000
21 C	0.1710	0.1941	A:	1.5430	1.4381	0.0283	0.0022
			B:	1.5296	1.2558	0.0295	0.0026
22 H	-0.1869	-0.0102	A:	0.5463	0.0394	0.0027	0.0000
			B:	0.5610	0.0350	0.0025	0.0000
23 O	-0.3840	-0.0006	A:	1.9107	2.2491	0.0289	0.0030
			B:	1.9107	2.2498	0.0289	0.0030
24 O	-0.3793	0.0043	A:	1.9101	2.2501	0.0286	0.0030
			B:	1.9100	2.2458	0.0287	0.0030
25 O	-0.4455	0.2768	A:	1.9448	2.3795	0.0330	0.0039
			B:	1.9398	2.1075	0.0330	0.0041
26 N	0.0333	0.3988	A:	1.7449	1.8779	0.0557	0.0042
			B:	1.7300	1.4966	0.0525	0.0048
27 C	0.3913	-0.0020	A:	1.6463	1.1037	0.0487	0.0046
			B:	1.6471	1.1049	0.0488	0.0046
28 C	0.3659	0.0050	A:	1.6634	1.1033	0.0483	0.0046
			B:	1.6645	1.0976	0.0479	0.0046
29 C	0.2297	0.0001	A:	1.5332	1.3205	0.0291	0.0024
			B:	1.5332	1.3204	0.0291	0.0024
30 H	-0.2022	0.0000	A:	0.5596	0.0388	0.0027	0.0000
			B:	0.5596	0.0388	0.0027	0.0000
31 C	0.1803	-0.0003	A:	1.5410	1.3365	0.0298	0.0024
			B:	1.5410	1.3368	0.0298	0.0024
32 H	-0.1942	0.0000	A:	0.5574	0.0371	0.0026	0.0000
			B:	0.5573	0.0372	0.0026	0.0000
33 C	0.2332	0.0001	A:	1.5328	1.3192	0.0291	0.0024
			B:	1.5328	1.3191	0.0291	0.0024
34 H	-0.2032	0.0000	A:	0.5600	0.0389	0.0027	0.0000
			B:	0.5600	0.0389	0.0027	0.0000
35 C	-0.0037	-0.0003	A:	1.5781	1.3816	0.0390	0.0030
			B:	1.5782	1.3819	0.0390	0.0030
36 C	0.5478	-0.0001	A:	1.4454	1.2598	0.0198	0.0010
			B:	1.4454	1.2599	0.0198	0.0010
37 C	0.1928	-0.0671	A:	1.5365	1.2990	0.0321	0.0026
			B:	1.5440	1.3631	0.0277	0.0023
38 H	-0.1923	0.0032	A:	0.5591	0.0361	0.0026	0.0000
			B:	0.5547	0.0372	0.0026	0.0000
39 C	0.1744	0.1748	A:	1.5415	1.4293	0.0271	0.0022
			B:	1.5298	1.2645	0.0286	0.0026

40 N	-0.1574	-0.0006	A:	1.6974	1.8481	0.0289	0.0040
			B:	1.6974	1.8487	0.0289	0.0040
41 C	0.1571	0.0016	A:	1.7076	1.1719	0.0391	0.0037
			B:	1.7078	1.1702	0.0390	0.0037
42 C	0.5438	0.0000	A:	1.4461	1.2611	0.0198	0.0011
			B:	1.4461	1.2611	0.0198	0.0011
43 H	-0.1653	0.0001	A:	0.5376	0.0422	0.0029	0.0000
			B:	0.5376	0.0421	0.0029	0.0000
44 H	-0.2282	0.0000	A:	0.5699	0.0412	0.0029	0.0000
			B:	0.5700	0.0412	0.0029	0.0000
45 H	-0.1554	0.0001	A:	0.5330	0.0418	0.0029	0.0000
			B:	0.5329	0.0418	0.0029	0.0000
46 H	-0.2267	0.0000	A:	0.5692	0.0412	0.0029	0.0000
			B:	0.5693	0.0412	0.0029	0.0000
47 H	-0.1614	0.0001	A:	0.5359	0.0419	0.0029	0.0000
			B:	0.5358	0.0419	0.0029	0.0000
48 H	-0.1605	0.0000	A:	0.5353	0.0421	0.0029	0.0000
			B:	0.5352	0.0421	0.0029	0.0000
49 H	-0.1593	-0.0074	A:	0.5341	0.0390	0.0028	0.0000
			B:	0.5438	0.0369	0.0026	0.0000
50 H	-0.1646	0.0001	A:	0.5373	0.0421	0.0029	0.0000
			B:	0.5373	0.0421	0.0029	0.0000
51 H	-0.1559	0.0001	A:	0.5333	0.0418	0.0029	0.0000
			B:	0.5332	0.0418	0.0029	0.0000
52 H	-0.2275	0.0000	A:	0.5696	0.0412	0.0029	0.0000
			B:	0.5696	0.0412	0.0029	0.0000
53 H	-0.1506	-0.0080	A:	0.5282	0.0403	0.0028	0.0000
			B:	0.5397	0.0371	0.0026	0.0000
54 H	-0.1611	0.0000	A:	0.5356	0.0420	0.0029	0.0000
			B:	0.5356	0.0420	0.0029	0.0000
55 H	-0.1604	0.0000	A:	0.5354	0.0419	0.0029	0.0000
			B:	0.5354	0.0419	0.0029	0.0000
56 H	-0.2265	0.0000	A:	0.5691	0.0412	0.0029	0.0000
			B:	0.5691	0.0412	0.0029	0.0000

#####

(η^2-*N,O-p*-TolNO)Mn(CO)$_2$(CNXyl)$_2$

Atom	Charge	Spin density		S	P	D	F
1 Mn	-0.2692	0.6953	A:	3.1207	6.6017	3.2525	0.0073
			B:	3.0809	6.3852	2.8134	0.0075
2 N	-0.1589	0.0394	A:	1.6973	1.8690	0.0289	0.0039
			B:	1.6957	1.8309	0.0291	0.0040
3 N	-0.1568	0.0388	A:	1.6972	1.8676	0.0290	0.0039
			B:	1.6955	1.8301	0.0293	0.0041
4 C	0.1514	-0.0026	A:	1.5322	1.3379	0.0492	0.0037
			B:	1.5332	1.3404	0.0483	0.0036
5 C	-0.0066	0.0051	A:	1.5792	1.3847	0.0390	0.0030
			B:	1.5785	1.3804	0.0390	0.0030
6 C	0.5414	-0.0003	A:	1.4457	1.2625	0.0198	0.0011
			B:	1.4458	1.2628	0.0198	0.0010
7 C	0.1508	-0.0081	A:	1.5323	1.3352	0.0494	0.0037
			B:	1.5335	1.3432	0.0483	0.0036
8 C	-0.0042	0.0162	A:	1.5787	1.3897	0.0389	0.0029
			B:	1.5775	1.3745	0.0390	0.0030
9 C	0.1814	0.0188	A:	1.5416	1.3451	0.0296	0.0024
			B:	1.5403	1.3275	0.0297	0.0024
10 C	0.1161	-0.0046	A:	1.6924	1.2026	0.0409	0.0037
			B:	1.7022	1.2001	0.0383	0.0037
11 C	0.2352	-0.0014	A:	1.5327	1.3174	0.0292	0.0024
			B:	1.5328	1.3188	0.0291	0.0024
12 C	0.3451	0.0635	A:	1.6728	1.1341	0.0479	0.0045
			B:	1.6751	1.0722	0.0438	0.0046
13 C	0.1171	-0.0013	A:	1.6924	1.2036	0.0411	0.0037
			B:	1.7018	1.1982	0.0384	0.0037
14 C	0.5395	-0.0012	A:	1.4464	1.2622	0.0199	0.0011
			B:	1.4468	1.2633	0.0198	0.0010
15 C	0.4023	-0.0106	A:	1.6541	1.0851	0.0498	0.0045
			B:	1.6481	1.1040	0.0476	0.0046
16 C	-0.0070	0.0163	A:	1.5791	1.3908	0.0389	0.0029

			B:	1.5779	1.3755	0.0390	0.0030
17 C	0.5398	-0.0011	A:	1.4455	1.2631	0.0199	0.0011
			B:	1.4459	1.2640	0.0197	0.0010
18 C	0.5370	-0.0005	A:	1.4465	1.2638	0.0199	0.0011
			B:	1.4466	1.2642	0.0198	0.0011
19 C	0.2311	-0.0015	A:	1.5331	1.3189	0.0292	0.0024
			B:	1.5333	1.3204	0.0291	0.0024
20 C	0.3492	0.0612	A:	1.6723	1.1316	0.0476	0.0045
			B:	1.6746	1.0720	0.0436	0.0046
21 O	-0.3799	-0.0067	A:	1.9096	2.2453	0.0288	0.0030
			B:	1.9107	2.2508	0.0288	0.0030
22 C	0.1802	0.0037	A:	1.5412	1.3384	0.0297	0.0024
			B:	1.5409	1.3349	0.0298	0.0024
23 O	-0.3513	0.0436	A:	1.9104	2.2553	0.0287	0.0030
			B:	1.9101	2.2116	0.0291	0.0031
24 C	0.2315	-0.0068	A:	1.5328	1.3162	0.0294	0.0024
			B:	1.5336	1.3227	0.0289	0.0024
25 C	-0.0033	0.0046	A:	1.5783	1.3837	0.0390	0.0030
			B:	1.5777	1.3798	0.0390	0.0030
26 O	-0.3505	0.0431	A:	1.9104	2.2546	0.0288	0.0029
			B:	1.9101	2.2114	0.0292	0.0031
27 C	0.2316	-0.0067	A:	1.5330	1.3161	0.0293	0.0024
			B:	1.5338	1.3224	0.0289	0.0024
28 H	-0.1649	0.0003	A:	0.5378	0.0419	0.0029	0.0000
			B:	0.5375	0.0419	0.0029	0.0000
29 H	-0.1551	0.0002	A:	0.5327	0.0420	0.0029	0.0000
			B:	0.5326	0.0420	0.0029	0.0000
30 H	-0.2242	-0.0001	A:	0.5680	0.0411	0.0029	0.0000
			B:	0.5681	0.0411	0.0029	0.0000
31 H	-0.1960	-0.0010	A:	0.5574	0.0374	0.0026	0.0000
			B:	0.5589	0.0370	0.0026	0.0000
32 H	-0.2044	0.0005	A:	0.5609	0.0389	0.0027	0.0000
			B:	0.5603	0.0389	0.0027	0.0000
33 H	-0.1678	0.0002	A:	0.5391	0.0420	0.0029	0.0000
			B:	0.5389	0.0420	0.0029	0.0000
34 H	-0.1575	0.0012	A:	0.5346	0.0419	0.0029	0.0000
			B:	0.5334	0.0419	0.0029	0.0000
35 H	-0.2248	0.0000	A:	0.5684	0.0411	0.0029	0.0000
			B:	0.5684	0.0411	0.0029	0.0000
36 H	-0.2244	0.0000	A:	0.5682	0.0411	0.0029	0.0000
			B:	0.5682	0.0411	0.0029	0.0000
37 H	-0.1612	0.0005	A:	0.5360	0.0419	0.0029	0.0000
			B:	0.5354	0.0420	0.0029	0.0000
38 H	-0.1606	0.0006	A:	0.5358	0.0419	0.0029	0.0000
			B:	0.5352	0.0419	0.0029	0.0000
39 H	-0.2230	0.0000	A:	0.5676	0.0410	0.0029	0.0000
			B:	0.5677	0.0410	0.0029	0.0000
40 H	-0.1593	0.0005	A:	0.5352	0.0418	0.0029	0.0000
			B:	0.5347	0.0418	0.0029	0.0000
41 H	-0.1661	0.0002	A:	0.5383	0.0419	0.0029	0.0000
			B:	0.5381	0.0419	0.0029	0.0000
42 H	-0.2037	0.0003	A:	0.5605	0.0388	0.0027	0.0000
			B:	0.5601	0.0389	0.0027	0.0000
43 H	-0.1949	-0.0002	A:	0.5575	0.0372	0.0026	0.0000
			B:	0.5578	0.0371	0.0026	0.0000
44 H	-0.2027	0.0003	A:	0.5600	0.0388	0.0027	0.0000
			B:	0.5596	0.0389	0.0027	0.0000
45 H	-0.2027	0.0003	A:	0.5601	0.0387	0.0027	0.0000
			B:	0.5597	0.0388	0.0027	0.0000

####

(η^2-*N,O*-*m*-TolNO)Mn(CO)$_2$(CNXyl)$_2$

Atom	Charge	Spin density		S	P	D	F
1 Mn	-0.0133	0.0186	A:	3.0771	6.4161	3.0124	0.0104
			B:	3.0785	6.4228	2.9863	0.0098
2 C	0.1522	0.0007	A:	1.5330	1.3391	0.0485	0.0037
			B:	1.5330	1.3383	0.0485	0.0037
3 N	-0.1583	-0.0008	A:	1.6975	1.8483	0.0289	0.0040

			B:	1.6975	1.8491	0.0289	0.0040
4 C	0.2295	0.0001	A:	1.5331	1.3207	0.0291	0.0024
			B:	1.5331	1.3205	0.0291	0.0024
5 H	-0.2011	0.0000	A:	0.5590	0.0389	0.0027	0.0000
			B:	0.5590	0.0389	0.0027	0.0000
6 C	0.1821	-0.0004	A:	1.5409	1.3357	0.0297	0.0024
			B:	1.5409	1.3360	0.0297	0.0024
7 H	-0.1952	0.0000	A:	0.5578	0.0372	0.0026	0.0000
			B:	0.5578	0.0372	0.0026	0.0000
8 H	-0.1548	-0.0079	A:	0.5301	0.0406	0.0028	0.0000
			B:	0.5416	0.0372	0.0026	0.0000
9 C	0.5516	-0.0001	A:	1.4446	1.2588	0.0198	0.0010
			B:	1.4446	1.2589	0.0198	0.0010
10 C	-0.0063	-0.0004	A:	1.5787	1.3823	0.0390	0.0030
			B:	1.5787	1.3827	0.0390	0.0030
11 C	0.5369	-0.0138	A:	1.4393	1.2629	0.0213	0.0011
			B:	1.4442	1.2741	0.0191	0.0010
12 C	0.1520	0.0008	A:	1.5329	1.3394	0.0485	0.0037
			B:	1.5328	1.3386	0.0485	0.0037
13 C	-0.0242	0.1882	A:	1.5820	1.4829	0.0385	0.0027
			B:	1.5694	1.3059	0.0396	0.0031
14 C	0.2332	0.0001	A:	1.5324	1.3195	0.0292	0.0024
			B:	1.5324	1.3193	0.0292	0.0024
15 H	-0.2042	0.0000	A:	0.5602	0.0391	0.0027	0.0000
			B:	0.5602	0.0391	0.0027	0.0000
16 C	0.2188	-0.0678	A:	1.5312	1.2914	0.0316	0.0025
			B:	1.5390	1.3560	0.0272	0.0023
17 C	0.5423	0.0000	A:	1.4464	1.2616	0.0198	0.0011
			B:	1.4464	1.2616	0.0198	0.0011
18 C	-0.0065	-0.0004	A:	1.5781	1.3829	0.0391	0.0030
			B:	1.5781	1.3833	0.0391	0.0030
19 C	0.2317	0.0000	A:	1.5329	1.3197	0.0291	0.0024
			B:	1.5329	1.3197	0.0291	0.0024
20 H	-0.2031	0.0002	A:	0.5601	0.0389	0.0027	0.0000
			B:	0.5599	0.0389	0.0027	0.0000
21 C	0.1798	-0.0004	A:	1.5414	1.3363	0.0298	0.0024
			B:	1.5414	1.3367	0.0297	0.0024
22 H	-0.1948	0.0000	A:	0.5576	0.0372	0.0026	0.0000
			B:	0.5576	0.0372	0.0026	0.0000
23 H	-0.2024	0.0029	A:	0.5622	0.0378	0.0027	0.0000
			B:	0.5580	0.0390	0.0027	0.0000
24 C	0.2320	0.0001	A:	1.5331	1.3195	0.0291	0.0024
			B:	1.5331	1.3193	0.0291	0.0024
25 C	0.5430	0.0000	A:	1.4461	1.2615	0.0198	0.0010
			B:	1.4461	1.2616	0.0198	0.0010
26 C	-0.0043	-0.0004	A:	1.5782	1.3818	0.0390	0.0030
			B:	1.5782	1.3822	0.0390	0.0030
27 H	-0.2031	0.0000	A:	0.5600	0.0389	0.0027	0.0000
			B:	0.5600	0.0389	0.0027	0.0000
28 C	-0.0071	-0.0004	A:	1.5789	1.3824	0.0390	0.0030
			B:	1.5789	1.3829	0.0390	0.0030
29 C	0.1602	0.0014	A:	1.7069	1.1709	0.0391	0.0037
			B:	1.7071	1.1694	0.0390	0.0037
30 H	-0.1587	0.0138	A:	0.5415	0.0419	0.0029	0.0000
			B:	0.5277	0.0419	0.0029	0.0000
31 C	0.5517	-0.0002	A:	1.4449	1.2584	0.0198	0.0010
			B:	1.4449	1.2585	0.0198	0.0010
32 N	-0.1584	-0.0010	A:	1.6977	1.8481	0.0289	0.0040
			B:	1.6978	1.8490	0.0289	0.0040
33 H	-0.1633	-0.0072	A:	0.5361	0.0392	0.0028	0.0000
			B:	0.5457	0.0369	0.0026	0.0000
34 O	-0.4492	0.2701	A:	1.9443	2.3786	0.0328	0.0039
			B:	1.9394	2.1132	0.0328	0.0041
35 C	0.1691	0.1741	A:	1.5440	1.4289	0.0273	0.0022
			B:	1.5322	1.2648	0.0288	0.0026
36 C	0.3667	0.0050	A:	1.6631	1.1033	0.0482	0.0045
			B:	1.6642	1.0976	0.0478	0.0045
37 O	-0.3849	-0.0006	A:	1.9105	2.2498	0.0288	0.0030
			B:	1.9105	2.2504	0.0288	0.0030
38 C	0.3886	-0.0020	A:	1.6471	1.1043	0.0486	0.0046
			B:	1.6479	1.1055	0.0487	0.0046
39 N	0.0250	0.3990	A:	1.7454	1.8821	0.0554	0.0041
			B:	1.7303	1.5004	0.0525	0.0048

40 C	0.1599	0.0014	A:	1.7073	1.1706	0.0391	0.0037
			B:	1.7075	1.1691	0.0390	0.0037
41 C	0.0496	-0.0760	A:	1.5485	1.3302	0.0544	0.0040
			B:	1.5586	1.4071	0.0441	0.0034
42 C	0.2261	-0.0666	A:	1.5311	1.2883	0.0317	0.0025
			B:	1.5389	1.3518	0.0273	0.0023
43 C	0.1772	0.1544	A:	1.5430	1.4156	0.0278	0.0022
			B:	1.5320	1.2705	0.0292	0.0026
44 O	-0.3802	0.0042	A:	1.9100	2.2507	0.0286	0.0030
			B:	1.9099	2.2465	0.0286	0.0030
45 H	-0.2301	0.0000	A:	0.5708	0.0413	0.0029	0.0000
			B:	0.5708	0.0413	0.0029	0.0000
46 H	-0.2305	0.0000	A:	0.5710	0.0413	0.0029	0.0000
			B:	0.5710	0.0413	0.0029	0.0000
47 H	-0.1650	0.0000	A:	0.5374	0.0421	0.0029	0.0000
			B:	0.5374	0.0421	0.0029	0.0000
48 H	-0.1553	0.0003	A:	0.5330	0.0419	0.0029	0.0000
			B:	0.5327	0.0419	0.0029	0.0000
49 H	-0.1943	0.0036	A:	0.5551	0.0410	0.0029	0.0000
			B:	0.5514	0.0411	0.0029	0.0000
50 H	-0.1938	0.0036	A:	0.5548	0.0410	0.0029	0.0000
			B:	0.5511	0.0411	0.0029	0.0000
51 H	-0.2012	0.0033	A:	0.5620	0.0376	0.0027	0.0000
			B:	0.5575	0.0387	0.0027	0.0000
52 H	-0.1582	0.0000	A:	0.5344	0.0419	0.0029	0.0000
			B:	0.5343	0.0419	0.0029	0.0000
53 H	-0.1633	0.0000	A:	0.5368	0.0420	0.0029	0.0000
			B:	0.5367	0.0420	0.0029	0.0000
54 H	-0.2261	0.0000	A:	0.5690	0.0412	0.0029	0.0000
			B:	0.5690	0.0412	0.0029	0.0000
55 H	-0.1585	0.0000	A:	0.5344	0.0419	0.0029	0.0000
			B:	0.5344	0.0419	0.0029	0.0000
56 H	-0.2265	0.0000	A:	0.5692	0.0411	0.0029	0.0000
			B:	0.5692	0.0412	0.0029	0.0000
57 H	-0.1637	0.0000	A:	0.5369	0.0420	0.0029	0.0000
			B:	0.5369	0.0420	0.0029	0.0000
58 H	-0.1551	0.0003	A:	0.5329	0.0419	0.0029	0.0000
			B:	0.5326	0.0419	0.0029	0.0000
59 H	-0.1646	0.0000	A:	0.5373	0.0421	0.0029	0.0000
			B:	0.5373	0.0421	0.0029	0.0000

2.8 Crystallographic Structure Determinations

General. Single-crystal Xray structure determinations were carried out using Bruker Platform or Kappa X-ray Diffractometers equipped with Mo or Cu radiation sources (sealed tube or rotating anode), low-temperature cryostats, and CCD detectors (Bruker APEX or Bruker APEX II). All structures were solved by direct methods using SHELXS[125] and refined by full matrix least-squares procedures utilizing SHELXL[125] within the Olex2 small-molecule solution, refinement and analysis software package.[126] Crystallographic data-collection and refinement information are listed in Table 2.3.

Due to a vacant coordination site, monoradical **1** crystallized with positional

disorder of the carbonyl ligands. Each CO ligand was fully refined to 0.75 occupancy and only one component of the disorder model is shown. Complex **3** crystallized with a 65:35 positional disorder of the $SnBu_3$ and CO groups. This disorder was modeled and fully refined. Complex **5** crystallized with 50% site disorder of the Cl ligand. This disorder was modeled and fully refined. Complex **7** possesses positional disorder of a $CNAr^{Dipp2}$ ligand, which was modeled and fully refined. Complexes **8** and **9** crystallized with an 85:15 and 90:10 positional disorder, respectively, of the PhNO and CO ligands. This disorder was modeled and fully refined. Complex **10** possessed positional disorder over a crystallographic mirror plane, which was modeled and fully refined. The triflate complex $(OTf)Mn(CO)_3(CNAr^{Dipp2})_2$ possessed an 80:20 positional disorder of the triflate group, which was modeled and fully refined. The carbon disulfide-bridged dimer contained a disordered $((CH_3)_3Si)_2O$ solvent molecule; this was treated with SQUEEZE and its electron density removed. $Mn(SbF_2)(CO)_3(CNAr^{Dipp2})_2$ possesses positional disorder of the (SbF_2)-unit and a pyridine solvent molecule, and was modeled and fully refined anisotropically. $Mn(THF{\cdot}AlCl_2)(CO)_3(CNAr^{Dipp2})_2$ possesses positional disorder of one Cl atom, and was modeled and fully refined anisotropically. $Mn(FHF)(CO)_3(CNAr^{Dipp2})_2$ possesses positional disorder of the (FHF)-unit and the *trans*-CO; this was modeled and refined anisotropically. One H atom in the disordered (FHF)-unit could be located in the electron density map and was included in the model.

Crystallographic Information Files (CIF) have been deposited with the Cambridge Crystallogaphic Data Center with the following reference codes:

$Mn(CO)_3(CNAr^{Dipp2})_2$ (**1**): **1412317**

$(Bu_3Sn)Mn(CO)_3(CNAr^{Dipp2})_2 \cdot 0.5(Et_2O)$ (**3**·0.5(Et_2O)): **1412319**

$(Cl_2HC)Mn(CO)_3(CNAr^{Dipp2})_2 \cdot 2(THF)$ (**4**·2(THF)): **1412312**

$ClMn(CO)_3(CNAr^{Dipp2})_2 \cdot 2.5(Et_2O)$ (**5**·2.5(Et_2O)): **1412313**

$(\mu_2\text{-}\kappa^1\text{:}\kappa^1\text{-}OC_6Me_4O)[Mn(CO)_3(CNAr^{Dipp2})_2]_2$ (**6**): **1412318**

cis,mer:trans,mer-$[Mn(CO)_3(CNAr^{Dipp2})_2]_2(\mu\text{-}\eta^1\text{:}\eta^1\text{-}P_4) \cdot 3(Et_2O)$ (**7**·3(Et_2O)): **1412315**

$(\eta^2\text{-}N,O\text{-PhNO})Mn(CO)_2(CNAr^{Dipp2})_2$ (**8**): **1412310**

$(\eta^2\text{-}N,O\text{-}m\text{-TolNO})Mn(CO)_2(CNAr^{Dipp2})_2$ (**9**): **1412311**

$(\eta^2\text{-}N,O\text{-}p\text{-TolNO})Mn(CO)_2(CNAr^{Dipp2})_2$ (**10**): **1412314**

$(OTf)Mn(CO)_3(CNAr^{Dipp2})_2 \cdot 0.5(n\text{-}C_5H_{12})$: **1412316**

$Mn(SbF_2)(CO)_3(CNAr^{Dipp2})_2$: **1538898**

$Mn(BiCl_2)(CO)_3(CNAr^{Dipp2})_2$: **1538895**

$Mn(FHF)(CO)_3(CNAr^{Dipp2})_2$: **1538897**

$Mn(AlCl_2 \cdot THF)(CO)_3(CNAr^{Dipp2})_2$: **1538896**

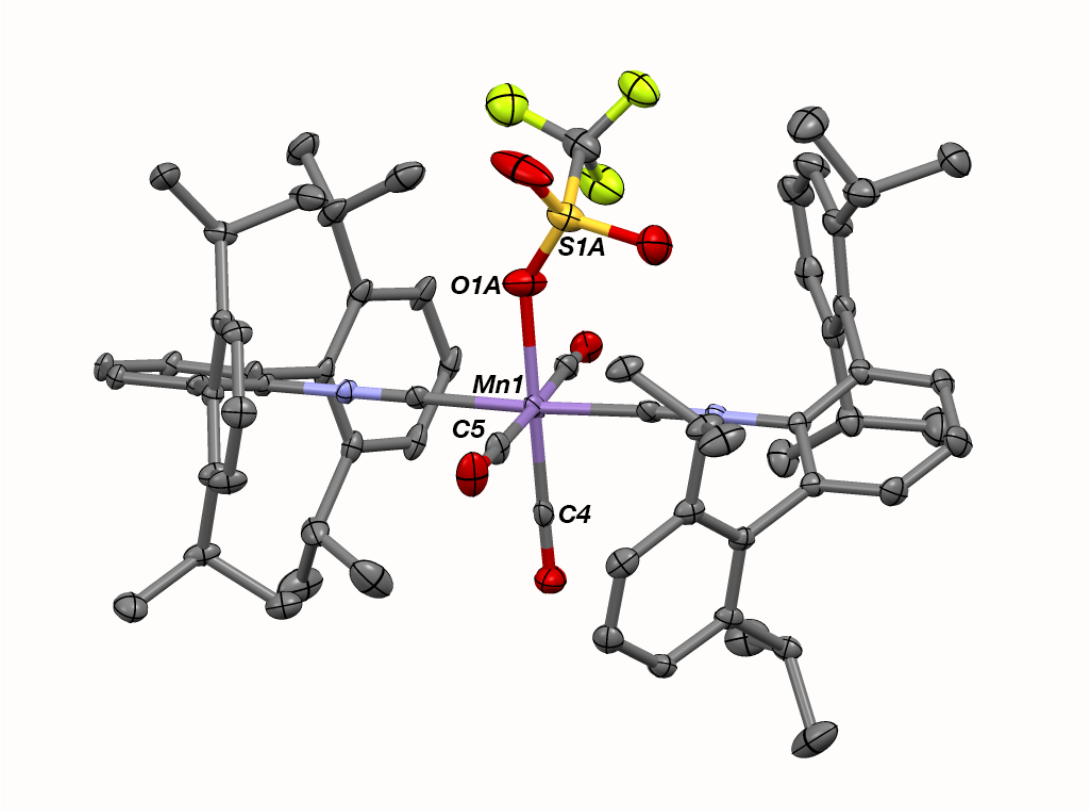

Figure 2.27. Molecular structure of $(OTf)Mn(CO)_3(CNAr^{Dipp2})_2$. Selected bond distances (Å) and angles (°): Mn1-O1A = 2.059(6); Mn1-C5 = 1.879(7); Mn1-C4 = 1.827(8); O1A-S1A = 1.388(7); Mn1-O1A-S1A = 143.9(5); C5-Mn1-C4 = 92.4(3).

Table 2.3. Crystallographic Data Collection and Refinement Information.

Name	$Mn(CO)_3(CNAr^{Dipp2})_2$ (**1**)	$(Bu_3Sn)Mn(CO)_3(CNAr^{Dipp2})_2 \cdot 0.5(Et_2O)$ (**3**·0.5(Et_2O))	$(Cl_2HC)Mn(CO)_3(CNAr^{Dipp2})_2 \cdot 2(THF)$ (**4**·2(THF))
Formula	$C_{65}H_{74}MnN_2O_3$	$C_{79}H_{106}MnN_2O_{3.5}Sn$	$C_{74}H_{91}Cl_2MnN_2O_5$
Crystal System	Monoclinic	Monoclinic	Monoclinic
Space Group	*C*2/*c*	$P2_1/c$	$P2_1/c$
a, Å	23.7399(13)	27.7726(8)	16.9829(9)
b, Å	23.5759(14)	11.4840(3)	16.6744(7)
c, Å	21.3554(14)	23.1053(7)	24.6720(13)
α, deg	90	90	90
β, deg	108.318(2)	93.774(2)	104.948(2)
γ, deg	90	90	90
V, $Å^3$	11346.7(12)	7325.2(4)	6750.2(6)
Z	8	4	4
Radiation (λ, Å)	Mo-Kα, 0.71073	Mo-Kα, 0.71073	Mo-Kα, 0.71073
ρ (calcd.), Mg/m^3	1.155	1.191	1.195
μ (Mo Kα), mm^{-1}	0.279	0.560	0.325
Temp, K	100	100	100
θ max, deg	25.417	25.385	26.757
data/parameters	10444/791	13411/1025	14277/733
R_1	0.0440	0.0506	0.0622
wR_2	0.0929	0.1213	0.1457
GOF	1.022	1.031	1.025

Table 2.4. Crystallographic Data Collection and Refinement Information.

Name	$ClMn(CO)_3(CNAr^{Dipp2})_2 \cdot 2.5(Et_2O)$ (**5**·2.5(Et_2O))	$(\mu_2\text{-}\kappa^1\text{:}\kappa^1\text{-}OC_6Me_4O)[Mn(CO)_3(CNAr^{Dipp2})_2]_2$ (**6**)	*cis,mer:trans,mer*-$[Mn(CO)_3(CNAr^{Dipp2})_2]_2(\mu\text{-}\eta^1\text{:}\eta^1\text{-}P_4)\cdot 3(Et_2O)$ (**7**·3(Et_2O))
Formula	$C_{75}H_{99}ClMnN_2O_{5.50}$	$C_{140}H_{160}Mn_2N_4O_8$	$C_{142}H_{178}Mn_2N_4O_9P_4$
Crystal System	Triclinic	Monoclinic	Triclinic
Space Group	*P*-1	*C*2/*c*	*P*-1
a, Å	14.702(2)	40.4433(17)	15.3515(9)
b, Å	15.465(2)	11.5056(4)	18.8775(12)
c, Å	17.102(3)	29.7226(13)	23.8175(14)
α, deg	75.357(4)	90	105.276(2)
β, deg	74.602(4)	116.1640(12)	90.744(2)
γ, deg	68.851(4)	90	94.059(2)
V, $Å^3$	3442.4(9)	12413.5(9)	6638.1(7)
Z	2	4	2
Radiation (λ, Å)	Mo-Kα, 0.71073	Mo-Kα, 0.71073	Mo-Kα, 0.71073
ρ (calcd.), Mg/m^3	1.164	1.143	1.160
μ (Mo Kα), mm^{-1}	0.281	0.261	0.295
Temp, K	100	100	100
θ max, deg	25.465	25.388	25.423
data/parameters	12605/700	11358/712	14379/1600
R_1	0.0776	0.0573	0.0565
wR_2	0.1920	0.1054	0.1285
GOF	1.048	1.006	1.023

Table 2.5. Crystallographic Data Collection and Refinement Information.

Name	(η^2-*N,O*-PhNO)Mn(CO)$_2$(CNAr^{Dipp2})$_2$ (**8**)	(η^2-*N,O*-*m*-TolNO)Mn(CO)$_2$(CNAr^{Dipp2})$_2$ (**9**)	(η^2-*N,O*-*p*-TolNO)Mn(CO)$_2$(CNAr^{Dipp2})$_2$ (**10**)
Formula	$C_{94}H_{103}MnN_3O_3$	$C_{83}H_{93}MnN_3O_3$	$C_{89}H_{99}MnN_3O_3$
Crystal System	Monoclinic	Monoclinic	Monoclinic
Space Group	*Cm*	*Cm*	C_2/m
a, Å	16.191(2)	16.2512(13)	16.1883(7)
b, Å	24.253(4)	24.293(3)	24.2117(10)
c, Å	12.1139(8)	12.1799(9)	12.0977(9)
α, deg	90	90	90
β, deg	129.891(4)	129.831(2)	129.662(2)
γ, deg	90	90	90
V, Å^3	3649.8(8)	3692.6(6)	3650.2(4)
Z	2	2	2
Radiation (λ, Å)	Mo-Kα, 0.71073	Mo-Kα, 0.71073	Mo-Kα, 0.71073
ρ (calcd.), Mg/m^3	1.254	1.111	1.195
μ (Mo Kα), mm^{-1}	0.237	0.227	0.233
Temp, K	100	100	100
θ max, deg	26.378	25.427	25.381
data/parameters	6905/420	6908/420	3454/237
R_1	0.0487	0.0411	0.0468
wR_2	0.1286	0.1105	0.1272
GOF	1.024	1.077	1.059

Table 2.6. Crystallographic Data Collection and Refinement Information.

Name	$(OTf)Mn(CO)_3(CNAr^{Dipp2})_2 \cdot 0.5(n\text{-}C_5H_{12})$	$((CO)_3(CNAr^{Dipp2})_2Mn(SCS)Mn(C{=}NAr^{Dipp2})(CO)_2(CNAr^{Dipp2})$.	$Mn(FHF)(CO)_3(CNAr^{Dipp2})_2 \cdot (Et_2O)$
Formula	$C_{68.50}H_{80}F_3MnN_2O_6S$	$C_{144}H_{185}Mn_2N_4O_{8.5}S_2Si_3$	$C_{67}H_{79}F_{1.2}MnN_2O_{3.47}$
Crystal System	Monoclinic	Monoclinic	Monoclinic
Space Group	*Cc*	*C*2/c	P 2 1/c
a, Å	23.487(5)	50.582(7)	19.1678(5)
b, Å	24.846(5)	15.3077(16)	16.5149(4)
c, Å	22.333(4)	40.553(6)	20.6165(5)
α, deg	90	90	90
β, deg	94.520(3)	113.998(5)	114.1020(10)
γ, deg	90	90	90
V, $Å^3$	12992(4)	28685(7)	5957.3(3)
Z	8	8	4
Radiation (λ, Å)	Mo-Kα, 0.71073	Mo-Kα, 0.71073	Cu-K_α, 1.54178
ρ (calcd.), Mg/m^3	1.143	1.096	1.181
μ (Mo Kα), mm^{-1}	0.294	0.283	2.217
Temp, K	100	100	100
θ max, deg	25.406	26.373	68.284
data/parameters	21256/1711	29307/1519	10877/749
R_1	0.0603	0.0582	0.0462
wR_2	0.1582	0.1560	0.1251
GOF	1.036	1.068	1.034

Table 2.7. Crystallographic Data Collection and Refinement Information.

Name	$Mn(BiCl_2)(CO)_3(CNAr^{Dipp2})_2\cdot(THF)$	$Mn(SbF_2)(CO)_3(CNAr^{Dipp2})_2\cdot 2(Pyridine)$	$Mn(THF\cdot AlCl_2)(CO)_3(CNAr^{Dipp2})_2$
Formula	$C_{73}H_{89}BiCl_2MnN_2O_5$	$C_{75}H_{84}F_2MnN_4O_3Sb$	$C_{69}H_{82}AlCl_2MnN_2O_4$
Crystal System	Monoclinic	Monoclinic	Monoclinic
Space Group	P 2 1/c	P 2 1/c	P 1 2/c
a, Å	17.0881(10)	15.9656(4)	13.6958(5)
b, Å	16.5315(9)	17.3952(4)	26.0232(9)
c, Å	24.8358	25.1885(6)	18.4253(6)
α, deg	90	90	90
β, deg	105.3620(10)	101.8090(10)	95.8827(17)
γ, deg	90	90	90
V, $Å^3$	6765.2(7)	6847.4(3)	6532.4(4)
Z	4	4	4
Radiation (λ, Å)	Mo-K_α, 0.71073	Mo-K_α, 0.71073	Mo-K_α, 0.71073
ρ (calcd.), Mg/m^3	1.384	1.265	1.176
μ (Mo Ka), mm^{-1}	2.913	0.633	0.344
Temp, K	100	100	100
θ max, deg	25.45	26.12	24.141
data/parameters	12473/773	13554/777	10356/742
R_1	0.0612	0.0557	0.0536
wR_2	0.1749	0.1555	0.1073
GOF	1.058	1.041	1.065

2.9 Acknowledgements

Chapter 2 is adapted in part from "Kinetic Destabilization of Metal-Metal Single Bonds: Isolation of a Pentacoordinate Manganese(0) Monoradical" by Douglas W. Agnew, Curtis E. Moore, Arnold L. Rheingold, and Joshua S. Figueroa, *Angewandte Chemie, International Edition* **2015** *54*, 12673-12677, Copyright 2015 Wiley-VCH Verlag GmbH & Co., and "Comparison of Nucelophilic- and Radical-

Based Routes to the Formation of Manganese-Group Element Single Bonds" by Douglas W. Agnew, Curtis E. Moore, Arnold L. Rheingold, and Joshua S. Figueroa, which has been submitted for publication. Permission to include published material in this dissertation has been obtained from all coauthors. The dissertation author is the first author of both papers.

2.10 References

1. M. C. Baird, *J. Organomet. Chem.* **2014**, *751*, 50.
2. C. D. Hoff, *Coord. Chem. Rev.* **2000**, *206–207*, 451.
3. M. C. Baird, *Chem. Rev.* **1988**, *88*, 1217.
4. D. C. Eisenberg, J. R. Norton, *Isr. J. Chem.* **1991**, *31*, 55.
5. R. L. Sweany, J. Halpern, *J. Am. Chem. Soc.* **1977**, *99*, 8335.
6. M. Wrighton, *Chem. Rev.* **1974**, *74*, 401.
7. S. A. Fairhurst, J. R. Morton, R. N. Perutz, K. F. Preston, *Organometallics* **1984**, *3*, 1389.
8. M. C. R. Symons, R. L. Sweany, *Organometallics* **1982**, *1*, 834.
9. J. A. Howard, J. R. Morton, K. F. Preston, *Chem. Phys. Lett.* **1981**, *83*, 226.
10. S. P.Church, M. Poliakoff, J. A. Timney, J. J. Turner, *J. Am. Chem. Soc.* **1981**, *103*, 7515.
11. W. L. Waltz, O. Hackelberg, L. M. Dorfman, A. Wojcicki, *J. Am. Chem. Soc.* **1978**, *100*, 7259.
12. A. Hudson, M. F. Lappert, P. W. Lednor, B. K. Nicholson, *J. Chem. Soc., Chem. Commun.* **1974**, 966.
13. A. S. Huffadine, B. M. Peake, B. H. Robinson, J. Simpson, P. A. Dawson, *J. Organomet. Chem.* **1976**, *121*, 391.
14. A. Hudson, M. F. Lappert, B. K. Nicholson, *J. Chem. Soc., Dalton Trans.* **1977**, 551.

15. D. R. Kidd, C. P. Cheng, T. L. Brown, *J. Am. Chem. Soc.* **1978**, *100*, 4103.

16. S. B. McCullen, T. L. Brown, *J. Am. Chem. Soc.* **1982**, *104*, 7496.

17. D. J. Kuchynka, C. Amatore, J. K. Kochi, *J. Organomet. Chem.* **1987**, *328*, 133.

18. G. B. Rattinger, R. L. Belford, H. Walker, T. L. Brown, *Inorg. Chem.* **1989**, *28*, 1059.

19. F. Bourrez, F. Molton, S. Chardon-Noblat, A. Deronzier, *Angew. Chem. Int. Ed.* **2011**, *50*, 9903.

20. J. M. Smieja, M. D. Sampson, K. A. Grice, E. E. Benson, J. D. Froehlich, .C. P. Kubiak, *Inorg. Chem.* **2013**, *52*, 2484.

21. M. D. Sampson, A. D. Nguyen, K. A. Grice, A. L. Rheingold, C. P. Kubiak, *J. Am. Chem. Soc.* **2014**, *136*, 5460.

22. A. E. Carpenter, C. C. Mokhtarzadeh, D. S. Ripatti, I. Havrylyuk, R. Kamezawa, C. E. Moore, A. L. Rheingold, J. S. Figueroa, *Inorg. Chem.* **2015**, *54*, 2936.

23. T. B. Ditri, B. J. Fox, C. E. Moore, A. L. Rheingold, J. S. Figueroa, *Inorg. Chem.* **2009**, *48*, 8362.

24. F. A. Cotton, F. Zingales, *J. Am. Chem. Soc.* **1961**, *83*, 351.

25. M. A. Stewart, C. E. Moore, T. B. Ditri, L. A. Labios, A. L. Rheingold, J. S. Figueroa, *Chem. Commun.* **2011**, *47*, 406.

26. A. W. Addison, T. N. Rao, J. Reedijk, J. van Rijn, G. C. Verschoor, *J. Chem. Soc., Dalton Transactions* **1984**, 1349.

27. M. Elian, R. Hoffmann, *Inorg. Chem.* **1975**, *14*, 1058.

28. W. J. Shaw, P. Kandandarachchi, J. A. Franz, T. Autrey, *Organometallics* **2004**, *23*, 2080.

29. Likely due to a *cis*-labilizing effect from the k^1-phosphido unit, **7** is obtained as a mixture of *trans:trans* and *cis:trans* (structurally characterized) isomers with respect to the $CNAr^{Dipp2}$ ligands. See text and Supporting Information.

30. M. Scheer, G. Balázs, A. Seitz, *Chem. Rev.* **2010**, *110*, 4236.

31. M. Caporali, L. Gonsalvi, A. Rossin, M. Peruzzini, *Chem. Rev.* **2010**, *110*, 4178.

32. O. J. Scherer, T. Hilt, G. Wolmershäuser, *Organometallics* **1998**, *17*, 4110.

33. S. Heinl, M. Scheer, *Chem. Sci.* **2014**, *5*, 3221.

34. S. Pelties, D. Herrmann, B. de Bruin, F. Hartl, R. Wolf, *Chem. Commun.* **2014**, *50*, 7014.

35. J. Lee, L. Chen, A. H. West, G. B. Richter-Addo, *Chem. Rev.* **2002**, *102*, 1019.

36. N. C. Tomson, L. A. Labios, T. Weyhermuller, J. S. Figueroa, K. Wieghardt, *Inorg. Chem.* **2011**, *50*, 5763.

37. M. L. H. Green, *J. Organomet. Chem.* **1995**, *500*, 127.

38. L. A. Labios, M. D. Millard, A. L. Rheingold, J. S. Figueroa, *J. Am. Chem. Soc.* **2009**, *131*, 11318.

39. S.-C. Chan, J. England, W.-C. Lee, K. Wieghardt, C.-Y. Wong, *ChemPlusChem* **2013**, *78*, 214.

40. M. S. Askari, B. Girard, M. Murugesu, X. Ottenwaelder, *Chem. Commun.* **2011**, *47*, 8055.

41. Iwasa, T.; Shimada, H.; Takami, A.; Matsuzaka, H.; Ishii, Y.; Hidai, M. *Inorg. Chem.* **1999**, *38*, 2851.

42. J. D. Atwood, T. L. Brown, *J. Am. Chem. Soc.* **1975**, *97*, 3380.

43. J. A. S. Howell, P. M. Burkinshaw, *Chem. Rev.* **1983**, *83*, 557.

44. R. D. Davy, M. B. Hall, *Inorg. Chem.* **1989**, *28*, 3524.

45. R. Bruce King. *Organometallic Syntheses*, Eisch, J. J., Ed. Elsevier: Amsterdam, 1988.

46. Maity, A.; Teets, T. S., *Chem. Rev.* **2016,** *116*, 8873-8911.

47. Lin, T.-P.; Peters, J. C., *J. Am. Chem. Soc.* **2014,** *136*, 13672-13683.

48. Niemeyer, J.; Kelly, M. J.; Riddlestone, I. M.; Vidovic, D.; Aldridge, S., *Dalton Trans.* **2015,** *44*, 11294-11305.

49. Braunschweig, H.; Radacki, K.; Seeler, F.; Whittell, G. R., *Organometallics* **2006,** *25*, 4605-4610.

50. Bauer, J.; Braunschweig, H.; Kraft, K.; Radacki, K., *Angewandte Chemie International Edition* **2011,** *50*, 10457-10460.

51. Cammarota, R. C.; Lu, C. C., *J. Am. Chem. Soc.* **2015,** *137*, 12486-12489.

52. Devillard, M.; Declercq, R.; Nicolas, E.; Ehlers, A. W.; Backs, J.; Saffon-Merceron, N.; Bouhadir, G.; Slootweg, J. C.; Uhl, W.; Bourissou, D., *J. Am. Chem. Soc.* **2016,** *138*, 4917-4926.

53. Jones, J. S.; Gabbaï, F. P., *Acc. Chem. Res.* **2016,** *49*, 857-867.

54. Jones, J. S.; Gabbai, F. P., *Chemistry – A European Journal* **2017,** *23*, 1136-1144.

55. Frank, R.; Howell, J.; Tirfoin, R.; Dange, D.; Jones, C.; Mingos, D. M. P.; Aldridge, S., *J. Am. Chem. Soc.* **2014,** *136*, 15730-15741.

56. Cassidy, J. M.; Whitmire, K. H., *Inorg. Chem.* **1991,** *30*, 2788-2795.

57. Braunschweig, H.; Brenner, P.; Cogswell, P.; Kraft, K.; Schwab, K., *Chem. Commun.* **2010,** *46*, 7894-7896.

58. Braunschweig, H.; Dewhurst, R. D.; Hupp, F.; Wolf, J., *Chemistry – A European Journal* **2015,** *21*, 1860-1862.

59. Scheer, M.; Vogel, U.; Becker, U.; Balazs, G.; Scheer, P.; Hönle, W.; Becker, M.; Jansen, M., *Eur. J. Inorg. Chem.* **2005,** *2005*, 135-141.

60. Groer, T.; Scheer, M., *J. Chem. Soc., Dalton Trans.* **2000**, 647-653.

61. Wallis, J. M.; Mueller, G.; Schmidbaur, H., *Inorg. Chem.* **1987,** *26*, 458-459.

62. Sasaki, S.; Sutoh, K.; Murakami, F.; Yoshifuji, a. M., *J. Am. Chem. Soc.* **2002,** *124*, 14830-14831.

63. Kuksis, I.; Baird, M. C., *Organometallics* **1994,** *13*, 1551-1553.

64. Kuksis, I.; Baird, M. C., *Organometallics* **1996,** *15*, 4755-4762.

65. See ref. 33.

66. Agnew, D. W.; Moore, C. E.; Rheingold, A. L.; Figueroa, J. S., *Angewandte Chemie International Edition* **2015,** *54*, n/a-n/a.

67. See ref. 25

68. Fox, B. J.; Sun, Q. Y.; DiPasquale, A. G.; Fox, A. R.; Rheingold, A. L.; Figueroa, J. S., *Inorg. Chem.* **2008,** *47*, 9010-9020.

69. Fox, B. J.; Millard, M. D.; DiPasquale, A. G.; Rheingold, A. L.; Figueroa, J. S., *Angewandte Chemie International Edition* **2009,** *48*, 3473-3477.

70. See ref. 23.

71. Labios, L. A.; Millard, M. D.; Rheingold, A. L.; Figueroa, J. S., *J. Am. Chem. Soc.* **2009,** *131*, 11318-11319.

72. Margulieux, G. W.; Weidemann, N.; Lacy, D. C.; Moore, C. E.; Rheingold, A. L.; Figueroa, J. S., *J. Am. Chem. Soc.* **2010,** *132*, 5033-5035.

73. Ditri, T. B.; Moore, C. E.; Rheingold, A. L.; Figueroa, J. S., *Inorg. Chem.* **2011,** *50*, 10448-10459.

74. Emerich, B. M.; Moore, C. E.; Fox, B. J.; Rheingold, A. L.; Figueroa, J. S., *Organometallics* **2011,** *30*, 2598-2608.

75. Carpenter, A. E.; Margulieux, G. W.; Millard, M. D.; Moore, C. E.; Weidemann, N.; Rheingold, A. L.; Figueroa, J. S., *Angewandte Chemie International Edition* **2012,** *51*, 9412-9416.

76. Ditri, T. B.; Carpenter, A. E.; Ripatti, D. S.; Moore, C. E.; Rheingold, A. L.; Figueroa, J. S., *Inorg. Chem.* **2013,** *52*, 13216-13229.

77. Barnett, B. R.; Moore, C. E.; Rheingold, A. L.; Figueroa, J. S., *J. Am. Chem. Soc.* **2014,** *136*, 10262-10265.

78. Carpenter, A. E.; McNeece, A. J.; Barnett, B. R.; Estrada, A. L.; Mokhtarzadeh, C. C.; Moore, C. E.; Rheingold, A. L.; Perrin, C. L.; Figueroa, J. S., *J. Am. Chem. Soc.* **2014,** *136*, 15481-15484.

79. Mokhtarzadeh, C. C.; Margulieux, G. W.; Carpenter, A. E.; Weidemann, N.; Moore, C. E.; Rheingold, A. L.; Figueroa, J. S., *Inorg. Chem.* **2015,** *54*, 5579-5587.

80. See ref. 22.

81. Barnett, B. R.; Moore, C. E.; Chandrasekaran, P.; Sproules, S.; Rheingold, A. L.; DeBeer, S.; Figueroa, J. S., *Chemical Science* **2015,** *6*, 7169-7178.

82. Carpenter, A. E.; Rheingold, A. L.; Figueroa, J. S., *Organometallics* **2016,** *35*, 2309-2318.

83. Mokhtarzadeh, C. C.; Rheingold, A. L.; Figueroa, J. S., *Dalton Trans.* **2016**.

84. Agnew, D. W.; Sampson, M. D.; Moore, C. E.; Rheingold, A. L.; Kubiak, C. P.; Figueroa, J. S., *Inorg. Chem.* **2016,** *55*, 12400-12408.

85. Agnew, D. W.; Gembicky, M.; Moore, C. E.; Rheingold, A. L.; Figueroa, J. S., *J. Am. Chem. Soc.* **2016,** *138*, 15138-15141.

86. Barnett, B. R.; Figueroa, J. S., *Chem. Commun.* **2016,** *52*, 13829-13839.

87. Deng, J.; Li, Q.-S.; Xie, Y.; King, R. B., *Dalton Trans.* **2012,** *41*, 6225.

88. Norman, N. C.; Webster, P. M.; Farrugia, L. J., *J. Organomet. Chem.* **1992,** *430*, 205-219.

89. Balch, A. L.; Catalano, V. J.; Chatfield, M. A.; Nagle, J. K.; Olmstead, M. M.; Reedy Jr, P. E., *J. Am. Chem. Soc.* **1991,** *113*, 1252-1258.

90. Wójcik, K.; Preda, A. M.; Mertens, L.; Ecorchard, P.; Rüffer, T.; Lang, H.; Mehring, M., *Inorg. Chem.* **2015,** *54*, 3905-3912.

91. Wójcik, K.; Ecorchard, P.; Schaarschmidt, D.; Rüffer, T.; Lang, H.; Mehring, M., *Z. Anorg. Allg. Chem.* **2012,** *638*, 1723-1730.

92. Errington, R. J.; Fisher, G. A.; Norman, N. C.; Guy Orpen, A.; Stratford, S. E., *Z. Anorg. Allg. Chem.* **1994,** *620*, 457-466.

93. Von Seyerl, J.; Huttner, G., *J. Organomet. Chem.* **1980,** *195*, 207-212.

94. Murphy, E. F.; Murugavel, R.; Roesky, H. W., *Chem. Rev.* **1997,** *97*, 3425-3468.

95. Doherty, N. M.; Hoffmann, N. W., *Chem. Rev.* **1991,** *91*, 553-573.

96. Orchin, M.; Becker, T. M.; Bauer, J. A. K.; Del Bene, J. E., **2001,** *629*, 165-170.

97. Drew, D.; Darensbourg, D. J.; Darensbourg, M. Y., *Inorg. Chem.* **2002,** *14*, 1579-1584.

98. Nahra, F.; Brill, M.; Gómez-Herrera, A.; Cazin, C. S. J.; Nolan, S. P., *Coord. Chem. Rev.* **2016,** *307, Part 1*, 65-80.

99. Murphy, V. J.; Hascall, T.; Chen, J. Y.; Parkin, G., *J. Am. Chem. Soc.* **1996,** *118*, 7428-7429.

100. Appelman, E. H.; Malm, J. G., *J. Am. Chem. Soc.* **1964,** *86*, 2297-2298.

101. Ball, N. D.; Sanford, M. S., *J. Am. Chem. Soc.* **2009,** *131*, 3796-3797.

102. Green, M. L. H., *J. Organomet. Chem.* **1995,** *500*, 127-148.

103. Braunschweig, H.; Gruss, K.; Radacki, K., *Angewandte Chemie International Edition* **2007,** *46*, 7782-7784.

104. Bauer, J.; Braunschweig, H.; Brenner, P.; Kraft, K.; Radacki, K.; Schwab, K., *Chemistry – A European Journal* **2010,** *16*, 11985-11992.

105. Fischer, R. A.; Schulte, M. M.; Weiss, J.; Zsolnai, L.; Jacobi, A.; Huttner, G.; Frenking, G.; Boehme, C.; Vyboishchikov, S. F., *J. Am. Chem. Soc.* **1998,** *120*, 1237-1248.

106. A. B. Pangborn, M. A. Giardello, R. H. Grubbs, R. K. Rosen, F. J. Timmers, *Organometallics* **1996**, *15*, 1518.

107. W. L. F. Armarego, C. L. L. Chai, *Purification of Laboratory Chemicals*; 5th ed. ed.; Elsevier, 2003.

108. See ref. 23.

109. See ref. 25.

110. D. Zhao, M. Johansson, J.-E. Bäckvall, *Eur. J. Org. Chem.* **2007**, *2007*, 4431.

111. H. G. Kuivila, A. K. Sawyer, A. G. Armour, *J. Org. Chem.* **1961**, *26*, 1426.

112. G. R. Fulmer, A. J. M. Miller, N. H. Sherden, H. E. Gottlieb, A. Nudelman, B. M. Stoltz, J. E. Bercaw, K. I. Goldberg, *Organometallics* **2010**, *29*, 2176.

113. S. Stoll, A. Schweiger, *Mag. Res.* **2006**, *178*, 42.

114. C. Fonseca Guerra, J. G. Snijders, G. te Velde, E. J. Baerends, *Theor. Chem. Acc.* **1998**, *99*, 391.

115. G. te Velde, F. M. Bickelhaupt, E. J. Baerends, C. Fonseca Guerra, S. J. A. van Gisbergen, J. G. Snijders, T. Ziegler, *J. Comput. Chem.* **2001**, *22*, 931.

116. ADF2012.01, SCM, Vrije Universiteit, Amsterdam, The Netherlands, 2012.

117. ADF-GUI, SCM, Vrije Universiteit, Amsterdam, The Netherlands, 2012.

118. See ref. 22.

119. E. van Lenthe, E. J. Baerends, J. G. Snijders, *J. Chem. Phys.* **1993**, *99*, 4597.

120. E. van Lenthe, J. G. Snijders, E. J. Baerends, *J. Chem. Phys.* **1996**, *105*, 6505.

121. S. H. Vosko, L. Wilk, M. Nusair, *Can. J. Phys.* **1980**, *58*, 1200.

122. A. D. Becke, *Phys. Rev. A* **1988**, *38*, 3098.

123. J. P. Perdew, *Phys. Rev. B* **1986**, *33*, 8822.

124. J. P. Perdew, *Phys. Rev. B* **1986**, *34*, 7406 (*erratum*).

125. G. M. Sheldrick, *Acta Crystallogr. A* **2008**, *64*, 112.

126. O. V. Dolomanov, L. J. Bourhis; R. J. Gildea, J. A. K. Howard, H. Puschmann, *J. Appl. Crystallogr.* **2009**, *42*, 339.

Chapter 3

Electrochemical Properties and CO_2-Reduction Ability of *m*-Terphenyl Isocyanide-Supported Manganese Tricarbonyl Complexes

3.1 Introduction

The electrochemical derivatization of carbon dioxide (CO_2) offers a promising route towards environmentally benign sources of fuel precursors and carbon feedstocks.[1-5] Known molecular catalysts in the homogenous reduction of CO_2 to CO include the group 7 bipyridine species *fac*-$XM(CO)_3$(bpy-R) (M = Mn or Re; X = halide, $[O_3SCF_3]^-$; bpy = 2,2'-bipyridine; R = alkyl or aryl; the prefix *fac*- will be omitted hereafter), which have demonstrated an exceptional selectivity for CO_2 reduction to CO versus H^+ reduction.[6-11] This selectivity has been attributed to the redox non-innocence of the basal bipyridine ligand, which enables a singlet diradical ground state for the catalytically active, formally M(1–) species.[12,13] Interestingly, it has been found that manganese-based catalysts, $XMn(CO)_3$(bpy-R) exhibit comparable activity to its rhenium-based analogues while operating at appreciably lower potentials.[7] This, in conjunction with the low cost and considerable availability of manganese, has made manganese-based catalysts particularly attractive as a system for eventual implementation.[14]

Until recently, the potential at which manganese-bipyridine catalysts operated was governed by the $2e^-$ reduction of the dimeric species $Mn_2(CO)_6(bpy\text{-}R)_2$, which are formed upon $1e^-$ reduction of monomeric $XMn(CO)_3(bpy\text{-}R)$ complexes.[6,7] While the initial reduction of $XMn(CO)_3(bpy\text{-}R)$ has been shown to be primarily bipyridine-based, $XMn(CO)_3(bpy\text{-}R)$ rapidly loses X after reduction to form the five-coordinate intermediate $Mn(CO)_3(bpy\text{-}R)$ prior to dimerization.[15,16] Despite variation of X between halide, solvento, and weakly coordinating anions, the potential for this reduction remains scarcely changed in polar organic solvents, and dimerization to Mn-Mn complexes is the typical end result. Additionally, the fast recombination of manganese monoradicals (*ca*. 2 X 10^9 $M^{-1}s^{-1}$)[17] prevent obviation of the dimerization pathway via fast electrochemical scan rates. However, it was recently shown that introduction of encumbering mesityl susbtituents on the 6 and 6' positions of the bipyridine ligand inhibits dimerization, reducing the necessary potential to reach the active Mn(1–) state.[8] While this improved the operating potential by *ca*. 300 mV, the potential for the initial reduction to the Mn(0) state remained essentially unchanged from that of the parent $XMn(CO)_3(bpy)$ system.[8] It is worth noting, however, that subtle differences are observed upon variation of the apical X ligand, with some evidence for change in the electrochemical mechanism during reduction.[8,18] Elucidation of these differences has proved difficult due to the redox-activity of the bipyridine ligand, precluding insight into the role of the Mn-X bond and the possibility of lowering the operating potential of this catalytic system even further. Accordingly, to develop an understanding of Mn-X bond effects on the Mn(I)/Mn(0) redox couple, we have studied the electrochemistry of the well-defined *m*-terphenyl isocyanide

complexes $[Mn(CO)_3(CNAr^{Dipp2})_2]^n$ (n = 1+, 0, 1–; Ar^{Dipp2} = 2,6-(2,6-(*i*-$Pr)_2C_6H_3)C_6H_3$)).[18,19] Furthermore, we have examined the reactivity of these complexes with CO_2 to delineate alternative reduction pathways for CO_2 with carbonyl manganates.

This system serves as an ideal complement to the $XMn(CO)_3$(bpy-R) electrocatalytic system, in that the formal oxidation state of the Mn center is unambiguous on the basis of both structural and spectroscopic features across the electron-transfer series.[12,19,20] Although well-defined oxidation states can also be ascribed to reduced species resulting from the pentacarbonyl complex $XMn(CO)_5$, the encumbering *m*-terphenyl isocyanide ligands inhibit the formation of Mn-Mn bonds, thereby permitting the study of monomeric low-valent manganese complexes without the complications associated with dimerization.[21-30] As has been previously reported, low-valent manganese mixed carbonyl/isocyanides are readily accessible due to kinetic stabilization imparted by the sterically encumbering *m*-terphenyl isocyanides.[19] The monoanionic complex $Na[Mn(CO)_3(CNAr^{Dipp2})_2]$ is thermally stable and does not display the insertion chemistry observed for other low-valent manganese isocyanides, thereby enabling it to provide analogous reactivity to $Na[Mn(CO)_5]$.[31] Additionally, we have recently reported the preparation of $[Mn(CO)_3(CNAr^{Dipp2})_2]^0$, the first isolable zerovalent manganese complex which acts as a functional mimic to the monoradical $Mn(CO)_5$.[20] Most importantly, $[Mn(CO)_3(CNAr^{Dipp2})_2]^0$ is readily accessible via comproportionation of the formally Mn(I) and Mn(1–) complexes, $(OTf)Mn(CO)_3(CNAr^{Dipp2})_2$ (OTf = $CF_3SO_3^-$) and $Na[Mn(CO)_3(CNAr^{Dipp2})_2]$,

respectively, illustrating the competency of this system for detailed chemical and electrochemical study.

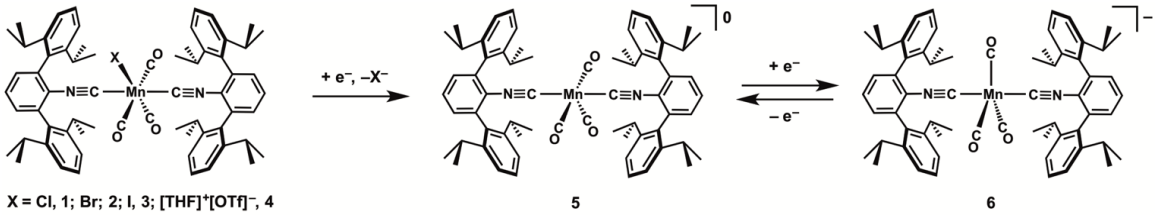

Scheme 3.1. A schematic view of the complexes involved in this study, where **1**, **2**, **3**, are the chloride, bromide, and iodide complexes, respectively, and **4** is the THF-bound cationic complex. Upon one-electron reduction, these complexes are converted to the stable zerovalent complex **5**, which can be further reduced to the anion **6**.

Section 3.2 Electrochemical Properties of $XMn(CO)_3(CNAr^{Dipp2})_2$ Complexes.

To probe the electrochemistry of low-valent manganese mixed carbonyl/isocyanides, and to provide a general comparison to the $XMn(CO)_3(bpy)$ system, we chose to study three halide complexes $ClMn(CO)_3(CNAr^{Dipp2})_2$ (**1**),[21] $BrMn(CO)_3(CNAr^{Dipp2})_2$ (**2**),[19] $IMn(CO)_3(CNAr^{Dipp2})_2$ (**3**), and the trifluoromethanesulfonate salt $[Mn(THF)(CO)_3(CNAr^{Dipp2})_2]OTf$ (**4**), which is generated upon addition of THF to $(OTf)Mn(CO)_3(CNAr^{Dipp2})_2$. To generate the iodide complex, $BrMn(CO)_3(CNAr^{Dipp2})_2$ (**2**) was stirred with excess KI in THF to provide analytically pure $IMn(CO)_3(CNAr^{Dipp2})_2$ (**3**) in 97% yield (Figure 3.1). The three halide complexes are isostructural in the solid state and all display a ν_{CN} band at 2118 cm^{-1} in their solution IR spectrum in THF. In comparison, $[Mn(THF)(CO)_3(CNAr^{Dipp2})_2]OTf$ shows a higher energy asymmetric ν_{CN} band at 2131

cm^{-1} in its IR spectrum, which reflects decreased π-basicity by the formally cationic Mn center.[21]

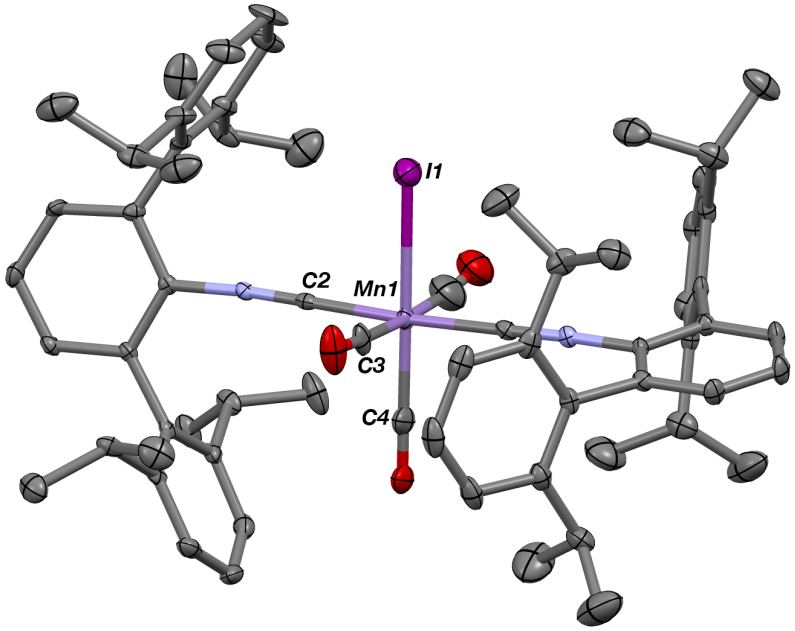

Figure 3.1. Molecular structure of $IMn(CO)_3(CNAr^{Dipp2})_2$ (**3**). Selected bond distances (Å) and angles (°): Mn1-I1 = 6273(7); Mn1-C2 = 1.902(4); Mn1-C4 = 1.846(5); C2-Mn1-C4 = 91.19(6); C4-Mn1-I1 = 178.18(15).

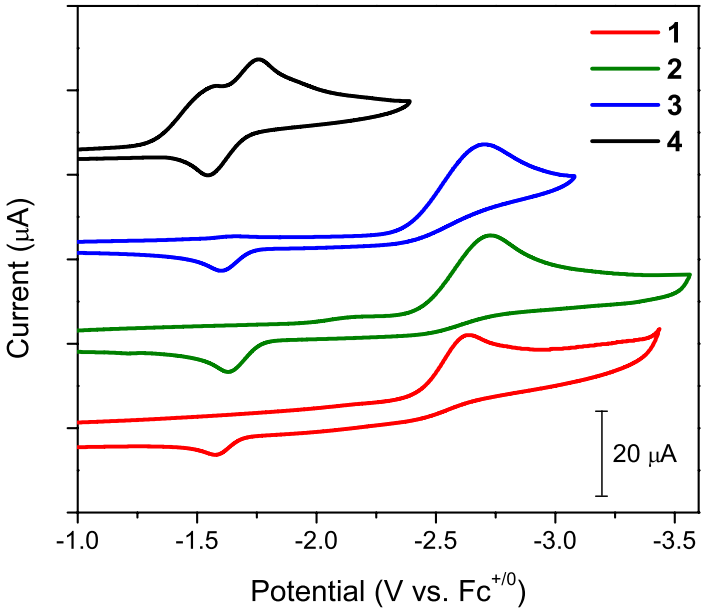

Figure 3.2. Cyclic voltammograms (CVs) of **1** (red), **2** (green), **3** (blue), and **4** (black) in THF with 0.1 M $TBAPF_6$ under dinitrogen. Conditions: 1 mM complex, scan rate = 100 mV/s, glassy carbon working electrode, Ag/AgCl psuedo-reference, Pt wire counter electrode.

Figure 3.2 shows the cyclic voltammograms (CVs) of complexes **1**-**4** obtained in dry THF under an N_2 atmosphere. The cationic complex **4** exhibits two one-electron reduction waves; an irreversible reduction at –1.50 V vs. Fc^+/Fc corresponding to the formation of neutral monoradical $Mn(CO)_3(CNAr^{Dipp2})_2$ (**5**) and a reversible reduction at $E_{1/2}$ = –1.67 V vs. Fc^+/Fc, corresponding to the generation of the monoanion $[Mn(CO)_3(CNAr^{Dipp2})_2]^-$ (**6**). The anodic portion of the aforementioned reversible couple is observed at –1.56 V vs Fc^+/Fc, which corresponds to the oxidation of **6** to **5**. Since dimerization is inhibited due to steric effects, the zerovalent and monoanionic states are electrochemically interchangeable and the reduction potentials are comparable to previously studied homoleptic and mixed phosphine/carbonyl Mn systems.[32,33]

Surprisingly, cyclic voltammograms of the three halide complexes **1**-**3** each show an irreversible reduction at *ca*. –2.7 V vs. Fc^+/Fc, which is over 1.0 V more negative than that of **4**. This reduction corresponds to the formation of the two-electron reduced anionic species, $[Mn(CO)_3(CNAr^{Dipp2})_2]^-$ (**6**), as evidenced by infrared spectroelectrochemistry (IR-SEC) experiments (*vide infra*). An oxidative wave is observed at –1.63 V vs. Fc^+/Fc, which we attribute to the formation of monoradical **5** and is similar to that observed for $[Mn(THF)(CO)_3(CNAr^{Dipp2})_2]OTf$. While the redox chemistry of **1**-**4** all originate from metal-based transformations, it is striking that such a large difference is observed in the first reduction potential between complexes **1**-**3** and **4**. Furthermore, the reduction of a six-coordinate Mn(I) species to the five-coordinate monoradical $[Mn(CO)_3(CNAr^{Dipp2})_2]^0$ involves minimal structural

reorientation,[20] suggesting that the disparity originates primarily within the character of the Mn-X bond.[34]

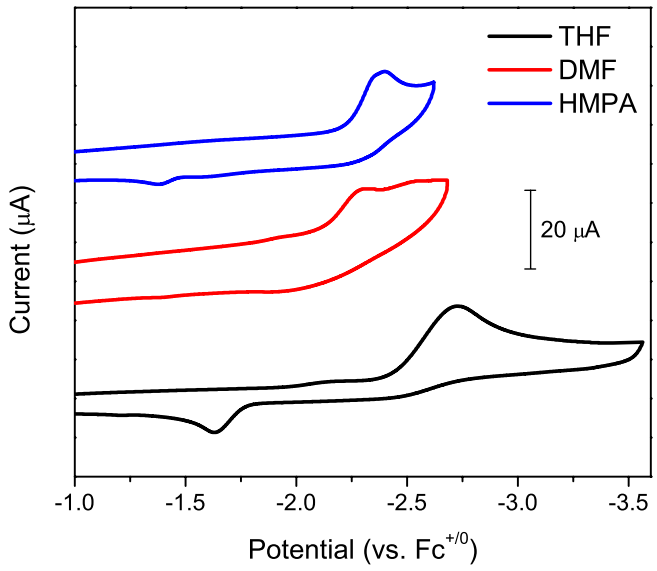

Figure 3.3. Cyclic voltammograms (CVs) of **2** in THF (black), DMF (red), and HMPA (blue). Conditions: 0.1 M $TBAPF_6$, scan rate = 100 mV/s, glassy carbon working electrode, Ag/AgCl reference electrode, Pt wire counter electrode, under dinitrogen.

To further probe the large difference in reduction potential between the halide complexes **1**-**3** and cationic complex **4**, cyclic voltammograms were acquired for the bromide complex **2** in dimethylformamide (DMF) and hexamethylphosphoramide (HMPA) (Figure 3.3). A potential source of the incongruity observed between the reduction potentials of the halide species **1**–**3** and **4** likely lies in the underlying equilibria governing anion dissociation in THF.[35-37] It was found that in these polar organic solvents the reduction of **2** shifted to a more positive potential at –2.29 V and –2.38 V vs Fc^+/Fc for DMF and HMPA, respectively, suggesting a strong relationship

between ion-pair affinity and redox potential in this system. Additionally, we studied **4** with increasing equivalents of acetonitrile (MeCN), which should bind more strongly to the Lewis acidic manganese center than THF. The results, shown in Figure 3.4, reveal that increasing equivalents of MeCN lead to a new complex with a single cathodic wave at –2.05 V vs. Fc^{+}/Fc. We assign this species as $[Mn(MeCN)(CO)_3(CNAr^{Dipp2})_2]OTf$, based on the increased potential necessary to effect reduction. The oxidative wave observed for **4** in THF (at *ca.* –1.6 V vs. Fc^{+}/Fc) is unchanged by the addition of MeCN, indicating that $[Mn(CO)_3(CNAr^{Dipp2})_2]^{-}$ (**6**) is

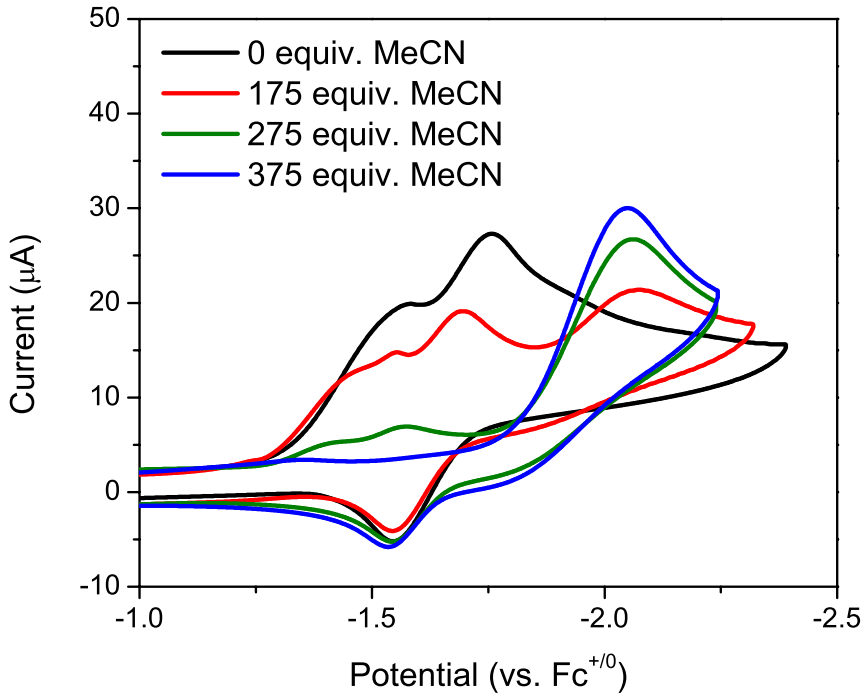

Figure 3.4. Cyclic voltammograms (CVs) of **4** in THF with 0.1 M $TBAPF_6$ under dinitrogen with the following equivalents of MeCN added: 0 equiv. (black), 175 equiv. (red), 275 equiv. (green), and 375 equiv. (blue). Conditions: 1 mM complex, scan rate = 100 mV/s, glassy carbon working electrode, Ag/AgCl reference electrode, Pt wire counter electrode.

also formed upon reduction of $[Mn(MeCN)(CO)_3(CNAr^{Dipp2})_2]OTf$ and is reoxidized in the return anodic wave. Perhaps most striking is that the negative shift in reduction potential upon MeCN addition is accompanied by a transition from two $1e^-$ reductions to a single $2e^-$ reduction wave, demonstrating the high sensitivity of the first reduction potential towards Mn-X (X = halide or solvent) binding strength.

Infrared-spectroelectrochemistry (IR-SEC) was performed on **2** and **4** to further understand the electrochemical processes in this system.[38] As shown in Figure 3.5, the cationic species **4** is reduced in two $1e^-$ steps (ECE mechanism). At resting potential, the starting material is characterized by an intense ν_{CN} band at 2131 cm^{-1}. At *ca.* –1.3 V,[39] complex **4** is reduced to the zerovalent species $Mn(CO)_3(CNAr^{Dipp2})_2$ (**5**),

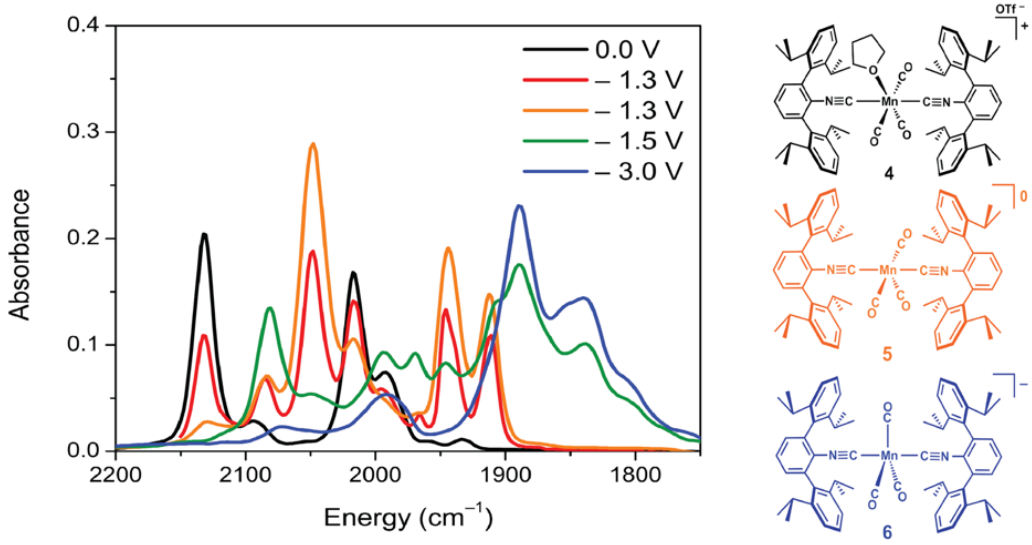

Figure 3.5. IR-SEC of **4** in THF with 0.1 M $TBAPF_6$ under dinitrogen. The starting material, $[Mn(CO)_3(CNAr^{Dipp2})_2(THF)]OTf$ (**4**) is observed at 0.0 V (black) with ν_{CN} = 2131 cm^{-1}; ν_{CO} = 2016, 1991 cm^{-1}. At –1.3 V (red), **4** is initially reduced, and upon holding the potential of the cell at –1.3 V (orange), **4** is fully reduced to the neutral species **5** (ν_{CN} = 2048 cm^{-1}; ν_{CO} = 1942, 1912 cm^{-1}). Slow formation of the hydride $HMn(CO)_3(CNAr^{Dipp2})_2$ (ν_{CN} = 2080 cm^{-1}) is apparent in the **5** to **6** conversion and likely results from deprotonation of either solvent or the supporting electrolyte (Hoffman elimination) by **6**.[39] At –1.5 V (green), **5** is reduced to anionic **6** (ν_{CN} = 1908 cm^{-1}; ν_{CO} = 1896 cm^{-1}), while a more negative potential, –3.0 V (blue), is necessary to reduce $HMn(CO)_3(CNAr^{Dipp2})_2$ to **6**.

as indicated by its ν_{CN} band at 2048 cm^{-1}. Upon further reduction at *ca.* –1.5 V vs Fc^{+}/Fc, this peak diminishes with a concurrent rise in absorption at 1890 cm^{-1} resulting from the ν_{CN}/ν_{CO} stretch of the anionic species $[Mn(CO)_3(CNAr^{Dipp2})_2]^-$ (**6**).[40]

In marked contrast to the behavior of cationic **4**, the halide complexes **1**-**3** are reduced in a single event to the anionic species **6**, as evidenced by IR-SEC experiments of the bromide complex **2** (Figure 3.6). At approximately –2.3 V vs Fc^{+}/Fc, **2** is converted directly to the anionic species **6**, with a small concurrent absorption resulting from the hydride complex, $HMn(CO)_3(CNAr^{Dipp2})_2$.[19] The latter

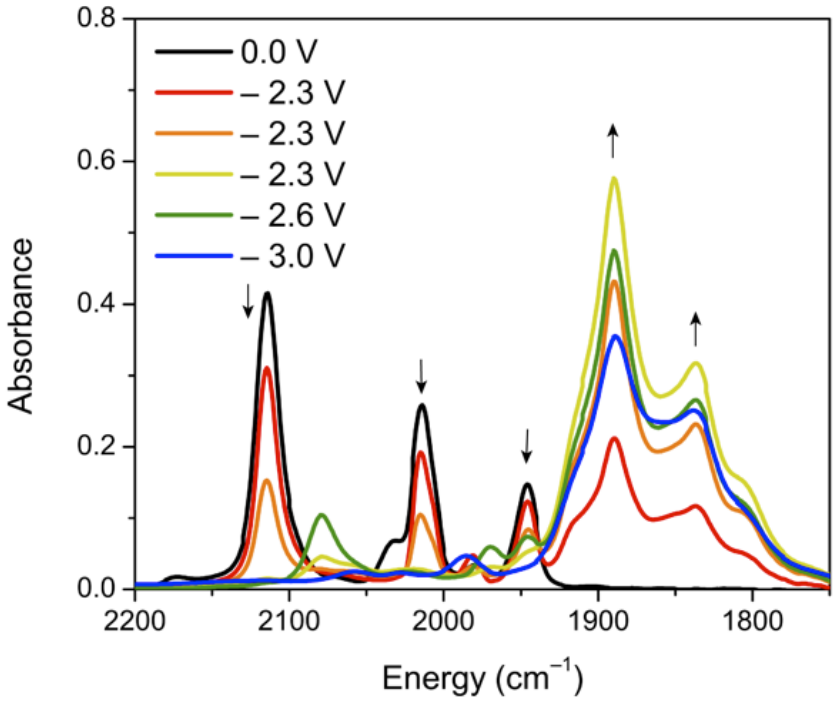

Figure 3.6. IR-SEC of **2** in THF with 0.1 M TBAPF6 under dinitrogen. The starting material, $BrMn(CO)_3(CNAr^{Dipp2})_2$ (**2**), is observed at 0.0 V (black) with ν_{CN} = 2117 cm^{-1} and ν_{CO} = 2015, 1943 cm^{-1}. At –2.3 V (red), **2** is initially reduced, and upon holding the potential of the cell at –2.3 V (orange, yellow), **2** is fully reduced by two electrons to **6** (ν_{CN} = 1908 cm^{-1} and νCO = 1896 cm^{-1}). A small amount of $HMn(CO)_3(CNAr^{Dipp2})_2$ (ν_{CN} = 2080 cm^{-1}) is generated upon holding the cell at –2.6 V (green), which is subsequently reduced at –3.0 V (blue).

likely arises from H^+ abstraction by **6** from either the solvent or supporting electrolyte.[39] Notably, however, no evidence for the formation of the zerovalent complex **5** or signals attributable to Mn–Mn dimers were observed throughout these IR-SEC experiments, providing strong evidence that the initial one-electron reduction of $XMn(CO)_3(CNAr^{Dipp2})_2$ (X = halide) occurs at a far lower reduction potential than the Mn(0)/Mn(1–) redox couple observed for complex **4**.

These electrochemical and spectroscopic data indicate that while both cationic and halide Mn(I) mixed carbonyl/isocyanide complexes undergo reduction following an ECE mechanism, the nature of the M-X bond has a significant effect upon the potential of the first reduction. For cationic complex **4**, the initial reduction of **4** to **5** occurs at a slightly more positive potential than the reduction of **5** to **6**, resulting in two sequential one-electron steps, where THF is lost between the two reductions. For the halide complexes **1**-**3**, a significant potential is necessary to charge the complex with one electron and facilitate X^- loss, resulting in reduction at far lower potentials and therefore ultimate reduction to $[Mn(CO)_3(CNAr^{Dipp2})_2]^-$. This behavior is best illustrated by the addition of MeCN, which in sufficient concentration causes a shift from a pronounced two-step reduction to a single cathodic wave.

Taken together, these data reveal a high sensitivity to the donor abilities of the apical ligand in Mn metal-based redox chemistry. Previous studies on cationic manganese carbonyl complexes have demonstrated a similar divergence in reduction potential correlating to the relative donor strength of the apical ligand, but a much smaller range of reduction potentials was observed.[32,41-43] It should be noted that the introduction of sterically demanding ligands does significantly affect the underlying

electron transfer mechanism, leading to altered transfer rates and noticeable changes in electrochemical behavior between halide and cationic salt species.[44-47] This partially accounts for the large negative reduction potential necessary to effect the first reduction in **1**-**3**, preventing the observable formation of the zerovalent state on the electrochemical timescale. Importantly, this behavior is mirrored in the chemical reduction of $BrMn(CO)_3(CNAr^{Dipp2})_2$ (**2**) by strong reducing agents such as Na/Hg or KC_8 in THF, which provide only the corresponding manganate salt (i.e. Na[**6**] or K[**6**]).

The above results suggest a significant dependency upon the Mn-X bond in the reduction of a formally Mn(I) complex to Mn(0). Considering that spectroscopic and computational studies have indicated that the isocyanides in this system do not act in a redox non-innocent fashion,[48] it is appropriate to ascribe these reductions of **1**-**4** as metal-based. Interestingly, the initial reduction of $[Mn(CO)_3(CNAr^{Dipp2})_2(THF)]OTf$ (**4**) occurs at *ca*. 0.4 V more positive than that of $ClMn(CO)_3(bpy)$ in THF (–1.89 V vs Fc^+/Fc)[17], whereas the reduction of **1**-**3** is found at *ca*. 0.6 V more negative. While significant evidence[16,49,50] points towards bipyridine being the initial site of reduction in $[Re(CO)_3(bpy\text{-}R)]^0$ complexes, with a formal charge assignment of $Re^I(CO)_3(bpy\text{-}R)^{\cdot-}$, the electronic state of the singly reduced manganese catalyst has yet to be fully characterized. Nevertheless, the results above, as well as other studies,[15,52,53] suggest that the Mn-X bond (X = halide, psuedohalide, solvent) may exert a significant influence on the eletrochemical properties of Mn-based CO_2 electrocatalysts possessing bipyridine and other diimine ligands.

3.3 Electrochemical and Stoichiometric Reactivity of $XMn(CO)_3(CNAr^{Dipp2})_2$ Complexes with CO_2.

In order to further compare the $XMn(CO)_3(CNAr^{Dipp2})_2$ and $XMn(CO)_3(bpy)$ systems, we investigated the ability of complexes **2** and **4** to electrocatalytically reduce CO_2 by monitoring the CVs of these species in CO_2-saturated THF. Under CO_2, the CV of **2** reveals a slight anodic shift and slight current increase of the $2e^-$ reduction wave, in addition to the disappearance of the oxidative feature at *ca*. –1.6 V vs Fc^+/Fc (Figure 3.7). These electrochemical features under CO_2 are consistent with reactivity of anionic **6** with CO_2. The current responses of **2** under CO_2 do not reflect catalytic activity, since the current enhancements are small. Additionally, headspace analysis of bulk electrolysis experiments of **2** in THF by GC-MS did not reveal measurable production of CO and further support our assignment of the reaction as non-catalytic.[54] Similarly, the CV of **4** under CO_2 displays slight anodic shifts of the two reduction waves, a slight change in the oxidative wave at ~ –1.6 V vs Fc^+/Fc, and very small current enhancement observed between –2.4 and –2.6 V vs. Fc^+/Fc (Figure 3.8). All of these features in the CV of **4** under CO_2 are much less pronounced than in the CV of **2**, despite the formation of **6** in both cases. As such, we undertook the direct reaction of CO_2 with $Na[Mn(CO)_3(CNAr^{Dipp2})_2]$ (i.e. Na[**6**]) to clarify the reactivity of monoanion **6** with CO_2.

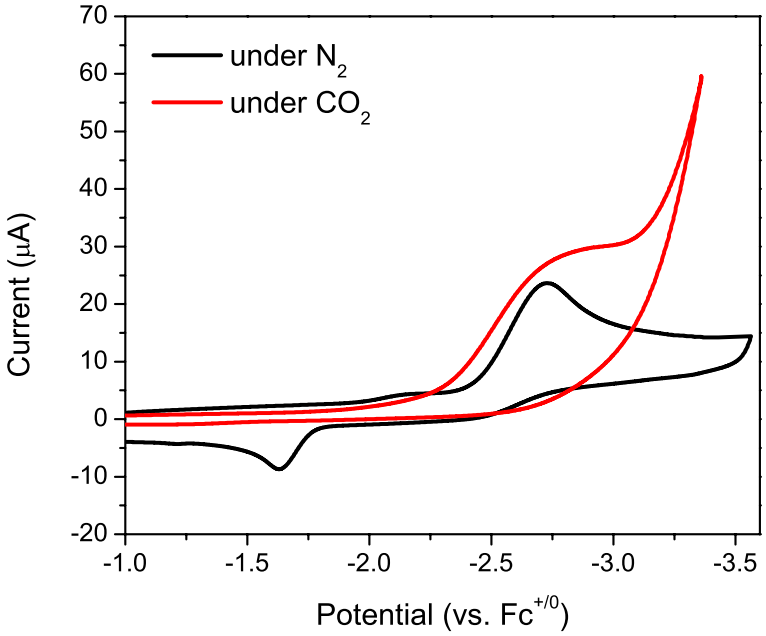

Figure 3.7. Cyclic voltammograms (CVs) of **2** in THF with 0.1 M $TBAPF_6$ under dinitrogen (black) and under CO_2 (red). Conditions: 1 mM complex, scan rate = 100 mV/s, glassy carbon working electrode, Ag/AgCl reference electrode, Pt wire counter electrode.

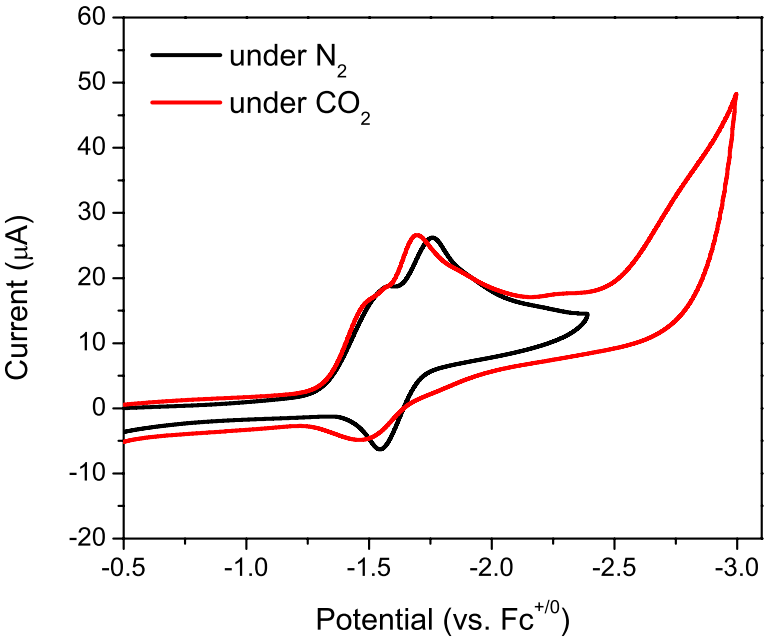

Figure 3.8. Cyclic voltammograms (CVs) of **4** in THF with 0.1 M TBAPF6 under dinitrogen (black) and under CO2 (red). Conditions: 1 mM complex, scan rate = 100 mV/s, glassy carbon working electrode, Ag/AgCl reference electrode, Pt wire counter electrode.

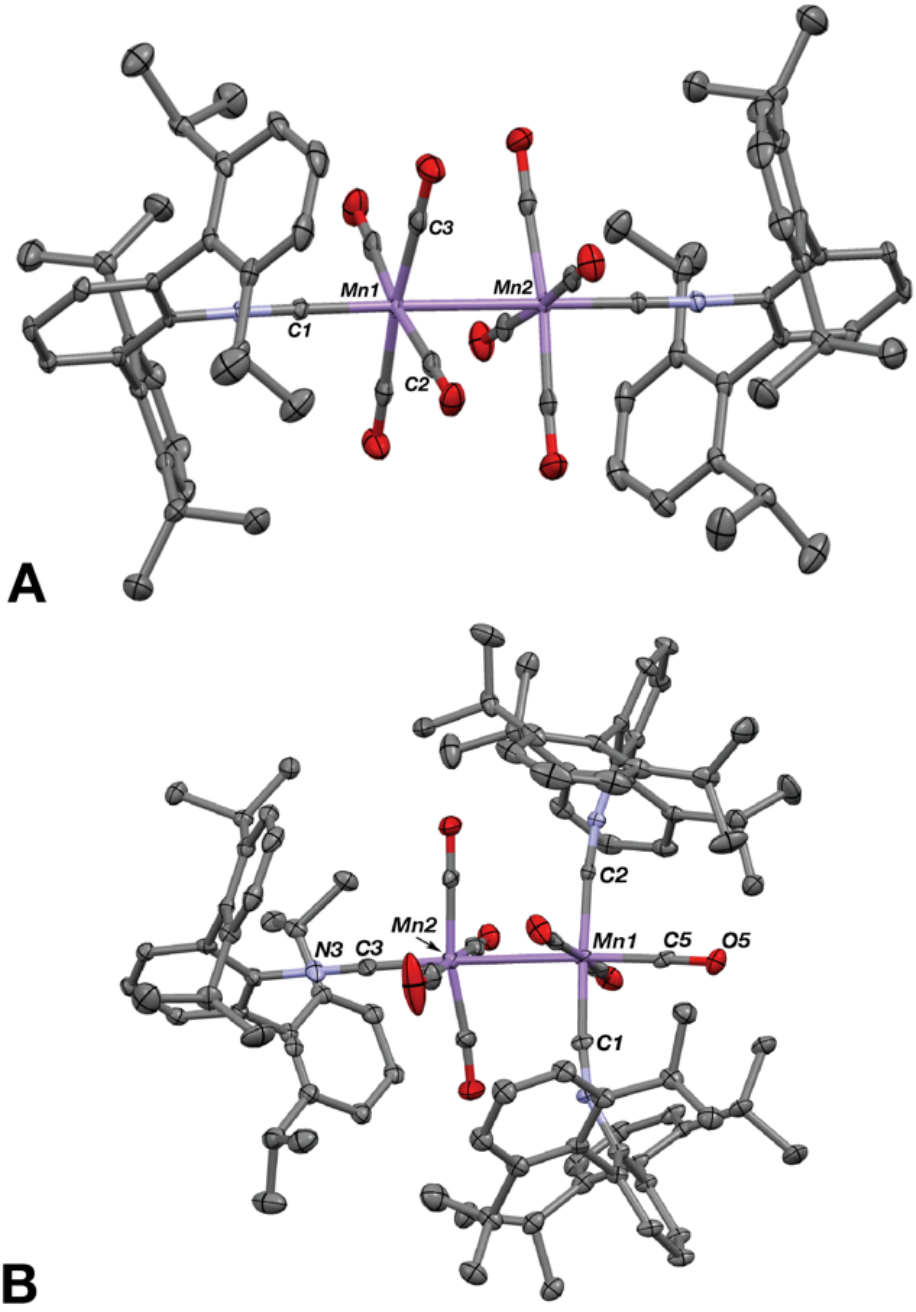

Figure 3.9. Solid state structures of $Mn_2(CO)_8(CNAr^{Dipp2})_2$ (**8**, A) and $Mn_2(CO)_7(CNAr^{Dipp2})_3$ (**7**, B) at 100K. Selected bond distances (Å) and angles (º): (A) Mn1-Mn1 = 2.9065(8); C1-N1 = 1.164(3); C4-O4 = 1.147(3); C1-Mn1-Mn1 = 178.71(9); C2-Mn1-C1 = 87.20(9). (B) Mn1-Mn2 = 2.999(5); C1-N1 = 1.169(9); C5-O5 = 1.149(9); C1-Mn1-Mn2 = 91.5(2); C1-Mn1-C5 = 90.5(3).

Stoichiometric addition of CO_2 to $Na[Mn(CO)_3(CNAr^{Dipp2})_2]$ in THF produces a light orange solution with a green precipitate over five minutes. Analysis of the product mixture showed the formation of the zerovalent complex **5**, as well as the dimeric products $Mn_2(CO)_7(CNAr^{Dipp2})_3$ (**7**) and $Mn_2(CO)_8(CNAr^{Dipp2})_2$ (**8**) (Figure 3.9). Notably, the free isocyanide, $CNAr^{Dipp2}$, and unreacted $Na[Mn(CO)_3(CNAr^{Dipp2})_2]$ were also observed in the reaction mixture, suggesting that the reactivity of CO_2 with $Na[Mn(CO)_3(CNAr^{Dipp2})_2]$ is not a straightforward process. Accordingly, we examined the reactivity of $Na[Mn(CO)_3(CNAr^{Dipp2})_2]$ with isotopically-labeled $^{13}CO_2$ to delineate the products formed from CO_2, as shown in Figure 3.10. Addition of a 10-fold excess of $^{13}CO_2$ led to the complete consumption of $Na[Mn(CO)_3(CNAr^{Dipp2})_2]$ and revealed ^{13}CO incorporation into the dimeric manganese species **7** and **8** with concomitant formation of $Na_2[^{13}CO_3]$, as established by a single $^{13}C\{^1H\}$ NMR resonance at δ = 168.3 ppm (D_2O) (Figure 3.11).[55] Importantly, no oxalate or formate was observed in the product mixture, suggesting an inner-sphere reductive disproportionation of CO_2 via a metallocarboxylate intermediate, which is similar to the reactivity of other carbonyl metallates with CO_2.[56-58]

Based upon the above evidence, we propose a mechanism (Scheme 3.2) in which two equivalents of $Na[Mn(CO)_3(CNAr^{Dipp2})_2]$ are necessary to effect the reductive disproportionation of CO_2. Addition of CO_2 to $Na[Mn(CO)_3(CNAr^{Dipp2})_2]$ forms the intermediate metallocarboxylate $Na[Mn(CO_2)(CO)_3(CNAr^{Dipp2})_2]$, which attacks a second equivalent of CO_2 to form a coordinated $-CO(O)CO_2$ ligand.[59] This species then decomposes to the tetracarbonyl complex $[Mn(CO)_4(CNAr^{Dipp2})_2]^+$

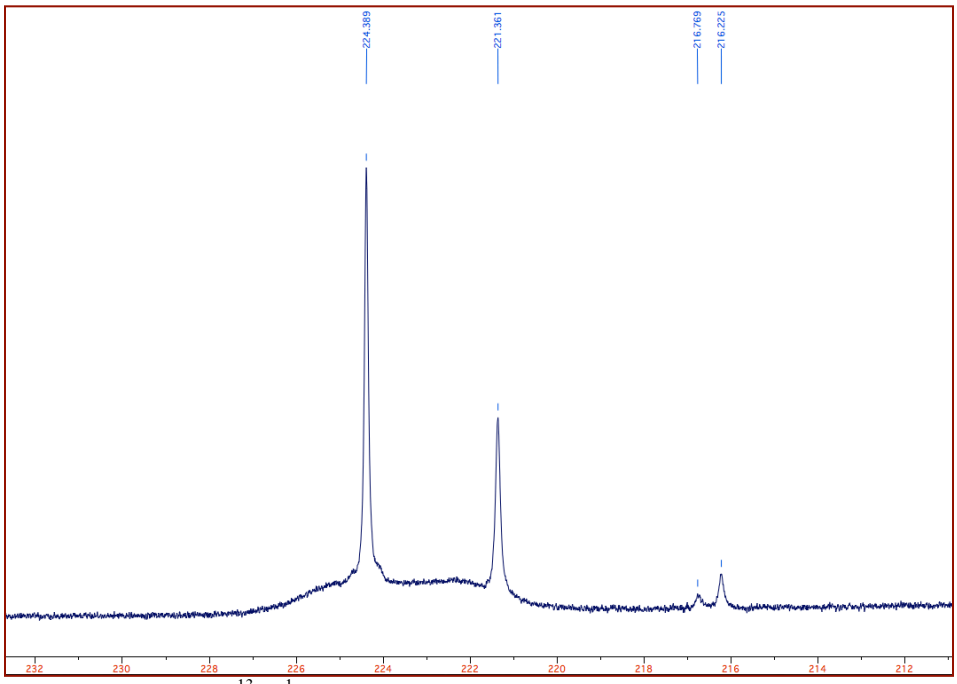

Figure 3.10. Inset view of $^{13}C\{^{1}H\}$ NMR spectrum in C_6D_6 of product mixture isolated from the addition of $^{13}CO_2$ to $Na[Mn(CO)_3(CNAr^{Dipp2})_2]$.

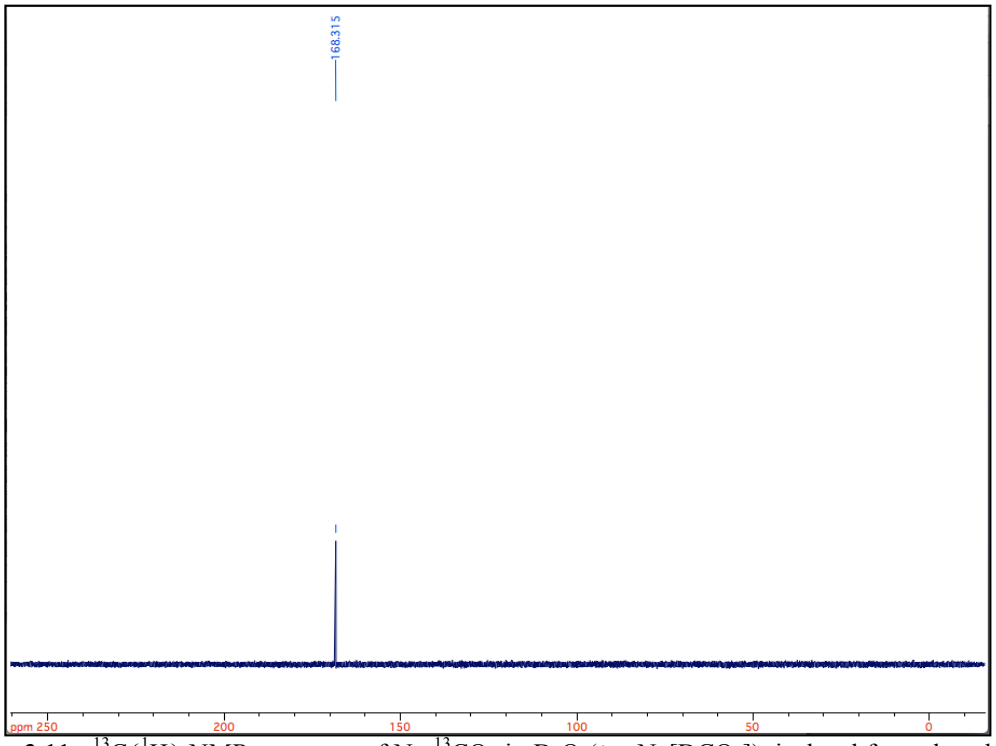

Figure 3.11. $^{13}C\{^{1}H\}$ NMR spectrum of $Na_2{}^{13}CO_3$ in D_2O (*i.e.* $Na[DCO_3]$), isolated from the addition of $^{13}CO_2$ to $Na[Mn(CO)_3(CNAr^{Dipp2})_2]$.

and $[CO_3]^{2-}$ in a manner similar to that proposed for CO_2 reductive disproportionation by homoleptic carbonyl metallates.[57,58] While $[Mn(CO)_4(CNAr^{Dipp2})_2]^+$ is expected to be stable in solution, in the presence of additional equivalents of $Na[Mn(CO)_3(CNAr^{Dipp2})_2]$ (or a negative potential in an electrochemical cell) it is likely reduced to form the zerovalent species **5** with concomitant release of CO. Most importantly, independent treatment of zerovalent **5** with CO leads rapidly to a mixture of the dimeric complexes $Mn_2(CO)_7(CNAr^{Dipp2})_3$ (**7**) and $Mn_2(CO)_8(CNAr^{Dipp2})_2$ (**8**), as well as free $CNAr^{Dipp2}$.[59] This CO-induced ligand redistribution/dimerization sequence is analogous to the classic syntheses of mixed carbonyl/phosphine Mn_2L_{10} dimers upon photolysis of $Mn_2(CO)_{10}$ in the presence of aryl and alkyl phosphines.[61,62] Accordingly, based upon this result, it is reasonable to suggest that the free CO generated in the course of CO_2 reductive disproportionation is rapidly trapped by monoradical $Mn(CO)_3(CNAr^{Dipp2})_2$ and therefore not detected in measurable quantities by headspace analysis experiments. In addition, this proposed mechanistic sequence suggests that initial formation of the metallocarboxylate species, $Na[Mn(CO_2)(CO)_3(CNAr^{Dipp2})_2]$, is slow relative to a second CO_2 addition, comproportionative electron transfer and CO trapping by the monoradical $Mn(CO)_3(CNAr^{Dipp2})_2$.

We postulate that the observed current increase of **2** under CO_2 versus that of **4** is derived primarily from the significantly larger reduction potential necessary to generate anionic **6** from the halide complexes **1**-**3**. Furthermore, the chemical reactivity of $Na[Mn(CO)_3(CNAr^{Dipp2})_2]$ with CO_2 clearly illustrates this process is not

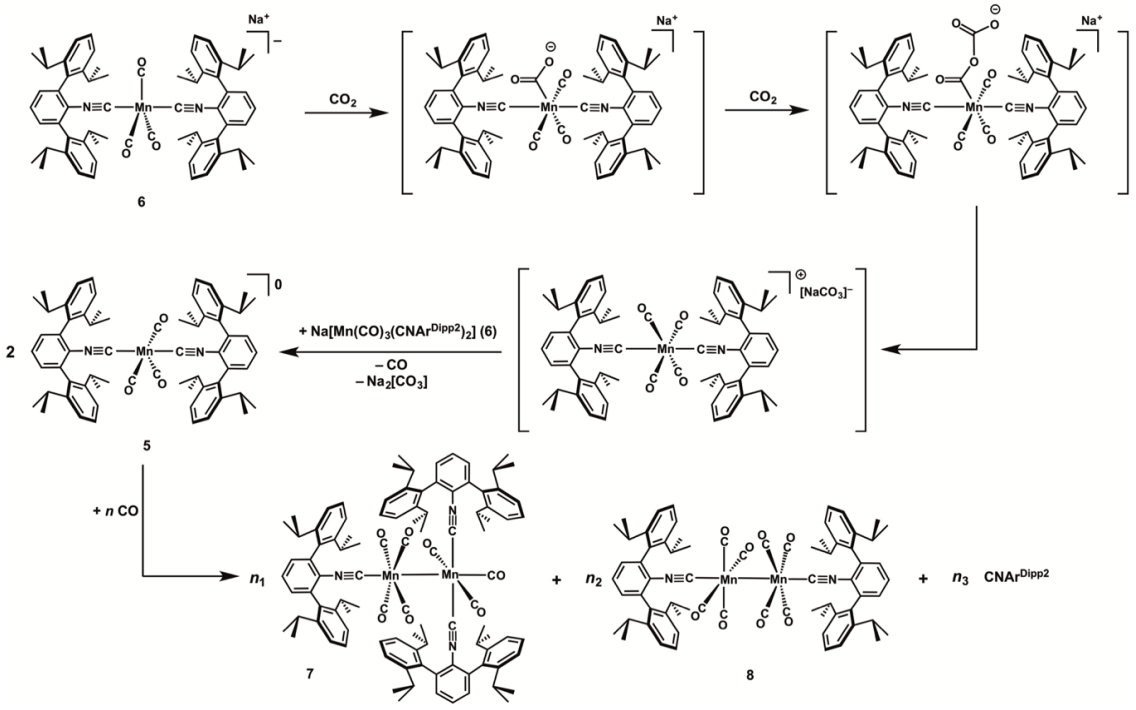

Scheme 3.2. Proposed mechanism for CO_2 reductive disproportionation by $Na[Mn(CO)_3(CNAr^{Dipp2})_2]$ to afford the observed products $Mn_2(CO)_7(CNAr^{Dipp2})_3$ (7), $Mn_2(CO)_8(CNAr^{Dipp2})_2$ (8), $CNAr^{Dipp2}$, and Na_2CO_3.therefore not detected in measurable quantities by headspace analysis experiments. In addition, this proposed mechanistic sequence suggests that initial formation of the metallocarboxylate species, $Na[Mn(CO_2)(CO)_3(CNAr^{Dipp2})_2]$, is slow relative to a second CO_2 addition, comproportionative electron transfer and CO trapping by the monoradical $Mn(CO)_3(CNAr^{Dipp2})_2$.

catalytic, given the range of redistribution products found. Surprisingly, reports of the reactivity of homoleptic carbonyl manganates with CO_2 are sparse,[63] making comparison to other manganese systems with π-acidic ligand fields and redox-innocent ligands difficult. However, the presence of zerovalent **5** and the dimeric complexes $Mn_2(CO)_7(CNAr^{Dipp2})_3$ (**7**) and $Mn_2(CO)_8(CNAr^{Dipp2})_2$ (**8**) indicate an operative reductive disproportionation mechanism and illustrates the dichotomous reactivity between this isocyanide system and the bipyridine-containing $XM(CO)_3(bpy)$ Group 7 metal complexes.[64]

Finally, in consideration of the currently held mechanism of CO_2 reduction by manganese-based electrocatalysts,[65] the reactivity of $XMn(CO)_3(CNAr^{Dipp2})$ and CO_2 in the presence of H^+ donors was examined. Notably, attempts at reducing CO_2 with $BrMn(CO)_3(CNAr^{Dipp2})$ under electrochemical conditions in the presence of H_2O or other weak Brønsted acids resulted in the exclusive formation of $HMn(CO)_3(CNAr^{Dipp2})_2$, which is unreactive towards CO_2. Similar results were found in attempts to chemically reduce CO_2 with $Na[Mn(CO)_3(CNAr^{Dipp2})_2]$ with an added H^+ source. These findings again highlight the unique electronic and/or structural features of manganese bipyridine catalysts, which enable resistance to metal-based protonation under electrochemical conditions.[64]

Section 3.4 Concluding Remarks

We have evaluated the electrochemistry of the well-defined manganese mixed carbonyl/isocyanide species $[Mn(CO)_3(CNAr^{Dipp2})_2]^n$ (n = –1, 0, +1) in THF under N_2 and CO_2. A striking dependence on the donor character of the apical ligand X in $XMn(CO)_3(CNAr^{Dipp2})_2$ has been shown to sizably affect the potential necessary for the initial reduction of Mn(I) to Mn(0) as well as to significantly alter the redox behavior of the system. Moving to more strongly s-donating ligands has a significant influence on the potential necessary for the first reduction, such that the redox behavior shifts from two sequential one-electron reductions to an observed single two-electron reduction. While the redox behavior of **1**-**4** is no doubt derived in part from the high Lewis acidity of manganese due to the π-acidic ligand field provided by the mixed

carbonyl/isocyanide system, the sensitivity observed here should provide guidance towards the engineering of manganese-based electrocatalysts with low operating potentials, especially those that feature the steric encumbrance necessary to prevent Mn-Mn single bond formation.

Reactivity studies of $Na[Mn(CO)_3(CNAr^{Dipp2})_2]$ with CO_2 reveal that reductive disproportionation to CO and $[CO_3]^{2-}$ is the operative mechanism of CO_2 reduction by isocyanide/carbonyl-supported manganates. The stability of zerovalent **5** enables the trapping of liberated CO and formation of the dimeric products $Mn_2(CO)_7(CNAr^{Dipp2})_3$ and $Mn_2(CO)_8(CNAr^{Dipp2})_2$. Importantly, these results suggest that the intermediate metallocarboxylate $Na[Mn(CO_2)(CO)_3(CNAr^{Dipp2})_2]$ can likely act as an effective nucleophile for a second equivalent of CO_2.[65] This divergence from the reactivity observed for $XMn(CO)_3$bpy catalysts emphasizes the need for further study of the reaction dynamics following CO_2 addition in Group 7 metal and related catalyst systems as a function of ancillary ligand properties and environment.[66]

3.5 Synthetic Procedures and Characterization Data

General Considerations. All manipulations were performed under an atmosphere of dry dinitrogen using standard Schlenk and glovebox techniques, unless otherwise stated. Solvents were dried and degassed according to standard procedures. Reagent grade starting materials were purchased from commercial sources and used without further purification, unless otherwise stated. The isocyanide ligand $CNAr^{Dipp2}$ was prepared according to literature procedure.[2]

The compounds $[Mn(CO)_3(CNAr^{Dipp2})_2]^0$, $Na[Mn(CO)_3(CNAr^{Dipp2})_2]$, $ClMn(CO)_3(CNAr^{Dipp2})_2$, $BrMn(CO)_3(CNAr^{Dipp2})_2$, and $[Mn(CO)_3(CNAr^{Dipp2})_2]OTf$ have been previously reported.[19, 20] Benzene-d_6 (Cambridge Isotope Laboratories) was stirred over NaK for two days, distilled, degassed, and stored over 4 Å molecular sieves. Bone dry CO_2 was purchased from Praxair and passed through a Drierite column prior to use. UHP-grade CO gas was purchased from Praxair and used as received. Tetrabutylammonium hexafluorophosphate ($TBAPF_6$, Aldrich, 98%) was twice recrystallized from methanol and dried under vacuum at 90°C overnight before use.

Solution ^1H and $^{13}C\{^1H\}$ NMR were recorded on a Varian X-Sens 500 spectrometer. ^1H and $^{13}C\{^1H\}$ NMR chemical shifts are reported in ppm relative to $SiMe_4$ (^1H and ^{13}C $\delta = 0.0$ ppm) with reference to residual proton resonances of 7.16 ppm (^1H) and 128.06 ppm (^{13}C) for benzene-d_6. Room temperature FTIR spectra of the isolated compounds were recorded on a Thermo-Nicolet iS10 FTIR spectrometer. Samples were prepared either as benzene-d_6 or THF solutions injected into a ThermoFisher solution cell equipped with KBr windows. Solvent peaks were digitally subtracted from all solution FTIR spectra using a previously recorded spectrum of the solvent. Electrochemical conditions are detailed in Section S3. Combustion analyses were performed by Midwest Microlabs of Indianapolis, IN (USA).

Synthesis of $IMn(CO)_3(CNAr^{Dipp2})_2$ (3). To a THF solution of $BrMn(CO)_3(CNAr^{Dipp2})_2$ (**2**, 0.038 g, 0.036 mmol, 5 ml) was added an excess of anhydrous KI. The mixture was stirred for 3 days, after which it was filtered through

filter pipette packed with Celite. The solvent was removed under reduced pressure to provide a yellow solid, which was dissolved in C_6H_6 and filtered through a fiberglass pipette packed with Celite. The volatiles were removed under reduced pressure to provide a light yellow solid (0.039 g, 97%). ^{1}H NMR (500.1 MHz, C_6D_6, 20 ºC) δ = 7.39 (t, 2H, *J* = 8 Hz, p-Ar), 7.20 (d, 4H, *J* = 8 Hz, m-Ar), 6.89 (m, 8H, m-Dipp), 6.81 (dd, 4H, *J* = 8, 7 Hz, p-Dipp), 2.64 (sept, 8H, *J* = 7 Hz, C*H*$(CH_3)_2$), 1.40 (d, 24H, *J* = 7 Hz, CH(*CH*$_3)_2$), 1.02 (d, 24H, *J* = 7 Hz, CH(C*H*$_3)_2$) ppm. ^{13}C{^{1}H} NMR (125.7 MHz, C_6D_6, 20 ºC) δ = 220.1 (*C*O), 210.5 (*C*O), 170.3 (*C*N), 146.4, 139.6, 134.4, 129.9, 129.7, 128.5, 123.6 31.4(C*H*$(CH_3)_2$), 24.7 (CH(C*H*$_3)_2$), 24.3 (CH(C*H*$_3)_2$) ppm. FTIR (C_6D_6, KBr windows): ν_{CN} = 2118 cm^{-1} (vs), ν_{CO} = 2015 cm^{-1} (vs), 2008 cm^{-1} (sh), 1942 cm^{-1} (s), also 2962, 2927, 2868, 1462, 755, 647, 630 cm^{-1}. Anal. Calcd for $C_{65}H_{74}IMnN_2O_3$: C, 70.13; H, 6.70; N, 2.52. Found C, 69.97; H, 6.80; N, 2.57.

Synthesis of $Mn_2(CO)_7(CNAr^{Dipp2})_3$ (7). $Mn_2(CO)_7(CNAr^{Dipp2})_3$ is recovered from the preparation of $Mn(CO)_3(CNAr^{Dipp2})_2$ via photolysis (Section S1.3); the red/orange pentane washings are concentrated, filtered, and stored overnight at –40 ºC to provide a mixture of red and orange crystals. The red crystals are manually isolated to provide $Mn_2(CO)_7(CNAr^{Dipp2})_3$ (**7**). ^{1}H NMR (500.1 MHz, C_6D_6, 20 ºC) δ = 7.40 (d, 2H, *J* = 8 Hz, m-Ar[a]), 7.37 (d, 4H, *J* = 8 Hz, m-Dipp), 7.30 (d, 8H, *J* = 8 Hz, m-Dipp), 7.25 (d, 4H, *J* = 8.5 Hz, m-Ar), 7.20 (dd, 1H, *J* = 8, 1.5 Hz, p-Ar), 7.07 (d, 4H, *J* = 8 Hz, p-Dipp), 6.98 (2H, *J* = 8 Hz, p-Ar), 6.89 (m, 2H, p-Dipp), 2.76 (sept, 8H, *J* = 7 Hz, C*H*(CH3)2), 2.66 (sept, 4H, *J* = 7 Hz, C*H*$(CH_3)_2$), 1.43 (d, 24 H, *J* = 7 Hz, CH(*CH3*)2), 1.30 (d, 12H, *J* = 7 Hz, CH(*CH3*)2), 1.16 (d, 12H, J = 7 Hz, CH(*CH3*)2),

1.01 (d, 24H, J = 7 Hz, CH(*CH3*)2) ppm. $^{13}C\{^{1}H\}$ NMR (125.7 MHz, C_6D_6, 20 ºC) δ = 224.4, 184.3, 169.2, 146.28, 146.17, 138.9, 137.8, 135.3, 135.2, 131.3, 129.5, 129.4, 129.35, 129.1, 129.0, 125.9, 123.4, 123.35, 31.4 (*C*H(CH_3)[a]), 31.1 (*C*H(CH_3)[a]), 25.7 (CH(*C*H_3)), 24.6 (CH(*C*H_3)[a]), 24.4 (CH(*C*H_3)[a]), 23.7 (CH(*C*H_3)) ppm. FTIR (C_6D_6, KBr windows, 20 ºC): $\nu_{CN/CO}$ = 2077 cm^{-1} (s), 2049 cm^{-1} (s), 2013 cm^{-1} (w), 1976 cm^{-1} (vs), 1953 cm^{-1} (m), 1927 cm^{-1} (w), also 2962, 2925, 1746, 1576, 1457, 1221, 1303 cm^{-1}. Despite multiple attempts a satisfactory elemental analysis could not be obtained.

Synthesis of $Mn_2(CO)_8(CNAr^{Dipp2})_2$ (8). To a 350 mL resealable ampoule was added a 7 mL *n*-hexane slurry of $Mn_2(CO)_{10}$ (0.102 g, 0.260 mmol), $CNAr^{Dipp2}$ (0.226 g, 0.533 mmol, 2.05 eq.), and a magnetic stirbar. The vessel was brought out of the glovebox, and the mixture was subjected to 4 freeze/pump/thaw cycles. The mixture was then irradiated for 5 minutes, after it was again subjected to freeze/pump/thaw cycles to remove liberated CO. This process was repeated 4 additional times, during which time the slurry became a clear orange solution. The ampoule was returned to the glovebox, and the solution was concentrated to ~ 2 mL and filtered through a fiberglass plug. All volatiles were then removed under reduced pressure, providing a light orange solid. Storage of a concentrated Et_2O solution at -35 ºC for 3 days produced large yellow needle crystals of the product, which were subsequently collected and dried. Yield: 0.231 g, 0.187 mmol, 72 %. ^{1}H NMR (300.1 MHz, C_6D_6, 20 ºC) δ = 7.40 (dd, 2H, *J* = 8, 1 Hz, p-Ar), 7.14 (d, 4H, *J* = 8 Hz, m-Ar), 6.93 (m, 8H, m-Dipp), 6.87 (dd, 4H, *J* = 8.5, 6.5 Hz, p-Dipp), 2.67 (sept, 8H, *J* = 7 Hz, C*H*(CH3)2),

1.28 (d, 24H, *J* = 7 Hz, CH(*CH3*)2), 1.05 (d, 24H, *J* = 7 Hz, CH(C*H*3)2) ppm. $^{13}C\{^{1}H\}$ NMR (125.7 MHz, C_6D_6, 20 ºC) δ = 223 (br s, *C*O), 146.4, 139.2, 134.7, 129.7, 129.4, 128.3, 123.5, 31.35 (*C*H(CH_3)), 24.5 (CH(*C*H_3)) 24.1 (CH(*C*H_3)) ppm. (Prolonged scanning failed to reveal a peak resulting from *C*NAr^{Dipp2}). FTIR (C_6D_6, KBr windows, 20 ºC): $\nu_{CN/CO}$ = 2130 cm^{-1} (w sh), 2094 cm^{-1} (s), 2039 cm^{-1} (m), 1977 cm^{-1} (vs), 1947 cm^{-1} (m sh), 1939 cm^{-1} (m sh), also 1459, 1416, 1363, 756, and 644 cm^{-1}. Anal. Calcd for $C_{70}H_{74}MnN_2O_8$: C, 71.18; H, 6.31;N, 2.37. Found C, 71.48; H, 6.46;, N, 2.34.

Preparation of [Mn(THF)(CO)$_3$(CNAr^{Dipp2})$_2$]OTF (4) in solution. The solvated cation **4** can be readily prepared by treating a C_6D_6 solution of Mn(OTf)(CO)$_3$(CNAr^{Dipp2})$_2$ (0.015 g, 0.013 mmol, 2 ml) with neat THF (1.2 μL, 0.015 mmol, 1.2 equiv.). ^{1}H NMR (500.1 MHz, C_6D_6, 20 ºC) δ = 7.40 (t, 2H, J = 8 Hz, p-Ar), 7.21 (d, 4H, J = 8 Hz, m-Ar), 6.93 (m, 8H, m-Dipp), 6.85 (dd, 4H, J = 8.5, 6.5 Hz, p-Dipp), 3.58 (br s, THF-C*H*$_2$), 2.65 (sept, 8H, J = 7 Hz, C*H*(CH_3)$_2$), 1.41 (br s, THF-C*H*$_2$), 1.35 (d, 24H, J = 7 Hz, CH(*CH*$_3$)$_2$), 1.00 (d, 24H, J = 7 Hz, CH(C*H*$_3$)$_2$) ppm. $^{13}C\{^{1}H\}$ NMR (125.7 MHz, C_6D_6, 20 ºC) δ = 218.7 (*C*O), 206.8 (*C*O), 168.4 (*C*NR), 146.8, 140.0, 134.2, 130.4, 129.9, 123.6, 67.8 (THF- *C*H$_2$) 31.4 (*C*H(CH_3)), 25.8 (THF-*C*H$_{2)}$, 25.0 (CH(*C*H_3)), 23.9 (CH(*C*H_3)) ppm. FTIR (C_6D_6, KBr windows): ν_{CN} = 2131 cm^{-1} (vs), 2090 cm^{-1} (w), ν_{CO} = 2032 cm^{-1} (vs), 1955 cm^{-1} (s), also 2963, 2926, 2867, 1459, 1233, 1203, 1178, 1010, 757, 637 cm^{-1}. Multiple attempts to acquire a satisfactory combustion analysis routinely provided data corresponding to

$Mn(OTf)(CO)_3(CNAr^{Dipp2})_2$, which we attribute to the lability of the bound THF under vacuum.

General Procedure for Addition of CO_2 to $Na[Mn(CO)_3(CNAr^{Dipp2})_2]$ (6). The anionic species $Na[Mn(CO)_3(CNAr^{Dipp2})_2]$ was prepared in a similar manner as described previously[2]; briefly, a THF solution of $BrMn(CO)_3(CNAr^{Dipp2})_2$ was stirred with Na/Hg amalgam (3.5 equivalents, 0.05%) for 2 hours and filtered, producing a deep purple solution. The solvent was removed *en vacuo* and the resulting solid dissolved in Et_2O, forming a red solution. The solution was transferred to an ampoule with a resealable Teflon screwcap, and the solution was degassed by three freeze/pump/thaw cycles. CO_2 was added via syringe to the frozen solution and the solution was allowed to warm to room temperature while stirring. The ampoule was returned to the glovebox, and all volatiles were removed under reduced pressure, providing a green/yellow solid. Examination of products by ^1H NMR revealed the formation of $[Mn(CO)_3(CNAr^{Dipp2})_2]^0$, $HMn(CO)_3(CNAr^{Dipp2})_2$, $Mn_2(CO)_7(CNAr^{Dipp2})_3$, $Mn_2(CO)_8(CNAr^{Dipp2})_2$, and free $CNAr^{Dipp2}$.

Addition of $^{13}CO_2$ to $Na[Mn(CO)_3(CNAr^{Dipp2})_2]$. To a degassed, frozen C_6D_6 solution of $Na[Mn(CO)_3(CNAr^{Dipp2})_2$ in a J. Young NMR tube was added 10 equivalents of $^{13}CO_2$ via syringe. The solution was allowed to thaw and was shaken vigorously for 10 minutes, changing the color of the solution from cherry red to light orange, and a clear precipitate emerged from the solution. Analysis of the solution by ^1H NMR demonstrated the same product mixture as in S1.2 and a large amount of

unreacted $^{13}CO_2$. $^{13}C\{^1H\}$ NMR spectroscopy revealed the incorporation of ^{13}CO into the diamagnetic products $Mn_2(CO)_7(CNAr^{Dipp2})_3$ (**7**) (δ_{CO} = 224.4 ppm) and $Mn_2(CO)_8(CNAr^{Dipp2})_2$ (**8**) (δ_{CO} = 221.4 ppm). The precipitate was dissolved into D_2O under an atmosphere of N_2, and a ^{13}C NMR spectrum revealed a singlet centered at 168.3 ppm. A reference spectrum of Na_2CO_3 in D_2O identified the carbonate resonance at δ = 168.1 ppm.

Dimerization of Zerovalent Manganese Under Additional Equivalents of CO. A C_6D_6 solution of $Mn(CO)_3(CNAr^{Dipp2})_2$ (0.019 g, 0.193 mmol) in J. Young NMR Tube was frozen and the headspace removed under dynamic vacuum. CO(1.5 equiv) was then added via syringe and the solution was allowed to thaw. Examination by ^1H and $^{13}C\{^1H\}$ NMR spectroscopy, and solution FT-IR spectroscopy, demonstrated the formation of $Mn_2(CO)_8(CNAr^{Dipp2})_2$, $Mn_2(CO)_7(CNAr^{Dipp2})_3$, free $CNAr^{Dipp2}$, as well as unreacted $Mn(CO)_3(CNAr^{Dipp2})_2$.

3.6 Representative Solution IR Spectra

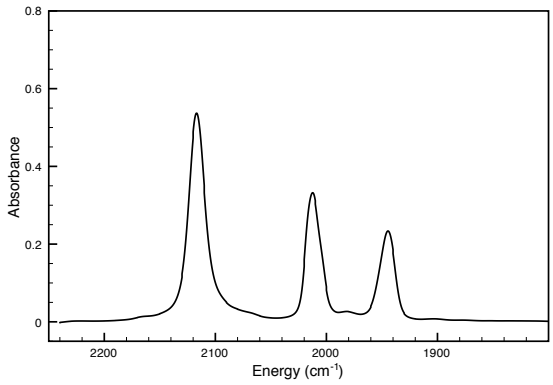

Figure 3.12. Infrared spectrum of $BrMn(CO)_3(CNAr^{Dipp2})_2$ (**2**) in C_6D_6.

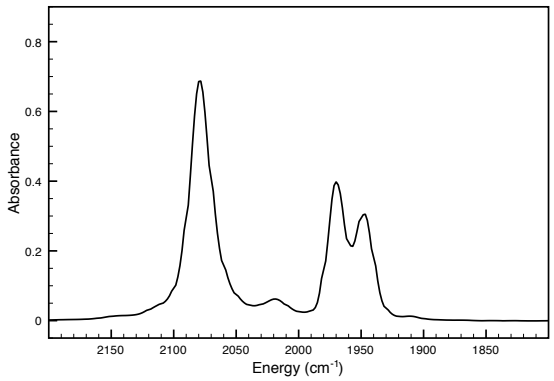

Figure 3.13. Infrared spectrum of $HMn(CO)_3(CNAr^{Dipp2})_2$ in THF.

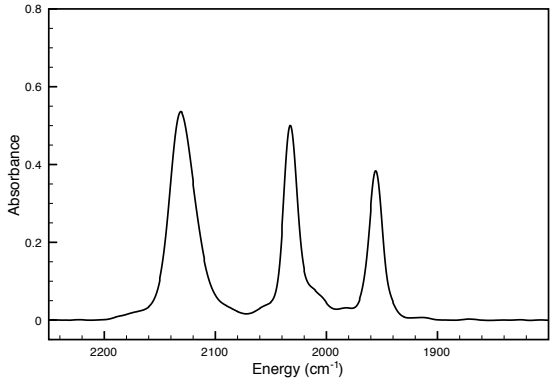

Figure 3.14. Infrared spectrum of $[Mn(CO)_3(CNAr^{Dipp2})_2]OTf$ (**4**) in THF.

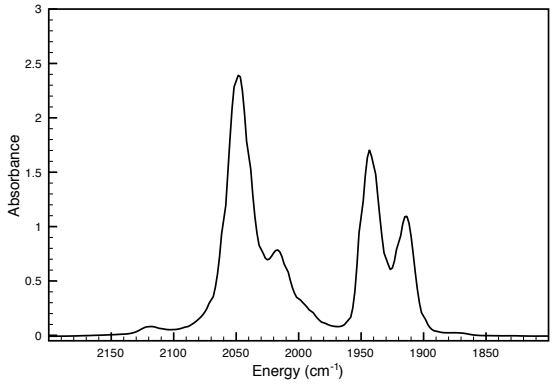

Figure 3.15. Infrared spectrum of $[Mn(CO)_3(CNAr^{Dipp2})_2]^0$ (**5**) in C_6D_6.

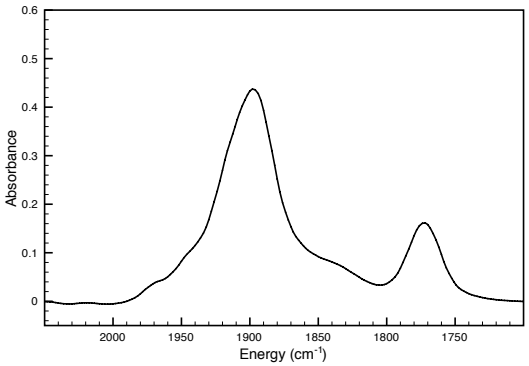

Figure 3.16. Infrared spectrum of $Na[Mn(CO)_3(CNAr^{Dipp2})_2]$ (**6**) in THF.

3.7 Experimental Design of Electrochemical Measurements.

General. Electrochemical samples were prepared in a glovebox under dry dinitrogen. Electrochemical experiments were performed using a BASi Epsilon potentiostat. A single-compartment cell was used for all cyclic voltammetry experiments with a glassy carbon working electrode (3 mm in diameter from BASi), a Pt wire counter electrode (flame annealed with a butane torch before use), and a Ag/AgCl pseudo-reference (separated from the bulk solution by a Vycor tip).[i] All electrochemical experiments were performed with 0.1 M tetrabutylammonium hexafluorophosphate ($TBAPF_6$) as the supporting electrolyte with ferrocene (Fc) added as an internal reference. Mn complex concentrations ranged from 0.25−2.0 mM in THF. All potentials were referenced vs Fc^+/Fc. For experiments under CO_2, electrochemical solutions were sparged with " bone dry" CO_2, which was run through a custom Drierite/activated 3Å molecular sieves drying column before use. These experiments under CO_2 were performed at gas saturation.

Infrared Spectroelectrochemistry (IR-SEC). The design of the IR spectroelectrochemical cell used for these studies has been reported previously.[67] For these experiments, a 4.5 mm glassy carbon disk working electrode, a Pt counter electrode, and an Ag pseudo-reference were used. All spectroelectrochemical experiments were carried out in a 0.1 M $TBAPF_6$ solution in THF, and all solutions were prepared in a glovebox under dry dinitrogen. Blank THF solutions with 0.1 M $TBAPF_6$ were used for FTIR solvent subtractions. A Gamry Reference 600 series three-electrode potentiostat was used to effect and monitor thin layer bulk electrolysis.

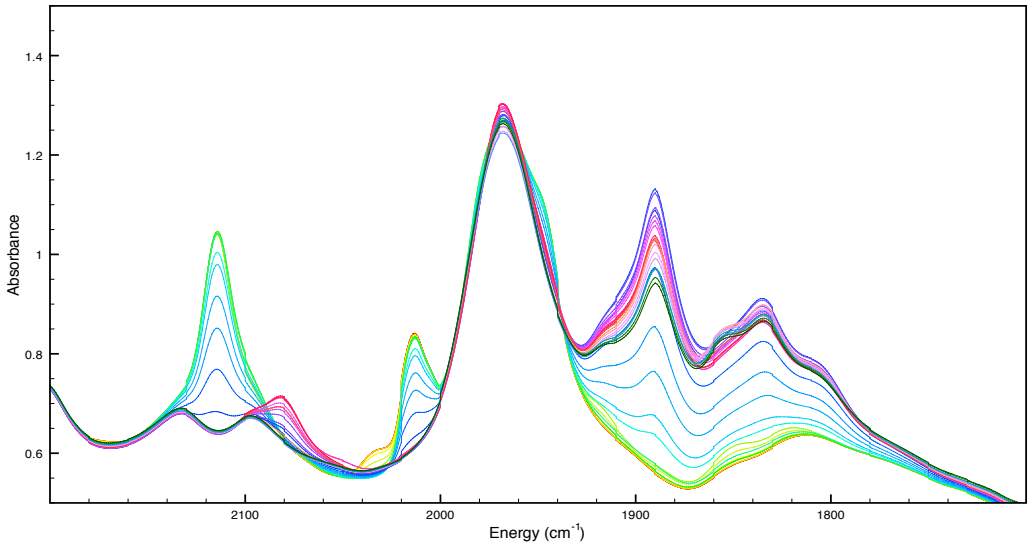

Figure 3.17. IR-SEC data for $BrMn(CO)_3(CNAr^{Dipp2})_2$ (**2**) without solvent subtraction. The green line represents the IR spectrum at no potential, and the purple line represents the IR spectrum at the final potential of –3.00 V.

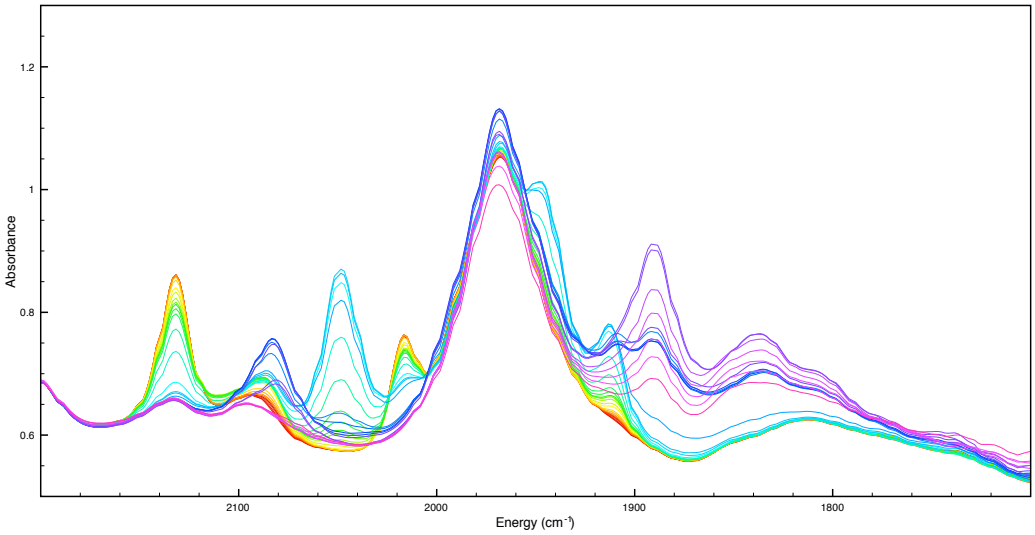

Figure 3.18. IR-SEC data for $[Mn(CO)_3(CNAr^{Dipp2})_2]OTf$ (**4**) without solvent subtraction. The orange line represents the IR spectrum at no potential, the light blue line represents the IR spectrum at –1.00 V, and the violet line represents the IR spectrum at the final potential of –4.00 V.

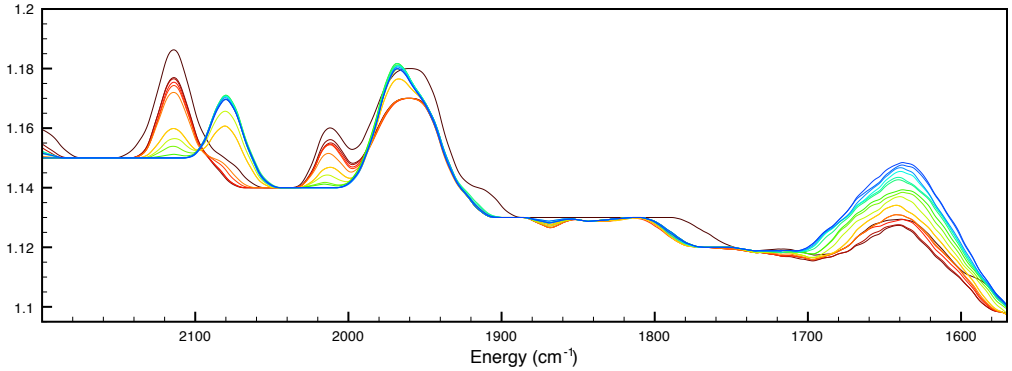

Figure 3.19. Raw IR-SEC data for $BrMn(CO)_3(CNAr^{Dipp2})_2$ (**2**) in $^{13}CO_2$-sparged THF without solvent subtraction or baseline normalization.

3.8 Crystallographic Structure Determinations.

General. Single crystal X-ray structure determinations were performed at low temperature on Bruker Kappa Diffractometers equipped with a Mo Kα radiation source and a Bruker APEX or APEX-II area detector. All structures were solved *via* direct methods with SIR 2004[68] and refined by full-matrix least-squares procedures

using SHELXL-2013[69] Crystallographic data collection and refinement information listed in Table 3.1. $Mn_2(CO)_7(CNAr^{Dipp2})_3$ possesses positional disorder of a $CNAr^{Dipp2}$ ligand and 4 CO ligands, and was modeled and fully refined.

Table 3.1 Crystallographic Data Collection and Refinement Information

Name	$Mn_2(CO)_8(CNAr^{Dipp2})_2 \cdot (Et_2O)$	$Mn_2(CO)_7(CNAr^{Dipp2})_3$	$IMn(CO)_3(CNAr^{Dipp2})_2 \cdot 2$ (THF)
Formula	$C_{78}H_{94}Mn_2N_2O_{10}$	$C_{100}H_{111}Mn_2N_3O_7$	$C_{73}H_{90}IMnN_2O_5$
Crystal System	Orthorhombic	Monoclinic	Monoclinic
Space Group	*Pccn*	$P2_1/c$	$P2_1/c$
a, Å	17.3739(16)	25.964(3)	16.7392(14)
b, Å	25.063(3)	11.7576(13)	17.0282(14)
c, Å	17.1374(17)	29.248(4)	24.298(2)
α, deg	90	90	90
β, deg	90	90.045(3)	102.184(3)
γ, deg	90	90	90
V, $Å^3$	7462.4(14)	8928.7(19)	6770.0(10)
Z	4	4	4
Radiation (λ, Å)	Mo-K_α, 0.71073	Mo-K_α, 0.71073	Mo-K_α, 0.71073
ρ (calcd.), Mg/m^3	1.183	1.173	1.234
μ (Mo Ka), mm^{-1}	0.395	0.338	0.700
Temp, K	100	100	100
θ max, deg	25.354	25.465	25.410
data/parameters	6779/443	16396/1277	12422/761
R_1	0.0443	0.1298	0.0577
wR_2	0.0877	0.2854	0.1346
GOF	1.026	1.207	1.034

3.9 Acknowledgements

Chapter 3 is adapted from "Electrochemical Properties and CO_2-Reduction Ability of *m*-Terphenyl Isocyanide Supported Manganese Tricarbonyl Complexes" by Douglas W. Agnew, Matthew D. Sampson, Curtis E. Moore, Arnold L. Rheingold, Clifford P. Kubiak, and Joshua S. Figueroa, *Inorganic Chemistry* **2016** *55* (23), 12400-12408. Copyright 2016, American Chemical Society. Permission to include published material in this dissertation has been obtained from all coauthors. The dissertation author is the first author of this paper.

3.10 References

1. Bell, A.T. Basic Research Needs: Catalysis for Energy (PNNL-17214), U.S. Department of Energy, Report from a Workshop held in August 6–8, 2007, Bethesda, Maryland (US) (http://www.sc.doe.gov/bes/reports/list.html).

2. Appel, A. M.; Bercaw, J. E.; Bocarsly, A. B.; Dobbek, H.; DuBois, D. L.; Dupuis, M.; Ferry, J. G.; Fujita, E.; Hille, R.; Kenis, P. J. A.; Kerfeld, C. A.; Morris, R. H.; Peden, C. H. F.; Portis, A. R.; Ragsdale, S. W.; Rauchfuss, T. B.; Reek, J. N. H.; Seefeldt, L. C.; Thauer, R. K.; Waldrop, G. L. *Chem. Rev.* 2013, *113*, 6621.

3. Centi, G.; Perathoner, S. *Catalysis Today*. 2009, *143*, 191.

4. Costentin, C.; Robert, M.; Savéant, J.-M. *Chem. Soc. Rev.* 2013, *42*, 2423.

5. Benson, E. E.; Kubiak, C. P.; Sathrum, A. J.; Smieja, J. M. *Chem. Soc. Rev.* 2008, *38,* 89.

6. Bourrez, M.; Molton, F.; Chardon-Noblat, S.; Deronzier, A. *Angew. Chem. Int. Ed.* 2011, *50,* 9903.

7. Smieja, J. M.; Sampson, M. D.; Grice, K. A.; Benson, E. E.; Froehlich, J. D.; Kubiak, C. P. *Inorg. Chem.* 2013, *52*, 2484.

8. Sampson, M. D.; Nguyen, A. D.; Grice, K. A.; Moore, C. E.; Rheingold, A. L.; Kubiak, C. P. *J. Am. Chem. Soc.* 2014, *136,* 5460.

9. Grice, K. A.; Kubiak, C. P. Chapter Five - Recent Studies of Rhenium and Manganese Bipyridine Carbonyl Catalysts for the Electrochemical Reduction of CO_2. In *Advances in Inorganic Chemistry*; Michele, A., Rudi van, E., Eds.; Academic Press, 2014; Vol 66, 163.

10. Agarwal, J.; Shaw, T. W.; Henry F Schaefer, I.; Bocarsly, A. B. *Inorganic Chemistry*. 2015, *54,* 5285.

11. Franco, F.; Cometto, C.; Ferrero Vallana, F.; Sordello, F.; Priola, E.; Minero, C.; Nervi, C.; Gobetto, R. *Chem. Commun*. 2014, *50,* 14670.

12. Benson, E. E.; Sampson, M. D.; Grice, K. A.; Smieja, J. M.; Froehlich, J. D.; Friebel, D.; Keith, J. A.; Carter, E. A.; Nilsson, A.; Kubiak, C. P. *Angew. Chem. Int. Ed.* 2013, *52*, 4841.

13). Scarborough, C. C.; Wieghardt, K. Electronic Structure of 2,2′-Bipyridine Organotransition-Metal Complexes. *Inorg. Chem*. 2011, *50,* 9773.

14. In addition to Mn-bipyridine complexes, related Mn-(α-diimine) complexes have also emerged as promising CO_2-reduction electrocatalysts.

15. Riplinger, C.; Sampson, M. D.; Ritzmann, A. M.; Kubiak, C. P.; Carter, E. A. *J. Am. Chem. Soc*. 2014, *136,* 16285–16298.

16. Scheiring, T.; Klein, A.; Kaim, W. *J. Chem. Soc., Perkin Trans. 2*. 1997, 2569.

17. Hughey, J. L., IV; Anderson, C. P.; Meyer, T. J. . *J. Organomet. Chem*. 1977, C49.

18. Hartl, F.; Rossenaar, B. D.; Stor, G. J.; Stufkens, D. J. *Rec. Trav. Chim. Pays-Bas*. 1995, *114,* 565.

19. Stewart, M. A.; Moore, C. E.; Ditri, T. B.; Labios, L. A.; Rheingold, A. L.; Figueroa, J. S. *Chem Comm*. 2011, *47*, 406.

20. Agnew, D. W.; Moore, C. E.; Rheingold, A. L.; Figueroa, J. S. *Angew. Chem. Int. Ed*. 2015, *54,* 12673.

21. Fox, B. J.; Sun, Q. Y.; DiPasquale, A. G.; Fox, A. R.; Rheingold, A. L.; Figueroa, J. S. *Inorg. Chem*. 2008 *47*, 9010.

22. Ditri, T. B.; Fox, B. J.; Moore, C. E.; Rheingold, A. L.; Figueroa, J. S. *Inorg. Chem*. 2009, *48*, 8362.

23. Fox, B. J.; Millard, M. D.; DiPasquale, A. G.; Rheingold, A. L.; Figueroa, J. S. *Angew. Chem. Int. Ed*. 2009, *48*, 3473.

24. Labios, L.A.; Millard, M.D.; Rheingold, A. L.; Figueroa, J. S. *J. Am. Chem. Soc.* 2009, *131*, 11318.

25. Margulieux, G. W.; Weidemann, N.; Lacy, D. C.; Moore, C. E; Rheingold, A. L.; Figueroa, J. S. *J. Am. Chem. Soc.* 2010, *132*, 5033.

26. Emerich, B. M.; Moore, C. E.; Fox, B. J.; Rheingold, A. L.; Figueroa, J. S. *Organometallics* 2011, *30*, 2598.

27. Carpenter, A. E.; Margulieux, G. W.; Millard, M. D.; Moore, C. E.; Weidemann, N.; Rheingold, A. L.; Figueroa, J. S. *Angew. Chem. Int. Ed.* 2012, *51*, 9412-9416.

28. Ditri, T. B.; Carpenter, A. E.; Ripatti, D. S.; Moore, C. E.; Rheingold, A. L.; Figueroa, J. S. *Inorg. Chem.* 2013, *52*, 13216.

29. Carpenter, A. E.; McNeece, A. J.; Barnett, B. R.; Estrada, A. L.; Mokhtarzadeh, C. C.; Moore, C. E.; Rheingold, A. L.; Perrin, C. L.; Figueroa, J. S. *J. Am. Chem. Soc.* 2014, *136*, 15481.

30. Carpenter, A. E.; Mokhtarzadeh, C. C.; Ripatti, D. S.; Havrylyuk, I.; Kamezawa, R.; Moore, C. E.; Rheingold, A. L.; Figueroa, J. S. *Inorg. Chem.* 2015, *54*, 2936.

31. L Utz, T.; A Leach, P.; J Geib, S.; John Cooper, N. *Chem. Comm.* 1997, 847–848.

32. Lacombe, D. A.; Anderson, J. E.; Kadish, K. M. *Inorg. Chem.* 1986, *25,* 2074.

33. Kuchynka, D. J.; Kochi, J. K.; Amatore, C. *J. Organomet. Chem.* 1987, *328*, 133.

34. Tulyathan, B.; Geiger, W. E. *J. Am. Chem. Soc.* 1985, *107,* 5960.

35. Grigoriev, V. A.; Cheng, D.; Hill, C. L.; Weinstock, I. A. *J. Am. Chem. Soc.* 2001, *123,* 5292.

36. Macchioni, A. *Chem. Rev.* 2005, *105,* 2039.

37. Carloni, P.; Eberson, L. *Acta Chem. Scand.* 1991, *45,* 373.

38. Machan, C. W.; Sampson, M. D.; Chabolla, S. A.; Dang, T.; Kubiak, C. P. *Organometallics.* 2014, *33*, 4550.

39. All IR-SEC measurements are made with reference to a Ag/AgCl pseudoreference. See Ref. 37 and S3.0 in the SI for details.

40. Upon formation of **6**, a small amount of the hydride complex, $HMn(CO)_3(CNAr^{Dipp2})_2$ (n_{CN} =2081 cm^{-1}) is also produced, likely by H^+ abstraction from the solvent or supporting electrolyte (Hoffman elimination); See for example: (a) Thielen, D. R.; Anderson, L. B. Electrochemical Irreducibility of the Cyclooctatetraene Radical Anion. *J. Am. Chem. Soc.* **1972**, *94*, 2521-2523. (b) Einsla, B. R.; Chempath, S.; Pratt, L. R.; Boncella, J. M.; Rau, J.; Macomber, C.; Pivovar, B. S. *ECS Trans.* **2007**, *11*, 1173-1180. Upon applying more negative potentials, $HMn(CO)_3(CNAr^{Dipp2})_2$ is reduced back to **6** at approximately –3.0 V.

41. Kuchynka, D. J.; Kochi, J. K. *Inorg. Chem.* **1989**, *28,* 855.

42. Treichel, P. M.; Mueh, H. J. *Inorg. Chem.* **1977**, *16,* 1167.

43. Rushman, P.; Brown, T. L. *J. Am. Chem. Soc.* **1987**, *109,* 3632.

44. Nielson, R. M.; Wherland, S. *J. Am. Chem. Soc.* **1985**, *107,* 1505.

45. Nielson, R.; Wherland, S. *Inorg. Chem.* **1984**, *23,* 1338.

46. Nielson, R. M.; Wherland, S. *Inorg. Chem.* **1985**, *24*, 1803.

47. Zizelman, P. M.; Amatore, C.; Kochi, J. K. *J. Am. Chem. Soc.* **1984**, *106*, 3771.

48 It is important to note that EPR spectroscopy studies and DFT calculations on neutral **5** have strongly suggested the presence of a metal-centered radical with only a small amount of spin-delocalization onto to the isocyanide C≡N π* system. In addition, the ν_{CN} stretching frequency of Na[**6**] is 221 cm^{-1} lower in energy than that of complex **4**, thereby signifying a strong and conventional π-backbonding interaction for the $2e^-$ reduced complex. See refs. 12, 18 and 19 for additional details.

49. Benson, E. E.; Grice, K. A.; Smieja, J. M.; Kubiak, C. P. *Polyhedron*. **2013**, *58,* 229.

50. Johnson, F. P. A.; George, M. W.; Hartl, F.; Turner, J. J. *Organometallics*. **1996**, *15,* 3374.

51. Suresh, C. H.; Koga, A. N. *J. Am .Chem. Soc.* **2002**,*124,* 1790.

52. Agarwal, J.; Stanton, C. J., III; Shaw, T. W.; Vandezande, J. E.; Majetich, G. F.; Bocarsly, A. B.; Schaefer, H. F., III. *Dalton Trans.* **2015**, *44,* 2122.

53. Machan, C. W.; Charles J Stanton, I.; Vandezande, J. E.; Majetich, G. F.; Henry F Schaefer, I.; Kubiak, C. P.; Agarwal, J. *Inorg. Chem.* **2015**, *54,* 8849.

54. Bulk electrolysis experiments of $BrMn(CO)_3(CNAr^{Dipp2})_2$ (**4**) in CO_2-saturated THF were very short lived and resulted in only a small amount of charged passed.

55. Mani, F.; Peruzzini, M.; Stoppioni, P. *Green Chem*. **2006**, *8,* 995.

56. Maher, J. M.; Cooper, N. J. *J. Am. Chem. Soc*. **1980**, *102,* 7604.

57. Maher, J. M.; Lee, G. R.; Cooper, N. J. *J. Am. Chem. Soc*. **1982**, *104,* 6797.

58. Lee, G. R.; Maher, J. M.; Cooper, N. J. *J. Am. Chem. Soc*. **1987**, *109,* 2956.

59. Herskovitz, T.; Guggenberger, L. J. *J. Am. Chem. Soc*. **1976**, *98* 1675.

60. The dimers $Mn_2(CO)_7(CNAr^{Dipp2})_3$ and $Mn_2(CO)_8(CNAr^{Dipp2})_2$ can also be prepared via photolysis of $Mn_2(CO)_{10}$ and either 2 or 3 equivalents of $CNAr^{Dipp2}$.

61. Wrighton, M. S.; Ginley, D. S. *J. Am. Chem. Soc*. **1975**, *97*, 2065.

62. Kidd, D. R.; Brown, T. L. *J. Am. Chem. Soc*. **1978**, *100*, 4095.

63. Evans, G. O.; Walter, W. F.; Mills, D. R.; Streit, C. A. *J. Organomet. Chem*. **1978**, *144,* C34..

64. Zeng, Q.; Tory, J.; Hartl, F. *Organometallics*. **2014**, *33,* 5002.

65. Keith, J. A.; Grice, K. A.; Kubiak, C. P.; Carter, E. A. *J. Am. Chem. Soc*. **2013**, *135,* 15823.

66. For a report of CO_2 reductive disproportionation by Mn(bpy-R) catalysts in the presence of Lewis acids, see: M. D. Sampson and C. P. Kubiak. *J. Am. Chem. Soc*. **2016**, *138*, 1386.

67. Machan, C. W.; Sampson, M. D.; Chabolla, S. A.; Dang, T.; Kubiak, C. P. *Organometallics*, **2014**, 33, 4550.

68. Burla, M.C.; Caliandro, R.; Camalli, M.; Carrozini, B.; Cascarano, G. L.; De Caro, L.; Giacovazzo, C.; Polidori, G.; Spagna, R. *J. Appl. Crystallogr.* **2005**, *38*, 381.

69. Sheldrick, G. M. *Acta Crystallogr. A*. **2008**, *64*, 112.

Chapter 4

Controlled *cis*-Labilization of CO from Manganese(I) Mixed Carbonyl/Isocyanides: An Entry Point to Coordinatively Unsaturated Metallo-Lewis Acids

4.1 Introduction

The unsaturated intermediates identified during the dissociative substitution of ligands on octahedral metal carbonyls stand among the earliest conceptual touchstones in the understanding of metal-based coordination chemistry.[1,2] In particular, studies of ligand exchange on group 7 pentacarbonyl halides $MX(CO)_5$ (M = Mn, Re; X = Cl, Br, I) has highlighted the intermediacy of the neutral 16 e^- species $MX(CO)_4$, which has only been observed directly in cryogenic matrix-isolation experiments.[3-6] Furthermore, there is a paucity of data relating to the corresponding isovalent 14 e^- divacant cations $[M(CO)_4]^+$ (M = Mn, Re), which are expected to be much stronger Lewis acids than their isoelectronic, neutral Group 6 metal $M(CO)_4$ counterparts (M = Cr, Mo, W).[7,8] Our interest in these species stems from previous studies by Kubas on a series of cationic complexes of the formulation $[Mn(CO)_3L_2]^+$, where L is typically a phosphine. These species have been shown to be potent electrophiles that can engage in a variety of s-interactions and are consequently used as models on which to delineate C-H bond activation and cleavage (Scheme 4.1).[9-12] Accordingly, further

development of these highly electrophilic Group 7 species may provide new inroads towards C-H functionalization and Lewis acid catalysis.[13]

To develop a systematic method of generating analogues to 14 e⁻ $[M(CO)_4]^+$ and 16 e⁻ $MX(CO)_4$ Group 7 metal species, we were inspired by the classic *cis*-labilizing effect of certain ligands within octahedral complexes.[3,14] This stereochemically controlled labilization is typically observed for X-type ligands[15] that feature significant π-basicity and can donate electron density into the metal d-orbital manifold to stabilize the 16 e⁻ transition state subsequent to CO dissociation.[16-18] Recently, it was found that singly reduced nitrosoarene radicals (*i.e.* $PhNO^-$) promote *cis*-CO dissociation in *m*-terphenyl isocyanide supported Mn(I) species

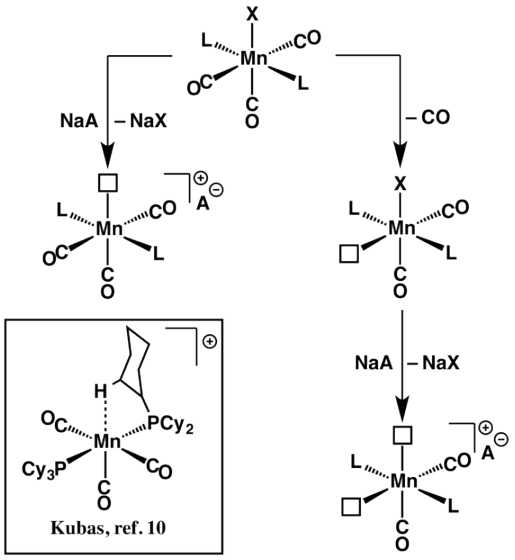

Scheme 4.1. *Left:* Scheme depicting the route typically used towards the generation of monovacant Mn(I) complexes, which engage in agostic interactions as in the complex shown in the bottom left. *Right*: Generalized scheme depicting the generation of *cis*-divacant Mn(I) fragments. L = neutral ligand; A = non-coordinating anion.

(η^1-PhNO)$Mn(CO)_3(CNAr^{Dipp2})_2$ (Ar^{Dipp2} = 2,6-(2,6-(*i*Pr)$_2C_6H_3$)C_6H_3)) to generate (η^2-PhNO)$Mn(CO)_2(CNAr^{Dipp2})_2$ and CO.[19] This result was found to be consistent with theoretical studies of ligands that exert *cis*-lability in octahedral complexes, but importantly, it highlighted the unique capacity available to certain bifunctional ligands to rapidly trap the $MnXL_4$ intermediate formed upon CO dissociation. We have therefore extended our studies to other ligands capable of not only fostering CO dissociation but also function to stabilize the resultant open site within the $[Mn(CO)_2(CNAr^{Dipp2})_2]^+$ scaffold. With appropriate synthetic elaboration, these "protected" species can thus serve as convenient starting materials for the generation of $MnXL_4$[15] and *cis*-divacant Mn(I) species.

The relative *cis*-labilizing ability of a wide range of ligands has been well documented from both theoretical and experimental investigations.[20] Of these, carboxylates (*i.e.* $[O_2CR]^-$) are strong σ- and π-donating anionic ligands and are among the strongest *cis*-labilizing ligands examined within the parent $XMn(CO)_5$ system.[21] Furthermore, they are well documented to bind in a κ^2-*O,O'* fashion as an LX chelate,[22-24] particularly to higher valent metals, and recent work by Ackermann has established the competency of a $BrMn(CO)_5$/carboxylate system for catalytic aryl C-H allylation.[25] As such, we have investigated the ability of several carboxylates to effect *cis*-CO labilization from the five-coordinate $[Mn(CO)_3(CNAr^{Dipp2})_2]^+$ core[19] and provide stabilization to the resulting open site. Within the supporting *m*-terphenyl isocyanide framework[26-34] we have subsequently investigated the liberation of carboxylate using a variety of reductants and Lewis acidic reagents to afford unique examples of Mn(I) and Mn(1-) mixed carbonyl/isocyanide complexes. Accordingly,

these synthetic studies have enabled us to access a range of unique Mn-based electrophiles for potential use in small-molecule binding applications.

4.2 Synthesis of Manganese(I) κ^2-Carboxylates via Dissociative Loss of CO.

To deliver a carboxylate group to the Mn center and facilitate decarbonylation, diethyl ether solutions of $Mn(OTf)(CO)_3(CNAr^{Dipp2})_2$[19] (OTf = $^-O_3SCF_3$) were treated with an alkali metal carboxylate (eg. M[O2CR]; M = Na, K, or Cs; R = alkyl, aryl, H) and heated at reflux. As a representative example, addition of cesium pivalate to $Mn(OTf)(CO)_3(CNAr^{Dipp2})_2$ produces $Mn(\kappa^2\text{-}(O_2C(t\text{Bu})))(CO)_2(CNAr^{Dipp2})_2$ (**1**) in 94% yield as a dark yellow solid. The ^{1}H NMR spectrum of **1** displays a single $CNAr^{Dipp2}$ environment, consistent with a *trans* orientation of *m*-terphenyl isocyanides. In addition, the isocyanide stretching frequency of **1** at 2075 cm^{-1} (C_6D_6) is red-shifted relative to the previously reported Mn(I) complexes $Mn(OTf)(CO)_3(CNAr^{Dipp2})_2$[19] and $MnBr(CO)_3(CNAr^{Dipp2})_2$[30] (2135 cm^{-1} and 2118 cm^{-1}, respectively), which indicates increased electron density at the metal center. A peak arising from the carboxylate moiety in the $^{13}C\{^1H\}$ NMR spectrum of **1** at 178.4 ppm, as well as peaks corresponding to the tert-butyl group at 39.6 and 27.3 ppm, confirms the incorporation of a single carboxylate into the Mn(I) scaffold. Significantly, a single carbonyl resonance is observed in the $^{13}C\{^1H\}$ NMR spectrum **1** (d = 222.9 ppm), which confirms that CO loss from the starting tricarbonyl complex $Mn(OTf)(CO)_3(CNAr^{Dipp2})_2$ occurs. Analogous IR and NMR spectral features are

observed upon reaction of $Mn(OTf)(CO)_3(CNAr^{Dipp2})_2$ with the carboxylate salts $NaO_2CC_6H_5$, NaO_2CCH_3, and KO_2CH, which afford the κ^2-carboxylate derivatives $Mn(\kappa^2\text{-}(O_2CCH_3))(CO)_2(CNAr^{Dipp2})_2$ (**2**), $Mn(\kappa^2\text{-}(O_2CC_6H_5))(CO)_2(CNAr^{Dipp2})_2$ (**3**) and $Mn(\kappa^2\text{-}(O_2CH))(CO)_2(CNAr^{Dipp2})_2$ (**4**), respectively (Scheme 4.2).[35] For carboxylates featuring moderately electron withdrawing substituents (*e.g.* $[O_2CC_6H_5]^-$, $[O_2CH]^-$), reaction times were increased to nearly two days to effect complete conversion to the decarbonylated product.

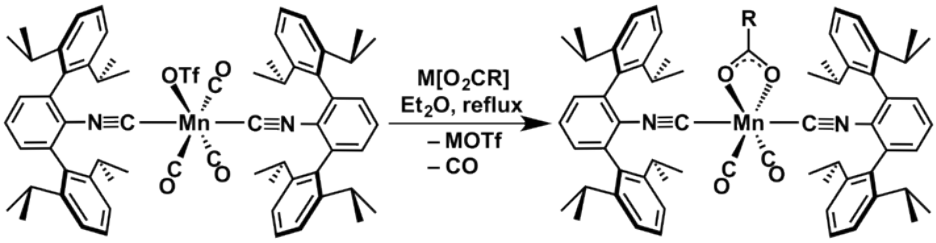

Scheme 4.2. Generalized synthesis of Mn(I) κ^2-carboxylates **1**-**4**. **1** = $Mn(\kappa^2\text{-}(O_2C(t\text{Bu})))(CO)_2(CNAr^{Dipp2})_2$, **2** = $Mn(\kappa^2\text{-}(O_2CCH_3))(CO)_2(CNAr^{Dipp2})_2$, **3** = $Mn(\kappa^2\text{-}(O_2CC_6H_5))(CO)_2(CNAr^{Dipp2})_2$ and **4** = $Mn(\kappa^2\text{-}(O_2CH))(CO)_2(CNAr^{Dipp2})_2$.

Table 4.1. Selected NMR and IR spectroscopic data for **1**-**4** with comparison to the σ_p value for the respective *R* group of the carboxylate.

Complex	$^{13}C\{^1H\}$ *C*NAr^{Dipp2} (ppm)	ν_{CN} (cm^{-1})	σ_p[36]
$Mn(\kappa^2\text{-}(O_2C(t\text{Bu})))(CO)_2(CNAr^{Dipp2})_2$ (**1**)[a]	192.5	2075 (vs)	–0.20
$Mn(\kappa^2\text{-}(O_2CCH_3))(CO)_2(CNAr^{Dipp2})_2$ (**2**)[a]	184.5	2090 (vs)	–0.17
$Mn(\kappa^2\text{-}(O_2CC_6H_5))(CO)_2(CNAr^{Dipp2})_2$ (**3**)[a]	178.6	2093 (vs)	–0.01
$Mn(\kappa^2\text{-}(O_2CH))(CO)_2(CNAr^{Dipp2})_2$ (**4**)	178.7[a]	2098 (vs)[b]	0

[a] Measured in C_6D_6, [b] Measured in $CDCl_3$

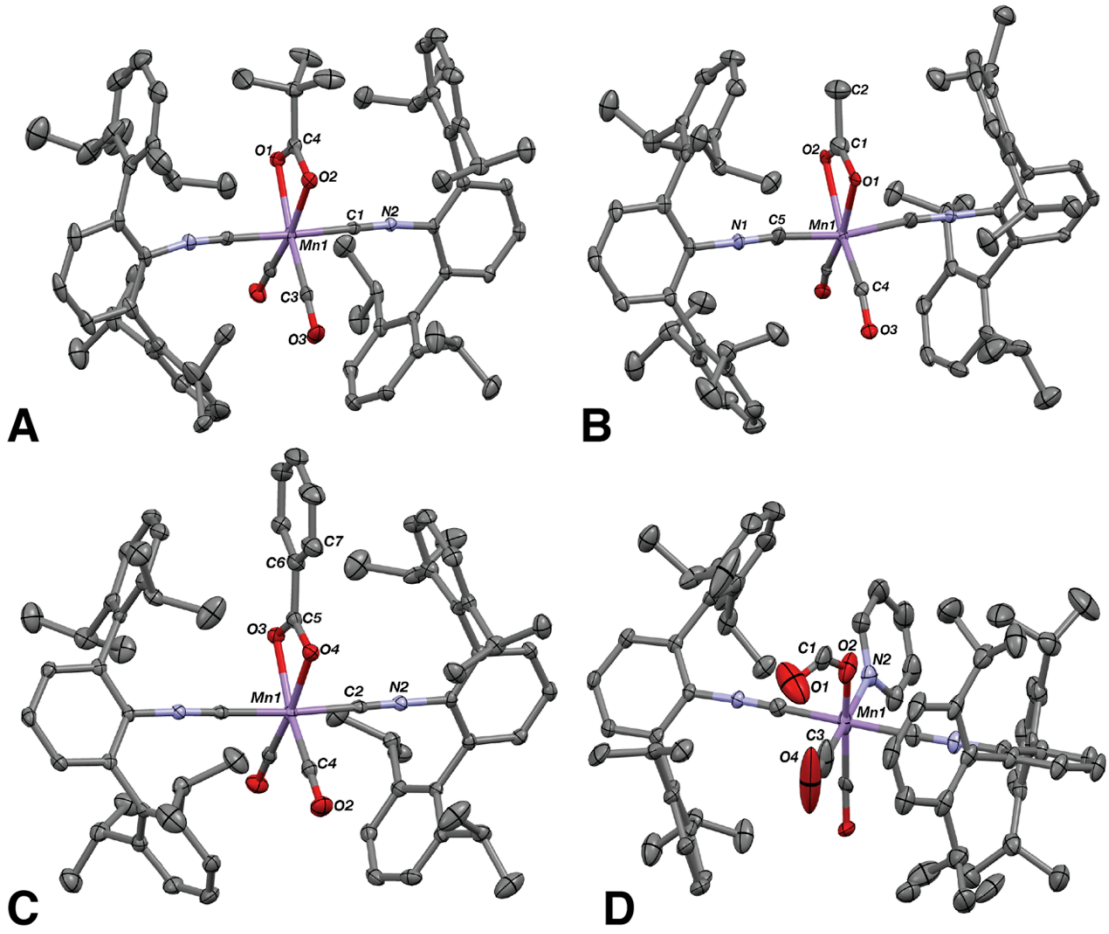

Figure 4.1. Solid-state structures of A) Mn(κ^2-(O_2C(*t*Bu)))($CO)_2$($CNAr^{Dipp2}$)$_2$ (**1**), B) Mn(κ^2-(O_2CCH_3))($CO)_2$($CNAr^{Dipp2}$)$_2$ (**2**), C) Mn(κ^2-($O_2CC_6H_5$))($CO)_2$($CNAr^{Dipp2}$)$_2$ (**3**) and D) Mn(κ^2-(O_2CH))(NC_5H_5)($CO)_2$($CNAr^{Dipp2}$)$_2$ (**4-pyr**). H atoms are omitted for clarity. Selected bond distances (Å) and angles (˚); (Mn(κ^2-(O_2C(*t*Bu)))($CO)_2$($CNAr^{Dipp2}$)$_2$ (**1**)): Mn1-O1 = 2.0716(16); Mn1-O2 = 2.0755(16); Mn1-C1 = 1.931(2); Mn1-C3 = 1.801(2); C4-O2 = 1.269(3); O1-Mn1-O2 = 64.00(6); O1-C4-O2 = 118.7(2); (Mn(κ^2-(O_2CCH_3))($CO)_2$($CNAr^{Dipp2}$)$_2$ (**2**): Mn1-O1 = 2.136(8); Mn1-O2 = 2.197(12); Mn1-C5 = 1.942(5); Mn1-C4 = 1.811(19); C1-O1 = 1.158(15); C1-O1 = 1.462(14); O2-C1-O1 = 128.9(12); O1-Mn1-O2 = 66.2(5); (Mn(κ^2-($O_2CC_6H_5$))($CO)_2$($CNAr^{Dipp2}$)$_2$ (**3**)): Mn1-O3 = 2.0997(14); Mn1-O4 = 2.0734(14); Mn1-C4 = 1.793(2); Mn1-C2 = 1.923(2); O3-C5-O4 = 118.47(19); O3-Mn1-O4 = 63.04(6); O4-C5-C6-C7 = -4.5(3); (Mn(κ^2-(O_2CH))(NC_5H_5)($CO)_2$($CNAr^{Dipp2}$)$_2$ (**4-pyr**)): Mn1-O2 = 1.80(2); Mn1-N2 = 2.078(4); O1-C1 = 1.105(19); O2-C1 = 1.24(2); N2-Mn1-O2 = 95.5(7); O1-C1-O2 = 123.6(18).

Further verification for the dissociation of CO and subsequent formation of κ^2-carboxylate adducts was gained from single crystal X-ray crystallography. As shown in Figure 4.1, the Mn centers in complexes **1-3** adopt pseudo-octahedral geometries,

with *trans*-disposed $CNAr^{Dipp2}$ and the CO ligands oriented *trans* to the respective carboxylate. This stereochemical configuration likely arises due to steric pressure from the bulky *m*-terphenyl substituents on $CNAr^{Dipp2}$, which forces them mutually *trans*-disposed, as well as the higher π-acidity of CO, which can stabilize the strongly σ- and π-donating carboxylate ligands. Notably, although attempts to structurally characterize the k^2-formate complex $Mn(k^2\text{-}O_2CH)(CO)_2(CNAr^{Dipp2})_2$ (**4**) were unsuccessful, crystals of $Mn(\kappa^1\text{-}(O_2CH))(CO)_2(NC_5H_5)(CNAr^{Dipp2})_2$ (**4-pyr**) could be obtained by dissolution of **4** in pyridine and storage at –35 °C. As shown in Figure 2, the presence of a donor ligand such as pyridine is sufficient to induce a κ^1-formate binding mode, highlighting the hemilability of the formate ligand in this system. When placed under high vacuum for several hours, **4** is regenerated quantitatively. Interestingly, **4-pyr** serves as a model complex to the proposed on-cycle intermediate of group 7 CO_2 reduction photocatalysts, in which CO_2 inserts into an *in-situ* generated metal hydride.[37] The observed *cis*-labilizing effect of formate indicates a possible deactivation pathway of this catalyst involving loss of CO followed by κ^2-coordination of the formate.

Insight into the mechanistic sequence leading to κ^2-coordination of the carboxylate can be garnered from the reaction of the S = ½ metalloradical $Mn(CO)_3(CNAr^{Dipp2})_2$[19] and benzoyl peroxide (Scheme 4.3). Addition of benzoyl peroxide to two equivalents $Mn(CO)_3(CNAr^{Dipp2})_2$ in a thawing Et_2O solution rapidly induces a color change to light yellow. Filtration of the cold solution followed by storage at –35 °C yields light yellow crystals, which upon analysis by X-ray

diffraction were shown to be *trans,mer*-(κ^1-($O_2CC_6H_5$))$Mn(CO)_3(CNAr^{Dipp2})_2$ (**5**) (Figure 4.2). Further warming of the solution to room temperature quickly generates the κ^2-benzoate complex **3**, which can be isolated in 88% yield and is comparable in yield to the salt-elimination route. Similar to the conversion of **4** to **4-pyr** described above, the tricarbonyl complex **5** can be regenerated from **3** by treatment with an excess of CO at room temperature. However, **3** is reformed upon removal

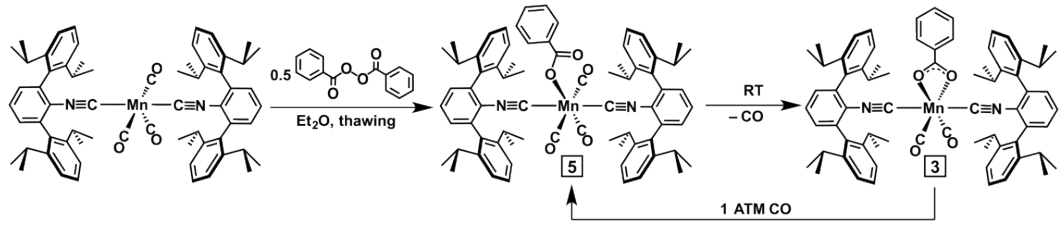

Scheme 4.3. Synthesis of *trans,mer*-(κ^1-($O_2CC_6H_5$))$Mn(CO)_3(CNAr^{Dipp2})_2$ (**5**) from $Mn(CO)_3(CNAr^{Dipp2})_2$ and benzoyl peroxide, and subsequent thermal decarbonylation to provide Mn(κ^2-($O_2CC_6H_5$))$(CO)_2(CNAr^{Dipp2})_2$ (**3**) and CO. Addition of one atmosphere CO regenerates **5** quantitatively.

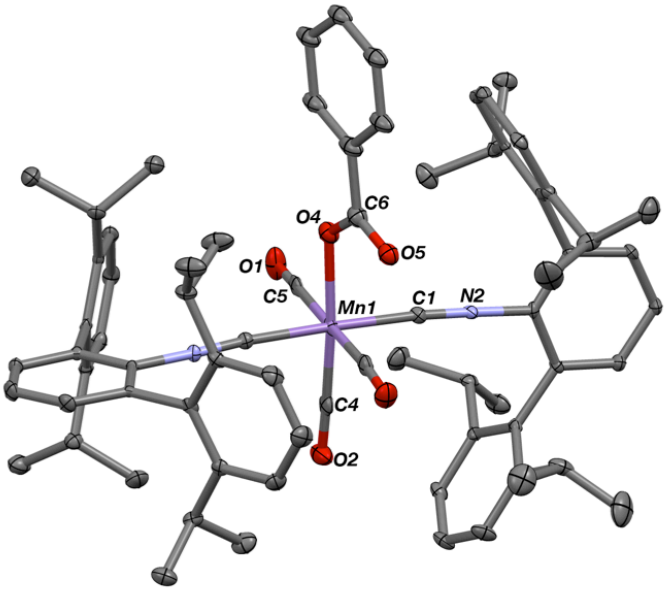

Figure 4.2. Solid state structure of *trans,mer*-(κ^1-($O_2CC_6H_5$))$Mn(CO)_3(CNAr^{Dipp2})_2$ (**5**), with H atoms omitted for clarity. Selected bond distances (Å) and angles (°): Mn1-O4 = 2.057(5); C6-O4 = 1.297(7); C6-O5 = 1.226(5); Mn1-C5 = 1.872(4); Mn1-C4 = 1.792(4); Mn1-C1 = 1.916(3); C1-Mn1-O4 = 91.88(15); O4-C6-O5 = 125.3(5).

of CO from the headspace, indicating κ^2-coordination to be preferred. This sequence supports the intermediacy of a κ^1-coordinated carboxylate prior to CO loss in the preparation of complexes **1**-**4**. Importantly, this observation was enabled by the ability to form the incipient κ^1-benzoate **5** via radical homolysis of benzoyl peroxide by $Mn(CO)_3(CNAr^{Dipp2})_2$ at low temperature, demonstrating the utility of $Mn(CO)_3(CNAr^{Dipp2})_2$ in assessing the reactivity available to low-valent manganese carbonyl/isocyanides.

As mentioned above, the inductive effect of the R substituent appears to strongly effect the *cis*-lablizing ability of a given carboxylate ligand within the Mn(I) octahedral framework, leading to longer reaction times and lower yields for carboxylates featuring less electron-releasing substituents. Accordingly, attempts to generate the corresponding κ^2-trifluoroacetate derivative from $Na[O_2CCF_3]$ and $Mn(OTf)(CO)_3(CNAr^{Dipp2})_2$ provided only the κ^1-carboxylate, *trans,mer-*(κ^1-$(O_2CCF_3)Mn(CO)_3(CNAr^{Dipp2})_2$ (**6**) (Figure 4.3), which is similar to the pentacarbonyl complex (κ^1-$O_2CCF_3)Mn(CO)_5$ prepared by Cotton and Darensbourg.[38] Notably, complex **6** is stable in refluxing toluene for several days, and efforts to induce decarbonylation under photolytic conditions led to intractable mixtures. This lack of *cis*-lability appears strongly correlated with the large inductive effect produced by the $-CF_3$ group (Hammett $\sigma_p = 0.54$),[36] which significantly attenuates the π-basicity of the carboxylate. Interestingly, comparison of Mn-C_{CO} bond lengths between **5** and **6** does not show appreciable dissimilarities, although a slight elongation is observed for Mn-C_{iso} in **6** compared to **5** (avg. 0.017(5) Å). Given the disparate thermal stabilities of

these two complexes, the ground state geometric structure of these two κ^1-carboxylate complexes appears relatively insensitive to the identity of the carboxylate. However, it is clear from the comparative stabilities of **5** and **6** that the combined s-donor and p-basicity properties of the carboxylate dramatically affect its *cis*-labilizing ability.

Within the Mn(I) tri-carbonyl/bis-isocyanide scaffold, the above results demonstrate a significant susceptibility towards *cis*-CO dissociation in the presence of

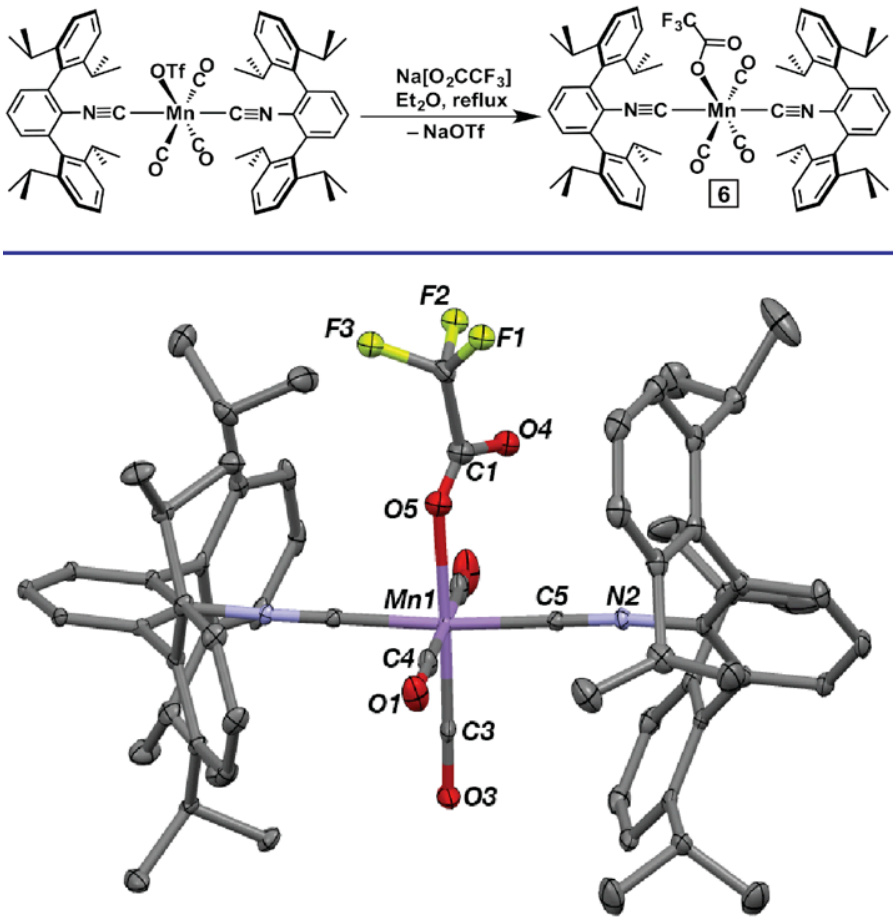

Figure 4.3. *Top*: Synthesis of *trans,mer*-(κ^1-O_2CCF_3)$Mn(CO)_3(CNAr^{Dipp2})_2$ (**6**). *Bottom*: Solid state structure of **6**, with disordered atoms and H atoms omitted for clarity. Selected bond distances (Å) and angles (˚): Mn1-O6 = 2.050(8); O5-C1 = 1.241(14); O4-C1 = 1.230(12); Mn1-C3 = 1.793(2); Mn1-C4 = 1.873(2); Mn1-C5 = 1.9372(17); Mn1-O5-C1 = 121.6(3); O5-C1-O4 = 130.6(3).

apical carboxylates with sufficient π-basicity. These results are consistent with previous studies, including the seminal work by Atwood and Brown on Mn(I) homoleptic carbonyl systems. It is therefore surprising that the examples shown above are among the first fully characterized Mn(I) κ^2-carboxylates. To date, only one structurally characterized Mn(I) κ^2-carboxylate has been reported, namely the acetate complex $Mn(\kappa^2\text{-}(O_2CCH_3))(CO)_2(P(C_6H_5)_3)_2$.[39] However, this compound is a byproduct of a multi-component reaction between the $Na[Mn(CO)_5]$, $ClSi(CH_3)_3$, $P(C_6H_5)_3$ and acetic acid. Furthermore, examples of analogous thiocarboxylate complexes are similarly sparse.[40] Nonetheless, it is clear that facile decarbonylation is achievable under the conditions described above, and can be used strategically to generate protected coordination sites for subsequent functionalization.

4.3 Carboxylate Removal to Generate Open Coordination Sites.

We hypothesized that removal of the κ^2- carboxylate ligand in these Mn(I) complexes, in effect a "deprotection" reaction, could be an effective strategy towards the generation of open coordination sites on the Mn center. Accordingly, several synthetic routes were envisioned for either the abstraction or displacement of the κ^2-carboxylate. As a test platform, the pivalate derivative **1** was used, as it is highly soluble in a variety of solvents and has a readily identifiable ^{1}H NMR resonance at 0.77 ppm corresponding to the *tert*-butyl group.

Initially, we focused on the reduction of complex **1,** as the carboxylate moiety can be viewed as a psuedohalide anion to the $[Mn(CO)_2(CNAr^{Dipp2})_2]^+$ fragment. This

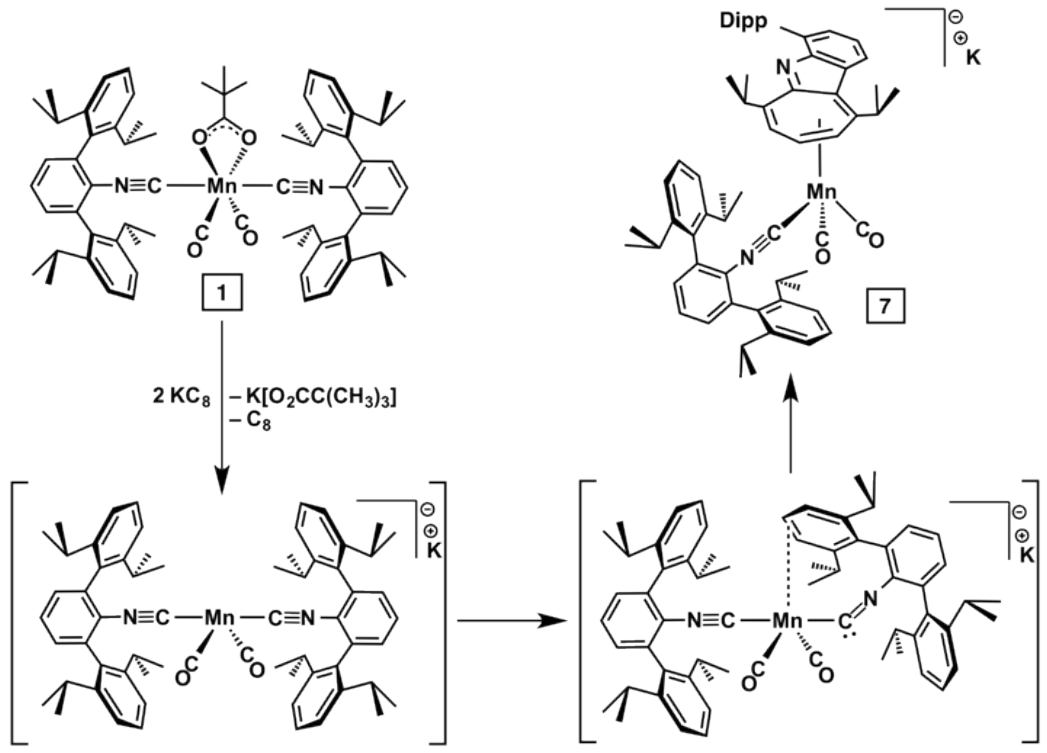

Scheme 4.4. Proposed mechanistic sequence leading to the formation of **7**, with pre-insertion complex on the bottom right.

metal-based reduction could then release pivalate as the corresponding metal salt. Multiple reductants, including cobaltacene, Na/Hg, and K[naphthalenide], were screened and found unable to reduce **1**. However, quick mixing of an Et_2O solution of **1** with 2.1 eq. KC_8 followed by filtration rapidly generated a single new product with notably de-symmetrized Ar^{Dipp2} resonances in the ^1H NMR spectrum. X-ray crystallographic analysis of this product revealed it to be the η^4-1-azabenz[*b*]azulene manganate complex $[K(Et_2O)][(\eta^4\text{-}4\text{-}Ar^{Dipp}\text{-}6,10\text{-diisopropylazabenz}[b]\text{azulene})\text{-}Mn(CO)_2(CNAr^{Dipp2})]$ (**7**) (Figure 4.4, bottom). Interestingly, complex **7** forms a one-dimensional coordination polymer in the solid-state (Figure 4.4, top), with isocarbonyl, imino and Dipp arene coordination to the potassium cation ($d_{avg.}$ K-O_{CO} = 2.650(6) Å; K-N_{aza} = 2.837(6)) establishing the bridging contacts. However, solution-

phase spectroscopic data are consistent with **7** being a discrete molecular species when dissolved. We contend complex **7** results from an *aza*-Büchner ring expansion[41,42] of the flanking Dipp ring of $CNAr^{Dipp2}$ stemming from the initial removal of $K[O_2CC(CH_3)_3]$. As shown in Scheme 4.4, initial reduction of **1** generates the transient tetracoordinate manganate $K[Mn(CO)_2(CNAr^{Dipp2})_2]$. However, in the absence of a

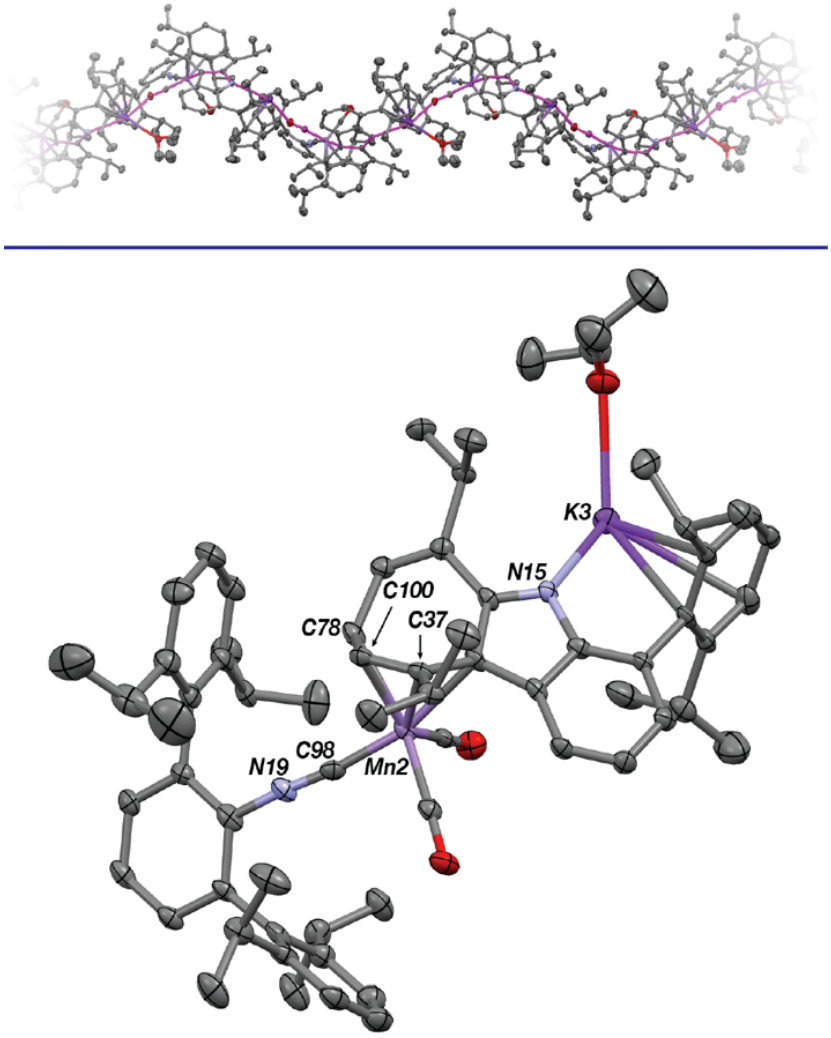

Figure 4.4. *Top*: Extended structure of 1-D coordination polymer formed by **7**, with purple line highlighting connectivity. *Bottom*: Molecular solid state structure of $[K(Et_2O)][(\eta^4\text{-}4\text{-}Ar^{Dipp}\text{-}6,10\text{-}$diisopropylazabenz[*b*]azulene)$Mn(CO)_2(CNAr^{Dipp2})]$ (**7**), with catenation to isocarbonyl and H atoms omitted. Selected bond distances (Å) and angles (˚): Mn2-C98 = 1.833(8); Mn2-C100 = 2.090(7); Mn2-C37 = 2.087(7); C78-C100 = 1.434(10); C100-C37 = 1.394(10); Mn2-C98-N2 = 173.4(6).

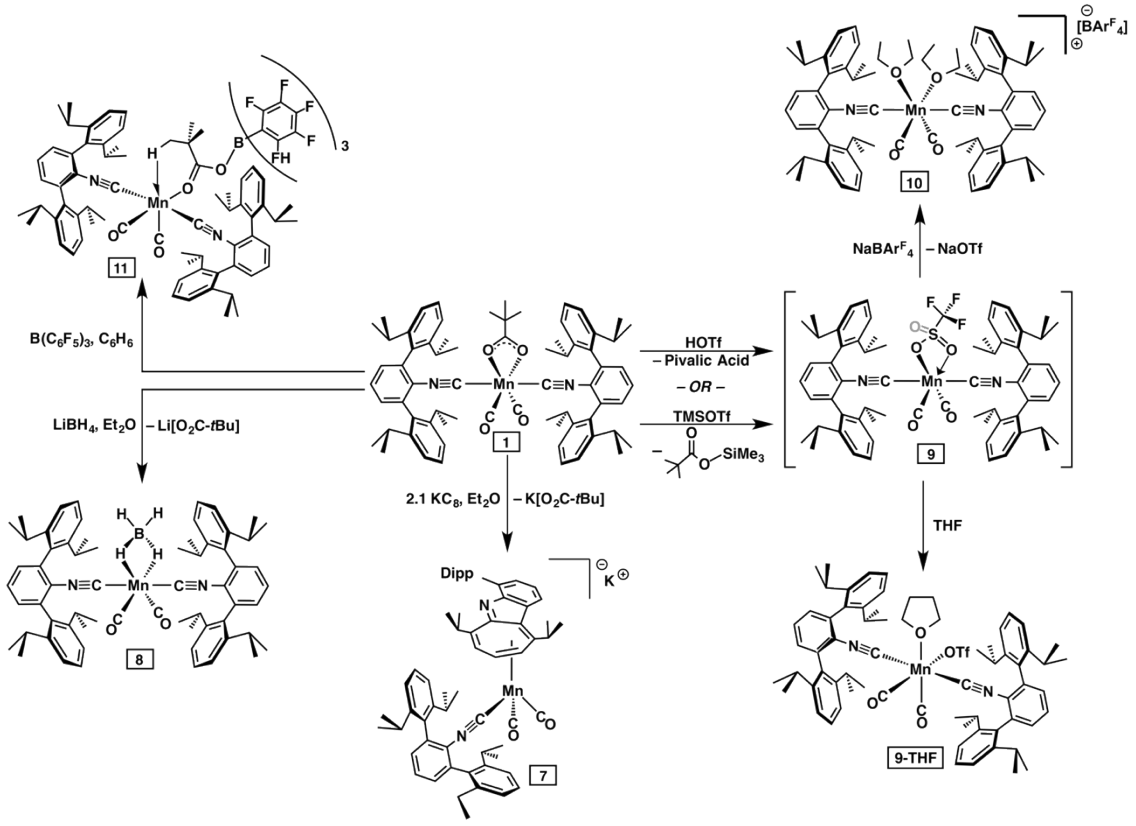

Scheme 4.5. Reaction pinwheel of **1** showing the deprotection strategies employed.In addition, Arnold has shown that the *m*-terphenyl isocyanide CNAr^{Mes2} similarly undergoes *aza*-Büchner ring expansion in the presence of reduced and coordinatively-unsaturated Zr centers.[45] Accordingly, this result is consistent with the generation of an electron-rich, low-coordinate manganate species. While this suggests metal-based reduction to be a potentially useful deprotection method, it is clear that under these conditions the Mn species thus formed is susceptible to decomposition.

sufficiently π-acidic ligand field to accommodate the anionic Mn center, excessive π-backdonation to the isocyanide induces an electrophilic carbenoid character at the isocyanide carbon. Additionally, the presence of an open coordination site can facilitate arene coordination to the Mn(1-) center, bending the isocyanide further and intensifying the carbenic character. We believe these two factors prime the isocyanide for insertion into the flanking Dipp ring, resulting in the formation of the azabenz[*b*]azulene. Importantly, we have recently reported a similar *aza*-Büchner ring expansion in a coordinatively unsaturated Co(I) complex,[43] and documented several

examples in zerovalent group 6 metal chemistry in which significant carbenoid character in the isocyanide results from arene coordination and subsequent C_{iso}-N-C_{ipso} bending.[44]

In accordance with the view of the k^2-pivalate group functioning as a psuedohalide counteranion, we sought to conduct an anion exchange reaction with a counteranion that could be protolytically degraded and released. Specifically, coordinated borohydride ($[BH_4]^-$) has been shown to be sensitive to H^+ addition to release H_2,[46] and furthermore is well-documented to bind in κ^1- and κ^2-modes.[47,48] Stirring of an excess of $LiBH_4$ with **1** facilitated the formation of Mn((κ^2-*H,H'*-BH_4))$(CO)_2(CNAr^{Dipp2})_2$ (**8**) and $LiO_2CC(CH_3)_3$. Complex **8** exhibits a ^{11}B resonance at –26.9 ppm, indicative of a four-coordinate boron center, and displays a broad singlet at –11.7 ppm in its ^1H NMR spectrum, suggesting a fluxional borohydride unit.

The solid-state structure of **8** (Figure 4.5) revealed a κ^2-coordinated borohydride group to the $Mn(CO)_2(CNAr^{Dipp2})_2$ framework,[47-49] and represents the first example of a low-valent molecular Mn-borohydride complex. Notably, **8** is thermally robust and does not decompose upon extended heating (toluene, 110 ºC, 5 days). However, addition of 1 equiv. HOTf to a thawing toluene solution of **8** led to a new species with a slightly downfield-shifted hydride resonance at -11.3 ppm, as well as higher energy isocyanide IR absorptions compared to **8** (ν_{CN} = 2104 cm^{-1} *vs*. 2097 cm^{-1} (**8**)). Analysis of single crystals grown from Et_2O revealed the formation of Mn(κ^2-*H,H'*-$F_3CSO_3BH_3$)$(CO)_2(CNAr^{Dipp2})_2$ (**8-OTf**), resulting from formal loss of H_2 from protonolysis (Figure 4.6). Interestingly, the ^{11}B NMR resonance of the

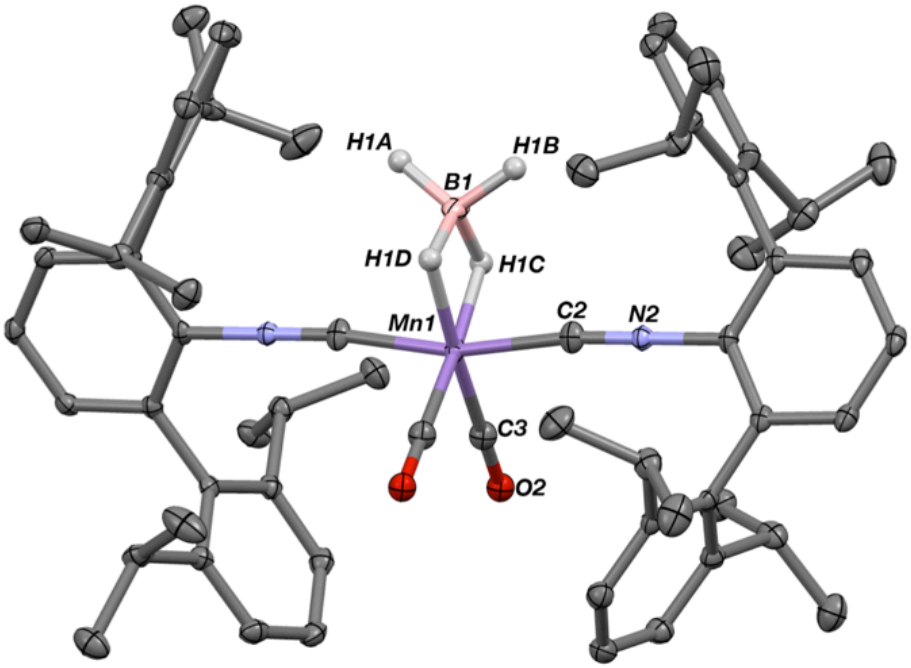

Figure 4.5. Solid state structure of $Mn((\kappa^2\text{-}H,H'\text{-}BH_4))(CO)_2(CNAr^{Dipp2})_2$ (**8**), with selected H atoms omitted for clarity. Selected bond distances (Å) and angles (˚): Mn1-C2 = 1.933(3); Mn-C3 = 1.813(6); Mn-H1D = 1.77(4); Mn1-H1C = 1.71(4); H1D-Mn1-H1C = 77(2); Mn1-H1D-B1 = 52.4(17); C2-Mn1-C3 = 85.87(13).

triflate-stabilized borane in **8-OTf** is observed at 28.8 ppm at 20 ºC, which is shifted upfield significantly from that expected for a four-coordinate boron center.[50-52] Unfortunately, attempts to further deprotonate **8-OTf** with additional equivalents of HOTf led to the formation of free $CNAr^{Dipp2}$ and intractable products. Accordingly, we sought a different route to low-coordinate Mn(I) centers.

Previous studies have established the efficacy of carboxylate esterification as an abstraction method, particularly to effect anion exchange.[53] Indeed, a simple Lewis acid abstraction of pivalate using trimethylsilyl triflate (TMSOTf) afforded the corresponding silyl ester $(CH_3)_3C(O)COSi(CH_3)_3$[54] and a new species, assigned as

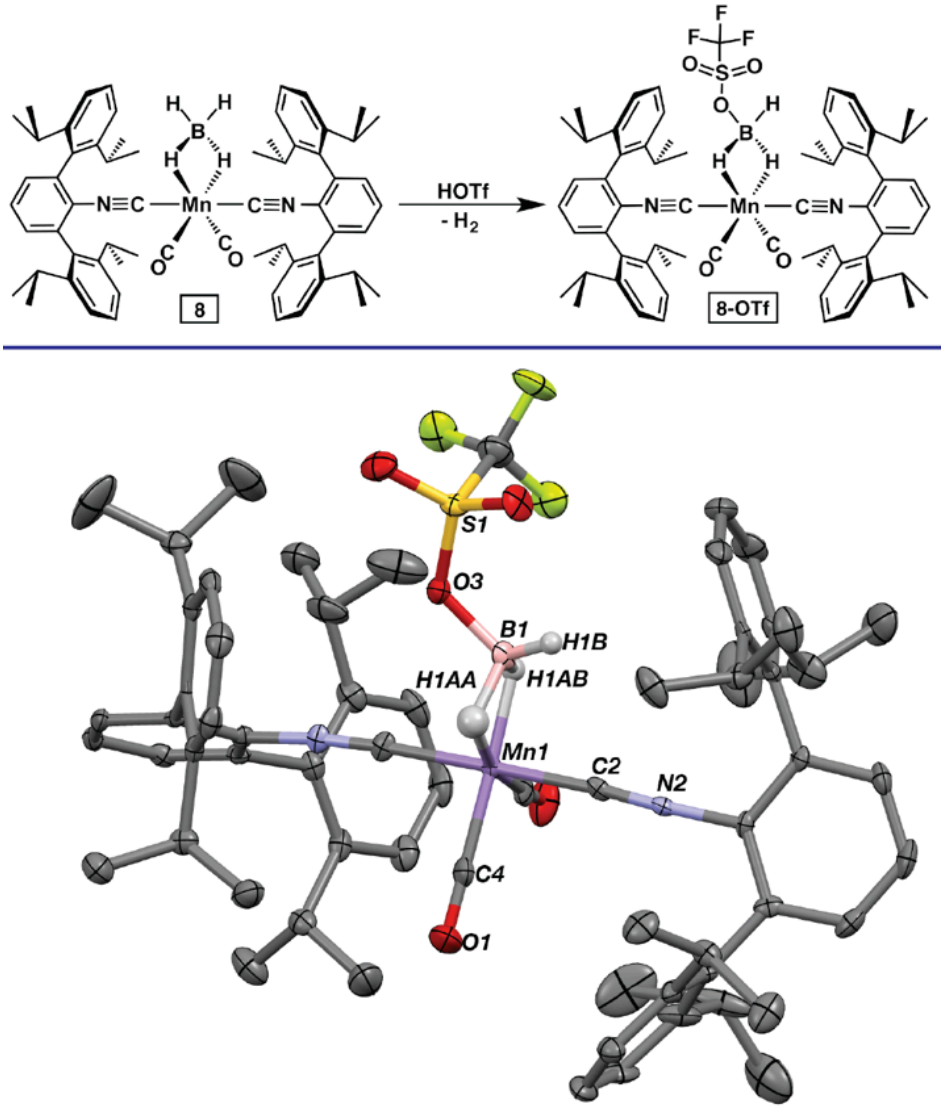

Figure 4.6. *Top*: Synthesis of $Mn(\kappa^2\text{-}F_3CSO_3BH_3)(CO)_2(CNAr^{Dipp2})_2$ (**8-OTf**). *Bottom*: Solid state structure of **8-OTf**, with disordered components and selected H atoms omitted for clarity. Selected bond distances (Å) and angles (˚): Mn1-C2 = 1.913(4); Mn1-C4 = 1.816(4); Mn1-H1AA = 1.73(4); Mn1-H1AB = 1.66(3); B1-O3 = 1.511(8); S1-O3 = 1.529(4); H1AA-Mn1-H1AB = 74.8(18); C2-Mn1-C4 = 89.31(18); H1B-B1-O3 = 113(3); O3-B1-H1AA = 107.1(19).

$Mn(OTf)(CO)_2(CNAr^{Dipp2})_2$ (**9**, Scheme 4.5). A single set of $CNAr^{Dipp2}$ resonances is observed in the ^1H NMR spectrum, indicating retention of the approximate C_{2v} symmetry of the starting complex. Furthermore, the solution IR

spectrum of **9** displays three strong bands at 2096, 1990 and 1934 cm^{-1}, again denoting a local C_{2v} symmetry about the Mn(I) center and supporting a *trans*, *cis* disposition of $CNAr^{Dipp2}$ and CO ligands, respectively. Dissolution of **9** in poorly-coordinating solvents such as *n*-pentane, benzene and toluene leads to ligand redistribution and the formation of the tricarbonyl $Mn(OTf)(CO)_3(CNAr^{Dipp2})_2$. However, addition of one equivalent of THF to **9** led to a new complex, $Mn(OTf)(THF)CO)_2(CNAr^{Dipp2})_2$ (**9-THF)** which displayed heightened stability at room temperature for several days. Single crystals of **9-THF** permitted structural analysis by X-ray crystallography, which revealed an octahedral Mn(I) complex in which the triflate anion and THF each occupy a coordination site (Figure 4.7, top). Importantly, coordination of $(CH_3)_3C(O)COSi(CH_3)_3$ was not observed by ^1H NMR or IR spectroscopy during the generation of **9** or **9-THF**. Accordingly, from this data, we believe that **9** is stabilized *via* κ^2-coordination of triflate, a well-known binding motif[27,55-57] and analogous to the aforementioned Mn(I) carboxylate species. However, conversion of the k^2-bound triflate ligand in **9** to the k^1-bound form can be readily induced by the relatively weak s-donor THF.

$Mn(OTf)(CO)_2(CNAr^{Dipp2})_2$ (**9)** can also be generated from the addition of a slight excess of HO_3SCF_3 in benzene with concomitant formation of pivalic acid. Similar to the reaction with TMSOTf, continued stirring over several hours generates $Mn(OTf)(CO)_3(CNAr^{Dipp2})_2$ and other intractable products. Nonetheless, this result indicates carboxylate lability in **1** may also be induced by Brønsted acids with acidities greater than pivalic acid, thereby providing an alternate means of generating open coordination sites in acidic media. Indeed, treatment of **1** with benzoic acid cleanly

afforded the κ^2-benzoate **3** with concomitant formation of pivalic acid, as indicated by IR and NMR spectroscopy. However, attempts to prepare $ClMn(CO)_2(CNAr^{Dipp2})_2$ by addition of HCl led to the coordinatively saturated complex $ClMn(CO)_3(CNAr^{Dipp2})_2$[19] via redistribution, thus suggesting that the conjugate base used in this protonolysis sequence must be able to occupy two coordination sites.

The observed ease by which pivalate could be exchanged for triflate *via* carboxylate esterification indicated that $Mn(OTf)(CO)_2(CNAr^{Dipp2})_2$ (**9**) could potentially serve as a starting point for the generation of a Mn(I) *cis*-divacant complex upon further exchange with a non-coordinating anion. The resultant tetra-coordinate d^6 complex would thus serve as an isoelectronic analogue to $Cr(CO)_4$, one of the archetypal binary unsaturated metal carbonyls[58,59] that has only been accessible through low-temperature matrix isolation.[60,61] Additionally, reports of tetra-coordinate d^6 Mn carbonyls are limited solely to gas phase photodissociation experiments, such that even a general description of their structure and reactivity remains unreported.[7,62] Accordingly, it was found that upon anion exchange of **9** in benzene with $NaBAr^F_4$ (BAr^F_4 = $B(C_6H_3(3,5\text{-}CF_3)_2)_4$) a dark red residue was produced after solvent lyophilization. Attempts to manipulate and characterize this complex led quickly to decomposition, with only free $CNAr^{Dipp2}$ observable by ^1H NMR spectroscopy. However, upon addition of Et_2O the color lightened to bright yellow, and single crystals suitable for structural analysis by X-ray crystallography could be obtained after storage at –40 ºC. The resultant complex was revealed to be $[Mn(OEt_2)_2(CO)_2(CNAr^{Dipp2})_2]BAr^F_4$ (**10**) (Figure 4.7, bottom), with diethyl ether molecules occupying *cis*-coordination sites on the formally Mn(I) center. Analysis by

^{1}H NMR spectroscopy shows the Et_2O ligands in **10** to be labile at 25 ºC, with a broadened resonance at 3.67

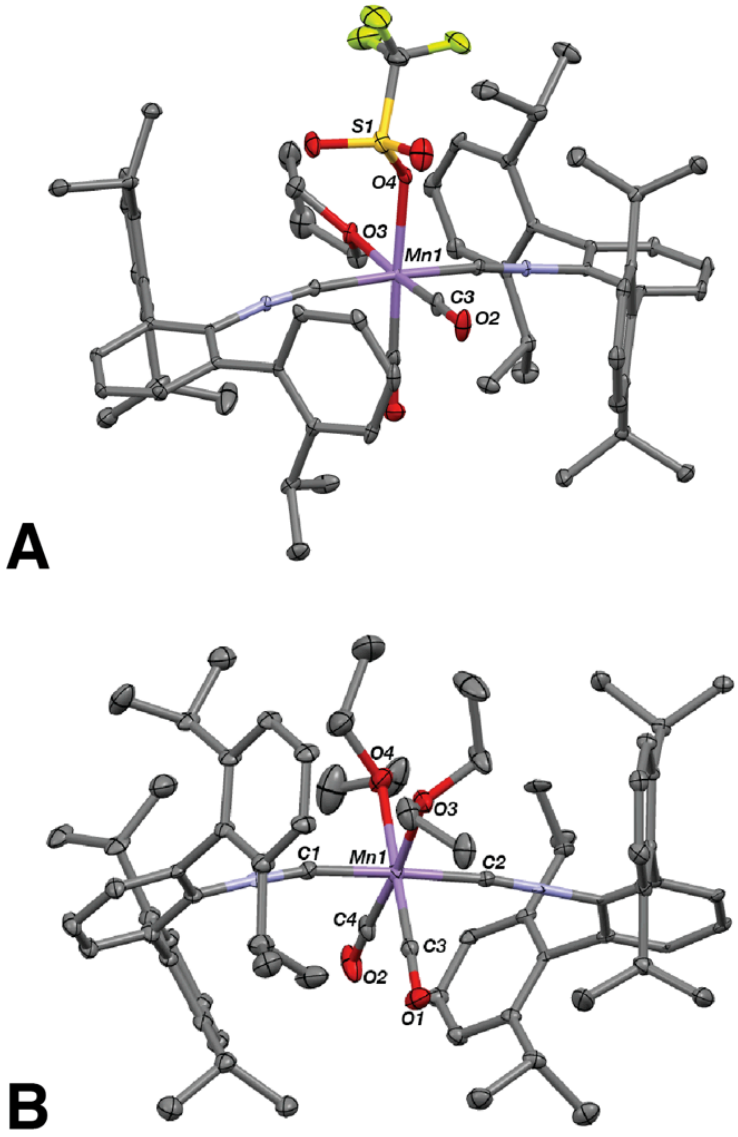

Figure 4.7. A) Solid state structure of $Mn(OTf)(THF)(CO)_2(CNAr^{Dipp2})_2$ (**9-THF**). B) Solid state structure of $[Mn(OEt_2)_2(CO)_2(CNAr^{Dipp2})_2]BAr^F_4$ (**10**), with BAr^F_4 counteranion omitted. H atoms have been omitted for both structures. Selected bond distances (Å) and angles (˚); ($Mn(OTf)(THF)(CO)_2(CNAr^{Dipp2})_2$ (**9-THF**))**:** Mn1-O4 = 2.101(3); Mn1-O3 = 2.070(3); Mn1-C3 = 1.813(4); O3-Mn-O4 = 81.44(11); O3-Mn1-C3 = 175.33; ($[Mn(OEt_2)_2(CO)_2(CNAr^{Dipp2})_2]BAr^F_4$ (**10**)): Mn1-O3 = 2.102(8); Mn-O4 = 2.104(9); Mn1-C3 = 1.783(14); Mn1-C4 = 1.818(15); Mn1-C1 = 1.959(11); O3-Mn1-O4 = 82.4(4); C3-Mn-C4 = 87.4(6); C2-Mn1-C1 = 176.3(4).

ppm corresponding to the Cα protons. Indeed, under dynamic vacuum the complex reassumes a dark red color, suggesting weak coordination of Et_2O, but as mentioned above attempts to isolate this species quickly caused decomposition. Nonetheless, the isolation of **10** indicates that carboxylate esterification followed by anion exchange is effective for the generation of *cis*-divacancies from κ^2-carboxylate Mn(I) starting complexes.

Based on the above results, extension of the Lewis abstraction strategy with larger main group Lewis acids was envisioned to allow for the single-step production of *cis*-divacant Mn(I) species. Accordingly, addition of $B(C_6F_5)_3$ to **1** was predicted to provide the corresponding trispentafluorophenyl borate ester, enabling the deprotection of the carboxylate and formation of the counteranion in one step. Indeed, upon addition of $B(C_6F_5)_3$ to **1**, analysis of the reaction mixture by ^{11}B NMR spectroscopy revealed a single resonance at –22.8 ppm, indicating the formation of a tetra-coordinate boron center. However, a diagnostic singlet resonance in the ^1H NMR spectrum at –0.60 ppm integrating to 9H suggested the simultaneous formation of a C-H—Mn agostic interaction.[63] Structural analysis of red single crystals at 100 K confirmed the presence of this interaction, revealing the generation of $Mn((\eta^2\text{-}H,C\text{-}CH_3)(CH_3)_2CCO_2B(C_6F_5)_3)(CO)_2(CNAr^{Dipp2})_2$ (**11**), in which the *t*-butyl group of the pivalate engages in an agostic interaction ($d_{Mn\text{-}H}$ = 1.94(2) Å) at the apical site on Mn (Figure 4.8). The broadening of the ^1H resonance at +0.60 ppm indicates fluxionality and suggests rapid interchange between the methyl protons on the *t*-butyl group. The *in-situ* generated borate forms a zwitterionic pair with the electrophilic Mn(I) center to

provide an overall charge-neutral compound featuring a stabilizing agostic interaction.[64,65] Complex **11** is stable in solution at room temperature for several days, but upon warming to 50 ºC decomposes to several products, including the isocyanide-borane adduct $(C_6F_5)_3B{\leftarrow}CNAr^{Dipp2}$ (Figure 4.9). However, this stability is markedly improved compared to the related agostic complexes $[Mn(CO)_3(PCy_3)_2]^+$ and $[Mn(CO)(dcpe)_2]^+$ (Cy = C_6H_{11}; dcpe = bis(dicyclohexylphosphino)ethane), which undergo disproportionation at room temperature.

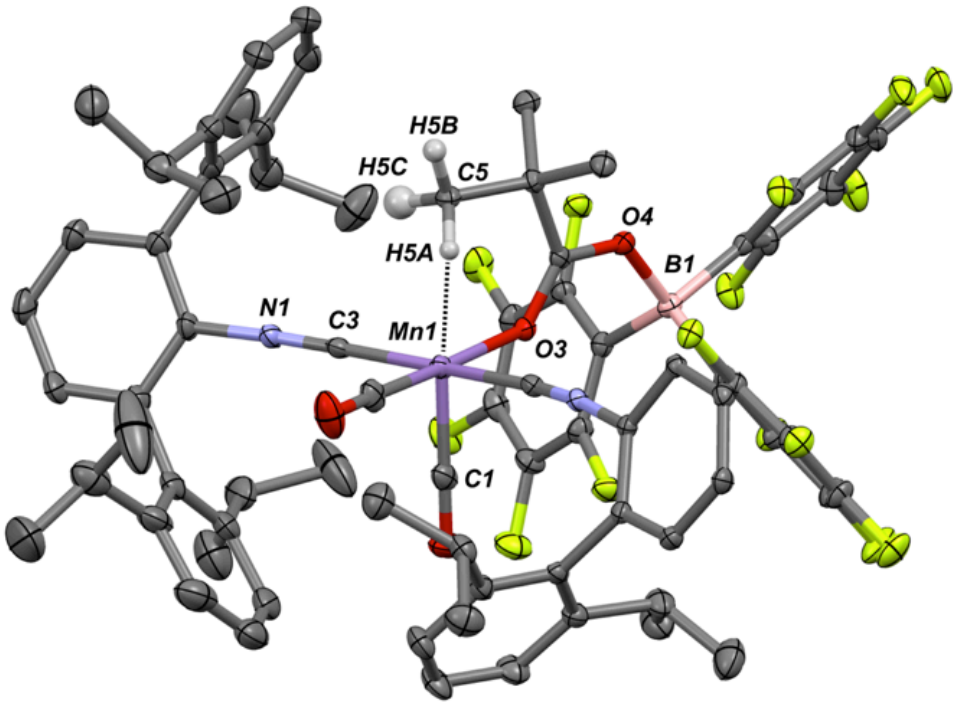

Figure 4.8. Solid state structure of $Mn(CO)_2(CNAr^{Dipp2})(\eta^2\text{-}(C,H\text{-}CH_3)(CH_3)_2CCO_2B(C_6F_5)_3)$ (**11**) with a Dipp ring and H atoms omitted for clarity. Selected bond distances (Å) and angles (˚): Mn1-C3 = 1.927(2); Mn1-O3 = 2.0371(15); Mn-C1 = 1.800(3); Mn1-H5A = 1.94(2); Mn1-C5 = 2.665(2); C3-Mn1-C1 = 90.70(9); C3-Mn1-O3 = 96.07(8); C1-Mn1-O3 = 92.83(9).

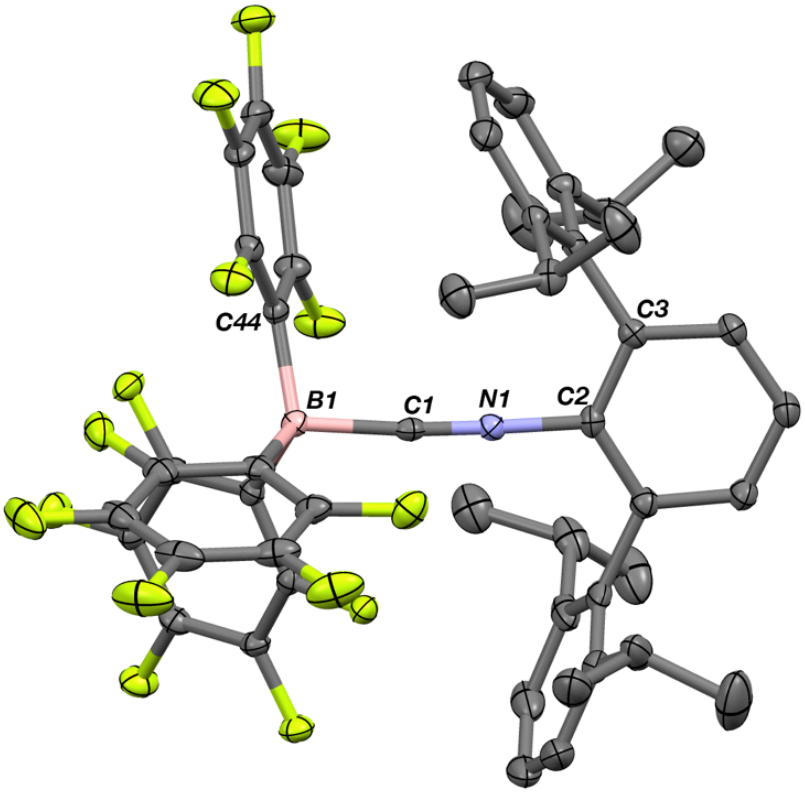

Figure 4.9. Molecular structure of $(C_6F_5)_3B{\leftarrow}CNAr^{Dipp2}$, with H atoms omitted for clarity. Selected bond distances (Å) and angles (˚): C1-N1 = 1.150(3); C2-N1 = 1.416(3); C1-B1 = 1.637(3); B1-C44 = 1.629(3); B1-C1-N1 = 175.2(2); C1-N2-C2 = 175.12(19).

Notably, no evidence for the formation of dinitrogen adducts was observed in solution IR measurements of complexes **9**-**11**. Previous studies by Kubas have highlighted the importance of a cationic, electron-rich metal center to effectively engage the π* orbitals of N_2.[10] Indeed, while there are many reported examples of neutral group 6 dinitrogen complexes, the few examples of isoelectronic Mn(I) dinitrogen species are typically supported by strong σ-donors, such as alkyl and aryl phosphines, which significantly increases the electron density on Mn.[66] The moderate π-acidity of the supporting $CNAr^{Dipp2}$ ligands, coupled with the strong π-acidity of CO, no doubt attenuates the ability of the Mn(I) center in **9**-**11** to backbond to N_2.

However, this absence only serves to underscore the Lewis acidity of the Mn(I) center within the mixed carbonyl/isocyanide framework, such that strong agostic interactions are capable of being formed upon synthetic elaboration.

In an attempt to extend the Lewis-acid abstraction chemistry of the pivalate group in **1**, the alkyl aluminane Al_2Me_6 was added with the intention similarly produce an ester-like trialkylaluminate (eg. (*t*BuC(O)O→$AlMe_3$) with concomitant formation of a low-coordinate Mn(I) center. Surprisingly, however, an apparent alkyl migration subsequent to this step provided the Mn(I) iminoacyl complex $Mn(CO)_2(\eta^2$-*C,N*-$(H_3CCNAr^{Dipp2}))(CNAr^{Dipp2})$ (**12**, Scheme 4.6). This deep blue species exhibits downfield ^{13}C resonances at 244.8 and 230.0 ppm for the carbonyls, indicative of an electron-rich Mn center. Iminoacyl formation is further denoted by the observation of a strong band at 1601 cm^{-1}, consistent with other observed η^2-iminoacyls.

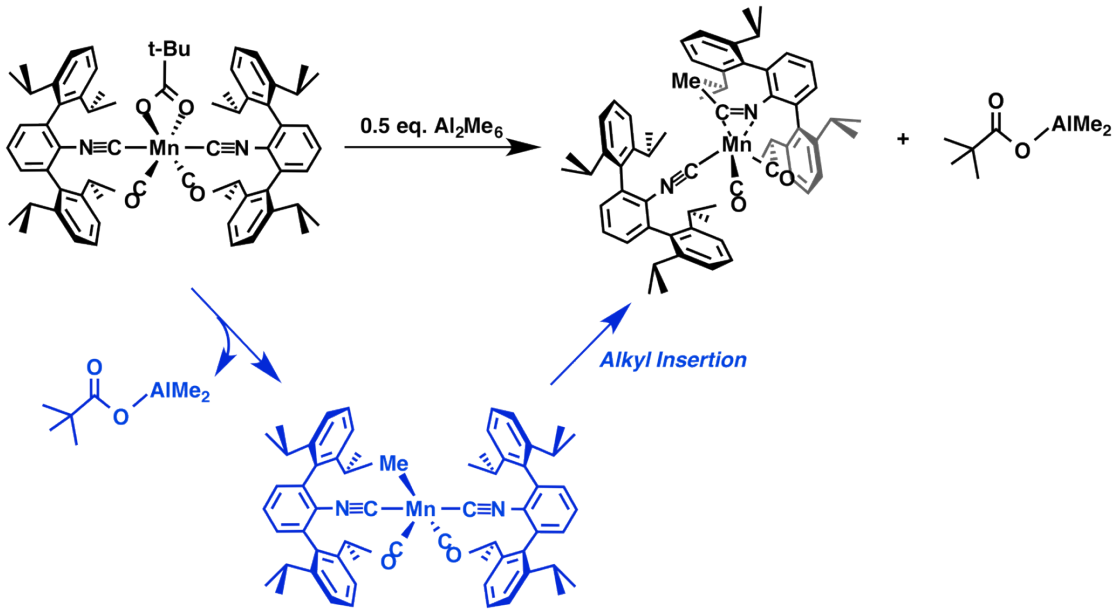

Scheme 4.6. Synthesis of $Mn(CO)_2(\eta^2$-*C,N*-$(H_3CCNAr^{Dipp2}))(CNAr^{Dipp2})$ (**12**) and *t*BuC(O)O$AlMe_3$.

Structural analysis of crystals grown from *n*-pentane using X-ray crystallography confirms the formation of $Mn(CO)_2(\eta^2$-*C,N*-$(H_3CCNAr^{Dipp2}))(CNAr^{Dipp2})$ (Figure 4.10). A significantly elongated iminoacyl C-N bond length is observed (d_{CN} = 1.301(6)), suggestive of substantial π-bonding with the electrophilic Mn(I) center. Indeed, this is to be expected of the formally 16 e^- complex, which likely derives its stability from the ability of the iminoacyl substituent to function as a 4 e^- donor ligand.[67] This uncommon electronic structure manifests in an unusual geometry for $Mn(CO)_2(\eta^2$-*C,N*-$(H_3CCNAr^{Dipp2}))(CNAr^{Dipp2})$, which adopts a distorted square pyramid with a Reedijk-Addison τ^5 value of 0.25. This species provides a unique example of a 5-coordinate Mn(I) species in a strong-ligand field environment.

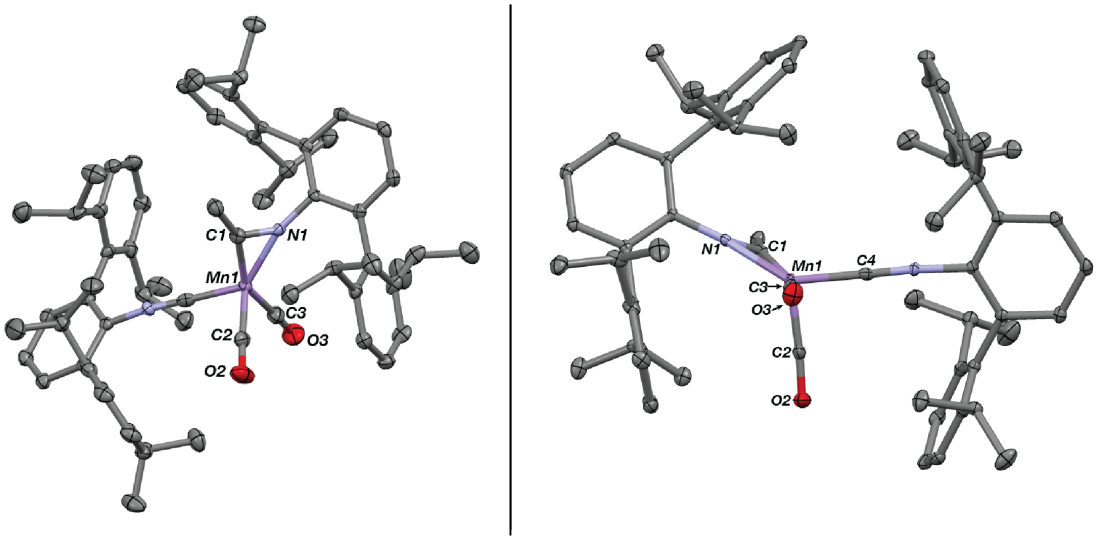

Figure 4.10. Two perspectives of the molecular structure of $Mn(CO)_2(\eta^2$-*C,N*-$(H_3CCNAr^{Dipp2}))(CNAr^{Dipp2})$ (**12**). Selected bond distances (Å) and angles (˚): C1-N1 = 1.301(6); C1-Mn1 = 1.908(5); N1-Mn1 = 1.957(4); Mn1-C4 = 1.817(6); C1-Mn1-N1 = 39.32; C1-Mn-C4 = 107.3(2).

Consistent with the formal 16 e^- assignment of the Mn(I) metal center, **12** reacts with nucleophilic L-type donor ligands to provide octahedral MXL_5 products.

This is illustrated by the addition of CO, which provides $Mn(CH_3)(CO)_3(CNAr^{Dipp2})_2$ (identified by comparison of spectra to those previously reported[30]) via an apparent migratory deinsertion of the alkyl group from the iminoacyl substituent (Scheme 4.7). This pathway is the microscopic reverse of the decarbonylation of the Mn-alkyl product; it therefore provides an interesting view into the possible generation of more highly electrophilic charge-neutral Mn(I) species via the inclusion of a X-type ligand.

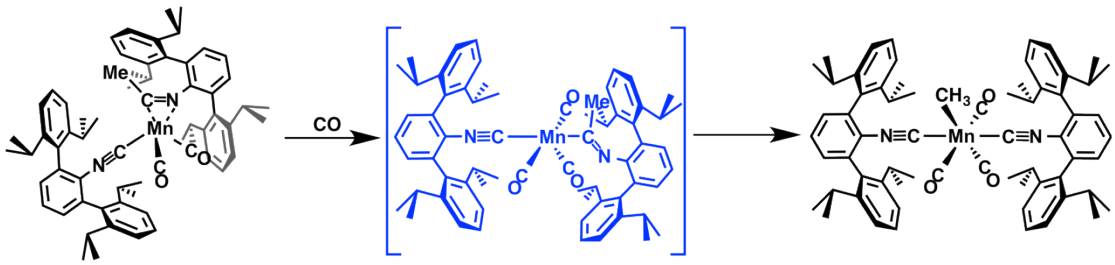

Scheme 4.7. The addition of CO to $Mn(CO)_2(\eta^2$-*C,N*-$(H_3CCNAr^{Dipp2}))(CNAr^{Dipp2})$ (**12**) causes the deinsertion of the alkyl group to provide the previously identified Mn-alkyl species $Mn(CH_3)(CO)_3(CNAr^{Dipp2})_2$.

4.4 Concluding Remarks

A series of Mn(I) κ^2-carboxylate derivatives have been prepared and establish carboxylate ligands to not only be effective *cis*-labilizing ligands within the Mn(I) mixed carbonyl/isocyanide framework, but also to function as LX chelates to stabilize the resulting open coordination site. This activity correlates well with the respective electronic inductive effect of the carboxylate *R* group, such that highly electronegative groups such as $–CF_3$ effectively inhibit *cis*-labilization. However, carboxylates featuring electron releasing groups are highly effective labilizing/protection agents and can be conveniently manipulated. Indeed, complete removal of the carboxylate ligand

is facilitated by a variety of reagents, demonstrating the versatility of κ^2-carboxylates for accessing Lewis-acidic Mn(I) centers for potential applications in small-molecule binding and catalysis. Accordingly, efforts aimed at systematically exploring this potential are underway.

4.5 Synthetic Procedures and Characterization Data

General Considerations. All manipulations were performed under an atmosphere of dry dinitrogen using standard Schlenk and glovebox techniques, unless otherwise stated. Solvents were dried and degassed according to standard procedures. Reagent grade starting materials were purchased from commercial sources and purified according to standard procedures. The compounds $CNAr^{Dipp2}$,[27] $Mn(OTf)(CO)_3(CNAr^{Dipp2})_2$,[19] $Mn(CO)_3(CNAr^{Dipp2})_2$,[19] and $Na[BAr^F_4]$[68] (Ar^F = 3,5-$(CF_3)_2C_6H_3$) were prepared according to literature procedures. $(CH_3)_3C(O)COSi(CH_3)_3$ was identified by comparison to previous ^1H and $^{13}C\{^1H\}$ NMR and IR spectra.[69] Benzene-d_6 (Cambridge Isotope Laboratories) was stirred over NaK alloy for 2 d, distilled, degassed, and stored over 4 Å molecular sieves. Solution ^1H, $^{13}C\{^1H\}$, ^{19}F, and $^{11}B\{^1H\}$ spectra were recorded on Bruker Advance 300, Varian Mercury 400, Varian X-Sens 500, and *J*EOL ECA-500 spectrometers. ^1H and $^{13}C\{^1H\}$ NMR chemical shifts are reported in ppm relative to $SiMe_4$ (^1H and $^{13}C\{^1H\}$ δ = 0.0 ppm) with reference to residual proton resonances of 7.16 ppm (^1H) and 128.06 ppm (^{13}C) for benzene-d_6.[70] Room temperature FTIR spectra were recorded on a Thermo-Nicolet iS10 FTIR spectrometer. Samples were prepared either as KBr pellets or as benzene-d_6

solutions injected into a ThermoFisher solution cell equipped with KBr windows. Solvent peaks were digitally subtracted from all solution FTIR spectra using a previously recorded spectrum of the solvent. The following abbreviations are used to describe the intensity and characteristics of important IR absorption bands: vs = very strong, s = strong, m = medium, w = weak, vw = very weak, b = broad, vb = very broad, sh = shoulder. HR-MS was recorded at the UCSD Molecular Mass Spectrometry Facility using an Agilent 6230 Accurate-Mass TOFMS. Combustion analyses were performed by Midwest Microlab, LLC of Indianapolis, Indiana (USA). Samples for combustion analysis were obtained from the first recrystallized batch of the reaction mixture. In a typical preparation, the crude, dry reaction mixture was dissolved in a minimum amount of solvent and stored at –40 ˚C for several days to produce crystalline material. This material was then collected, thoroughly dried under vacuum and then packaged under vacuum for shipment. In most cases, this material was also used for single-crystal X-ray structure determination.

Synthesis of Mn(κ^2-*O*,*O*-($O_2CC(CH_3)_3$))$(CO)_2(CNAr^{Dipp2})_2$ (1). A 50 mL Schlenk tube with a 14/20 side-arm adapter was charged with an Et_2O solution of $Mn(OTf)(CO)_3(CNAr^{Dipp2})_2$ (0.265 g, 0.233 mmol, 20 mL) and cesium pivalate (0.234 g, 0.100 mmol, 1.3 equiv.) under a N_2 atmosphere. The sealed tube was brought out and a reflux adapter was fitted under a N_2 purge, and the solution was brought to reflux for 16 h. The deep orange mixture was cooled, brought into a glovebox, filtered through a Celite plug, and the Et_2O was removed under reduced pressure. 3 portions of pentane (10 mL) were used to extract the deep orange solution, and all volatiles

were removed under reduced pressure to yield a deep orange solid. Yield: 0.245 g, 0.219 mmol, 94%. Single crystals suitable for X-ray diffraction were prepared in a saturated $Et_2O/(Me_3Si)_2O$ solution at –40 ˚C overnight. ^{1}H NMR (500.1 MHz, C_6D_6, 20 ˚C) δ = 7.35 (t, 2H, *J* = 8 Hz, *p*-Ar), 7.22 (d, 4H, *J* = 8 Hz, *m*-Ar), 6.90 (m, 8H, *m*-Dipp), 6.83 (dd, 4H, *J* = 8, 7 Hz, *p*-Dipp), 2.76 (sept, 8H, *J* = 7 Hz, C*H*$(CH_3)_2$), 1.36 (d, 24H, *J* = 7 Hz, CH(*CH*$_3)_2$), 1.07 (d, 24H, *J* = 7 Hz, CH(C*H*$_3)_2$), 0.77 (s, 9H, C(C*H*$_3)_3$) ppm. ^{13}C{^{1}H} NMR (125.7 MHz, C_6D_6, 20 ˚C) δ = 222.9 (*C*O), 192.5 (*C*N), 178.4 ((t-Bu)*C*O_2), 146.5, 139.4, 134.8, 130.4, 129.5, 128.3, 123.7, 39.6 (*C*$(CH_3)_3$), 31.4 (*C*H$(CH_3)_2$), 27.3 (C(*C*H$_3)_3$), 24.7 (CH(*C*H$_3)_2$), 24.2 (CH(*C*H$_3)_2$) ppm. FTIR (C_6D_6, KBr windows): ν_{CN} = 2075 cm^{-1} (vs), ν_{CO} = 1967 cm^{-1} (m), 1910 cm^{-1} (s), also 2962, 2926, 2867, 1510, 1460, 1384, 758, 638, 586 cm^{-1}. Anal. Calcd for $C_{69}H_{83}MnN_2O_4$: C, 78.23; H, 7.90; N, 2.64. Found: C, 77.92; H, 8.01; N, 2.78.

Synthesis of Mn(κ^2-*O*,*O*-(O_2CCH_3))$(CO)_2(CNAr^{Dipp2})_2$ (2). A 50 mL Schlenk tube with a 14/20 side-arm adapter was charged with an Et_2O solution of $Mn(OTf)(CO)_3(CNAr^{Dipp2})_2$ (0.069 g, 0.061 mmol, 15 mL) and sodium acetate (0.007 g, 0.079 mmol, 1.3 equiv.) under a N_2 atmosphere. The sealed tube was brought out and a reflux adapter was fitted under an N_2 purge, and the solution was brought to reflux for 18 h. The deep yellow mixture was cooled, brought into a glovebox, and the Et_2O was removed under reduced pressure. The resultant yellow solid was slurried in benzene and filtered through a Celite pad. The filter cake was extracted with benzene (5 x 2 mL), and all volatiles from the yellow filtrate were removed *en vacuo* to provide a yellow solid. Yield 0.055 g, 0.056 mmol, 92%. ^{1}H NMR (500.1 MHz, C_6D_6, 20 ˚C)

δ = 7.33 (t, 2H, *J* = 8 Hz, *p*-Ar), 7.17 (d, 4H, *J* = 8 Hz, *m*-Ar), 6.89 (m, 8H, *m*-Dipp), 6.84 (dd, 4H, *J* = 8, 7 Hz, *p*-Dipp), 2.70 (sept, 8H, *J* = 7 Hz, C*H*$(CH_3)_2$), 1.35 (d, 24H, *J* = 7 Hz, CH(*CH*$_3)_2$), 1.22 (s, 3H, C(C*H*$_3$)), 1.05 (d, 24H, *J* = 7 Hz, CH(C*H*$_3)_2$) ppm. $^{13}C\{^1H\}$ NMR (125.7 MHz, C_6D_6, 20 ˚C) δ = 222.9 (*C*O), 184.5 (*C*N), 178.9 ((CH$_3$)*C*O$_2$), 146.1, 139.3, 134.2, 129.4, 129.1, 127.9, 123.2, 31.1 (*C*H(CH$_3)_2$), 24.5 (C(*C*H$_3$)), 24.1 (CH(*C*H$_3)_2$), 23.9 (CH(*C*H$_3)_2$) ppm. FTIR (C_6D_6, KBr windows): ν_{CN} = 2090 cm^{-1} (vs), ν_{CO} = 1965 cm^{-1} (m), 1907 cm^{-1} (s), also 2962, 2921, 1599, 1465, 1024, 758 cm^{-1}. Anal. Calcd. for $C_{66}H_{77}MnN_2O_4$: C, 77.93; H, 7.63; N, 2.75. Found: C, 76.76; H, 7.40; N, 2.51. Note, multiple attempts to obtain a satisfactory combustion analysis were made. We suspect that the discrepancy between the calculated and found combustion analyses arises from the presence of residual NaOTf, which is not completely removed during the filtration/crystallization purification procedures.

Synthesis of Mn(κ^2-*O*,*O*-((C$_6$H$_5$)CO$_2$))(CO)$_2$(CNAr^{Dipp2})$_2$ (3). Method A. A 50 mL Schlenk tube with a 14/20 side-arm adapter was charged with an Et_2O solution of Mn(OTf)(CO)$_3$(CNAr^{Dipp2})$_2$ (0.073 g, 0.064 mmol, 15 mL) and sodium benzoate (0.011 g, 0.076 mmol, 1.2 equiv.) under a N_2 atmosphere. The sealed tube was brought out and a reflux adapter was fitted under an N_2 purge, and the solution was brought to reflux for 30 h. The deep yellow mixture was cooled, brought into a glovebox, filtered through a Celite plug, and the Et_2O was removed under reduced pressure to provide a light orange solid. Yield, 0.062 g, 0.058 mmol, 90 %. Single crystals suitable for X-ray analysis were prepared by slow evaporation of a benzene

solution at room temperature in N_2 atmosphere. ^{1}H NMR (400.1 MHz, C_6D_6, 20 ˚C) δ = 7.68 (d, 2H, *J* = 7 Hz, *o*-Bz), 7.24 (m, 1H, *p*-Bz), 7.20 (m, 2H, *m*-Bz), 7,15 (t, 2H, *J* = 8 Hz, *p*-Ar), 7.09 (d, 4H, *J* = 8 Hz, *m*-Ar), 6.99 (d, 8H, *J* = 8 Hz, *m*-Dipp), 6.83 (m, 4H, *p*-Dipp), 2.60 (sept, 8H, *J* = 7 Hz, C*H*(CH_3)$_2$), 1.24 (d, 24H, *J* = 7 Hz, CH(C*H*$_3$)$_2$), 0.98 (d, 24H, *J* = 7 Hz, CH(C*H*$_3$)$_2$) ppm. ^{13}C{^{1}H} NMR (125.7 MHz, C_6D_6, 20 ˚C) δ = 223.3 (*C*O), 178.6 (*C*N), 177.8 (Bn-*C*O_2-Mn), 146.1, 139.9, 134.3, 131.0, 130.1, 129.7, 129.6, 128.9, 128.8, 128.6, 128.3, 127.9, 127.6, 127.5, 126.9, 123.4, 31.41 (*C*H(CH_3)$_2$), 24.5 (CH(*C*H_3)$_2$), 24.2 (CH(*C*H_3)$_2$) ppm. FTIR (C_6D_6, KBr windows): ν_{CN} = 2093 cm^{-1} (vs), ν_{CO} = 1964 cm^{-1} (m), 1910 cm^{-1} (s), also 2963, 2864, 1516, 1456, 1439, 756 cm^{-1}. Anal. Calcd for $C_{71}H_{79}MnN_2O_4$: C, 78.96; H, 7.38; N, 2.59. Found: C, 77.06; H, 7.38; N, 2.81. Note, multiple attempts to obtain a satisfactory combustion analysis were made. We suspect that the discrepancy between the calculated and found combustion analyses arises from the presence of residual NaOTf, which is not completely removed during the filtration/crystallization purification procedures.

Synthesis of Mn(κ^2-*O*,*O*-(C_6H_5)CO_2))$(CO)_2$($CNAr^{Dipp2}$)$_2$ (3). Method B. To a stirring orange solution of Mn$(CO)_3$($CNAr^{Dipp2}$)$_2$ in Et_2O (98 mg, 0.0994 mmol, 16 mL) was added a solution of benzoyl peroxide in Et_2O (0.013 g, 0.0545 mmol, 3 mL) at room temperature. After 5 minutes the color of the solution lightened, and the solution was stirred an additional 16 hours. The solvent was removed under reduced pressure, and the orange solid was washed with *n*-pentane (2 x 5 mL). The solid was collected and dried under vacuum. Yield: 0.094 g, 0.088 mmol, 88 %.

Synthesis of Mn(κ^2-*O*,*O*-(C_6H_5)CO_2))($CO)_2$($CNAr^{Dipp2}$)$_2$ (3) from 1 and benzoic acid. A Et_2O solution of benzoic acid (0.002 g, 0.016 mmol, 1.01 equiv., 1 mL) was added to a stirring Et_2O solution of **1** (0.022 g, 0.0197 mmol, 2 mL). The solution was stirred for ten minutes and then all volatile were removed under reduced pressure. ^{1}H NMR and IR analysis (C_6D_6) indicated complete formation of **3** with concomitant generation of pivalic acid. Washing of the resultant yellow solid with pentane (1 x 3 mL) provided **3** as a pure solid. Yield: 0.019 g, 0.018 mmol, 92%.

Synthesis of Mn(κ^2-*O*,*O*-(O_2CH))($CO)_2$($CNAr^{Dipp2}$)$_2$) (4). A 50 mL Schlenk tube with a 14/20 adapter was charged with an Et_2O solution of Mn(OTf)($CO)_3$($CNAr^{Dipp2}$)$_2$OTf (0.078 g, 0.069 mmol, 15 mL) and sodium formate (0.005 g, 0.074 mmol, 1.1 equiv.) under a N_2 atmosphere. The sealed tube was brought out and a reflux adapter was fitted under an N_2 purge, and the solution was brought to reflux for 36 h. The yellow mixture was cooled, brought into a glovebox, and filtered through a medium porosity fritted funnel. The filter cake was washed with Et_2O (2 x 5 mL) and then extracted with CH_2Cl_2 (3 x 10 mL). All volatiles were then removed under reduced pressure to provide a yellow solid. Yield: 0.064 g, 0.065 mmol, 94%. ^{1}H NMR (500.1 MHz, C_6D_6, 20 ˚C) δ = 8.0 (s, 1H, O_2CH), 7.38 (t, 2H, *J* = 8 Hz, *p*-Ar), 7.19 (d, 4H, *J* = 8 Hz, *m*-Ar), 6.87 (m, 8H, *m*-Dipp), 6.79 (dd, 4H, *J* = 8, 7 Hz, *p*-Dipp), 2.61 (sept, 8H, *J* = 7 Hz, $CH(CH_3)_2$), 1.35 (d, 24H, *J* = 7 Hz, $CH(CH_3)_2$), 1.02 (d, 24H, *J* = 7 Hz, $CH(CH_3)_2$) ppm. . $^{13}C\{^1H\}$ NMR (125.7 MHz, C_6D_6, 20 ˚C) δ = 223.5 (*C*O), 178.7 (O_2CH), 172.9 (*C*N), 150.4, 146.4, 139.7, 134.4,

134.2, 129.8, 123.6, 123.5, 31.4 (CH(CH$_3$)$_2$), 24.6 (CH(CH$_3$)$_2$), 24.0 (CH(CH$_3$)$_2$) ppm (three resonances corresponding to aryl carbons are obscured by the C_6D_6 signal). FTIR ($CDCl_3$, KBr windows): ν_{CN} = 2098 cm^{-1} (vs), ν_{CO} = 2018 cm^{-1} (w), 1971 cm^{-1} (m), 1907 cm^{-1} (m) also 2966, 2930, 2869, 1607, 1546, 1461, 1364, 1108 cm^{-1}. Anal. Calcd for $C_{65}H_{75}MnN_2O_4$: C, 77.82; H, 7.53; N, 2.79. Found: C, 77.90; H, 7.50; N, 2.58.

Synthesis of Mn(κ^1-*O*-(O_2CH))(CO)$_2$(Pyr)(CNAr^{Dipp2})$_2$) (4-pyr). A concentrated pyridine solution of Mn(κ^2-(O_2CH))(CO)$_2$(CNAr^{Dipp2})$_2$) (**4**) was allowed to stand at –40 ˚C for 3 d, forming dark orange crystals. ^{1}H NMR (500.1 MHz, C_6D_6, 20 ˚C) δ = 8.33 (s, 1H, O_2C*H*), 7.99 (d, 2H, *J* = 5 Hz, *o*-pyr), 7.34 (t, 2H, *J* = 8 Hz, *p*-Ar), 7.16 (d, 4H, *J* = 8 Hz, *m*-Ar), 6.86 (m, 8H, *m*-Dipp), 6.82 (dd, 4H, *J* = 8, 7 Hz, *p*-Dipp), 6.67 (br s, 1H, *p*-pyr), 6.56 (br s, 2H, *m*-pyr), 2.62 (sept, 8H, *J* = 7 Hz, C*H*(CH$_3$)$_2$), 1.38 (d, 6H, *J* = 7 Hz, CH(*CH*$_3$)$_2$),), 1.35 (d, 6H, *J* = 7 Hz, CH(*CH*$_3$)$_2$), 1.12 (m, 12H, CH(C*H*$_3$)$_2$) 1.03 (m, 24H, CH(C*H*$_3$)$_2$) ppm. ^{13}C{^{1}H} NMR (125.7 MHz, C_6D_6, 20 ˚C) δ = 221.7 (*C*O), 209.9 (*C*O), 178.7 (*C*N), 167.7 (O_2*C*H), 153.5, 146.5, 146.4, 139,8, 139.7, 139,5, 134.7, 134.4, 129.9, 129.7, 129.5, 124.6, 123.5, 31.5 (CH(CH$_3$)$_2$), 31.4 (CH(CH$_3$)$_2$), 24.7 (CH(CH$_3$)$_2$), 24.6 (CH(CH$_3$)$_2$), 24.2 (CH(CH$_3$)$_2$), 24.0 (CH(CH$_3$)$_2$) ppm. FTIR (C_6D_6, KBr windows): ν_{CN} = 2081 cm^{-1} (vs), ν_{CO} = 1969 cm^{-1} (m), 1909 cm^{-1} (m), 1895 cm^{-1} (m) also 2962, 2926, 2869, 1597, 1462, 1243, 1157, 1030, 758, 641 cm^{-1}. Anal. Calcd for $C_{70}H_{80}MnN_3O_4$: C, 77.68; H, 7.45; N, 3.88. Found: C,

78.46; H, 7.87; N, 3.15. Combustion analysis reflects the presence of residual pyridine which is not removed upon prolonged exposure to vacuum.

Synthesis of Mn(κ^1-*O*-((C_6H_5)CO_2))(CO)$_3$($CNAr^{Dipp2}$)$_2$ (5). A C_6D_6 solution of Mn(κ^2-$C_6H_5O_2$)(CO)$_2$($CNAr^{Dipp2}$)$_2$ (**3**; 0.011 g, 0.010 mmol, 1 mL) was added to a J. Young NMR tube. The solution was subjected to two freeze-pump-thaw cycles, after which 1 atmosphere of CO was introduced. Spectroscopic analysis demonstrated a complete conversion to the κ^1-benzoate complex. ^{1}H NMR (500.1 MHz, C_6D_6, 20 ˚C) δ = 8.14 (d, 2H, *J* = 7 Hz, *o*-Bz), 7.37 (t, 1H, *J* = 7 Hz, *p*-Bz), 7.31 (t, 2H, *J* = 8 Hz, *p*-Ar), 7.20 (m, 2H, *m*-Bz), 7.16 (d, 4H, *J* = 8 Hz, *m*-Ar), 6.83 (d, 8H, *J* = 7 Hz, *m*-Dipp), 6.78 (m, 4H, *p*-Dipp), 2.57 (sept, 8H, *J* = 7 Hz, C*H*(CH_3)$_2$), 1.28 (d, 24H, *J* = 7 Hz, CH(C*H*$_3$)$_2$), 1.00 (d, 24H, *J* = 7 Hz, CH(C*H*$_3$)$_2$) ppm. ^{13}C{^{1}H} NMR (125.7 MHz, C_6D_6, 20 ˚C) δ = 217.1(Bn-*C*O-Mn), 210.7 (*C*O), 184.5 (*C*O), 172.6 (*C*N), 169.8, 146.3, 139.8, 138.7, 137.8, 134.2, 131.1, 129.8, 129.7, 128.5, 128.3 126.9, 123.6, 31.4(*C*H(CH_3)$_2$), 24.5 (CH(*C*H$_3$)$_2$), 24.2 (CH(*C*H$_3$)$_2$) ppm. IR spectroscopic analysis was impeded due to the dissociation of CO at elevated temperatures. Single crystals of Mn(κ^1-$C_6H_5O_2$)(CO)$_3$($CNAr^{Dipp2}$)$_2$ were retrieved from storage of the reaction mixture of **S1.5** at 238K immediately after addition of benzoyl peroxide. Satisfactory elemental analysis could not be attained due to thermal decomposition to Mn(κ^2-(C_6H_5)CO_2)(CO)$_2$($CNAr^{Dipp2}$)$_2$ (**3**) and CO.

Synthesis of Mn(κ^1-*O*-(O_2CCF_3))($CO)_3$($CNAr^{Dipp2}$)$_2$ (6). A 50 mL Schlenk tube with a 14/20 side-arm adapter was charged with an Et_2O solution of $Mn(OTf)(CO)_3(CNAr^{Dipp2})_2$ (0.030 g, 0.026 mmol, 20 mL) and sodium trifluoroacetate (0.005 g, 0.037 mmol, 1.5 equiv.) under a N_2 atmosphere. The sealed tube was brought out and a reflux adapter was fitted under an N_2 purge, and the solution was brought to reflux for 18 h. The light yellow mixture was cooled, brought into a glovebox, filtered through a Celite plug, and the Et_2O was removed under reduced pressure. This residue was taken up in *ca.* 10 mL pentane and filtered through a Celite plug, and all volatiles were removed under reduced pressure to provide a dark yellow solid. Yield 0.025 g, 0.023 mmol, 87%. Single crystals suitable for X-ray diffraction were grown from a concentrated diethyl ether solution at –40 ˚C overnight. ^{1}H NMR (500.1 MHz, C_6D_6, 20 ˚C) δ = 7.44 (t, 2H, *J* = 8 Hz, *p*-Ar), 7.19 (d, 4H, *J* = 8 Hz, *m*-Ar), 6.85 (m, 8H, *m*-Dipp), 6.80 (dd, 4H, *J* = 8, 7 Hz, *p*-Dipp), 2.59 (sept, 8H, *J* = 7 Hz, C*H*(CH_3)$_2$), 1.32 (d, 24H, *J* = 7 Hz, CH(*C*H_3)$_2$), 1.00 (d, 24H, *J* = 7 Hz, CH(C*H*$_3$)$_2$) ppm. ^{13}C{^{1}H} NMR (125.7 MHz, C_6D_6, 20 ˚C) δ = 217.6 (*C*O), 208.6 (*C*-O), 170.4 (*C*N), 162.5 (q, *J* = 36 Hz, *C*F_3), 146.5, 140.0, 134.1, 129.9, 123.6, 31.4 (C*H*(CH_3)$_2$), 24.5 (CH(C*H*$_3$)$_2$), 24.1 (CH(C*H*$_3$)$_2$) ppm. ^{19}F NMR (470.6 MHz, C_6D_6, 20 ˚C) δ = –72.3 ppm. FTIR (C_6D_6, KBr windows): ν_{CN} = 2119 cm^{-1} (vs), ν_{CO} = 2024 cm^{-1} (s), 1946 cm^{-1} (s), also 2963, 2927, 2869, 1687 (w), 1596, 1463, 1193, 1138, 755, 647 cm^{-1}. Anal. Calcd for $C_{67}H_{74}F_3MnN_2O_5$: C, 73.21; H, 6.78; N, 2.55. Found: C, 73.79; H, 6.95; N, 2.61. Note, we suspect that the discrepancy between the calculated and found combustion analyses arises from the presence of residual NaOTf, which is not completely removed during the filtration/crystallization purification procedures.

Synthesis of K[(η^4-4-Ar^{Dipp}-6,10-diisopropylazabenz[*b*]azulene)Mn(CO)$_2$(CNAr^{Dipp2})] (7). A room temperature toluene solution of Mn(κ^2-($O_2CC(CH_3)_3$)(CO)$_2$(CNAr^{Dipp2})$_2$) (**1**, 0.037 g, 0.033 mmol, 2 mL) was added to KC_8 (0.009 g, 0.066 mmol, 2 equiv.) and manually mixed with a pipette for five minutes. The mixture was filtered through a filter pipette to provide a red solution, and all volatiles were removed *en vacuo* to yield a red solid. Storage of a concentrated Et_2O/$(Me_3Si)_2O$ solution at –40 ˚C provides red crystals suitable for crystallographic analysis. Yield: 0.019 g, 0.020 mmol, 60%. ^{1}H NMR (400.1 MHz, C_6D_6, 20 ˚C) δ = 7.85 (d, 1H, *J* = 8 Hz, *4-H*), 7.41 (t, 1H, *J* = 8 Hz, *5-H*), 7.32 (m, 4H), 7.20 (m, 2H), 7.10 (m, 2H), 6.96 (m, 2H), 6.87 (m, 4H), 6.14 (d, 1H, *J* = 8 Hz, *10-H*), 5.08 (d, 1H, *J* = 8 Hz, *12-H*), 3.84 (sept, 1H, *J* = 7 Hz, C*H*(CH_3)$_2$), 2.86 (m, 6H, C*H*(CH_3)$_2$), 2.23 (sept, 1H, *J* = 7 Hz, C*H*(CH_3)$_2$), 1.73 (d, 3H, *J* = 7 Hz, C*H*(CH_3)$_2$), 1.55 (d, 6H, *J* = 7 Hz, C*H*(CH_3)$_2$), 1.54 (d, 6H, *J* = 7 Hz, C*H*(CH_3)$_2$), 1.31 (d, 3H, *J* = 7 Hz, C*H*(CH_3)$_2$), 1.16 (m, 15H, C*H*(CH_3)$_2$) 1.07 (d, 3H, *J* = 7 Hz, C*H*(CH_3)$_2$), 0.97 (d, 3H, *J* = 7 Hz, C*H*(CH_3)$_2$), 0.89 (m, 6H, C*H*(CH_3)$_2$), 0.83 (d, 3H, *J* = 7 Hz, C*H*(CH_3)$_2$) ppm. ^{13}C{^{1}H} NMR (125.7 MHz, C_6D_6, 20 ˚C) δ = 246.6 (*C*O), 223.4 (*C*N), 150.0, 149.2, 147.4, 146.9, 146.8, 146.5, 140.8, 140.3, 138.4, 137.5, 136.4, 135.8, 130.8, 129.5, 128.8, 124.2, 123.07, 122.1, 121.9, 120.6, 119.8, 91.3, 47.9, 31.7 (*C*H(CH_3)$_2$), 31.3 (*C*H(CH_3)$_2$), 31.2 (*C*H(CH_3)$_2$), 30.8 (*C*H(CH_3)$_2$), 25.2 (CH(*C*H_3)$_2$), 24.8 (CH(*C*H_3)$_2$) 24.6 (CH(*C*H_3)$_2$), 24.4 (CH(*C*H_3)$_2$), 23.7 (CH(*C*H_3)$_2$), 23.2 (CH(*C*H_3)$_2$) ppm (three resonances corresponding to aryl carbons are obscured by the C_6D_6 signal). FTIR (C_6D_6, KBr windows): ν_{CN} = 2048 cm^{-1} (s), 2016 cm^{-1} (vs), ν_{CO} = 1888 cm^{-1} (vs), 1809 cm^{-1} (s), also 2956, 2863, 1610, 1580, 1566, 1460, 1416, 1386,

1253, 1056, 844, 825, 760 cm^{-1}. Anal. Calcd for $C_{64}H_{74}KMnN_2O_2$: C, 77.08; H, 7.48; N, 2.81. Found: C, 77.06; H, 7.77; N, 2.42.

Synthesis of Mn(κ²-*H*,*H*-(BH_4))($CO)_2$($CNAr^{Dipp2}$)$_2$ (8). To a diethyl ether solution of Mn(κ²-($O_2CC(CH_3)_3$))($CO)_2$($CNAr^{Dipp2}$)$_2$ (**1**; 0.072 g, 0.068 mmol, 2 mL) was added a slurry of Li[BH_4] in diethyl ether (0.005 g, 0.023 mmol, 3 equiv., 1 mL). The mixture was allowed to stir at room temperature for 16 h, after which it was filtered through a Celite pad and all volatiles removed under reduced pressure. The resulting residue was re-dissolved in *n*-pentane (2 mL) and filtered through a fiberglass pad. All volatiles were removed under reduced pressure, providing a yellow solid. Yield: 0.060 g, 0.062 mmol, 91%. Single crystals are grown from a concentrated diethyl ether solution at –40 ˚C overnight. ^{1}H NMR (400.1 MHz, C_6D_6, 20 ˚C) δ = 7.31 (t, 2H, *J* = 8 Hz, p-Ar), 7.16 (d, 8H, *J* = 8 Hz, m-Dipp), 6.92 (d, 4H, *J* = 8 Hz, m-Ar), 6.86 (m, 4H, p-Dipp), 2.69 (sept, 8H, *J* = 7 Hz, C*H*(CH_3)$_2$), 1.31 (d, 24H, *J* = 7 Hz, CH(C*H*$_3$)$_2$), 1.04 (d, 24H, *J* = 7 Hz, CH(C*H*$_3$)$_2$), -11.71 (br s, *H*$_4$B) ppm. ^{13}C{^{1}H} NMR (125.7 MHz, C_6D_6, 20 ˚C) δ = 221.1 (*C*O), 178.0 (*C*N), 146.4, 139.6, 134.6, 129.9, 129.6, 128.6, 128.3, 123.5, 31.4 (C*H*(CH_3)$_2$), 24.7 (CH(C*H*$_3$)$_2$), 24.1 (CH(C*H*$_3$)$_2$) ppm (three resonances corresponding to aryl carbons are obscured by the C_6D_6 signal). ^{11}B{^{1}H} NMR (160.4 MHz, C_6D_6, 20 ˚C) δ = –26.9 ppm. FTIR (C_6D_6, KBr windows): ν_{BH} = 2467 cm^{-1} (w), 2428 cm^{-1} (w), ν_{CN} = 2097 cm^{-1} (vs), ν_{CO} = 2043 cm^{-1} (w), 1983 cm^{-1} (s), 1936 cm^{-1} (s), also 2961, 2925, 2867, 1597, 1458, 1260, 1118,

755, 652 cm^{-1}. Anal. Calcd for $C_{64}H_{78}BMnN_2O_2$: C, 78.98; H, 8.08; N, 2.88. Found C, 78.84; H, 7.97; N, 2.90

Synthesis of Mn(κ²-*H*,*H*-($F_3CSO_3BH_3$))($CO)_2$($CNAr^{Dipp2}$)$_2$ (8-OTf). To a stirred thawing toluene solution of **7** (0.046 g, 0.047 mmol, 2 mL) was added neat triflic acid (4.4 μl, 0.049 mmol, 1.05 equiv.), and the solution was allowed to warm over 30 min. Thereafter the solution was filtered and all volatiles were removed, providing a dark yellow residue. The solid was dissolved in *n*-pentane (2 mL), filtered, and the solvent removed *en vacuo* to provide a yellow solid. Yield: 0.045 g, 0.040 mmol, 86%. Diffraction quality crystals were grown from a concentrated diethyl ether solution at –40 ˚C. ^{1}H NMR (500.2 MHz, C_6D_6, 20 ˚C) δ = 7.38 (t, 1H, *J* = 8 Hz, *p*-Ar), 7.30 (t, 1H, *J* = 8 Hz, p-Ar), 7.20 (d, 8H, *J* = 8 Hz, *m*-Dipp), 6.90 (d, 4H, *J* = 8 Hz, *m*-Ar), 6.86 (m, 4H, *p*-Dipp), 2.69 (sept, 4H, *J* = 7 Hz, C*H*(CH_3)$_2$), 2.62 (sept, 4H, *J* = 7 Hz, C*H*(CH_3)$_2$), 1.35 (d, 12H, *J* = 7 Hz, CH(C*H*$_3$)$_2$), 1.25 (d, 12H, *J* = 7 Hz, CH(C*H*$_3$)$_2$), 1.03 (m, 24H, CH(C*H*$_3$)$_2$), –11.3 (br s, *H*$_3$B) ppm. ^{13}C{^{1}H} NMR (125.7 MHz, C_6D_6, 20 ˚C) δ = 219.5 (*C*O), 173.5 (*C*N), 172.5 (*C*N), 146.4, 146.2, 139.9, 139.7, 134.4, 134.0, 130.6, 130.0, 129.9, 129.7, 123.6, 31.4 (C*H*(CH_3)$_2$), 24.7 (CH(C*H*$_3$)$_2$), 24.6 (CH(C*H*$_3$)$_2$), 24.0 (CH(C*H*$_3$)$_2$), 23.9 (CH(C*H*$_3$)$_2$) ppm. ^{11}B{^{1}H} NMR (160.4 MHz, C_6D_6, 20 ˚C) δ = 28.8 ppm. FTIR (C_6D_6, KBr windows): ν_{BH} = 2467 cm^{-1} (w), 2428 cm^{-1} (w), ν_{CN} = 2104 cm^{-1} (vs), ν_{CO} = 2032 cm^{-1} (w), 2004 cm^{-1} (m), 1958 cm^{-1} (s), also 2963, 2925, 2868, 1615, 1457, 1396, 1249, 1202, 955, 755, 633 cm^{-1}. A satisfactory elemental analysis for this compound could not be obtained despite repeated attempts.

Synthesis of $Mn(OTf)(CO)_2(CNAr^{Dipp2})_2$ (9). Method A. In a typical preparation, $Mn(\kappa^2\text{-}(O_2CC(CH_3)_3))(CO)_2(CNAr^{Dipp2})_2$ (**1**, 0.047 g, 0.042 mmol) was dissolved in pentane and stirred as neat Me_3SiOTf (10 μl, 0.055 mmol, 1.3 equiv.) added. The reaction mixture was stirred for 25 minutes, during which time the solution became light red. At this time all volatiles were removed *en vacuo* to provide a red-orange residue. ^1H NMR analysis of this residue demonstrated full conversion to $Mn(CO)_2(CNAr^{Dipp2})_2(OTf)$ and $(CH_3)_3C(O)COSi(CH_3)_3$. *Note*: Continued stirring of the solution leads to decomposition of $Mn(OTf)(CO)_2(CNAr^{Dipp2})_2$ to form $Mn(OTf)(CO)_3(CNAr^{Dipp2})_2$ and other intractable products.

Method B. In a representative reaction, $Mn(\kappa^2\text{-}(O_2CC(CH_3)_3))(CO)_2(CNAr^{Dipp2})_2$ (**1**, 0.021 g, 0.019 mmol) was dissolved in benzene (2 mL) and stirred to generate a yellow-orange solution. Neat triflic acid (1.75 μl, 0.020 mmol, 1.05 equiv.) was added to the solution and stirred for 2 minutes, during which time the solution became orange. ^1H NMR analysis confirmed the production of $Mn(OTf)(CO)_2(CNAr^{Dipp2})_2$ with concomitant formation of pivalic acid, as well as small amount of $Mn(OTf)(CO)_3(CNAr^{Dipp2})_2$ resulting from decomposition of $Mn(OTf)(CO)_2(CNAr^{Dipp2})_2$.

Characterization data for $Mn(OTf)(CO)_2(CNAr^{Dipp2})_2$ (9): ^1H NMR (500.1 MHz, C_6D_6, 20 ˚C) δ = 7.33 (t, 2H, *J* = 8 Hz, *p*-Ar), 7.20 (d, 4H, *J* = 8 Hz, *m*-Ar), 6.93 (m, 12H, *m*-Dipp and *p*-Dipp), 2.74 (sept, 8H, *J* = 7 Hz, C*H*$(CH_3)_2$), 1.35 (m, 24H, CH(*CH*$_3)_2$), 1.04 (d, 24H, *J* = 7 Hz, CH(C*H*$_3)_2$) ppm. $^{13}C\{^1H\}$ NMR (125.7 MHz,

C_6D_6, 20 ˚C) δ = 223.9 (*C*O), 171.7 (*C*N), 146.4, 140.0, 134.3, 130.6, 129.8, 123.7, 31.4 (*C*H(CH_3)$_2$), 24.9 (CH(*C*H_3)$_2$), 23.8 (CH(*C*H_3)$_2$) ppm. ^{19}F NMR (282.2 MHz, C_6D_6, 20 ˚C) δ = -76.9 (s) ppm. FTIR (C_6D_6, KBr windows): ν_{CN} = 2096 cm^{-1} (vs), ν_{CO} = 1990 cm^{-1} (m), 1934 cm^{-1} (s), also 2962, 2925, 2869, 1402, 1342, 1211, 1156, 1006, 849, 755, 626 cm^{-1}. Due to the instability of Mn(OTf)(CO)$_2$(CNAr^{Dipp2})$_2$ a satisfactory combustion analysis was not obtained.

Characterization data for Mn(OTf)(THF)(CO)$_2$(CNAr^{Dipp2})$_2$ (9-THF). ^{1}H NMR (400.1 MHz, C_6D_6, 20 ˚C) δ = 7.29 (t, 2H, *J* = 8 Hz, *p*-Ar), 7.17 (d, 4H, *J* = 8 Hz, *m*-Ar), 6.88 (m, 12H, *m*-Dipp and *p*-Dipp), 2.75 (sept, 8H, *J* = 7 Hz, C*H*(CH_3)$_2$), 2.58 (m, 4H, *THF*), 1.44 (d, 12H, *J* = 7 Hz, CH(*CH*$_3$)$_2$), 1.40 (d, 12H, *J* = 7 Hz, CH(*CH*$_3$)$_2$), 1.12 (m, 4H, *THF*), 1.03 (d, 24H, *J* = 7 Hz, CH(C*H*$_3$)$_2$) ppm. ^{13}C{^{1}H} NMR (125.7 MHz, C_6D_6, 20 ˚C) δ = 225.2 (*C*O), 219.1 (*C*O), 173.4 (*C*N), 147.1, 147.0, 139.7, 135.0, 130.8, 129.6, 123.6, 123.3, 74.2 (THF), 31.4 (*C*H(CH_3)$_2$), 26.7 (THF), 24.9 (CH(*C*H_3)$_2$), 24.7 (CH(*C*H_3)$_2$), 24.2 (CH(*C*H_3)$_2$), 24.0 (CH(*C*H_3)$_2$) ppm. FTIR (C_6D_6, KBr windows): ν_{CN} = 2093 cm^{-1} (vs), 2032 cm^{-1} (w), ν_{CO} = 1993 cm^{-1} (m), 1954 cm^{-1} (w), 1918 cm^{-1} (s), also 2963, 2928, 2868, 1594, 1460, 1395, 1322, 1234, 1210, 1172, 1024, 963, 626 cm^{-1}. Anal. Calcd for $C_{69}H_{82}F_3MnN_2O_6S$: C, 70.28; H, 7.01; N, 2.37. Found: C, 70.73; H, 6.99; N, 2.76.

Synthesis of [Mn(CO)$_2$(CNAr^{Dipp2})$_2$(OEt$_2$)$_2$]BAr$^F_4$ (10). To a *n*-pentane solution of Mn(OTf)(CO)$_2$(CNAr^{Dipp2})$_2$ (**9**), prepared as in S1.10 (Method A), was added solid

$NaBAr^F_4$ (0.039 g, 1.05 equiv. based on $Mn(OTf)(CO)_2(CNAr^{Dipp2})_2$). A red precipitate quickly evolved from solution, and the mixture was stirred for an additional 20 minutes. The mixture was then filtered through a Celite plug, and the residual solid was washed with *n*-pentane (3 x 5 mL). The solid was extracted with benzene (2 x 5 mL) from the Celite to provide a deep red solution. All volatiles were then removed *en vacuo* to provide a red-brown residue. Dissolution of this residue in a minimal amount of Et_2O, followed by storage at –40 ˚C for 4 d produced light yellow crystals, which were collected and washed with 2 mL *n*-pentane. Yield: 0.046 g, 0.023 mmol, 56% (based on $Mn(\kappa^2\text{-}(O_2CC(CH_3)_3))(CO)_2(CNAr^{Dipp2})$). ^{1}H NMR (500.1 Hz, C_6D_6, 20 ˚C) δ = 8.39 (s, 8H, *o*-Ar^F), 7.72 (s, 4H, *p*-Ar^F), 7.20 (m, 2H, *p*-Ar), 7.07 (d, 4H, *J* = 8 Hz, *m*-Ar), 6.83 (m, 12H, *p*-Dipp and *m*-Dipp), 3.67 (br s, Et_2O), 2.48 (sept, 8H, *J* = 7 Hz, C*H*$(CH_3)_2$), 1.09 (d, 24H, *J* = 7 Hz, CH(*CH*$_3)_2$), 0.99 (d, 24H, *J* = 7 Hz, CH(C*H*$_3)_2$) ppm. ^{13}C{^{1}H} NMR (125.7 MHz, C_6D_6, 20 ˚C) δ = 220.5 (*C*O), 182.7(*C*-N), 162.3 (q, *J* = 50 Hz, *C*F_3), 146.3, 146.1, 139.3, 135.1, 134.0, 133.5, 130.1, 129.6, 129.4, 126, 123.8, 123.2, 117.7, 74.9 (O(*C*$H_2CH_3)_2$, 30.9 (*C*$(CH_3)_3$), 23.9 (CH(*C*$H_3)_2$), 23.2 (CH(*C*$H_3)_2$), 14.9 (O(CH_2*C*H_3) ppm. ^{19}F NMR (470.6 MHz, C_6D_6, 20 ˚C) δ = -62.5 (s, Ar^F-C*F*$_3$) ppm. FTIR (C_6D_6, KBr windows): ν_{CN} = 2111 cm^{-1} (vs), 2010 cm^{-1} (m), ν_{CO} = 1991 cm^{-1} (m), 1932 cm^{-1} (s), also 2958, 2926, 2866, 1356, 1280, 1163, 1130, 712, 685, 674 cm^{-1}. Despite repeated attempts, a satisfactory elemental analysis could not be obtained.

Synthesis of $Mn(CO)_2(CNAr^{Dipp2})(\eta^2\text{-}(C,H\text{-}CH_3)(CH_3)_2CCO_2B(C_6F_5)_3)$ (11). To a stirring benzene solution of $Mn(\kappa^2\text{-}(O_2CC(CH_3)_3)(CO)_2(CNAr^{Dipp2})_2)$ (**1**, 0.020 g, 0.018 mmol, 2 mL) was added a solution of $B(C_6F_5)_3$ (0.010 g, 0.020 mmol, 1.1 equiv., 1 mL). Over the course of 1 h the orange solution gradually became dark red, after which the solvent was removed under reduced pressure to provide a tacky red solid. Recrystallization from diethyl ether at –40 ˚C provided $Mn(CO)_2(CNAr^{Dipp2})(\eta^2\text{-}(C,H\text{-}CH_3)CCO_2B(C_6F_5)_3)$ as a red solid. Yield: 0.018 g, 0.015 mmol, 85%. ^{1}H NMR (500.1 Hz, C_6D_6, 20 ˚C) δ = 7.35 (t, 2H, *J* = 8 Hz, *p*-Ar), 7.11 (d, 4H, *J* = 8 Hz, *m*-Ar), 6.97 (m, 4H, *p*-Dipp), 6.90 (m, 8H, *m*-Dipp), 2.69 (sept, 4H, *J* = 7 Hz, C*H*$(CH_3)_2$), 2.57 (sept, 4H, *J* = 7 Hz, C*H*$(CH_3)_2$), 1.22 (m, 24H, CH(*CH*$_3)_2$), 1.04 (d, 12H, *J* = 7 Hz, CH(C*H*$_3)_2$), 1.00 (d, 12H, *J* = 7 Hz, CH(C*H*$_3)_2$), -0.60 (br s, 9H, C(C*H*$_3)_3$) ppm. ^{13}C{^{1}H} NMR (125.7 MHz, C_6D_6, 20 ˚C) δ = 222.0 (*C*O), 186.5 (*C*N), 168.1 ((t-Bu)*C*O_2), 147.4 (B(*C*$_6F_5$)), 146.7, 146.4, 139.4, 138.5 (B(*C*$_6F_5$)), 136.5 (B(*C*$_6F_5$)), 134.8, 131.5, 130.7, 123.6, 36.9 (*C*$(CH_3)_3$), 31.2 (*C*H$(CH_3)_2$), 30.8 (*C*H$(CH_3)_2$), 25.3 (C(*C*H$_3)_3$), 25.2 (CH(*C*H$_3)_2$), 25.0 (CH(*C*H$_3)_2$), 23.5 (CH(*C*H$_3)_2$), 23.4 (CH(*C*H$_3)_2$) ppm. ^{19}F NMR (282.2 MHz, C_6D_6, 20 ˚C) δ = –131.1 (br s), –145.0 (br s), –161.2 (br s) ppm. ^{11}B NMR (96.2 MHz, C_6D_6, 20 ˚C) δ = -22.8 ppm. FTIR (C_6D_6, KBr windows): ν_{CN} = 2124 cm^{-1} (w), 2104 cm^{-1} (vs), ν_{CO} = 2012 cm^{-1} (m), 1946 cm^{-1} (s), $\nu_{C=O}$ = 1646 cm^{-1} (m), also 2964, 2928, 2869, 1594, 1518, 1471, 1382, 1285, 1099, 979, 759, 668 cm^{-1}. A small amount of $(F_5C_6)_3B\leftarrow CNAr^{Dipp2}$ generated during the reaction prevented the acquisition of a satisfactory combustion analysis.

Synthesis of $(F_5C_6)_3B\leftarrow CNAr^{Dipp2}$. The isocyanide-borane adduct can be readily prepared in quantitative yield by addition of solid $CNAr^{Dipp2}$ to a solution of $B(C_6F_5)_3$ in C_6D_6 in a 1:1 stoichiometry. Characterization data: ^{1}H NMR (500.1 Hz, C_6D_6, 20 ˚C) δ = 7.24 (t, 2H, *J* = 8 Hz, *p*-Dipp), 7.19 (d, 2H, *J* = 8 Hz, *m*-Ar), 6.96 (d, 4H, *m*-Dipp), 6.85 (m, 1H, *p*-Ar), 2.43 (sept, 4H, *J* = 7 Hz, C*H*$(CH_3)_2$), 1.09 (d, 12H, *J* = 7 Hz, CH(*CH*$_3)_2$), 0.87 (d, 12H, *J* = 7 Hz, CH(C*H*$_3)_2$) ppm. ^{13}C{^{1}H} NMR (125.7 MHz, C_6D_6, 20 ˚C) δ = 149.0 (*C*N), 147.1 (B(*C*$_6F_5$)), 146.4, 141.9 (B(*C*$_6F_5$)), 141.0, 138.4 (B(*C*$_6F_5$)), 136.4 (B(*C*$_6F_5$)), 132.0, 131.6, 131.5, 130.6, 123.4, 31.4 (*C*$(CH_3)_3$), 25.3 (C(*C*$H_3)_3$), 22.7 (CH(*C*H_3) ppm. ^{19}F NMR (282.2 MHz, C_6D_6, 20 ˚C) δ = -131.5 (d, 6 F, *J* = 37 Hz, *o*-F), -155.9 (t, 3 F, *J* = 20 Hz, *p*-F), -162.6 (m, 6 F, *m*-F). ^{11}B NMR (96.2 MHz, C_6D_6, 20 ˚C) δ = –21.7 ppm. Anal. Calcd for $C_{49}H_{37}BF_{15}N$: C, 62.89; H, 3.98; N, 1.50. Found: C, 63.89; H, 4.64; N, 1.63.

Synthesis of $Mn(CO)_2(\eta^2$-*C,N*-$(H_3CCNAr^{Dipp2}))(CNAr^{Dipp2})$ (12). To a stirring solution of κ^2-$(O_2CC(CH_3)_3Mn(CO)_2(CNAr^{Dipp2})_2)$ in thawing pentane (0.055 g, 0.057 mmol, 5 ml) was added Al_2Me_6 (0.009 g, 11.5 μl, 1,05 eq.) as a neat liquid. The yellow reaction solution slowly becomes deep red, after which it becomes green and finally deep blue over the course of 20 minutes. The resultant solution is then filtered through a fiberglass plug, and the volatiles are removed under reduced pressure to yield a deep blue solid. Yield 0.036 g, 67 %. Single crystals are grown from a slowly evaporating pentane solution at 298K. ^{1}H NMR (400.1 MHz, C_6D_6, 20 ºC) δ = 7.32 (t, 2H, J = 8 Hz, p-Ar), 7.20 (d, 4H, J = 8 Hz, m-Dipp), 7.13 (d, 2H, J = 8 Hz, m-Ar),

7.04 (d, 4H, J = 8 Hz, m-Dipp), 6.94 (d, 2H, J = 8 Hz, m-Ar), 6.86 (m, 2H, p-Dipp), 2.76 (sept, 4H, J = 7 Hz, C*H*$(CH_3)_2$), 2.64 (sept, 4H, J = 7 Hz, C*H*$(CH_3)_2$), 2.38 (s, 3H, (H_3CCN)), 1.25 (d, 12H, J = 7 Hz, CH(C*H*$_3)_2$), 1.21 (d, 12H, J = 7 Hz, CH(C*H*$_3)_2$), 1.12 (d, 12H, J = 7 Hz, CH(C*H*$_3)_2$), 1.03 (d, 12H, J = 7 Hz, CH(C*H*$_3)_2$) ppm. $^{13}C\{^1H\}$ NMR (125.7 MHz, C_6D_6, 20 ºC) δ = 244.8 (*C*O), 230 (*C*O), 194.7 (η^2-*C*N), (CN), 146.7, 145.9, 143.0, 138.1, 135.8, 135.3, 133.9, 131.3, 129.7, 129.1, 129.0, 128.3, 125.7, 125.5, 123.4, 123.2, 31.5 (C*H*$(CH_3)_2$), 30.9 (C*H*$(CH_3)_2$), 26.2 (CH(C*H*$_3)_2$), 24.6 (CH(C*H*$_3)_2$), 24.5 (H_3*C*CN), 24.4 (CH(C*H*$_3)_2$), 23.1 (CH(C*H*$_3)_2$) ppm. FTIR (C_6D_6, KBr windows): ν_{CN} = 2069 cm^{-1} (s), ν_{CO} = 1934 cm^{-1} (vs), 1890 cm^{-1} (s), $\nu_{iminoacyl}$ = 1601 cm^{-1} (s), also 2963, 2927, 2868, 1491, 1449, 1384, 1196, 1056, 754, 702 cm^{-1}. Despite repeated attempts, a satisfactory elemental analysis was not obtained.

4.6 Selected ^{1}H NMR Spectra

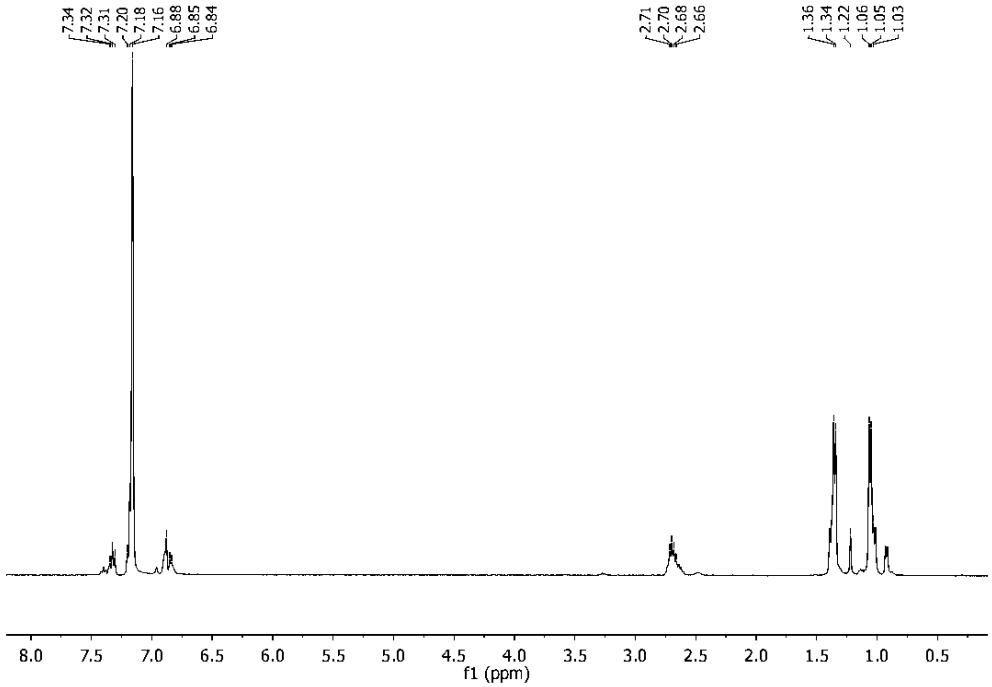

Figure 4.11. ^{1}H NMR spectrum (500.1 MHz, 20 ˚C, C_6D_6) of Mn(κ^2-*O*,*O*-(O_2CCH_3))($CO)_2$($CNAr^{Dipp2}$)$_2$

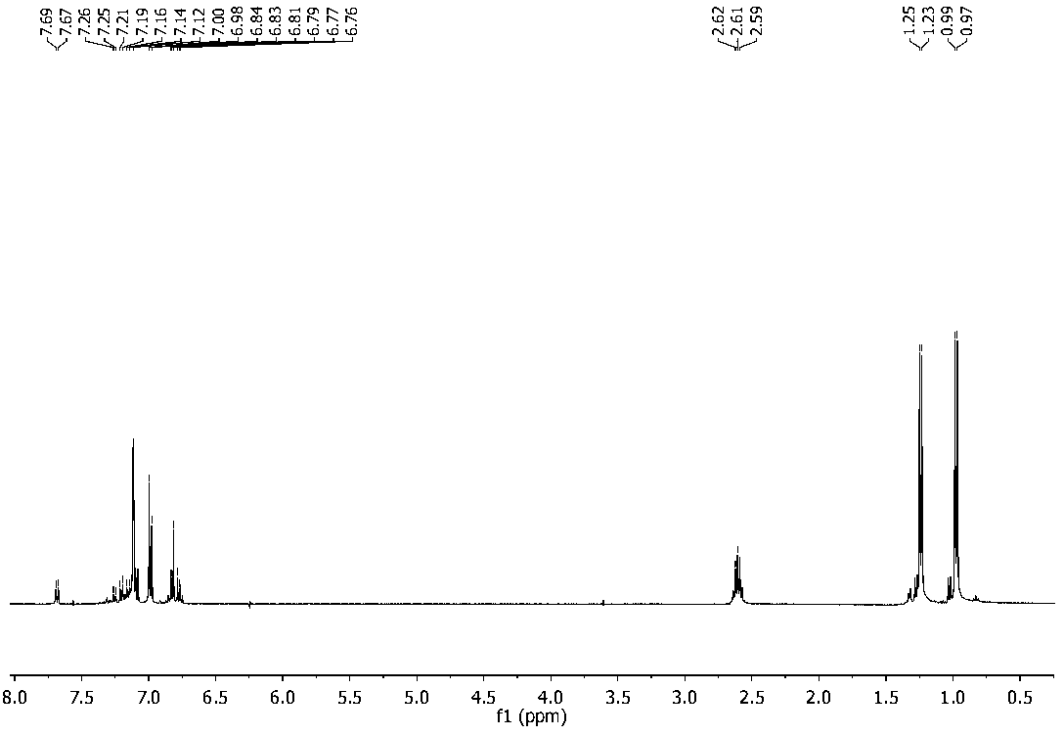

Figure 4.12. ^{1}H NMR spectrum (400.1 MHz, 20 ˚C, C_6D_6) of Mn(κ^2-*O*,*O*-($O_2C(C_6H_5)$))($CO)_2$($CNAr^{Dipp2}$)$_2$ (**3**).

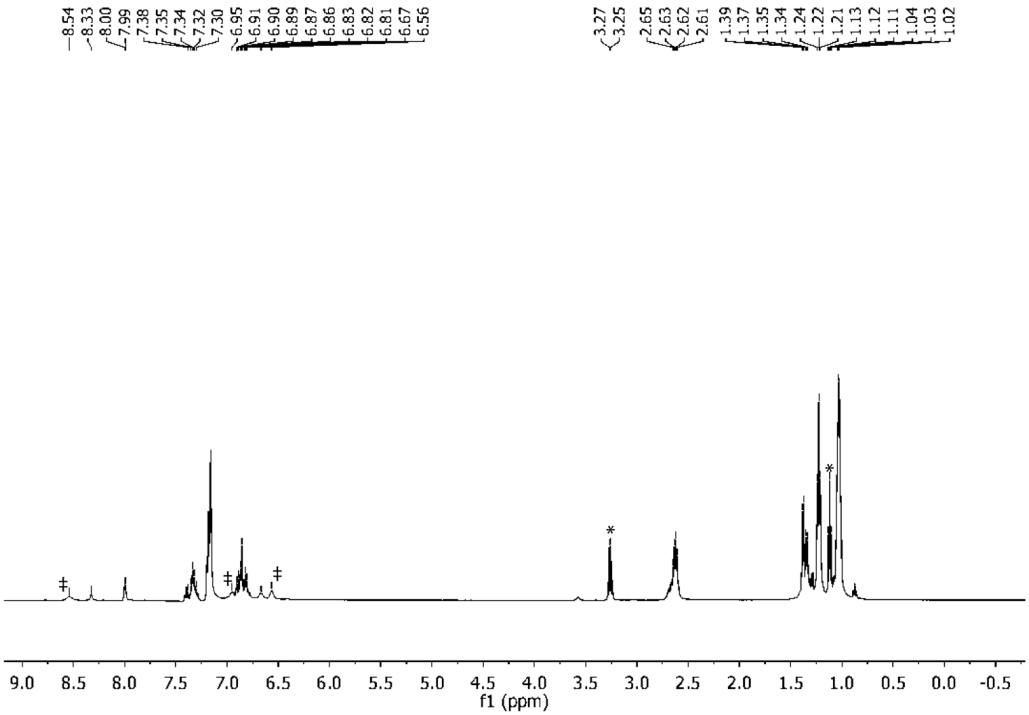

Figure 4.13. ^{1}H NMR spectrum (500.1 MHz, 20 ˚C, C_6D_6) of Mn(κ^1-*O*-(O_2CH))($CO)_2$(Pyr)($CNAr^{Dipp2}$)$_2$) **(4-pyr)**. The symbols (‡) and (*) denote free pyridine and free Et_2O, respectively.

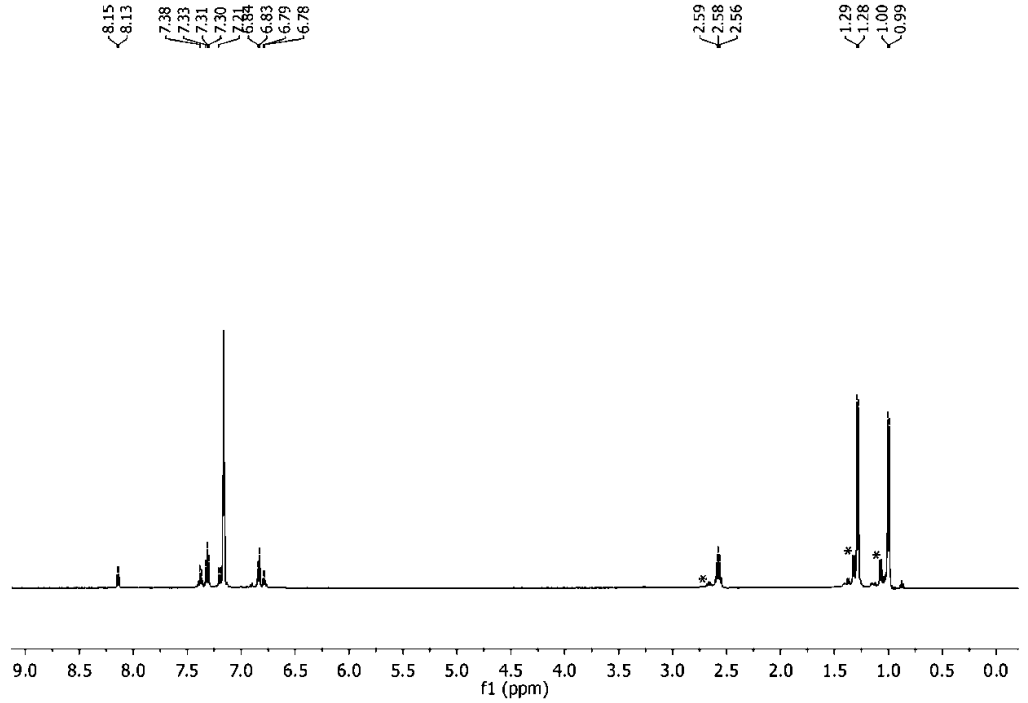

Figure 4.14. ^{1}H NMR spectrum (500.1 MHz, 20 ˚C, C_6D_6) of Mn(κ^1-*O*-((C_6H_5)CO_2))$(CO)_3$($CNAr^{Dipp2}$)$_2$ **(5)**. The symbol (*) denotes residual Mn(κ^2-*O*,*O*-($O_2C(C_6H_5)$)$(CO)_2$($CNAr^{Dipp2}$)$_2$ (**3**).

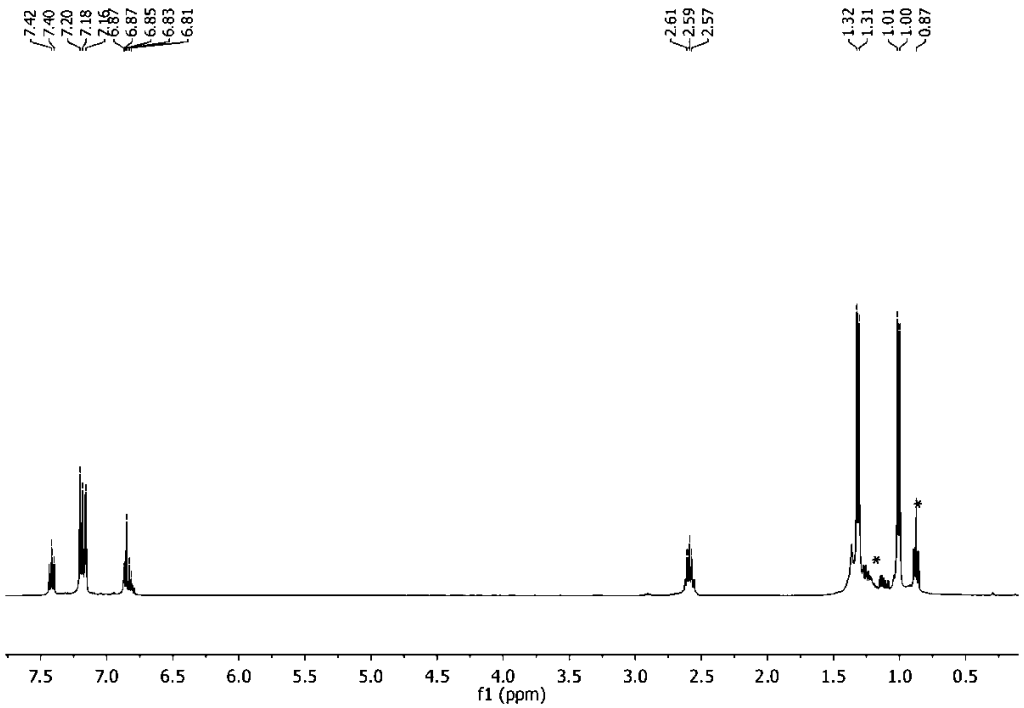

Figure 4.15. ^{1}H NMR spectrum (500.1 MHz, 20 ˚C, C_6D_6) of Mn(κ^1-*O*-(O_2CCF_3))$(CO)_3(CNAr^{Dipp2})_2$ **(6)**. The symbol (*) denotes residual *n*-pentane.

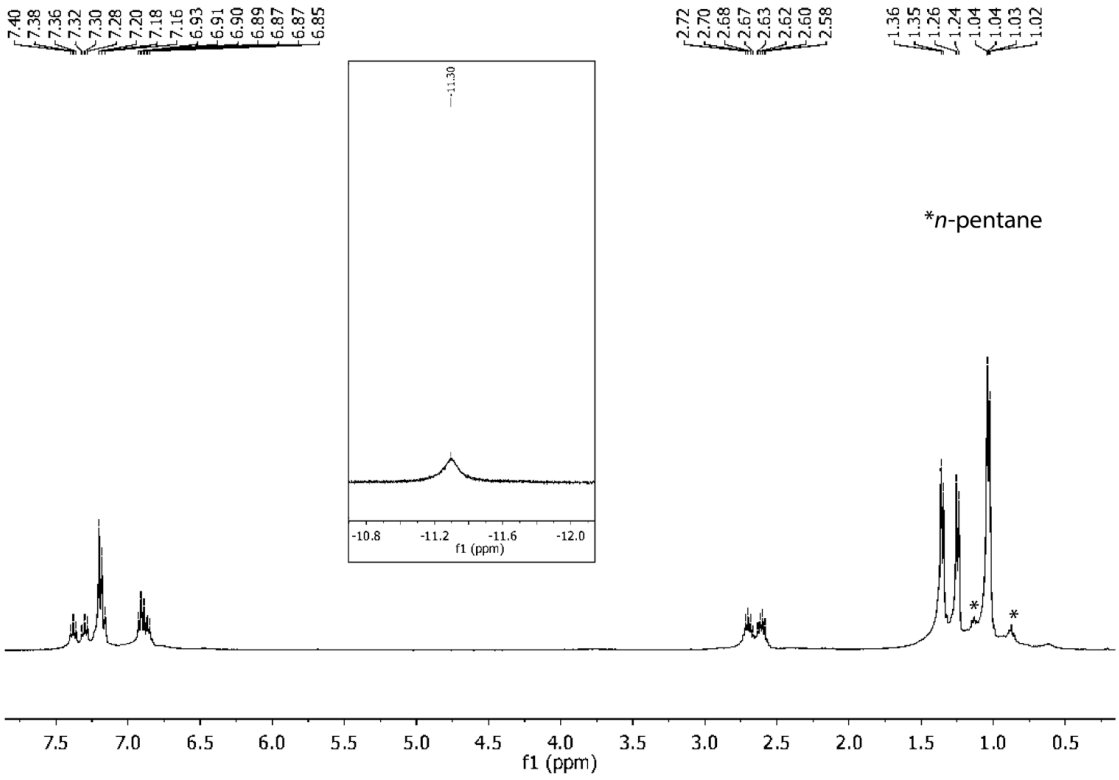

Figure 4.16. ^{1}H NMR spectrum (500.1 MHz, 20 ˚C, C_6D_6) of Mn(κ^2-*H*,*H*-($F_3CSO_3BH_3$))$(CO)_2(CNAr^{Dipp2})_2$ **(8-OTf)**. The inset shows the upfield borohydride resonance.

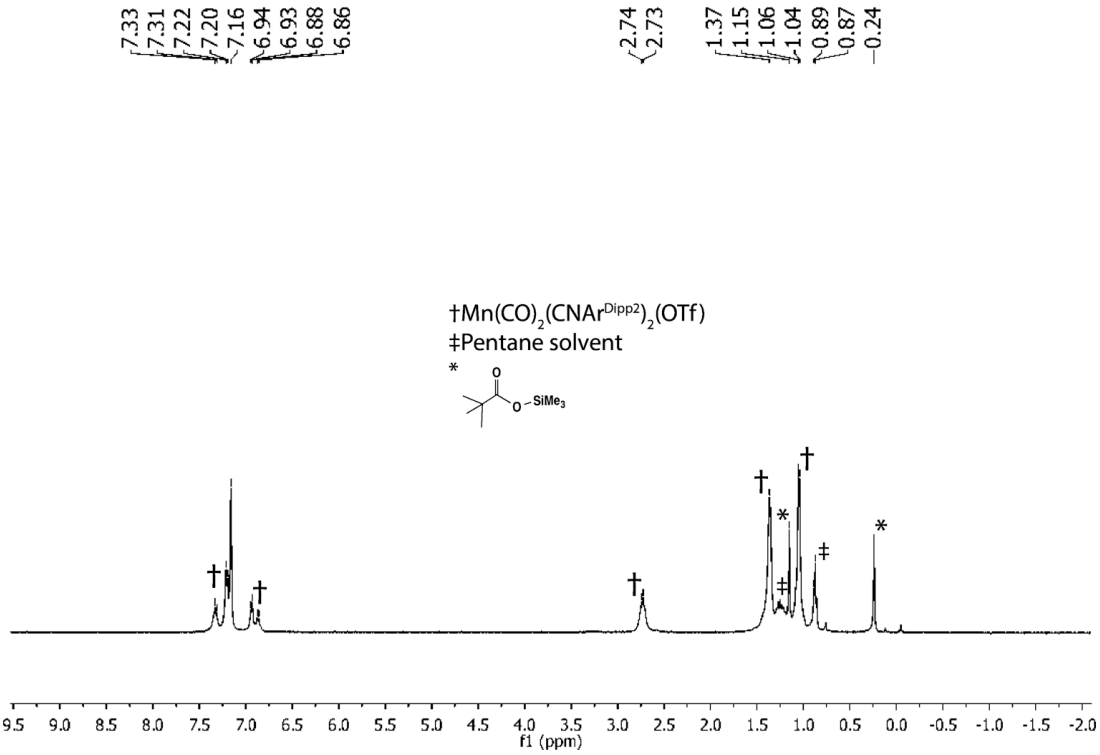

Figure 4.17. ^{1}H NMR spectrum (400.1 MHz, 20 ˚C, C_6D_6) of $Mn(OTf)(CO)_2(CNAr^{Dipp2})_2$ **(9)** in reaction mixture resulting from S1.14, Method A.

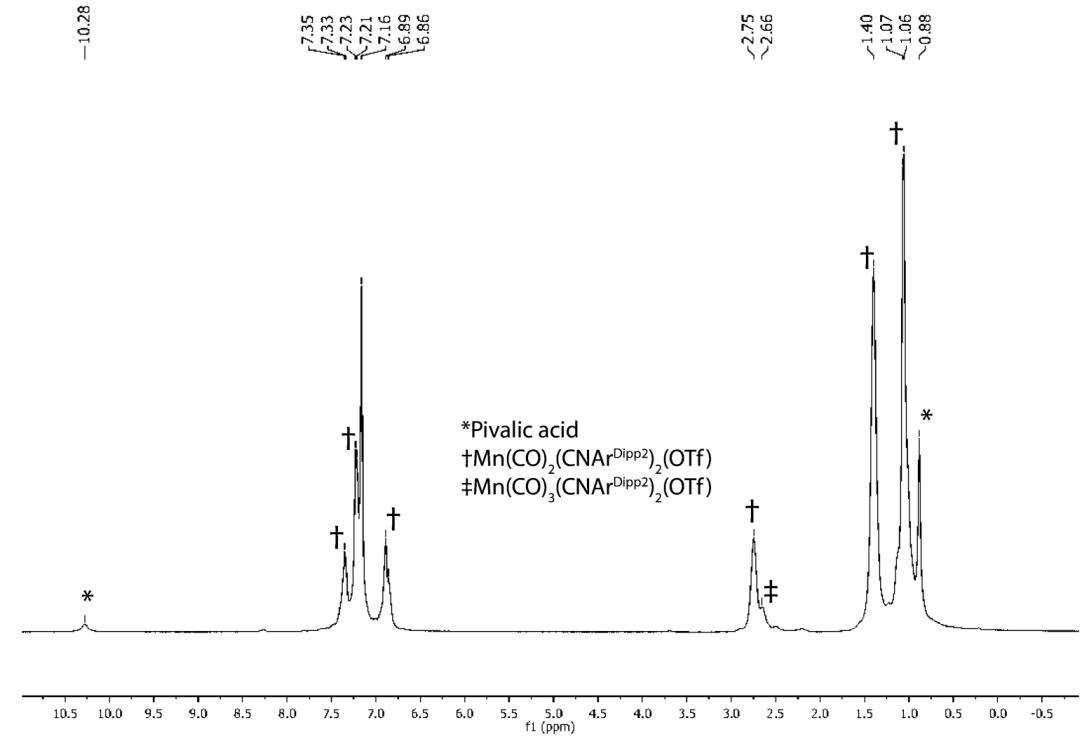

Figure 4.18 ^{1}H NMR spectrum (400.1 MHz, 20 ˚C, C_6D_6) of $Mn(OTf)(CO)_2(CNAr^{Dipp2})_2$ **(9)** in reaction mixture resulting from S1.14, Method B.

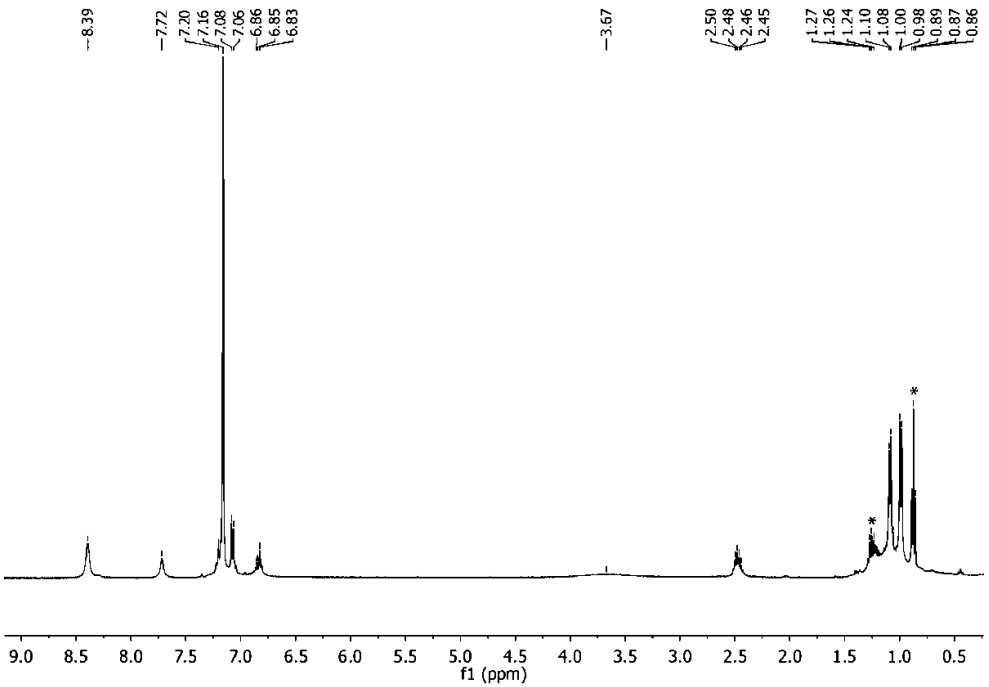

Figure 4.19. ^{1}H NMR spectrum (500.1 MHz, 20 ˚C, C_6D_6) of $[Mn(CO)_2(CNAr^{Dipp2})_2(OEt_2)_2]BAr^F{}_4$ **(10)**. The symbol (*) denotes free *n*-pentane.

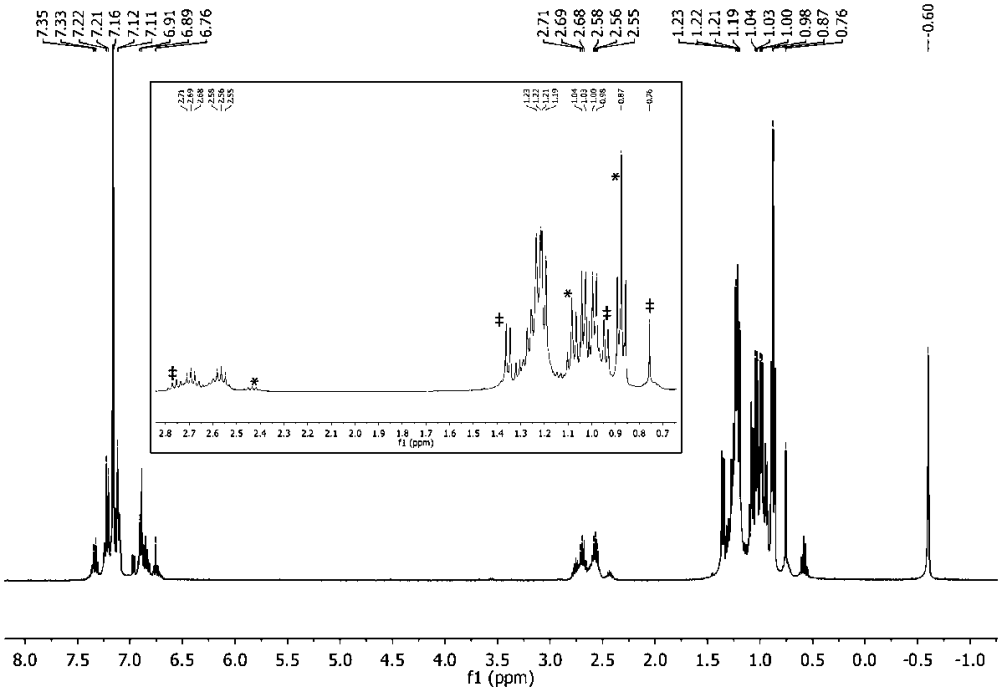

Figure 4.20. ^{1}H NMR spectrum (500.1 MHz, 20 ˚C, C_6D_6) of $Mn(CO)_2(CNAr^{Dipp2})(\eta^2\text{-}(C,H\text{-}CH_3)(CH_3)_2CCO_2B(C_6F_5)_3)$ **(11)**. The symbols (‡) and (*) in the inset denote the starting material $Mn(\kappa^2\text{-}O,O\text{-}(O_2CC(CH_3)_3))(CO)_2(CNAr^{Dipp2})_2$ **(1)** and $(F_5C_6)_3B{\leftarrow}CNAr^{Dipp2}$, respectively.

4.7 Crystallographic Structure Determinations

General. Single crystal X-ray structure determinations were performed at low temperature on Bruker Kappa Diffractometers equipped with a Mo Kα or Cu Kα radiation source and a Bruker APEX or APEX-II area detector. All structures were solved *via* direct methods with SHELXS[71] and refined by full-matrix least-squares procedures using SHELXL[71] within the Olex2[72] software. In cases of highly disordered solvent molecules, the Platon routine SQUEEZE[73] was used to account for the corresponding electrons as a diffuse contribution to the overall scattering without specific atom positions. Crystallographic data collection and refinement information is listed in Table S3.1.

Notes on Structure Solutions.

$Mn((\kappa^2\text{-}CH_3CO_2))(CO)_2(CNAr^{Dipp2})_2$ (2). Positional disorder exists for the acetate and *trans*-CO ligands; this was treated as two-site positional disorder, modeled and refined anisotropically.

$Mn(\kappa^1\text{-}(O_2CH))(CO)_2(Pyr)(CNAr^{Dipp2})_2$ (4-pyr). Positional disorder exists for the formate and *trans*-CO ligands; this was treated as two-site positional disorder, modeled and refined anisotropically.

$Mn(\kappa^1\text{-}(O_2CCF_3))(CO)_3(CNAr^{Dipp2})_2$) (5). The trifluoroacetate ligand is rotationally disordered over two positions and was modeled and refined anisotropically.

$Mn((\kappa^1\text{-}C_6H_5O_2))(CO)_3(CNAr^{Dipp2})_2$ (6). The benzoate ligand is rotationally disordered over two positions and was modeled and refined anisotropically. A

significantly disordered diethyl ether solvent molecule was treated with SQUEEZE and its electron density removed.

K[(η^4-4-Ar^{Dipp}-6,10-diisopropylazabenz[*b*]azulene)Mn(CO)$_2$(CNAr^{Dipp2})] (7). Significant disorder was found for co-crystallization solvent molecules consisting of two molecules of diethyl ether and two molecules of hexamethyldisiloxane. These were treated with SQUEEZE and their electron density removed.

Mn(κ^2-(BH$_4$))(CO)$_2$(CNAr^{Dipp2})$_2$ (8). Positional disorder exists for the borohydride ligand and the two *trans*-CO ligands. These were treated as two-site positional disorder, modeled and refined anisotropically. The hydrogen atoms of the borohydride were located in the electron density map.

Mn(κ^2-(F$_3$CSO$_3$BH$_3$))(CO)$_2$(CNAr^{Dipp2})$_2$ (8-OTf). Positional disorder exists for the $F_3CSO_3BH_3$ moeity; these were treated as two-site positional disorder, modeled and refined anisotropically. The hydrogen atoms of one $–BH_3$ group were located in the electron density map.

Mn(CO)$_2$(CNAr^{Dipp2})(η^2-*C*,*H*-CH$_3$)CCO$_2$B(C$_6$F$_5$)$_3$) (11). Significant disorder was found for co-crystallization solvent molecules consisting of three molecules of toluene and two molecules of diethyl ether. These were treated with SQUEEZE and their electron density removed. Rotational disorder in the *tert*-butyl group of one molecule of $Mn(CO)_2(CNAr^{Dipp2})(\kappa^1\text{-}(CH_3)CCO_2B(C_6F_5)_3)$ was modeled and refined anisotropically. The methyl hydrogen atoms engaged in agostic interactions with the Mn^I metal center were located in the electron density map and were refined without the use of constraints.

Table 4.2 Crystallographic Data Collection and Refinement Information.

Name	2·Mn(κ^2-($O_2CC(CH_3)_3$))$(CO)_2$($CNAr^{Dipp2}$)$_2$·(Et_2O) (**1**)	2·Mn($\kappa^2CH_3CO_2$)$(CO)_2$($CNAr^{Dipp2}$)$_2$ (**2**)	Mn(κ^2-$C_6H_5O_2$)$(CO)_2$($CNAr^{Dipp2}$)$_2$ ·(C_6H_6) (**3**)
Formula	$C_{142}H_{175}Mn_2N_2O_9$	$C_{66}H_{77}MnN_2O_4$	$C_{74}H_{82}MnN_2O_4$
Crystal System	Monoclinic	Monoclinic	Monoclinic
Space Group	$P2_1/c$	$P2_1/c$	C2/c
a, Å	25.996(2)	16.862(2)	46.2914(10)
b, Å	21.874(2)	16.736(2)	16.5737(4)
c, Å	25.178(2)	41.454(5))	16.9876(4)
α, deg	90	90	90
β, deg	116.3112(13)	100.020(2)	104.9100(10)
γ, deg	90	90	90
V, $Å^3$	12834(2)	11520(2)	12594.4(5)
Z	4	8	8
Radiation (λ, Å)	Mo-K_α, 0.71073	Mo-K_α, 0.71073	Mo-K_α, 0.71073
ρ (calcd.), Mg/m^3	1.135	1.173	1.180
μ (Mo Ka), mm^{-1}	0.254	0.278	0.260
Temp, K	100	100	100
θ max, deg	27.159	24.416	25.328
data/parameters	28414/1447	18988/1473	11494/746
R_1	0.0614	0.0927	0.0439
wR_2	0.1589	0.1970	0.0910
GOF	1.029	1.119	1.015

Table 4.3. Crystallographic Data Collection and Refinement Information.

Name	$Mn(O_2CH)(CO)_2(C_5H_5N)(CNAr^{Dipp2})_2$) (**4-pyr**)	$Mn(C_6H_5O_2)(CO)_3(CNAr^{Dipp2})_2 \cdot 2(Et_2O)$ (**5**)	$Mn(O_2CCF_3)(CO)_3(CNAr^{Dipp2})_2) \cdot (Et_2O)$ (**6**)
Formula	$C_{78}H_{100}MnN_3O_6$	$C_{80}H_{99}MnN_2O_7$	$C_{69}H_{79}F_3MnN_2O_{5.5}$
Crystal System	Monoclinic	Triclinic	Monoclinic
Space Group	$P2_1/c$	P-1	$P2_1/c$
a, Å	15.7361(3)	12.2792(15)	20.5450(4)
b, Å	17.6996(3)	16.609(2)	16.6493(3)
c, Å	26.0679(5)	19.630(3)	20.6945(4)
α, deg	90	97.684(4)	90
β, deg	102.6390	91.435(4)	117.2250(10)
γ, deg	90	96.967(9)	90
V, Å^3	7084.6(2)	3934.6(9)	6294.5
Z	4	2	4
Radiation (λ, Å)	Mo-K_α, 0.71073	Mo-K_α, 0.71073	Mo-K_α, 0.71073
ρ (calcd.), Mg/m^3	1.154	1.060	1.119
μ (Mo Ka), mm^{-1}	0.239	0.217	0.269
Temp, K	100	100	100
θ max, deg	24.776	25.440	26.414
data/parameters	12137/874	14439/902	12643/850
R_1	0.0892	0.0570	0.0440
wR_2	0.2284	0.1253	0.1127
GOF	1.087	1.019	1.023

Table 4.4. Crystallographic Data Collection and Refinement Information.

Name	2·(K(Et_2O)[(η^4-azabenz[*b*]azulene)Mn(CO)$_2$(CNAr^{Dipp2})]·(Et_2O)) (**7**)	2·Mn(BH_4)(CO)$_2$(CNAr^{Dipp2})$_2$ (**8**)	Mn($F_3CSO_3BH_3$)(CO)$_2$(CNAr^{Dipp2})$_2$ (**8-OTf**)
Formula	$C_{68}H_{83.5}KMnN_2O_3$	$C_{64}H_{76B}MnN_2O_3$	$C_{65}H_{80}F_3MnN_2O_5S$
Crystal System	Monoclinic	Monoclinic	Monoclinic
Space Group	$P2_1/n$	C2/c	$P2_1$
a, Å	19.142(5)	23.7213(8)	13.1452(7)
b, Å	27.610(8)	23.5514(9)	15.6184(9)
c, Å	27.492(8)	21.3816(9)	15.2093(7)
α, deg	90	90	90
β, deg	104.977(4)	108.664(2)	93.025(2)
γ, deg	90	90	90
V, Å^3	14037(7)	11317.1(8)	3118.2(3)
Z	8	8	2
Radiation (λ, Å)	Mo-K$_\alpha$, 0.71073	Mo-K$_\alpha$, 0.71073	Mo-K$_\alpha$, 0.71073
ρ (calcd.), Mg/m^3	1.014	1.159	1.197
μ (Mo Ka), mm^{-1}	0.287	0.279	0.302
Temp, K	100	100	100
θ max, deg	20.865	26.059	25.392
data/parameters	14754/1428	11162/713	11473/5964
R_1	0.0854	0.0589	0.0447
wR_2	0.1982	0.1609	0.0841
GOF	1.065	1.111	1.022

Table 4.5. Crystallographic Data Collection and Refinement Information.

Name	$Mn(CO)_2(CNAr^{Dipp2})_2(OC_4H_8)(O_3SCF_3)\cdot(Et_2O)$ (**9-THF**)	$2\cdot[Mn(CO)_2(CNAr^{Dipp2})_2(OEt_2)_2](BC_{32}H_{12}F_{24})\cdot(Et_2O)$ (**10**)	$2\cdot Mn(CO)_2(CNAr^{Dipp2})((CH_3)_3CCO_2B(C_6F_5)_3)\cdot(Et_2O)$ (**11**)
Formula	$C_{73}H_{92}F_3MnN_2O_7S$	$C_{78}H_{100}MnN_3O_6$	$C_{89}H_{88}BF_{15}MnN_2O_{4.5}$
Crystal System	Monoclinic	Monoclinic	Triclinic
Space Group	Cc	$P2_1/c$	P-1
a, Å	19.600(3)	25.384(3)	14.7941(8)
b, Å	15.2051(19)	16.256(2)	24.7433(13)
c, Å	23.552(3)	49.409(6)	26.5070(14)
α, deg	90	90	97.8460(10)
β, deg	96.6829(16)	101.988(6)	98.6420(10)
γ, deg	90	90	90.6020(10)
V, $Å^3$	6971.2(15)	19944(4)	9498.3(9)
Z	4	8	4
Radiation (λ, Å)	Mo-K_α, 0.71073	Mo-K_α, 0.71073	Mo-K_α, 0.71073
ρ (calcd.), Mg/m^3	1.196	1.312	1.125
μ (Mo Ka), mm^{-1}	0.280	0.228	0.213
Temp, K	100	100	100
θ max, deg	26.387	21.000	25.449
data/parameters	13378/856	21546/2577	35043/2119
R_1	0.0353	0.1376	0.0452
wR_2	0.0877	0.3216	0.1120
GOF	1.025	1.190	1.027

Table 4.6. Crystallographic Data Collection and Refinement Information.

Name	$(C_6F_5)_3B{\leftarrow}CNAr^{Dipp2}$	$Mn(CO)_2(\eta^2\text{-}C,N\text{-}(H_3CCNAr^{Dipp2}))(CNAr^{Dipp2})$ (**12**)
Formula	$C_{49}H_{37}BF_{15}N$	$C_{65}H_{77}MnN_2O_{1.97}$
Crystal System	Monoclinic	Monoclinic
Space Group	$P2_1/n$	Pn
a, Å	12.8109(16)	18.3757(5)
b, Å	22.635(3)	11.8713(3)
c, Å	15.620(2)	26.7056(8)
α, deg	90	90
β, deg	106.705(7)	106.3370(10)
γ, deg	90	90
V, Å^3	4338.2(10)	5590.4(3)
Z	4	4
Radiation (λ, Å)	Cu-K$_\alpha$, 1.54178	Mo-K$_\alpha$, 0.71073
ρ (calcd.), Mg/m^3	1.432	1.156
μ (Mo Ka), mm^{-1}	1.117	0.280
Temp, K	100	100
θ max, deg	63.687	24.75
data/parameters	7051/603	18128/1304
R_1	0.0422	0.0515
wR_2	0.0999	0.1164
GOF	1.047	0.966

4.8 Acknowledgements

Chapter 4 is adapted from "Controlled cis Labilization of CO from Manganese(I) Mixed Carbonyl/Isocyanide Complexes: An Entry Point to Coordinatively Unsaturated Metallo-Lewis Acids" by Douglas W. Agnew, Curtis E. Moore, Arnold L. Rheingold, and Joshua S. Figueroa, *Organometallics* 2017 *36* (2),

363-371. Copyright 2017, American Chemical Society. Permission to include published material in this dissertation has been obtained from all coauthors. The dissertation author is the first author of this paper.

4.9 References

1. Atwood, J. D. *Inorganic and Organometallic Reaction Mechanisms*, 2nd ed.; Wiley-VCH, Inc.: New York, 1997.

2. Howell, J. A. S.; Burkinshaw, P. M. *Chem. Rev.* **1983**, *83*, 557.

3. Atwood, J. D.; Brown, T. L. *J. Am. Chem. Soc.* **1975**, *97*, 3380.

4 Atwood, J. D.; Brown, T. L. *J. Am. Chem. Soc.* **1976**, *98*, 3155.

5. Atwood, J. D.; Brown, T. L. *J. Am. Chem. Soc.* **1976**, *98*, 3160.

6. McHugh, T. M.; Rest, A. J.; Taylor, D. J. *J. Chem. Soc., Dalton Trans.* **1980**, 1803.

7. Dearden, D. V.; Hayashibara, K.; Beauchamp, J. L.; Kirchner, N. J.; Van Koppen, P. A. M.; Bowers, M. T. *J. Am. Chem. Soc.* **1989**, *111*, 2401.

8. Beck, W.; Suenkel, K. *Chem. Rev.* **1988**, *88*, 1405.

9. King, W. A.; Luo, X.-L.; Scott, B. L.; Kubas, G. J.; Zilm, K. W. *J. Am. Chem. Soc.* **1996**, *118*, 6782.

10. Toupadakis, A.; Kubas, G. J.; King, W. A.; Scott, B. L.; Huhmann-Vincent, J. *Organometallics* **1998**, *17*, 5315.

11. Huhmann-Vincent, J.; Scott, B. L.; Kubas, G. J. *Inorg Chem* **1999**, *38*, 115.

12. Fang, X.; Scott, B. L.; John, K. D.; Kubas, G. J. *Organometallics* **2000**, *19*, 4141.

13. Valyaev, D. A.; Lavigne, G.; Lugan, N. *Coord. Chem. Rev.* **2015**, *308*, 191.

14. Cohen, M. A.; Brown, T. L. *Inorg Chem* **1976**, *15*, 1417.

15. Green, M. L. H. *J. Organomet. Chem.* **1995**, *500*, 127.

16. Lichtenberger, D. L.; Brown, T. L. *J. Am. Chem. Soc.* **1978**, *100*, 366.

17. Macgregor, S. A.; MacQueen, A. D. *Inorg Chem* **1999**, *38*, 4868.

18. Kovacs, A.; Frenking, G. *Organometallics* **2001**, *20* , 2510.

19. Agnew, D. W.; Moore, C. E.; Rheingold, A. L.; Figueroa, J. S. *Angew. Chem. Int. Ed.* **2015**, *54*, 12673.

20. Atwood, J. D.; Wovkulich, M. J.; Sonnenberger, D. C. *Acc. Chem. Res.* **1983**, *16*, 350.

21. Schmidt, G.; Paulus, H.; Van Eldik, R.; Elias, H. *Inorg Chem* **1988**, *27*, 3211.

22. Darensbourg, D. J.; Rokicki, A. *Organometallics* **1982**, *1*, 1685.

23. Darensbourg, D. J.; Wiegreffe, H. P. *Inorg Chem* **1990**, *29*, 592.

24. Cotton, F. A.; Darensbourg, D. J.; Kolthammer, B. W. S. *J. Am. Chem. Soc.* **1981**, *103*, 398.

25. Liu, W.; Richter, S. C.; Zhang, Y.; Ackermann, L. *Angew. Chem. Int. Ed.* **2016**, *55*, 7747.

26. Fox, B. J.; Millard, M. D.; DiPasquale, A. G.; Rheingold, A. L.; Figueroa, J. S. *Angew. Chem. Int. Ed. Engl.* **2009**, *48*, 3473.

27. Ditri, T. B.; Fox, B. J.; Moore, C. E.; Rheingold, A. L.; Figueroa, J. S. *Inorg Chem* **2009**, *48*, 8362.

28. Labios, L. A.; Millard, M. D.; Rheingold, A. L.; Figueroa, J. S. *J. Am. Chem. Soc.* **2009**, *131*, 11318.

29. Margulieux, G. W.; Weidemann, N.; Lacy, D. C.; Moore, C. E.; Rheingold, A. L.; Figueroa, J. S. *J. Am. Chem. Soc.* **2010**, *132*, 5033.

30. Stewart, M. A.; Moore, C. E.; Ditri, T. B.; Labios, L. A.; Rheingold, A. L.; Figueroa, J. S. *Chem. Commun.* **2011**, *47*, 406.

31. Emerich, B. M.; Moore, C. E.; Fox, B. J.; Rheingold, A. L.; Figueroa, J. S. *Organometallics* **2011**, *30*, 2598.

32. Mokhtarzadeh, C. C.; Margulieux, G. W.; Carpenter, A. E.; Weidemann, N.; Moore, C. E.; Rheingold, A. L.; Figueroa, J. S. *Inorg Chem* **2015**, *54*, 5579.

33. Barnett, B. R.; Moore, C. E.; Rheingold, A. L.; Figueroa, J. S. *J. Am. Chem. Soc.* **2014**, *136*, 10262.

34. Carpenter, A. E.; Rheingold, A. L.; Figueroa, J. S. *Organometallics* **2016**, *35*, 2309.

35. The reactivity of the metal carboxylate is invariant with regard to the metal cation; similar results were found using Na, K and Cs salts for all four carboxylates.

36. Hansch, C.; Leo, A.; Taft, R. W. *Chem. Rev.* **1991**, *91*, 165.

37. Agarwal, J.; Johnson, R. P.; Li, G. *J. Phys. Chem. A* **2011**, *115*, 2877.

38. Cotton, F. A.; Darensbourg, D. J.; Kolthammer, B. W. S. *Inorg Chem* **1981**, *20*, 1287.

39. Dean, W. K.; Simon, G. L.; Treichel, P. M.; Dahl, L. F. **1973**, *50*, 193.

40. Mace, W. J.; Main, L.; Nicholson, B. K.; Hagyard, M. *J. Organomet. Chem.* **2002**, *664*, 288.

41. Buchner, E.; Curtius, T. *Ber. Dtsch. Chem. Ges.* **1885**, *18*, 2377.

42. Boyer, J. H.; De Jong, J. *J. Am. Chem. Soc.* **1969**, *91*, 5929.

43. Mokhtarzadeh, C. C.; Rheingold, A. L.; Figueroa, J. S. *Dalton Trans.* **2016**, *45*, 14561.

44. Ditri, T. B.; Carpenter, A. E.; Ripatti, D. S.; Moore, C. E.; Rheingold, A. L.; Figueroa, J. S. *Inorg Chem* **2013**, *52*, 13216.

45. Chomitz, W. A.; Sutton, A. D.; Krinsky, J. L.; Arnold, J. *Organometallics* **2009**, *28*, 3338.

46. Ruiz, D. A.; Ung, G.; Melaimi, M.; Bertrand, G. *Angew. Chem. Int. Ed.* **2013**, *52*, 7590.

47. Darensbourg, M. Y.; Bau, R.; Marks, M. W.; Burch, R. R.; Deaton, J. C.; Slater, S. *J. Am. Chem. Soc.* **1982**, *104*, 6961.

48. Chantler, V. L.; Chatwin, S. L.; Jazzar, R. F. R.; Mahon, M. F.; Saker, O.; Whittlesey, M. K. *Dalton Trans.* **2008**, 2603.

49. Carreno, R.; Riera, V.; Ruiz, M. A.; Bois, C.; Jeannin, Y. *Organometallics* **1993**, *12*, 1946.

50. Maria, L.; Paulo, A.; Santos, I. C.; Santos, I.; Kurz, P.; Spingler, B.; Alberto, R. *J. Am. Chem. Soc.* **2006**, *128*, 14590.

51. Tang, C. Y.; Thompson, A. L.; Aldridge, S. *J. Am. Chem. Soc.* **2010**, *132*, 10578.

52. Phillips, N.; Tang, C. Y.; Tirfoin, R.; Kelly, M. J.; Thompson, A. L.; Gutmann, M. J.; Aldridge, S. *Dalton Trans.* **2014**, *43*, 12288.

53. Cotton, F. A.; Dunbar, K. R.; Poli, R. *Inorg Chem* **1986**, *25*, 3700.

54. Pola, J.; Jakoubkova, M.; Papouskova, Z.; Chvalovsky, V. *Collect. Czech. Chem. Commun.* **1977**, *42*, 1540.

55. Vela, J.; Cirera, J.; Smith, J. M.; Lachicotte, R. J.; Flaschenriem, C. J.; Alvarez, S.; Holland, P. L. *Inorg Chem* **2007**, *46*, 60.

56. Whited, M. T.; Kosanovich, A. J.; Janzen, D. E. *Organometallics* **2014**, *33*, 1416.

57. Andrella, N. O.; Sicard, A. J.; Gorelsky, S. I.; Korobkov, I.; Baker, R. T. *Chem. Sci.* **2015**, *6*, 6392.

58. Elian, M.; Hoffmann, R. *Inorg Chem* **1975**, *14*, 1058.

59. Burdett, J. K. *Inorg Chem* **1975**, *14,* 375.

60. Burdett, J. K.; Graham, M. A.; Perutz, R. N.; Poliakoff, M.; Rest, A. J.; Turner, J. J.; Turner, R. F. *J. Am. Chem. Soc.* **1975**, *97*, 4805.

61. Fletcher, T. R.; Rosenfeld, R. N. *J. Am. Chem. Soc.* **1985**, *107*, 2203.

62. Reed, Z. D.; Duncan, M. A. *J Am Soc Mass Spectrom* **2010**, *21*, 739.

63. Brookhart, M.; Green, M. L. H.; Parkin, G. *PNAS* **2007**, *104*, 6908.

64. Brookhart, M.; Lamanna, W.; Pinhas, A. R. *Organometallics* **1983**, *2*, 638.

65. Brookhart, M.; Lukacs, A. *Organometallics* **1983**, *2*, 649.

66. Perthuisot, C.; Fan, M.; Jones, W. D. *Organometallics* **1992**, *11*, 3622.

67. Durfee, L. D.;Rothwell, I. P. *Chem. Rev.* **1988,** *88* 1059.

68. Yakelis, N. A.; Bergman, R. G. *Organometallics.* **2005**, 14, 3579.

69. Pola, *J.*; *J*akoubkova, M.; Papouskova, Z.; Chvalovsky, V. *Collection of Czechoslovak Chemical Communications*. **1977**, 5, 1540–1550.

70. Fulmer, G. R.; Miller, A. *J.* M.; Sherden, N. H.; Gottlieb, H. E.; Nudelman, A.;

Stoltz, B. M.; Bercaw, *J*. E.; Goldberg, K. I. *Organometallics* **2010**, 29, 2176.

71. Sheldrick. G. M. Acta Crystallogr. A. **2008**, 64, 112.

72. Dolomanov, O. V.; Bourhis, L. *J*.; Gildea, R. *J*.; Howard, *J*. A. K.; Puschmann, H. *J*. *Appl. Cryst.* **2009**, *42*, 339.

73. van der Sluis, P.; Spek. A. L. *Acta Crystallogr.* **1990**, *A46*, 194-201.

Chapter 5

Robust, Transformable and Crystalline Single-Node Organometallic Networks Constructed from Ditopic *m*-Terphenyl Isocyanides

5.1 Introduction

Control over the metal coordination environment has become a defining hallmark in the evolution of porous coordination polymers (PCPs) and metal-organic frameworks (MOFs), and has given rise to significant topological and structural diversity within this class of materials.[1-4] To achieve targeted and/or emergent properties, techniques such as thermal activation, reticular linker substitution[5,6] and post-synthetic modification[7] have been employed to create highly tailored, functional materials for applications in separations,[8] gas storage,[9] sensing,[10] and catalysis.[11] In many cases, such enhanced properties are enabled by open metal-coordination sites at the secondary building unit (SBU) or framework linker. While recent progress in defect engineering has provided a means to consistently impart some structures with open metal sites,[12] there remain few approaches to reliably control the formation of low-coordinate metal centers within a framework material.[13] However, in molecular systems it is well established that sterically encumbering ligands can exert substantial control over the coordination number and geometry at a metal site, and this strategy has allowed for the preparation of numerous complexes possessing coordinative

unsaturation.[14-16] In some cases, the increased steric profile of the ligand can additionally engender high thermal and moisture stability to the resulting complex.[17,18]

In recent years, we have extensively studied a class of encumbering, monodentate *m*-terphenyl[19] isocyanide ligands that are highly effective at controlling the coordination number and geometry of mono- and multinuclear coordination complexes.[20-25] Like the metal ligand bonds in carboxylate- and imidazolate-based MOFs, the metal-isocyanide linkage is recognized to be robust on account of strong ligand-to-metal s-donation and the potential for significant secondary p-backbonding interactions.[24,26] However, multitopic isocyanides represent an under-explored linker group for coordination networks. This is despite the fact that some of the earliest reported catalytically-active amorphous coordination polymers consisted of ill-defined mixtures of diaryldiisocyanides and Rh(I) single-metal nodes.[27-29] Accordingly, here we report the development of diisocyanide ligands featuring *meta*-terphenyl substituents that enable coordinative control and stabilization of highly-robust crystalline coordination frameworks possessing mononuclear Cu(I) nodes. Most importantly, the same principles that allow for the manipulation of coordination geometry and number of mononuclear centers in solution[20] are shown to be transported to a solid-state network when significantly encumbering, neutral ligands are utilized as linker groups.

5.2 Preparation and Properties of Cu(I)-Isocyanide Coordination Polymers

The ditopic *m*-terphenyl isocyanide, $[CNAr^{Mes2}]_2$ (Figure 1), was prepared *via* Suzuki-Miyaura coupling of the *para*-bromo aniline 4-$BrAr^{Mes2}NH_2$ and is available in

an overall 73% yield from the known aniline H_2NAr^{Mes2}.[30] Ditopic $[CNAr^{Mes2}]_2$ is an off-white solid with a $^{13}C\{^1H\}$ NMR isocyanide carbon resonance of 172.2 ppm and a ν_{CN} stretching band of 2118 cm^{-1} in C_6D_6 solution, which are similar to those of the monotopic isocyanide $CNAr^{Mes2}$.[20] Notably, crystallographic structure determination of $[CNAr^{Mes2}]_2$ revealed a near-planar biphenyl core with a torsion angle approaching 0º (Figure S2.7), which contrasts with the equilibrium torsion angle for unsubstituted biphenyl of 44.4º.[31] Based upon the calculated torsional barriers in $[CNAr^{Mes2}]_2$ (2.0 kcal/mol at 0º and 3.3 kcal/mol at 90º; Table S4.1), we attribute the observed absence

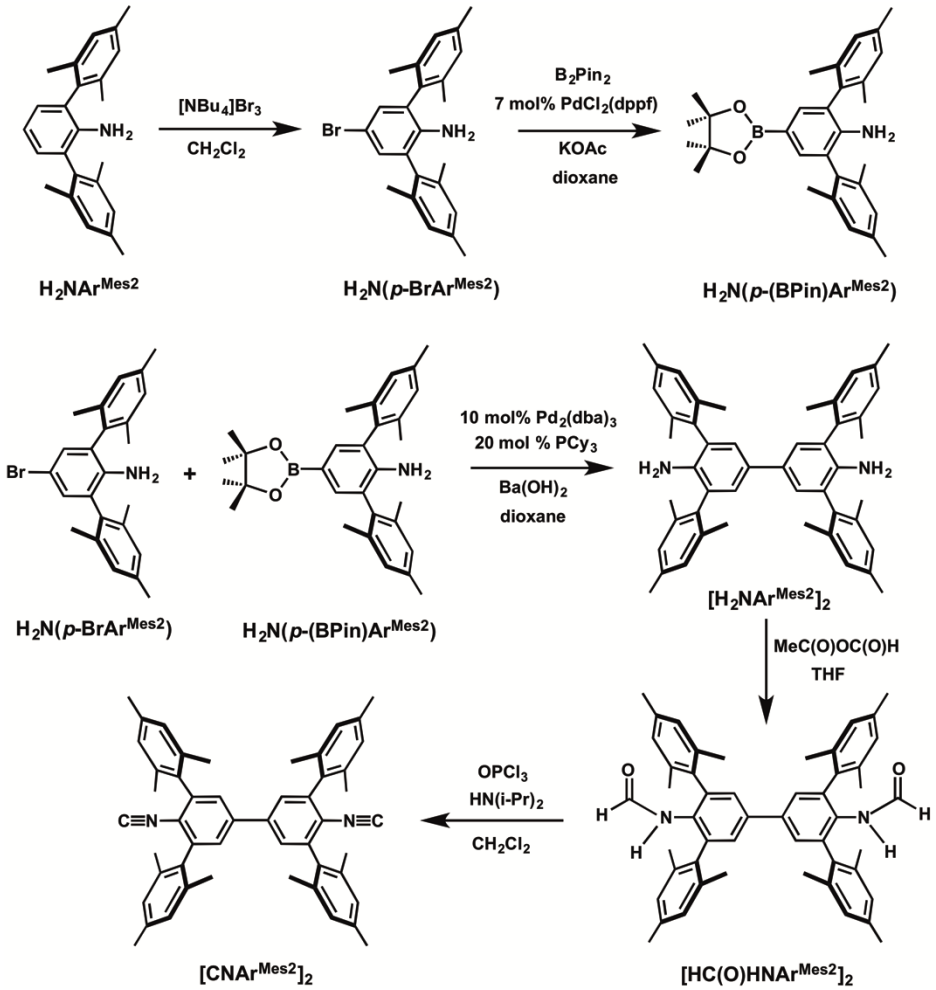

Scheme 5.1. Synthesis of the ditopic isocyanide $[CNAr^{Mes2}]_2$.

of torsion to be predominantly derived from crystal packing forces. Importantly, this low-barrier rotation element remains the only significant structural flexibility in the ligand, which otherwise provides a rigid, linear scaffold for the formation of coordination frameworks.

With $[CNAr^{Mes2}]_2$ in hand, we sought to examine the effect of *meta*-terphenyl substitution in coordination frameworks composed of Cu(I)-isocyanide nodes. Mechanically mixing solid $[CNAr^{Mes2}]_2$ with $[Cu(MeCN)_4]PF_6$, followed by addition of THF and heating at 80ºC for 16 h in a pressure tube afforded large colorless, octahedral-shaped crystals of Cu-^{ISO}CN-1 (^{ISO}CN = isocyanide coordination network). The observed isocyanide IR stretching frequency at 2118 cm^{-1} (ATR-IR) indicated little activation of the σ-bond of the isocyanide and insignificant π-backdonation, as expected for a Cu(I) isocyanide material.[20,32] Structural analysis by single crystal X-ray crystallography revealed a 2-fold interpenetrated diamondoid framework (Figure 1, B) in the *F*dd2 space group composed of four-coordinate Cu(I) units of approximate tetrahedral geometry, (Houser τ_4[33] = 0.95). The $[CNAr^{Mes2}]_2$ ligands bridging the Cu(I) nodes form *ca*. 9.8 X 9.8 Å rectangular channels along the *a* and *c* axes, which are partially occupied by *meta*-mesityl groups which narrow the pore size to *ca*. 2.1 X 3.2 Å. Cu-^{ISO}CN-1 is, to our knowledge, the first structurally characterized three-dimensional framework assembled from diisocyanide building blocks.

Attempts at thermal activation (50 ºC to 125ºC, 25 ºC intervals) of Cu-^{ISO}CN-1 for gas sorption analysis repeatedly generated samples with distinctly broadened IR spectra in the isocyanide region (Figure 5.24). Holding a solid sample of Cu-^{ISO}CN-1

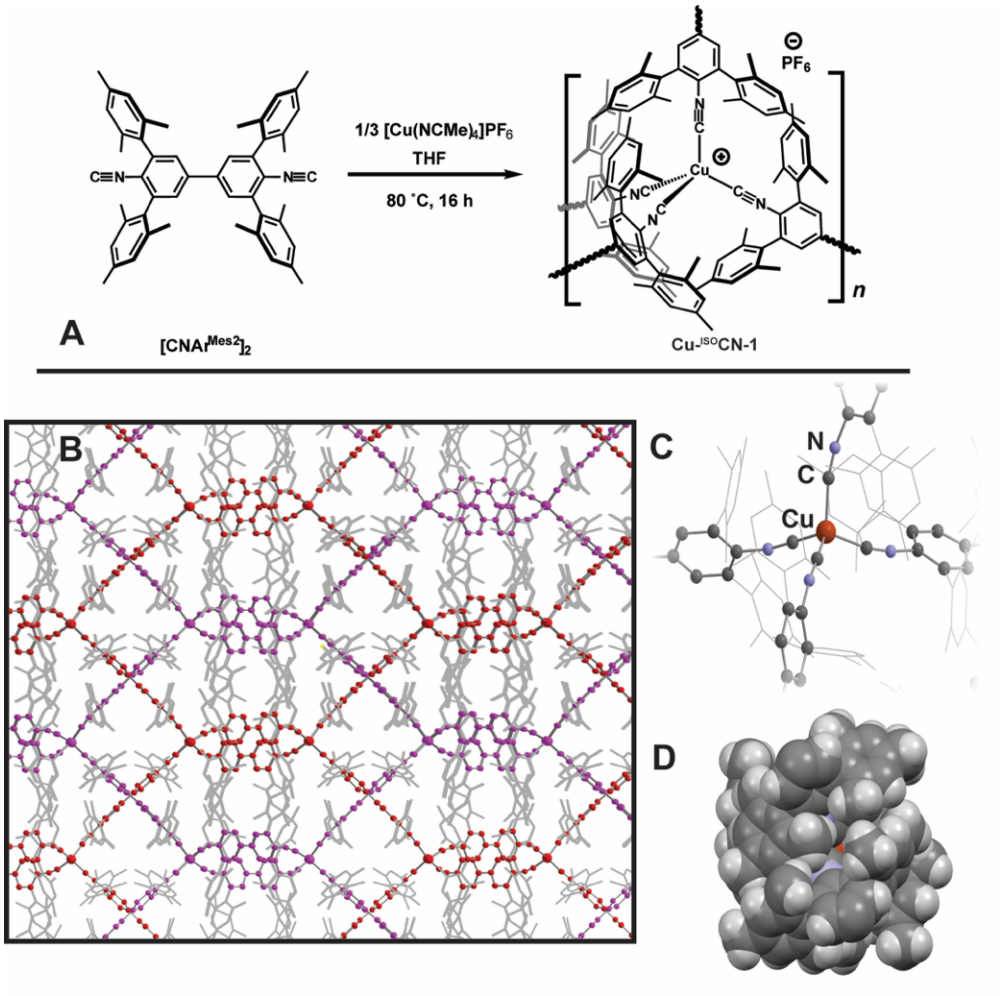

Figure 5.1. **A**: Synthesis of Cu-^{ISO}CN-1. **B**: The interpenetrated diamondoid lattice of Cu-^{ISO}CN-1 along the *ac* plane, with *m*-terphenyl groups displayed in wireframe and THF and $[PF_6]^-$ omitted for clarity. **C**: Cu(I) tetrakis-isocyanide node. **D**: Space-filling diagram of Cu(I) tetrakis-isocyanide node.

at 125 ºC for 1.5 d resulted in a significant change in its ATR-IR spectrum and produced a discernible shift in ν_{CN} to *ca*. 2149 cm^{-1} (Figure 2), indicating increased σ-donation from the isocyanides to the Cu(I) center.[34] Furthermore, PXRD analysis of Cu-^{ISO}CN-1 after thermolysis (Figure S1.13) showed that an alternate crystalline phase of lower symmetry was being accessed. In our initial report on mononuclear Cu(I) complexes supported by the monodentate isocyanide CNAr^{Mes2},[20] tetrakis-isocyanide species were not observed in solution by traditional spectroscopic methods,

even in the presence of additional equivalents of free $CNAr^{Mes2}$. This suggested that tris-$CNAr^{Mes2}$ coordination is kinetically preferred, and is attributed to the steric profile of the flanking mesityl rings. However, within coordination frameworks, kinetically "trapped," metastable coordination sites can occur due to the specific set of synthetic conditions employed,[35-38] which can transform under thermal conditions to provide the corresponding thermodynamically-preferred framework.[39] Accordingly, the transformation of Cu-^{ISO}CN-1 in the solid-state indicates steric destabilization of the framework, despite the stability often observed in interpenetrated diamondoid frameworks.[40] Indeed, substantial congestion is observed in the space-filling diagram of the Cu(I) tetrakis-isocyanide node (Figure 1, D), revealing significant steric pressures from the presence of *m*-terphenyl substituents. Consequently, the alleviation of this congestion could then enable the formation of lower-coordinate Cu(I) nodes, similar to that observed for mononuclear species in solution.

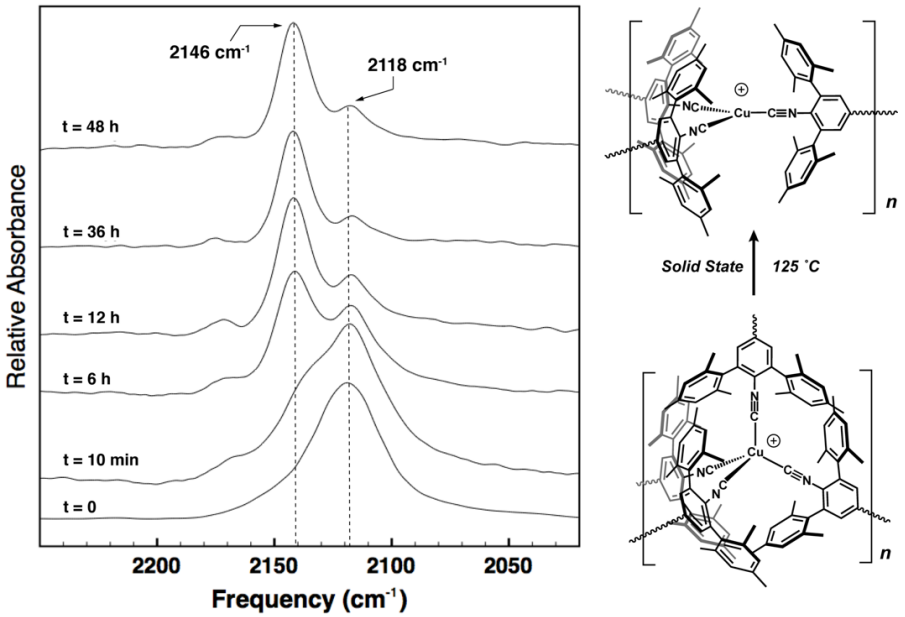

Figure 5.2. Stacked ATR-IR spectra for the thermolysis of Cu-^{ISO}CN-1 in the solid state at 125 ºC over the course of 2 days. After 36 h, no further changes in relative ν_{CN} intensity were observed. The residual band centered at 2118 cm^{-1} after 48 h of heating is free $[CNAr^{Mes2}]_2$ present in the solid-state sample.

In an effort to further investigate this solid-state transformation,[41,42] we found that heating of a suspension of Cu-^{ISO}CN-1 in THF at 100 ºC in a sealed pressure tube for five days followed by slow cooling provided large colorless block crystals of this new phase, denoted Cu-^{ISO}CN-2. The solid-state IR spectrum of Cu-^{ISO}CN-2 displayed a single strong absorbance at 2146 cm^{-1}, which is consistent with the band observed upon heating solid Cu-^{ISO}CN-1 and is suggestive of a tris-isocyanide arrangement about the Cu(I) center (Figure 2).[34] Additionally, analysis of the mother liquor indicated the presence of free $[CNAr^{Mes2}]_2$, thereby indicating linker ejection en route to the formation of Cu(I) centers featuring fewer isocyanide ligands than found in the original network. These coordination properties were confirmed by structural analysis of Cu-^{ISO}CN-2 by single-crystal X-ray crystallography, which reveals a 2-fold interpenetrated framework composed of overlapping 2D sheets (Figure 3). The 2D sheets conform to a hexagonal pattern (*hcb* net) with Cu(I) tris-isocyanide nodes capped by a coordinated THF molecule. Like Cu-^{ISO}CN-1, small rectangular channels (*ca*. 11 X 10 Å) are formed along the *b* axis that are partly occupied by the *m*-terphenyl groups, creating smaller channels (*ca*. 4.5 X 5.1 Å). This 3D to 2D transformation of Cu-^{ISO}CN-1 to Cu-^{ISO}CN-2 is noteworthy, as it represents a significant lattice rearrangement concurrent with alteration of the metal coordination environment. While the precise mechanism of this transformation is unknown at this time, this result nonetheless demonstrates that the generation of metal nodes with labile solvent ligands as the thermodynamically preferred product can be done in a straightforward manner using encumbering, multi-topic *m*-terphenyl isocyanides. As

such, we targeted the *in situ* formation of a porous framework composed of Cu(I) tris-isocyanide nodes *via* a direct approach.

Notably, a simple alteration in the synthetic protocol provided a new coordination polymer composed solely of Cu(I) tris-isocyanide nodes. Addition of a dilute solution of $[CNAr^{Mes2}]_2$ to dissolved $[Cu(MeCN)_4]PF_6$ produced an amorphous, off-white polymer with a single isocyanide band centered at 2145 cm^{-1}. Heating of this polymer at 100 ºC for 24 h followed by slow cooling over 16 h generated Cu-^{ISO}CN-3 as a colorless crystalline solid. Analysis by single crystal X-ray crystallography showed a stacked-layer, non-interpenetrated 2D coordination network ($P2_1/n$ space group) with a matching *hcb* net to Cu-^{ISO}CN-2 (Figure 3). The honeycomb network is composed of pyramidalized (C-Cu-centroid = 12.7º) tris-isocyanide Cu(I) nodes with an apically bound THF molecule, similar to that of the interpenetrated framework of Cu-^{ISO}CN-2. Additionally, a CP-MAS ^{13}C NMR spectrum of Cu-^{ISO}CN-3 identified the isocyanide carbon resonance at ~ 144 ppm (Figure 5.3), quite similar to that of molecular $[Cu(CNAr^{Mes2})_3]OTf$ (δ = 146 ppm).[20] In Cu-^{ISO}CN-3, the free THF is pointed inwards to long, narrow rectangular channels (*ca*. 23.1 X 3.7 Å) along the *a* axis. Accordingly, this spatial orientation of bound THF in Cu-^{ISO}CN-3, coupled with known solution-phase lability of the THF ligand in the monomeric species $[(THF)Cu(CNAr^{Mes2})_3]^+$,[20] prompted us to further investigate the physical properties of this material.

Purification of Cu-^{ISO}CN-3 involves three cycles of slow stirring in THF followed by centrifugation and removal of the supernatant, and provides Cu-^{ISO}CN-3 as a free-flowing microcrystalline solid. Thermogravimetric analysis (Figure 5.41)

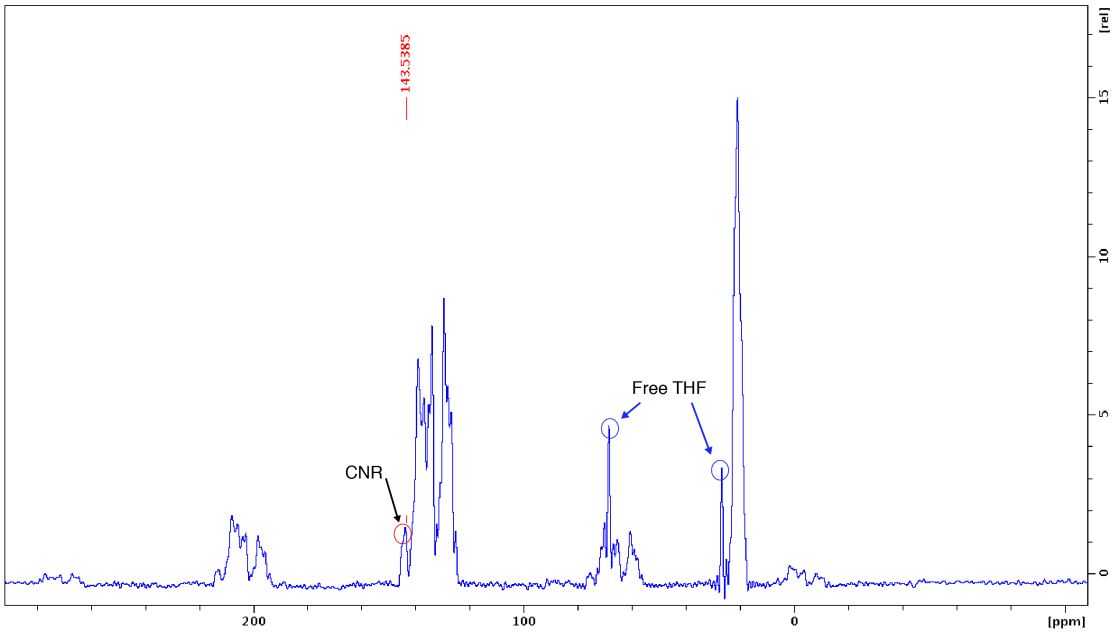

Figure 5.3. Solid-state CP-MAS ^{13}C NMR spectrum of Cu-^{ISO}CN-1.

reveals a small mass loss at 281 ºC, attributable to shallow-depth THF loss, followed by decomposition at 487 ºC, which demonstrates the remarkably high thermal stability of the framework. Surface area analysis after activation at 200 ºC by N_2 showed negligible adsorption; however, further analysis with CO_2 provided a Langmuir value of 200 m^2/g. Although many materials outcompete Cu-^{ISO}CN-3 in measured internal surface area, this Langmuir value is comparable to some zeolitic materials[43] and as

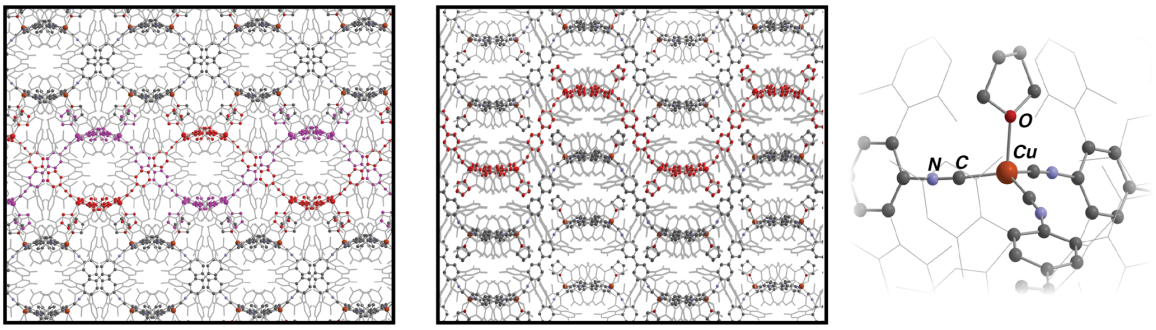

Figure 5.4. *Left*: View down the *c* axis of Cu-^{ISO}CN-2. *Middle*: View of Cu-^{ISO}CN-3 down the *ac* plane. Free solvent and $[PF_6]^-$ anions have been removed for clarity. *Right*: $[Cu(THF)([CNAr^{Mes2}]_2)_3]^+$ node of Cu-^{ISO}CN-3, similar to that found in Cu-^{ISO}CN-2.

such we believe this result supports the viability of *meta*-substituent incorporation into bridging ligands without greatly sacrificing material performance.

Cu-^{ISO}CN-3 is stable under atmospheric conditions indefinitely, but is readily dissolved by strongly polar aprotic solvents such as DMF and acetone. However, Cu-^{ISO}CN-3 shows marked stability in H_2O and other protic polar solvents, such as MeOH and ^{i}PrOH. Cu-^{ISO}CN-3 also displays remarkable stability towards 1 N HCl, 1 N HNO_3, and 1 N NaOH (2 days, 293K), conditions which typically lead to the decomposition of transition metal-isocyanide complexes as well as many carboxylate-based MOFs.[44] Analysis of Cu-^{ISO}CN-3 soaked in these solvents by ATR-IR demonstrates retention of the tris-isocyanide Cu(I) nodes within the framework, while PXRD analysis confirms preservation of crystallinity within Cu-^{ISO}CN-3 (Figure 4). We attribute the slight attenuation (~ 8 cm^{-1}) in the IR spectra of soaked Cu-^{ISO}CN-3 to the formation of new solvento species upon exchange with THF. Importantly, gas sorption analyses of Cu-^{ISO}CN-3 soaked in 1 N HNO_3 and 1 N NaOH showed only minor diminishment in measured surface area (158 m^2/g and 133 m^2/g, respectively) after activation at 200 ºC. This stability can be correlated to the high observed hydrophobicity (contact angle > 120º) for Cu-^{ISO}CN-3, likely derived from the presence of the encumbering mesityl groups. These data demonstrate significant stability can be gained from the inclusion of sterically protecting groups about the metal center for single-node coordination networks.[44]

In summary, we have demonstrated that linear, ditopic isocyanides can function as effective metal linkers in the construction of 3D and 2D coordination

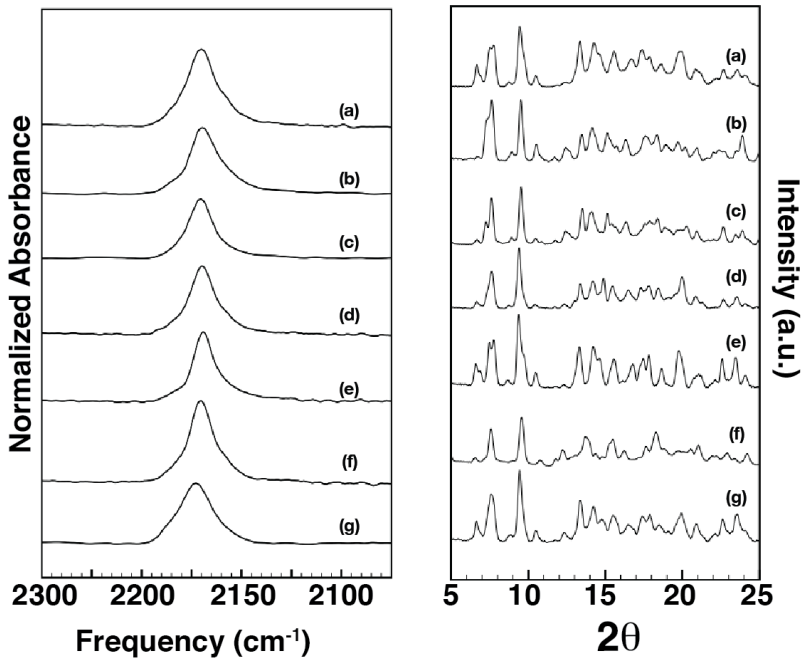

Figure 5.5. ATR-IR (left) and PXRD (right) of Cu-^{ISO}CN-3 after 2 day exposure to a) 1 N NaOH, b) 1 N HCl, c) 1 N HNO_3, d) iPrOH, e) MeOH, f) H_2O. Shown in g) as-prepared Cu-^{ISO}CN-3.

networks. Importantly, the inclusion of sterically encumbering *m*- mesityl substituents on the central biphenyl linker forces the thermodynamically favorable formation of a 2D infinite sheet consisting of solvated tris-isocyanide Cu(I) nodes over that of a tetrakis-isocyanide 3D framework. This result mirrors the solution-phase chemistry observed for Cu(I) *m*-terphenyl isocyanides, enabling a predictive ability when designing new low-coordinate coordination polymers. In addition, the steric protection afforded by the *m*-terphenyl framework confers significant thermal and aqueous stability to the extended network. This is exceptional among coordination solids containing single metal ion nodes, as structural stability in MOFs is often attributed to high nuclearity SBUs with high connectivity using high oxidation state, strongly Lewis acid metal ions with hard Lewis basic ligands. Accordingly, the application of this ligand system in the development of other frameworks constructed from low-coordinate metal nodes is underway.

5.3 Nanoscale Morphological Characteristics of Cu-^{ISO}CN-3

Given the ability to selectively form an extended planar network of Cu(I) tris-isocyanide centers, we were interested in the morphological characteristics of Cu-^{ISO}CN-3. Specifically, owing to the weak π-π stacking and van der Waals interactions that enable the formation of the 3-D lattice, we hypothesized that under appropriate conditions the individual, covalently-linked sheets could be exfoliated into single layers. These layers could then be utilized as metal organic membrane materials, which are currently under intensive study for use in separations and flow catalysis.[45] Indeed, the preparation of phase-pure materials that can be subsequently utilized in this capacity is extremely difficult, and has only recently been made possible with the aid of mixed-membrane polymers.[46] Accordingly, we have prepared of ultrathin, discrete layers of a crystalline Cu-isocyanide network for future study as a membrane material.

The high sensitivity that low-coordinate metal complexes display with regards to their coordination, dependent on the matrix environment (see Chapter 1), suggested that the geometry of the Cu(I) tris-isocyanide node could be influenced by replacement of the apical donor ligand. As an example, the pyramidilization of the Cu(I) center in [Cu(THF)(CNAr^{Mes2})$_3$]OTf (as defined in Figure 5.6), was found to be 6.96º at 100K in the solid state. However, if the apical THF ligand is substituted for the much more strongly σ-donating PMe_3 ligand, then this pyramidalization is increased to 16.37º (Figure 5.7). Accordingly, this electronic influence could be expected to have a profound influence over the macroscale properties of an arrayed Cu(I) tri-isocyanide material like Cu-^{ISO}CN-3.

Interestingly, the pyramidalization observed for the Cu(I) centers in Cu-^{ISO}CN-3 is 12.8º (average of two crystallographically distinct Cu sites), significantly more than the molecular analogue [Cu(THF)(CNAr^{Mes2})$_3$]OTf. While we attribute this distortion to be predominantly packing forces in the crystal, it can be taken as portentous that this variability is observed. Indeed, computational studies of several abbreviated Cu tris-isocyanide models incorporating different neutral donor ligands (THF, PMe_3, OH_2) show significant geometric distortions (Table 5.1 and Figure 5.8). Importantly, a difference of 4.11º was found between the models incorporating THF and OH_2 as the apical ligand, suggesting that simply substituting these two ligands would have an observable effect. Based on this large variance, we expect that in general the ligand properties of the surrounding medium to be particularly efficacious in dictating the resultant nanoscale morphology.

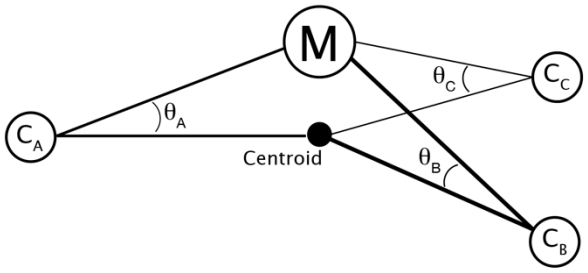

Figure 5.6. Generalized illustration of the geometric parameters used to define the pyramilization of $[Cu(L_a)(L_b)_3]^+$ species. The following equation was used to define the pyramidilization (**P**) from true trigonal-planarity: $P = \frac{\theta_a + \theta_b + \theta_c}{3}$, where θ_a, θ_b, and θ_c are the angles between M-C_n-Centroid.

Table 5.1. Comparison of the calculated *vs*. experimental values for **P** for the set of complex under study.

Model	Calculated	Experimental
$[Cu(CNXyl)_3]^+$	3.57º	n/a
$[Cu(OH_2)(CNXyl)_3]^+$	3.80º	n/a
$[Cu(PMe_3)(CNXyl)_3]^+$	17.15º	16.37º ([Cu(PMe$_3$)(CNAr^{Mes2})$_3$]OTf)
$[Cu(THF)(CNXyl)_3]^+$	7.91º	6.96º ([Cu(THF)(CNAr^{Mes2})$_3$]OTf)

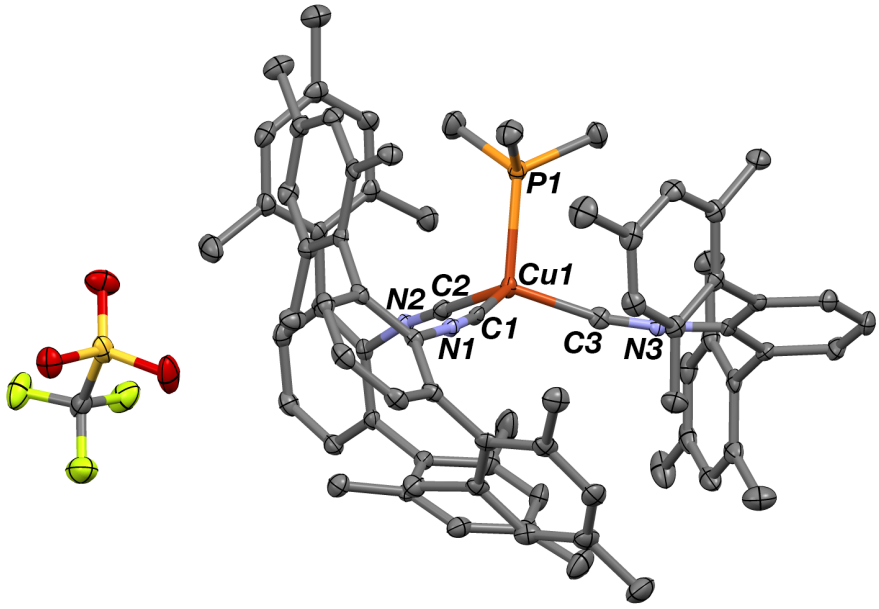

Figure 5.7. Molecular structure of $[Cu(PMe_3)(CNAr^{Mes2})_3]OTf$ (OTf = O_3SCF_3), with THF solvent molecules omitted for clarity. Selected bond distances (Å) and angles (º): Cu1-P1 = 2.3036(7); Cu1-C1 = 1.950(2); Cu1-C2 = 1.942(2); Cu1-C3 = 1.944(2); C1-Cu1-P1 = 106.51(6); P1-Cu1-C2 = 107.97(6); P1-Cu1-C3 = 104.66(6). Pyramidilization from trigonal planar geometry (calculated from centroid position between C1-C2-C3) = 16.37º.

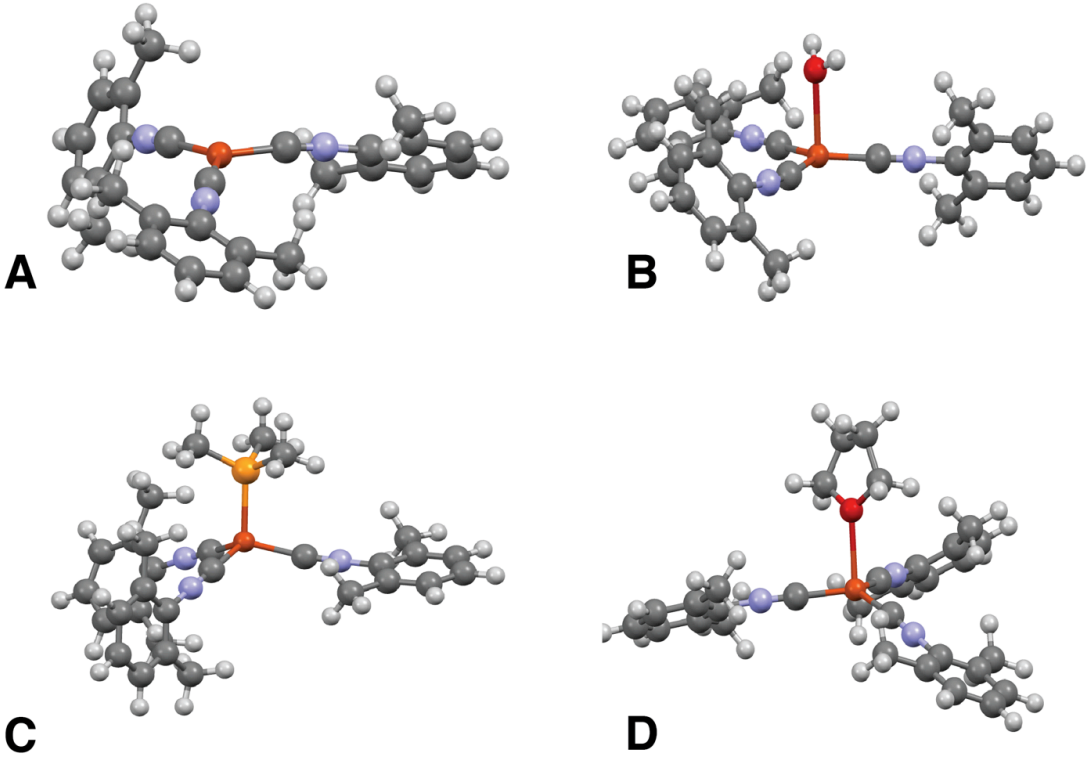

Figure 5.8. Optimized structures of $[Cu(CNXyl)_3]^+$ (**A**), $[Cu(OH_2)(CNXyl)_3]^+$ (**B**), $[Cu(PMe_3)(CNXyl)_3]^+$ (**C**), and $[Cu(THF)(CNXyl)_3]^+$ (**D**).

This "flexibility" at the molecular level led us to consider a second driving force towards the formation of discrete sheet of Cu-^{ISO}CN-3. As described above, Cu-^{ISO}CN-3 was found to be superhydrobic on account of the aryl backbone of $[CNAr^{Mes2}]_2$. With enough added energy, this hydrophobicity could aid in the separation of layers. Indeed, it was found that sonication of powdered samples of Cu-^{ISO}CN-3 in ultrapure water for 3 hours led to the formation of well-separated layers. This was established with dry-state transmission electron microscopy (TEM) of deposited Cu-^{ISO}CN-3 on Cu grid foil, as shown in Figures 5.9 to 5.12. The observed material is deposited as layers onto the grid, with contrast providing evidence for thickness. This morphology appears to be general for the bulk of the sample, as demonstrated by micrometer-scale imaging (Figure 5.12).

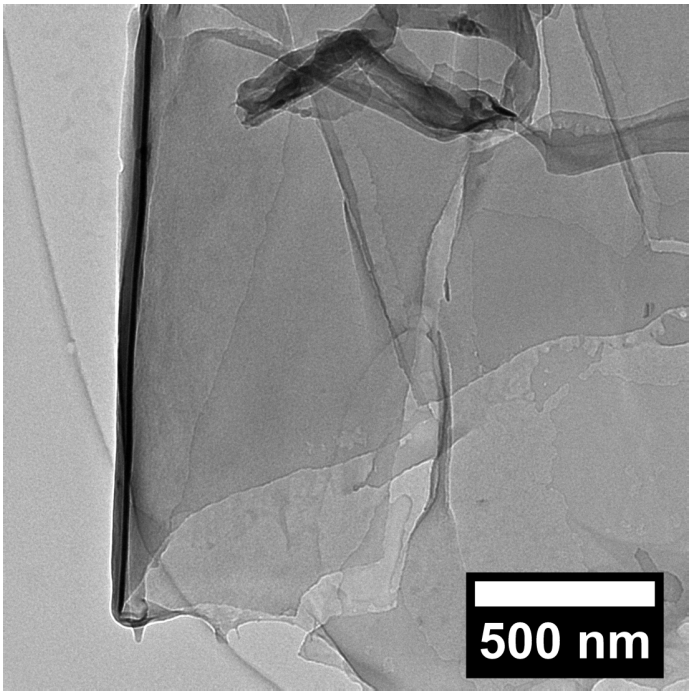

Figure 5.9. TEM image of Cu-^{ISO}CN-3 sheets prepared by sonication in H_2O.

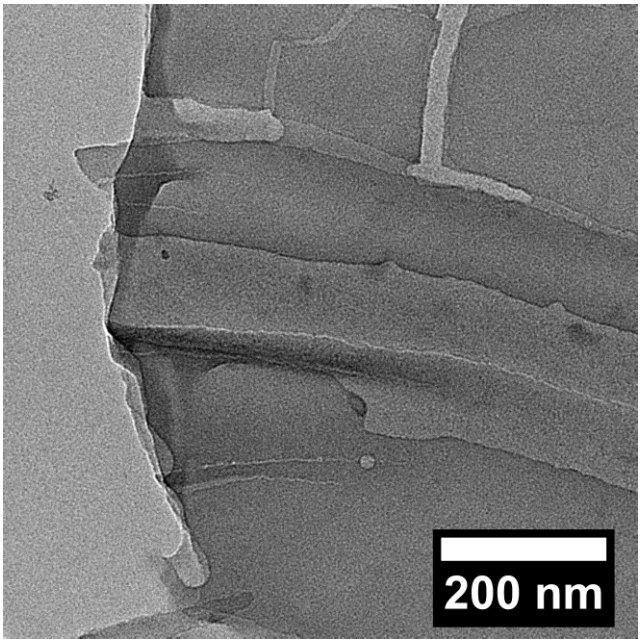

Figure 5.10. TEM image of Cu-^{ISO}CN-3 sheets prepared by sonication in H_2O.

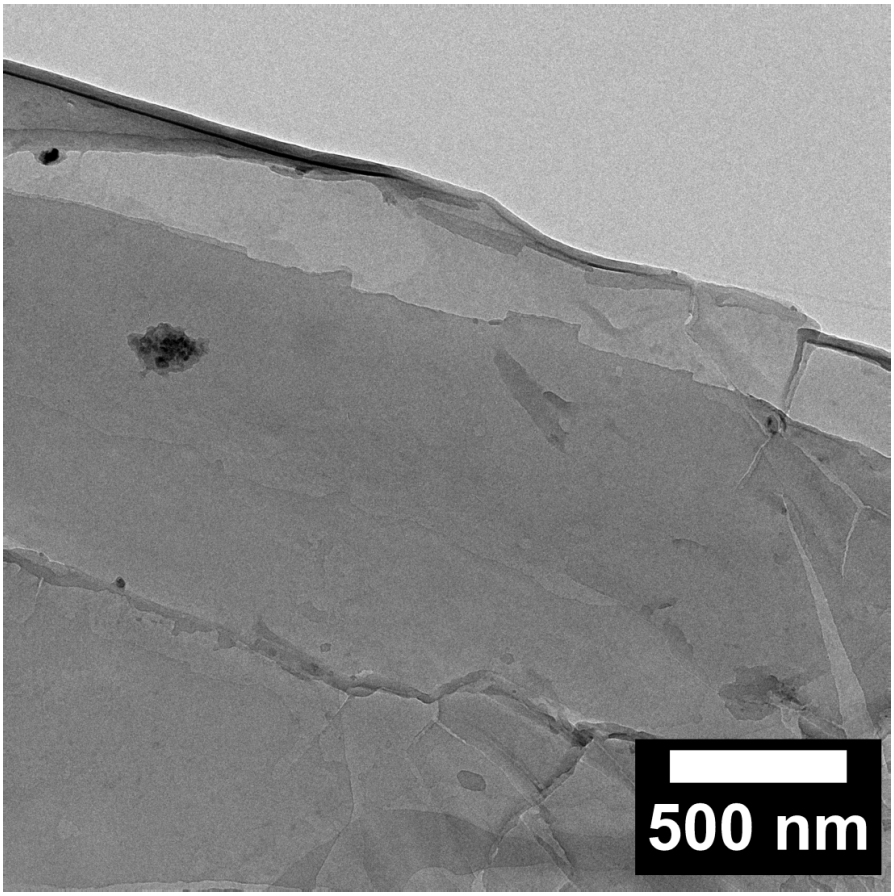

Figure 5.11. TEM image of Cu-^{ISO}CN-3 sheets prepared by sonication in H_2O.

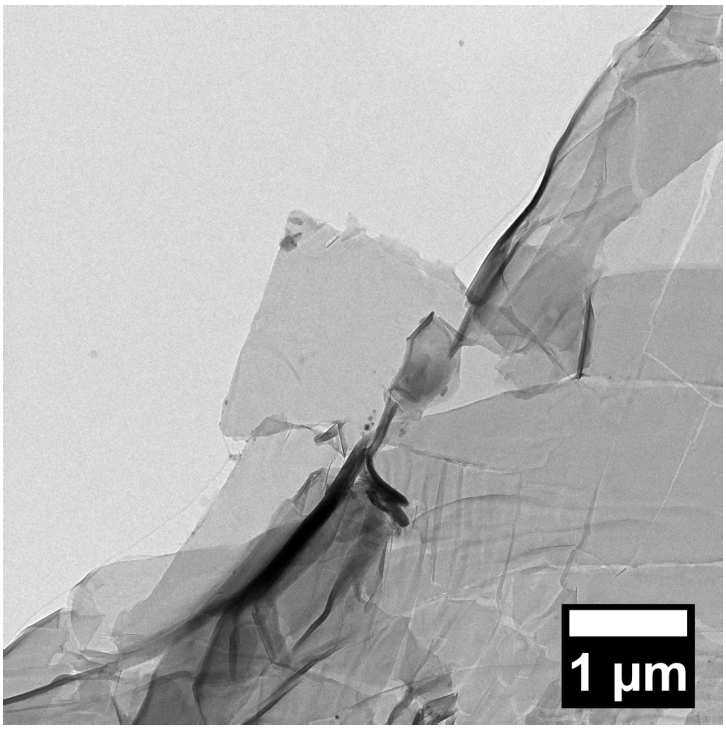

Figure 5.12. TEM image of Cu-^{ISO}CN-3 sheets prepared by sonication in H_2O.

Inspired by these results, we sought out different pathways towards functionalized morphologies for Cu-^{ISO}CN-3. An alternate means of causing layer exfoliation could be found in anion exchange, particularly for large, non-coordinating variants. To test this, we sonicated Cu-^{ISO}CN-3 in a MeOH solution of NaBAr^F (BAr^F = tetrakis[3,5-bis(trifluoromethyl)phenyl]borate) for three hours, and analyzed the resulting sample by TEM. The results, shown in Figure 5.13, indicate this method of preparation was not satisfactory towards the formation of discrete layers. Indeed, the simple sonication method in neat H_2O appears to currently be the superior form of preparing these nanoscale 2-D sheets.

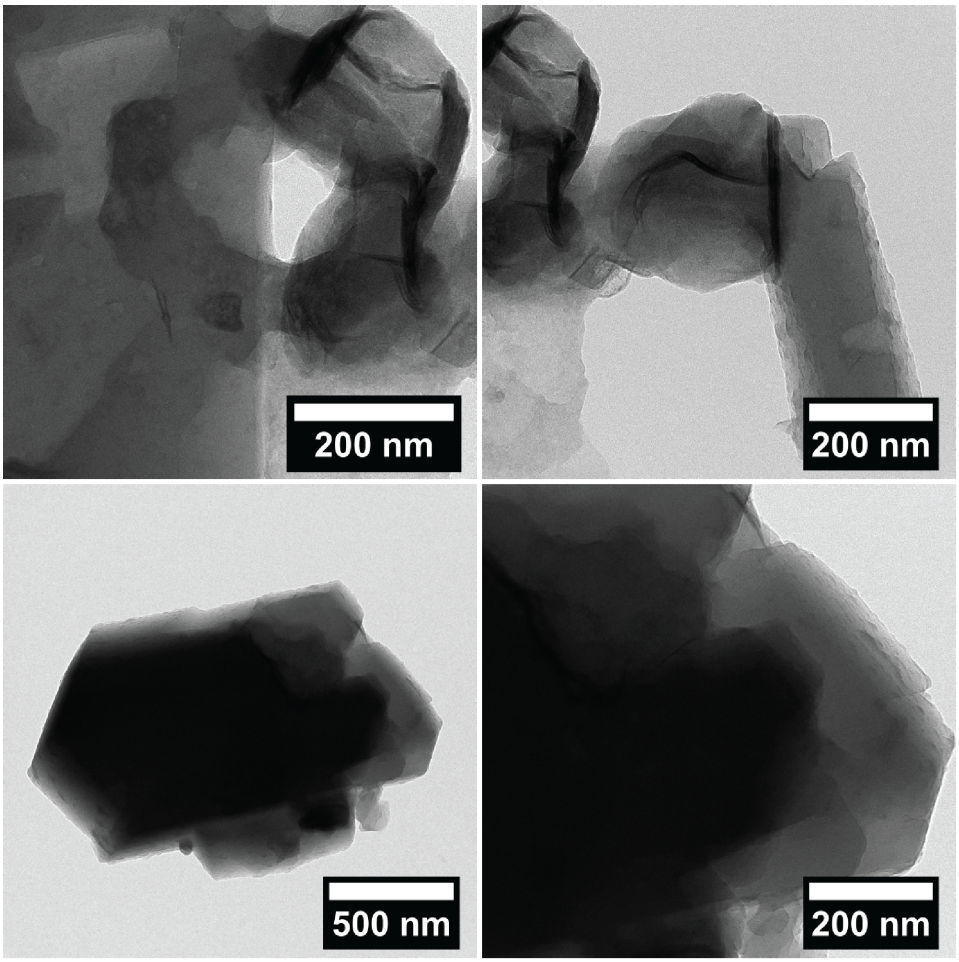

Figure 5.13. TEM images of Cu-^{ISO}CN-3 after sonication in a 20 mM solution of NaBAr^{F} in MeOH.

5.4 Concluding Remarks

The preparation of the first crystallographically characterized metal isocyanide polymers has been described. These materials show unique characteristics on account of the *m*-terphenyl isocyanide linker [CNAr^{Mes2}]$_2$, such as in the thermal decomposition of the three-dimensional material Cu-^{ISO}CN-1 to Cu-^{ISO}CN-2. Additionally, these low-coordinate materials are remarkably thermally robust, and show significant resilience to both acidic and basic aqueous conditions. Finally, a

preliminary study of the nanoscale properties of these materials was undertaken, providing for future work towards the development of specific applications.

5.5 Synthetic Procedures and Characterization Data

General Considerations. Unless otherwise stated, all manipulations were performed under an atmosphere of dry dinitrogen using standard Schlenk and glovebox techniques. Solvents were dried and degassed according to standard procedures. Unless otherwise stated, reagent grade starting materials were purchased from commercial sources and used without further purification, H_2NAr^{Mes2} and $[Cu(THF)(CNAr^{Mes2})_3]OTf$ (OTf = O_3SCF_3) was prepared as described previously.[47] $PdCl_2$(dppf) (dppf = 1,1′-bis(diphenylphosphino)ferrocene) and $(C_6H_6)[Cu(OTf)]_2$ was prepared according to literature procedures.[48,49] Solution ^1H and $^{13}C\{^1H\}$ NMR were recorded on a Bruker 300 spectrometer, a Varian 400 spectrometer, a Varian X-Sens 500 spectrometer, or a JEOL ECA-500 spectrometer. ^1H and $^{13}C\{^1H\}$ NMR chemical shifts are reported in ppm relative to $SiMe_4$ (^1H and $^{13}C\{^1H\}$ δ = 0.0 ppm) with reference to residual proton resonances of 7.26 ppm (^1H, C_6D_6) and 7.26 ppm (^1H, $CDCl_3$).[50] Solid-state CP-MAS ^{13}C NMR spectra were recorded on a 600 MHz Varian instrument using a homebuilt probe. Solution FTIR spectra were recorded on a Thermo-Nicolet iS10 FTIR spectrometer. Samples were prepared as benzene-d_6 or $CDCl_3$ solutions and injected into a ThermoFisher solution cell equipped with KBr windows. Solvent peaks were digitally subtracted from all solution FTIR spectra using a previously recorded spectrum of the solvent. Solid-state IR spectra were collected at 2 cm^{-1} resolution as either a KBr pellet or using a Bruker Platinum Alpha ATR-IR equipped with a diamond crystal. The following abbreviations are used to

describe the intensity and characteristics of important IR absorption bands: vs = very strong, s = strong, m = medium, w = weak, vw = very weak, b = broad, vb = very broad, sh = shoulder. Samples for powder X-ray diffraction were mounted on nylon loops with minimal Paratone oil, and were analyzed at 300K under a dinitrogen stream using Cu-Kα radiation (λ = 1.54178 Å) on a Bruker Kappa diffractometer equipped with a VÅNTEC-500 area detector and an Oxford Cryostream 700. HR-MS was recorded at the UCSD Molecular Mass Spectrometry Facility using an Agilent 6230 Accurate-Mass TOFMS.

Synthesis of $H_2N(p\text{-}BrAr^{Mes2})$. A CH_2Cl_2 solution of $[N(n\text{Bu})_4][Br_3]$ (7.35 g, 150 ml, 100 mM) was added quickly to a stirring solution of H_2NAr^{Mes2} in CH_2Cl_2 (4.88 g, 150 ml, 100 mM) under air. The solution changed from orange to light yellow over 1 minute, and the solution was allowed to stir for an additional hour. The mixture was then stripped of volatiles with a rotary evaporator, and the resultant solid was dissolved in 200 ml Et_2O. This solution was washed with 1 M NaOH (2 x 100 ml), deionized water (100 ml), dried over $MgSO_4$ and filtered. All volatiles were removed *in vacuo*, providing an off-white microcrystalline solid. Yield, 5.837 g, 97%. ^{1}H NMR (400.1 MHz, $CDCl_3$, 20 ˚C) δ = 7.04 (s, 2H, *m*-Ar), 6.96 (s, 4H, *m*-Mes), 3.17 (s, 2H, NH_2) 2.32 (s, 6 H, *p*-(Mes-CH_3)), 2.06 (s, 12H, *o*-(Mes-CH_3)). ^{13}C{^{1}H} NMR (125.7 MHz, $CDCl_3$, 20 ˚C) δ = 152.1, 140.3, 137.5, 137.0, 134.0, 131.1, 128.6, 127.8, 21.3 (*p*-Mes-*C*H$_3$), 20.2 (*o*-Mes-*C*H$_3$) ppm. FTIR ($CDCl_3$, KBr windows, 20 ˚C): 3485 (w), 3389 (w), 2950 (w), 2921 (m), 2858 (w), 1599 (w), 1453 (s), 1378 (w), 1234 (w),

854 (w) cm^{-1}. HR-MS (ESI-TOFMS): predicted for $[M+H]^+ = C_{24}H_{27}NBr$, 408.1321, found m/z = 408.1323.

Synthesis of $H_2N(p\text{-}(BPin)Ar^{Mes2})$ (Pin = 1,1,2,2-$Me_4C_2O_2$). A resealable ampoule was charged with $H_2N(Ar^{Mes2}\text{-}p\text{-}Br)$ (0.898 g, 2.20 mmol), $PdCl_2(dppf)$ (0.816 g, 0.154 mmol, 7 mol %), B_2Pin_2 (0.613 g, 2.41 mmol, 1.1 eq.), KOAc (0.646 g, 6.59 mmol, 3 eq.), and dioxane (7 ml). The ampoule was then sealed under an N_2 atmosphere and stirred at 80 ˚C for 14 h. The mixture was cooled and all volatiles were removed under reduced pressure. The resultant residue was then purified by column chromatography (silica gel, with Celite packing on top) using a 2% EtOAc/hexanes solution to elute $H_2N(p\text{-}(BPin)Ar^{Mes2})$. The fractions were collected and concentrated to a solid by rotatory evaporation to afford a colorless solid. Yield: 0.880 g, 88%. ^1H NMR (400.1 MHz, $CDCl_3$, 20 ˚C) δ = 7.35 (s, 2H, *m*-Ar), 6.93 (s, 4H, *m*-Mes), 3.39 (s, 2H, NH_2) 2.30 (s, 6 H, *p*-(Mes-CH_3)), 2.04 (s, 12H, *o*-(Mes-CH_3)), 1.30 (s, 12 H, , BPin-CH_3). $^{13}C\{^1H\}$ NMR (125.7 MHz, $CDCl_3$, 20 ˚C) δ = 143.9, 137.2, 136.8, 135.7, 135.1, 134.9, 128.4, 127.9, 125.0, 83.2 (BO*C*$(CH_3)_2$), 25.1 (BOC(*C*$H_3)_2$), 21.2 (*p*-Mes-*C*H_3), 20.3 (*o*-Mes-*C*H_3) ppm. FTIR ($CDCl_3$, KBr windows, 20 ˚C): 3493 (w), 3392 (w), 2980 (m), 2919 (w), 2860 (w), 1605 (s), 1365 (vs), 1141 (s), 964 (w), 920 (w), 853 (m) cm^{-1}. HR-MS (ESI-TOFMS): predicted for $[M+H]^+ = C_{30}H_{39}NBO_2$, 456.3704, found m/z = 456.3074.

Synthesis of $[H_2NAr^{Mes}]_2$. A resealable ampoule was charged with $H_2N(p\text{-}BrAr^{Mes2})$ (0.879 g, 1.93 mmol), $H_2N(p\text{-}(BPin)Ar^{Mes2})$ (0.790 g, 1.93 mmol), Pd_2dba_3 (0.177 g,

0.193 mmol, 10 mol %, dba = dibenzylideneacetone), PCy_3 (0.108 g, 0.386 mmol, 20 mol %), and $Ba(OH)_2$ (1.156 g, 6.57 mmol, 3.5 eq.) and dioxane (20 ml). To this was added degassed, deionized H_2O (5.5 ml), and the mixture was vigorously stirred at 80 ˚C for 16 h under an atmosphere of N_2. The mixture was cooled, filtered through a medium porosity fritted funnel packed with Celite, and the filter cake was extracted with CH_2Cl_2 (3 x 15 ml). The mixture was stripped of volatiles under reduced pressure, providing a brown residue. The residue was dissolved in 100 ml CH_2Cl_2 and washed with H_2O (100 ml, pH ≈ 6, acidified with 1.0 M HCl), H_2O (100 ml, neutral pH), and brine (150 ml). The aqueous washes were then combined and extracted with CH_2Cl_2 (3 x 100 ml). The organic extracts were combined, dried over $MgSO_4$, filtered, and volatiles were removed by rotary evaporation. The resultant solid was purified by column chromatography (silica gel) using a gradient of 0 to 5% EtOAc/hexanes, collecting the middle fractions. The fractions were combined and concentrated under reduced pressure to provide $[H_2NAr^{Mes}]_2$ as an off-white solid. Yield: 1.10 g, 86%. ^{1}H NMR (400.1 MHz, $CDCl_3$, 20 ˚C) δ = 7.16 (s, 4H, *m*-Ar), 6.95 (s, 8H, *m*-Mes), 3.14 (s, 4H, N*H*$_2$), 2.31 (s, 12 H, *p*-Mes-C*H*$_3$)), 2.08 (s, 24H, *o*-Mes-C*H*$_3$). ^{13}C{^{1}H} NMR (125.7 MHz, $CDCl_3$, 20 ˚C) δ = 152.1, 139.3, 137.1, 136.9, 135.6, 128.5, 126.3, 126.2, 21.3 (*p*-*C*H$_3$), 20.4 (*o*-*C*H$_3$) ppm. FTIR ($CDCl_3$, KBr windows, 20 ºC): 3483 (w), 3382 (w), 2922 (m), 2856 (w), 1611 (w), 1448 (s), 1256 (w), 1016 (w), 855 (w), 655 (w) cm^{-1}. HR-MS (ESI-TOFMS): predicted for $[M+H]^+$ = $C_{48}H_{53}N_2$, 657.4203, found *m/z* = 657.4201.

Synthesis of [HC(O)HNAr^{Mes2}]$_2$. Formic acid (0.770 g, 16.7 mmol, 10 eq.) was added dropwise via syringe to stirring acetic anhydride (1.37 g, 13.4 mmol, 8 eq.). The mixture was warmed to 50 ˚C for 1 h to generate formyl acetic anhydride, cooled to RT, and transferred to a stirring THF solution of [H_2NAr^{Mes}]$_2$ (1.098 g, 1.67 mmol, 50 ml). This mixture was stirred for 16 h, after which all volatiles were removed by rotary evaporation. Excess formic acid and acetic acid are removed upon heating the mixture to 80 ºC for 2 h under dynamic vacuum. The resultant white solid, [HC(O)HNAr^{Mes2}]$_2$, is used without further purification. Yield: 1.110 g, 93%. ^{1}H NMR (400.1 MHz, $CDCl_3$, 20 ˚C) δ = 7.66 (d, 2H, *J* = 11 Hz, NHC(O)*H*), 7.37 (s, 4H, *m*-Ar), 6.96 (s, 8 H, *m*-Mes), 6.61 (d, 2H, *J* = 11 Hz, N*H*C(O)H), 2.31 (s, 6 H, *p*-Mes-C*H*$_3$), 2.04 (s, 12H, *o*-Mes-C*H*$_3$). ^{13}C{^{1}H} NMR (125.7 MHz, $CDCl_3$, 20 ºC) δ = 162.5 (H*C*(O)N), 138.3, 135.9, 134.3, 133.8, 132.0, 129.1, 128.2, 126.9, 21.2 (*p*-Mes-*C*H$_3$), 20.6 (*o*-Mes-*C*H$_3$) ppm. FTIR ($CDCl_3$, KBr windows, 20 ˚C): ν_{CO} = 1682 cm^{-1} (s), ν_{NH} = 3359 (w), also 2919 (w), 2849 (w), 1602 (m), 1417 (w), 1363 (m), 1258 (m), 1220 (w) cm^{-1}. HR-MS (ESI-TOFMS): predicted for $[M+H]^+$ = $C_{50}H_{53}O_2N_2$, 713.4102, found *m/z* = 713.4102.

Synthesis of [CNAr^{Mes2}]$_2$. To a stirring CH_2Cl_2 solution of [HC(O)HNAr^{Mes2}]$_2$ (1.110 g, 1.56 mmol, 50 ml) was added diisopropylamine (0.68 g, 6.70 mmol, 4 equiv.) via syringe. After stirring for 5 minutes, $POCl_3$ (0.64 g, 4.19 mmol, 2.7 equiv.) was added dropwise via syringe, and the solution was stirred for 5 hours. Aqueous Na_2CO_3 (1.5 M, 50 ml) was added, and the resulting mixture was stirred for 2 h. The organic and aqueous layers were then separated, and the organic layer was

washed with 50 ml H_2O. The aqueous layers were combined and extracted with CH_2Cl_2 (3 X 50 ml). The organic extracts were combined, dried over $MgSO_4$, filtered, and volatiles were removed *in vacuo*. A minimal amount of MeCN was added to the resultant residue, which was then briefly heated to reflux followed by cooling to – 40 ˚C. The off-white solid was collected by filtration and dried under reduced pressure. Yield: 0.946 g, 90%. ^{1}H NMR (400.1 MHz, $CDCl_3$, 20 C˚) δ = 7.44 (s, 4H, *m*-Ar), 6.97 (s, 8 H, *m*-Mes), 2.33 (s, 6 H, *p*-Mes-C*H*$_3$), 2.07 (s, 12H, *m*-Mes-C*H*$_3$). ^{13}C{^{1}H} NMR (125.7 MHz, $CDCl_3$, 20 ˚C) δ = 168.2 (*C*N), 140.4, 140.3, 138.2, 135.6, 133.8, 128.6, 127.8, 125.7. 21.8 (*p*-Mes-*C*H$_3$)), 20.4 (*o*-Mes-*CH$_3$*) ppm. ^{13}C{^{1}H} NMR (125.7 MHz, C_6D_6, 20 ˚C) = 172.2 (*C*N), 153.9, 141.1, 139.9, 138.2, 135.8, 134.3, 129.0, 128.6, 127.5, 21.2 (*p*-Mes-*C*H$_3$), 20.3 (*o*-Mes-*CH$_3$*) ppm. FTIR ($CDCl_3$, KBr windows, 20 ˚C): ν_{CN} = 2125 cm^{-1} (s), also 2924 (m), 2855 (w), 1612 (s), 1592 (s), 1444 (m), 1262 (w), 854 (m), 790 (w) cm^{-1}. FTIR (C_6D_6, KBr windows, 20 ˚C): ν_{CN} = 2118 cm^{-1} (s). HR-MS (ESI-TOFMS): predicted for $[M+H]^+$ = $C_{48}H_{49}N_2$, 676.3890, found *m/z* = 676.3886. Melting point (uncorrected, 3 runs) = 200 ºC.

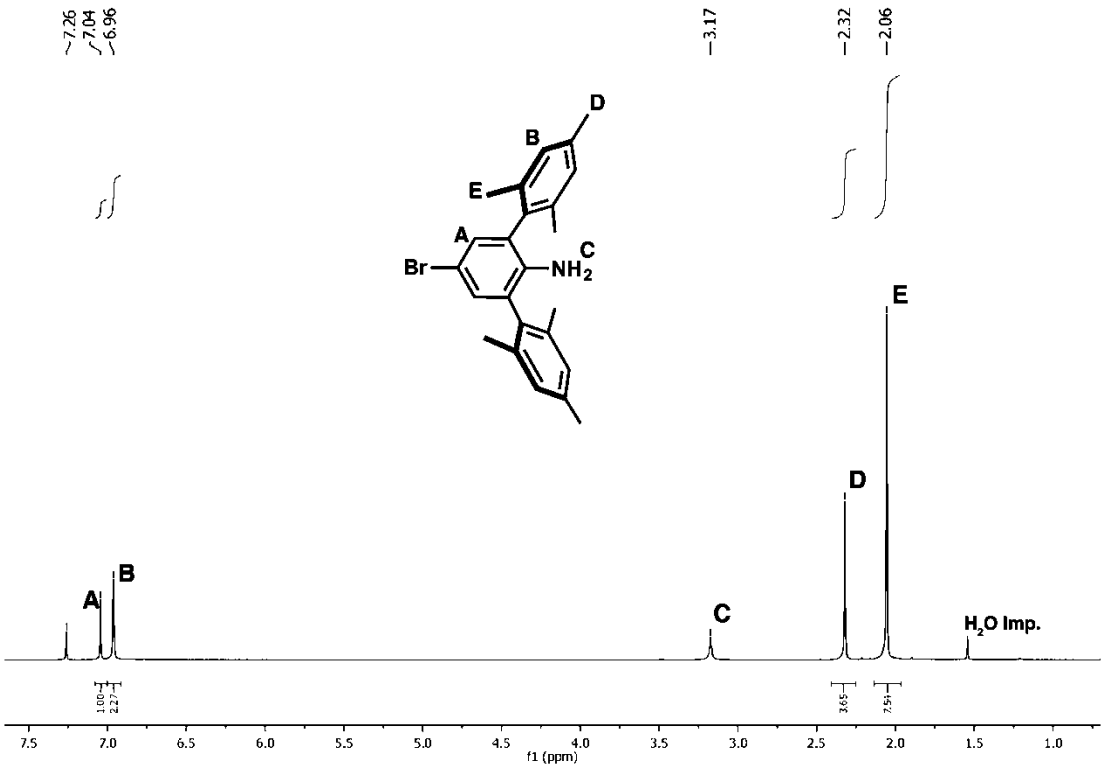

Figure 5.14. ^{1}H NMR spectrum ($CDCl_3$, 400.1 MHz, 20 °C) of H_2N(*p*-$BrAr^{Mes2}$).

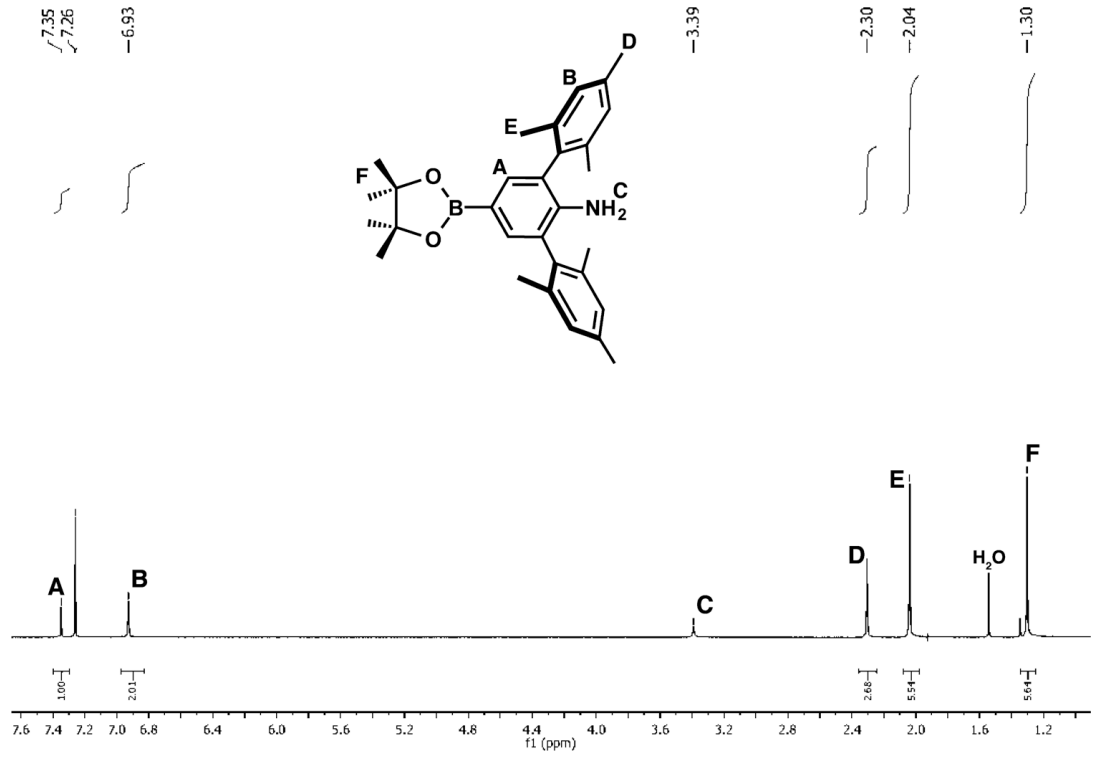

Figure 5.15. ^{1}H NMR spectrum ($CDCl_3$, 400.1 MHz, 20 °C) of H_2N(*p*-(BPin)Ar^{Mes2}).

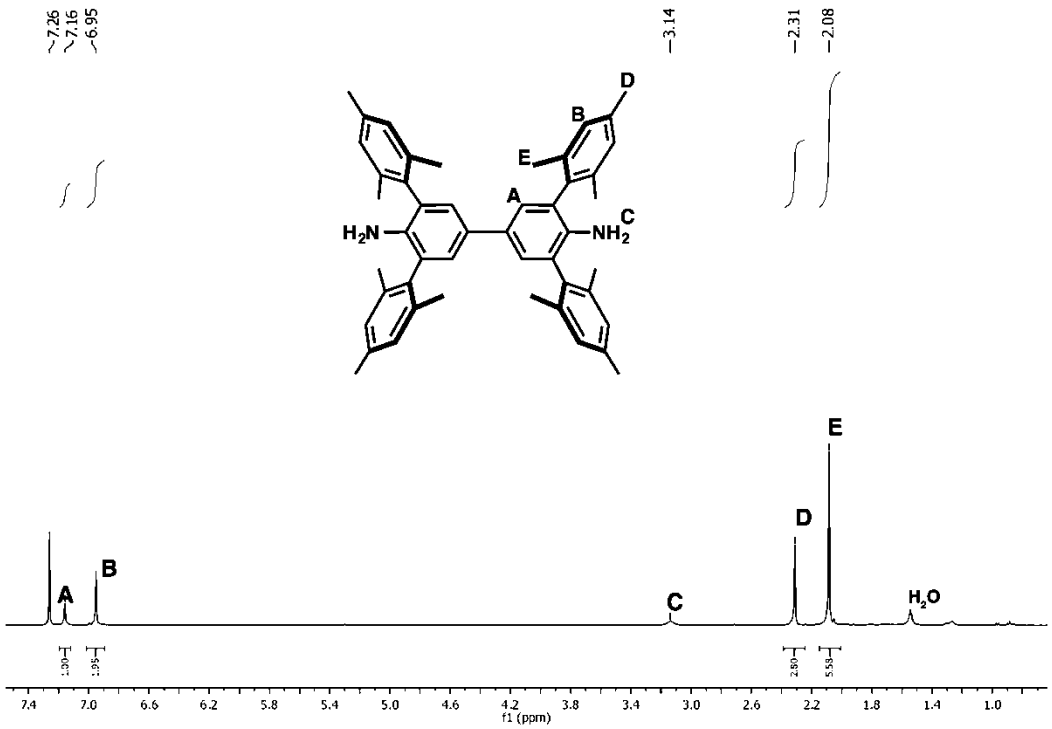

Figure 5.16. ^{1}H NMR spectrum ($CDCl_3$, 400.1 MHz, 20 °C) of $[H_2NAr^{Mes2}]_2$.

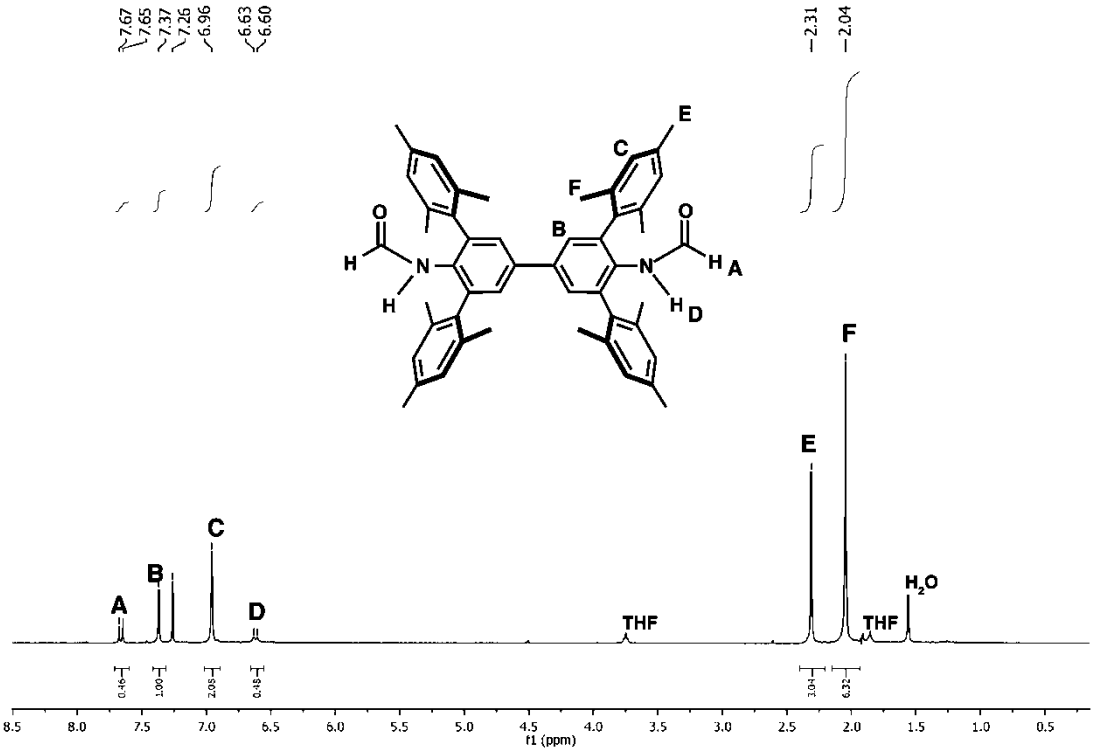

Figure 5.17. ^{1}H NMR spectrum ($CDCl_3$, 400.1 MHz, 20 °C) of $[HC(O)HNAr^{Mes2}]_2$.

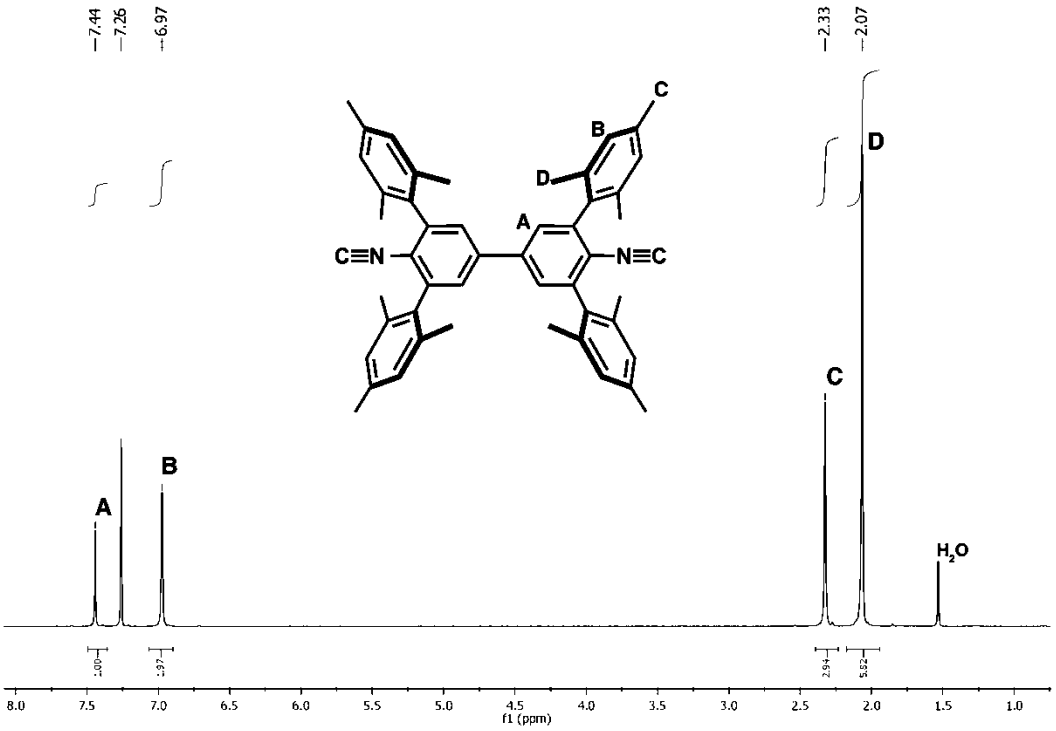

Figure 5.18. ^{1}H NMR spectrum ($CDCl_3$, 400.1 MHz, 20 °C) of $[CNAr^{Mes2}]_2$.

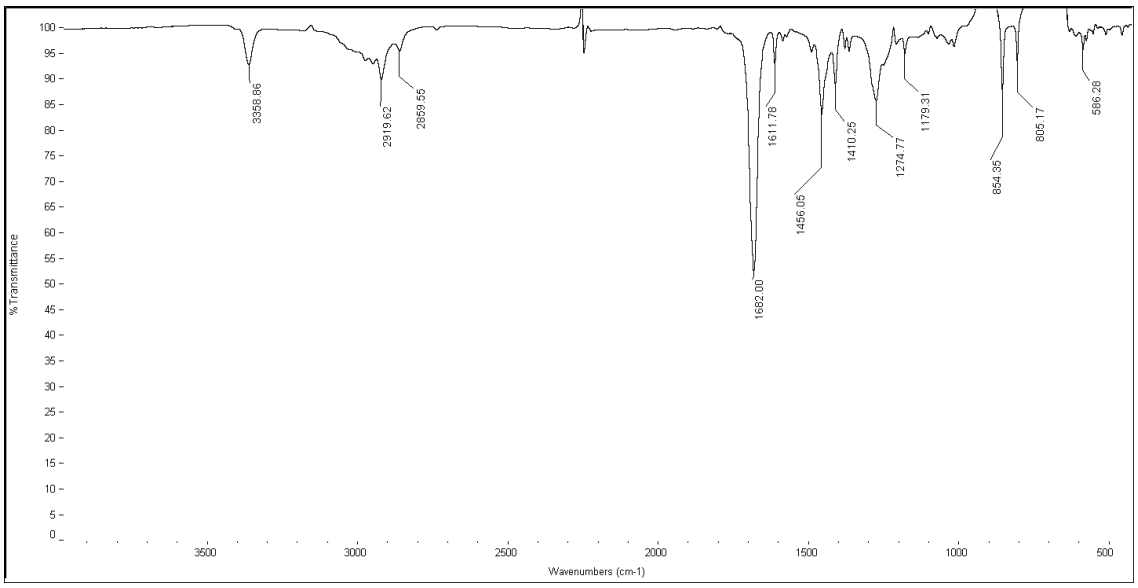

Figure 5.19. Solution IR spectrum ($CDCl_3$, 20 °C) of $[HC(O)HNAr^{Mes2}]_2$.

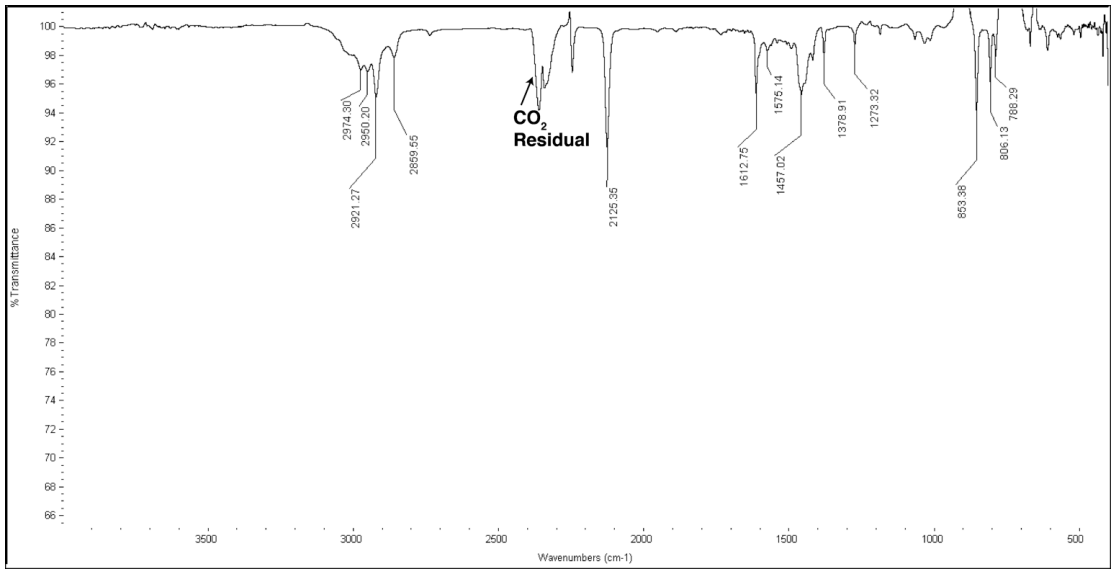

Figure 5.20. Solution IR spectrum ($CDCl_3$, 20 ˚C) of $[CNAr^{Mes2}]_2$.

Preparation of Cu(I) Networks

Note: All preparations were performed under an atmosphere of dry dinitrogen or argon. Once produced, the materials Cu-^{ISO}CN-1, Cu-^{ISO}CN-2, and Cu-^{ISO}CN-3 are stable under normal atmospheric conditions.

Caution! Significant pressures can be generated during the preparations of these materials. Care must be taken to ensure adequate safety measures are in place.

Cu-^{ISO}CN-1. $[Cu(MeCN)_4]PF_6$ (0.013 g, 0.035 mmol) and $[CNAr^{Mes2}]_2$ (0.070 g, 0.104 mmol) were mixed using a mortar and pestle for 1 min to form a white powder.

This was then added to a thick-walled pressure tube and 0.5 ml THF was added to form a thick paste. The mixture was heated at 80 ˚C for 16 h in an oven, removed and then allowed to cool rapidly to room temperature. This procedure produced Cu-^{ISO}CN-1 as large colorless crystals, which were suitable for X-ray crystallographic analysis. Bulk collection was performed via addition of THF (3 ml) and sonication for 30 min in a room temperature bath. The suspended solid is centrifuged, and the supernatant removed. Fresh THF (5 ml) was added and the suspension stirred for 24 h, after which centrifugation was used to separate the solid from the supernatant, the latter of which was removed and discarded. This process was repeated two more times, followed by removal of the volatiles *in vacuo*, to provide Cu-^{ISO}CN-1 as a microcrystalline solid. Yield: 0.054 g.

Solid state thermal decomposition of Cu-^{ISO}CN-1. A solid sample of Cu-^{ISO}CN-1 (~0.02 g) was placed in a 10 ml scintillation vial under air. The vial was placed in a sand bath within an oven at 125 ºC, and samples were taken at regular intervals by cooling the sample to room temperature.

Cu-^{ISO}CN-2. A sample of Cu-^{ISO}CN-1 (0.015 g) was suspended in THF (2 ml) and heated at 100 ºC inside a pressure tube for 5 days. The solution was allowed to cool to room temperature slowly over 24 h. The supernatant was removed and the crystals were gently washed with THF once. The crystals were re-suspended in 5 ml THF and were gently swirled, followed by centrifugation to isolate Cu-^{ISO}CN-2. The crystals

were placed under dynamic vacuum at room temperature for 4 h to produce a free-flowing microcrystalline solid. Yield: 0.009 g.

Synthesis of Cu-^{ISO}CN-3. To a quickly stirred THF solution of $[Cu(MeCN)_4]PF_6$ (0.004 g, 0.011 mmol, 2 ml) in a thick-walled pressure tube was added a THF solution of $[CNAr^{Mes2}]_2$ (0.023 g, 0.034 mmol, 2 ml) over 5 minutes. Upon addition of approximately half the solution of $[CNAr^{Mes2}]_2$, a white suspension evolved and remained throughout the rest of the addition. The combined reagents were allowed to stir for 40 min, and an amorphous suspension was deposited on the tube wall. The supernatant was removed, and the solid was gently washed with THF (3 X 10 ml). Upon removal of the final wash, with residual solvent still remaining, the tube was sealed with a Teflon screw cap equipped with a Viton O-ring. The tube was placed in an oven at 100 ºC for 48 h and allowed to cool slowly to room temperature over 24 h. In place of the amorphous polymer was a colorless crystalline solid, from which single crystals could be selected for X-ray crystallographic analysis. Bulk collection of the material is performed via the addition of 5 ml THF, followed by 30 min sonication in a room temperature bath. The suspended solid is centrifuged and the supernatant removed, and all volatiles are removed *in vacuo* to afford microcrystalline Cu-^{ISO}CN-3. Yield: 0.016 g.

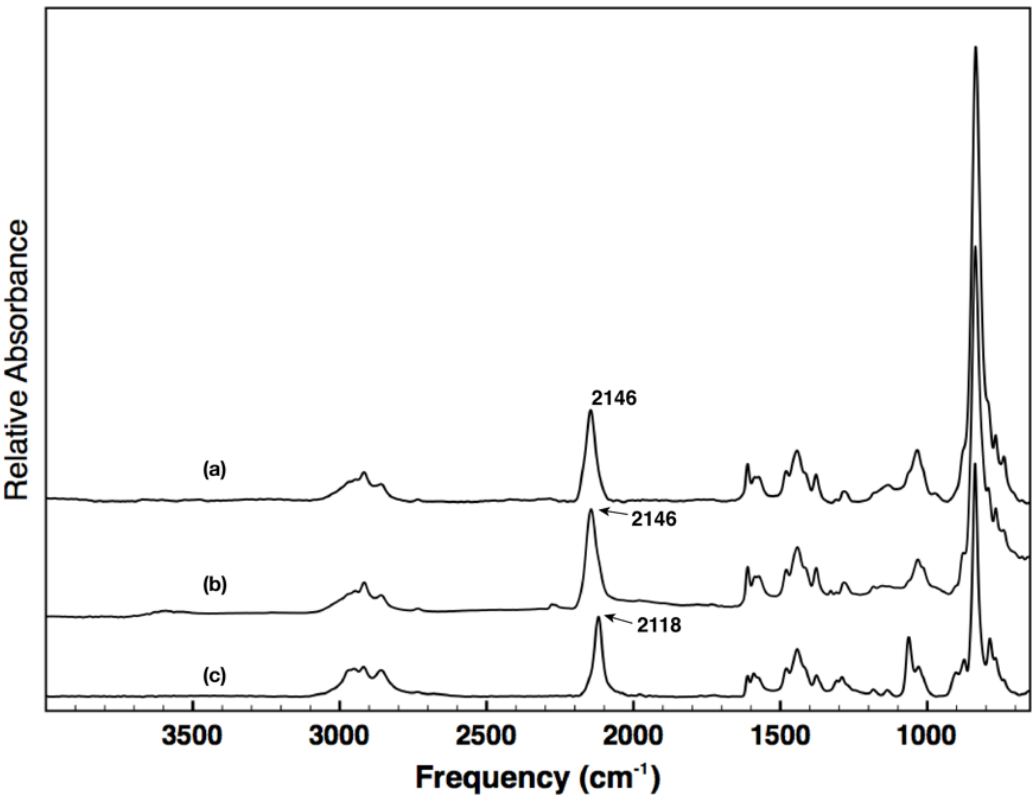

Figure 5.21. Solid-state ATR-IR spectra of **(a)** Cu-^{ISO}CN-3, **(b)** Cu-^{ISO}CN-2, and **(c)** Cu-^{ISO}CN-1.

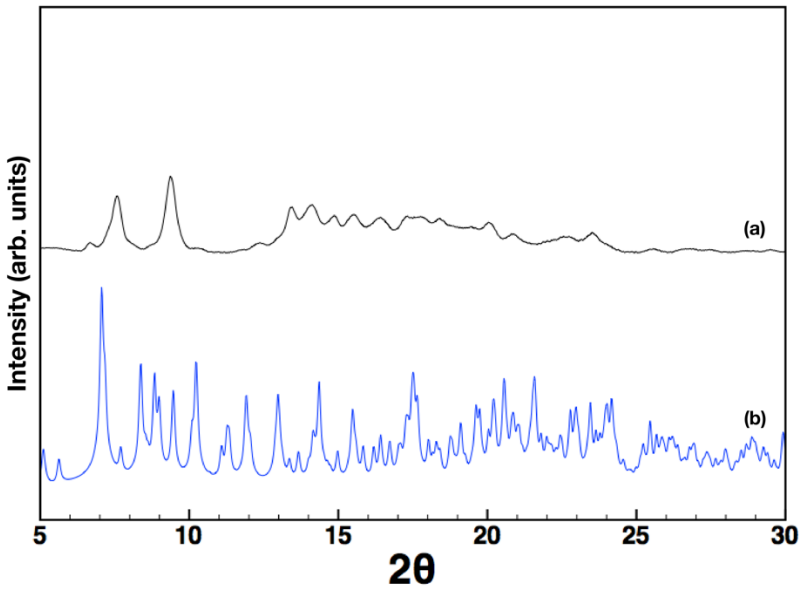

Figure 5.22. Experimental and predicted powder X-ray diffraction patterns for Cu-^{ISO}CN-3. **(a)** As-isolated crystalline phase; **(b)** predicted pattern of Cu-^{ISO}CN-3 from single-crystal X-ray structure.

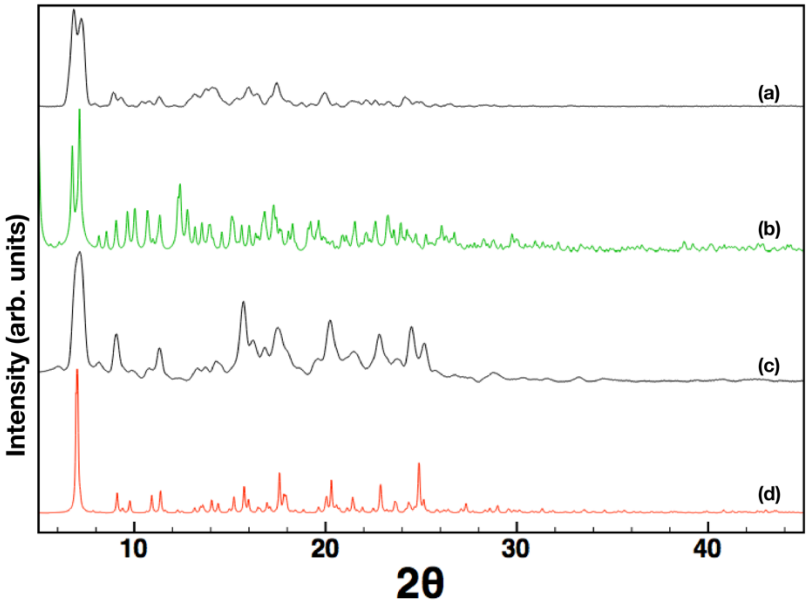

Figure 5.23. Experimental and predicted powder X-ray diffraction patterns for **(a)** Cu-^{ISO}CN-2 (experimental), **(b)** Cu-^{ISO}CN-2 (predicted), **(c)** Cu-^{ISO}CN-1 (experimental), **(d)** Cu-^{ISO}CN-1 (predicted). All predicted patterns were generated from structural solutions attained from single-crystal X-ray diffraction studies.

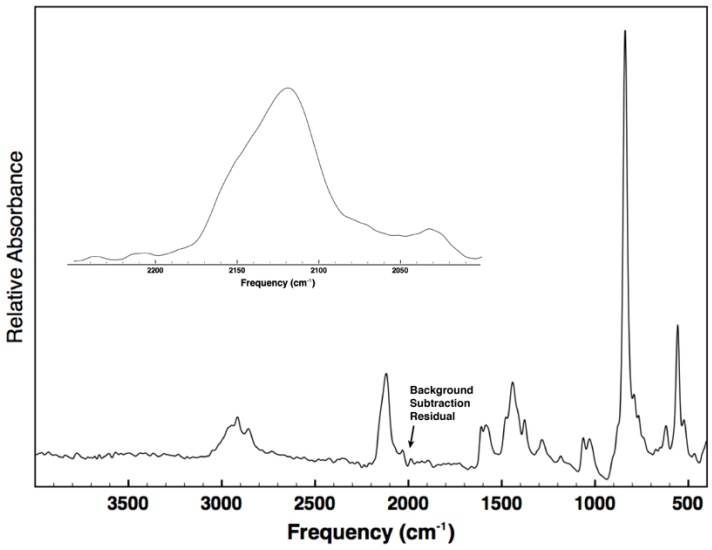

Figure 5.24. ATR-IR of Cu-^{ISO}CN-1 heated at 50 ºC for 5 days. Inset view shows the isocyanide region.

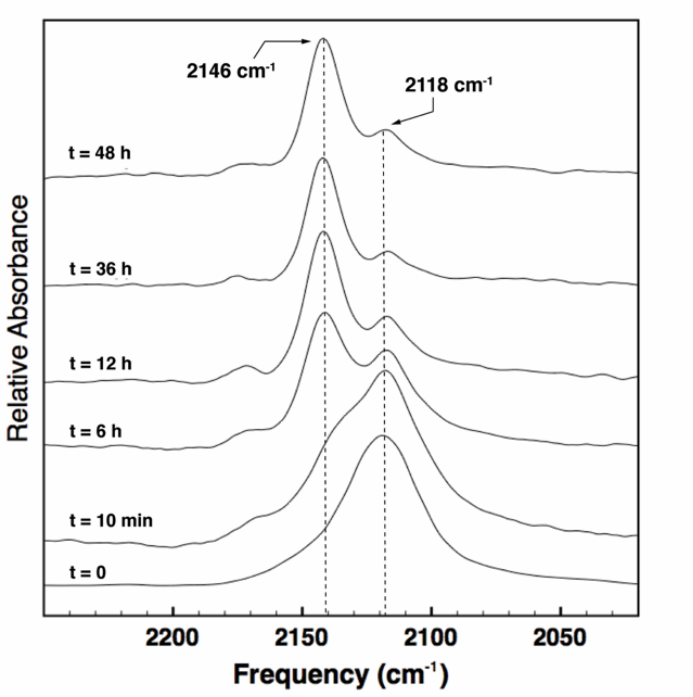

Figure 5.25. ATR-IR of Cu-^{ISO}CN-1 heated at 125 ˚C over a 48 h period. No further changes in the ATR-IR spectra are observed after 36 h.

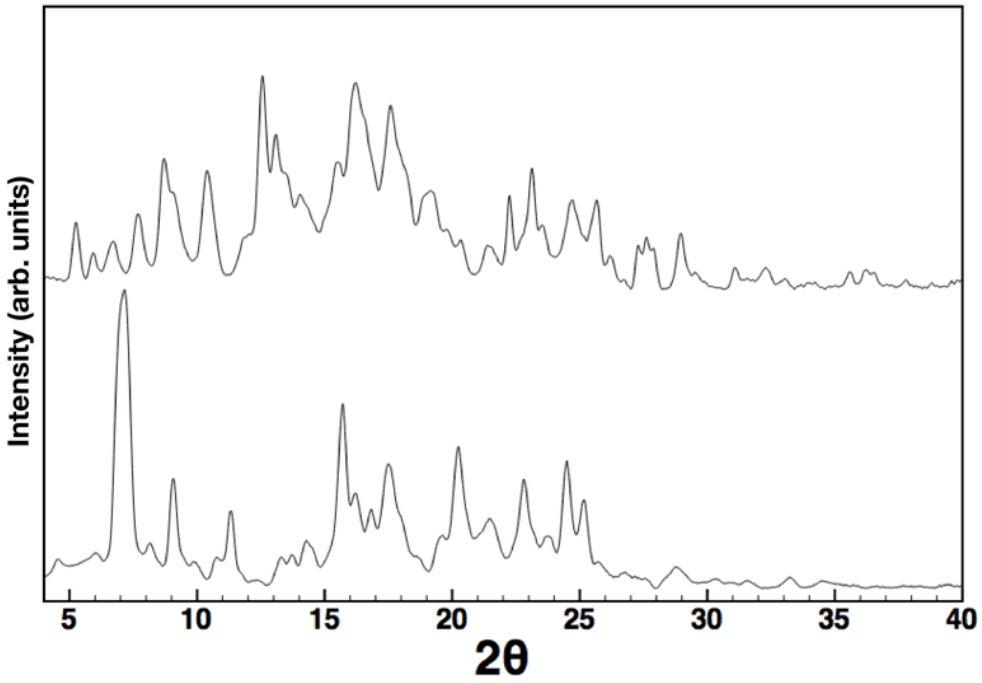

Figure 5.26. Powder X-ray diffraction pattern of Cu-^{ISO}CN-1 heated at 125 ºC for 2 days in the solid state (**top**) and representative pattern of Cu-^{ISO}CN-1 as prepared (**bottom**).

Environmental Stability Studies on Cu-^{ISO}CN-3.

In a typical preparation, 0.005 g of Cu-^{ISO}CN-3 was placed in a 2 mL scintillation vial with the corresponding solution under study. The suspension was allowed to stand for 2-4 days, with minor agitation interspersed. All aqueous solutions were prepared using H_2O tested to 18.2 MΩ resistance. The solvent was then removed *via* rotary evaporation; in the case of acidic/basic solutions, the material was suspended in 1 ml Et_2O and washed with H_2O (3 X 3 ml). Volatiles were then removed *in vacuo*.

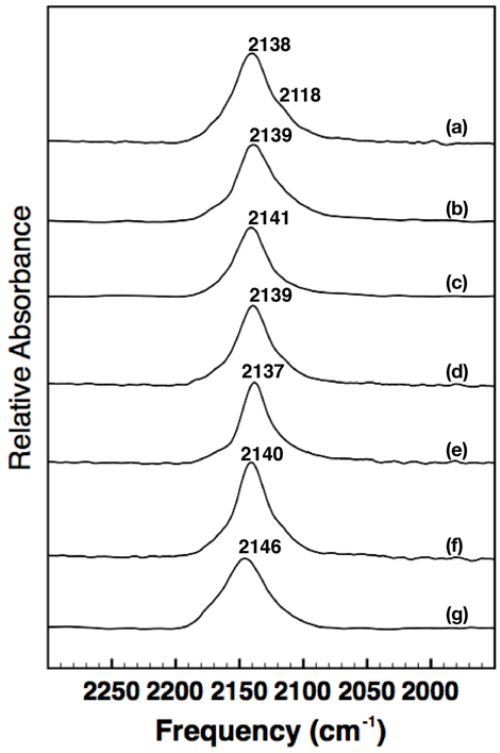

Figure 5.27. Solid-state ATR-IR spectra of the isocyanide region of Cu-^{ISO}CN-3 after suspension under ambient conditions. **(a)** 1 N NaOH, **(b)** 1 N HCl, **(c)** 1 N HNO_3, **(d)**, iPrOH, **(e)** MeOH, (**f**) H_2O, (**g**) as-prepared Cu-^{ISO}CN-3 for reference.

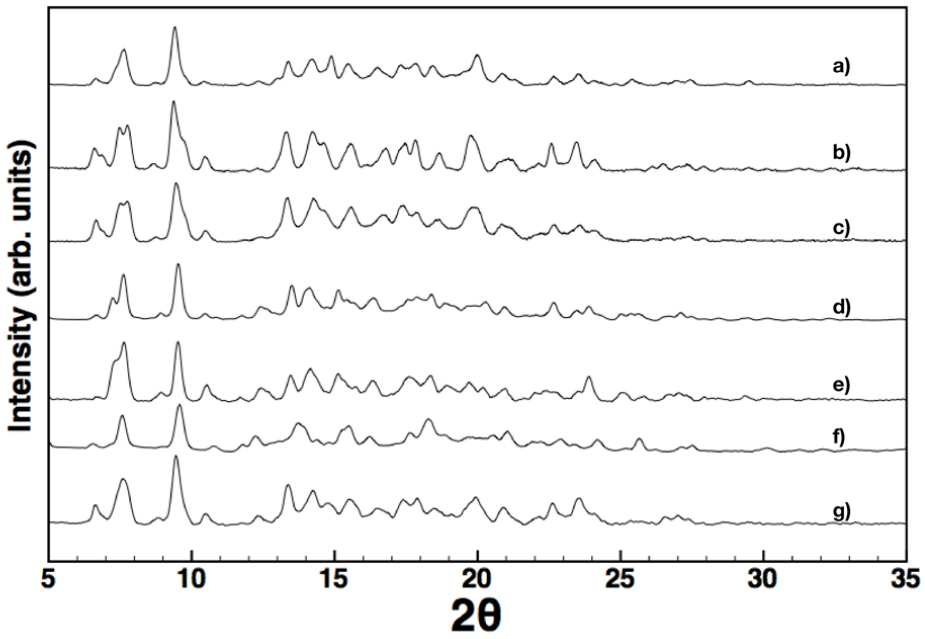

Figure 5.28. Powder X-ray diffraction of Cu-^{ISO}CN-3 after suspension in **(a)** MeOH, **(b)** iPrOH, **(c)** 1 N NaOH, **(d)** 1 N HNO_3, **(e)** 1 N HCl, **(f)** H_2O. Provided for reference is **(g)** the experimental pattern for Cu-^{ISO}CN-3 after synthesis.

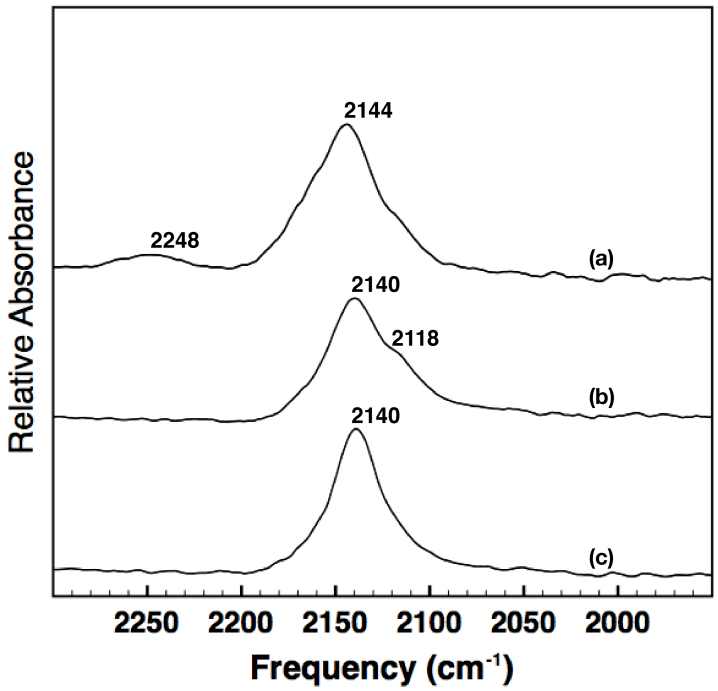

Figure 5.29. Solid-state ATR-IR spectra of the isocyanide region of Cu-^{ISO}CN-3 after activation at 200 ºC and gas sorption analysis. Samples prepared under basic/acidic conditions were treated as described in **S1.9** prior to activation; **(a)** 1 N HNO_3, **(b)** 1 N NaOH. The spectrum in **(c)** is representative of Cu-^{ISO}CN-3 after activation.

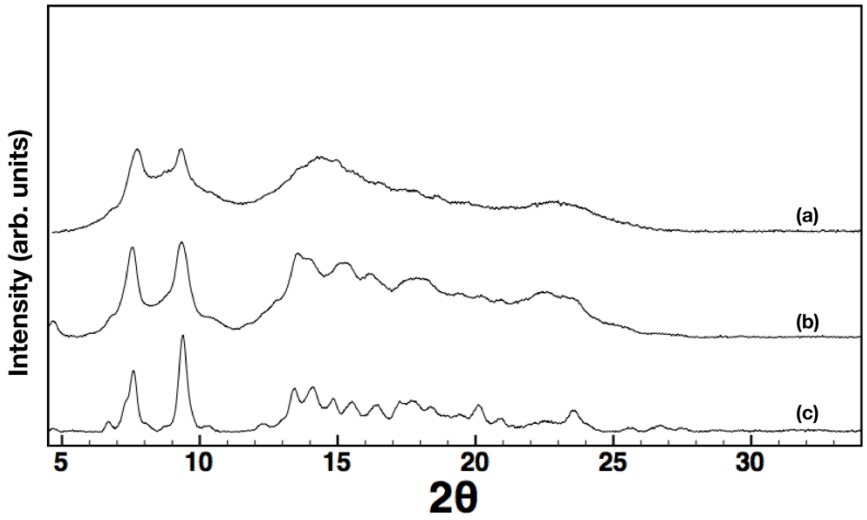

Figure 5.30. Powder X-ray diffraction of Cu-^{ISO}CN-3 after activation at 200 ºC and gas sorption analysis. Samples prepared under basic/acidic conditions were treated as described in **S1.9** prior to activation; **(a)** 1 N HNO_3, **(b)** 1 N NaOH. The pattern in **(c)** is representative of Cu-^{ISO}CN-3 after activation.

5.6 Crystallographic Structure Determinations

General. Single X-ray structure determinations were performed at 100 K on Bruker Kappa Diffractometers equipped with a Mo-Kα or Cu-Kα radiation source and an APEX-II CCD area detector. All structures were solved *via* direct methods with SHELXS[51] and refined by full-matrix least-squares procedures using SHELXL[51] within the Olex2[52] software. In cases of highly disordered solvent molecules of co-crystallization, the Platon routine SQUEEZE[53] was used to account for the corresponding electrons as a diffuse contribution to the overall scattering without specific atom positions. Crystallographic data collection and refinement information is listed in Table S2.1.

Notes on Structure Solutions.

Cu-^{ISO}CN-1. The $[PF_6]^-$ counteranion is positionally disordered and was modeled and refined anisotropically. Significant disorder was observed for one THF solvent molecule of co-crystallization. This was treated with SQUEEZE and the electron density removed.

Cu-^{ISO}CN-2. The $[PF_6]^-$ counteranion is rotationally disordered and was modeled and refined anisotropically. Significant disorder was observed for two THF solvent molecules of co-crystallization. These were treated with SQUEEZE and their electron density removed.

Cu-^{ISO}CN-3. The $[PF_6]^-$ counteranion is positionally disordered and was modeled and refined anisotropically.

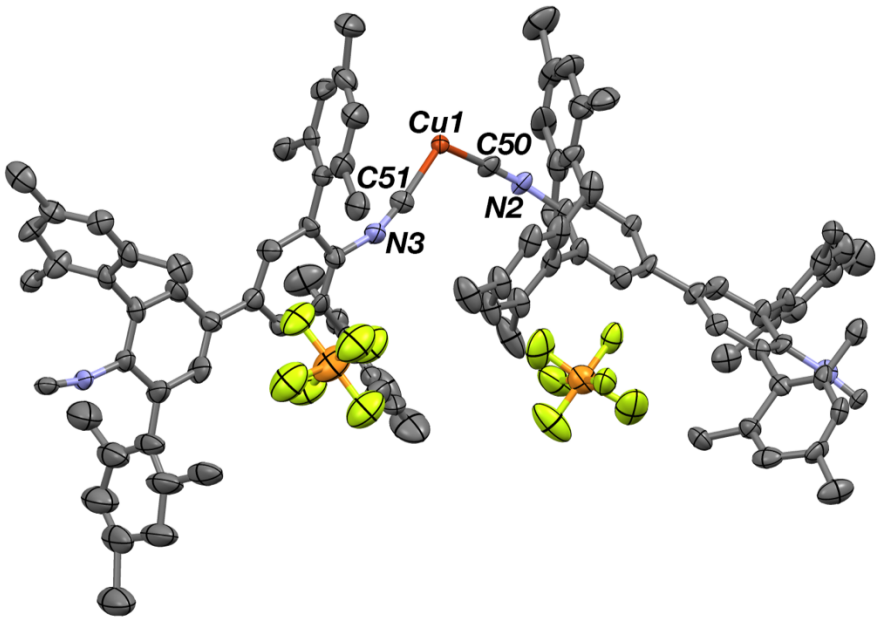

Figure 5.31. Asymmetric unit of Cu-^{ISO}CN-1, with THF solvent molecules of co-crystallization omitted for clarity and disordered $[PF_6]^-$ shown.

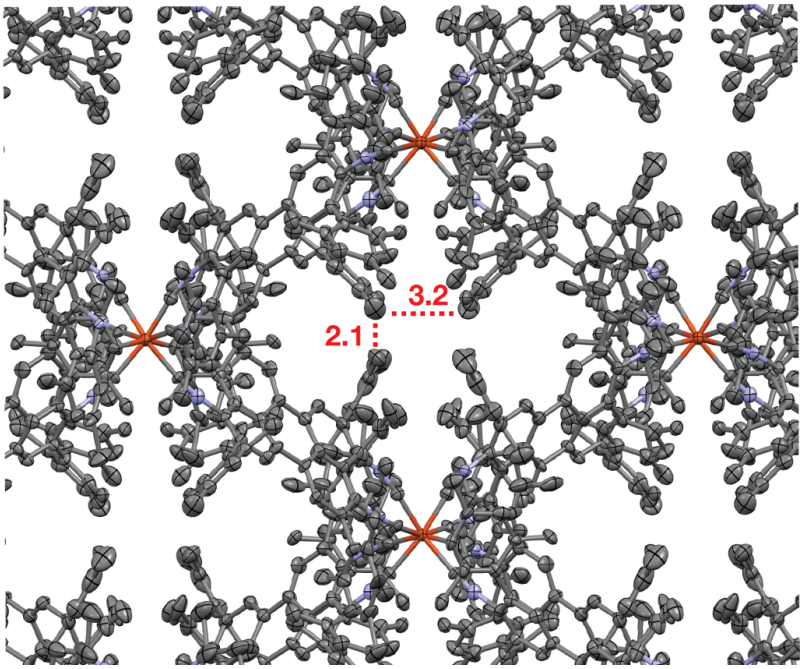

Figure 5.32. Channels formed along *a* axis in Cu-^{ISO}CN-1. The channels along the *c* axis are crystallographically identical.

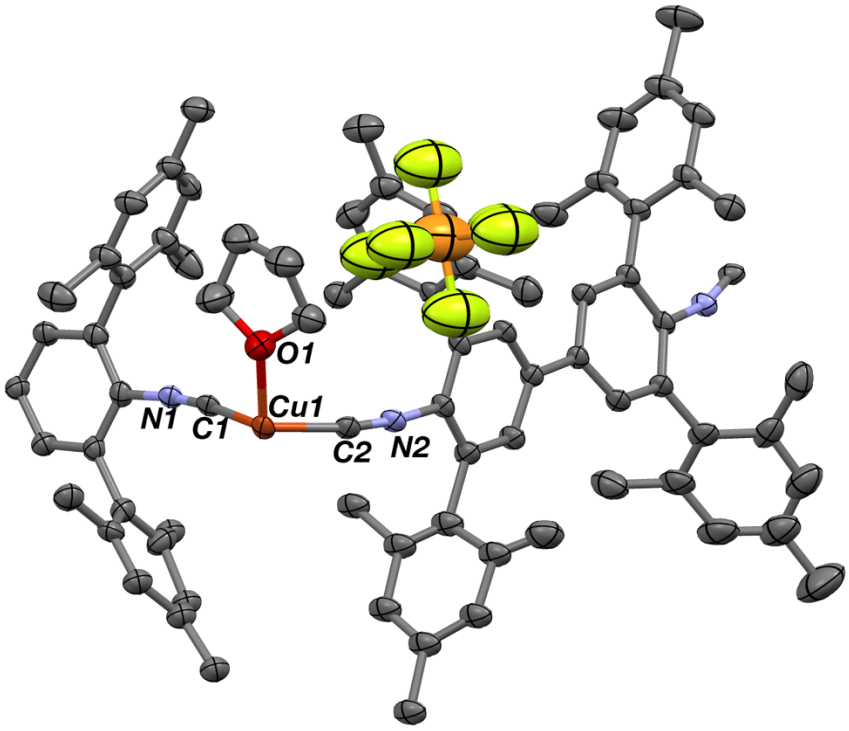

Figure 5.33. Asymmetric unit of Cu-^{ISO}CN-2, with disordered $[PF_6]^-$ anions omitted for clarity.

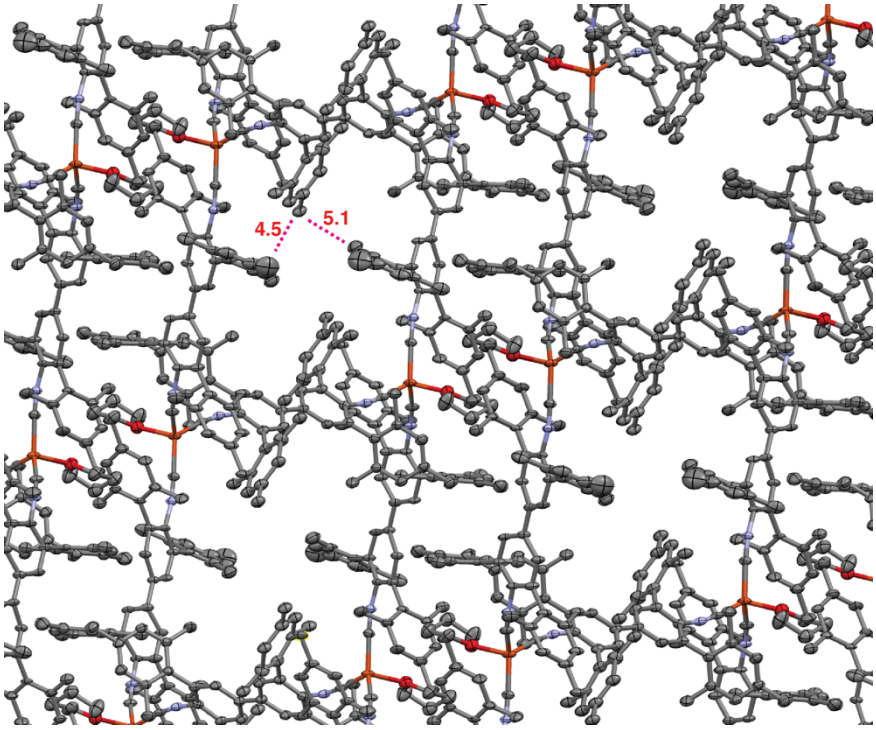

Figure 5.34. Channels along the *b* axis in Cu-^{ISO}CN-2.

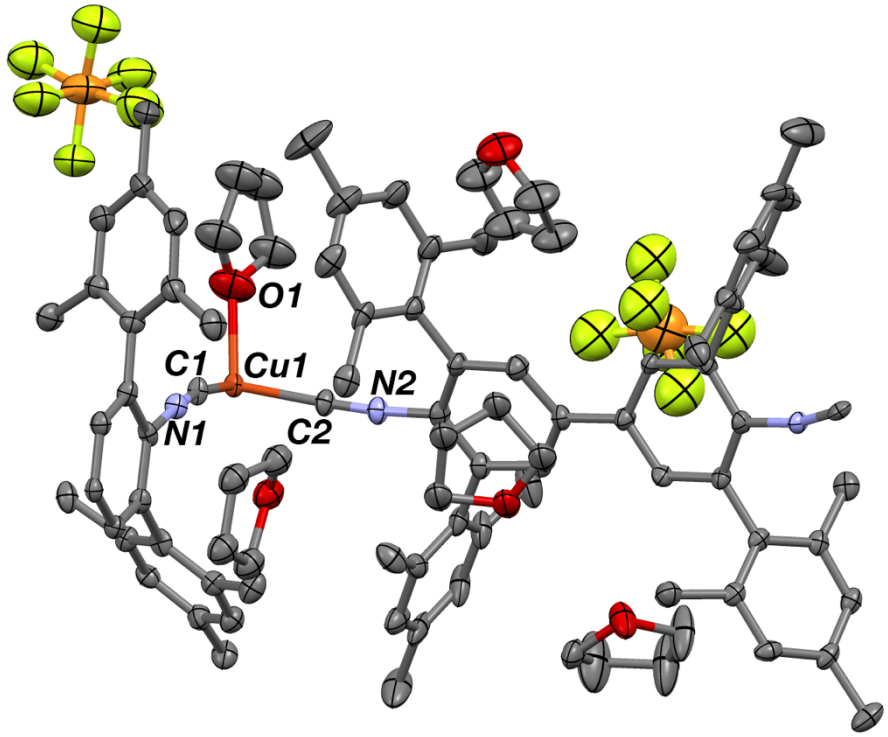

Figure 5.35. Asymmetric unit of Cu-^{ISO}CN-3, with positionally disordered $[PF_6]^-$ counteranions included.

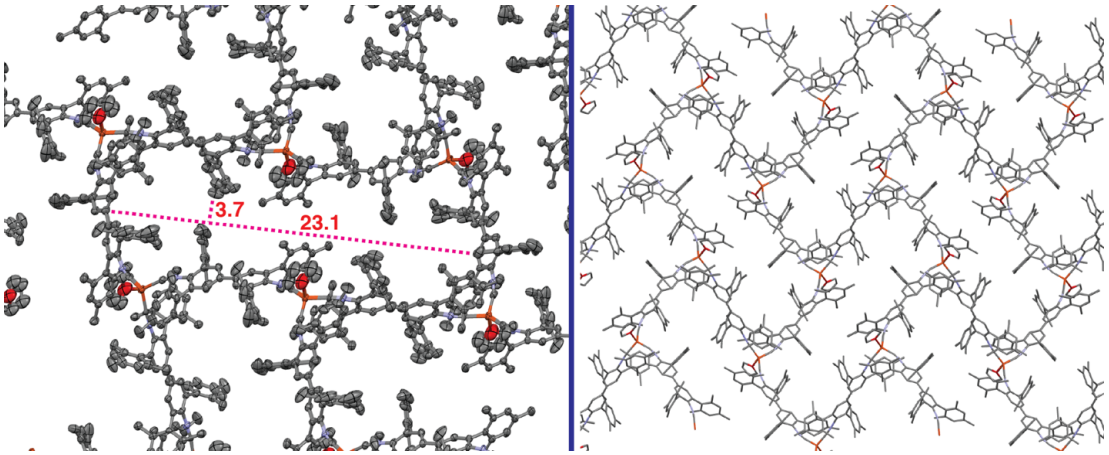

Figure 5.36. View along the *a* axis of Cu-^{ISO}CN-3. *Left*: Inset view of pore, showing Cu-THF unit pointed towards channel. *Right*: Zig-zag pattern formed by channels.

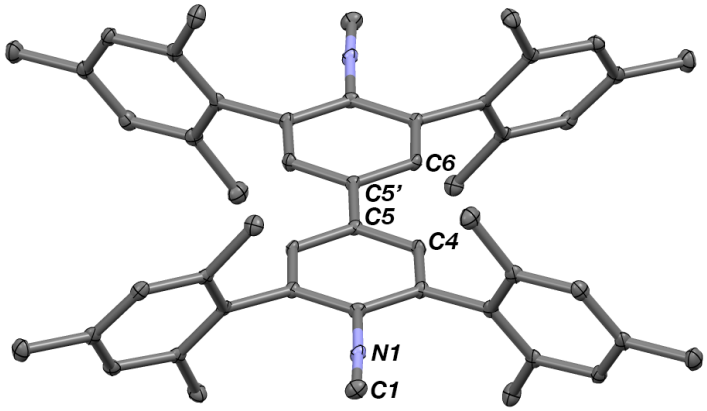

Figure 5.37. Molecular structure of [CNAr^{Mes2}]$_2$, with diethyl ether solvent molecules of co-crystallization omitted for clarity. Selected bond distances (Å), and torsion angles (º): N1-C1 = 1.160(2); C4-C5 = 1.398(2); C5-C5' = 1.494(3); C4-C5-C5'-C4' = 0.62(2).

Table 5.2. Crystallographic Data Collection and Refinement Information.

Name	Cu-^{ISO}CN-3·3(THF)	Cu-^{ISO}CN-2	Cu-^{ISO}CN-1·2(THF)
Formula	$C_{91}H_{104}CuF_6N_3O_4P$	$C_{79}H_{79}CuF_6N_3OP$	$C_{112}H_{121}CuF_6N_4O_3P$
Crystal System	Monoclinic	Monoclinic	Orthorhombic
Space Group	$P2_1/n$	$C2/c$	$Fdd2$
a, Å	13.740(3)	38.4955(14)	30.4380(14))
b, Å	31.382(6)	17.5041(6)	44.985(2)
c, Å	21.010(4)	27.6236(10)	30.3992(14)
α, deg	90	90	90
β, deg	99.681(3)	113.737(2)	90
γ, deg	90	90	90
V, Å^3	8930(3)	17038.9(11)	41625(3)
Z	4	8	16
Radiation (λ, Å)	Mo-K$_\alpha$, 0.71073	Mo-K$_\alpha$, 0.71073	Cu-K$_\alpha$, 1.54178
ρ (calcd.), Mg/m^3	1.125	1.010	1.136
μ (Mo Ka), mm^{-1}	0.322	0.326	0.926
Temp, K	100	100	100
θ max, deg	24.817	20.816	59.037
data/parameters	15303/955	8922/829	14992/1208
R_1	0.1230	0.0999	0.0887
wR_2	0.3825	0.3390	0.2708
GOF	1.222	1.295	1.052

Table 5.3. Crystallographic Data Collection and Refinement Information.

Name	$[CNAr^{Mes}]_2 \cdot 2(Et_2O)$	$[Cu(PMe_3)(CNAr^{Mes2})_3]OTf \cdot 2(THF)$
Formula	$C_{58}H_{68}N_2O_2$	$C_{87}H_{99}CuF_3N_3O_5PS$
Crystal System	Triclinic	Triclinic
Space Group	P-1	P-1
a, Å	12.6957(8)	12.307(2)
b, Å	13.7455(7)	16.871(3)
c, Å	15.3667(9)	20.318(4)
α, deg	104.296(2)	83.160(7)
β, deg	90.301(2)	72.800(7)
γ, deg	104.170(2)	85.159(7)
V, Å^3	2513.3(3)	3996.2(13)
Z	2	2
Radiation (λ, Å)	Mo-K$_\alpha$, 0.71073	Mo-K$_\alpha$, 0.71073
ρ (calcd.), Mg/m^3	1.090	1.205
μ (Mo Ka), mm^{-1}	0.065	0.378
Temp, K	100	100
θ max, deg	25.358	25.416
data/parameters	9209/575	14655/931
R_1	0.0442	0.0391
wR_2	0.0985	0.0914
GOF	1.002	1.023

5.7 Contact Angle Measurements, TGA/DSC and Gas Sorption Analyses.

Thermal Analysis. Thermogravimetric analysis was performed on ~5–15 mg of material that had been dried under dynamic vacuum. Analysis was conducted under a stream of dry dinitrogen gas (80 mL/min) using a Mettler Toledo TGA/DSC 1 STAR^e System running from 30 ˚C to 800 ˚C with a ramping rate of 5 ˚C/min.

Surface Area Analysis. Samples were prepared on and measured using a Micrometrics ASAP 2020 Adsorption Analyzer. Approximately 30 mg of material was transferred to a pre-weighed sample tube and degassed at 200 ˚C for at least 10 hours or until the outgas rate was below 5 mmHg. The sample tube was reweighed to obtain a mass for the sample. Measurements were collected on three independent samples at 195 K employing CO_2 of 99.999% purity using the volumetric technique. Analyses performed on Cu-^{ISO}CN-3, degassed at 35 ˚C, 50 ˚C, 105 ˚C, and 150 ˚C, revealed insignificant surface areas. Analyses performed on Cu-^{ISO}CN-2 displayed no significant porosity under N_2 or CO_2 gas.

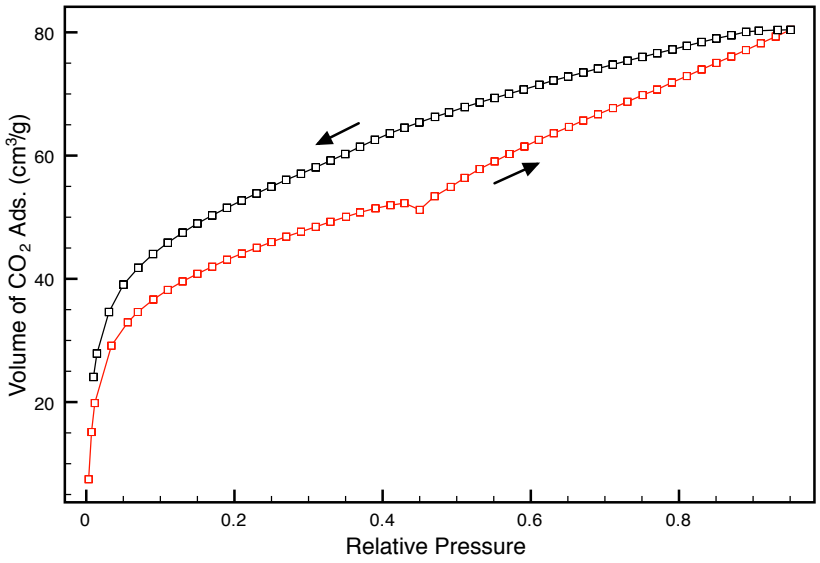

Figure 5.38. CO_2 sorption isotherms of activated Cu-^{ISO}CN-3; red = adsorption, black = desorption.

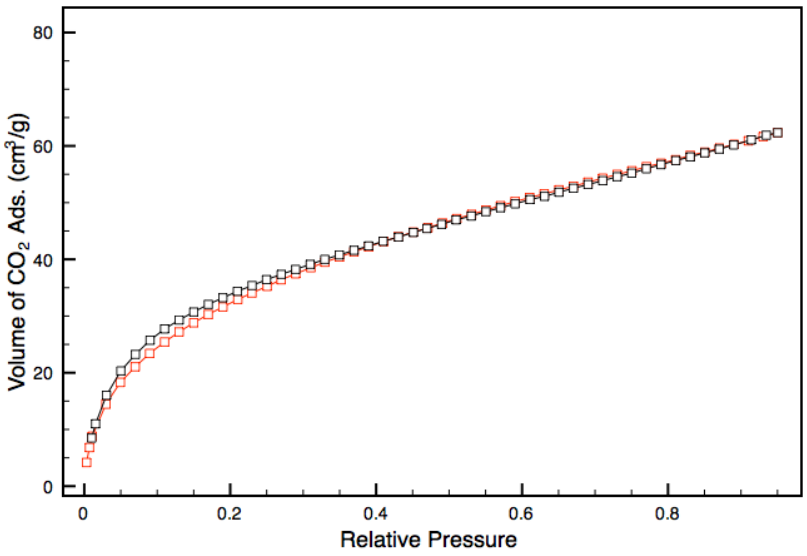

Figure 5.39. CO_2 sorption isotherms of activated Cu-^{ISO}CN-3 after exposure to 1 N HNO_3; red = adsorption, black = desorption.

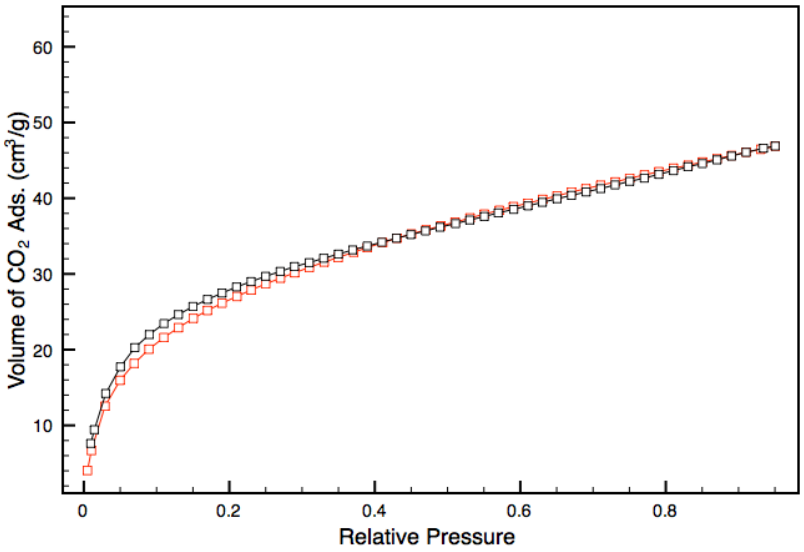

Figure 5.40. CO_2 sorption isotherms of activated Cu-^{ISO}CN-3 after exposure to 1 M NaOH; red = adsorption, black = desorption.

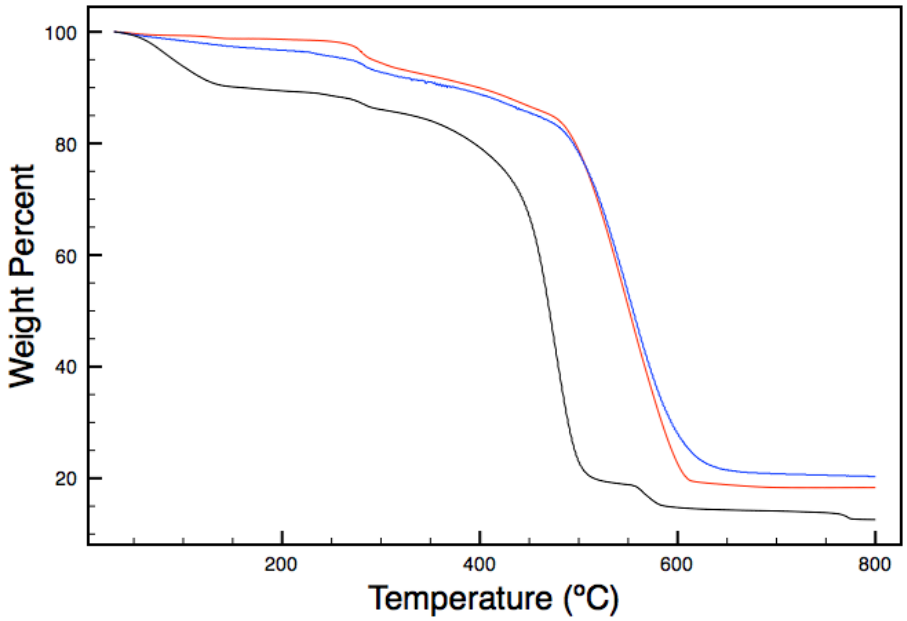

Figure 5.41. Thermogravimetric analyses of Cu-^{ISO}CN-3 (red), Cu-^{ISO}CN-2 (blue), and Cu-^{ISO}CN-1 (black).

Contact Angle Measurements on Cu-^{ISO}CN-3. Contact angle measurements were recorded using a Tantec CAM-micro Contact Angle Meter. Samples of Cu-^{ISO}CN-3 were prepared as described in Section S1.8 and dried under dynamic vacuum prior to analysis. Samples were then pressed onto a glass slide using a spatula. A drop of water (tested to 18.2 MΩ) was slowly dropped from a microsyringe and the contact angle measured.

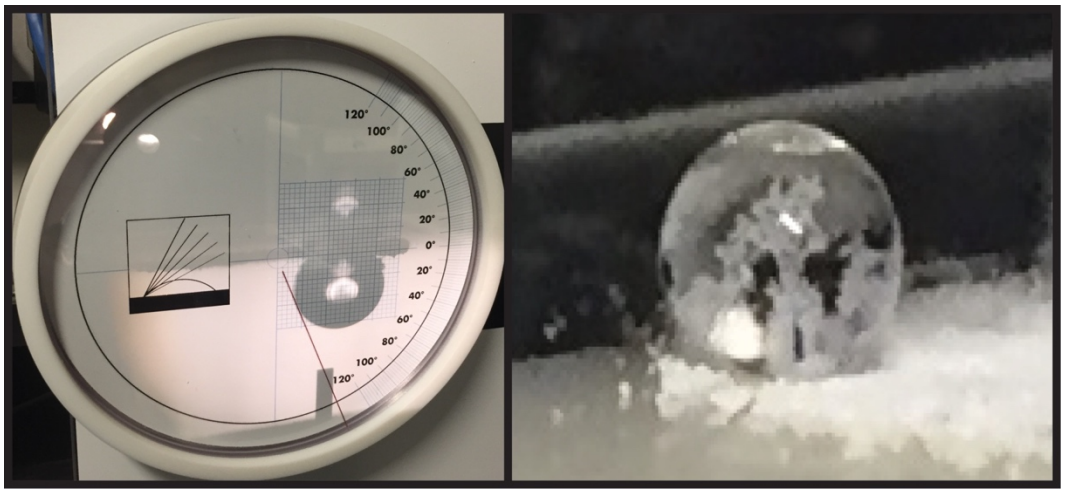

Figure 5.42. A representative image of the contact angle meter upon addition of a drop of H_2O to Cu-^{ISO}CN-3 (left). Close-up view of a bead of water on top of Cu-^{ISO}CN-3 (right).

5.8 Computational Studies

Computational Details. Density Functional Theory calculations on $[CNAr^{Mes2}]_2$ were performed using the ORCA program package[54] with the B3LYP/G hybrid functional and the 6-31G* basis set.[55-57] An atom-pairwise dispersion correction with Becke-Johnson damping was applied to all geometry optimizations.[58] Using crystallographic atomic coordinates, the geometry of $[CNAr^{Mes2}]_2$ optimized with a torsion angle of 36.65˚. The barriers to rotation (ΔE^0 and ΔE^{90}) were calculated by comparison to the optimized structures of $[CNAr^{Mes2}]_2$ with the torsion angles constrained to 0º and 90º, respectively. Calculations were carried out at the W. M. Keck Laboratory for Integrated Biology II, which is supported in part by the W. M. Keck Foundation.

Table 5.4. Calculated Relative Energies as a Function of Linker Torsion Angle for $[CNAr^{Mes2}]_2$.

Calculation/State	Torsion Angle	Relative Energy (ΔE, kcal/mol)
$[CNAr^{Mes2}]_2$ – Optimized	36.65˚	0.0
$[CNAr^{Mes2}]_2$ – 0˚	0˚	+ 2.0
$[CNAr^{Mes2}]_2$ – 90˚	90˚	+ 3.3

Input and Results

Input for geometry optimization of $[CNAr^{Mes2}]_2$

```
#UKS opt #
#
%pal nprocs 8 end
! UKS OPT  B3LYP/G 6-31G* D3 XYZFile
%SCF
MaxIter 300
end
* xyz 0 1
N   7.77014562478634      7.52662986033379      6.93522659145288
N   2.29419844104112     13.96031662763004     12.05269428448421
C   6.84402209542803      8.24279528883058      9.03944428828579
C   5.63512177911213     10.40141474142694      7.72693271192683
H   5.17757776829699     11.22705452280236      7.18462387359622
C   6.06677316748026      9.16337705693644      9.74032325442550
H   5.95931257291707      9.00110079221376     10.81155393541914
C   5.44583268304455     10.25959239194208      9.11374161354021
C   6.40129202783582      9.50732647189501      6.98090249694228
C   7.48644777880467      7.09638814906067      9.73687941066335
C   1.34958617278676     14.20493126032415      8.60677418012279
C   7.00449206008117      8.42601001718049      7.65211884407731
C   3.22774486867550     13.24371407124506      9.95198227300404
C   6.57988226182063      9.69121119144136      5.51544115974265
C   3.66112393737398     11.97819113317477     12.01144808681545
C   4.62289165905061     11.22464081889775      9.88205517447085
C   4.42956740961740     11.08337122780893     11.26861514186929
H   4.88034131876918     10.25447900200329     11.81190609191426
C   2.58734116269675     14.38930304833500      9.25163125566657
C   3.47964858042745     11.79761593404880     13.47704764492472
C   6.74460925829595      5.92375902220304      9.97550990242625
C   5.77746709836254      8.96441204860659      4.61539347317011
C   8.83411672940633      7.18564642722265     10.13420699147097
C   7.55726214731974     10.58729607915640      5.04198136025027
C   4.00528398833040     12.32143605059009      9.25362328752172
H   4.12039417713718     12.48647173411902      8.18372930127816
C   5.95710273458432      9.16286267558001      3.24286956991396
H   5.32996932374607      8.60461172425149      2.54314796355722
C   3.06139611861631     13.06022676898218     11.33824838704922
C   0.76309774091390     15.29275371849812      7.95227705385754
H   -0.20148375609991     15.15342464301622      7.45759730301703
C   6.91708448789065     10.05013984725430      2.74495177412274
C   0.65565329744288     12.86686373589946      8.64355122799807
```

```
H    1.25336222561231     12.08500707579570      8.15149340466371
H   -0.31920534843909      12.91795121738490      8.14247083903603
H    0.49140078319873     12.53291376552382      9.67918074781230
C    7.36565868231714      4.85621406123671     10.63151741246668
H    6.79377542903772      3.94210585096737     10.81001179650193
C    2.59477256944400     16.71024959247027      8.58575604972115
H    3.07938496439890     17.68987377877767      8.58808717492000
C    3.21387852003540     15.64989301046536      9.25496385881543
C    1.37192731036966     16.55206186237502      7.92501302170428
C    7.70666871953794     10.75280484187467      3.66140285009019
H    8.46596633888803     11.44701298882593      3.29246713151928
C    4.45921144432783     12.28319321369068     14.36379803422601
C    3.14450438588360     11.45070128721184     16.24881028299707
C    8.69810118706417      4.92419201198189     11.05230710809672
C    9.41550236943936      6.09614505305328     10.79025095884776
H   10.46191340014333      6.16370197773174     11.09841125421550
C    9.64431643864183      8.42151516459625      9.83779232325007
H    9.82777626303266      8.52192120317146      8.75670979053628
H   10.61921439304249      8.38042202519832     10.33984892214317
H    9.12505515097005      9.33475045080228     10.16247262455183
C    5.31499102381032      5.80961493440477      9.51031502131936
H    4.66404318267706      6.54014987339229     10.01368682612011
H    4.91841362433777      4.80602940628628      9.70920837123977
H    5.23076282557712      6.00399206866654      8.43058675369237
C    2.32793721911966     11.15115668267283     13.96446685598247
C    4.27470155532266     12.09736237902918     15.73766561300126
H    5.03407900967103     12.47397579055916     16.42763821524423
C    0.73737436771922     17.70239425248635      7.18641286378809
H    1.08482957871009     17.73850414685765      6.14145708943374
H    0.99223492956150     18.66500824006058      7.65034005078079
H   -0.35696236049989      17.60914863104297      7.16528782198871
C    2.18413281887803     10.98340539577358     15.34511992200885
H    1.29372327980685     10.47572552515276     15.72459946928779
C    7.12058552150677     10.21678216630811      1.26098578112396
H    7.86396401412494      9.49596433693488      0.88482181479176
H    7.48682297582811     11.22336316028469      1.01697092667123
H    6.18778568575304     10.04478433637247      0.70676171345622
C    4.75383199850062      7.97887259594318      5.11801090066973
H    5.24196106533380      7.10354157168122      5.57402667756255
H    4.12147157139375      7.61839260526470      4.29682181281676
H    4.10505385806673      8.42271029319340      5.88682193932308
C    8.42591653000174      6.75808941415337      6.32176416399158
C    8.43979927902008     11.34263550379446      6.00325019187339
H    7.86103571810927     12.04476241664300      6.62234208809403
H    9.20432852316291     11.91566171803336      5.46364153197611
H    8.94948087378626     10.65764340188166      6.69711528279202
C    4.51456453830781     15.86124523196406      9.98670620026138
H    4.36826090204347     15.79621040056940     11.07617117988929
H    4.93309756483419     16.85095113645636      9.76441932600068
H    5.26065983905014     15.09981516047632      9.71720321290087
C    9.33761016821967      3.77335502408589     11.78577284875662
H    9.19827930763567      3.87436551381160     12.87404955654825
H   10.41872449837995      3.72933474377142     11.59606256731693
H    8.89587551463183      2.81320829011332     11.48620679561275
C    5.67574540243078     13.00715202637198     13.84502014689264
H    6.29348379209463     12.35949153717045     13.20504884245413
|H   6.30033456531398      13.36521441540043     14.67310022282173
H    5.38975264983602     13.87511137592784     13.23196534705533
```

```
C   2.94794878962820     11.29439679395339     17.73486164387705
H   3.90942784738401     11.25496193267648     18.26464705882423
H   2.38589586364971     10.38038881180711     17.97092300367100
H   2.38001603180478     12.14426183246334     18.14580044948732
C   1.26134391010600     10.66271907428354     13.01811585187887
H   0.74649153654856     11.50805692787179     12.53558212720330
H   0.50615054584010     10.07111042414012     13.55079623694352
H   1.68417719492638     10.04322706498258     12.21401621877909
C   1.63558092511575     14.72855891878283     12.66349496870184
*
```

Optimized coordinates for $[CNAr^{Mes2}]_2$

```
  N   7.78143178926238      7.55178591246989      6.95059984441509
  N   2.30071485698881     13.94649429069539     12.03606857758267
  C   7.15031098785198      8.51885530937729      9.06040685284084
  C   5.34429549056108     10.18412945563717      7.70603836992359
  H   4.62528074153201     10.80216725853736      7.17741372163947
  C   6.36299024035091      9.43547334143742      9.75674958470796
  H   6.48532947194166      9.50630186327166     10.83336573066962
  C   5.45341302528085     10.27782783201661      9.10093029513555
  C   6.10994508310435      9.28210655172212      6.96735421274344
  C   8.10650415743932      7.63125804459557      9.78036222702023
  C   2.21580498163039     14.91451419390912      8.54882803139310
  C   7.01263569572365      8.45453230146479      7.66123728227963
  C   3.55367816674550     13.42451025595593     10.05068334223229
  C   5.96366128688215      9.18740907393808      5.48771034525382
  C   3.34237685625370     11.78452368469838     11.87119551939381
  C   4.62606611592176     11.23700619387126      9.86446050944112
  C   4.12083642406935     10.89801484654589     11.12789774037432
  H   4.31184312803918      9.91149601744005     11.53731615836020
  C   3.25618778780246     14.77002339325540      9.48426681810355
  C   2.81673461481359     11.40149729493645     13.21181540811367
  C   7.62823860481481      6.46786493044351     10.41041188552217
  C   5.19766679954304      8.15038974671648      4.92434000775650
  C   9.47507237926994      7.95323804630976      9.81763620756984
  C   6.59402414919486     10.13804406529349      4.66460843423462
  C   4.32928841473081     12.50546587810802      9.34487202442550
  H   4.73245207449833     12.80305060842690      8.38244780236064
  C   5.06175920483984      8.09194206870774      3.53534340929480
  H   4.46436566462651      7.29445813522346      3.09873489363992
  C   3.06768392594425     13.04870045624083     11.31712596371816
  C   1.95159141384168     16.18249482732178      8.02526581596401
  H   1.14118365169577     16.29759600296810      7.30835381407088
  C   5.67500640082594      9.02549066725359      2.69575324176182
  C   1.37908269865186     13.72714201341706      8.13385913044260
  H   1.98333924165157     12.95586793973643      7.64161405623337
  H   0.58800001855219     14.02928171775012      7.44141098080208
  H   0.90708839986218     13.25016461084448      9.00135300781827
  C   8.53343629819576      5.64772397833666     11.08802312447116
  H   8.16683887968038      4.74371669482404     11.56918916799370
  C   3.71299738301423     17.13574979632352      9.34579866690270
  H   4.29262673730369     17.99942244157625      9.66371599241128
  C   4.00622452303388     15.88631366720192      9.89688208464575
  C   2.69259356249023     17.30430542475936      8.40596594133797
  C   6.43606126691523     10.04143524669261      3.27980966736176
  H   6.92318186876137     10.77600702032377      2.64220175256751
```

C	3.67037979525790	11.44781453428727	14.32915840461532
C	1.84317706201998	10.66102061922426	15.74373783076238
C	9.89518111295402	5.95467745072757	11.15505500305635
C	10.34642958402427	7.10922788849247	10.51024110250690
H	11.40511258366809	7.35792246100135	10.54188178846171
C	10.00179572938060	9.17661365042543	9.10645816790408
H	9.96691422650427	9.04410303213188	8.01750909807752
H	11.04140640592847	9.37285862467344	9.38395519868550
H	9.40976251735955	10.06800766635484	9.34129763287847
C	6.16615164465088	6.09516035540572	10.33637105991969
H	5.53038998593229	6.83767168702582	10.83322789898074
H	5.98584519733561	5.12642542000390	10.81093727517825
H	5.82268969752204	6.03460132282691	9.29712535611337
C	1.47689455139399	10.99614796101135	13.35332966598763
C	3.16750717606876	11.07427690442272	15.57796463116502
H	3.82638525061874	11.11076536281477	16.44290415851640
C	2.41249131462806	18.65872533605680	7.80213531352296
H	3.01915090990600	18.82349013565365	6.90220587449152
H	2.64634819400122	19.46566305098931	8.50467627188457
H	1.36210109916464	18.75581259950371	7.50914882566600
C	1.01537935899179	10.62495787689637	14.61834785260218
H	-0.01750768787145	10.30190798833270	14.72629104984128
C	5.54490457566683	8.91934060464332	1.19572212663514
H	6.33582472518461	8.28395597098874	0.77538387270372
H	5.62466835276287	9.89985275465920	0.71504569603749
H	4.58573817942765	8.47624302842815	0.90768242513084
C	4.54128256343114	7.10964479668387	5.79932454845788
H	5.28846338104189	6.43521640498837	6.23661745377518
H	3.84081134207593	6.49805574656922	5.22271409032514
H	3.99366779121592	7.56557879622069	6.63130845914052
C	8.44017646917676	6.77930499719957	6.34797532997904
C	7.44272456731545	11.23631698462499	5.26052960454643
H	6.85000522500646	11.92057828057688	5.87923567015278
H	7.92529294057446	11.82500538915712	4.47502782274160
H	8.22686382615598	10.82722014299406	5.90880426500852
C	5.09639796428563	15.74465581071479	10.93150508015317
H	4.67600616890621	15.50719323017804	11.91651314578826
H	5.66621206300577	16.67337363530732	11.02931039898129
H	5.79372221205568	14.93888228642713	10.67664371032711
C	10.85038201438987	5.07295743477477	11.92212099170002
H	10.93832152636536	5.39941571299922	12.96696105068651
H	11.85493322116758	5.09911280654988	11.48753783840720
H	10.51072106520023	4.03182928028477	11.93384191855378
C	5.10213840038276	11.91067021757663	14.19164700982646
H	5.68295592403408	11.25225486024226	13.53507439825484
H	5.59794847500211	11.93873732370306	15.16596540960921
H	5.15421178568020	12.91510138969340	13.75483678918167
C	1.31117856596933	10.29272833104384	17.10729930490028
H	2.10918810846302	9.93104621829727	17.76424941394168
H	0.54408726506421	9.51345750587095	17.04028404495813
H	0.85151119435940	11.16061791537652	17.59843241400861
C	0.54530559846361	10.97029516253132	12.16545336263348
H	0.29588398534671	11.98779846670752	11.84098760769065
H	-0.39158259084346	10.46409441304447	12.41493148350949
H	0.99403426762537	10.45783888501323	11.30761374739787
C	1.64639067246706	14.71278618709105	12.65132140910685

Optimized coordinates for [CNAr^{Mes2}]$_2$, torsion constrained to 0°.

N	7.78606208081577	7.52939972265837	6.93993051716559
N	2.30238238631248	13.96992102138948	12.05097792722298
C	6.85584384637812	8.25061003402918	9.03779099436958
C	5.65588766794218	10.40844114069435	7.72654090469862
H	5.20270318473006	11.22775560336717	7.18216768000587
C	6.08092190067253	9.17348432761920	9.73741918974808
H	5.97255277074859	9.00884072706394	10.80269444008766
C	5.46339723609055	10.27029453628614	9.11177350597413
C	6.42123560982317	9.51163005835247	6.98299058739700
C	7.48889880087360	7.09845478034583	9.74035289473649
C	1.36820122050054	14.18751289057415	8.57810125019233
C	7.02103818437108	8.43174807276525	7.65373312805060
C	3.23833610779179	13.25319121074107	9.95384242677959
C	6.59326139897754	9.69259934037979	5.51380146947274
C	3.67039356296023	11.98984326486411	12.00793148022027
C	4.63767500301523	11.23826571882976	9.88094326560621
C	4.44052802189687	11.09656720821240	11.26515944931517
H	4.88505778680760	10.27154338460700	11.80777161637797
C	2.58715422575511	14.39360169455942	9.24900261068382
C	3.48696955317944	11.80159846697089	13.47485870717488
C	6.73421371049246	5.93873359944382	9.99261191684509
C	5.82107879920223	8.92950429483118	4.61950055463724
C	8.83775039764792	7.17242851050501	10.13131743824399
C	7.53001074309851	10.62487666142282	5.03234008131606
C	4.01908288831883	12.33444987653037	9.25523351886673
H	4.13371941888133	12.50337147953105	8.19132199155276
C	5.98658927633598	9.12904993402566	3.24688265583657
H	5.38378224053631	8.54518407602668	2.55462883849106
C	3.07154400930300	13.07060431651096	11.33762209481113
C	0.76836794637588	15.26608893360890	7.92394027658939
H	-0.17799048487192	15.11069569004247	7.41131847895601
C	6.90619889212927	10.05232389277262	2.74296919093410
C	0.70253376433026	12.83126583801307	8.58593310728108
H	1.32395251706478	12.07040195507826	8.09991964880809
H	-0.25912637396680	12.86485186169808	8.06685846546239
H	0.52319389123806	12.48284801923646	9.61010926285140
C	7.34223615071242	4.86963101851890	10.65507782582127
H	6.76150215900792	3.96985132612588	10.84539269361654
C	2.55175798143521	16.71906883819981	8.60561334889318
H	3.01098504489386	17.70500087193943	8.62442898177689
C	3.18168732464564	15.66786822036311	9.27574284337841
C	1.34708898314895	16.53798700360142	7.92102060805778
C	7.66825188911863	10.79050778871284	3.65201368398004
H	8.39271133471119	11.51098494162924	3.27825610848735
C	4.50128701838265	12.20935116078979	14.36005275706235
C	3.15223889163003	11.43821868262350	16.24241668857381
C	8.67553762221658	4.92469023463030	11.06960291422919
C	9.40723867676649	6.08298031294865	10.79472826000954
H	10.44975162929075	6.13897072786600	11.09937534552422
C	9.66624826823966	8.39546229602661	9.81809830332187
H	9.85399563837049	8.47663562513291	8.74041069117152
H	10.63533546164737	8.35168976334796	10.32201651126325
H	9.16088038535620	9.31703501001754	10.12674948040211
C	5.29954243630407	5.83665141454469	9.53208123222236

H	4.66961505184301	6.60930483123041	9.98705751160400
H	4.87636233908681	4.86088994652475	9.78779058224250
H	5.22101757770528	5.96594138660864	8.44561057745259
C	2.30164990046336	11.22330358982415	13.96446837365575
C	4.31657818778423	12.01759472931916	15.73140001736750
H	5.09960624325401	12.33302980300332	16.41736656627173
C	0.69878721519687	17.68232484499933	7.18058464620598
H	1.07189358470282	17.74905366445013	6.15022408267134
H	0.90941694538139	18.64143427765006	7.66509895024529
H	-0.38809856657876	17.55891895362194	7.12611154451242
C	2.15840382250820	11.04456332683350	15.34233570775884
H	1.24592808571946	10.59000956827287	15.72163914199447
C	7.09425278685871	10.22371587723177	1.25514330945598
H	7.82939658528004	9.50715777100607	0.86565025369335
H	7.45639610761612	11.22747341195484	1.01030282481665
H	6.15854819193961	10.05762888103694	0.71078247676006
C	4.84132248845190	7.89839247009836	5.12675374773318
H	5.36694426070660	7.02016322322596	5.52218386030575
H	4.18293170548202	7.55629286324052	4.32316741443105
H	4.21857996377974	8.29238346276810	5.93729847003668
C	8.44084018656972	6.75720378907449	6.33233508689282
C	8.38942206258672	11.42055687124226	5.98616826850513
H	7.79002029086704	12.07808916206356	6.62675738437852
H	9.10515053722930	12.04280689061442	5.44095581081182
H	8.95485484474662	10.76097548779236	6.65545723885638
C	4.46479687826251	15.90680143329821	10.03482003999670
H	4.29954936736729	15.83854440631023	11.11746413558377
H	4.86406433614053	16.90284245434283	9.82174913104497
H	5.23188696809175	15.16727455691656	9.77939811508303
C	9.30418714522900	3.77074993263286	11.81198058789643
H	9.17771368087251	3.88139470065126	12.89779954198004
H	10.37953746875992	3.70661406475570	11.61395797411640
H	8.84878185234337	2.81688177764322	11.52681569165374
C	5.76207568950045	12.86232975207269	13.84382900715282
H	6.33706247742201	12.18793862824032	13.19869249394450
H	6.40764562865889	13.17158396978056	14.67071973410751
H	5.53174542039783	13.75019155625092	13.24273211536711
C	2.95850386085952	11.27144567885191	17.73008122452415
H	3.91646775207138	11.17216479782613	18.25011711607606
H	2.35204576909098	10.38824635301413	17.95788988872000
H	2.44193241334231	12.14009112708422	18.16009312665572
C	1.19282865950792	10.81477088990527	13.02439909390549
H	0.67409495382073	11.69529563986707	12.62554789732037
H	0.44984681170973	10.19839375413644	13.53997745116554
H	1.57398405053145	10.24971345210021	12.16707474660815
C	1.64395133520226	14.73776061002503	12.66012619388309

Optimized coordinates for [CNAr^{Mes2}]$_2$, torsion constrained to 90°.

N	7.76698053680047	7.55018343452742	6.95147353705048
N	2.29621459573277	13.94077768425861	12.03886439727655
C	6.85142473671649	8.25406222838938	9.05957536030727
C	5.62745900226207	10.41728612010103	7.75349564139967
H	5.14948513995576	11.25090779404179	7.24827509326284
C	6.07460722564275	9.17224339102311	9.76972385089683
H	5.95263070175644	9.03724735556791	10.84032537534492
C	5.45957445594581	10.25490942303359	9.13260951398977

C	6.39383656339845	9.52391325737836	7.00169306233883
C	7.49734755643720	7.10101876760099	9.74734254620548
C	0.53134578604437	10.77324216211041	11.90459855443421
C	7.00080999497934	8.44730583932047	7.67410250722592
C	2.45482845540881	11.90474596097463	10.77003336532345
C	6.56013598460214	9.70469818468041	5.53247068500282
C	4.45025194218236	13.27953296824593	11.20016213423524
C	4.63015862439674	11.21967200824494	9.90704987989878
C	5.21124400647384	12.35488824495057	10.48101667938230
H	6.27765891801745	12.52762831817563	10.37142889229159
C	0.99164473245209	11.67045688589524	10.92396748975373
C	5.08132298302737	14.48855286023007	11.79971413974380
C	6.74364662897670	5.94527040907916	10.02092250332228
C	5.79643545739928	8.93040956147582	4.64032240541141
C	8.85609673967216	7.16896100909048	10.10412927464534
C	7.48152741317250	10.65085815978399	5.04818117308445
C	3.25602180174473	11.00759457812222	10.06057953501412
H	2.79431384011980	10.13146183942506	9.61573545062947
C	5.95621707391021	9.13148795567905	3.26725586042295
H	5.36005955825878	8.53882054355873	2.57670112372676
C	3.07091066331580	13.03743061336682	11.33340263636142
C	-0.84351801108382	10.56086281451024	12.03208167792332
H	-1.20095583495064	9.87258218365113	12.79520248150112
C	6.86138133449961	10.06738910260848	2.76049311825779
C	1.50095760844265	10.07045069032865	12.82455892633207
H	2.18292001999110	9.41218630914202	12.27312635157180
H	0.96887377530037	9.46256166100367	13.56224143612197
H	2.12763119668929	10.78910976444557	13.36654038258705
C	7.36360876198588	4.87353559799501	10.66786403184217
H	6.78387942324196	3.97653558113425	10.87376969325300
C	-1.28519572224797	12.11116870976660	10.25617763579613
H	-1.98994365434995	12.63924744468761	9.61747575964622
C	0.08123143484421	12.35517739317292	10.09887186217259
C	-1.76774900980691	11.21505874584648	11.21340966798599
C	7.61437063919877	10.81739220323332	3.66746858805190
H	8.32703061371500	11.54845042622848	3.29151875389049
C	5.37360705276322	15.59593649125818	10.98248427354764
C	6.29720799770946	16.76494575891840	12.91625416340271
C	8.70761763794181	4.92206497701343	11.04727619597703
C	9.43707815115001	6.07698621924409	10.75320559630374
H	10.48729100161225	6.12838871417689	11.03133772650717
C	9.68230674499168	8.38852287476802	9.77223022503741
H	9.85298326374198	8.46524788152806	8.69139313491602
H	10.65932082481569	8.34373355273872	10.26054672089297
H	9.18444839883839	9.31221953852851	10.08662176520352
C	5.29712567252183	5.84862206677974	9.59724109819850
H	4.68064705684850	6.62093710193994	10.07088721273625
H	4.87821653907198	4.87301007705126	9.86031352585139
H	5.19157526652396	5.98231888978286	8.51366119249106
C	5.38228087584914	14.51590916802340	13.17361385617602
C	5.97989002274147	16.71617071335023	11.55616396108997
H	6.20647010635666	17.57270832533839	10.92496617748328
C	-3.24678620262965	10.94479038695146	11.34502049993725
H	-3.56225840039604	10.13384852264398	10.67507106246751
H	-3.83987230807600	11.82868243315363	11.08732898262822
H	-3.50890368843158	10.64515928337491	12.36481442518911
C	5.99248008612925	15.65391369298067	13.70679566313291
H	6.23428975098427	15.67241478355693	14.76711857747803

C	7.04394685522588	10.24034625654432	1.27225949062181
H	7.79216051427350	9.53747540509751	0.88272584724789
H	7.38649809520849	11.25050832227070	1.02561705540852
H	6.11086873387083	10.05536545393607	0.72941962263423
C	4.83020947134721	7.88794901674602	5.15007054329387
H	5.36693355073587	7.01958115610894	5.55194687010307
H	4.17950424992963	7.53249515536840	4.34604172269185
H	4.19887474020884	8.27762550015706	5.95615562851734
C	8.42148682443320	6.78423231860671	6.33639562408099
C	8.33034748551355	11.46071454691244	5.99957206760221
H	7.72181560274545	12.11135541335623	6.63872301686723
H	9.03684765248517	12.09179369116589	5.45244602513383
H	8.90511998627458	10.81059882549703	6.67019564702085
C	0.56473043410258	13.35561627947818	9.07626583578496
H	0.92813156208826	14.26974074198140	9.56217315028832
H	-0.24241082194321	13.64045943891087	8.39540210750682
H	1.39296136480836	12.95725901508655	8.47991023842649
C	9.35025991672957	3.76532049521482	11.77303410191981
H	9.25385440441413	3.87718985338966	12.86182074143554
H	10.41940229380802	3.69578303082818	11.54592310150771
H	8.88249857069061	2.81361242040100	11.50079537225624
C	5.02287469305497	15.58745940286166	9.51307960498595
H	5.56692805902668	14.80853012002167	8.96684012747783
H	5.25900162726053	16.55043773879736	9.05089624167436
H	3.95493692360925	15.39058365205340	9.36152758645329
C	6.92484706263040	17.99725275505640	13.52111568469400
H	7.54265551360808	18.53113160776152	12.79105526558822
H	7.55437013633753	17.74519168154663	14.38099046719577
H	6.15633476265444	18.69810591838727	13.87289005404315
C	5.04326152739902	13.34469094747228	14.06441689661031
H	3.95991166201541	13.27047218503804	14.22017462628180
H	5.51266493081922	13.45143448165210	15.04605620234558
H	5.37301231112641	12.39575233701629	13.62820560064730
C	1.63639000817696	14.71111506608914	12.64263648008858

Optimized coordinates for $[Cu(PMe_3)(CNXyl)_3]^+$.

Cu	11.55473759341691	6.11811839520098	13.64228239105454
P	13.33617289860690	4.72705342246005	12.93977279935571
N	12.45430769402322	9.08776375997612	13.35450087706209
N	9.18352037937573	4.55915458780986	12.36499006422628
N	11.19523061020675	6.08421353371858	16.76160451678501
C	8.61983719385443	4.43534816528239	9.56085640408639
C	7.61383870253155	2.82970799993014	12.90286693762240
H	15.63403825314507	4.07017689905865	13.50707540834546
C	11.00932186449136	6.15885226513049	18.13697303765469
C	8.23577639784082	3.63707711512535	11.93600778575341
C	11.90347339399485	5.47185379753810	18.97336495989750
H	14.31121681778547	6.02310976342102	11.11596198062165
C	10.79614460990141	10.73104565787595	14.96015803401044
H	12.62278544176062	2.60110208900759	13.88733782095360
C	12.86281007366047	10.40518718858102	13.52742024434668
C	10.00190083756338	5.27309527555992	12.78256134857193
C	9.93052486574787	6.91495088915420	18.62415635250896
C	11.32979030925483	6.04041533712371	15.60724809675670
C	14.04560156207530	10.84396462973957	12.91202410907435
C	14.43818695687055	12.15724087253789	13.15376309565982

H	15.34663638250932	12.52625081204066	12.69584259452074
C	12.06501009059486	7.99216052858359	13.31983323813938
C	6.68961080570928	1.89224667087709	12.45282147553510
H	6.19337431741113	1.25623166211809	13.17386797541140
H	14.67074540238910	4.44402809721887	14.95020987550742
C	14.87013135482989	9.93410297065790	12.04524579542383
C	7.93201824063164	2.96952502539615	14.36336967772523
C	7.02610166737137	2.58081018107447	10.16952959712332
H	6.78987571874529	2.47752984796692	9.11807306138947
C	7.95354309475368	3.54059045156340	10.56371346243893
C	12.51518712557383	12.53231934142899	14.55518246253708
H	13.74887683716691	2.33886843679923	12.53699767603718
C	10.62963290658669	6.29850027699753	20.85700597235916
C	13.04595538249162	4.67858873296411	18.40674222044608
C	12.07080842165796	11.23203797860284	14.34327724685630
C	6.40032801059536	1.76446849086948	11.10112138811375
H	5.68071960548960	1.02686599016283	10.77161177101244
C	8.99499380226493	7.62840202010186	17.69294818897366
H	10.47589547258941	6.35388524227057	21.92714482323905
H	12.06411130100189	2.79028946768229	12.22452163932201
H	11.93078652417838	13.19141142729577	15.18425587714624
C	12.91161568889560	2.94200361826942	12.89310918581997
C	13.95355646153628	4.99953281001593	11.23049775633282
H	15.29518090177944	5.75580384234331	13.94466868651297
C	14.88556270968286	4.74559747779257	13.92470497211449
C	11.68805130812386	5.55897097792203	20.34504489583395
H	12.35959319752060	5.03865157009476	21.01634370608458
C	9.76450338975974	6.97041770257104	20.00427016458537
H	8.94631413218822	7.54837536334010	20.41374696455706
C	13.68832538696447	12.99122421730591	13.97161431502417
H	14.02222916391818	14.00363429948952	14.15832189850876
H	13.14236786584006	4.84032084072928	10.52000693436525
H	14.76862211146453	4.31344228880148	10.99459140011899
H	8.44245152066416	5.48932457758354	9.78921547305312
H	8.24002417606251	4.23866500699757	8.56035945879061
H	9.70212999122212	4.27981476346726	9.54627114450758
H	10.98412774619862	9.89741713854502	15.64025631454767
H	10.09945968710002	10.37374909484511	14.19881733328936
H	10.30833014111798	11.52294553053351	15.52566741740624
H	15.64565996906947	10.49812013130649	11.53005202743702
H	14.25911330079547	9.43092387055712	11.29446852569189
H	15.36021579456643	9.15994089812628	12.64217288023043
H	8.98115963449245	2.74249835423927	14.56969223432896
H	7.31957351927391	2.29167282130071	14.95398293521688
H	7.74638762651979	3.98691858655030	14.71574989211718
H	13.60829052376476	4.18986347940713	19.20054325964957
H	13.73349143414017	5.31963566114499	17.84870903127307
H	12.69136980237146	3.90777342715525	17.71842602142888
H	8.44302618948281	6.92534605471028	17.06398104505975
H	9.53658049074111	8.29942384156373	17.02236052575734
H	8.27286874409258	8.21872730638645	18.25423678675057

Optimized coordinates for $[Cu(THF)(CNXyl)_3]^+$.

C	2.89510487223113	4.59722427126568	5.93635404163850
C	4.67647791361274	2.84473962387312	3.80016201631306
C	2.87366717557559	5.52883020440700	2.76830304836674

C	2.45913941395011	4.90338614921733	8.42696036497115
C	2.44629508405879	6.18043922721516	9.00805609678348
C	2.30701582329896	6.24522626367940	10.39124437352432
H	2.29863267591320	7.21373214298722	10.87479181905569
C	2.17511877347604	5.09154747763236	11.15309927756589
H	2.07297985665108	5.16634566458163	12.22801987061649
C	2.15255861143531	3.84439419364517	10.54338649099043
H	2.02270559064492	2.95185582986228	11.14187020187022
C	2.28696327062627	3.71985296792892	9.16516152197197
C	2.57187527189860	7.42321671540356	8.17369943721790
C	8.46374719479865	0.07477688500073	4.63284664492087
H	8.97264190086076	-0.26605560177681	5.52467363924378
C	8.92187478690827	-0.31542912664979	3.38335143920169
H	9.78861229848335	-0.95789427601878	3.30316139683979
C	8.27249235324442	0.11553816554716	2.23541681608627
H	8.63571554529421	-0.19174195589092	1.26332952836933
C	7.15525245247492	0.94107928160145	2.30689485936724
C	6.88139715096665	1.32777616715462	6.12831504898331
H	0.13422251558278	4.74178203117854	4.60760980947467
N	2.66674039144093	4.78922922501815	7.05889946459442
N	5.60099714408184	2.14818929511789	3.69213109680134
N	2.61139809925482	6.38496905298699	2.02902594753178
O	1.11741523076667	3.09955216459433	3.83758481064808
C	-0.74550043899049	1.62163281184389	3.87201978529269
H	-1.09510812093151	1.52116909423009	2.84300282886500
H	-1.13334508020445	0.77640802613491	4.43810640639273
C	-1.16654595498138	2.97778800779100	4.45414858144932
H	-1.16025583098161	2.94943267641869	5.54599425758543
C	7.35372333874866	0.90209608575628	4.76736742129508
C	2.23700940933547	2.37873104291481	8.49085452667697
C	2.36005426299432	7.42527429803394	1.14556136268253
C	2.28221413081490	7.13230776406411	-0.22531772495542
C	2.10049149792456	8.20306557800607	-1.09404955733089
H	2.04153408202260	8.01474321158961	-2.15842549711131
C	1.99147659182466	9.50135033180470	-0.61360562477698
H	1.85844266004573	10.32220967162322	-1.30599584846893
C	2.03463245237531	9.75383261338389	0.75126464105978
H	1.92661437114396	10.76659913579862	1.11741196144004
C	2.21391053261245	8.72177487580519	1.66519926094564
C	6.46965506343370	1.40734099672476	1.05515116904571
H	-2.15768696096744	3.29285196985623	4.12989389759161
C	-0.07444256116105	3.90633983104693	3.93900628619740
C	2.25621788932129	8.97901049379012	3.14398216257574
C	0.77845660983490	1.69746024431744	3.91880812411225
H	1.17537434867334	1.29881437070391	4.85696023121783
C	2.39384731603935	5.72101343714252	-0.72489085765145
Cu	3.28397582623152	4.16371312475045	4.08107584023532
H	1.26181862073219	1.17881310347627	3.09064106279237
H	-0.31732305978791	4.30657862052521	2.94977234541828
C	6.71433641024680	1.32146715453710	3.58669052434692
H	3.54133542295548	7.47651650655723	7.67223702776031
H	2.46111881809466	8.30984491374500	8.79511207987196
H	1.80686904421094	7.45778968065080	7.39472680093254
H	7.45409988514127	0.81891529067358	6.90037676383552
H	5.82507496662527	1.09362518193741	6.27951156833633
H	7.00695303556302	2.40432590933028	6.27248149816912
H	3.18909975254960	2.13076585404935	8.01479491634397
H	1.47481813583009	2.35490048176056	7.70883828960307

H	2.00454853166852	1.59762489861062	9.21214971853067
H	6.57312628880843	2.48866469444122	0.92835054025219
H	5.40213075411845	1.17623645267394	1.06869839746599
H	6.90718149351353	0.92575963322978	0.18348514029544
H	3.25701126286602	8.80742267636314	3.54907648299376
H	1.57527668554158	8.31822485957065	3.68337398582011
H	1.97314603360557	10.00708426368757	3.36396518648750
H	3.41627192908039	5.34600787654640	-0.62930064894266
H	2.10815096423184	5.66157996170005	-1.77386222354729
H	1.75118001171461	5.04503450283962	-0.15945971407893

Optimized coordinates for $[Cu(OH_2)(CNXyl)_3]^+$.

C	2.92662756937300	4.99796739059220	5.91964847436980
C	4.98482269435841	3.49848241669379	3.95208173042088
C	3.07846981154236	6.13605897660262	2.71145655032838
C	2.09180367999601	4.65313540379963	8.30266685304290
C	1.98124363228704	5.70750988383450	9.22251744296276
C	1.58205456150112	5.37996094531692	10.51540134277636
H	1.48569670213729	6.17117635201356	11.24787596133944
C	1.30335673818827	4.06990498991988	10.87332231437879
H	0.99368762566013	3.84157978830663	11.88465684901463
C	1.40007099813024	3.05098977998691	9.93467620124851
H	1.16081238104992	2.03358482073608	10.21584694983402
C	1.79372125151378	3.31667192084408	8.62884612341823
C	2.29494535059970	7.13289508884718	8.86568652280424
C	8.02885021582038	0.10846003623804	5.35715438112986
H	8.37191222918706	-0.25472390428356	6.31727939696167
C	8.50717627370603	-0.46955765321190	4.18992007518538
H	9.22029750978132	-1.28150929132602	4.24335940377839
C	8.07588865014927	-0.00691017879456	2.95579981198343
H	8.45551361156240	-0.45806459066608	2.04864750518462
C	7.15900233304533	1.03465151328618	2.85673317937365
C	6.60466748092489	1.76576426184261	6.59560926437674
H	1.53557480934676	1.27872395468524	8.03537283954300
N	2.52373929995165	4.91327604033981	7.00563434156705
N	5.76308428980783	2.63556244627246	3.98878504150390
N	2.73811477998721	6.89471235782129	1.89928248156728
O	1.71698004640003	3.21264574801869	3.55887559567150
H	5.62697903120812	1.35679190505064	1.37441429938412
H	7.22200905025785	0.98809925789620	0.72115237802459
H	5.08247053314429	7.10894344868418	0.25494506910657
H	5.11753863568282	8.37303572103955	1.48097507381009
H	5.47120733949924	8.76742990630827	-0.20074792573761
C	7.11198504757128	1.15355398243721	5.32164650041307
C	1.88586737317704	2.21734678286744	7.61021056672081
C	2.37289091642961	7.80956741658901	0.91482134425721
C	1.00816763593677	8.05962481806417	0.69022892677395
C	0.68020639451761	8.97728600878358	-0.30296198015324
H	-0.36276149830859	9.18791972343892	-0.50330623582434
C	1.66679146923718	9.62335486772199	-1.03455050465184
H	1.38944243077538	10.33535117961737	-1.80065112569504
C	3.00641447396165	9.35975757430851	-0.78789647590964
H	3.77011236391656	9.86768152006033	-1.36146417408977
C	3.39337777561141	8.44596695332922	0.18779823091495
C	6.69913098787240	1.52063661976943	1.51226067178832
H	-0.03942344077132	6.28709461044325	1.31335837216983
H	0.84993712870714	3.57912885952126	3.35135399778514

C	4.84322138710530	8.15814553810149	0.44550316863440
H	1.84760888026221	2.48413449183336	2.94149860685639
H	-1.04604968175755	7.72889747814834	1.18971223043728
C	-0.06207755990147	7.36774346203466	1.48159285998283
Cu	3.57780437502225	4.85004191898223	4.07663230783601
H	0.05692566762000	7.54375092492273	2.55367100850546
H	6.88926943008201	2.58887652546676	1.38442503923344
C	6.68882697378713	1.59842324707717	4.05589377267940
H	3.36628084937567	7.33323729649782	8.95496760268760
H	1.78067481229626	7.81168057935326	9.54341124411951
H	1.99273763575904	7.37874935959164	7.84747311609265
H	7.09821860793455	1.31361601180966	7.45301045286570
H	5.52803438105624	1.61094723694333	6.70876695895061
H	6.79098570038519	2.84183526814974	6.62814256867603
H	2.91286651290707	2.07097796569101	7.26754991054806
H	1.28706767364487	2.43702529173815	6.72423694904321

Optimized coordinates for $[Cu(CNXyl)_3]^+$.

C	2.66568117353489	4.27844520183926	5.56534610353857
C	5.02992774910217	2.75554365868938	3.71502846142005
C	3.08583778518162	5.41064130404768	2.61004705251916
C	1.69742293149256	4.87892048122246	7.84176798963967
C	1.46597746482178	6.23558095960090	8.12433517340486
C	1.05671100730604	6.55037683958668	9.41520414725072
H	0.87206001188800	7.58554587798174	9.67180384969969
C	0.88066791237766	5.55873468480199	10.37105851145779
H	0.56800793485831	5.82852779966179	11.37111822170462
C	1.08103411069990	4.22357265347599	10.04740221021479
H	0.91448165306763	3.45708800715335	10.79282145904665
C	1.48844019474879	3.84857531306153	8.77252991693815
C	1.63666991250718	7.30064100936565	7.07934237298500
C	8.65127475795026	-0.15230596627402	4.77118137712653
H	9.10986142009832	-0.49269874380065	5.69013451858327
C	9.14679588336683	-0.58467589742301	3.54982844510163
H	9.99206855444330	-1.25926556742650	3.51942441410076
C	8.55987830442669	-0.15867038870771	2.36690651894880
H	8.94847454495485	-0.50377207723188	1.41778333270209
C	7.47307020042012	0.70901451953639	2.37296673761204
C	7.04561250868089	1.17844880311872	6.17213380337047
H	1.40551381880960	1.75762883650905	9.22922187336090
N	2.18410886422114	4.54047539500765	6.58767076686233
N	5.91855093541399	2.01000272705698	3.66733382723228
N	2.77397083894172	6.39563153536591	2.08214507739532
H	7.17849090334710	2.25646329852969	6.29816560983339
H	5.78084209421025	0.94221248652830	1.05365439484754
H	7.32098902621560	0.66470310460528	0.24141828955787
H	5.17254388087644	7.35720413861104	0.99946200748445
H	5.07696641990905	8.02239041399548	2.62262652786228
H	5.51119693568667	9.06659477156330	1.26646880910385
C	7.56674018934282	0.71486620432875	4.84233225783441
C	1.67466464935329	2.40619297641061	8.39795729748153
C	2.41153382633740	7.63094993437173	1.56133322949226
C	1.05180022801869	7.88981992468358	1.32287802542254
C	0.72099598676925	9.16592233707705	0.87952415359348
H	-0.31694000155746	9.40307139313325	0.68452053698607
C	1.69891233071911	10.13169130178588	0.68340469275503
H	1.41598763556189	11.11930145086210	0.34383111940985

C	3.03668127762708	9.83425886666924	0.90300401989964
H	3.79264429852289	10.58851658204648	0.72810573180714
C	3.42850981154810	8.57481414602523	1.34178767167100
C	6.85022369096747	1.16426555900143	1.08495960806965
H	0.20613704189128	5.94799033044860	0.92560971723725
H	2.70793667793399	2.19086525029757	8.11554990530871
C	4.87413250989255	8.23846024762692	1.57059320948028
H	1.04735479093562	2.13597724355761	7.54595642262026
H	-0.97760859664857	7.21989722470729	1.23188461977855
C	-0.00114680849101	6.83788293009857	1.52330090075739
Cu	3.59788130097638	4.03502177700454	3.87921454725396
H	-0.06143651155406	6.51691639603871	2.56604245612093
H	6.96897367529047	2.24226736938655	0.94556806735514
C	6.99770368609706	1.13502642186148	3.62613150105270
H	2.67165171039655	7.37233724766316	6.73646528258071
H	1.34572199730142	8.27100904333651	7.47697461614461
H	1.01973407146048	7.09600996031732	6.20179329417718
H	7.57884468087108	0.68051400265171	6.97871013996288
H	5.98105193687716	0.95934194855540	6.28517661484243

5.9 Acknowledgements

Chapter 5 is in part adapted from "Robust, Transformable, and Crystalline Single-Node Organometallic Networks Constructed from Ditopic *m*-Terphenyl Isocyanides" by Douglas W. Agnew, Milan Gembicky, Curtis E. Moore, Arnold L. Rheingold, and Joshua S. Figueroa, *Journal of the American Chemical Society* **2016** *138* (46), 15138-15141. Copyright 2016, American Chemical Society. Permission to include published material in this dissertation has been obtained from all coauthors. The dissertation author is the first author of this paper. Chapter 5 contains unpublished material produced in collaboration with Professor Nathan Gianneschi, Dr. Joseph Patterson, and Mollie Touve, who are thanked for the acquisition of TEM images of Cu-^{ISO}CN-3. Professor Stanley Opella and Dr. Anna de Angelis are thanked for the acquisition of the CP-MAS ^{13}C NMR spectrum of Cu-^{ISO}CN-3. Professor Seth Cohen and Michael S. Denny, Jr., are thanked for helpful discussions and assistance with physical measurements.

5.10 References

1. Yaghi, O. M.; Li, H.; Eddaoudi, M.; O'Keeffe, M. *Nature* **1999**, *402*, 276.

2. Long, J. R.; Yaghi, O. M. *Chem Soc Rev* **2009**, *38*, 1213.

3. Kitagawa, S.; Kitaura, R.; Noro, S.-I. *Angew. Chem. Int. Ed.* **2004**, *43*, 2334.

4. Yaghi, O. M.; O'Keeffe, M.; Ockwig, N. W.; Chae, H. K.; Eddaoudi, M.; Kim, J. *Nature* **2003**, *423*, 705.

5. Farha, O. K.; Shultz, A. M.; Sarjeant, A. A.; Nguyen, S. T.; Hupp, J. T. *J. Am. Chem. Soc.* **2011**, *133*, 5652.

6. Feng, D.; Chung, W.-C.; Wei, Z.; Gu, Z.-Y.; Jiang, H.-L.; Chen, Y.-P.; Darensbourg, D. J.; Zhou, H.-C. *J. Am. Chem. Soc.* **2013**, *135*,17105.

7. Wang, Z.; Cohen, S. M. *Chem Soc Rev* **2009**, *38*, 1315.

8. Li, J.-R.; Sculley, J.; Zhou, H.-C. *Chem. Rev.* **2012**, *112*, 869.

9. Murray, L. J.; Dinca, M.; Long, J. R. *Chem Soc Rev* **2009**, *38*, 1294.

10. Kreno, L. E.; Leong, K.; Farha, O. K.; Allendorf, M.; Van Duyne, R. P.; Hupp, J. T. *Chem. Rev.* **2012**, *112*, 1105.

11. Lee, J.; Farha, O. K.; Roberts, J.; Scheidt, K. A.; Nguyen, S. T.; Hupp, J. T. *Chem Soc Rev* **2009**, *38*, 1450.

12. Shearer, G. C.; Chavan, S.; Bordiga, S.; Svelle, S.; Olsbye, U.; Lillerud, K. P. *Chem. Mater.* **2016**, *28*, 3749.

13. Furukawa, H.; Müller, U.; Yaghi, O. M. *Angew. Chem. Int. Ed.* **2015**, *54*, 3417.

14. Eller, P. G.; Bradley, D. C.; Hursthouse, M. B.; Meek, D. W. *Coord. Chem. Rev.* **1977**, *24*, 276.

15. Alvarez, S. *Coord. Chem. Rev.* **1999,** *193,* 13.

16. Power, P. P. *J. Organomet. Chem.* **2004**, *689*, 3904.

17. Phillips, N.; Rowles, J.; Kelly, M. J.; Riddlestone, I.; Rees, N. H.; Dervisi, A.; Fallis, I. A.; Aldridge, S. *Organometallics*. **2012**, *31*, 8075.

18. Arrowsmith, M.; Maitland, B.; Kociok-Köhn, G.; Stasch, A.; Jones, C.; Hill, M. S. *Inorg Chem* **2014**, *53*, 10543.

19. Kays, D. *Dalton Trans*. **2011**, *40*, 769.

20. Fox, B. J.; Sun, Q. Y.; DiPasquale, A. G.; Fox, A. R.; Rheingold, A. L.; Figueroa, J. S. *Inorg Chem* **2008**, *47*, 9010.

21. Fox, B. J.; Millard, M. D.; DiPasquale, A. G.; Rheingold, A. L.; Figueroa, J. S. *Angew. Chem. Int. Ed. Engl.* **2009**, *48*, 3473.

22. Margulieux, G. W.; Weidemann, N.; Lacy, D. C.; Moore, C. E.; Rheingold, A. L.; Figueroa, J. S. *J. Am. Chem. Soc.* **2010**, *132*, 5033.

23. Carpenter, A. E.; Margulieux, G. W.; Millard, M. D.; Moore, C. E.; Weidemann, N.; Rheingold, A. L.; Figueroa, J. S. *Angew. Chem. Int. Ed. Engl.* **2012**, *51*, 9412.

24. Carpenter, A. E.; Mokhtarzadeh, C. C.; Ripatti, D. S.; Havrylyuk, I.; Kamezawa, R.; Moore, C. E.; Rheingold, A. L.; Figueroa, J. S. *Inorg Chem* **2015**, *54*, 2936.

25. Agnew, D. W.; Moore, C. E.; Rheingold, A. L.; Figueroa, J. S. *Angew. Chem. Int. Ed.* **2015**, *54*, 12673.

26. Cotton, F. A.; Zingales, F. *J. Am. Chem. Soc.* **1961**, *83*, 351.

27. Efraty, A.; Feinstein, I.; Frolow, F.; Wackerle, L. *J. Am. Chem. Soc.* **1980**, *102*, 6341.

28. Efraty, A.; Feinstein, I.; Frolow, F. *Inorg Chem* **1982**, *21*, 485.

29. Efraty, A.; Feinstein, I. *Inorg Chem* **1982**, *21*, 3115.

30. Gavenonis, J.; Tilley, T. D. *Organometallics* **2002**, *21*, 5549.

31. Johansson, M. P.; Olsen, J. *J. Chem. Theory Comput.* **2008**, *4*, 1460.

32. Dias, H. V. R.; Jin, W. *Inorg Chem* **1996**, *35* (12), 3687.

33. Yang, L.; Powell, D. R.; Houser, R. P. *Dalton Trans*. **2007**, 955.

34. ν_{CN} ([Cu(THF)($CNAr^{Mes2}$)$_3$]OTf, KBr) = 2160 cm^{-1}; see Ref. 20.

35. Bernini, M. C.; la Peña-O'Shea, de, V. A.; Iglesias, M.; Snejko, N.; Gutierrez-Puebla, E.; Brusau, E. V.; Narda, G. E.; Illas, F.; Monge, M. A. *Inorg Chem* **2010**, *49*, 5063.

36. Martí-Rujas, J.; Islam, N.; Hashizume, D.; Izumi, F.; Fujita, M.; Kawano, M. *J. Am. Chem. Soc.* **2011**, *133*, 5853.

37. Liu, D.; Liu, T.-F.; Chen, Y.-P.; Zou, L.; Feng, D.; Wang, K.; Zhang, Q.;

Yuan, S.; Zhong, C.; Zhou, H.-C. *J. Am. Chem. Soc.* **2015**, *137*, 7740.

38. Naumov, P.; Bharadwaj, P. K. *CrystEngComm* **2015**, *17*, 8775.

39. Martí-Rujas, J.; Kawano, M. *Acc. Chem. Res.* **2013**, *46*, 493.

40. Jiang, H.-L.; Makal, T. A.; Zhou, H.-C. *Coord. Chem. Rev.* **2003**, *257*, 2232.

41. Kole, G. K.; Vittal, J. J. *Chem Soc Rev* **2013**, *42*, 1755.

42. Bloch, W. M.; Sumby, C. J. *Chem. Comm.* **2012**, *48*, 2534.

43. Ma, Y.; Tong, W.; Zhou, H.; Suib, S. L. *Microporous and Mesoporous Materials* **2017**, *37*, 243.

44. Howarth, A. J.; Liu, Y.; Li, P.; Li, Z.; Wang, T. C.; Hupp, J. T.; Farha, O. K. *Nat. Rev. Mater.* **2016**, *1*, 15018.

45. Denny Jr, M. S.; Moreton, J. C.; Benz, L.; Cohen, S. M. *Nat. Rev. Mater.* **2016,** *1*, 16078.

46. Denny Jr, M. S.; Cohen, S. M. *Angew. Chem. Int. Ed.* **2015**, *54,* 9029.

47. Fox, B. J.; Sun, Q. Y.; DiPasquale, A.G.;Fox, A. R.; Rheingold, A. L.; Figueroa, J. S. *Inorg. Chem.* **2008**, *47*, 9010.

48. Butler, I. R.; Cullen, W. R.; Kim, T.-J.; Rettig, S. J.; Trotter, J. *Organometallics* **1985**, *4*, 972.

49. Salomon, R. G.; Kochi, J. K. J. Am. Chem. Soc. 1973, *95*, 3300.

50. Fulmer, G. R.; Miller, A. J. M.; Sherden, N. H.; Gottlieb, H. E.; Nudelman, A.; Stoltz, B. M.; Bercaw, J. E.; Goldberg, K. I. *Organometallics* **2010**, *29*, 2176.

51. Sheldrick. G. M. *Acta Crystallogr. A.* **2008**, *64*, 112.

52. Dolomanov, O. V.; Bourhis, L. J.; Gildea, R. J.; Howard, J. A. K.; Puschmann, H. J. *Appl. Cryst.* **2009**, *42*, 339.

53. van der Sluis, P.; Spek. A. L. *Acta Crystallogr.* **1990**, *A46*, 194-201.

54. F. Neese, *Wiley Interdiscip. Rev.: Comput. Mol. Sci.* **2012**, *2*, 73.

55. A. D. Becke, *Phys. Rev. A* **1988**, *38*, 3098.

56. J. P. Perdew, *Phys. Rev. B* **1986**, *33*, 8822.

57. J. P. Perdew, *Phys. Rev. B* **1986**, *34*, 7406 (Erratum).

58. S. Grimme, J. Antony, S. Ehrlich, and H. Krieg. *J. Chem. Phys.*, **2010**, *132*, 154104.

Chapter 6

Further Development of Multi-Topic *m*-Terphenyl Isocyanide Ligands for Supramolecular Chemistry

6.1 Introduction

The ability to generate highly divergent architectures through simple alteration of metal ion identity is perhaps one of the most powerful principles underlying coordination driven self-assembly.[1-5] As a result, multiple supramolecular configurations can be achieved within the same ligand set, allowing for the facile synthesis of novel multinuclear species.[6-9] Additionally, simple synthetic elaboration of a given ligand type, while retaining the important steric and electronic factors governing the ultimate identity of the metal-ligand coordinative bond, can be used to extend the qualities of known discrete materials.[10-13] While these features have been exhaustively investigated for high-valent metal ions, typically with pyridine-based or nitrile-based ligand sets, there remain far fewer reports of multinuclear metal complexes linked together with a multitopic isocyanide.[14-20] In continuation of our interest in supramolecular species derived from sterically encumbering, *m*-terphenyl multitopic isocyanides, we report here recent progress in the preparation of novel molecular complexes as well as new ligand sets to diversify previously obtained materials.

Inspired by the previously surveyed chemistry with Cu(I) ions with $[CNAr^{Mes2}]_2$,[21] we have investigated the formation of multinuclear metal species using easily available organometallic precursors. This work has been performed with an

emphasis on generating molecular fragments that can be further elaborated upon to generate framework materials. We have found that under certain conditions, these fragments can aggregrate following well-defined organometallic reaction pathways to form unique, fluorescent molecules. In alignment with this, we have also prepared a linear Co(II) coordination polymer, which is the first example of a Co(II)-isocyanide coordination polymer. Additionally, we report here the synthesis of the ditopic isocyanide *p*-QTPh-[$CNAr^{Mes2}$]$_2$ and tritopic isocyanide 1,3,5-($CNAr^{Mes2}$)-triphenylbenzene, which rely upon very similar synthetic procedures to that of [$CNAr^{Mes2}$]$_2$.

6.2 Multinuclear Complexes Bridged by [$CNAr^{Mes2}$]$_2$

The complimentary electronic features of isocyanides for low-valent metal species – namely the low-lying, cylindrically symmetric π*-orbital (see Chapter 1) – prompted us to investigate the formation of multinuclear supramolecular complexes in which a low-valent metal center determined overall framework architecture. While there are numerous examples utilizing divalent or trivalent metal centers, there are comparatively few examples in which a zerovalent metal ion acts as the node.[1] Accordingly, we have investigated the reactivity of [$CNAr^{Mes2}$]$_2$ with several zerovalent metal precursors, including $Fe(CO)_5$, $Cr(CO)_6$, and $Mo(CO)_6$ to gain a foothold in this relatively underexplored chemistry. Additionally, in recognition of the strong σ-donating character of aryl isocyanides,[22-23] we have examined the ability of [$CNAr^{Mes2}$]$_2$ to function as a linker ligand with high-valent metals while still providing directional steric influence over metal node coordination. To this end, we report the formation of a dinuclear Pd(II) dimer, which promises to be amenable to the formation

of framework materials. We have also prepared an interesting 1-dimensional coordination polymer using $CoCl_2$, which provides an excellent example of the steric forces that $[CNAr^{Mes2}]_2$ dictate.

Reaction of $[CNAr^{Mes2}]_2$ with two equiv $Fe(CO)_5$ readily forms the deep yellow dimeric species $[(CO)_4FeCNAr^{Mes2}]_2$ in the course of thirty minutes (Scheme 6.1) with loss of two equiv CO. A single set of resonances from $[CNAr^{Mes2}]_2$ in the ^1H NMR is consistent with the formation a highly symmetric species. Indeed, crystallographic analysis reveals the formation a dinuclear Fe(0) complex, in which the Fe···Fe distance is 15.844(4) Å (Figure 6.1). Infrared spectral analysis of $[(CO)_4FeCNAr^{Mes2}]_2$ gives rise to a strong isocyanide band at 2157 cm^{-1}, consistent with the previously reported mono-isocyanide, tetracarbonyl Fe species $Fe(CO)_4(CNAr^{Mes2})$.[24] Unfortunately, attempts at further substitution at the Fe center with $[CNAr^{Mes2}]_2$ did not prove tractable, suggesting that alternative Fe(0) starting materials with more labile ligands are necessary for supramolecular complex formation.

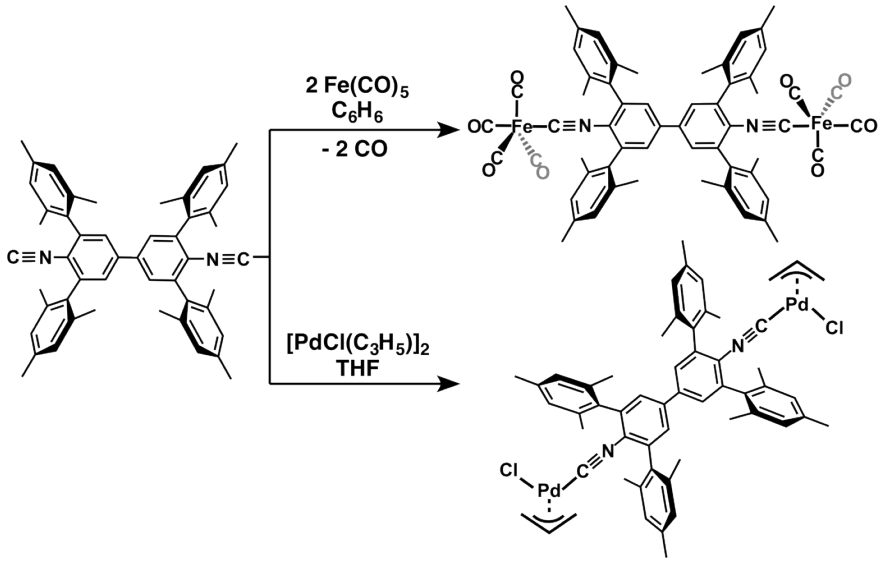

Scheme 6.1. Preparation of $[(CO)_4FeCNAr^{Mes2}]_2$ and $[PdCl(\eta^3\text{-allyl})CNAr^{Mes2}]_2$

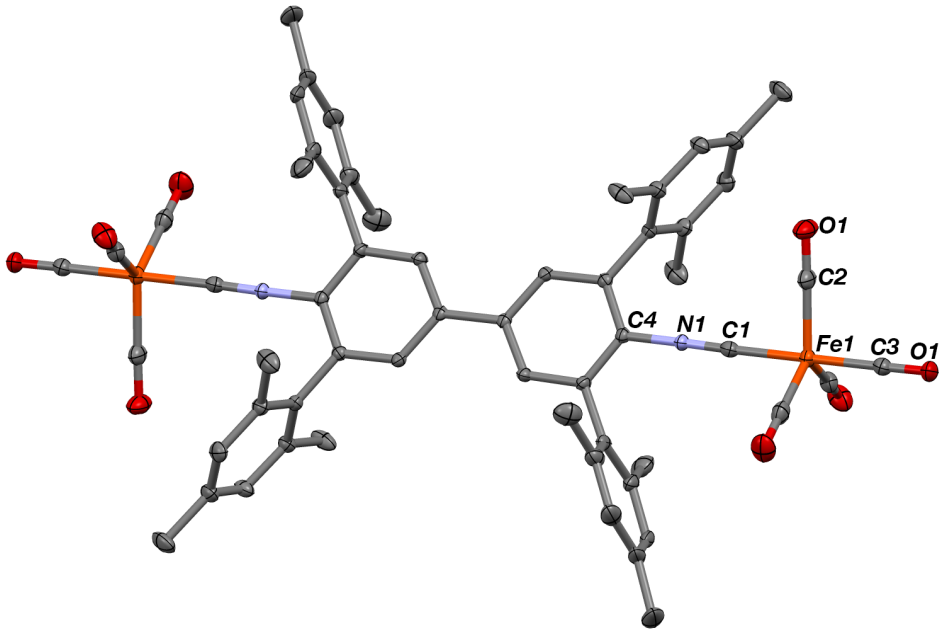

Figure 6.1. Molecular structure of $[(CO)_4FeCNAr^{Mes2}]_2$, with H atoms omitted for clarity. Selected bond angles (°) and distances (Å): Fe1-Fe1' = 15.844(4); Fe1-C1 = 1.862(3); C1-N1 = 1.144(4); C3-O1 = 1.140(3); C2-Fe1-C1 = 88.65(13).

With the need for easily removed ligands in mind, we turned to the formation of a Pd(II) dimer which could be reduced to Pd(0). It has been previously shown in the Figueroa laboratory by Dr. Liezel Labios that $PdCl(\eta^3\text{-allyl})(CNAr^{Dipp2})$ could be reduced with $Li[HBEt_3]$ to form a homoleptic *m*-terphenyl isocyano Pd trimer.[25] With $[CNAr^{Mes2}]_2$ ligation, we envisioned this transformation could be utilized for the formation of infinite framework materials with catalytically active trimeric Pd nodes. Gratifyingly, addition of 1 equiv $[CNAr^{Mes2}]_2$ to $[PdCl(\eta^3\text{-allyl})]_2$ resulted in the formation of the dimer $[PdCl(\eta^3\text{-allyl})(CNAr^{Mes2})]_2$ (Scheme 6.1). Interestingly, $[PdCl(\eta^3\text{-allyl})CNAr^{Mes2}]_2$ exhibits two distinct isocyanide bands at 2171 (s) cm^{-1} and 2113 (m) cm^{-1}, which is due to vibronic coupling of the two symmetrically-related isocyanide groups (for comparison, ν_{CN} = 2173 cm^{-1} for $PdCl(\eta^3\text{-allyl})(CNAr^{Dipp2})$).[26]

The solid state structure (Figure 6.2) confirms this symmetry, and suggests that [PdCl(η^3-allyl)CNAr^{Mes2}]$_2$ is indeed poised to be a versatile synthon for framework materials. However, initial attempts at generating extended supramolecular complexes have thus far produced amorphous products, therefore suggesting a need for more tailored reaction conditions.

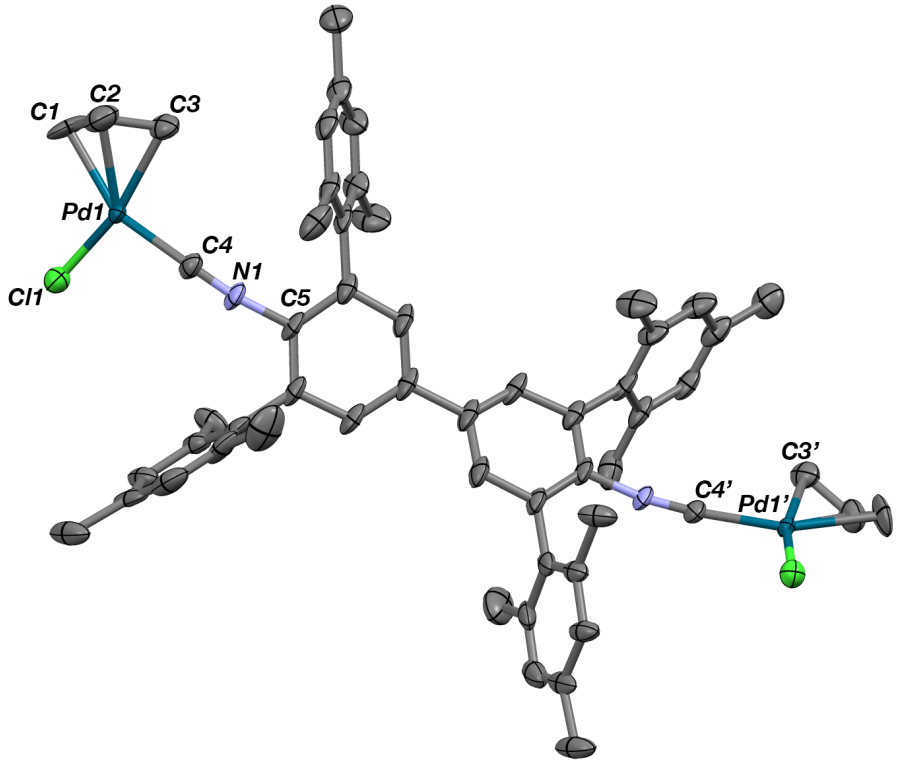

Figure 6.2. Molecular structure of [PdCl(η^3-allyl)CNAr^{Mes2}]$_2$, with FBz solvent molecule and H atoms omitted for clarity. Selected bond angles (°) and distances (Å): Pd-Pd1' = 15.827(9); Pd1-Cl1 = 2.3508(15); Pd1-C4 = 1.976(5); C1-C2 = 1.559(9); C2-C3 = 1.372(9); C4-N2 = 1.142(5); Cl1-Pd1-C4 = 98.07(16); C1-C2-C3 = 120.8(7); C4-N1-C5 = 170.8(5).

In an attempt to discern any electronically distinct properties of [CNAr^{Mes2}]$_2$ from that of the parent monoisocyanide CNAr^{Mes2}, we prepared the dinuclear –Cr(CO)$_5$ dimer using (THF)Cr(CO)$_5$ (Scheme 6.2 and Figure 6.3). We have previously disclosed a through examination of the electronic properties of a variety of aryl

isocyanides, using the comparison measure of ^{13}C resonances for the equatorial and axial carbonyl ligands and the CO stretching force constants to assess the σ-donating/π-accepting ratio for the isocyano substituent.[27] The ^{13}C resonances for CO_{axial} and CO_{eq} were found at δ = 216.7 and 214.2 ppm (C_6D_6, 20 ˚C), respectively, close to the values reported for $Cr(CO)_5(CNAr^{Mes2})$ (δ = 217.0 and 214.3 ppm, respectively). However, direct comparison of the isocyanide stretching frequency, and therefore the CO force constant, was not possible due to the strong vibronic coupling in $[(CO)_5CrCNAr^{Mes2}]_2$, which notably gives rise to a medium intensity stretch at 2137 cm^{-1}, which is attributed to the formally forbidden symmetric –CN stretch. However, it worth mentioning that the antisymmetric isocyanide stretching band is observed at 2050 cm^{-1} does compare well with that of $Cr(CO)_5(CNAr^{Mes2})$ (ν_{CN} = 2054 cm^{-1}), providing some gauge as to the comparative electronic properties between $[CNAr^{Mes2}]_2$ and $CNAr^{Mes2}$.

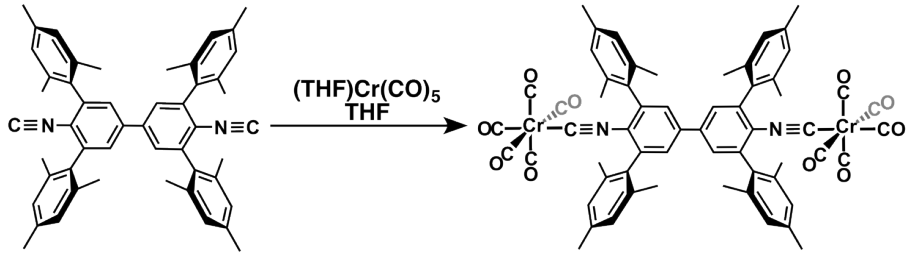

Scheme 6.2. Synthesis of $[(CO)_5CrCNAr^{Mes2}]_2$.

With a fair handle on the electronic properties of $[CNAr^{Mes2}]_2$, we were interested in examining the feasibility of its use in generating coordination polymers of higher valence metal ions. In particular, despite a surfeit of examples of coordination polymers derived for M(II) nodes, there remains just two examples in which a linker ligand employed sterically encumbering substituents was used to

facilitate low-coordination at the metal node. In two communications from Clyburne *et al.*,[28-29] a dibenzoic acid ligand with 3,5-dimesityl substitution

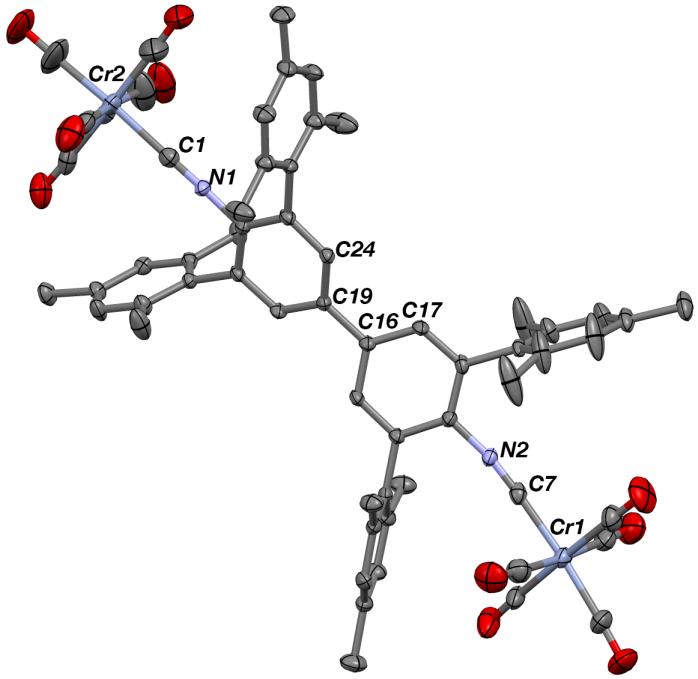

Figure 6.3. Molecular structure of $[(CO)_5CrCNAr^{Mes2}]_2$, with H atoms omitted for clarity. Selected dihedral angles (˚), bond angles (˚) and distances (Å): Cr1-Cr2 = 16.024(6); Cr2-C1 = 1.970(4); C1-N1 = 1.144(5); Cr1-C7 = 1.972(4); C7-N2 = 1.153(4); Cr1-C7-N2 = 175.7(3); C24-C19-C16-C17 = -30.0(5).

was used to prepare Zn(II), Cu(II) and Ag(II) frameworks that adopt a 2-D sheet morphology. While these materials were extremely sensitive to moisture, crystallographic analysis indicated that the presence of *m*-mesityl substituents produced the desired effect of low-coordination at the linking node, with free solvent occupying the open coordination sites. Accordingly, the use of $[CNAr^{Mes2}]_2$ was expected to produce similarly low isocyanide-coordination metal sites in high valent metals.

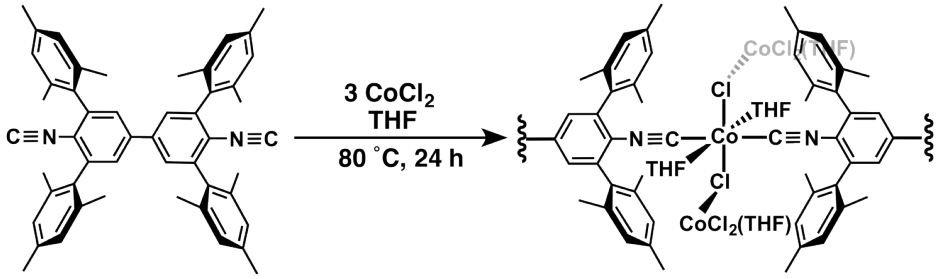

Scheme 6.3. Preparation of the 1-D coordination polymer Co-^{ISO}CN-1.

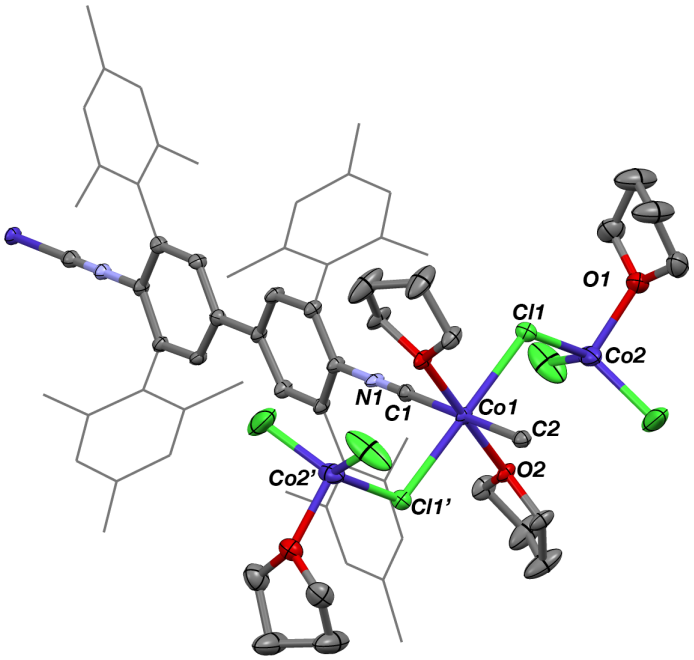

Figure 6.4. Unit cell of Co-^{ISO}CN-1, with *m*-terphenyl groups displayed in wireframe and free THF solvent molecule and H atoms omitted for clarity. Selected bond angles (°) and distances (Å): Co1-Cl1 = 2.4972(10); C1-Co2 = 2.2895(12); Co1-O2 = 2.092(2); Co1-C1 = 2.096(5); Co2-O1 = 2.034(3); Cl1-Co1-Cl1' = 179.63(6); C1-Co1-O2 = 90.47(7).

To test this, we examined the use of [CNAr^{Mes2}]$_2$ with divalent cobalt. Addition of [CNAr^{Mes2}]$_2$, dissolved in THF, to a stirring solution $CoCl_2$ in THF readily produced a deep blue solution. Heating this solution at 80 °C for 24 h, followed by slow cooling, produces deep blue crystals of Co-^{ISO}CN-1 (Scheme 6.3 and Figure 6.4). Solid-state ATR-IR analysis of these crystals reveals two bands in the isocyanide region at 2184 cm^{-1} (w) and 2117 cm^{-1} (m), supporting the retention of Co(II)

oxidation state and a highly symmetric environment about the metal node. These crystals are somewhat sensitive to ambient moisture, causing slow degradation to free isocyanide, as evidenced by a decrease in intensity in the 2184 cm^{-1} band and visible decomposition of the crystalline integrity.

Single crystal X-ray diffraction was undertaken to understand the structure of this polymer more completely. As shown in Figure 6.4, $[CNAr^{Mes2}]_2$ coordinates to Co(II) in a linear arrangement, with *trans*-oriented THF molecules bound *cis* to the isocyanides. At the two remaining coordination sites, $[CoCl_3(THF)]$ groups are bound via a bridging μ^2-Cl, which provide charge balance to the Co metal node. The linear arrangement of bound isocyanides thus form a 1-dimensional coordination polymer (Figure 6.5). The *trans*-coordination of the bridging isocyanide $[CNAr^{Mes2}]_2$ is likely enforced by the steric imposition of the *m*-terphenyl substituents, which enables the generation of open sites on the Co(II) center which are occupied by THF solvent molecules. This favoring of open coordination sites is encouraging, and suggests that further exploration of high-valent coordination polymers formed with $[CNAr^{Mes2}]_2$ is warranted. In particular, the prospect

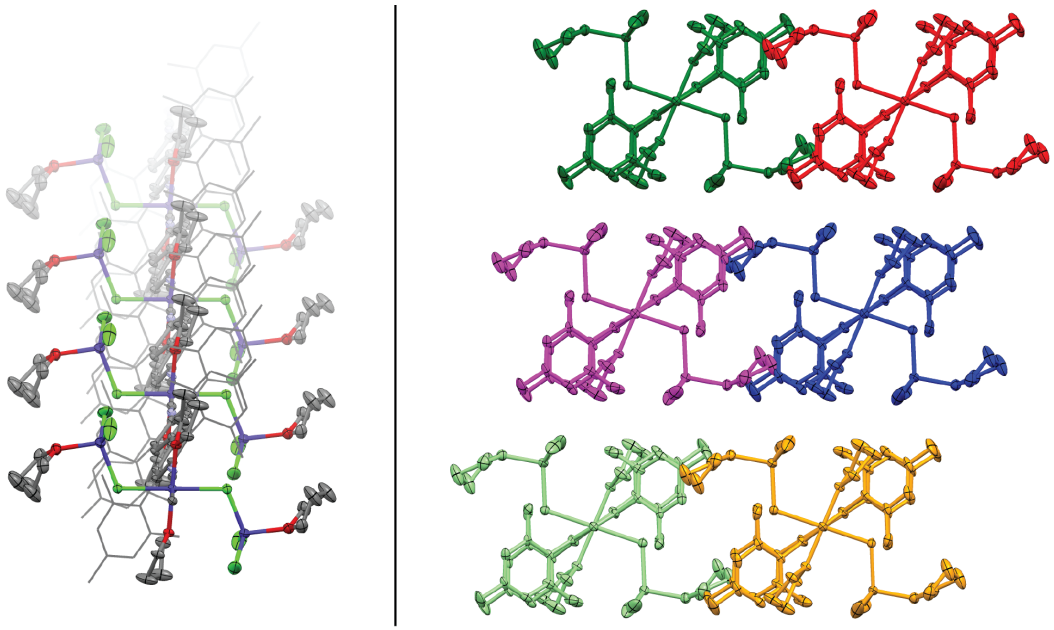

Figure 6.5. (*Left*) Covalent connectivity in Co-^{ISO}CN-1, revealing the formation of a 1-D Co(II) coordination polymer. (*Right*) Packing of 1-D chains into the lattice, which is reinforced through weak van der Waals interactions.

of using these as-formed coordination polymers for redox-active applications, which the isocyanide ligands have been demonstrated to support, is recommended by this author to be a particularly attractive application.

Finally, returning to the subject of discrete supramolecular complexes outlined above, we turned our attention to the formation of multinuclear Mo complexes bridged by [CNAr^{Mes2}]$_2$. It has been previously shown by Dr. Treffly Ditri that Mo(CO)$_6$ reacts with three equiv of CNAr^{Mes2} to generate *fac*-Mo(CO)$_3$(CNAr^{Mes2})$_3$.[30] This coordinative arrangement suggested that the [Mo(CO)$_3$] fragment could be used as a directing metal node for the formation of supramolecular polyhedra. Specifically, based upon the octahedral geometry of the zerovalent Mo center, the formation of a cube-shaped polyhedron could be envisioned with *fac*-substitution of three CO ligands. Accordingly, we have explored the multinuclear complexes formed via the

decarbonylation of $Mo(CO)_6$ and substitution of $[CNAr^{Mes2}]_2$, following the principles of supermolecular self-assembly.[1]

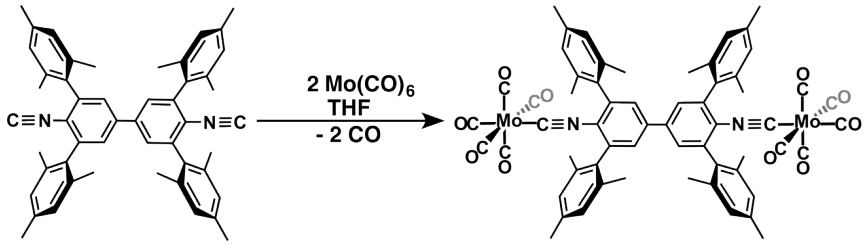

Scheme 6.4. Preparation of the dinuclear complex $[(CO)_5MoCNAr^{Dipp2}]_2$ from $Mo(CO)_6$.

Ligand substitution is well known to occur on group 6 carbonyls via a dissociative mechanism, and is particularly accelerated under illumination and in the presence of coordinating solvents.[31-33] To modulate the pace of reaction, we initially carried out substitution reactions with the exclusion of light. Stirring of a THF of solution of $Mo(CO)_6$ and $[CNAr^{Mes2}]_2$ for thirty minutes in the dark produces a light yellow colored solution, which when assayed by ^1H NMR indicates the formation of a single product (Scheme 6.4). Isolation of this product and characterization by X-ray crystallography reveals the formation of the dimeric complex $[(CO)_5MoCNAr^{Dipp2}]_2$, resulting from loss of one CO ligand per Mo center (Figure 6.6). The infrared spectrum exhibits five bands in the isocyanide/CO region, with a weak band at 2133 cm^{-1} likely originating from the forbidden symmetric stretch for $[CNAr^{Mes2}]_2$. Additionally, three resonances are observed in the downfield region of the $^{13}C\{^1H\}$ NMR spectrum at δ = 206.4, 203.2, and 166.7 ppm, which correspond to the CO_{axial}, CO_{eq}, and CNR carbons, respectively.

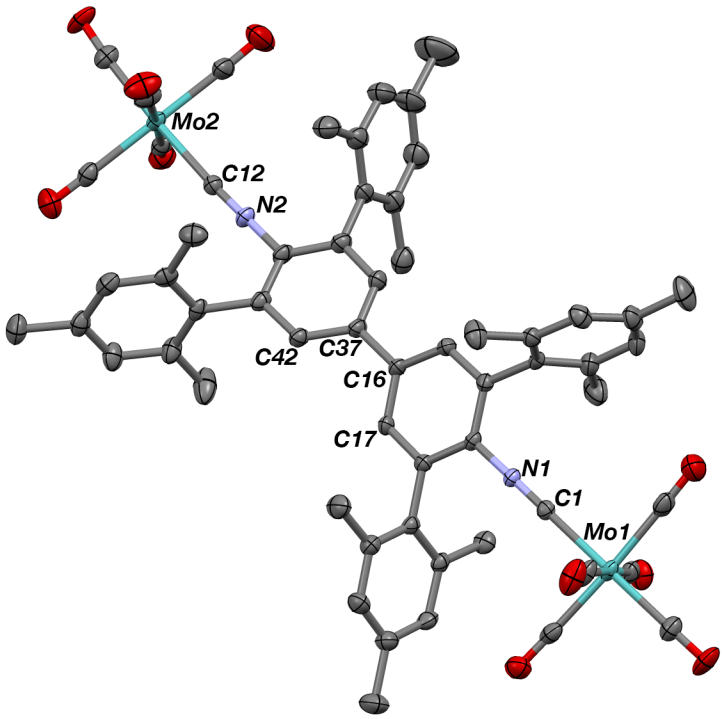

Figure 6.6. Molecular structure of $[(CO)_5MoCNAr^{Mes2}]_2$, with H atoms omitted for clarity. Selected dihedral angles (°), bond angles (°) and distances (Å): Mo1-Mo2 = 16.300(5); Mo1-C1 = 2.122(3); C1-N1 = 1.154(4); Mo2-C12 = 2.122(3); C42-C37-C16-C17 = 34.7(5).

Interestingly, continued stirring of $[(CO)_5MoCNAr^{Dipp2}]_2$ leads to the slow generation of a new product, as evidenced by a second set of signals from $[CNAr^{Mes2}]_2$ in the ^1H NMR spectrum. Intrigued by the possibility that second CO dissociation event was occurring to produce $[Mo(CO)_4]$ nodes with bridging $[CNAr^{Mes2}]_2$ ligands, we reran the reaction with a 1:1 stoichiometry between $[CNAr^{Mes2}]_2$ and $Mo(CO)_6$. After 4 h stirring, a single set of peaks were observed in the ^1H NMR that were identical to those seen in the decomposition of $[(CO)_5MoCNAr^{Dipp2}]_2$, suggesting a product with equal parts Mo centers and $[CNAr^{Mes2}]_2$ (Scheme 6.5). Additionally, new CO peaks with equal intensity in the $^{13}C\{^1H\}$ NMR spectrum were observed at δ = 208.6 and 204.3 ppm, while a single peak was observed for the $[CNAr^{Mes2}]_2$ isocyanide carbon at δ = 171.5 ppm (Figure 6.7). These data are consistent with the formation of a

$Mo(CO)_4(CNR)_2$ node, with *cis* disposition of the isocyanide ligands, resulting in the formation of the tetranuclear square $[(CO)_4Mo(CNAr^{Dipp2})_2]_2$ (Scheme 6.5, right). Indeed, *trans*-disposed isocyanides would result in a single chemical environment for the CO ligands, resulting in just one corresponding resonance in the $^{13}C\{^1H\}$ NMR spectrum. Unfortunately, attempts at preparing single crystals for X-ray crystallography have thus far failed to yield suitable material. Additionally, mass spectrometric analysis (ESI-TOFMS, 160.0 V cone voltage) did indicate high molecular weight species (highest observed = 2383.1423 amu) but failed to uncover a mass corresponding to $[(CO)_4Mo(CNAr^{Dipp2})_2]_2$. This may be due to the high cone voltage employed in the experiment. Nonetheless, from the spectroscopic data it is likely that $[(CO)_4Mo(CNAr^{Dipp2})_2]_2$ is the generated species.

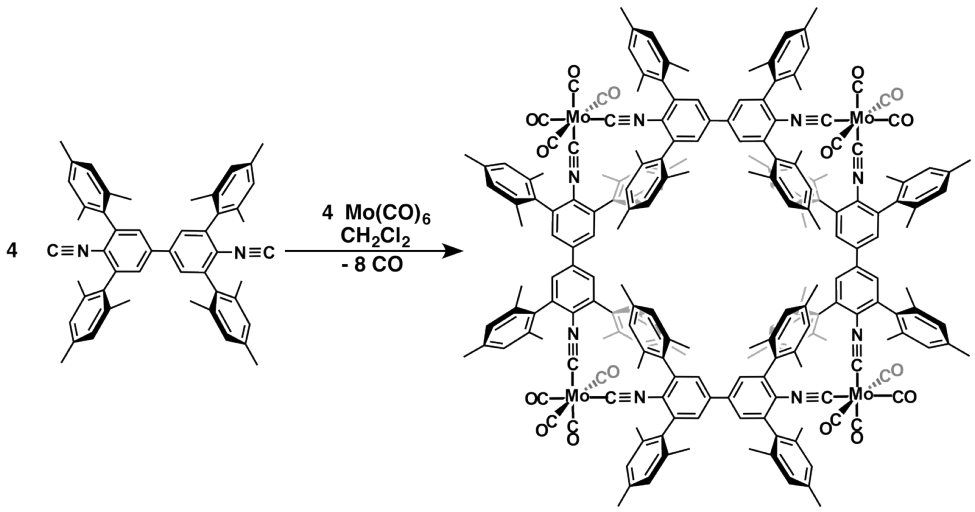

Scheme 6.5. Formation of the tetranuclear complex $[(CO)_4Mo(CNAr^{Mes2})_2]_4$.

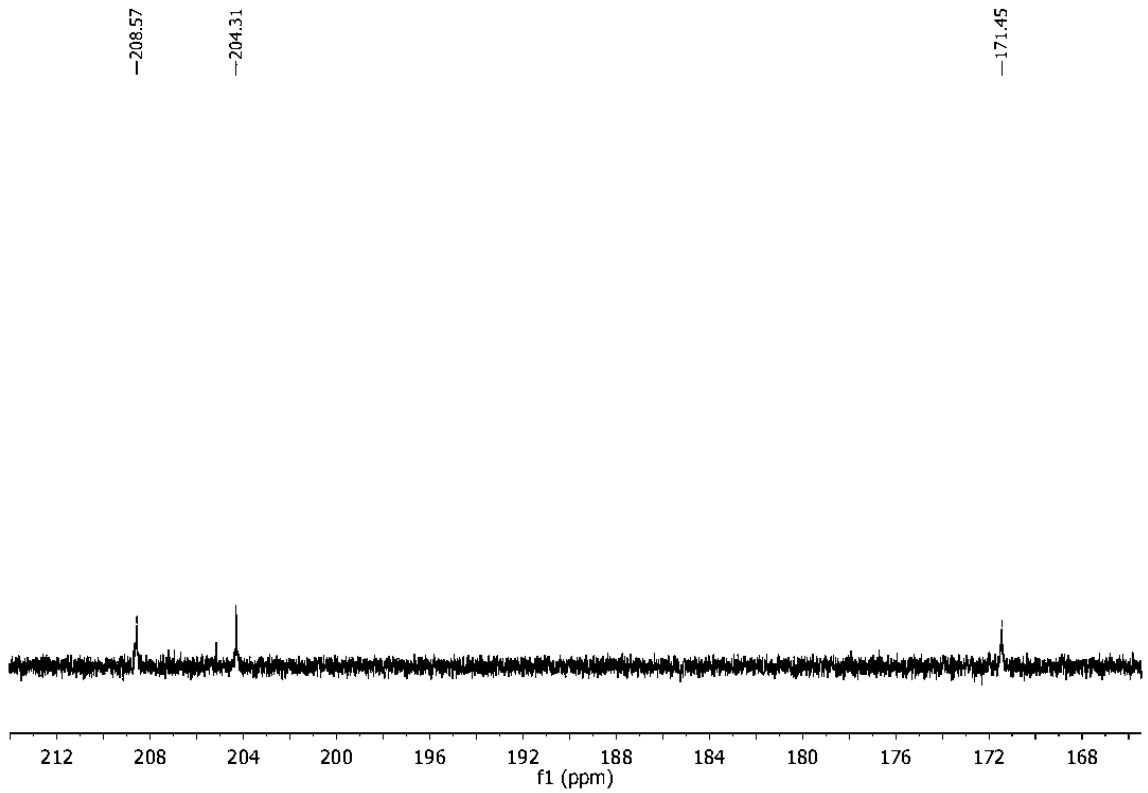

Figure 6.7. Downfield region of the $^{13}C\{^{1}H\}$ NMR spectrum of $[(CO)_4Mo(CNAr^{Mes2})_2]_4$.

As isocyanide ligation increases at the Mo center in moving from $[(CO)_4MoCNAr^{Dipp2}]_2$ to $[(CO)_4Mo(CNAr^{Dipp2})_2]_2$, it was observed that the solution color became increasingly reddened. As shown in Figure 6.8, UV-Vis spectra acquired from a C_6H_6 solution of $[(CO)_4MoCNAr^{Dipp2}]_2$ displayed three bands at λ = 287, 326 and 380 nm. The high-energy bands likely originate from the aromatic backbone of $[CNAr^{Mes2}]_2$, and obscure the observation of the L→M charge-transfer band observed for similar mononuclear species.[34] However, upon formation of $[(CO)_4Mo(CNAr^{Dipp2})_2]_2$ the low-energy band shifts to λ_{max} = 430 nm as a result of diminished energy spacing between the HOMO and LUMO d-orbitals. Interestingly, continued stirring of $[(CO)_4Mo(CNAr^{Dipp2})_2]_2$ in C_6H_6 gives rise to a deep-red solution

which is strongly fluorescent under ultraviolet irradiation (λ_{max} = 624 cm^{-1}) (Figure 6.9). ^{1}H NMR analysis of this mixture reveals $[(CO)_4Mo(CNAr^{Dipp2})_2]_2$ to be the dominant product, but additional peaks arising from $[CNAr^{Mes2}]_2$ are observed indicating a new product is being formed. Two new low-energy bands are also observed at λ_{max} = 497 and 555 nm, suggesting the formation of a Mo complex with higher isocyanide ligation. Notably, dissolution of this decomposition product into coordinating solvents, such as THF, MeCN or pyridine, completely quenches the observed fluorescence. It is also important to note that none of the previously surveyed Mo carbonyl/isocyanides in our laboratory have exhibited any observable fluorescence.[30, 35-36]

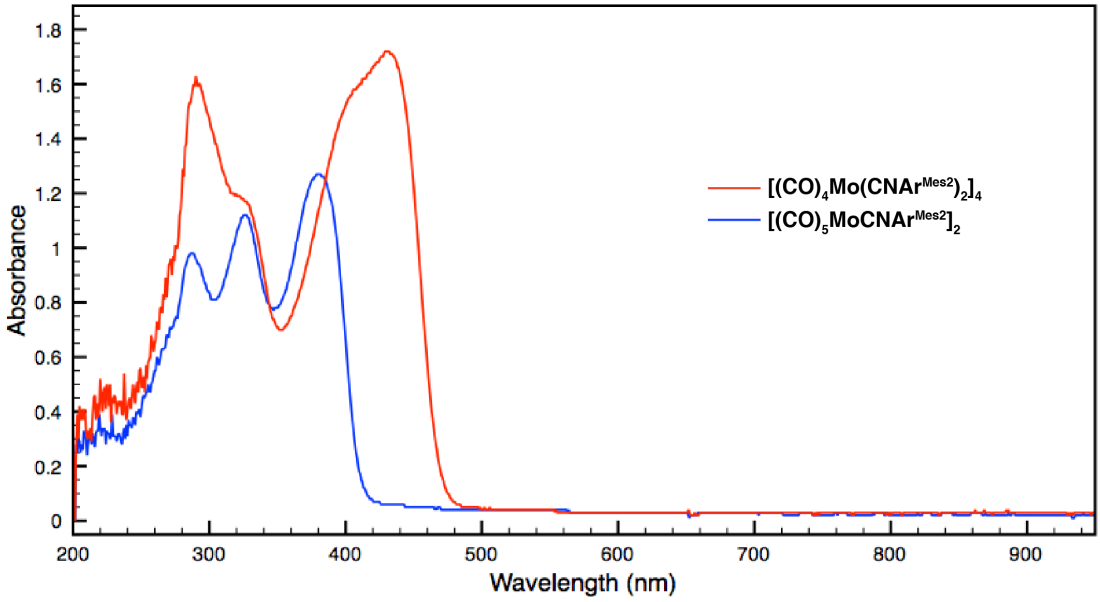

Figure 6.8. UV-Vis spectra (C_6H_6, 20 °C) of $[(CO)_5MoCNAr^{Dipp2}]_2$ (blue) and $[(CO)_4Mo(CNAr^{Dipp2})_2]_2$ (red).

Attempts to isolate and characterize this new complex have to date been unsuccessful. There exist two possibilities for the decomposition of

$[(CO)_4Mo(CNAr^{Dipp2})_2]_2$. The first involves the well-documented ability of *cis*-$Mo(CO)_4L_2$ derivatives to isomerize to the corresponding *trans*-isomer.[37] This would result in the producton of a linear, 1-D coordination polymer with a [*trans*-$Mo(CO)_4(CNAr^{Mes2})_2$] repeating unit. If this process is slow, however, then a congested ^1H NMR spectrum would be expected; this is consistent with experimental observation. The second possibility involves dissociation of CO from the $[Mo(CO)_4]$ node, followed by re-assembly of the complex to form a cubic structure with [*fac*-$Mo(CO)_3$] vertices. This reaction progression is also consistent with previous studies of Mo mixed carbonyl/isocyanides.[34] In attempt to corroborate this possibility, 2 equiv $[CNAr^{Mes2}]_2$ was added to 3 equiv $Mo(CO)_3(\eta^6\text{-}C_6H_6)$ (the molar equivalents for the formation of an octanuclear cube) in THF and stirred at room temperature, forming a deep red solution that exhibited similar optical properties as that of the decomposition product from $[(CO)_4Mo(CNAr^{Dipp2})_2]_2$. Notably, ^1H NMR analysis of this mixture showed nearly identical properties to that of the $[(CO)_4Mo(CNAr^{Dipp2})_2]_2$ decomposition. We therefore tentatively assign this new species as a cubic, octanuclear Mo_8 supramolecular complex. Future work will be aimed towards new synthetic routes that enable complete formation of this fluorescent complex.

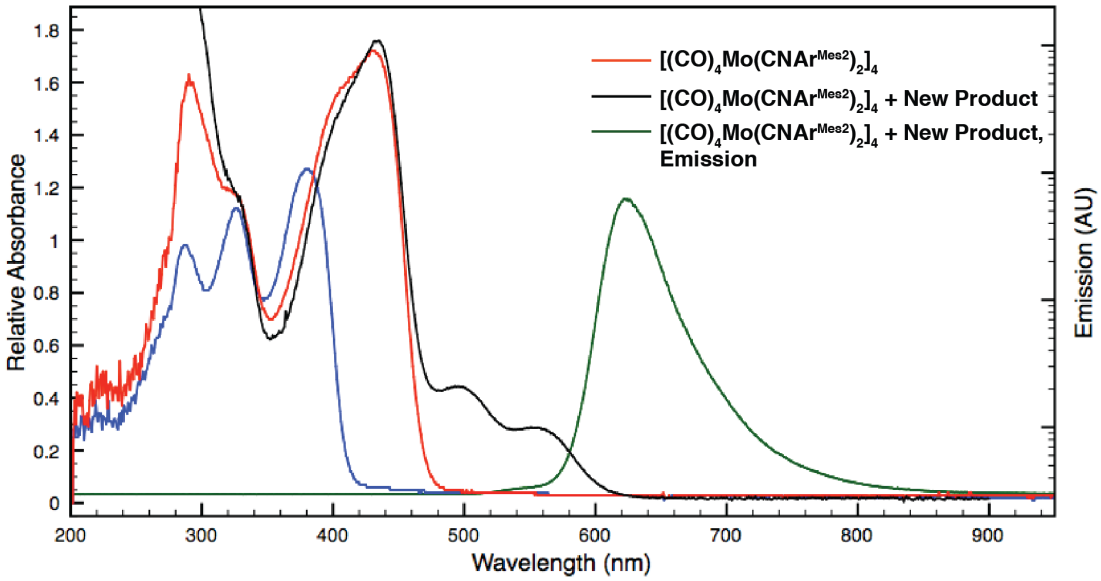

Figure 6.9. UV-Vis spectra (C_6H_6, 20 ˚C) of $[(CO)_4Mo(CNAr^{Dipp2})_2]_2$ (red) and its decomposition product (black). The emission spectrum for the decomposition product is displayed in green. It is important to note that all values spectra are relative in intensity.

6.3 Development of Additional Ditopic and Tritopic *m*-Terphenyl Isocyanide Ligands

While $[CNAr^{Mes2}]_2$ has enabled a satisfactory preliminary examination of the available framework architectures to a sterically encumbering linear diisocyanide, it was quickly rationalized that a longer linker length would be necessary to create materials with high porosity. This is due to the fact that although the *m*-terphenyl groups are effective towards determining metal node coordination number and geometry, the free space they simultaneously occupy negatively affects the material surface area. Accordingly, new multitopic ligands were synthesized that borrowed the design elements of $[CNAr^{Mes2}]_2$, while enabling much greater metal-metal spacing as well as higher dimensionality in framework materials. Importantly, it was found that the synthetic methodology utilized in the preparation of $[CNAr^{Mes2}]_2$ could be easily

transferred to the synthesis of these new ligands, and signified that many new ligands employing a *m*-terphenyl isocyanide binding group could be prepared.

The critical step to preparing the ditopic isocyanide $[CNAr^{Mes2}]_2$ laid in the Suzuki coupling of H_2NAr^{Mes2}-Br and H_2NAr^{Mes2}-BPin to form the dianiline $[H_2NAr^{Mes2}]_2$.[21] Accordingly, under these conditions any combination of aryl dibromide with $H_2N(p\text{-(BPin)}Ar^{Mes2})$, or conversely, aryl diboronic acid with $H_2N(p\text{-BrAr}^{Mes2})$, could be imagined to provide the corresponding dianiline. Indeed, it was found the coupling conditions for the formation of $[H_2NAr^{Mes2}]_2$ could be used in preparing *p*-QTPh-$[H_2NAr^{Mes2}]_2$ (*p*-QTPH = *para*-quaterphenyl) from 4,4'-dibromobiphenyl and $H_2N(p\text{-(BPin)}Ar^{Mes2})$ in 78% yield (Scheme 6.6). Once in hand, *p*-QTPh-$[H_2NAr^{Mes2}]_2$ could be readily converted to the diisocyanide *p*-QTPh-$[CNAr^{Mes2}]_2$ via formylation of the aniline followed by dehydration with $POCl_3$. The diisocyanide *p*-QTPh-$[CNAr^{Mes2}]_2$ exhibits identical spectroscopic signatures as $CNAr^{Mes2}$ and $[CNAr^{Mes2}]_2$ for the isocyanide moiety,

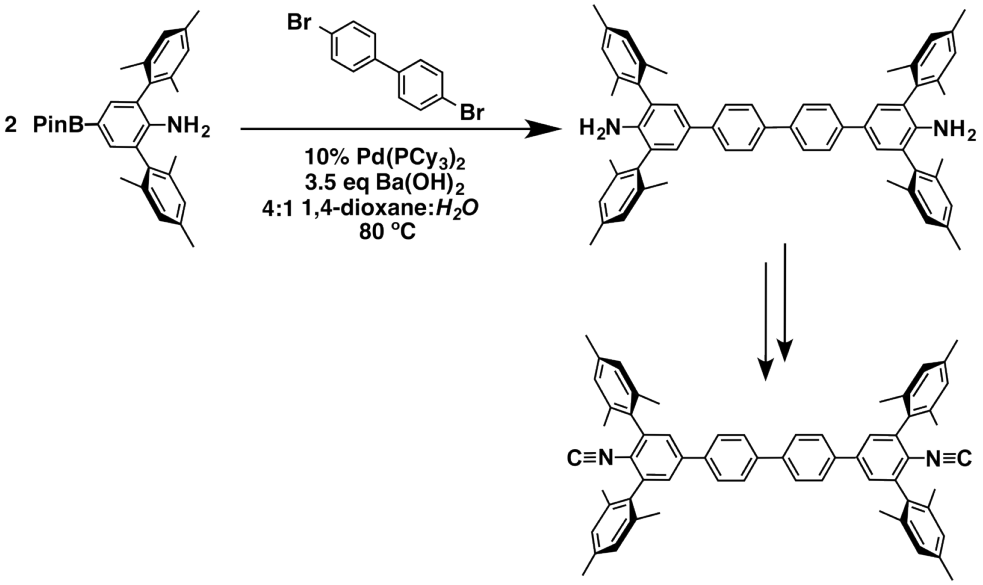

Scheme 6.6. Preparation of *p*-QTPh-$[CNAr^{Mes2}]_2$ from $H_2N(p\text{-(BPin)}Ar^{Mes2})$ and 4,4'-dibromobiphenyl, with the last two steps consisting of formylation followed by dehydration abbreviated.

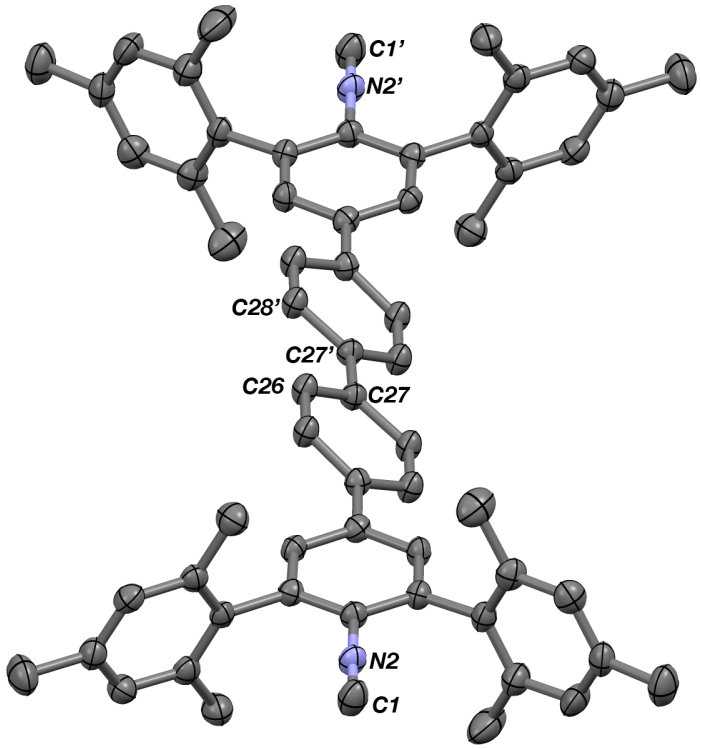

Figure 6.10. Molecular structure of *p*-QTPh-[CNAr^{Mes2}]$_2$. Selected dihedral angles (°), bond angles (°) and distances (Å): C1-C1' = 20.740(3); C1-N2 = 1.146(3).

with ν_{CN} = 2118 cm^{-1} (C_6D_6) and $^{13}C\{^1H\}$ (CNR) = 167.7 ppm ($CDCl_3$). The solid state structure of *p*-QTPh-[CNAr^{Mes2}]$_2$ reveals the C_{iso}-C_{iso} interatomic distance to be 20.740(3) Å, significantly longer than that of [CNAr^{Mes2}]$_2$, thus portending *p*-QTPh-[CNAr^{Mes2}]$_2$ to be a particularly effective ligand in generating high-porosity frameworks with low-coordinate metal nodes.

Encouraged by this result, we next moved to the development of a tritopic isocyanide which incorporated *m*-terphenyl groups. Coupling of H_2N(*p*-(BPin)Ar^{Mes2}) and 1,3,5-(4-bromophenyl)benzene in a 3-to-1 mixture readily afforded the trianiline 1,3,5-(H_2NAr^{Mes2})$_3$-triphenylbenzene in 47% yield (Scheme 6.7). Formylation with formyl acetic anhydride, followed by dehydration with $POCl_3$, provided 1,3,5-(CNAr^{Mes2})$_3$-triphenylbenzene as a light yellow solid. Both the infrared and ^{13}C NMR

signatures for the isocyanide compared well with $CNAr^{Mes2}$ and $[CNAr^{Mes2}]_2$, indicating a similar electronic profile for the isocyano group. Although a definite structural data has not yet been attained, the combined infrared, NMR, and mass spectrometric analysis of 1,3,5-$(CNAr^{Mes2})_3$-triphenylbenzene confirm its preparation. Accordingly, it is expected that the use of 1,3,5-$(CNAr^{Mes2})_3$-triphenylbenzene in framework preparation will provide new topologies on account of the tridentate binding capability.

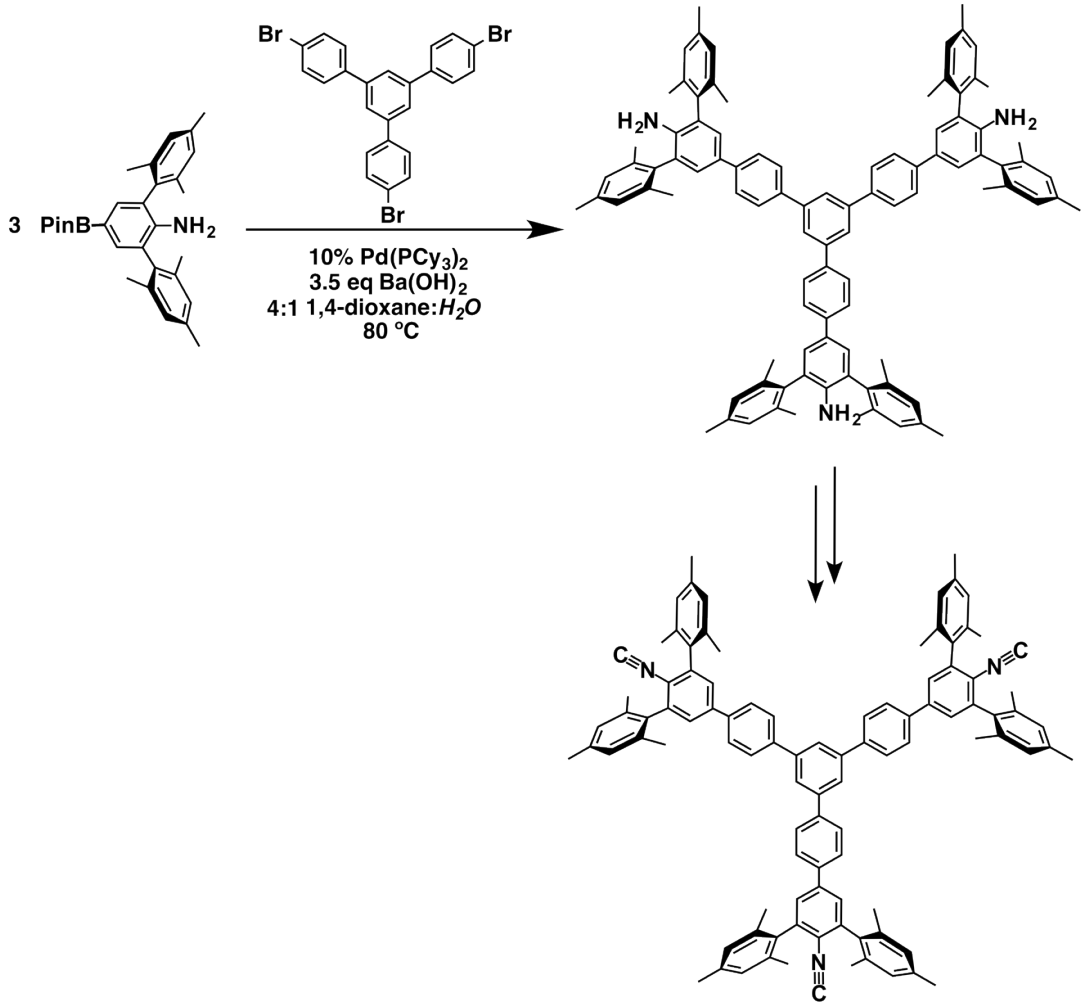

Scheme 6.7. Preparation of 1,3,5-$(CNAr^{Mes2})_3$-triphenylbenzene from $H_2N(p\text{-}(BPin)Ar^{Mes2})$ and 1,3,5-tris(4-bromophenyl)benzene, with the last two steps consisting of formylation followed by dehydration abbreviated.

6.4 Concluding Remarks

The preparation of several dinuclear metal species linked by $[CNAr^{Mes2}]_2$, as well as the first cobalt oligomer formed with $[CNAr^{Mes2}]_2$, is described. The dinuclear complexes hold promise for subsequent functionalization into interesting supramolecular compounds, as suggested by the observed degradation of $[(CO)_4Mo(CNAr^{Dipp2})_2]_2$. Additionally, two new multitopic isocyanides that incorporate bulky *m*-terphenyl groups are reported, which promise to provide new, highly tailored materials that incorporate the design principles described here and in Chapters 5 & 7. These results will therefore provide an excellent strating point for future investigations into the supramolecular chemistry of low-valent metal ions linked by *m*-terphenyl multitopic isocyanides.

6.5 Synthetic Procedures and Characterization Data

General Considerations.

All manipulations were performed under an atmosphere of dry dinitrogen using standard Schlenk and glovebox techniques, unless otherwise stated. Solvents were dried and degassed according to standard procedures. Reagent grade starting materials were purchased from commercial sources and used without further purification, unless otherwise stated. The isocyanide ligand $[CNAr^{Mes2}]_2$, $H_2N(p\text{-}BrAr^{Mes2})$ and $H_2N(p\text{-}(BPin)Ar^{Mes2})$ were prepared according to literature procedures.[21] Benzene-d_6 (Cambridge Isotope Laboratories) was stirred over NaK for two days, distilled, degassed, and stored over 4 Å molecular sieves; $CDCl_3$ was

degassed via four freeze-pump-thaw cycles, and stored over 3 Å molecular sieves for at least one day prior to use.

Solution ^{1}H and ^{13}C NMR were recorded on a Bruker 300 spectrometer, a Varian 400 spectrometer, a Varian X-Sens 500 spectrometer, or a JEOL ECA-500 spectrometer. ^{1}H and ^{13}C NMR chemical shifts are reported in ppm relative to $SiMe_4$ (^{1}H and ^{13}C δ = 0.0 ppm) with reference to residual proton resonances of 7.16 ppm (^{1}H) and 128.06 ppm (^{13}C) for benzene-d_6 and $CDCl_3$.[38] Room temperature FTIR spectra were recorded on a Thermo-Nicolet iS10 FTIR spectrometer. Samples were prepared as benzene-d_6 or $CDCl_3$ solutions injected into a ThermoFisher solution cell equipped with KBr windows. Solvent peaks were digitally subtracted from all solution FTIR spectra using a previously recorded spectrum of the solvent. UV-VIS absorption spectra were collected using an Ocean Optics UV-Vis-NIR spectrometer with a deuterium light source. Emission spectra were collected on the same instrument with UV irradiation from an Ocean Optics DT-MINI-2-GS light source (λ = 365 nm). Combustion analyses were performed by Robertson Microlit Laboratories of Madison, New Jersey (USA) and Midwest Microlabs of Indianapolis, Indiana. HR-MS was recorded at the UCSD Molecular Mass Spectrometry Facility using an Agilent 6230 Accurate-Mass TOFMS with acetonitrile as the eluent.

Synthesis of $[(CO)_4FeCNAr^{Mes2}]_2$. To a stirring benzene solution of $Fe(CO)_5$ (0.005 g, 0.026 mmol, 2 ml) was added a benzene solution of $[CNAr^{Mes2}]_2$ (0.009 g, 0.0134, 0.5 equiv., 1 ml). The resultant solution was allowed to stir for 2 h, during which time the color became deep yellow. Thereafter, all volatiles were removed under reduced

pressure to provide a yellow solid. Yield: 0.016 g, 93%. Single crystals were grown from a concentrated THF solution stored at –40 ˚C overnight. ^{1}H NMR (500.1 MHz, C_6D_6, 20 ºC) δ = 7.53 (s, 4H, *m*-Ar), 6.92 (s, 8H, *m*-Mes), 2.21 (s, 12H, *p*-C*H*$_3$), 2.01 (s, 24H, *m*-C*H*$_3$) ppm. ^{13}C{^{1}H} NMR (125.7 MHz, C_6D_6, 20 ºC) δ = 212.6 (CO), 212.4 (CO), 172.9 (CNR), 152.2, 140.2, 139.5, 138.9, 135.7, 133.5, 129.1, 128.4, 127.3, 21.1 (*p*-CH_3), 20.3 (*m*-CH_3) ppm. FTIR (C_6D_6, KBr windows): ν_{CN} = 2157 cm^{-1} (m), $\nu_{CO/CN}$ = 2048 cm^{-1} (s), 1994 cm^{-1} (m), 1967 cm^{-1} (vs), also 2973, 2919, 2861, 1612, 1380, 1118, 883, 852, 813, 628 cm^{-1}. A satisfactory combustion analysis for this compound has not been obtained.

Synthesis of [(CO)$_5$Cr[CNAr^{Mes2}]$_2$. A 50 ml resealable ampoule was charged with 0.018 g $Cr(CO)_6$ dissolved in 10 ml THF. The solution was then subjected to three freeze-pump-thaw cycles, after which it was irradiated for 2 h using a mercury arc lamp (Oriel Corporation, Model 66023, 1000 W). Following this, the now light-yellow solution was brought into a glovebox, and treated with a THF solution of [CNAr^{Mes2}]$_2$ (0.022 g, 0.032 mmol, 1 ml), causing the solution to become a deeper yellow. This solution was stirred for 1.5 h, after which all volatiles were removed under reduced pressure. Unreacted $Cr(CO)_6$ was recovered from this solid by sublimation (50 mTorr, 40 ˚C). Dissolution of the remaining solid with THF, followed by cooling to –40 ˚C over 1 day, provided light yellow single crystals. Yield: 0.019 g, 83%. ^{1}H NMR (500.1 MHz, C_6D_6, 20 ºC) δ = 7.52 (s, 4H, *m*-Ar), 6.92 (s, 8H, *m*-Mes), 2.22 (s, 12H, *p*-C*H*$_3$), 2.00 (s, 24H, *m*-C*H*$_3$) ppm. ^{13}C{^{1}H} NMR (125.7 MHz, C_6D_6, 20 ºC) δ = 216.7 (CO), 214.2 (CO), 175.7 (CNR), 140.9, 139.3,

138.9, 135.6, 133.7, 129.1, 128.6, 128.3, 127.1, 21.1 (*p*-CH_3), 20.3 (*m*-CH_3) ppm. FTIR (C_6D_6, KBr windows): ν_{CN} = 2136 cm^{-1} (m), $\nu_{CO/CN}$ = 2050 cm^{-1} (s), 1997 cm^{-1} (vw), 1959 cm^{-1} (vs), also 2975, 2921, 2860, 1448, 669, 657 cm^{-1}. A satisfactory combustion analysis for this compound has not been obtained.

Synthesis of [PdCl(η^3-allyl)CNAr^{Mes2}]$_2$. To a stirring solution of [PdCl(C_3H_5)]$_2$ in THF (0.021 g, 0.057 mmol, 4 ml) was added a THF solution of [CNAr^{Mes2}]$_2$ (0.039 g, 0.057 mmol, 1 equiv., 1 ml). The solution was stirred for 30 min., during which time the color became light yellow. The solution was then filtered through a fiberglass plug, and all volatiles were removed *en vacuo* to provide a yellow solid. Yield: 0.059 g, 99%. Crystals suitable for X-ray analysis were prepared in a saturated THF solution stored at – 40 ˚C overnight. ^{1}H NMR (500.1 MHz, C_6D_6, 20 ºC) δ = 7.56 (s, 4H, *m*-Ar), 6.91 (s, 8H, *m*-Mes), 2.98 (m, 2H, *CH* allyl), 2.64 (d, J = 8 Hz, 4H, CH_2 allyl), 2.15 (s, 12H, *p*-CH_3), 2.11 (s, 24H, *m*-CH_3) ppm. The second CH_2 allyl resonance could not be identified. ^{13}C{^{1}H} NMR (125.7 MHz, C_6D_6, 20 ºC) δ = 152.4 (*C*NR), 141.4, 140.0, 138.8, 136.0, 133.3, 129.2, 126.8, 116.6, 73.5, 57.1, 21.2 (*p*-CH_3), 20.5 (*m*-CH_3) ppm. FTIR (C_6D_6, KBr windows): ν_{CN} = 2171 cm^{-1} (s), 2113 cm^{-1} (m), also 2918, 2853, 1613, 1572, 1443, 1373, 1289, 1193, 1068, 883, 852 cm^{-1}. A satisfactory combustion analysis for this compound has not been obtained.

Synthesis of [(CO)$_5$MoCNAr^{Mes2}]$_2$. A THF solution of $Mo(CO)_6$ (0.012 g, 0.046 mmol, 2 ml) was treated with a THF solution of [CNAr^{Mes2}]$_2$ (0.016 g, 0.023 mmol, 0.5 equiv., 1 ml) and allowed to stir for 30 min *in the dark*. During this time the solution

became light yellow. Thereafter, all volatiles were removed under reduced pressure to provide a light yellow solid. Recrystallization from a concentrated THF solution stored at –40 ˚C for 2 days provided light yellow single crystals suitable for X-ray diffraction. Yield: 0.012 g, 63%. ^{1}H NMR (500.1 MHz, C_6D_6, 20 ºC) δ = 7.51 (s, 4H, *m*-Ar), 6.92 (s, 8H, *m*-Mes), 2.22 (s, 12H, *p*-C*H*$_3$), 1.99 (s, 24H, *m*-C*H*$_3$) ppm. ^{13}C{^{1}H} NMR (125.7 MHz, C_6D_6, 20 ºC) δ = 206.4 (CO), 203.2 (CO), 166.7 (CNR), 141.0, 139.4, 138.9, 135.6, 133.6, 129.1, 128.3, 127.2, 21.1 (*p*-CH_3), 20.3 (*m*-CH_3) ppm. FTIR (C_6D_6, KBr windows): ν_{CN} = 2136 cm^{-1} (m), $\nu_{CO/CN}$ = 2053 cm^{-1} (s), 1958 cm^{-1} (vs), also 2920, 2860, 1613, 1417, 1378, 1331, 1032, 883, 852, 597, 558 cm^{-1}. A satisfactory combustion analysis for this compound has not been obtained.

Synthesis of [(CO)$_4$Mo(CNAr^{Mes2})$_2$]$_4$. To a stirring CH_2Cl_2 solution of $Mo(CO)_6$ (0.009 g, 0.036 mmol, 2 ml) was added a CH_2Cl_2 solution of [CNAr^{Mes2}]$_2$ (0.024 g, 1 equiv. 1 ml). The combined solution was allowed to stir for 4 h, during which time the color became orange. All volatiles were then removed under reduced pressure to provide a yellow/orange solid. Yield: 0.017 g, 91%. ^{1}H NMR (500.1 MHz, C_6D_6, 20 ºC) δ = 7.55 (s, 4H, *m*-Ar), 6.95 (s, 8H, *m*-Mes), 2.31 (s, 12H, *p*-C*H*$_3$), 2.03 (s, 24H, *m*-C*H*$_3$) ppm. ^{13}C{^{1}H} NMR (125.7 MHz, C_6D_6, 20 ºC) δ = 208.6 (CO), 204.3 (CO), 171.5 (CNR), 140.5, 138.7, 138.2, 135.6, 134.1, 129.1, 128.6, 127.6, 127,4, 21.4 (*p*-CH_3), 20.4 (*m*-CH_3) ppm. FTIR (C_6D_6, KBr windows): ν_{CN} = 2133 cm^{-1} (w), $\nu_{CO/CN}$ = 2065 cm^{-1} (m), 2011 cm^{-1} (m), 1944 cm^{-1} (vs), 1922 cm^{-1} (s), also 2919, 2859, 1613, 1480, 1441, 1417, 1377, 1032, 882, 851, 589 cm^{-1}. A satisfactory combustion analysis for this compound has not been obtained.

Generation of Fluorescent Mo Complex

A) from $[(CO)_4Mo(CNAr^{Mes2})_2]_4$. A CH_2Cl_2 solution of $[(CO)_4Mo(CNAr^{Mes2})_2]_4$ was allowed to stir for 24 h at ambient temperature and lighting. During this time the solution color became deep red, and a noticeable fluorescence became apparent. ^1H NMR analysis of this mixture in C_6D_6 indicated that an additional complex had formed, although $[(CO)_4Mo(CNAr^{Mes2})_2]_4$ was still the dominant product.

B) from $Mo(CO)_3(\eta^6\text{-}C_6H_6)$ and $[CNAr^{Mes2}]_2$. To a benzene solution of $Mo(CO)_3(\eta^6\text{-}C_6H_6)$ (0.004 g, 0.015 mmol, 2 ml, 2 equiv) was added a solution of $[CNAr^{Mes2}]_2$ (0.015, 0.022 mmol, 2 ml, 3 equiv), causing an immediate color change to yellow. The solution was allowed to stir for 2 h, during which time the color became deep red and was noticeably fluorescent. ^1H NMR analysis of this mixture in C_6D_6 indicated formation of $[(CO)_4Mo(CNAr^{Mes2})_2]_4$ as well as a second product. The resonances resulting from this second product matched those found from (**A**).

Synthesis of Co-^{ISO}CN-1. To a stirring THF solution of $CoCl_2$ (0.035 g, 0.269 mmol, 2 ml, 3 equiv) in a 15 ml glass pressure tube was slowly added a THF solution of $[CNAr^{Mes2}]_2$ (0.061 g, 0.090 mmol, 2 ml) over the course of 5 min. The solution was then allowed to stir for 1 h, after which the stir bar was removed, the tube capped with a Teflon screw-cap, and the sealed tube placed in a 80 ˚C sand bath inside an oven. The tube was kept at this temperature for 24 h, after which it was allowed to slowly cool to RT over the course of 24 h. This resulted in the formation of brilliant blue

single crystals on the side of the tube, which were collected on a fine porosity frit and used for further analysis.

Ligand Syntheses.

Synthesis of *p*-QTPh-[H_2NAr^{Mes2}]$_2$. A resealable ampoule was charged with H_2N(*p*-$BPinAr^{Mes2}$) (0.141 g, 0.310 mmol), 4,4'-dibromobiphenyl (0.048 g, 0.155 mmol), Pd_2dba_3 (0.009 g, 0.016 mmol, 10 mol %, dba = dibenzylideneacetone), PCy_3 (0.009 g, 0.032 mmol, 20 mol %), and $Ba(OH)_2$ (0.093 g, 0.544 mmol, 3.5 eq.) and dioxane (3 ml). To this was added degassed, deionized H_2O (1.5 ml), and the mixture was vigorously stirred at 80 ˚C for 16 h under an atmosphere of N_2. The mixture was cooled, filtered through a medium porosity fritted funnel packed with Celite, and the filter cake was extracted with CH_2Cl_2 (3 x 15 ml). The mixture was stripped of volatiles under reduced pressure, providing a brown residue. The residue was dissolved in 50 ml CH_2Cl_2 and washed with H_2O (25 ml, pH ≈ 6, acidified with 1.0 M HCl), H_2O (50 ml, neutral pH), and brine (50 ml). The aqueous washes were then combined and extracted with CH_2Cl_2 (3 x 50 ml). The organic extracts were combined, dried over $MgSO_4$, filtered, and volatiles were removed by rotary evaporation. The resultant solid was purified by column chromatography (silica gel) using a gradient of 0 to 2% EtOAc/hexanes, collecting the middle fractions. The fractions were combined and concentrated under reduced pressure to provide *p*-QTPh-[H_2NAr^{Mes2}]$_2$ as an off-white solid. Yield: 0.098 g, 78%. ^{1}H NMR (500.1 MHz, $CDCl_3$, 20 ºC) δ = 7.64 (s, 8H, biphenyl), 7.29 (s, 4H, *m*-Ar), 7.00 (s, 8H, *m*-Mes), 2.34 (s, 12H, *p*-C*H*$_3$), 2.11 (s, 24H, *m*-C*H*$_3$) ppm. ^{13}C{^{1}H} NMR (125.7 MHz, $CDCl_3$, 20 ºC) δ

= 139.8, 138.5, 137.3, 137.2, 135.2, 130.4, 128.6, 127.3, 127.1, 126.4, 126.5, 21.3 (*p*-CH_3), 20.4 (*m*-CH_3) ppm. FTIR ($CDCl_3$, KBr windows, 20 ºC): 3483 (w), 3382 (w), 2922 (m), 2856 (w), 1611 (w), 1448 (s), 1256 (w), 1016 (w), 855 (w), 655 (w) cm^{-1}. HR-MS (ESI-TOFMS): predicted for $[M+H]^+$ = $C_{60}H_{61}N$, 809.4829, found *m/z* = 809.4824.

Synthesis of *p*-QTPh-[HOC(O)NAr^{Mes2}]$_2$. Formic acid (0.071 g, 1.55 mmol, 10 eq.) was added dropwise via syringe to stirring acetic anhydride (0.079 g, 0.755 mmol, 5 eq.) in 2 ml THF. The mixture was warmed to 50 ˚C for 1 h to generate formyl acetic anhydride, cooled to RT, and transferred to a stirring THF solution of *p*-QTPh-[H_2NAr^{Mes2}]$_2$ (0.098 g, 0.155 mmol, 25 ml). This mixture was stirred for 16 h, after which all volatiles were removed by rotary evaporation. Excess formic acid and acetic acid are removed upon heating the mixture to 80 ºC for 2 h under dynamic vacuum. The resultant white solid, *p*-QTPh-[HOC(O)NAr^{Mes2}]$_2$, is used without further purification. Yield: 0.125 g, 99%. ^{1}H NMR (500.1 MHz, $CDCl_3$, 20 ºC) δ = 7.70 (s, 8H, biphenyl), 7.67 (d, 2H, J = 11 Hz, *H*C(O)NH), 7.47 (s, 4H, *m*-Ar), 6.99 (s, 8H, *m*-Mes), 6.86 (d, 2H, J = 11 Hz, *H*C(O)NH), 2.39 (s, 12H, *p*-C*H*$_3$), 2.08 (s, 24H, *m*-C*H*$_3$) ppm. FTIR (C_6D_6, KBr windows): ν_{NH} = 3360 cm^{-1} (w), ν_{CO} = 1682 cm^{-1} (s), also 3030, 2917, 2851, 1559, 1464, 1279, 900, 826, 793, 647 cm^{-1}.

Synthesis of *p*-QTPh-[CNAr^{Mes2}]$_2$. To a stirring CH_2Cl_2 solution of *p*-QTPh-[HOC(O)NAr^{Mes2}]$_2$ (0.126 g, 0.153 mmol, 25 ml) was added diisopropylamine (0.060 g, 0.612 mmol, 4 equiv.) via syringe. After stirring for 5 minutes, $POCl_3$ (0.057 g,

0.382 mmol, 2.5 equiv.) was added dropwise via syringe, and the solution was stirred for 5 hours. Aqueous Na_2CO_3 (1.5 M, 10 ml) was added, and the resulting mixture was stirred for 2 h. The organic and aqueous layers were then separated, and the organic layer was washed with 20 ml H_2O. The aqueous layers were combined and extracted with CH_2Cl_2 (3 X 20 ml). The organic extracts were combined, dried over $MgSO_4$, filtered, and volatiles were removed *in vacuo*. A minimal amount of MeCN was added to the resultant residue, which was then briefly heated to reflux followed by cooling to – 40 ˚C. The off-white solid was collected by filtration and dried under reduced pressure. Yield: 0.113 g, 89%. ^{1}H NMR (500.1 MHz, $CDCl_3$, 20 ºC) δ = 7.71 (s, 8H, biphenyl), 7.54 (s, 4H, *m*-Ar), 7.00 (s, 8H, *m*-Mes), 2.34 (s, 12H, *p*-C*H*$_3$), 2.10 (s, 24H, *m*-C*H*$_3$) ppm. ^{13}C{^{1}H} NMR (125.7 MHz, $CDCl_3$, 20 ºC) δ = 167.6 (CN), 141.5, 140.3, 140.1, 138.5, 138.1, 135.8, 134.3, 128.7, 127.8, 127.7, 127.6, 22.9 (*p*-CH_3), 20.4 (*m*-CH_3) ppm. FTIR ($CDCl_3$, KBr windows): ν_{CN} = 2117 cm^{-1} (s), 2957, 2922, 2859, 2733, 1613, 1593, 1438, 1378, 1004, 852, 825 cm^{-1}.

Synthesis of 1,3,5-(H_2NAr^{Mes2})$_3$-Triphenylbenzene. A resealable ampoule was charged with H_2N(*p*-$BPinAr^{Mes2}$) (0.83 g, 0.182 mmol, 3 equiv), 1,3,5-tris(*p*-bromophenyl)benzene (0.033 g, 0.061 mmol), Pd_2dba_3 (0.016 g, 0.009 mmol, 15 mol %, dba = dibenzylideneacetone), PCy_3 (0.016 g, 0.018 mmol, 30 mol %), and $Ba(OH)_2$ (0.109 g, 0.214 mmol, 3.5 eq.) and dioxane (5 ml). To this was added degassed, deionized H_2O (2 ml), and the mixture was vigorously stirred at 90 ˚C for 16 h under an atmosphere of N_2. The mixture was cooled, filtered through a medium porosity fritted funnel packed with Celite, and the filter cake was extracted with CH_2Cl_2 (3 x 20

ml). The mixture was stripped of volatiles under reduced pressure, providing a brown residue. The residue was dissolved in 50 ml CH_2Cl_2 and washed with H_2O (25 ml, pH ≈ 6, acidified with 1.0 M HCl), H_2O (50 ml, neutral pH), and brine (50 ml). The aqueous washes were then combined and extracted with CH_2Cl_2 (3 x 50 ml). The organic extracts were combined, dried over $MgSO_4$, filtered, and volatiles were removed by rotary evaporation. The resultant solid was purified by column chromatography (silica gel) using a gradient of 0 to 3% EtOAc/hexanes, collecting the middle fractions. The fractions were combined and concentrated under reduced pressure to provide 1,3,5-$(H_2NAr^{Mes2})_3$-triphenylbenzene as an light yellow solid. Yield: 0.061 g, 47%. ^{1}H NMR (500.1 MHz, $CDCl_3$, 20 ºC) δ = 7.80 (s, 3H, C_6H_3-), 7.71 (d, J = 6 Hz, 12H, -C_6H_4-), 7.31 (s, 6H, *m*-Ar), 7.00 (s, 12H, *m*-Mes), 3.26 (s, 6H, -NH_2), 2.34 (s, 18H, *p*-CH_3), 2.12 (s, 36H, *m*-CH_3) ppm. ^{13}C{^{1}H} NMR (125.7 MHz, $CDCl_3$, 20 ºC) δ = 142.2, 140.8, 140.4, 139.0, 137.3, 137.2, 135.4, 130.1, 128.7, 127.8, 127.2, 126.6, 126.5, 124.8, 22.9 (*p*-CH_3), 20.4 (*m*-CH_3) ppm. FTIR ($CDCl_3$, KBr windows): ν_{NH} = 3486 cm^{-1} (w), 3389 cm^{-1} (w), also 2957, 2921, 2851, 1711, 1458, 1224 cm^{-1}.

Synthesis of 1,3,5-$(HOC(O)NAr^{Mes2})_3$-Triphenylbenzene. Formic acid (0.049 g, 1.07 mmol, 20 eq.) was added dropwise via syringe to stirring acetic anhydride (0.109 g, 0.1.07 mmol, 20 eq.) in 2 ml THF. The mixture was warmed to 50 ˚C for 1 h to generate formyl acetic anhydride, cooled to RT, and transferred to a stirring THF solution of 1,3,5-$(H_2NAr^{Mes2})_3$-triphenylbenzene (0.069 g, 0.048 mmol, 15 ml). This mixture was stirred for 16 h, after which all volatiles were removed by rotary

evaporation. Excess formic acid and acetic acid are removed upon heating the mixture to 80 ºC for 2 h under dynamic vacuum. The resultant white solid, 1,3,5-(HOC(O)NAr^{Mes2})$_3$-triphenylbenzene, is used without further purification. Yield: 0.065 g, 99%. ^{1}H NMR (500.1 MHz, $CDCl_3$, 20 ºC) δ = 7.83 (s, 3H, C_6H_3-), 7.73 (d, J = 6 Hz, 12H, -C_6H_4-), 7.69 (d, 3H, J = 11 Hz, *H*C(O)NH), 7.49 (s, 6H, *m*-Ar), 7.00 (s, 12H, *m*-Mes), 6.65 (d, 3H, J = 11 Hz, *H*C(O)NH), 2.34 (s, 18H, *p*-C*H*$_3$), 2.09 (s, 36H, *m*-C*H*$_3$) ppm. ^{13}C{^{1}H} NMR (125.7 MHz, $CDCl_3$, 20 ºC) δ = 162.6 (H*C*(O)NH), 142.1, 140.4, 139.6, 139.1, 138.3, 137.9, 136.1, 134.6, 133.8, 131.9, 129.5, 129.2, 128.6, 128.03, 127.4, 125.2, 21.3 (*p*-CH_3), 20.7 (*m*-CH_3) ppm. FTIR ($CDCl_3$, KBr windows): ν_{NH} = 3360 cm^{-1} (w), ν_{CO} = 1683 cm^{-1} (s), also 2919, 2850, 1577, 1558, 1515, 1465, 1436, 1423, 1280, 1014, 975, 854, 833 cm^{-1}. HR-MS (ESI-TOFMS): predicted for $[M+H]^+ = C_{99}H_{94}N_3O_3$, 1372.7290, found *m/z* = 1372.7260.

Synthesis of 1,3,5-(CNAr^{Mes2})$_3$-Triphenylbenzene. To a stirring CH_2Cl_2 solution of 1,3,5-(HOC(O)NAr^{Mes2})$_3$-triphenylbenzene (0.065 g, 0.048 mmol, 15 ml) was added diisopropylamine (0.054 g, 0.535 mmol, 10 equiv.) via syringe. After stirring for 5 minutes, $POCl_3$ (0.032 g, 0.214 mmol, 4 equiv.) was added dropwise via syringe, and the solution was stirred for 5 hours. Aqueous Na_2CO_3 (1.5 M, 5 ml) was added, and the resulting mixture was stirred for 2 h. The organic and aqueous layers were then separated, and the organic layer was washed with 10 ml H_2O. The aqueous layers were combined and extracted with CH_2Cl_2 (3 X 20 ml). The organic extracts were combined, dried over $MgSO_4$, filtered, and volatiles were removed *in vacuo*. A minimal amount of MeCN was added to the resultant residue, which was then briefly

heated to reflux followed by cooling to – 40 ˚C. The light yellow solid was collected by filtration and dried under reduced pressure. Yield: 0.050 g, 80%. ^{1}H NMR (500.1 MHz, C_6D_6, 20 ºC) δ = 7.99 (s, 3H, C_6H_3-), 7.67 (d, J = 6 Hz, 12H, -C_6H_4-), 7.47 (s, 6H, *m*-Ar), 6.91 (s, 12H, *m*-Mes), 2.20 (s, 18H, *p*-CH_3), 2.16 (s, 36H, *m*-CH_3) ppm. $^{13}C\{^{1}H\}$ NMR (125.7 MHz, $CDCl_3$, 20 ºC) δ = 171.9 (*C*N), 143.1, 141.9, 141.7, 141.0, 139.2, 138.4, 138.3, 136.2, 136.1, 135.1, 129.3, 126.8, 21.6 (*p*-CH_3), 20.7 (*m*-CH_3) ppm. FTIR (C_6D_6, KBr windows): ν_{CN} = 2117 cm^{-1} (s), also 2973, 2933, 2854, 1620, 1596, 1456, 1263, 1218, 1162, 851, 833, 743 cm^{-1}. HR-MS (ESI-TOFMS): predicted for $[M+H]^+ = C_{99}H_{88}N_3$, 1318.6947, found *m/z* = 1318.6973.

6.6 Crystallographic Structure Determinations

General. Single crystal X-ray structure determinations were performed at low temperature on Bruker Kappa Diffractometers equipped with a Mo-Kα or Cu-Kα radiation source and a Bruker APEX or APEX-II area detector. All structures were solved *via* direct methods with SIR 2004 and refined by full-matrix least-squares procedures using SHELXL-2013. Crystallographic data collection and refinement information listed in Table 6.1 and 6.2.

Table 6.1. Crystallogrpahic Data Collection andRefinement Information.

Name	$[(CO)_4FeCNAr^{Mes2}]_2$	$[(CO)_5CrCNAr^{Mes2}]_2$	Co-^{ISO}CN-1·(THF)
Formula	$C_{29}H_{24}FeNO_4$	$C_{60}H_{48}Cr_2N_2O_{10}$	$C_{112}H_{121}CuF_6N_4O_3P$
Crystal System	Monoclinic	Orthorhombic	Monoclinic
Space Group	$P2_1/n$	$Pbca$	$C2/c$
a, Å	13.1377(5)	27.389(2)	21.0162(14)
b, Å	15.1289(5)	14.2241(11)	16.3599(10)
c, Å	13.1761(5)	28.569(2)	22.1931(16)
α, deg	90	90	90
β, deg	93.4350(10)	90	101.005(3)
γ, deg	90	90	90
V, Å^3	2614.16(16)	11130.2(15)	7490.2(9)
Z	4	8	4
Radiation (λ, Å)	Mo-Kα, 0.71073	Mo-Kα, 0.71073	Mo-Kα, 0.71073
ρ (calcd.), Mg/m^3	1.287	1.266	1.328
μ (Mo Ka), mm^{-1}	0.610	0.449	0.921
Temp, K	100	100	100
θ max, deg	25.439	25.415	25.695
data/parameters	4800/322	10245/670	7103/473
R_1	0.0506	0.0671	0.0556
wR_2	0.1432	0.1763	0.1271
GOF	1.043	1.028	1.023

Table 6.2. Crystallogrpahic Data Collection andRefinement Information.

Name	$[(CO)_5MoCNAr^{Mes2}]_2$·(FBz)	*p*-QTPh-$[CNAr^{Mes2}]_2$	$[Cl(\eta^3\text{-allyl})PdCNAr^{Mes2}]_2$
Formula	$C_{66}H_{53}FMo_2N_2O_{10}$	$C_{62}H_{56}N_2$	$C_{28}H_{29}ClNPd$
Crystal System	Triclinic	Trigonal	Monoclinic
Space Group	*P-1*	*R-3*	*C2/c*
a, Å	11.3365(7)	43.757(7)	24.8621(7)
b, Å	15.6222(9)	43.757(7)	15.0846(4)
c, Å	19.2269(10)	8.2370(14)	15.7427(4)
α, deg	91.145(2)	90	90
β, deg	92.767(2)	90	109.1530(10)
γ, deg	91.866(2)	120	90
V, $Å^3$	3398.5(3)	13658(5)	5577.2(3)
Z	2	9	8
Radiation (λ, Å)	Mo-Kα, 0.71073	Mo-Kα, 0.71073	Mo-Kα, 0.71073
ρ (calcd.), Mg/m^3	1.217	0.907	1.242
μ (Mo Ka), mm^{-1}	0.424	0.052	0.774
Temp, K	100	100	100
θ max, deg	24.745	23.529	24.736
data/parameters	11608/734	4481/290	4763/285
R_1	0.0418	0.0628	0.0462
wR_2	0.1021	0.1672	0.1083
GOF	1.052	1.035	1.042

6.7 Acknowledgements

Professor Michael Sailor, Nicole Chan, and Dr. Tushar Kumeria are thanked for their assistance with UV-Vis measurements, particularly with the design of the air-free system utilized in the described study.

6.8 Refererences

1. Cook, T. R.; Zheng, Y.-R.; Stang, P. J., *Chem. Rev. (Washington, DC, U. S.)* **2013,** *113*, 734-777.

2. Carlucci, L.; Ciani, G.; Proserpio, D. M., *Coord. Chem. Rev.* **2003,** *246*, 247-289.

3. Kitagawa, S.; Kitaura, R.; Noro, S.-i., *Angewandte Chemie International Edition* **2004,** *43*, 2334-2375.

4. Moulton, B.; Zaworotko, a. M. J., *Chem. Rev. (Washington, DC, U. S.)* **2001,** *101*, 1629-1658.

5. Yaghi, O. M.; O'Keeffe, M.; Ockwig, N. W.; Chae, H. K.; Eddaoudi, M.; Kim, J., *Nature* **2003,** *423*, 705-714.

6. Stang, P. J.; Olenyuk, B., *Acc. Chem. Res.* **1997,** *30*, 502-518.

7. Chakrabarty, R.; Mukherjee, P. S.; Stang, P. J., *Chem. Rev. (Washington, DC, U. S.)* **2011,** *111*, 6810-6918.

8. Fujita, M., *Chem. Soc. Rev.* **1998,** *27*, 417-425.

9. Fujita, D.; Ueda, Y.; Sato, S.; Mizuno, N.; Kumasaka, T.; Fujita, M., *Nature* **2016,** *540*, 563-566.

10. Cohen, S. M., *Chem. Rev. (Washington, DC, U. S.)* **2012,** *112*, 970-1000.

11. Yaghi, O. M.; Li, H.; Eddaoudi, M.; O'Keeffe, M., *Nature* **1999,** *402*, 276-279.

12. Long, J. R.; Yaghi, O. M., *Chem. Soc. Rev.* **2009,** *38*, 1213-1214.

13. Chen, T.-H.; Popov, I.; Kaveevivitchai, W.; Miljanić, O. Š., *Chem. Mater.* **2014,** *26*, 4322-4325.

14. Maher, T. R.; Meyers, J. J.; Spaeth, A. D.; Lemley, K. R.; Barybin, M. V., *Dalton Trans.* **2012,** *41*, 7845-7848.

15. Hahn, F. E., *Angewandte Chemie International Edition* **1993,** *32*, 650-665.

16. Tanase, T.; Goto, E.; Begum, R. A.; Hamaguchi, M.; Zhan, S.; Iida, M.; Sakai, K., *Organometallics* **2004,** *23*, 5975-5988.

17. Fournier, E.; Sicard, S.; Decken, A.; Harvey, P. D., *Inorg. Chem.* **2004,** *43*, 1491-1501.

18. Paek, J. H.; Song, K. H.; Jung, I.; Kang, S. O.; Ko, a. J., *Inorg. Chem.* **2007,** *46*, 2787-2796.

19. Rommel, J. S.; Weinrach, J. B.; Grubisha, D. S.; Bennett, D. W., *Inorg. Chem.* **1988,** *27*, 2945-2949.

20. Ko, C.-C.; Cheung, A. W.-Y.; Yiu, S.-M., *Polyhedron* **2015,** *86*, 17-23.

21. Agnew, D. W.; Gembicky, M.; Moore, C. E.; Rheingold, A. L.; Figueroa, J. S., *J. Am. Chem. Soc.* **2016,** *138*, 15138-15141.

22. Sarapu, A. C.; Fenske, R. F., *Inorg. Chem.* **1975,** *14*, 247-253.

23. Cotton, F. A.; Zingales, F., *J. Am. Chem. Soc.* **1961,** *83*, 351-355.

24. Mokhtarzadeh, C. C.; Margulieux, G. W.; Carpenter, A. E.; Weidemann, N.; Moore, C. E.; Rheingold, A. L.; Figueroa, J. S., *Inorg. Chem.* **2015,** *54*, 5579-5587.

25. Barnett, B. R.; Labios, L. A.; Stauber, J. M.; Moore, C. E.; Rheingold, A. L.; Figueroa, J. S., *Organometallics* **2017,** *36*, 944-954.

26. Roos, B. O.; Andersson, K.; Fülscher, M. P.; Malmqvist, P.-â.; Serrano-Andrés, L.; Pierloot, K.; Merchán, M., Multiconfigurational Perturbation Theory: Applications in Electronic Spectroscopy. In *Adv. Chem. Phys.*, John Wiley & Sons, Inc.: 1996; pp 219-331.

27. Carpenter, A. E.; Mokhtarzadeh, C. C.; Ripatti, D. S.; Havrylyuk, I.; Kamezawa, R.; Moore, C. E.; Rheingold, A. L.; Figueroa, J. S., *Inorg. Chem.* **2015,** *54*, 2936-2944.

28. Dickie, D. A.; Jennings, M. C.; Jenkins, H. A.; Clyburne, J. A. C., *Inorg. Chem.* **2005,** *44*, 828-830.

29. Dickie, D. A.; Schatte, G.; Jennings, M. C.; Jenkins, H. A.; Khoo, S. Y. L.; Clyburne, J. A. C., *Inorg. Chem.* **2006,** *45*, 1646-1655.

30. Ditri, T. B.; Fox, B. J.; Moore, C. E.; Rheingold, A. L.; Figueroa, J. S., *Inorg. Chem.* **2009,** *48*, 8362-8375.

31. Atwood, J. D.; Brown, T. L., *J. Am. Chem. Soc.* **1976,** *98*, 3160-3166.

32. Cohen, M. A.; Brown, T. L., *Inorg. Chem.* **1976,** *15*, 1417-1423.

33. Lichtenberger, D. L.; Brown, T. L., *J. Am. Chem. Soc.* **1978,** *100*, 366-373.

34. Connor, J. A.; Jones, E. M.; McEwen, G. K.; Lloyd, M. K.; McCleverty, J. A., *Journal of the Chemical Society, Dalton Transactions* **1972**, 1246.

35. Ditri, T. B.; Moore, C. E.; Rheingold, A. L.; Figueroa, J. S., *Inorg. Chem.* **2011,** *50*, 10448-10459.

36. Ditri, T. B.; Carpenter, A. E.; Ripatti, D. S.; Moore, C. E.; Rheingold, A. L.; Figueroa, J. S., *Inorg. Chem.* **2013,** *52*, 13216-13229.

37. Darensbourg, D. J.; Kump, R. L., *Inorg. Chem.* **1978,** *17*, 2680-2682.

38. Fulmer, G. R.; Miller, A. J. M.; Sherden, N. H.; Gottlieb, H. E.; Nudelman, A.; Stoltz, B. M.; Bercaw, J. E.; Goldberg, K. I., *Organometallics* **2010,** *29*, 2176-2179.

Chapter 7

Development of Multidimensional Coordination Polymers of Ni(0)

7.1 Introduction

The heart of coordination polymers and metal organic frameworks lies at the dynamism found in transition metal coordination chemistry. Manipulations at the atomic level have led to increasingly diverse and targeted materials for a range of applications. However, the current library of building materials used to construct multidimensional frameworks is largely reliant upon high valent metal ions that dictate not only the resulting framework architecture but to a large extent the properties available in these materials. In this report, we show that a coordination polymer with 16 e^- Ni(0) nodes is easily accessed using a linear ditopic isocyanide, and that this material displays robust thermal and aqueous stability. Importantly, by basing this polymer design on low-valent metal ions we observe capabilities not available to metal-organic hybrid materials comprised of high-valent metal ions. The chemistry described here, we believe, opens new routes to coordination polymers with unprecedented functionality.

7.2 A Redox-Active Coordination Polymer Derived from Tricoordinate Ni(0) Nodes

A key feature found in almost all coordination polymers reported to date has been the employment of high-valent metal ions for nodal formation, whether in the

traditional metal-oxide secondary building units (SBUs) of metal organic frameworks (MOFs)[1-2] or in the coordination complexes underpinning porous coordination polymers (PCPs).[3-4] Accordingly, a series of complimentary ligand types have been employed for network formation, including carboxylates, imidazolates, pyridines, and nitriles, which has resulted in an abundance of framework motifs.[5-6] While significant effort to modulate the properties of these ligands has been undertaken in the last 20 years, the consistent use of high-valent metal ions effectively restricts the potential of coordination polymers to address certain challenges in heterogeneous catalysis and gas separations.[7-10] Moreover, although the use of tailored ligands that allow the incorporation of low-valent, low-coordinate organometallic substrates has expanded the scope of applications, these specialized materials have in many cases been shown to be susceptible to metal leaching and low-stability.[11-13] To address this shortcoming, we have developed a coordination polymer system that utilizes substrate-accessible zerovalent metals at the nodal site.

Although nitriles and pyridines are neutral ligands, they offer poor stabilization to reduced metal centers on account of their inability to effectively π-backbond. Isocyanides, by comparison, are excellent ligands for reduced, electron-rich metal ions owing to their measurable π-acidity, and have found widespread use in studies of low-valent organometallic complexes of the transition metals.[14-24] Despite its prevalence as a stabilizing ligand for reduced mononuclear species, few examples exist in which multitopic isocyanides have been employed in the preparation of oligomeric, low-valent metal species.[25-29] Recently, we demonstrated that the linear diisocyanide $[CNAr^{Mes2}]_2$ ($[CNAr^{Mes2}]_2$ = 1,1'-biphenyl-4,4'diisocyano-3,3',5,5'-tetramesityl) was

amenable to the formation of 2D and 3D crystalline arrays consisting of Cu(I)-isocyanide nodes.[30] The inclusion of sterically encumbering *m*-terphenyl units facilitated predictive control over metal-node geometry and ligand coordination number, and was reminiscent of the solution-phase chemistry of the corresponding mononuclear Cu(I) isocyanide species previously investigated in our laboratory.[31] While these results established a rationale for the preparation of extended networks of coordinatively unsaturated metal sites, we were intrigued by the prospect of using low-valent transition metals at the nodal center to take advantage of the π-acidic diisocyanide ligand. Accordingly, our earlier studies[32-33] of isoelectronic, mononuclear Ni(0) isocyanides prompted us to examine the extension to low-valent metal ions in infinitely networked materials.

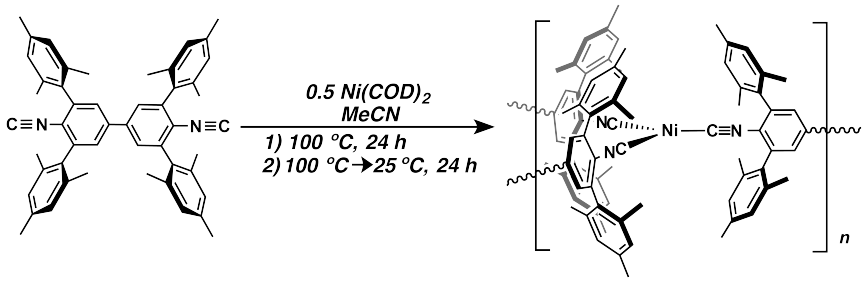

Scheme 7.1. Synthesis of Ni-^{ISO}CN-1.

Mixing acetonitrile solutions of $Ni(COD)_2$ (COD = 1,5-cyclooctadiene) and $[CNAr^{Mes2}]_2$ in a 1:2 ratio, followed by placement in a sealed tube in an oven at 100 °C for 2 days produces large, red/black single crystals of Ni-^{ISO}CN-1 (^{ISO}CN = isocyanide coordination network) that assume a parallelepiped morphology (Fig. 7.35 and 7.36). Structural analysis of Ni-^{iso}CN-1 by single crystal X-ray diffraction (SXRD) reveals the formation of a framework material (*P*-1 space group) composed of Ni(0) tris-isocyanide nodal sites. Surprisingly, these nodes ensemble to form infinite, 1-D

ladder-like polymers (Fig. 7.1) instead of a 2-D honeycomb lattice expected from trigonal planar metal geometries.[34] This framework architecture results in a local C_s symmetry for the Ni(0) tris-isocyanide metal centers, leading to three observed isocyanide bands ($\nu_{CN(symm)}$ = 2085 cm^{-1}; ν_{CN} = 1969 cm^{-1}; $\nu_{CN(assym)}$ = 1908 cm^{-1}) in the ATR-IR spectrum (Fig. 7.2). Powder X-ray diffraction (PXRD) analysis of Ni-^{iso}CN-1 (Fig. 7.10) shows the framework arrangement determined by SXRD to be representative of the bulk sample. This symmetry-breaking deviation from the expected geometry of homoleptic, tricoordinate Ni(0) is reinforced by the structural rigidity of the polymeric framework, which is a known but often unpredictable feature of many structurally inflexible coordination polymers. As expected of an extended multidimensional framework facilitated by π-π stacking and other weak electrostatic interactions of the *m*-terphenyl groups, the 3-D lattice of Ni-^{ISO}CN-1 is unstable towards vacuum desolvation, as indicated by PXRD of the material after removal of guest solvent molecules. Nonetheless, the unaffected IR spectrum of Ni-^{ISO}CN-1 after desolvation demonstrates retention of the covalent linkages forming the 1-D polymer chain.

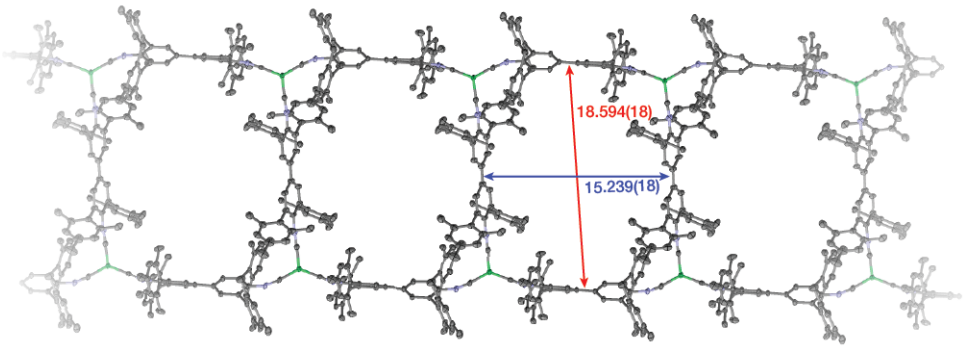

Figure 7.1. A linear strand of Ni-^{ISO}CN-1, showing the ladder-like topology.

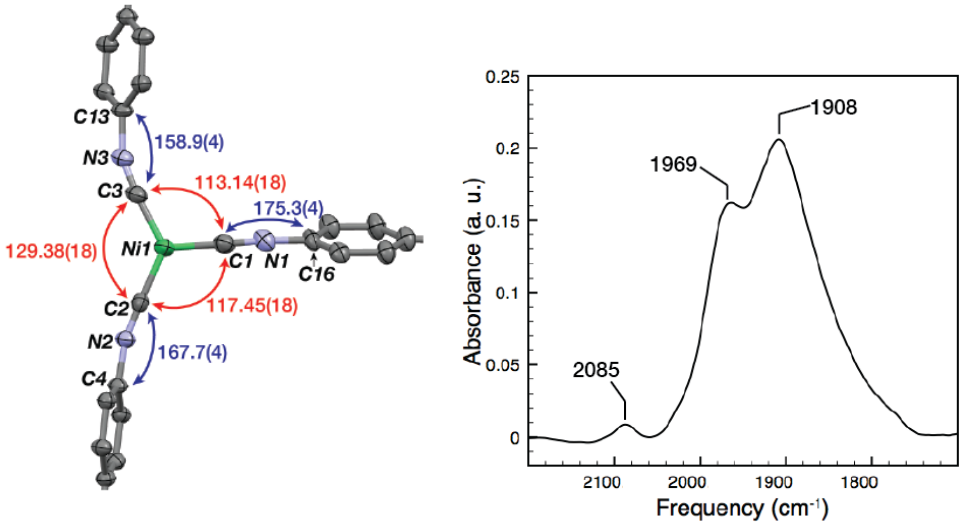

Figure 7.2. (*left*) the unusual C_s-symmetry about Ni enforced by the rigid framework of Ni-^{ISO}CN-1; (*right*) plot of the isocyanide region in the ATR-IR spectrum of Ni-^{ISO}CN-1.

While the IR frequency of ligated isocyanides can provide good evidence of metal oxidation state[35], Ni K-edge X-ray absorption spectra (XAS) studies were conducted to provide resolute proof of Ni(0) valency in Ni-^{ISO}CN-1 (Fig 7.3). We chose to use Ni(CNAr^{Mes2})$_3$ as a benchmark for oxidation state and ligand coordination number, as it provides a good molecular analogue to the node found in Ni-^{ISO}CN-1. Viewing the near-edge portion of the spectrum (XANES), a strong band originating from a Ni 1s → CNR π* metal-to-ligand charge transfer (MLCT) is observed for the d^{10} Ni(0) species and materials at *ca.* 8332.3 eV. Notably, the appearance of a second band corresponding to a 1s → 3d transition is absent from the spectra of Ni-^{ISO}CN-1, verifying Ni(0) valency. Comparison of the MLCT band of Ni(CNAr^{Mes2})$_3$ with Ni-^{ISO}CN-1 provides further confirmation of ligand coordination number. Importantly, the slight blue-shift (*ca.* 0.6 eV) of the MLCT band for Ni-^{iso}CN-1 is in agreement

with calculations on a C_s-symmetric Ni(CNAr^{Mes2})$_3$ model incorporating the small distortion from trigonal planar geometry observed for Ni-^{iso}CN-1.

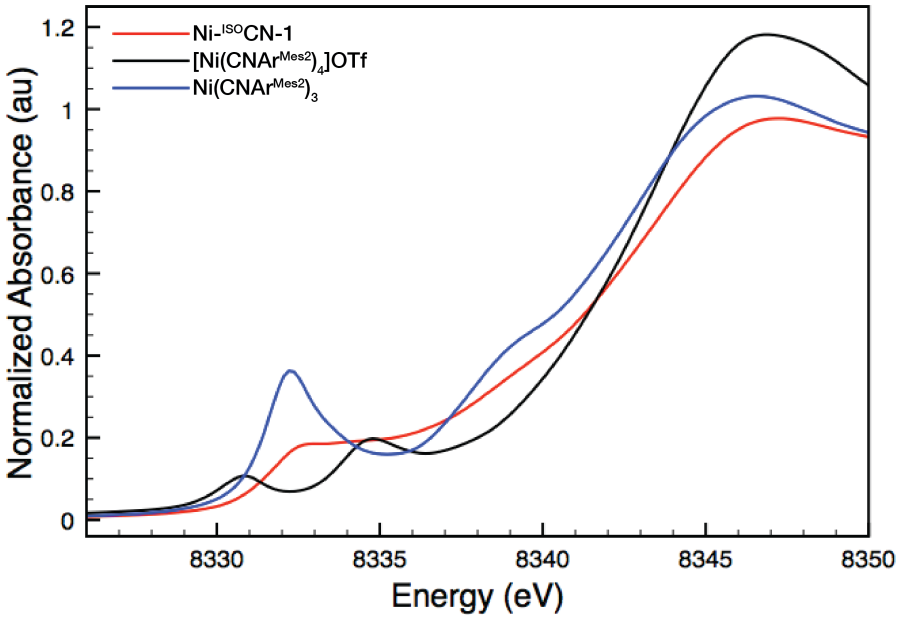

Figure 7.3. Synchrotron XANES data for Ni-^{ISO}CN-1, [Ni(CNAr^{Mes2})$_4$]OTf , and Ni(CNAr^{Mes2})$_3$.

Consistent with this Ni(0) valency, Ni-^{ISO}CN-1 is extremely sensitive to the presence of O_2, causing rapid degradation to a mixture of free [CNAr^{Mes2}]$_2$ as well as oxidized isocyanate (ν_{OCN} = 2242 cm^{-1}).[36] Surprisingly, however, this material is stable for several days in degassed H_2O (Figure 7.17), perhaps owing to the high hydrophobicity engendered by [CNAr^{Mes2}]$_2$ that has been observed previously.[30] Ni-^{ISO}CN-1 remains an insoluble solid in many organic solvents as well, including benzene, THF, and MeCN. However, it is perhaps unsurprising that visible degradation is observed upon addition of an excess of PMe_3 or CO, no doubt due to the complimentary ligand qualities of these substrates for Ni(0). Regarding its thermal stability, initial studies of Ni-^{ISO}CN-1 reveal it be stable to 261 °C, as indicated by differential scanning coulometry (DSC) under dinitrogen.

The presence of tricoordinate Ni(0) nodes in Ni-^{ISO}CN-1, which can function as Lewis basic metal sites towards σ- and π-acidic substrates[37], is a significant departure from the capabilities of traditional coordination polymers. This is illustrated by the ability of Ni-^{ISO}CN-1 to chemically absorb Lewis acidic Tl^+ ions (as TlOTf) via reverse-dative binding from the lone $3d_z^2$ orbital on Ni (Fig. 7.4). Placement of Ni-^{ISO}CN-1 in MeCN solutions of TlOTf results in uptake and binding of Tl^+, and the occupancy of Tl^+ at the apical site can be varied depending on solution concentration. At 100 mM concentration, full occupancy of Tl^+ is achieved to provide Ni(TlOTf)-^{ISO}CN-1 as red crystals. Crystallographic analysis by single-crystal X-ray diffraction reveals binding of acetonitrile *trans* to the Ni-Tl dative interaction ($d_{Ni\text{-}NCMe(AVG)}$ = 2.038(8) Å) to form an approximate trigonal pyramidal metal center. Examination of the near-edge portion of the XAS spectrum of Ni(TlOTf)-^{ISO}CN-1 confirms retention of zero-valency at the Ni node (Fig. 7.5), with an identical MLCT band as Ni-^{ISO}CN-1. Binding of Tl^+ nonetheless results in higher energy isocyanide IR bands as a result

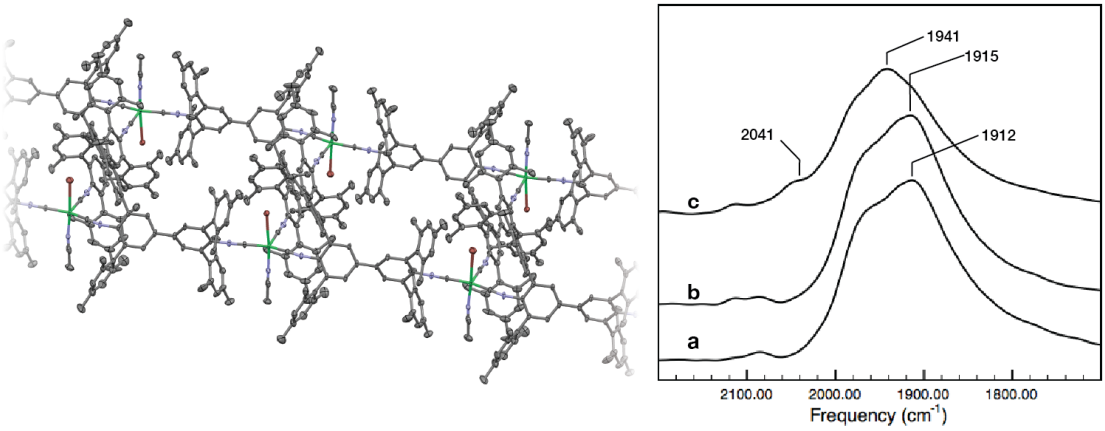

Figure 7.4. (*Left*) Solid-state structure of Ni(TlOTf)-^{ISO}CN-1; (*Right*) Stacked plot of ATR-IR spectra of Ni-^{ISO}CN-1 exposed to 1 mM (**a**), 10 mM (**b**), and 100mM (**c**) MeCN solutions of TlOTf.

of attenuated π-backbonding from Ni due to the dative nature of the interaction (Fig. 2). Taken together, this data underscores the unusual nature surrounding *trans* ligation of MeCN in Ni(TlOTf)-^{ISO}CN-1, as no formal oxidative process has occurred. Indeed, this "turn-on" secondary binding of exogenous Lewis base has been attributed to Z-ligand promoted Lewis acidity at d^{10} metal centers[38], and presents an interesting opportunity to tune the chemisorption abilities of this class of coordination polymers.

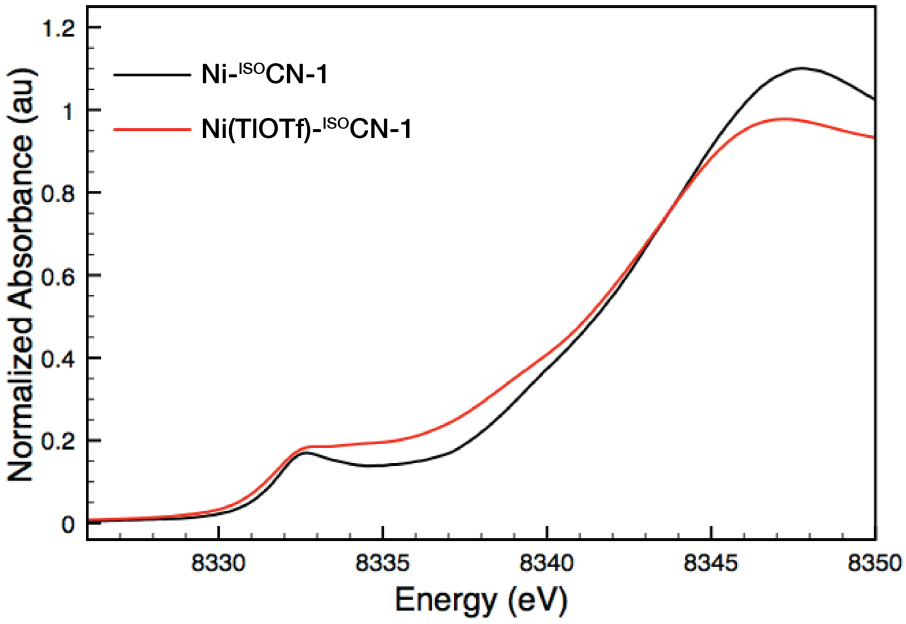

Figure 7.5. XANES spectra for Ni(TlOTf)-^{ISO}CN-1 and Ni-^{ISO}CN-1, verify retention of Ni(0) oxidation state after addition of TlOTf.

As isocyanides are significantly stronger σ-donating ligands compared to CO, the organometallic complexes derived from them are typically capable of multi-electron cycling between oxidation states.[15, 39] To test this ability in Ni-^{ISO}CN-1, we exposed single crystals to a 100 μM solution of FcOTf in MeCN (Fc = ferrocenium; OTf = O_3SCF_3), which has been shown to be a capable oxidant of molecular Ni($CNAr^{Mes2}$)$_3$. A clear blue-shift in the low energy isocyanide bands in the IR

spectrum, as well as a new band centered at 2121 cm^{-1}, indicates an increase in isocyanide bond order consistent with oxidation of the Ni(0) nodes. Crystallographic analysis of this material indicates a substantial decrease in unit cell volume (–892.4(3) $Å^3$) with space group retention. Modeling of the electron density at the Ni site reveals partial oxidation to Ni(I) (SOF = 0.26), which causes pyramidalization of the Ni center and binding of MeCN at the apical coordination site. Attempts to prepare material with a higher percentage of Ni(I) sites repeatedly led to destruction of the single-crystal matrix, which is consistent with the large structural distortions imposed by this geometric change of the Ni node. Notably, however, exposure of Ni-^{ISO}CN-1 to high concentrations of FcOTf (10 mM) resulted in the formation of a yellow, MeCN-insoluble powder, which exhibited a strong IR band centered at 2121 cm^{-1} as well as a shoulder at 2109 cm^{-1}. These energies closely match those of molecular $Ni(OTf)(CNAr^{Mes2})_3$ (ν_{CN} = 2126 and 2112 cm^{-1})[32], supporting the assignment of monovalent Ni centers in this material. Free $[CNAr^{Mes2}]_2$ was not detectable by ^1H NMR analysis of MeCN washings of this powder, providing strong evidence that the covalent Ni-C linkage remains intact throughout the oxidative event. Furthermore, PXRD analysis of this material indicates a substantial phase transformation from native Ni-^{ISO}CN-1, consistent with the large geometric distortion expected from oxidation to Ni(I) and based upon that observed from structural analysis of the mixed-valence species.

In lieu of definitive structural data of this Ni(I) polymer, termed Ni(I)-^{ISO}CN-1, we studied the isolated powder using X-band EPR spectroscopy to understand the local geometry at the Ni node. A spectrum of the Ni(I)-^{ISO}CN-1 at 295K reveals a

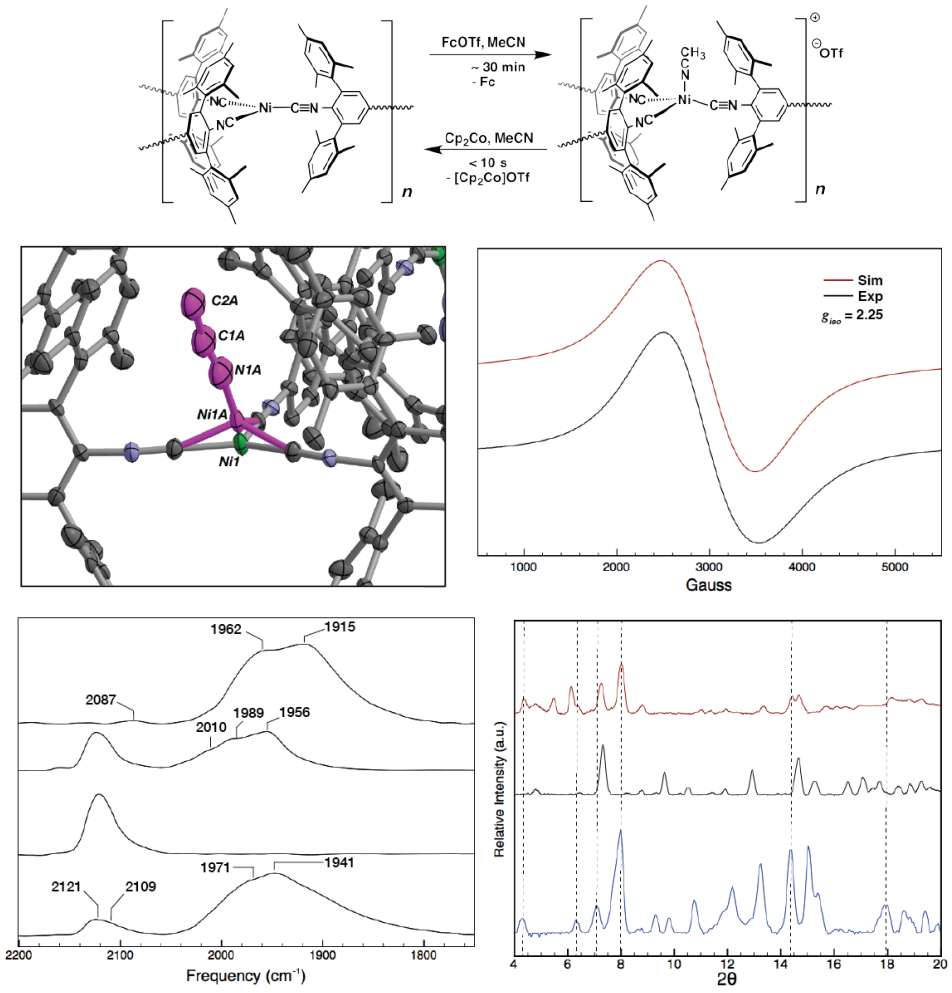

Figure 7.6. Redox activity of Ni-^{ISO}CN-1. (*Top*) Reaction of Ni-^{ISO}CN-1 with FcOTf in MeCN generates the singly-oxidized material Ni(I)-^{ISO}CN-1, which can be re-reduced to Ni-^{ISO}CN-1 with either Cp_2Co or Fc^*; (*middle left*) crystal structure of mixed-valence Ni-^{ISO}CN-1, showing the Ni(I)-NCMe disorder in magenta; (*middle right*) CW-EPR spectrum (298K) of Ni(I)-^{ISO}CN-1, with the experimental spectrum displayed in black and the simulated spectrum displayed in red; (*bottom left*) stacked plot of ATR-IR spectra of Ni-^{ISO}CN-1 during redox process, **a**) mixed-valence Ni-^{ISO}CN-1, **b**) Ni(I)-^{ISO}CN-1, **c**) partially reduced Ni(I)-^{ISO}CN-1, **d**) completely re-reduced Ni-^{ISO}CN-1; (*bottom right*) PXRD (298K) of as-prepared Ni-^{ISO}CN-1 (blue), Ni(I)-^{ISO}CN-1 (black), and re-reduced Ni-^{ISO}CN-1 (red).

highly broadened isotropic signal with g_{iso} = 2.25, a value consistent with other mononuclear Ni(I) complexes.[40] We attribute the broadening to a short spin-spin relaxation time due to close proximity of the Ni(I) ions, which has been observed in other framework materials with paramagnetic metal ions.[41] However, upon cooling to 150K the spectrum assumes a broadened rhombic lineshape, with measured g_z = 3.15,

g_y = 2.17 and g_x = 1.19 (Fig. 7.21). These low-field and high-field values are outside those reported for typical three- and four-coordinate Ni(I) ions, and simulations suggest these likely result from significant *g*-strain induced by a distorted geometry at Ni. Comparison to a rhombic spectrum of Ni(OTf)($CNAr^{Mes2}$)$_3$ at 150K, measured in toluene glass, shows a similarly broad low field transition at g_z = 3.07, with g_y = 2.14 and g_x = 2.03. Future work will be performed using higher frequency EPR, pulsed EPR, and magnetometry studies to further delineate the electronic character of Ni(I)-^{ISO}CN-1 as well as the mixed valence polymer

The above data support the ability of Ni-^{ISO}CN-1 to undergo Ni-based oxidation to monovalent nodes without collapse of the polymeric structure. While oxidation of framework nodes is by no means unprecedented[41-43], the stability observed for this oxidative process in Ni-^{ISO}CN-1 suggested to us that this polymer might be capable of redox cycling between Ni(0) and Ni(I). Indeed, upon exposure to a solution of Cp_2Co (5 mM in MeCN; Cp = cyclopentadienyl), Ni(I)-^{ISO}CN-1 immediately reassumes a black color, and again no free [$CNAr^{Mes2}$]$_2$ is observed in the surrounding liquor. IR bands corresponding to Ni-^{ISO}CN-1 are observed in the ATR-IR spectrum, and the powder diffraction pattern assumes that of the starting material prior to oxidation, albeit with lower intensity for high angle reflections. Although slower (1 day), this reduction process can also be mediated by MeCN solutions of decamethylferrocene (Fig. 7.14 and 7.20), indicating that a Ni(0)/Ni(I) redox couple can be realized within a voltage window of 0.44 V (in MeCN) for Ni-^{ISO}CN-1. While this redox process is mediated by exogenous chemical agents, we expect a similar redox response on account of the strong covalency in the Ni-isocyanide bond.[44]

Accordingly, we are currently investigating the ability of Ni-^{ISO}CN-1 to undergo distinct redox events *via* applied potential to the solid material.

Ni-^{ISO}CN-1 is to our knowledge the first authenticated metal-organic material developed from zerovalent metal nodes. Consistent with this formulation, the open coordination sites on Ni permit the chemisorption of Lewis acidic metal ions in solution as indicated by the incorporation of TlOTf. This ability is a unique result of the Lewis basic Ni(0) center and stands in contrast to most known free-ion absorption mechanisms for framework materials. Finally, Ni-^{ISO}CN-1 provides a rare example of a chemically redox-active framework material, and is the first to exhibit this process with low-valent metals. We are consequently exploring the ability of Ni-^{ISO}CN-1 to mediate redox-transformations as well as investigating its physical properties towards a variety of conditions in more detail.

7.3 Preparation of a 3-Dimensional Porous Framework with Zerovalent Ni Nodes

We have previously shown that addition of four equiv. of the monoisocyanide CNAr^{Mes2} leads to the exclusive formation of Ni(CNAr^{Mes2})$_4$, which adopts an expected tetrahedral geometry about Ni(0).[32] With this coordination environment in mind, we sought to construct a three-dimensional framework in which the nodes are comprised entirely of zerovalent metal atoms. Borrowing from the preparation of Ni(CNAr^{Mes2})$_4$, we found that the slow addition of 3 equiv. [CNAr^{Mes2}]$_2$ to a stirring THF solution of Ni(COD)$_2$ (COD = 1,5-cyclooctadiene) leads to the precipitation of an amorphous, maroon solid. Subsequent annealing in a THF suspension at 100 ˚C inside a thick-walled glass pressure tube for 2 days generates Ni-^{ISO}CN-2 (^{ISO}CN =

isocyanide coordination network) as a free-flowing microcrystalline solid, with a strong peak at 2θ = 7.30° in the powder X-ray diffraction (PXRD) pattern. Additionally, ATR-IR analysis of this material reveals a single broad absorbance centered at 1950 cm^{-1}, slightly red-shifted from that of four-coordinate $Ni(CNAr^{Mes2})_4$ but is nonetheless indicative of high symmetry about Ni.

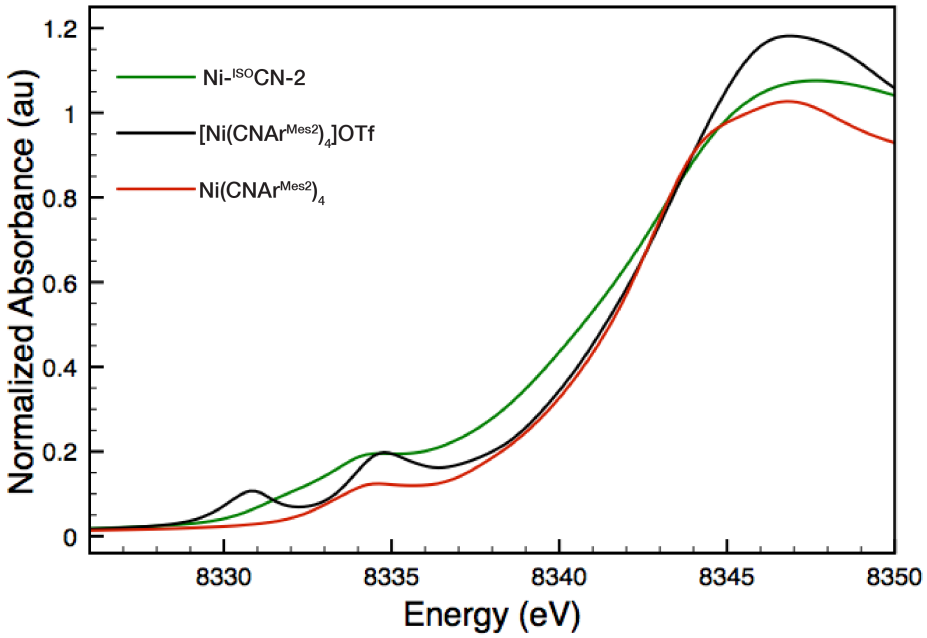

Figure 7.7. Synchrotron XANES data for Ni-^{ISO}CN-2, $[Ni(CNAr^{Mes2})_4]OTf$, and $Ni(CNAr^{Mes2})_4$.

To verify Ni valency in Ni-^{ISO}CN-2, we performed X-ray absorption spectroscopy (XAS) at the Ni K-edge on the isolated solid with comparison to the molecular standards $Ni(CNAr^{Mes2})_4$ and $[Ni(CNAr^{Mes2})_4]OTf$ (OTf = trifluoromethanesulfonate, $F_3CSO_3^-$). As shown in Figure 7.7, a small, broadened band is observed in the near-edge portion of the spectrum (XANES) at 8334.5 eV for Ni-^{ISO}CN-2, with an otherwise featureless rising edge. Calculations indicate this band arises from a spin-allowed Ni 1s → CNR π* metal-to-ligand charge transfer (MLCT),

rather than a Ni-based 1s → 3d transition. Indeed, the near-edge spectrum of [Ni(CNAr^{Mes2})$_4$]OTf exhibits two distinct bands at 8330.8 eVand 8334.8 eV, which are assigned as the Ni 1s → 3d transition and Ni 1s → CNR π* MLCT, respectively. Importantly, due to the d^{10} electron configuration of Ni(CNAr^{Mes2})$_4$ this Ni 1s → 3d transition is unavailable, and as such only a single band at 8334.5 eV resulting from a MLCT is observed. This band energy is in close agreement with that found for Ni-^{ISO}CN-2, and accordingly we assign a Ni(0) valency for Ni-^{ISO}CN-2.

Attempts at preparing crystalline material of Ni-^{ISO}CN-2 suitable for single crystal X-ray diffraction via other heating/cooling programs failed to provide particles of suitable size. However, it was found that an alternate synthesis, involving the mechanical grinding of Ni(COD)$_2$ and an excess of [CNAr^{Mes2}]$_2$ followed by heating at 100 ˚C in the presence of THF, led to the formation of large, black/red single crystals which adopt a cubic habit. Crystallographic analysis of these crystals at 100K reveals a doubly-interpenetrated diamondoid framework in the *C2/c* space group, with [CNAr^{Mes2}]$_2$ serving as the linker ligand. The framework architecture derives from tetrakis-isocyanide Ni nodal sites with tetrahedral geometry (Houser $\tau^4 = 0.98$).[45] This common structural motif results in the formation of *ca*. 4.2 X 3.6 Å and 6.3 X 4.5 Å channels along the 001 axis; the pore size in this case being limited by the *m*-terphenyl groups of [CNAr^{Mes2}]$_2$. Notably, this material represents the first structurally characterized three-dimensional material derived from zerovalent metal nodes, making this material effectively isoelectronic with Ni metal.

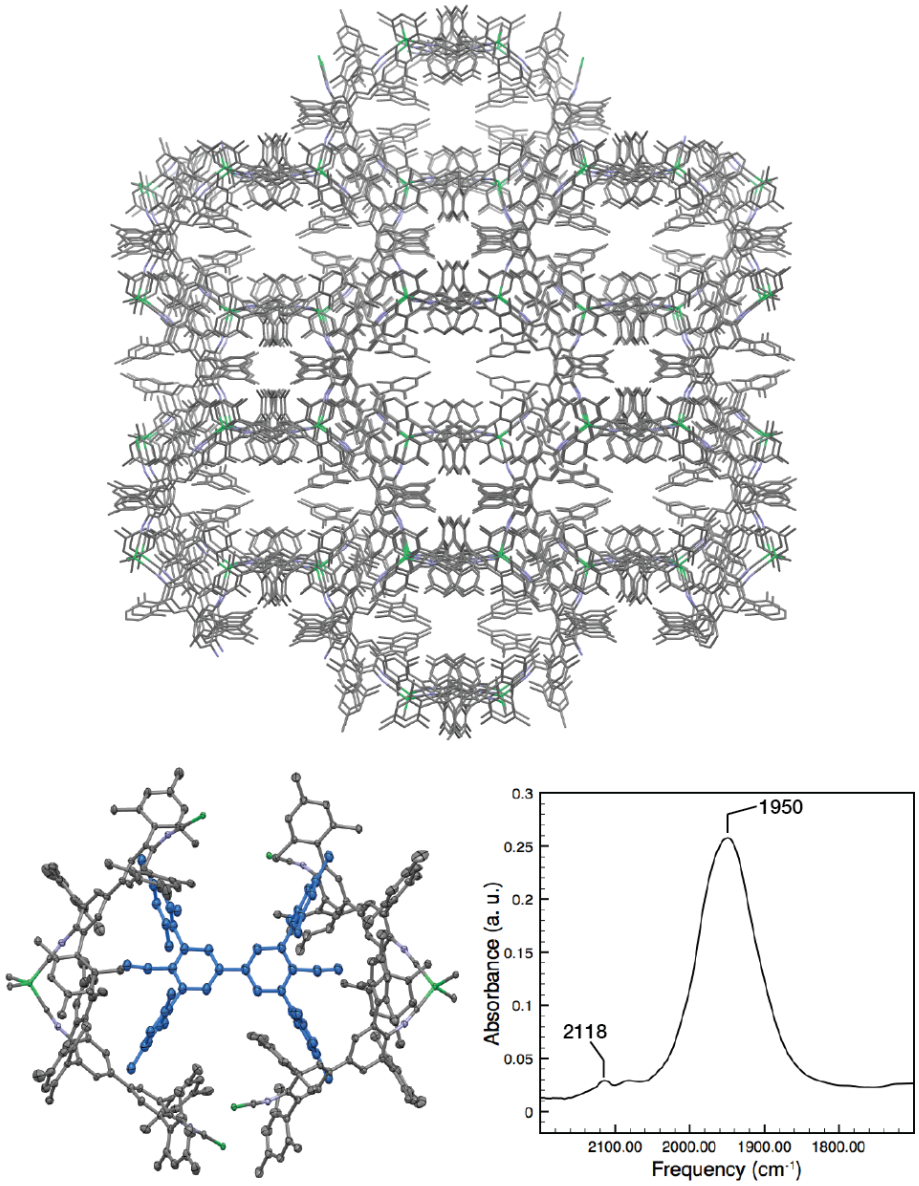

Figure 7.8. (*top*) View down 100 axis of Ni-^{ISO}CN-2·([CNAr^{Mes2}]$_2$)$_{0.5}$, with free [CNAr^{Mes2}]$_2$ omitted; (*bottom left*) Pore generated by two unique Ni(0) nodes, with the partially occupied free [CNAr^{Mes2}]$_2$ shown in blue; (*bottom right*) ATR-IR spectrum of Ni-^{ISO}CN-2.

Careful examination of the void space generated by this 3-D architecture indicated partial occupation of the larger pore (SOF = 50%) by free [CNAr^{Mes2}]$_2$. This is confirmed by ATR-IR analysis of these crystals showing two bands in the isocyanide region at 2114 cm^{-1} and 1960 cm^{-1}. We contend that the inclusion of free

$[CNAr^{Mes2}]_2$ in the larger pores leads to the preservation of framework stability, and consequently the ability to form large single crystals. This enforced stability via packing has been observed in multidimensional materials, particularly for those containing counteranionic moieties. Indeed, comparison of the predicted pattern from the structurally characterized single crystals, which we term Ni-^{ISO}CN-2·($[CNAr^{Mes2}]_2$)$_{0.5}$, and the PXRD pattern of Ni-^{ISO}CN-2 suggests structurally distinct phases. This is likely the result of framework collapse in Ni-^{ISO}CN-2.[46] Indeed, without the support of free $[CNAr^{Mes2}]_2$ providing electrostatic and π-π interactions in the large pore, the known kinetic lability inherent to four-coordinate Ni(0) metal centers in strong ligand[47] fields likely enables isocyanide dissociation and subsequent framework destabilization. This is consistent with our prior studies on isoelectronic Cu(I)-isocyanide frameworks, in which we demonstrated that the steric pressure exerted by the *m*-terphenyl groups in $[CNAr^{Mes2}]_2$ was sufficient to induce framework collapse to a material with a lower isocyanide coordination number at Cu(I). This structural instability in Ni-^{ISo}CN-2 is further demonstrated by heating a sample for several days at 100 ˚C in a THF suspension, which leads to a noticeable red shift (ν_{CN} = 2040 cm^{-1}, Δ = -10 cm^{-1}) in the ATR-IR spectrum, indicating an increase in π-backbonding from Ni. As there is no redox event possible (eg. reduction of Ni(0)), we surmise this is due to dissociation of $[CNAr^{Mes2}]_2$ to form three coordinate Ni(0) nodes in the framework. Moreover, ^{1}H NMR analysis of the mother liquor after heating shows minor amounts of free $[CNAr^{Mes2}]_2$. Indeed, the stability of tricoordinate Ni centers is well established from prior work on both discrete molecular analogues as well as in oligomeric frameworks.

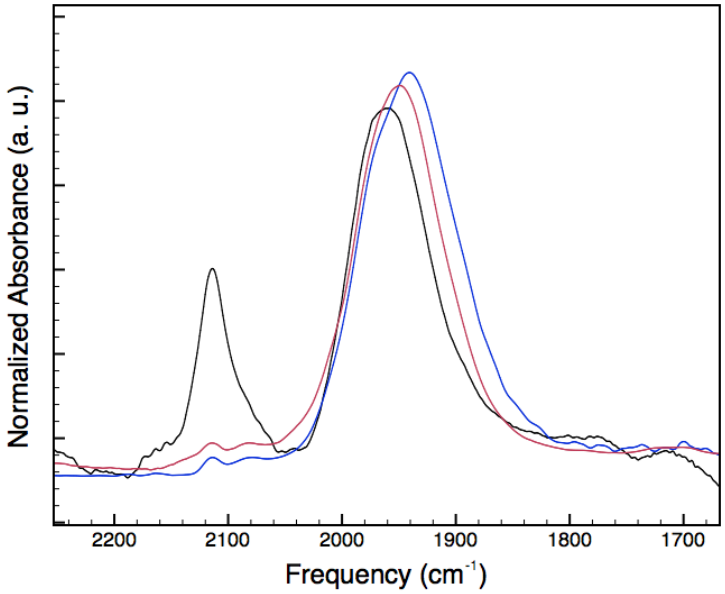

Figure 7.9. ATR-IR spectra of Ni-^{ISO}CN-2·([CNAr^{Mes2}]$_2$)$_{0.5}$ (black), as prepared Ni-^{ISO}CN-2 (red), and Ni-^{ISO}CN-2 after heating in THF (blue).

Consistent with the identified Ni(0) valency, solid Ni-^{ISO}CN-2 is unstable towards aerobic conditions and slowly decomposes to free [CNAr^{Mes2}]$_2$ (Figure X). However, ATR-IR analysis of Ni-^{ISO}CN-2 indicates indefinite stability under a dinitrogen atmosphere (several months) and confirms no degradation after suspension in a variety of common organic solvents, including benzene, acetonitrile, and diethyl ether. Initial examination of the thermal stability of solid Ni-^{ISO}CN-2 by differential scanning coulometry (DSC) under a dinitrogen atmosphere indicates stability to 191 ˚C, and a substantive phase transformation at 294 ˚C. This suggests that as-prepared Ni-^{ISO}CN-2, which appears to be a collapsed framework, is thermally stable after vacuum desolvation and when not in the presence of solvent (*vide supra*).

In conclusion, we report the first three-dimensional material derived from zerovalent metal atom nodes. While direct structural characterization of Ni-^{ISO}CN-2 was not available, we were able to develop a framework basis with the isolation of Ni-

^{ISO}CN-2·([CNAr^{Mes2}]$_2$)$_{0.5}$, showing the framework to likely be of a two-fold interpenetrated, diamondoid type.

7.4 Synthetic Procedures and Experimental Details

General Considerations. All manipulations were performed under an atmosphere of dry dinitrogen using standard Schlenk and glovebox techniques, unless otherwise stated. Solvents were dried and degassed according to standard procedures. Ni(COD)$_2$ and TlOTf were purchased from Strem Chemicals, Inc. and used without further purification. [CNAr^{Mes2}]$_2$ was prepared as described previously, and recrystallized twice prior to use.[30] FcOTf (Fc = ferrocenium; OTf = O_3SCF_3) was prepared according to literature procedures.[48] Fc* (Fc* = $(C_5(CH_3)_5)_2Fe$) was purchased from Sigma-Aldrich Corp. and used as received. Elemental analysis was performed by Midwest Microlabs, Inc. of Indianapolis, IN.

Synthesis of Ni-^{ISO}CN-1. A suspension of Ni(COD)$_2$ in MeCN (0.008 g, 0.029 mmol, 2 ml) was stirred at room temperature for 8 minutes, generating a dark mixture. This mixture was transferred to a 15 ml pressure tube, which had been warmed to *ca*. 75 ºC. A second MeCN solution of [CNAr^{Mes2}]$_2$ (0.040 g, 0.059 mmol, 2 equiv., 2 ml) was then added quickly to form a reddish-black mixture. The tube was capped with a Teflon screw-cap and immediately placed in a sand bath in an oven at 100 ºC. The tube was heated at 100 ºC for 24 h, followed by cooling to 35 ºC over a 24 h period. The tube was removed, brought into a glovebox, and the MeCN mother liquor was gently removed. The crystals thus prepared were transferred as a slurry in MeCN (1.5

ml) to a scintillation vial, and the MeCN was decanted off. The crystals were gently washed again with MeCN (3 ml), which was subsequently decanted, to provide Ni-^{ISO}CN-1 as black/red single crystals. Multiple attempts failed to provide satisfactory combustion analysis; we believe this is due to the high sensitivity of Ni-^{ISO}CN-2 to O_2, which is typically in 50 ppm concentration in sample preparation.

Addition of TlOTf to Ni-^{ISO}CN-1. Formation of Ni(TlOTf)-^{ISO}CN-1.

A) Representative procedure for Ni(TlOTf)-^{ISO}CN-1: Approximately 0.01 g of freshly washed Ni-^{ISO}CN-1 was transferred to a scintillation vial. This was then treated with 100 mM TlOTf in MeCN (2 ml) and allowed to stand for 6 h. Thereafter, some crystals were collected and subjected to analysis by single crystal X-ray diffraction. The remaining sample was gently washed with pure MeCN (4 ml) for 1 min and the solvent decanted, and the crystalline material was used for other analyses.

B) Ni(TlOTf)-^{ISO}CN-1 (61.6% occupancy): The same procedure outlined above for Ni(TlOTf)-^{ISO}CN-1 was used, with the exception that 10 mM TlOTf in MeCN was used.

C) Ni(TlOTf)-^{ISO}CN-1 (23.5% occupancy): The same procedure outlined above for Ni(TlOTf)-^{ISO}CN-1 was used, with the exception that 1 mM TlOTf in MeCN was used.

Formation of Mixed Valence Ni-^{ISO}CN-1. Approximately 0.01 g of freshly washed Ni-^{iso}CN-1 was transferred to a scintillation vial. This material was treated with a blue 100 μM solution of FcOTf in MeCN (2 ml). After approximately 4 h, the color of the

solution had become yellow, and inspection of the crystalline material indicated a concomitant color change to light red. A few crystals were then selected and subjected to analysis by single crystal X-ray diffraction. The remaining sample was gently washed with MeCN (2 ml) twice, with the solution decanted after each wash. The material thus prepared was subsequently used for other analyses.

Formation of Ni(I)-^{ISO}CN-1. Approximately 0.02 g of freshly washed Ni-^{ISO}CN-1 was transferred as a suspension in MeCN (2 ml) to a 10 ml scintillation vial. This material was then treated with 5 mM FcOTf in MeCN (1 ml), and allowed to stand for 4 h. By this time, the formerly blue supernatant had assumed a yellow color, and Ni-^{ISO}CN-1 had become yellow as well. The surrounding liquor was removed by decantation, and Ni(I)-^{ISO}CN-1 was washed with *n*-pentane 5 times (2 ml), with the washings being removed via decantation.

Reduction of Ni(I)-^{ISO}CN-1 to Ni-^{ISO}CN-1.

A) With Cp_2CO: To a 10 ml scintillation vial containing Ni(I)-^{ISO}CN-1 (0.015 g) was added 1 ml MeCN. This was then treated with 3 ml of a 5 mM MeCN solution of Cp_2Co, causing the yellow, suspended Ni(I)-^{ISO}CN-1 to immediately become black. This solid was allowed to settle, and the mother liquor was decanted. This solid was washed twice with MeCN, followed by decantation, and was subsequently analyzed.

B) With Fc^*: The process for **A** was repeated, except using 2 ml of a 20 mM MeCN solution of Fc^*. This mixture was allowed to stand for one day, after which the now-black material was collected and washed with MeCN.

Synthesis of Ni-^{ISO}CN-2. To a stirring solution of $Ni(COD)_2$ in THF (0.009 g, 0.033 mmol, 4 ml), was added a THF solution of $[CNAr^{Mes2}]_2$ (0.065 g, 0.096 mmol, 3 equiv., 4 ml) over a 5 minute period, causing the formation and precipitation of a deep red powder. This mixture was stirred for 30 minutes at room temperature, after which it was transferred to a 15 ml pressure tube and capped with a Teflon screw-cap. The tube was then placed in a sand bath inside an oven set to 100 ˚C for a 48 h period, after which it was allowed to cool to room temperature over a 5 h period. The deep maroon solid was transferred to a scintillation vial and the supernatant was decanted off. Following two wash cycles (consisting of gentle agitation in 4 ml THF followed by decantation), all volatiles were removed under dynamic vacuum for 6 h to provide 0.037 g of a deep maroon, free-flowing solid.

Preparation of Ni-^{ISO}CN-2·$([CNAr^{Mes2}]_2)_{0.5}$. Single crystals of Ni-^{ISO}CN-1·$([CNAr^{Mes2}]_2)_{0.5}$ were prepared as follows: $Ni(COD)_2$ (0.004 g, 0.0146 mmol) mechanically mixed with $[CNAr^{Mes2}]_2$ (0.059 g, 0.087 mmol, 6 equiv.) with a mortar and pestle, and the resulting solid mixture was transferred to a 15 ml pressure tube. To this mixture was added *ca*. 0.1 ml THF, and the tube was placed in a sand bath inside an oven set to 100 ˚C for one day, followed by cooling to room temperature over 24 h. The deep black/red cubic crystals thus prepared are amenable to analysis by single crystal X-ray diffraction.

XAS Spectroscopy

Ni K-edge XAS spectra were collected on the 16 pole, 2 T wiggler beamline 9-3 at the Stanford Synchrotron Radiation Lightsource (SSRL) under ring conditions of 3 GeV and 500 mA. Samples were diluted in BN, pressed into 1 mm aluminum spacers and sealed with 37 μm Kapton tape. Samples were maintained at 10 K in a liquid He cryostat during data collection. A Si(220) double-crystal monochromator was used for energy selection and a Rh-coated mirror (set to an energy cutoff of 13 keV) was used for harmonic rejection. Internal energy calibration was performed by assigning the first inflection point of a Ni foil spectrum to 8331.6 eV. Data on $Ni(CNAr^{Mes2})_3$**,** Ni-^{ISO}CN-1 and Ni(TlOTf)-^{ISO}CN-1 were collected in transmission mode, with X-rays detected by ionization chambers immediately upstream and downstream of the sample. Data on samples $[Ni(CNAr^{Mes2})_3]OTf$, Ni(I)-^{ISO}CN-1, and Ni(0/I)-^{ISO}CN-1 were collected in fluorescence mode with a Canberra 100-element Ge monolith solid-state detector perpendicular to the incident beam. Data on samples $Ni(CNAr^{Mes2})_4$, $[Ni(CNAr^{Mes2})_4]OTf$, $Ni(COD)_2$, and Ni-^{ISO}CN-2 were collected in fluorescence mode with a Lytle detector. For spectra measured by fluorescence detection, elastic scatter into the detector was attenuated using a Soller slit with an upstream Co filter.

Powder X-ray Diffraction Data.

Low-temperature powder X-ray diffraction was collected using Cu-Kα radiation (λ = 1.54178 Å) on a Bruker Kappa diffractometer equipped with a VÅNTEC-500 area detector and an Oxford Cryostream 700, and were collected to 2θ = 45˚. Samples were prepared on a nylon loop using minimal Paratone oil. Crystalline material, as prepared,

was used without grinding to preserve structural integrity; we therefore believe discrepancies in peak intensity are due to preferential orientation of the crystallites. Corrections for the anomalous scattering caused by the nylon loop and Paratone oil were performed by subtracting a background scan consisting solely of these materials. The PXRD pattern for desolvated Ni-^{ISO}CN-1 at ambient temperature was collected using an air-free sample holder on a Bruker D8 Advance diffractometer at 40 kV, 40 mA for Cu Kα (λ= 1.5418 Å), with a scan speed of 1 sec/step. The experimental background of the collected patterns was corrected using the DIFFRAC.SUITE EVA software package from Bruker Corporation.

ATR-IR Spectroscopy

Solid-state IR spectra were collected at 2 cm^{-1} resolution using a Bruker Platinum Alpha ATR-IR equipped with a diamond crystal. Air-free analyses were collected using this instrument inside a nitrogen-filled glovebox. Samples were deposited either as a drop-cast suspension or as a powder.

EPR Spectroscopy

X-Band continuous wave (CW) EPR spectra were measured on a Bruker E500 spectrometer equipped with a Bruker ER 041 X Microwave Bridge and a liquid nitrogen cooling system. Spectra were recorded in 4 mm quartz tubes, and the magnetic field was calibrated with DPPH. The isotropic spectrum of Ni(I)-^{ISO}CN-1 was simulated using the EasySpin module[49] in Matlab.

EPR spectrometer conditions:

[Ni(CNAr^{Mes2})$_3$]OTf (0.5 mM, 150K): X-band (9.3913 GHz): centerfield/sweep-width = 3130 G//4000 G; microwave power = 0.2021 mW; modulation amplitude = 1.00 G; modulation frequency = 100.0 KHz; time constant = 20.48 ms; scans = 4.

Ni(I)-^{ISO}CN-1 (295K): X-band (9.3907 GHz): centerfield/sweep-width = 3000 G/5000 G; microwave power = 0.2021 mW; modulation amplitude = 5 G; modulation frequency = 100.0 KHz; time constant = 20.48 ms; scans = 8.

Ni(I)-^{ISO}CN-1 (150K): X-band (9.4054 GHz): centerfield/sweep-width = 4000 G/7000 G; microwave power = 0.2017 mW; modulation amplitude = 2 G; modulation frequency = 100.0 KHz; time constant = 40.96 ms; scans = 4.

Differential Scanning Coulemetry

Measurements on Ni-^{ISO}CN-1 were performed under a stream of dry dinitrogen gas (80 mL/min) using a Mettler Toledo TGA/DSC 1 STAR^e System running from 35 ˚C to 500 ˚C with a ramping rate of 5 ˚C/min. Samples were prepared in a dinitrogen-filled glovebox and placed in a 30 μl stainless steel high-pressure crucible (Mettler-Toledo) with a gold pan lid. Sample sizes varied from 5-15 mg. A background measurement of an empty crucible with the pan lid was collected and used as to correct for background.

7.5 Characterization Data

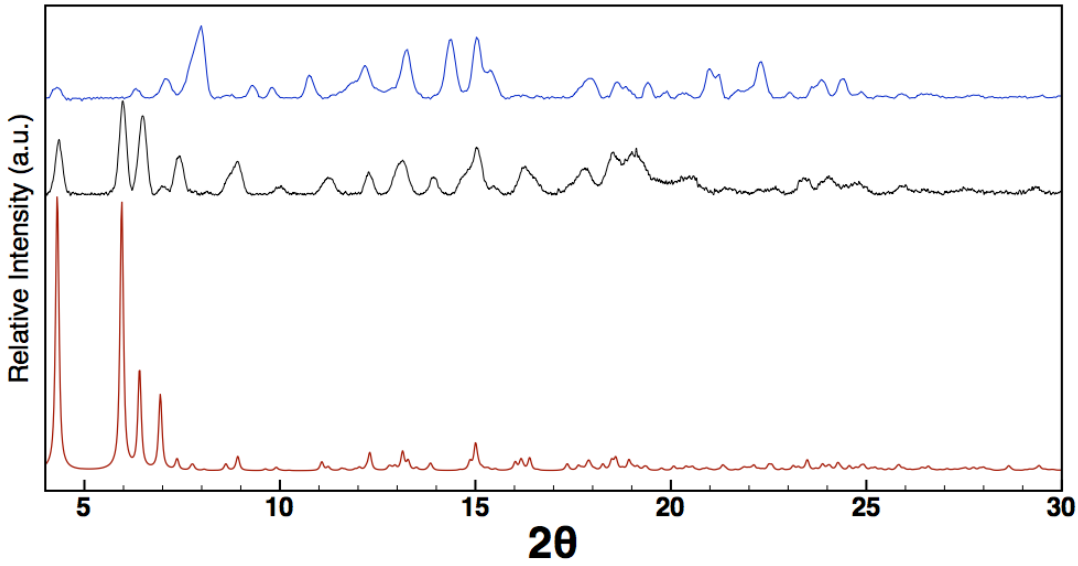

Figure 7.10. PXRD pattern of as-synthesized Ni-^{ISO}CN-1 at 100K (middle, black) and the predicted pattern from SXRD (bottom, red). The top pattern, collected at 295K, in blue results for Ni-^{ISO}CN-1 upon desolvation under vacuum.

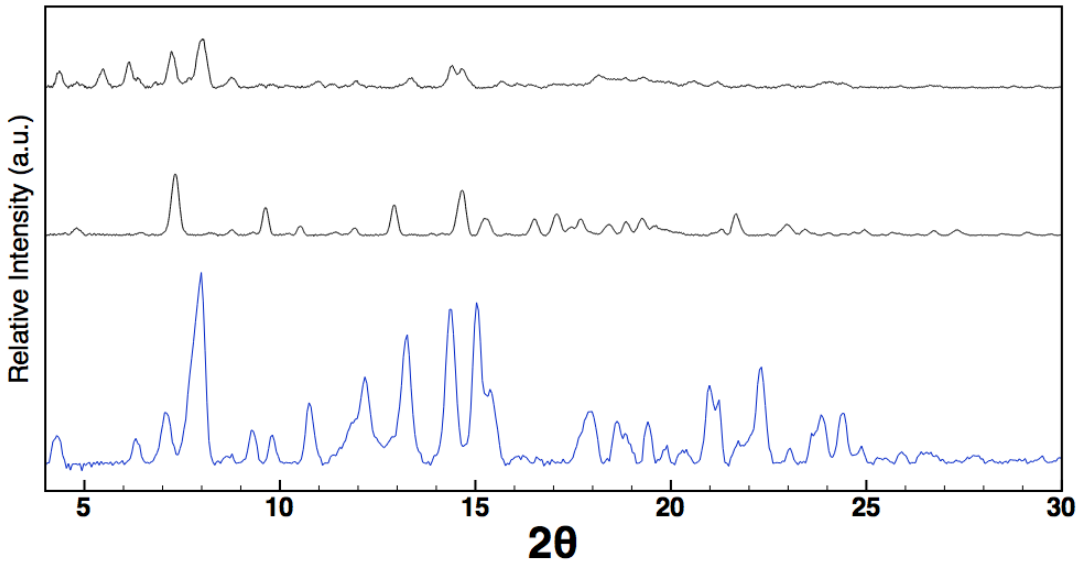

Figure 7.11. Full PXRD patterns of Ni-^{ISO}CN-1 undergoing redox-cycling. Starting Ni-^{ISO}CN-1 (bottom, blue); after full oxidation to Ni(I) using FcOTf (middle); after reduction to Ni(0) using Cp_2Co (top).

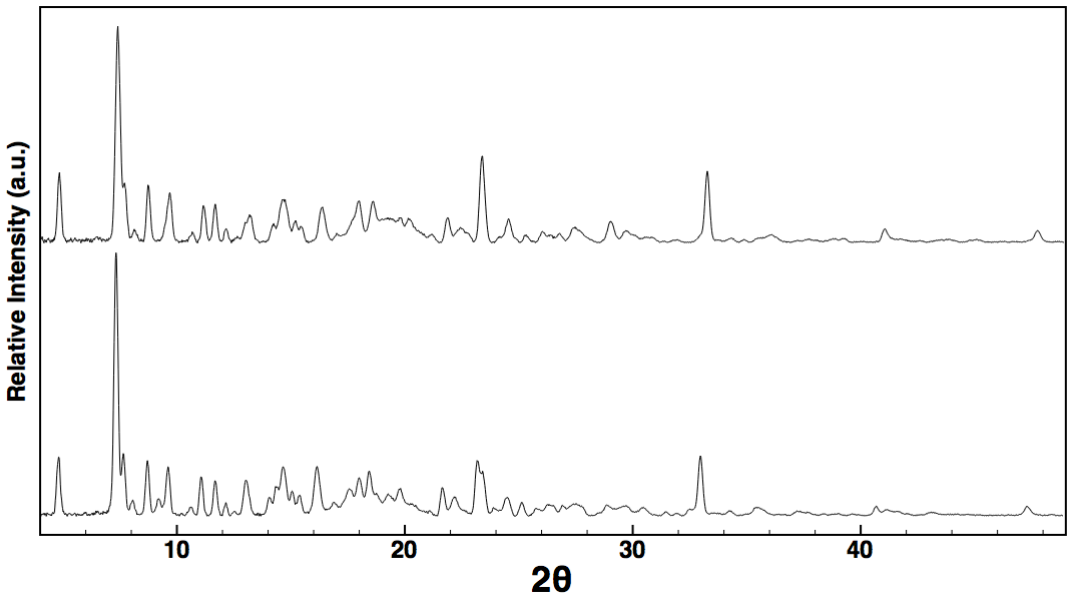

Figure 7.12. PXRD pattern for Ni(TlOTf)-^{ISO}CN-1; (*top)* 100K, (*bottom*) 295K.

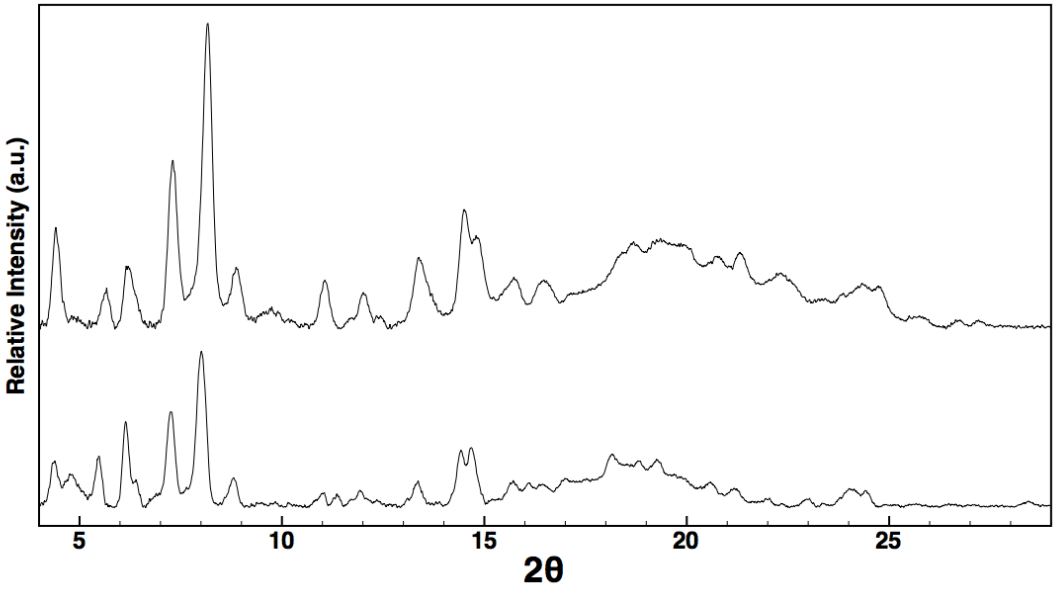

Figure 7.13. PXRD pattern for Ni-^{ISO}CN-1 after reduction from Ni(I)-^{ISO}CN-1; (*top)* 100K, (*bottom*) 295K.

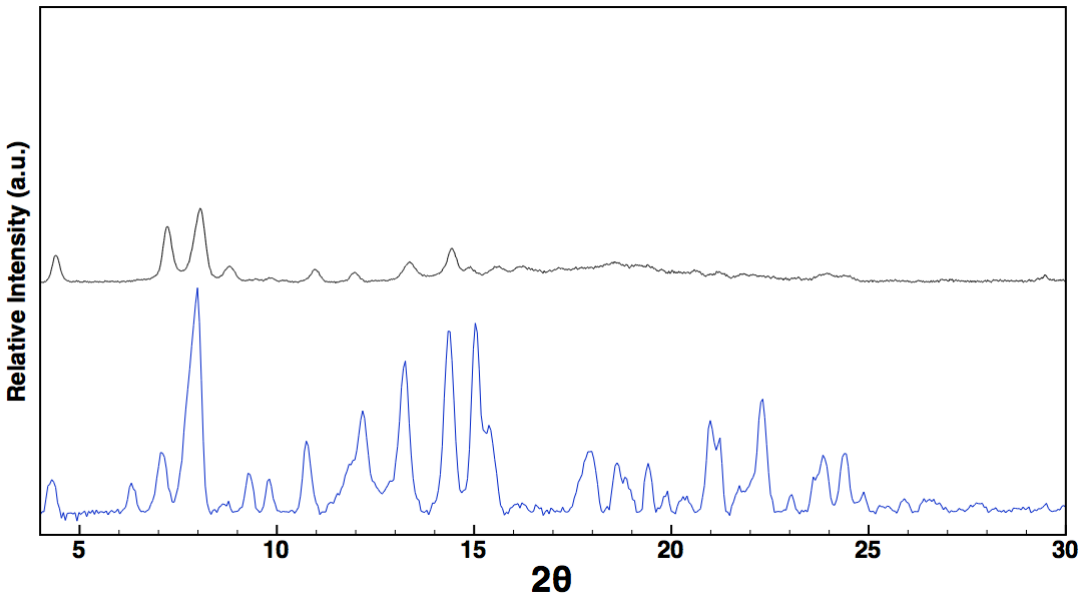

Figure 7.14. Comparison of PXRD patterns (298K) of Ni-^{ISO}CN-1 (blue) and re-reduced Ni-^{ISO}CN-1 after exposure of Ni(I)-^{ISO}CN-1 to Fc^{*} for one day.

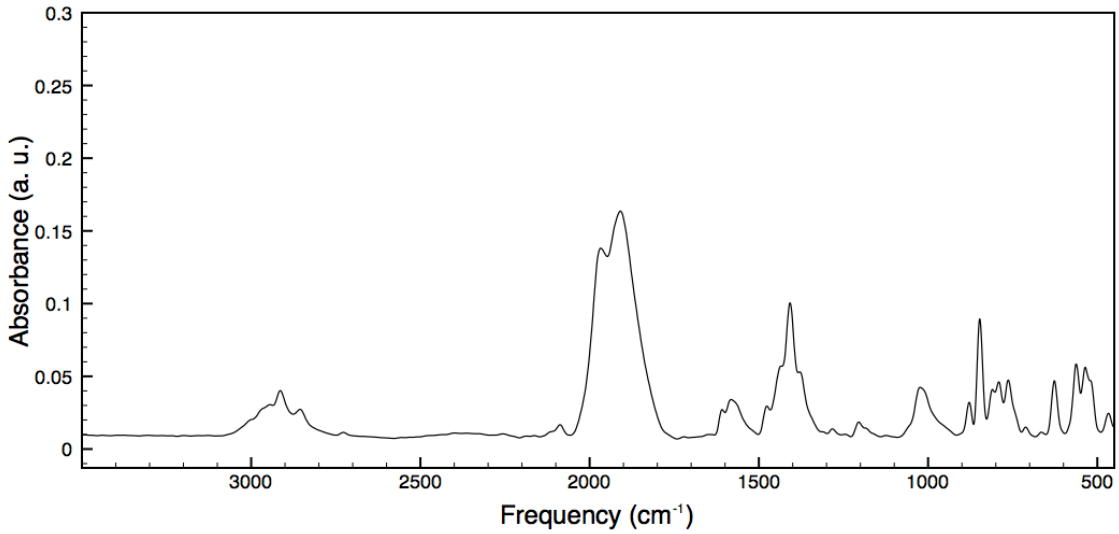

Figure 7.15. Solid-state ATR-IR spectrum of Ni-^{ISO}CN-1.

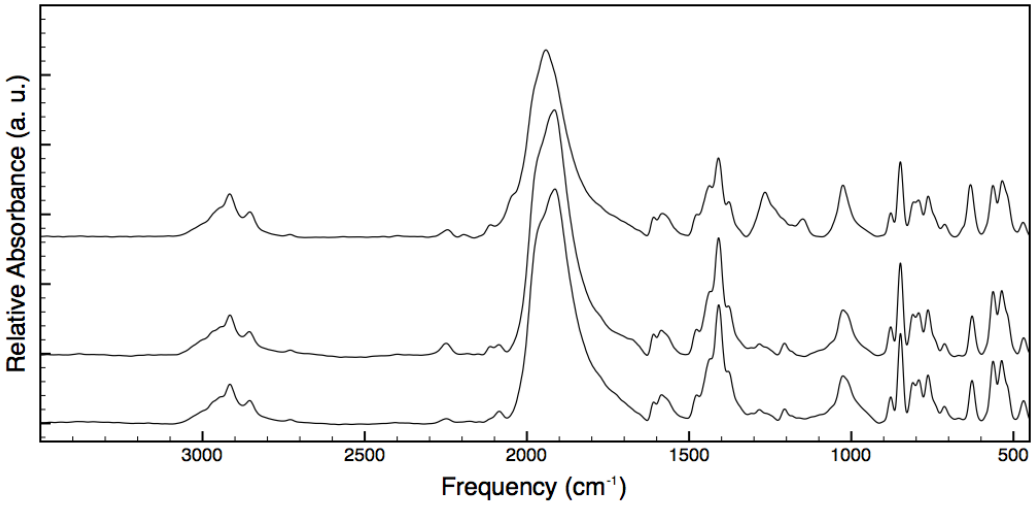

Figure 7.16. Solid-state ATR-IR spectra of Ni-^{ISO}CN-1 after exposure to MeCN solutions of TlOTf; (top) 100mM, (middle) 10 mM, (bottom) 1 mM.

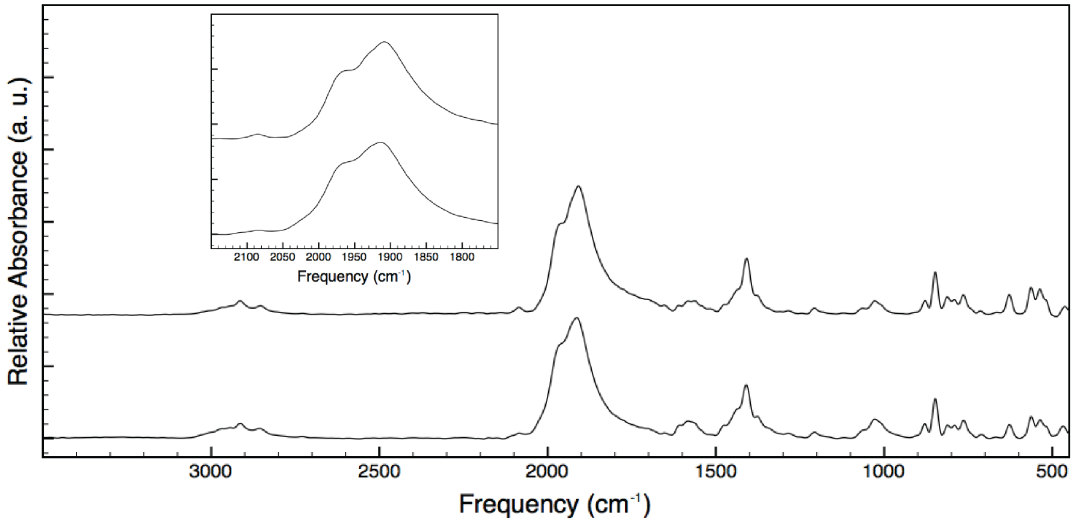

Figure 7.17. View of isocyanide region for ATR-IR spectra of Ni-^{ISO}CN-1 after placement in degassed H_2O under a N_2 atmosphere; (bottom*)* two days, (top) four days.

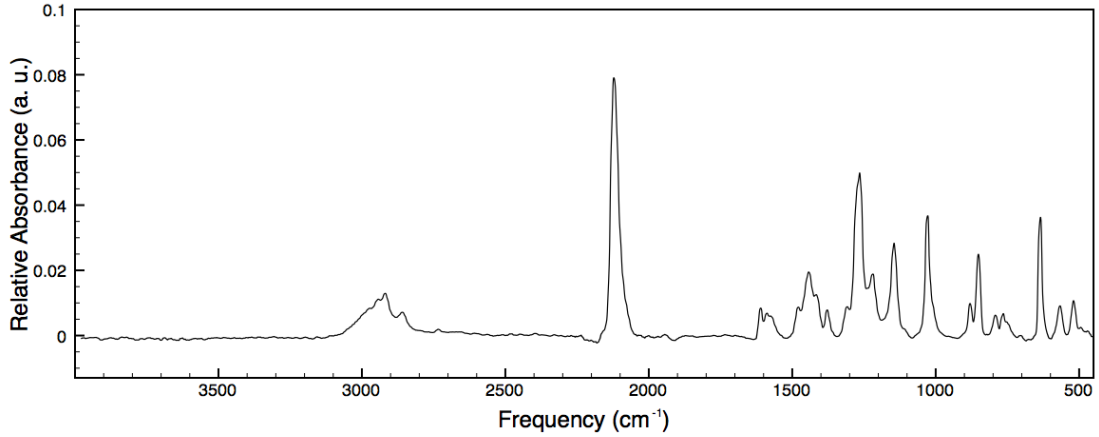

Figure 7.18. ATR-IR of Ni(I)-^{ISO}CN-1.

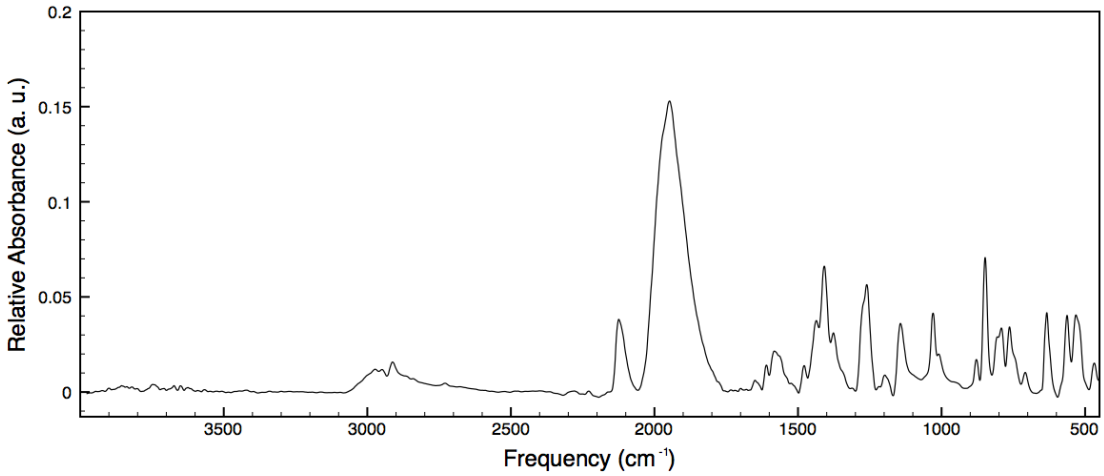

Figure 7.19. ATR-IR of mixed-valence Ni-^{ISO}CN-1.

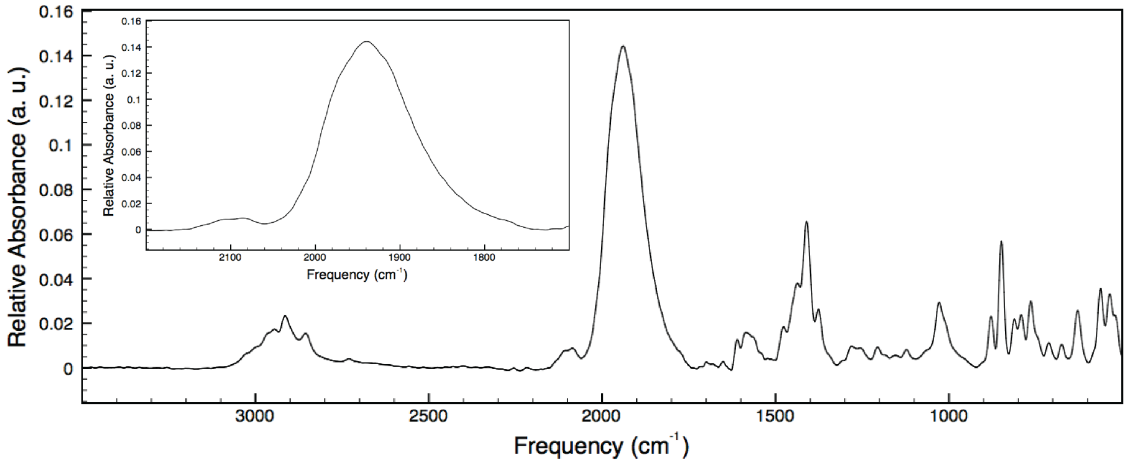

Figure 7.20. ATR-IR of Ni-^{ISO}CN-1 after reduction with Fc^{*} in MeCN; inset shows isocyanide region.

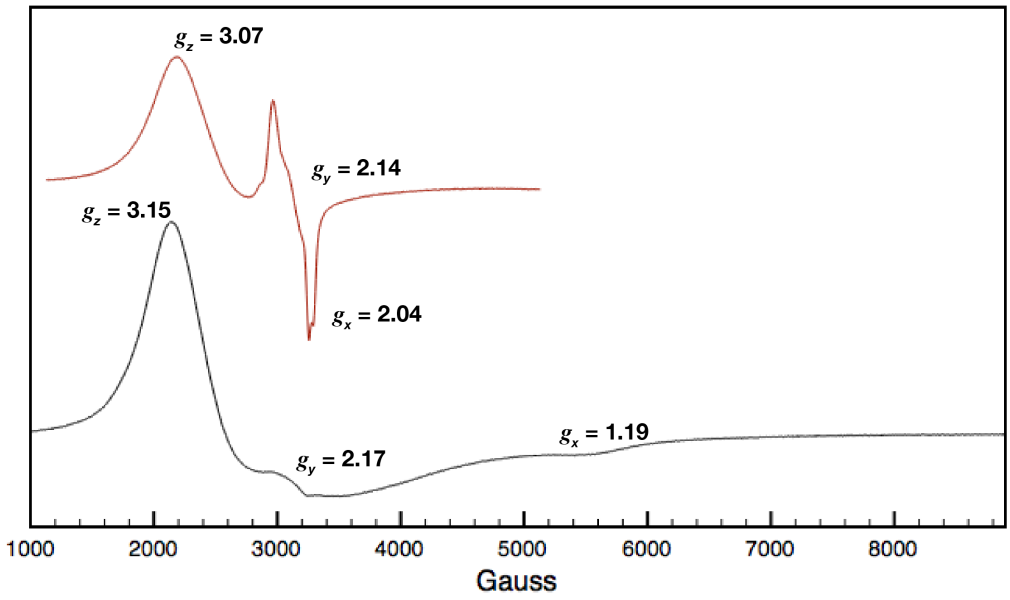

Figure 7.21. X-band EPR spectra of [Ni(CNAr^{Mes2})$_3$]OTf (top, red) and Ni(I)-^{ISO}CN-1 (bottom, black) collected at 150K.

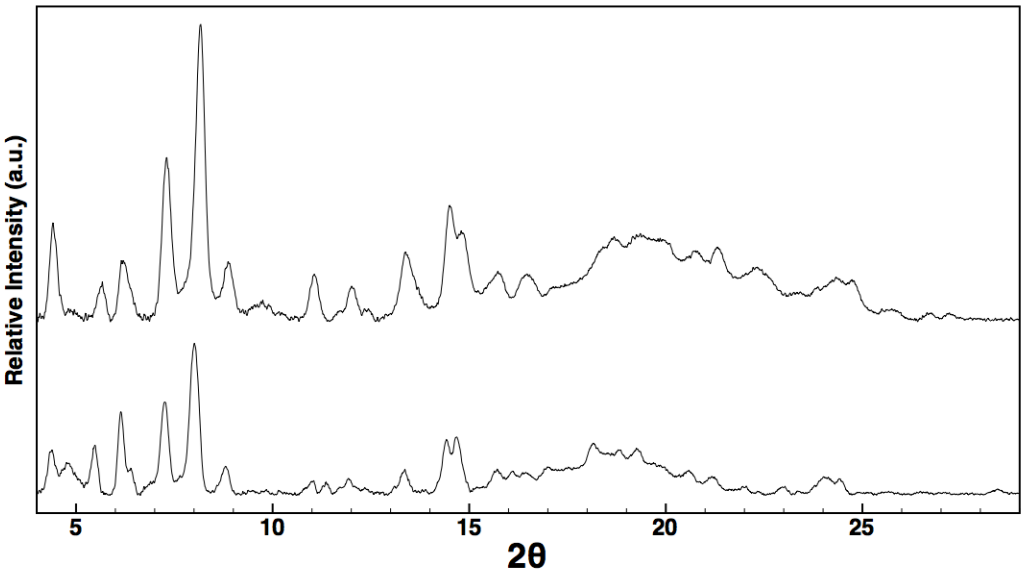

Figure 7.22. PXRD pattern of Ni-^{ISO}CN-1 after reduction from Ni(I)-^{ISO}CN-1; (*top*) 100K, (*bottom*) 295K.

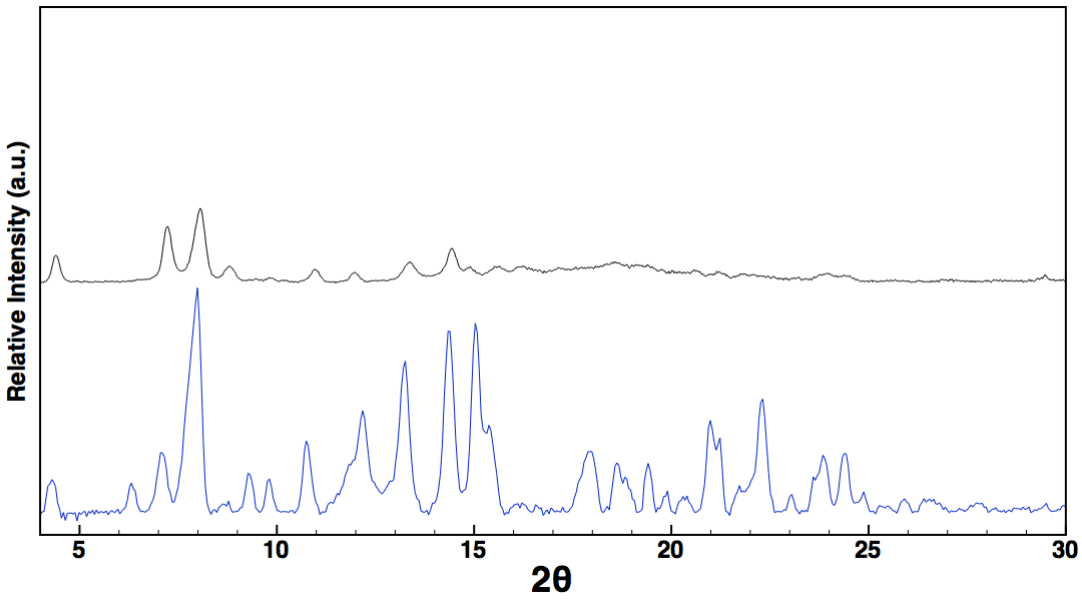

Figure 7.23. Comparison of PXRD patterns (298K) of Ni-^{ISO}CN-1 (blue) and re-reduced Ni-^{ISO}CN-1 after exposure of Ni(I)-^{ISO}CN-1 to Fc^* for one day.

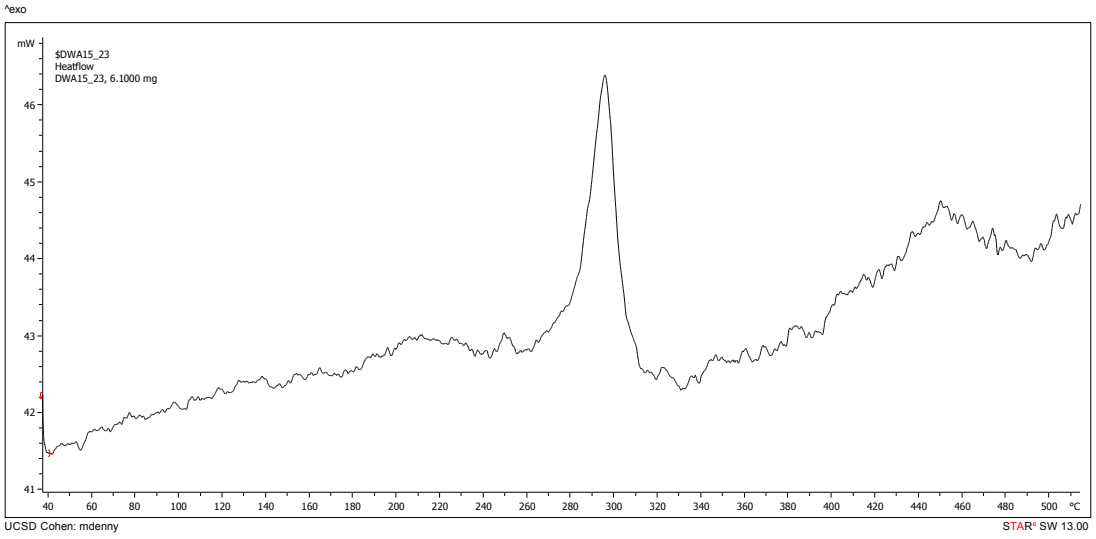

Figure 7.24. Representative DSC trace for Ni-^{ISO}CN-1. The large exotherm has an onset temperature of 261 ˚C.

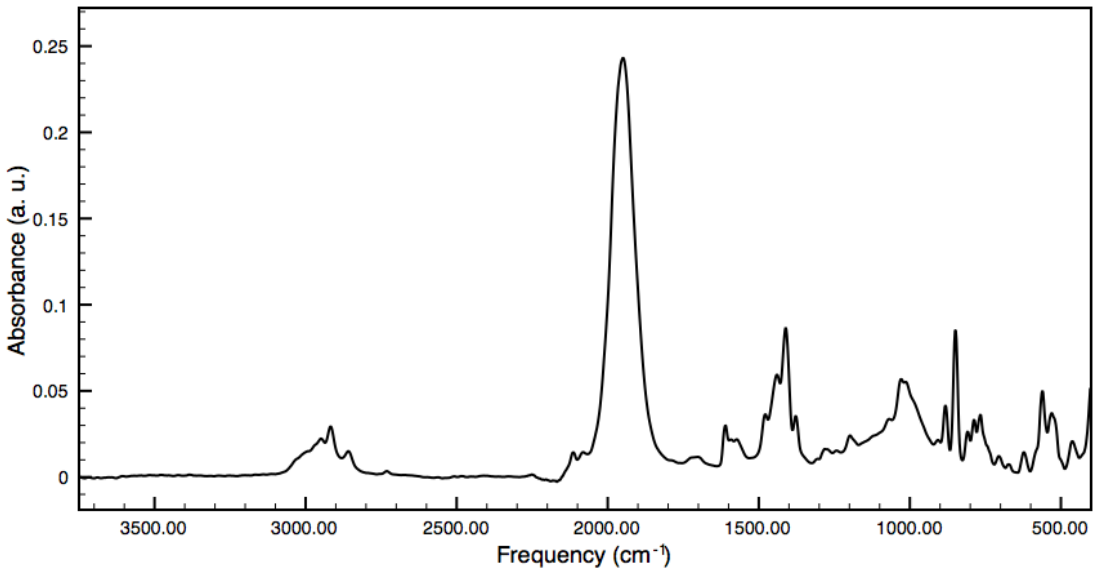

Figure 7.25. Solid-state ATR-IR spectrum of Ni-^{ISO}CN-2.

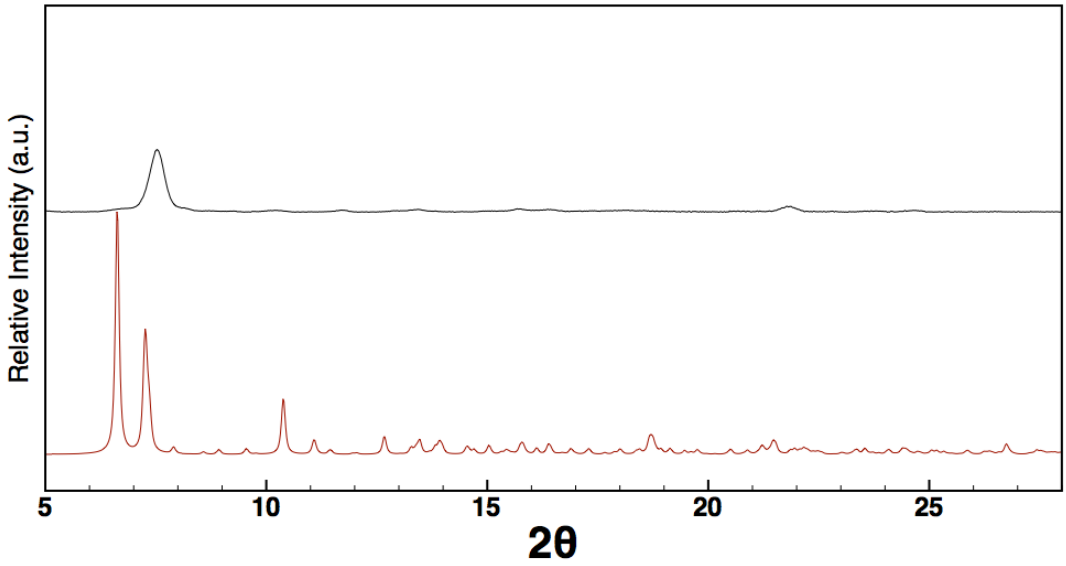

Figure 7.26. PXRD pattern of as-synthesized, desolvated Ni-^{ISO}CN-1 (top, black) and the predicted pattern of Ni-^{ISO}CN-1·[CNAr^{Mes2}]$_2$ from SC-XRD (bottom, red).

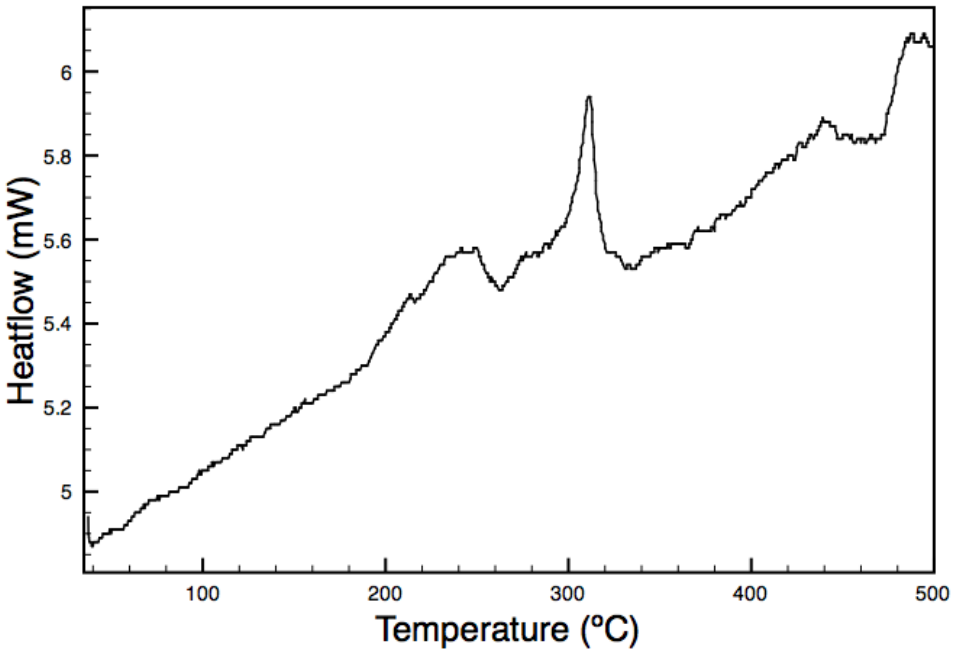

Figure 7.27. Representative DSC trace for Ni-^{ISO}CN-2. The large exotherm has an onset temperature of 302 ˚C.

7.6 Crystallographic Structure Determinations

Single X-ray structure determinations were performed at 100K on Bruker Kappa Diffractometers equipped with a Cu-Kα radiation source and an APEX-II CCD area detector. All structures were solved *via* direct methods with SHELXS[50] and refined by full-matrix least-squares procedures using SHELXL[50] within the Olex2[51] software. In cases of highly disordered solvent molecules, the Platon routine SQUEEZE[52] was used to account for the corresponding electrons as a diffuse contribution to the overall scattering without specific atom positions. Crystallographic data collection and refinement information is listed in Table 7.2-7.3.

Notes on Structure Solutions

Ni-^{ISO}CN-1. Significant disorder was observed for six MeCN solvent molecules. These were treated with SQUEEZE and their electron density removed.

Ni(TlOTf)-^{ISO}CN-1. Significant disorder was observed for two MeCN solvent molecules. These were treated with SQUEEZE and their electron density removed. Positional disorder was observed for one thallium atom; this was modeled as two-part disorder and refined anisotropically.

Ni(TlOTf)-^{ISO}CN-1-62%. Positional disorder was observed for one thallium atom; this was modeled as two-part disorder and refined anisotropically. The *trans*-MeCN corresponding to the low occupancy (SOF = 22%) Tl was not located in the electron density map. Significant disorder was observed for one MeCN solvent moleucles. This was treated with SQUEEZE and its electron density removed.

Ni(TlOTf)-^{ISO}CN-1-24%. Positional disorder of the *trans*-MeCN was observed and modeled as two-part disorder by allowing both groups to refine freely. Electron density corresponding to the trifluoromethanesulfonate counteranion was observed in the electron density map; however, attempts to model this group revealed significant crystallographic disorder. It was therefore treated with SQUEEZE and its electron density removed.

Ni(0/I)-^{ISO}CN-1. The compositional disorder resulting from the Ni(I/0) sites was modeled as a two-part disorder using freely assigned site occupancy factors for the Ni-$NCCH_3$ groups.

Ni-^{ISO}CN-2. Three mesityl rings were found to be positionally disordered and were modeled and refined anisotropically. Free $[CNAr^{Mes2}]_2$ and a THF solvent molecule were modeled at 50% occupancy in the void space. This resulted in a higher wR_2 value than if the corresponding electron density was treated with SQUEEZE and removed; however, inclusion of these modeled components was determined to provide a more accurate description of the structure. Residual electron density which could not be satisfactorily modeled was then treated with SQUEEZE and its electron density removed.

Table 7.1. Tl occupancy data determined from crystallographic analysis.

Material	Tl^+ Occupancy	Unit Cell Volume (Å)	Conc. TlOTf (mM)
Ni(TlOTf)-^{ISO}CN-1	100%	8539.6(5)	100
Ni(TlOTf)-^{ISO}CN-1 (61.6% occupancy)	61.6%	3435.5(4)	10
Ni(TlOTf)-^{ISO}CN-1 (23.5% occupancy)	23.5%[a]	7728.2(10)	1

[a] Determined from the average of two crystallographically distinct Tl^+ sites

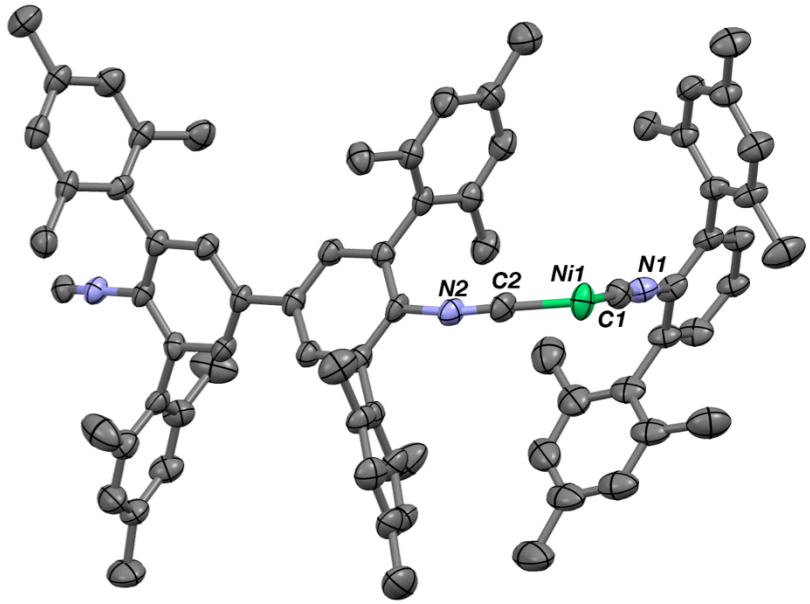

Figure 7.28. Asymmetric unit of Ni-^{ISO}CN-1, with MeCN solvent molecules omitted for clarity.

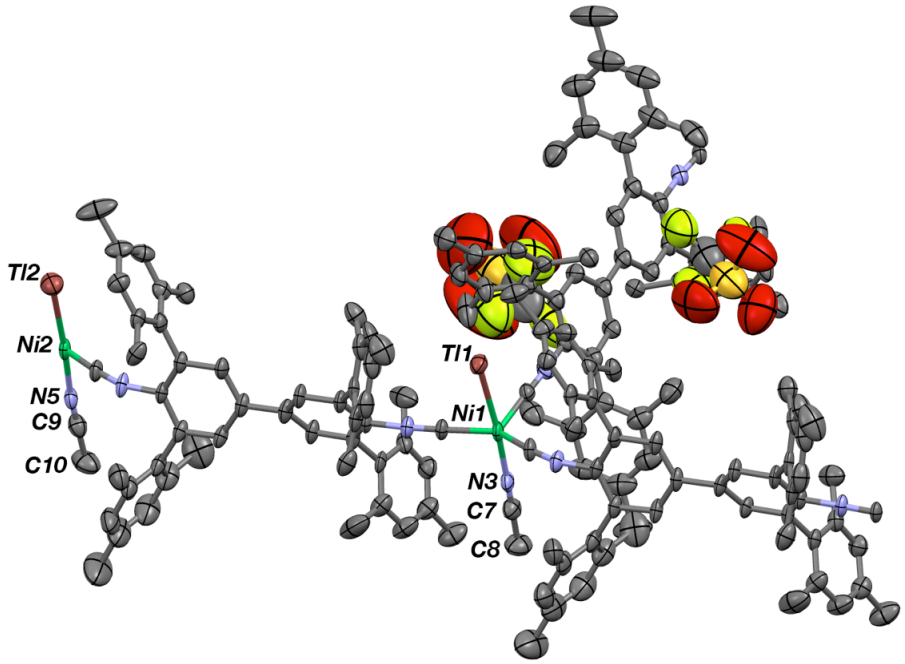

Figure 7.29. Asymmetric unit of Ni(TlOTf)-^{ISO}CN-1, with one MeCN solvent molecule and disordered Tl^{+} omitted for clarity.

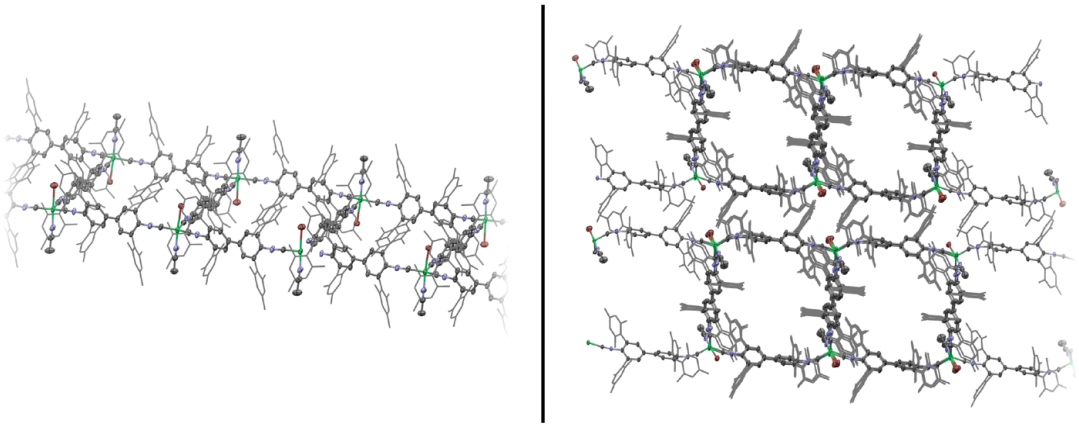

Figure 7.30. (Left) View of single polymer of Ni(TlOTf)-^{ISO}CN-1; (Right) View down the *ab* plane. The *meta*-terphenyl substituents are displayed in wireframe for clarity. Additionally, the triflate counteranion has also been omitted for clarity.

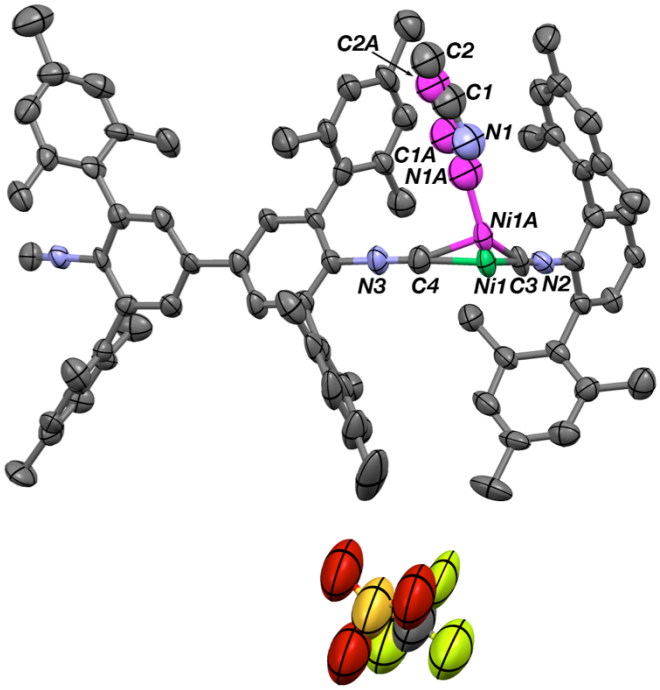

Figure 7.31. Asymmetric unit of Ni(0/I)-^{ISO}CN-2. The disordered Ni site was modeled and refined anisotropically, with a SOF = 0.26 for Ni(I) (shown in magenta).

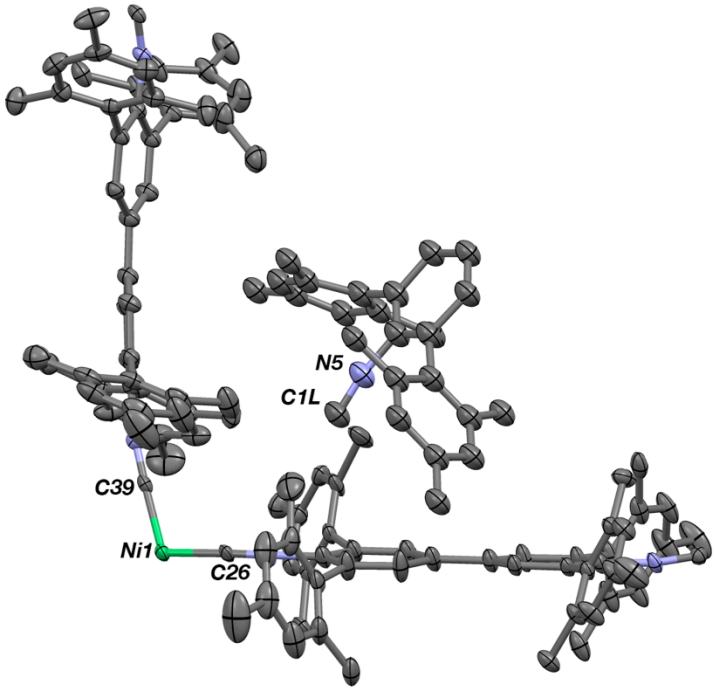

Figure 7.32. Asymmetric unit of Ni-^{ISO}CN-2·[CNAr^{Mes2}]$_2$, with THF solvent molecule and disordered mesityl rings omitted for clarity.

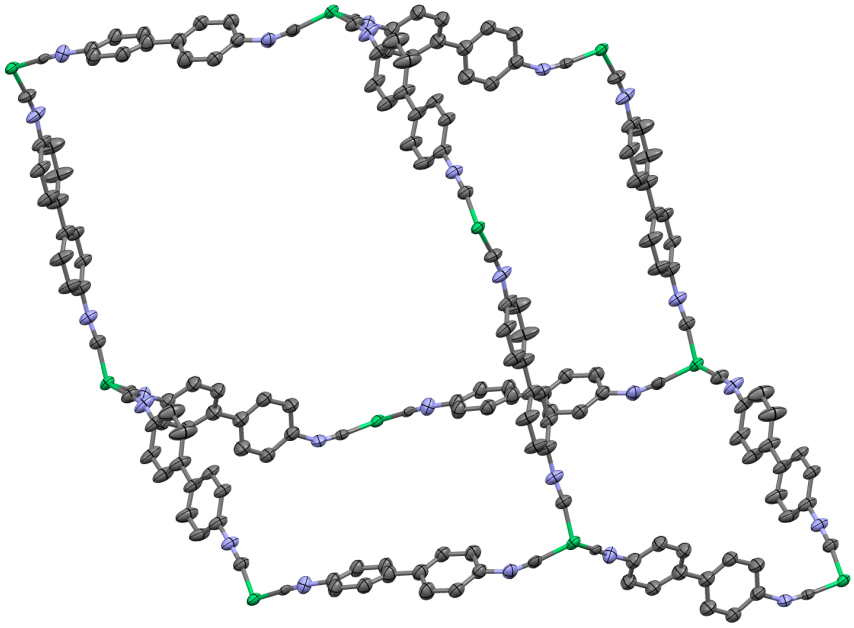

Figure 7.33. Adamantoid cage formed by 10 Ni(0) nodes in Ni-^{ISO}CN-2. The mesityl groups on [CNAr^{Mes2}]$_2$ have been omitted for clarity.

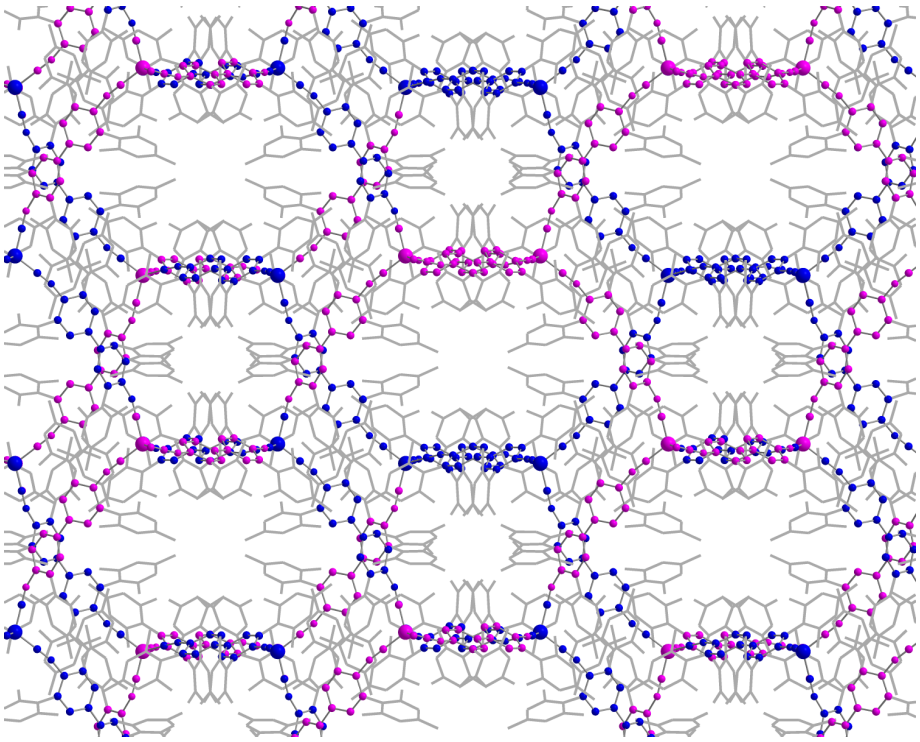

Figure 7.34. View down the 100 axis, with free $[CNAr^{Mes2}]_2$ omitted. The independent nets are colored in blue and pink, respectively, highlighting the two-fold interpenetration in Ni-^{ISO}CN-2.

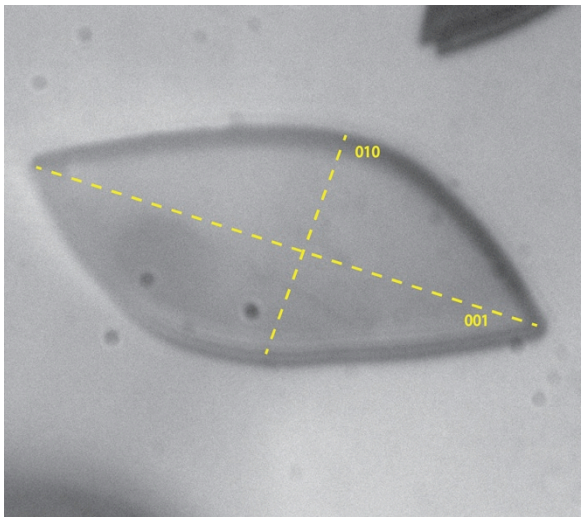

Figure 7.35. Optical microscope photograph of a single crystal of Ni-^{ISO}CN-1. The 100 axis lies approximately orthogonal to the face of the parallelogram. The Ni-^{ISO}CN-2 polymers are aligned along the 010 axis.

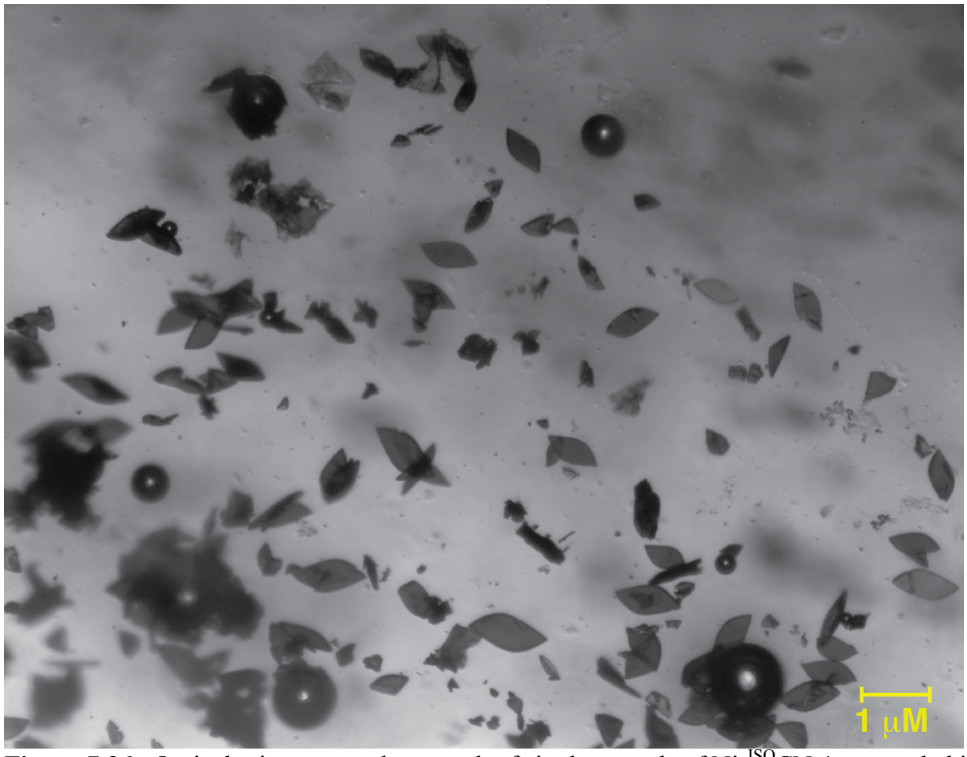

Figure 7.36. Optical microscope photograph of single crystals of Ni-^{ISO}CN-1 suspended in Trilene oil.

Table 7.2 Crystallographic Data Collection and Refinement Information

Name	Ni-^{ISO}CN-1	Ni(0/I)-^{ISO}CN-1	Ni(TlOTf)-^{ISO}CN-1
Formula	$C_{81}H_{81}N_6Ni$	$C_{77.2}H_{75}F_{0.59}N_4NiO_{0.59}S_{0.2}$	$C_{158}H_{153}F_6N_9Ni_2O_6S_2Tl_2$
Crystal System	Triclinic	Triclinic	Triclinic
Space Group	P-1	P-1	P-1
a, Å	14.1305(3)	13.7559(7)	18.1437(7)
b, Å	15.2387(3)	15.3622(7)	21.2536(7)
c, Å	20.6963(5)	18.8794(10)	22.5989(8)
α, deg	95.506(2)	74.822(4)	90.106(2)
β, deg	94.303(2)	74.463(4)	96.873(2)
γ, deg	101.617(2)	64.825(4)	99.164(2)
V, Å^3	4324.72(17)	3428.3(3)	8539.6(5)
Z	2	2	2
Radiation (λ, Å)	Cu-Kα, 1.54178	Cu-K$_{\alpha}$, 1.54178	Cu-Kα, 1.54178
ρ (calcd.), Mg/m^3	0.919	1.109	1.158
μ (Mo Ka), mm^{-1}	0.607	0.810	4.472
Temp, K	100	100	100
θ max, deg	50.588	44.674	57.896
data/parameters	9065/814	5408/832	23504/1712
R_1	0.0574	0.0738	0.0733
wR_2	0.1429	0.2030	0.2026
GOF	1.019	1.034	1.013

Table 7.3 Crystallographic Data Collection and Refinement Information

Name	Ni(TlOTf)-^{ISO}CN-1-62%	Ni(TlOTf)-^{ISO}CN-1-24%	Ni-^{ISO}CN-1·($[CNAr^{Mes2}]_2$)$_{0.5}$
Formula	$C_{76.5}H_{73.28}F_{1.94}N_{3.43}NiO_{1.94}S_{0.65}Tl_{0.65}$	$C_{153.56}H_{149.34}N_{7.78}Ni_2Tl_{0.4}$	$C_{114.29}H_{111.62}N_{4,5}NiO_{0.5}$
Crystal System	Triclinic	Triclinic	Monoclinic
Space Group	P-1	P-1	C2/c
a, Å	13.6009(9)	15.2756(10)	29.5994(12)
b, Å	15.3746(10)	24.1502(17)	34.1170(11)
c, Å	19.0456(13)	24.3135(17)	25.9158(9)
α, deg	74.343(5)	106.488(5)	90
β, deg	74.963(5)	101.720(5)	124.556(2)
γ, deg	65.333(4)	108.383(5)	90
V, Å^3	3435.5(4)	7728.2(10)	21553.6(14)
Z	2	2	2
Radiation (λ, Å)	Cu-Kα, 1.54178	Cu-K$_\alpha$, 1.54178	Cu-Kα, 1.54178
ρ (calcd.), Mg/m^3	1.276	0.996	0.995
μ (Mo Ka), mm^{-1}	3.823	1.558	0.595
Temp, K	100	100	100
θ max, deg	45.731	42.458	50.589
data/parameters	5394/829	10662/1504	11351/1086
R_1	0.01214	0.1130	0.0982
wR_2	0.2599	0.2961	0.2507
GOF	1.0114	1.016	0.987

7.7 Acknowledgements

Chapter 7 is adapted from two manuscripts currently being prepared for publication by D. W. Agnew, I. D. Dimucci, C. E. Moore, S. N. MacMillan, A. L. Rheingold, K. M. Lancaster, and J. S. Figueroa. Permission to include published

material in this dissertation has been obtained from all coauthors. The dissertation author is the first author of these papers.

7.8 References

1. Moulton, B.; Zaworotko, a. M. J., *Chem. Rev. (Washington, DC, U. S.)* **2001,** *101*, 1629-1658.

2. Tranchemontagne, D. J.; Mendoza-Cortes, J. L.; O'Keeffe, M.; Yaghi, O. M., *Chem. Soc. Rev.* **2009,** *38*, 1257-1283.

3. Cook, T. R.; Zheng, Y.-R.; Stang, P. J., *Chem. Rev.***2013,** *113*, 734-777.

4. Kitagawa, S.; Kitaura, R.; Noro, S.-i., *Angewandte Chemie Int. Ed.* **2004,** *43*, 2334-2375.

5. Chen, T.-H.; Popov, I.; Kaveevivitchai, W.; Miljanić, O. Š., *Chem. Mater.* **2014,** *26*, 4322-4325.

6. Long, J. R.; Yaghi, O. M., *Chem. Soc. Rev.* **2009,** *38*, 1213-1214.

7. Lee, J.; Farha, O. K.; Roberts, J.; Scheidt, K. A.; Nguyen, S. T.; Hupp, J. T., *Chem. Soc. Rev.* **2009,** *38*, 1450-1459.

8. Farha, O. K.; Shultz, A. M.; Sarjeant, A. A.; Nguyen, S. T.; Hupp, J. T., *J. Am. Chem. Soc.* **2011,** *133*, 5652-5655.

9. Kreno, L. E.; Leong, K.; Farha, O. K.; Allendorf, M.; Van Duyne, R. P.; Hupp, J. T., *Chem. Rev.* **2012,** *112*, 1105-1125.

10. Li, J.-R.; Sculley, J.; Zhou, H.-C., *Chem. Rev.* **2012,** *112*, 869-932.

11. Gascon, J.; Corma, A.; Kapteijn, F.; Llabrés i Xamena, F. X., *ACS Catalysis* **2014,** *4*, 361-378.

12. Chughtai, A. H.; Ahmad, N.; Younus, H. A.; Laypkov, A.; Verpoort, F., *Chem. Soc. Rev.* **2015,** *44*, 6804-6849.

13. Sawano, T.; Lin, Z.; Boures, D.; An, B.; Wang, C.; Lin, W., *J. Am. Chem. Soc.* **2016,** *138*, 9783-9786.

14. Yamamoto, Y., *Coord. Chem. Rev.* **1980,** *32*, 193-233.

15. Sarapu, A. C.; Fenske, R. F., *Inorg. Chem.* **1975,** *14*, 247-253.

16. Ditri, T. B.; Fox, B. J.; Moore, C. E.; Rheingold, A. L.; Figueroa, J. S., *Inorg. Chem.* **2009,** *48*, 8362-8375.

17. Labios, L. A.; Millard, M. D.; Rheingold, A. L.; Figueroa, J. S., *J. Am. Chem. Soc.* **2009,** *131*, 11318-11319.

18. Stewart, M. A.; Moore, C. E.; Ditri, T. B.; Labios, L. A.; Rheingold, A. L.; Figueroa, J. S., *Chem. Commun.* **2010,** *47*, 406-408.

19. Carpenter, A. E.; Margulieux, G. W.; Millard, M. D.; Moore, C. E.; Weidemann, N.; Rheingold, A. L.; Figueroa, J. S., *Angewandte Chemie Int. Ed.* **2012,** *51*, 9412-9416.

20. Ditri, T. B.; Carpenter, A. E.; Ripatti, D. S.; Moore, C. E.; Rheingold, A. L.; Figueroa, J. S., *Inorg. Chem.* **2013,** *52*, 13216-13229.

21. Mokhtarzadeh, C. C.; Margulieux, G. W.; Carpenter, A. E.; Weidemann, N.; Moore, C. E.; Rheingold, A. L.; Figueroa, J. S., *Inorg. Chem.* **2015,** *54*, 5579-5587.

22. Agnew, D. W.; Moore, C. E.; Rheingold, A. L.; Figueroa, J. S., *Angewandte Chemie Int. Ed.* **2015,** *54*, 12673-12677.

23. Carpenter, A. E.; Rheingold, A. L.; Figueroa, J. S., *Organometallics* **2016,** *35*, 2309-2318.

24. Agnew, D. W.; Sampson, M. D.; Moore, C. E.; Rheingold, A. L.; Kubiak, C. P.; Figueroa, J. S., *Inorg. Chem.* **2016,** *55*, 12400-12408.

25. Maher, T. R.; Meyers, J. J.; Spaeth, A. D.; Lemley, K. R.; Barybin, M. V., *Dalton Trans.* **2012,** *41*, 7845-7848.

26. Efraty, A.; Feinstein, I.; Frolow, F.; Wackerle, L., *J. Am. Chem. Soc.* **1980,** *102*, 6341-6343.

27. Feinstein-Jaffe, I.; Efraty, A., *J. Mol. Catal.* **1986,** *35*, 285-302.

28. Feinstein-Jaffe, I.; Maisuls, S. E., *J. Organomet. Chem.* **1988,** *350*, 57-75.

29. Feinstein-Jaffe, I.; Efraty, A., *J. Mol. Catal. 40*, 1-7.

30. Agnew, D. W.; Gembicky, M.; Moore, C. E.; Rheingold, A. L.; Figueroa, J. S., *J. Am. Chem. Soc.* **2016,** *138*, 15138-15141.

31. Fox, B. J.; Sun, Q. Y.; DiPasquale, A. G.; Fox, A. R.; Rheingold, A. L.; Figueroa, J. S., *Inorg. Chem.* **2008,** *47*, 9010-9020.

32. Fox, B. J.; Millard, M. D.; DiPasquale, A. G.; Rheingold, A. L.; Figueroa, J. S., *Angewandte Chemie International Edition* **2009,** *48*, 3473-3477.

33. Emerich, B. M.; Moore, C. E.; Fox, B. J.; Rheingold, A. L.; Figueroa, J. S., *Organometallics* **2011,** *30*, 2598-2608.

34. O'Keeffe, M.; Yaghi, O. M., *Chem. Rev.* **2012,** *112*, 675-702.

35. Cotton, F. A.; Zingales, F., *J. Am. Chem. Soc.* **1961,** *83*, 351-355.

36. Otsuka, S.; Nakamura, A.; Tatsuno, Y., *Chemical Communications* **1967**, 836a-836a.

37. Barnett, B. R.; Figueroa, J. S., *Chem. Commun.* **2016,** *52*, 13829-13839.

38. Barnett, B. R.; Moore, C. E.; Chandrasekaran, P.; Sproules, S.; Rheingold, A. L.; DeBeer, S.; Figueroa, J. S., *Chemical Science* **2015,** *6*, 7169-7178.

39. Barybin, M. V.; Meyers, J. J.; Neal, B. M., Renaissance of Isocyanoarenes as Ligands in Low-Valent Organometallics. In *Isocyanide Chemistry*, Wiley-VCH Verlag GmbH & Co. KGaA: 2012; pp 493-529.

40. Saraev, V. V.; Kraikivskii, P. B.; Svoboda, I.; Kuzakov, A. S.; Jordan, R. F., *The Journal of Physical Chemistry A* **2008,** *112*, 12449-12455.

41. Brozek, C. K.; Dincă, M., *J. Am. Chem. Soc.* **2013,** *135*, 12886-12891.

42. Bloch, E. D.; Murray, L. J.; Queen, W. L.; Chavan, S.; Maximoff, S. N.; Bigi, J. P.; Krishna, R.; Peterson, V. K.; Grandjean, F.; Long, G. J.; Smit, B.; Bordiga, S.; Brown, C. M.; Long, J. R., *J. Am. Chem. Soc.* **2011,** *133*, 14814-14822.

43. Aubrey, M. L.; Long, J. R., *J. Am. Chem. Soc.* **2015,** *137*, 13594-13602.

44. Chu, C.; Ayres, J. A.; Stefanescu, D. M.; Walker, B. R.; Gorman, C. B.; Parsons, G. N., *The Journal of Physical Chemistry C* **2007,** *111*, 8080-8085.

45. Yang, L.; Powell, D. R.; Houser, R. P., *Dalton Trans.* **2007**, 955-964.

46. Bratten, S. R.; Neville, S. M.; Turner, D. R., *Coordination Polymers: Design, Analysis and Application*. The Royal Society of Chemistry: 2009.

47. Muetterties, E. L.; Band, E.; Kokorin, A.; Pretzer, W. R.; Thomas, M. G., *Inorg. Chem.* **1980,** *19*, 1552-1560.

48. Bailey, B. C.; Basuli, F.; Huffman, J. C.; Mindiola, D. J., *Organometallics* **2006,** *25*, 2725-2728.

49. Stoll, S.; Schweiger, A., *J. Magn. Reson.* **2006,** *178*, 42-55.

50. Sheldrick, G., *Acta Crystallographica Section A* **2008,** *64*, 112-122.

51. Dolomanov, O. V.; Bourhis, L. J.; Gildea, R. J.; Howard, J. A. K.; Puschmann, H., *J. Appl. Crystallogr.* **2009,** *42*, 339-341.

52. van der Sluis, P.; Spek, A. L., *Acta Crystallographica Section A* **1990,** *46*, 194-201.